High-Dimensionality Free-running Cardiovascular Phase-Contrast Magnetic Resonance Imaging Applications

Baginha Da Lança Falcão Mariana

Baginha Da Lança Falcão Mariana, 2023, High-Dimensionality Free-running Cardiovascular Phase-Contrast Magnetic Resonance Imaging Applications

Originally published at : Thesis, University of Lausanne

Posted at the University of Lausanne Open Archive http://serval.unil.ch
Document URN : urn:nbn:ch:serval-BIB_3825B322BA653

UNIL | Université de Lausanne
Faculté de biologie et de médecine

Département de Radiologie Médicale,
Centre hospitalier universitaire Vaudois (CHUV)

High-Dimensionality Free-running Cardiovascular Phase-Contrast Magnetic Resonance Imaging Applications

Thèse de doctorat ès sciences de la vie (PhD)

présentée à la

Faculté de biologie et de médecine
de l'Université de Lausanne

par

Mariana Baginha da Lança FALCÃO

Master en Ingénierie Biomédicale
Instituto Superio Técnico, Universidade de Lisboa, Portugal.

Jury

Prof. Margret Schottelius, Présidente
Prof. Matthias Stuber, Directeur de thèse
Dr. Christopher W. Roy, Co-directeur de thèse
Prof. Daniel Kim, Expert
PD Dr. Fabio Becce, Expert

Lausanne
2023

UNIL | Université de Lausanne
Faculté de biologie et de médecine

Département de Radiologie Médicale,
Centre hospitalier universitaire Vaudois (CHUV)

High-Dimensionality Free-running Cardiovascular Phase-Contrast Magnetic Resonance Imaging Applications

Thèse de doctorat ès sciences de la vie (PhD)

présentée à la

Faculté de biologie et de médecine
de l'Université de Lausanne

par

Mariana Baginha da Lança FALCÃO

Master en Ingénierie Biomédicale
Instituto Superio Técnico, Universidade de Lisboa, Portugal.

Jury

Prof. Margret Schottelius, Présidente
Prof. Matthias Stuber, Directeur de thèse
Dr. Christopher W. Roy, Co-directeur de thèse
Prof. Daniel Kim, Expert
PD Dr. Fabio Becce, Expert

Lausanne
2023

UNIL | Université de Lausanne
Faculté de biologie et de médecine

Ecole Doctorale
Doctorat ès sciences de la vie

Imprimatur

Vu le rapport présenté par le jury d'examen, composé de

Président·e	Madame	Prof.	Margret	**Schottelius**
Directeur·trice de thèse	Monsieur	Prof.	Matthias	**Stuber**
Co-directeur·trice	Monsieur	Dr	Christopher W.	**Roy**
Expert·e·s	Monsieur	Prof.	Daniel	**Kim**
	Monsieur	Dr	Fabio	**Becce**

le Conseil de Faculté autorise l'impression de la thèse de

Mariana Baginha Da Lanca Falcão

Master in Biomedical engineering, Universidade de Lisboa, Portugal

intitulée

High-dimensionality free-running cardiovascular phase-contrast magnetic resonance imaging applications

Lausanne, le 9 mars 2023

pour le Doyen
de la Faculté de biologie et de médecine

Prof. Margret Schottelius

Abstract

Phase-contrast magnetic resonance imaging (PC-MRI) is increasingly used in the diagnosis and management of congenital heart diseases. In particular, three-dimensional (3D) PC-MRI, commonly named 4D flow MRI, provides 3D coverage of anatomical structures, and, from it, it is possible to quantify the volume of blood flowing through a vessel over time, and to visualize the complex pattern of blood flowing through the great vessels and chambers of the heart. However, to mitigate respiratory motion artifacts, conventional 4D flow MRI uses prospective respiratory navigation that limits the acquisition to the end-expiratory phase of respiration, while discarding a large portion of data. This leads to long and unpredictable scan times that depend on each patient's respiratory pattern.

A push-button research sequence, called the free-running PC-MRI framework, was recently developed in an effort to create a time efficient and easy-to-use alternative to 4D flow MRI. In this sequence, data are continuously acquired over a fixed scanning time, then, respiratory and cardiac signals are extracted from the data and used to sort it retrospectively prior to reconstruction, to mitigate motion artifacts and improve image quality.

To date, the free-running PC-MRI framework is still under development. Each of the building blocks of the framework (sequence, signal extraction, reconstruction) presents its own limitations. For example, respiratory and cardiac signal extraction strategies are strongly tied to specific sequence parameters, and this coupled interaction limits the optimization of the sequence, that would benefit from new acquisition schemes to reduce scan times, improve image quality, or even provide higher spatial resolution data, that is essential to monitor pediatric congenital heart disease populations. Moreover, the study of respiratory and cardiac motion has not been fully exploited in this framework, and the development of new mechanisms to better mitigate motion-related artifacts could enable better image quality, and benefit sequence and reconstruction optimization efforts. Additionally, while sequence optimization is limited by multiple factors, the overall goal is to generate high quality flow datasets in an easy-to-use fashion at short scan times, with high spatial resolution and good image quality in both anatomical and flow information.

This doctoral dissertation addresses some of the practical limitations described above, through the development and implementation of novel acquisition and reconstruction strategies for the free-running PC-MRI framework. Chapter 1 provides an overview containing basic concepts and definitions to follow the remainder of this dissertation.

In Chapter 2, an MR image-independent motion detection system, named Pilot Tone navigation system, is integrated in the free-running PC-MRI framework to detect respiratory and cardiac motion signals. Prior to Pilot Tone, self-gating data was used for signal extraction, by integrating additional imaging readouts into the sequence trajectory. This, however, can limit future improvements in sequence design, and therefore a sequence-independent alternative is

desirable. This study describes the signal extraction framework for Pilot Tone and validates the obtained physiological signals to self-gated signals as well as to the reference standard for cardiac activity, electrocardiography. Then, using Pilot Tone signals, respiratory and cardiac resolved 5D flow datasets were reconstructed and shown to provide accurate flow measurements when compared to gold-standard modalities. Finally, and contrarily to self-gating, Pilot Tone was shown to be unaffected by changes in sequence design, suggesting that the imaging sequence and the extracted physiological signals are decoupled from each other, which sets up new opportunities for improving sequence design.

In Chapter 3, the untapped potential of respiratory self-gating signals is leveraged to estimate and correct for the spatial displacement of the heart due to respiration in the free-running PC-MRI framework, thus improving the quality of the resulting images. The algorithm used to perform this respiratory motion correction is called focused navigation (fNAV), and in this thesis will be shown its first validation in PC-MRI datasets to obtain 4D flow motion-corrected images. Using fNAV, respiratory motion displacements were accurately corrected, and the quantification of flow measurements from 4D flow image reconstructions of these corrected datasets was shown to be in accordance with reference-standard measurements. Correcting respiratory motion in the free-running PC-MRI framework instead of resolving it, which had been previously done, reduces the dimensionality of these datasets, thus increasing the sampling size per imaging volume (which improves image quality) and simplifying image reconstruction and analysis. As a result, using fNAV may also benefit sequence optimization, by facilitating shorter scan times and possibly empowering in the acquisition of higher resolution PC-MRI images.

In Chapter 4, the Pilot Tone navigation system described in Chapter 2 is combined with the respiratory motion-correction method validated in Chapter 3 to create a novel strategy to synchronize and combine two sequentially acquired free-running sequences. Using the proposed method, called Synchronization of Neighboring Acquisitions by Physiological Signals (SyNAPS), one anatomical free-running sequence and one free-running PC-MRI sequence, were combined into one comprehensive 4D ‘anatomy + flow’ imaging dataset. Merging anatomy and flow information using SyNAPS improves the visualization of cardiovascular structures in flow data that now can be segmented dynamically, without the need for contrast injection. This will, consequently, improve the delineation of vessels of interest, which in turn increases the precision of flow quantification.

In conclusion, this doctoral dissertation addressed different practical challenges and presented new solutions that can help to further optimize and improve the building blocks of the free-running PC-MRI framework. The impact of this work will hopefully drive sequence improvements regarding higher spatial resolution, shorter scan times and improved flow quantification. Thanks to the technical advances here described, as well as the scientific and clinical collaborations derived from this work, the free-running PC-MRI framework is one step closer to becoming a valuable tool in the diagnosis and management of congenital heart diseases.

Résumé

L'imagerie par résonance magnétique à contraste de phase (PC-IRM) est de plus en plus utilisée pour le diagnostic et la prise en charge des cardiopathies congénitales. En particulier, la PC-IRM tridimensionnelle (3D), communément appelée IRM de flux 4D, fournit une couverture 3D des structures anatomiques, permettant alors de quantifier le volume de sang en circulation dans un vaisseau donné ainsi que de visualiser le schéma complexe de circulation du sang dans les grands vaisseaux et les chambres du cœur. Cependant, dans le but d'atténuer les artéfacts dus au mouvement respiratoire, l'IRM de flux 4D conventionnelle utilise des navigateurs diaphragmatiques qui rejettent une grande partie des données car limitent l'acquisition à la phase expiratoire. Cela conduit à des durées d'acquisition longues et imprévisibles car dépendants du schéma respiratoire de chaque patient.

Une séquence de recherche "*push-button*", nommée "*PC-MRI free-running framework*", a récemment été développée comme alternative efficace (en termes de temps) et plus facile à utiliser par rapport à l'IRM de flux 4D conventionnelle. Avec cette séquence, les données sont acquises en continu durant l'intégralité du scan, avec une durée fixe et connue à l'avance pour tous les patients. Après l'acquisition, les signaux respiratoires et cardiaques sont extraits des données et utilisés comme guide pour la reconstruction, afin de diminuer les artéfacts de mouvement et ainsi d'améliorer la qualité des images.

À ce jour, le *PC-MRI free-running framework* est toujours en cours de développement. Chacun des éléments qui le composent (c'est-à-dire la séquence IRM, l'algorithme d'extraction des signaux de mouvement, la reconstruction) présente ses propres limites. Par exemple, les stratégies d'extraction des signaux respiratoires et cardiaques sont fortement liées à des paramètres spécifiques de la séquence, et cette interaction couplée limite l'optimisation de cette dernière. L'élaboration de nouveaux schémas d'acquisition permettrait de réduire le temps de scan, d'améliorer la qualité des images, ou encore d'acquérir des données à plus haute résolution spatiale, ce qui est essentiel pour l'étude des cardiopathies congénitales pédiatriques. De plus, l'étude des mouvements respiratoires et cardiaques n'a pas été pleinement exploitée au sein du *framework*, et le développement de nouveaux mécanismes permettant de minimiser les artéfacts de mouvements améliorerait la qualité d'image et profiterait aux efforts d'optimisation de la séquence et de la reconstruction. En complément, bien que l'optimisation de la séquence soit limitée par de multiples facteurs, l'objectif global est de générer de manière simple des données de flux de haute qualité, dans des temps d'acquisition fixes et réduits, à haute résolution spatiale tout en assurant une bonne qualité d'image en fin de processus.

Cette thèse de doctorat aborde certaines des limites pratiques décrites ci-dessus, par le développement et la mise en œuvre de nouvelles stratégies d'acquisition et de reconstruction au sein du *PC-MRI free-running framework*. Le chapitre 1 fournit au lecteur une introduction abordant les concepts et définitions de base requis à la compréhension des chapitres suivants.

Dans le chapitre 2, un système de détection de mouvement indépendant de l'IRM, appelé système de navigation Pilot Tone, est intégré dans le *framework* pour détecter les signaux de mouvement respiratoire et cardiaque. Précédemment, la technique d'extraction de signaux dite de "*self-gating*" se faisait par intégration de mesures supplémentaires dans la trajectoire de la séquence IRM. Cependant, cela limite les opportunités d'amélioration de la séquence car cela contraint cette dernière à suivre un certain schéma; une méthode alternative et indépendante du type de séquence est donc souhaitable. L'étude présentée décrit un cadre complet d'extraction de signaux pour le Pilot Tone et propose une validation des signaux physiologiques obtenus par comparaison aux signaux de *self-gating* ainsi qu'à l'électrocardiographie. Ensuite, en utilisant les signaux Pilot Tone, des données de flux 5D résolus pour la respiration et le battement cardiaque ont été reconstruits, et fournissant des mesures de flux précises par rapport aux modalités de référence. Enfin, contrairement à la technique *self-gating*, le Pilot Tone n'est pas affecté par de potentielles modifications de séquence, ce qui suggère que la séquence utilisée et les signaux de Pilot Tone sont découplés l'un de l'autre, et permet donc d'optimiser la séquence, notamment concernant le schéma d'échantillonnage.

Dans le chapitre 3, les signaux de respiration obtenus par *self-gating* sont étudiés afin d'estimer et corriger le déplacement spatial du cœur dû à la respiration, dans le cadre du *PC-MRI free-running framework*, ce qui améliore considérablement la qualité des images obtenues. L'algorithme utilisé pour effectuer cette correction du mouvement respiratoire est appelé navigation focalisée (fNAV), et dans cette thèse, nous montrerons sa première validation appliquée à des données PC-IRM pour obtenir des images flux 4D. En utilisant l'algorithme fNAV, les déplacements du mouvement respiratoire ont été corrigés avec précision, et la quantification des mesures de flux à partir des images de flux 4D obtenues s'est avérée être en accord avec les mesures de référence. La correction du mouvement respiratoire, en opposition à sa résolution qui fut validée précédemment dans le cadre d'acquisitions free-running PC-IRM, réduit la dimensionnalité de ces données, augmentant ainsi la densité d'échantillons par volume d'imagerie (ce qui améliore la qualité de l'image) et simplifiant la reconstruction et l'analyse des images. L'utilisation de fNAV peut également être bénéfique pour l'optimisation de la séquence, en permettant des temps de scannage plus courts et en aidant éventuellement à l'acquisition d'images PC-IRM de plus haute résolution spatiale.

Dans le chapitre 4, le système de navigation Pilot Tone développé dans le chapitre 2 est combiné à la méthode de fNAV dans le chapitre 3 afin de créer une nouvelle stratégie de synchronisation et de combinaison de deux séquences *free-running* acquises séquentiellement. La méthode proposée, appelée "*Synchronization of Neighboring Acquisitions by Physiological Signals*" (SyNAPS), permet de combiner une séquence free-running anatomique et une séquence free-running PC-IRM en un ensemble complet de données d'imagerie "anatomie + flux" 4D. La fusion des informations sur l'anatomie et le flux à l'aide de SyNAPS améliore la visualisation des structures cardiovasculaires dans les données de flux, qui peuvent désormais être segmentées de manière dynamique, sans qu'il soit nécessaire d'injecter un produit de contraste. Ceci améliore par conséquent le suivi des vaisseaux d'intérêt, ce qui augmente la précision de la quantification du flux dans ces vaisseaux.

En conclusion, cette thèse de doctorat aborde différents limites pratiques liées au *PC-MRI free-running framework*, et présente de nouvelles solutions pour son optimisation. Potentiellement, l'impact de ce travail et ces résultats prometteurs sera d'améliorer la séquence

en termes de résolution spatiale (plus élevée), de durée d'acquisition (plus courte) et de permettre, au bout de la chaîne, une meilleure quantification du flux sanguin. Grâce aux progrès techniques décrits ici, ainsi qu'aux collaborations scientifiques et cliniques nées de ce travail, le *PC-MRI free-running framework* se rapproche un peu plus de sa forme optimale, formant un outil précieux pour le diagnostic et la gestion des cardiopathies congénitales.

Acknowledgements

First and foremost, I would also like to acknowledge the grant that funded my work, supported by the Swiss National Science Foundation, grant number 173129.

I would like to acknowledge my supervisor **Dr. Christopher W. Roy**, for showing me how science can be exciting, and for always guiding me with such positive energy. I am forever thankful for everything that you taught me.

I would also like to acknowledge **Prof. Matthias Stuber**, for the mentorship, the guidance, and for helping me to always take a step back and to think about the bigger picture.

Additionally, I need to acknowledge all those with whom I have been fortunate to collaborate with. The following collaborators contributed to my personal development as a researcher, through their teachings and through the fruitful scientific discussions that kept my passion for science alive. I would, thus like to thank Liliana Ma, Lorenzo Di Sopra, Mario Bacher, Giulia Rossi, Adèle Mackowiak, Justin Baraboo, Elizabeth Weiss, Michael Markl, Peter Speier, Jonas Richiardi, Tobias Rutz, Estelle Tenisch, Milan Prša, Anna Giulia Pavon, Pierre Monney, Panagiotis Antiochos, Jean Baptiste Ledoux, David Rodrigues, and Chantal Rohner.

To everyone at the CHUV-UNIL Translational MR Research team, I would like to thank for all the great moments together, for laughing and crying with me and for all the support received. In particular, I would like to thank Adèle and Giulia, with whom I shared so much of this journey, and who carried me at every step of the way.

Moreover, I need to acknowledge all of my friends, who have supported me, even from far, through the good and the bad days. In particular, I would also like to thank Elisabetta, Joana, Sandra, Laura and Marisa. I feel so lucky to have found you in my life, and I am thankful for your constant love and support.

Finally, to my family:

Maria João, obrigada por seres uma irmã forte, inteligente, e carinhosa. Obrigada por sempre me teres apoiado e aconselhado com tanto amor e carinho.

Ao meu pai, **José Carlos**, quero agradecer-te pelo amor, carinho, e por me ensinares a ter sentido critico e a questionar tudo em meu redor. Sempre apoiaste as minhas decisões, e todos os dias me incentivas a ser melhor do que no dia anterior.

À minha mãe, **Maria José**, obrigada por todo o amor, paciência, apoio, pelas chamadas matinais, e acima de tudo por me teres ensinado a seguir sempre os meus sonhos. És o meu modelo de vida, e espero poder algum dia poder tornar-me uma mulher tão incrível como tu.

Foi graças ao vosso apoio que consegui este doutoramento. A minha eterna gratidão aos três, que mesmo longe estão sempre comigo.

List of abbreviations

2D	two-dimensional image
3D	three-dimensional volume
4D	four-dimensional volume
5D	five-dimensional volume
AAo	ascending aorta
bSSFP	balanced steady-state free precession
CHD	congenital heart disease
CHUV	Centre hospitalier universitaire vaudois
CMR	cardiovascular magnetic resonance
CMRA	coronary magnetic resonance angiography
CS	compressed sensing
DAo	descending aorta
ECG	electrocardiogram
F	female
FCNN	fully convolutional neural network
FFT	fast Fourier transform
FISS	fast interrupted steady-state
fNAV	focused navigation
FOV	field-of-view
FRF	free-running framework
GRE	gradient echo
ICA	independent component analysis
IRB	institutional review board
ISMRM	International Society for Magnetic Resonance in Medicine
MPA	main pulmonary artery
MRA	magnetic resonance angiography
MRI	magnetic resonance imaging
NV	net volume
PC-MRI	phase contrast magnetic resonance imaging
PCA	principal component analysis
PF	peak flow rate
PT	Pilot Tone
RF	radio frequency
ROI	region of interest
SCMR	Society for Cardiovascular Magnetic Resonance
SG	self-gating

SI	superior-inferior
SMRA	Society for Magnetic Resonance Angiography
SNR	signal-to-noise ratio
SyNAPS	synchronization of neighboring acquisitions by physiological signals
TE	echo time
TR	repetition time
UTE	ultra short echo
venc	velocity encoding
XD-GRASP	extra-dimensional golden-angle radial sparse parallel

Table of Contents

Chapter 1.
Introduction

Congenital heart diseases (CHD) are the most common birth defects, affecting an estimated 1.3% of newborns in Switzerland and 0.8% overall in European countries according to a population study performed in 2011[1]. While some defects can resolve on their own without significant impact during the first years of infancy, there is still a large amount of cases (~30%) where surgical intervention remains the only solution of care. The most recent data points to an expected >90% survival rate in CHD related-interventions (with variation depending on complexity)[2,3], enabling the affected patients to reach adult life. Nevertheless, the consequences of such invasive procedures, together with aging effects, etc., create the need to continuously follow-up on these now chronic cases, in order to ensure long term survival and quality of life[4].

CHD is a broad term that includes a wide range of abnormalities that require personalized care, thus requiring different imaging protocols. Considering the patients' increased life expectancy and the recurrent need for follow-up with imaging modalities, the use of x-ray angiographic exams as well as computed tomography may add a large radiation toll to these cases[5], that could have negative effects in the future, and therefore radiation-free alternatives are preferred when possible. Therefore, depending on their characteristics, CHD cases are regularly recommended for a cardiovascular magnetic resonance imaging (CMR) exam, to visualize anatomy and study quantitative measures, such as blood flow intake in the pulmonary and systemic circulations (Chapter 1.1)[6].

Imaging the heart in CMR is a complex problem due to the heart's anatomical and functional constraints (Chapter 1.2). The heart moves continuously over time, to pump blood to the entire body through the cardiovascular system. Additionally, the heart is located inside the thorax and above the diaphragm, which work together to continuously expand and deflate the lungs, leading to displacement of the heart due to respiratory motion. Finally, there can be spontaneous motion of the patient inside the scanner, which can be attenuated by asking the patient not to move while being scanned, or by using sedation[7]. As a result, the heart is already under a very complex setup that constrains how CMR can be performed[8].

However, motion sensitivity is not always considered a disadvantage in MRI. In regular CMR protocols, the motion of the heart is captured along the cardiac cycle and the acquired readouts can be sorted to create dynamic cardiac images that can be used to study heart function[9,10]. Using dynamic imaging can also be useful to capture the velocity of blood running throughout the heart and the vessels, which can provide information on the severity of certain diseases[6]. Blood flow can be comprehensively quantified using MRI, by manipulating the MRI imaging sequences such to increase their sensitivity to either vessel contrast (Magnetic Resonance Angiography) or to blood velocity[11]. The second case, where blood velocity is

encoded into MR information, is commonly called Phase-Contrast MRI (PC-MRI) and uses imaging gradients to modulate changes in voxel-wise velocity (Chapter 1.3)[12]. PC-MRI is now an important component of CMR, particularly to monitor and follow-up CHD cases, which often involve defects in the vasculature of the larger vessels[6].

2D PC-MRI is the current gold-standard for non-invasively measuring blood flow for clinical diagnosis as well as for patient follow-up and treatment planning[7,13]. Nevertheless, slice planning is cumbersome and time consuming, as imaging planes need to be placed perpendicularly to the vessels of interest for an optimal flow assessment[7]. As a consequence of the long setup time required per plane, a clinical protocol can only include a limited number of 2D PC-MRI acquisitions[14]. Alternatively, three-dimensional (3D) PC-MRI sequences that are also cardiac-resolved are an ideal replacement to the gold-standard 2D PC-MRI cardiac-resolved protocol (Chapter 1.4).

The most conventional sequence for 3D PC-MRI is commonly called 4D flow MRI (3D anatomical volume + 1D cardiac motion information + velocity encoding)[15]. 4D flow MRI acquires data throughout the cardiac cycle, but only for a portion of the respiratory cycle, requiring diaphragmatic navigators to prospectively select end-expiration time points to be used for the MR acquisition. However, prospective respiratory navigation often leads to long and unpredictable scanning times, and as a result, there has been a large effort in developing 3D PC-MRI sequences that can address the constraints of cardiac and respiratory motion while collecting data within a fixed scan time[16–21]. Among different strategies, one recent work introduced a free-running MRI framework[22], which was extended to include phase-contrast properties and named the free running PC-MRI framework (Chapter 1.5)[19]. In this framework, velocity-encoded imaging data is continuously acquired over a fixed period of time, and retrospectively processed to reconstruct whole-heart multi-dimensional respiratory and cardiac resolved flow datasets with isotropic resolution[19].

The free-running PC-MRI framework provides a paradigm shift on how flow imaging is performed, but to date it still presents some limitations, such as low spatial resolution and low image contrast, that need to be addressed in order to improve the framework's overall performance and increase its clinical utility in the monitoring of CHD.

1.1. Congenital heart disease and cardiovascular magnetic resonance imaging

The heart (Figure 1) is a muscular organ that pumps blood through vessels to distribute oxygen, nutrients, and many other compounds to the entire body. The heart pumps with periodic motion, following a sequence of muscle contractions and relaxations to collect new blood and then send it to the rest of the body through the pulmonary and the systemic circulations[23]. The adequate distribution of oxygenated blood throughout the tissues is vital, but it can sometimes be disrupted, due to either heart or vascular defects.

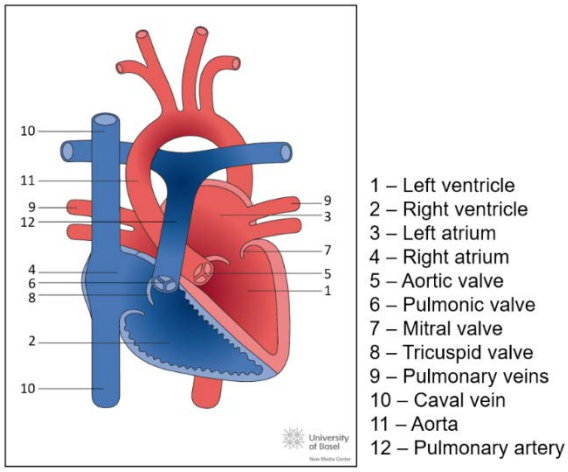

Figure 1. Illustration of the healthy heart and the main vessels surrounding it. The heart has four chambers, named the right/left atria and the right/left ventricles. The right atrium collects de-oxygenated blood from the caval veins (superior and inferior), sends it to the right ventricle, which in turn will send it to the lungs, where it will be re-oxygenated, through the main pulmonary artery and pulmonary circulation. The re-oxygenated blood will then be sent back to the heart through the pulmonary veins, arrive to the left atrium, move to the left ventricle, and finally be sent back to the entire body through the aorta and the systemic circulation. *Illustration taken from http://www.chd-diagrams.com, licensed under Creative Commons Attribution-NonCommercial-NoDerivatives 4.0 International License by the New Media Center of the University of Basel.*

In order to detect or monitor complications in the heart and major vessels, we can perform a CMR exam, where the periodic motion of the heart is taken into account to inform the image acquisition and minimize image artifacts[13].

CMR can be used for a large variety of applications, such as to monitor heart failure[24], coronary artery disease[25], a broad variety of cardiomyopathies[26–28], valvular diseases [29,30], and CHD in both pediatric and adult populations[7]. In particular, CHD patients require regular CMR follow-up exams to monitor possible post-surgical comorbidities over time[2,3,6], in conjunction with other imaging modalities such as echocardiography, invasive angiography, and cardiac computed tomography[6].

One of the sequences included for monitoring and follow-up of CHD patients in CMR is the PC-MRI[12], which quantifies blood velocity along the cardiac cycle. Quantifying the flow of blood going through a vessel is important to understand the proper functioning of the circulatory system as well as the heart itself. This is particularly relevant in some CHD cohorts, where anatomical defects may lead to flow abnormalities, such as stenosis and regurgitation[4,6] , which can, in turn, lead to additional heart and vessel damage[4]. From PC-MRI, different blood flow measurements can be quantified, such as the cardiac output, the pulmonary-to-systemic flow ratio, valvular regurgitation, etc[7,31].

The following subsections describe some examples of CHD that in most cases require surgical intervention, and where the use of PC-MRI is an integral part in patient follow-up[6,7].

Coarctation of the aorta

Aortic coarctation is defined by a discrete or relatively discrete narrowing of the aorta[32], most commonly on the proximal descending thoracic aorta (Figure 2), and has an incidence of around 409 per million live births[32], representing ~7% of the diagnosed CHDs[6,33]. The

narrowing of the aorta causes severe circulatory issues, including high blood pressure and flow return in the left ventricle, that can cause hypertrophy and lead to cardiac malfunction, and, in the worst case, heart failure.

In general, echocardiography is the first line imaging modality for coarctation of the aorta, but CMR can be useful to provide complementary anatomic and hemodynamic information[34] for intervention preplanning[35] and post-surgical repair follow-up[34]. In particular, flow assessment and collateral flow quantification using PC-MRI are important measures that contribute to an improved understanding of the physiology of each aortic coarctation pre- and post-surgery.

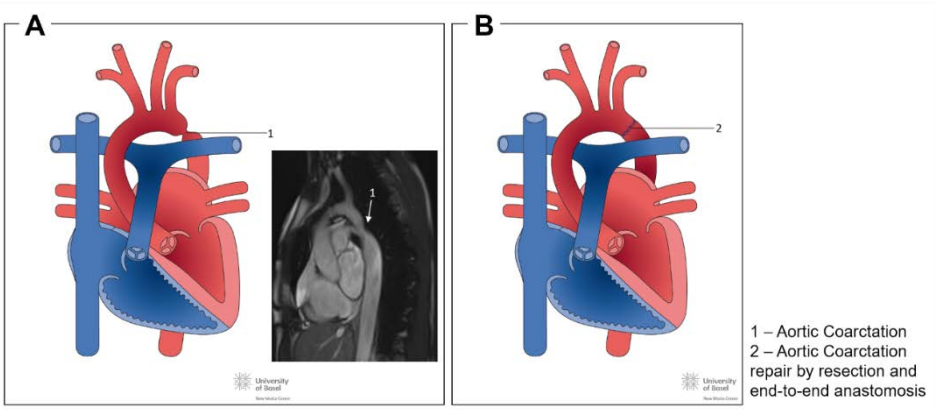

Figure 2. Illustrations of one case of coarctation of the aorta (A) and its repair by resection and end-to end anastomosis (B). *Illustration taken from http://www.chd-diagrams.com, licensed under Creative Commons Attribution-NonCommercial-NoDerivatives 4.0 International License by the New Media Center of the University of Basel.*

Single Ventricle before and after the Fontan procedure

The single ventricle defect describes a very complex group of defects mainly characterized by a partial or complete absence of the ventricular septum development before birth (Figure 3). Each specific defect has a different incidence within the population, but the overall incidence of the single ventricular defect is estimated to be around 805 cases per million births[32].

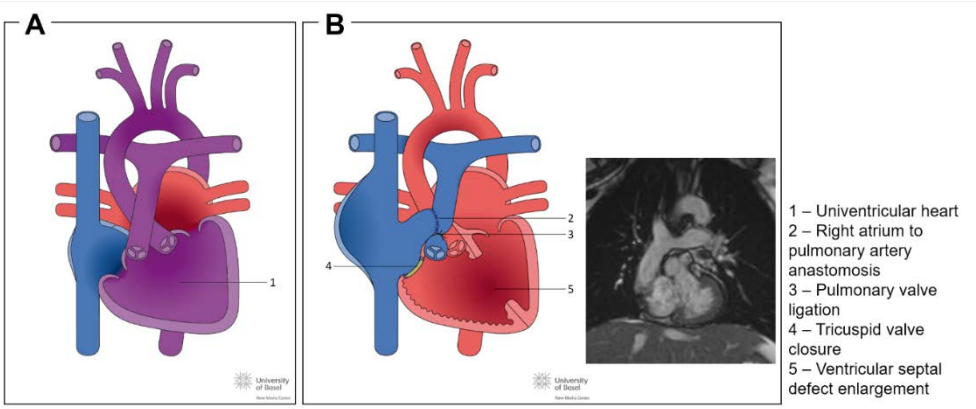

Figure 3. Illustrations of one case of Single Ventricle (A) and its repair by a Classic Fontan operation (RA-PA) for DORV (B). *Illustration taken from http://www.chd-diagrams.com, licensed under Creative Commons Attribution-NonCommercial-NoDerivatives 4.0 International License by the New Media Center of the University of Basel.*

Due to the consequences in blood oxygenation level changes traveling to all tissues, nearly all patients require either reconstructive surgery or heart transplantation. The most common surgery is the Fontan procedure (Figure 3B)[36,37], where the right atrium is "ventriclized" to direct the blood from the vene cava to the lungs. Due to the complexity of the procedure, adverse outcomes post-surgery become increasingly frequent with aging[37], and may lead to heart failure and death[38,39]. To monitor these comorbidities, CMR is recommended as a regular follow-up exam for post-Fontan cases, and particularly PC-MRI is recommended to evaluate measurements such as systemic to pulmonary collateral flow, as well as flow to both lungs[6].

Tetralogy of Fallot

Tetralogy of Fallot (Figure 4) is described by a deviation of the developing conal septum that causes a misalignment with the ventricular septum (creating a ventricular septal defect), an "overriding aorta" (aorta positioned above the septal defect), and right-ventricular hypertrophy[40]. This defect has an average incidence of 32.6 per 100,000 live births[32] and an estimated prevalence of 6% from all CHDs[41]. Surgical repair is generally performed at early stages and ensures a high survival rate (>98%)[42,43] and life expectancy of the patients[44]. With time, complications related to residual anatomic and hemodynamic abnormalities are very common, thus patient follow-up is recommended[6].

Although echocardiography often performed, CMR is already the gold standard for reliably and accurately measuring 3D ventricular volumes. Additionally, PC-MRI is mainly used to quantify flow in the pulmonary arteries[6].

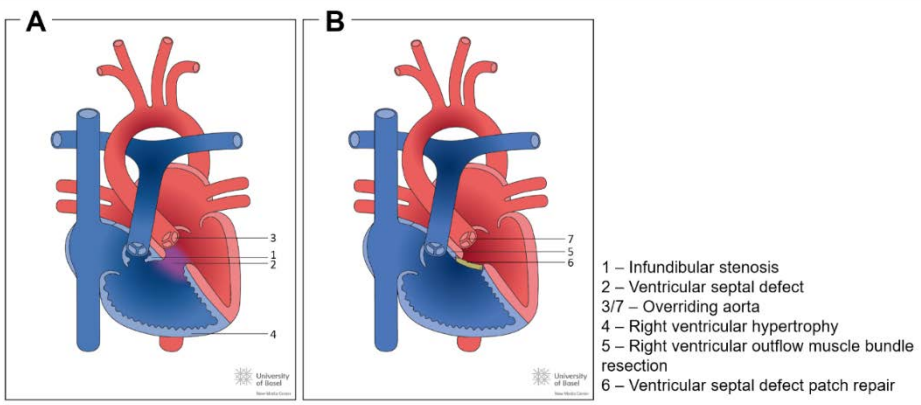

Figure 4. Illustrations of the most common defects in the tetralogy of Fallot (A) and of one possible repair strategy (B). *Illustration taken from http://www.chd-diagrams.com, licensed under Creative Commons Attribution-NonCommercial-NoDerivatives 4.0 International License by the New Media Center of the University of Basel.*

Transposition of the great arteries

Transposition of the great arteries, as the name indicates, defines the defect where the two main arteries (aorta and main pulmonary artery) are transposed with each other (Figure 5). It has an estimated incidence of around 300 live births per million[32].

Depending on the type of transposition of the great arteries, surgical repair is often done with an arterial switch operation (Figure 5B). This procedure, has a high success rate, but postoperative complications are common, and include ventricular dysfunction, pulmonary or

aortic stenosis, coronary artery stenosis/occlusion, valve regurgitation and aortic root dilation[45]. As a result, these patients are also recommended for clinical follow-up to ensure all these complications are under control.

For the follow-up, CMR is recommended complimentary to echocardiography, and can help detect all of the postoperative complications mentioned above. In particular, PC-MRI is very important for these cases, as it helps evaluate arterial stenosis.

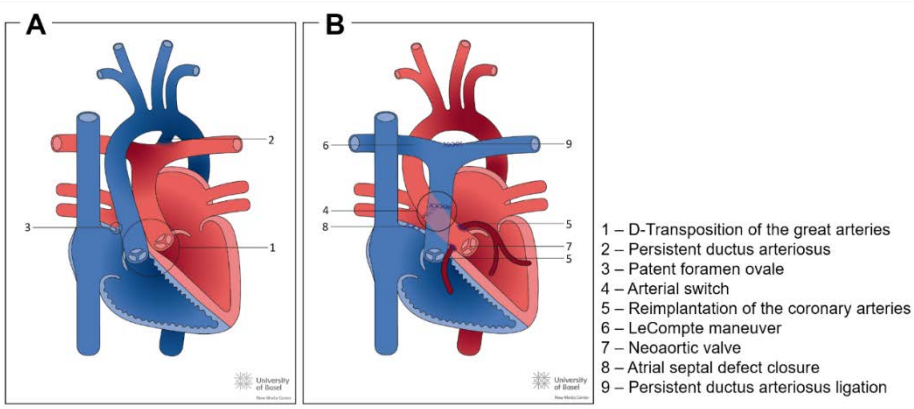

Figure 5. Illustrations of a Simple D-Transposition of the great arteries (A) and of one common arterial switch operation (Jatene procedure) (B). *Illustration taken from http://www.chd-diagrams.com, licensed under Creative Commons Attribution-NonCommercial-NoDerivatives 4.0 International License by the New Media Center of the University of Basel.*

Imaging heart defects from CMR is very complex due to the intrinsic changes in heart anatomy caused by each defect, creating additional imaging challenges for these cases. Additionally, respiratory-derived motion and the heart's heartbeat add further acquisition constraints[8].

1.2. Detection of cardiac and respiratory motion

The adequate detection of cardiac motion is essential to capture static and dynamic MRI information from the heart and vessels with minimized image artifacts, and is especially important to quantify blood flow with PC-MRI. During a CMR exam, the contraction and relaxation of the heart is usually monitored using MRI compatible electrocardiography (ECG) devices[13]. In particular, the R-wave of the ECG signal, which coincides with the end-diastolic (maximum volume) time point in the cardiac cycle, can be used to identify the beginning and end of each heartbeat. In this way, user-defined windows can be prospectively chosen to acquire imaging data for one or multiple time-points after detection of the R-wave resulting in static or motion-resolved images respectively (Figure 6A)[46]. Alternatively, to take advantage of data from the entire cardiac-cycle, the ECG signal can be used to retrospectively combine data across multiple heartbeats also providing motion-resolved images (Figure 6B)[47,48].

Although using ECG is the most common method to monitor cardiac motion, its use in clinical context introduces additional setup time. Additionally, signal quality may sometimes be corrupted due to poor ECG lead placement or due to MR-derived magneto hydrodynamic

effects and gradient switching that can induce additional electrical currents, all which compromise the ECG signal detection[49]. Alternatively to ECG, other MR-compatible devices such as pulse oximeters or Doppler ultrasound can be used to monitor cardiac motion and inform the image acquisition[50]. Moreover, imaging-based solutions (e.g. self-gating)[51] or Pilot Tone navigation[52] are also able to detect cardiac motion and are mainly used for retrospective motion-resolved imaging. Albeit different, the cardiac motion information from these ECG-alternatives can be similarly used to either resolve the entire cardiac motion or select specific windows for acquisition (Figure 6).

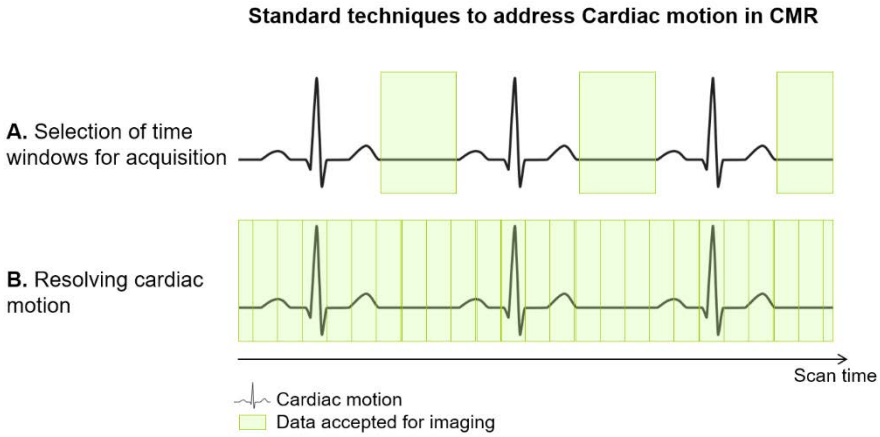

Figure 6. Examples of techniques to compensate cardiac motion in CMR. A) User-defined windows can be prospectively chosen to acquire imaging data for one or multiple time-points after detection of the R-wave, resulting in static or motion-resolved images respectively. **B)** Alternatively, to take advantage of data form the entire cardiac-cycle, data can be combined across multiple heartbeats to provide motion-resolved images.

In addition to its periodic motion, the heart is also affected by respiratory-derived motion caused by the motion of the diaphragm as well as the expansion (inspiration) and deflation (expiration) of the thorax. This motion also affects image quality in CMR, but can be mitigated using different modalities.

In short 2D acquisitions, patients are often requested to hold their breath (Figure 7A)[6,7,13]. However, the breath-hold duration governs the maximal spatial resolution, temporal resolution, volumetric coverage allowed, thus limiting the image acquisition. Additionally, difficulties performing breath-holds may arise in patients of older age or affected by cardiopulmonary deficiency, or in non-compliant patients, such as early age infants[7]. Furthermore, CMR exams requiring multiple breath-holds often suffers from poor reproducibility, leading to misregistration errors in the obtained k-space data, which influences the clinical outcome[53,54]. Alternatively, the patient can be instructed to breathe regularly and quietly, and free-breathing (Figure 7B) multiple signal averaging can be performed, albeit with consequent worsening in image quality[13].

When moving to 3D image acquisition, several strategies have been developed to mitigate respiratory motion in CMR. A few examples will be described below and will be focused on what has been reported for PC-MRI.

First, data can be acquired in free-breathing (Figure 7B), but, just like in 2D, without additional respiratory compensation there will be a decrease in the accuracy of flow measurements and overall visualization of the vessels of interest [55,56].

One strategy that has become commonly used in the field is the use of a one-dimensional (1D) navigator echo, prescribed along the lung liver interface to monitor respiratory motion to limit data collection to a manually defined acceptance window during the end-expiratory phase[57,58] (Figure 7C). Nonetheless, the efficiency of selectively acquiring only a portion of the data over time, while rejecting data acquired during the remaining respiratory stages, is highly driven by the breathing pattern of each patient, and thus leads to unpredictable scan times.

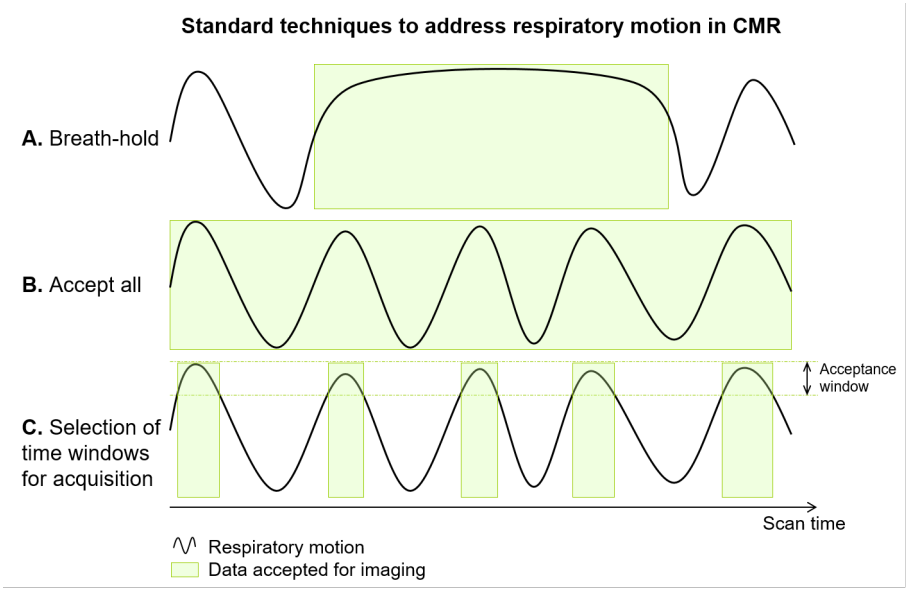

Figure 7. Examples of techniques to compensate respiratory motion in CMR. A) The most common approach to mitigate respiratory motion is to perform short 2D scans with breath-hold, which can still be demanding in some patient cohorts. **B)** Alternatively, the acquisition can be in free breathing, which corrupts the obtained imaging information, although strategies to prospective or retrospectively compensate motion in free-breathing data can be used to improve image quality. **C)** Finally, prospective respiratory navigation can be used to limit data collection to a manually defined acceptance window.

Beyond these two common strategies for 3D PC-MRI modalities, there have also been some efforts in the development of alternative respiratory motion compensation tools that acquire data continuously in free-breathing, using image navigators, self-gating[59] or Pilot Tone navigation[52].

For example, adaptive navigator gating techniques take advantage of 1D respiratory navigators to prospectively adapt the k-space sampling pattern[55,60–62] and ensuring that the central portion of k-space, which is more sensitive to respiratory motion, is acquired during end-expiration while the periphery is acquired during the remaining respiratory phases. This technique has been shown to mitigate respiratory motion artifacts, though its performance may be limited by large motion variations, providing better results when combined with additional data rejection[55,61], which decreases acquisition efficiency.

Alternatively, soft-gating techniques[16,63,64] weight the acquired readouts according to the amount of motion occurring at each time point and has also been shown to successfully

compensate respiratory motion while maintaining image quality at high sampling efficiency. However, in cases of large respiratory motion amplitudes, residual motion artifacts may not be fully suppressed.

The use of respiratory resolved image reconstruction techniques[19–21,64,65] incorporates the respiratory cycle as an additional dimension to reconstruct images at different respiratory stages[19,21,37], which could be utilized to study respiratory-driven hemodynamics in certain patient population, such as post-Fontan patients. Nonetheless, for clinical pathologies that do not benefit from the study of respiratory dependent flow, the increased reconstruction and analysis times required for each respiratory-dependent dataset may be impractical.

Finally, a wide range of respiratory motion correction methods[17,65–68] utilize data from the entire respiratory cycle while minimizing motion related artifacts.

1.3. Phase-Contrast Magnetic Resonance Imaging

MRI signals are complex, providing both magnitude and phase information. This Chapter outlines how the phase information in particular can be exploited to measure blood flow using Phase-Contrast Magnetic Resonance Imaging (PC-MRI).

Magnetic field gradients provide spatial encoding in MR images, by perturbing the main magnetic field, and causing hydrogen protons in different locations to precess at slightly different rates[69]. If the imaged tissue is static, these gradients apply phase changes in the magnetization of tissues that are predictable with the strength and duration of these gradients. In non-static tissues (such as blood flowing through a vessel), however, the spins will be subjected to local magnetic fields of different strengths as they move (Figure 8). As a result, the phase precession of these moving spins will be modulated by different MR spatial encodings, leading to image artifacts[14].

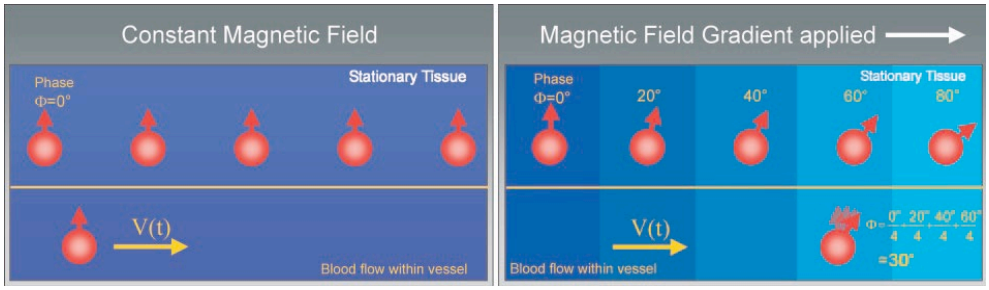

Figure 8. Influence of spatial encoding gradients in static tissue and non-static tissue. The moving spins accumulate phase errors as they move through different points where the magnetic field gradient is changing, causing phase detection errors that lead to image artifacts. *Figure extracted from Lotz et al, RadioGraphics, 2002*[14].

Although phase accumulation in moving spins can be detrimental to image quality, it can fortunately be manipulated to our advantage and instead, utilized to estimate spin motion[70,71]. In phase-contrast MRI (PC-MRI)[72–75], using a bipolar phase gradients' design, the static tissue phase information cancels out, while moving structures have a non-zero phase output that is proportional to tissue velocity (Figure 9)[14].

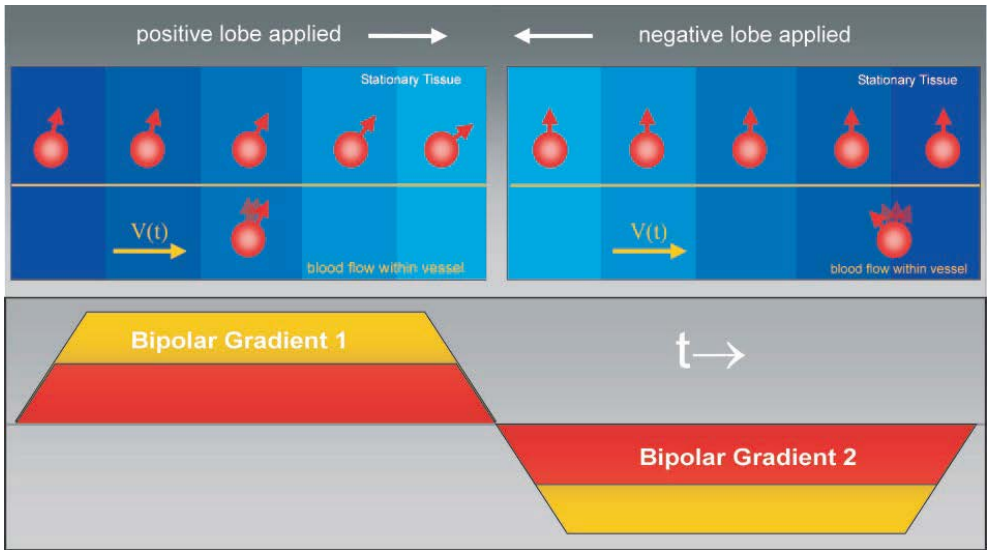

Figure 9. In Phase-Contrast MRI, Gradient encoding is played out in two steps, a positive gradient and a negative gradient, symmetric to the first one. This bipolar gradient scheme enables the annulment of the phase in static tissue, whereas non-static tissue is phased out. The phase of the moving spins can then be used to estimate their velocity. *Figure extracted from Lotz et al, RadioGraphics, 2002*[14].

The effects of these bipolar gradients can be mathematically explained in a few steps[12]. The Larmor frequency ω_L of spins at a certain spatial location $\vec{r} = (x, y, z)$ in a static magnetic field B_0, local field inhomogeneity ΔB_0, and an added gradient encoding waveform G(t) is given by:

$$\omega_L(\vec{r}, t) = \gamma B_z(\vec{r}, t) =$$
$$= \gamma B_0 + \gamma \Delta B_0 + \gamma \vec{r}(t)\vec{G}(t)$$

With γ being the gyromagnetic ratio, $\gamma B_0 = \omega_{L,0}$ symbolizing the Larmor frequency of the main magnetic field, $\gamma \Delta B_0$ representing the influence of field inhomogeneities in the precession frequency, and $\gamma \vec{r}(t)\vec{G}(t)$ representing the gradient encoding effects.

From the moment an excitation pulse is applied to the field (t=0), up to the echo time (t=TE), where the phase will be detected, the phase at a location $\vec{r}$ can be calculated as the integral of ω_L[12].

$$\phi(\vec{r}, TE) = \int_0^{TE} \omega_L(\vec{r}, t)dt = \omega_{L,0} \times TE + \gamma \Delta B_0 \times TE + \gamma \int_0^{TE} \vec{r}(t)\vec{G}(t)$$

For simplification, the phase accumulation from the main field B_0 can be eliminated from the equation, as the free induction decay signal is demodulated with respect to $\omega_{L,0}$[12]. Additionally, we can simplify the term $\gamma \Delta B_0 \times TE = \phi_0$, which represents an unknown, field inhomogeneity's phase contribution that can be caused by several factors such as field imperfections and magnetic susceptibility at tissue boundaries. Assuming that each set of protons in a specific spatial location can be characterized by an original position $\vec{r}_0$ and a constant velocity v,

$$\vec{r}(t) = \vec{r}_0 + \vec{v}t + \cdots$$

We can expand the equation of $\phi(\vec{r}, TE)$ above into the Taylor series:

$$\phi(\vec{r}, TE) = \phi_0 + \gamma\vec{r}_0 \int_0^{TE} \vec{G}(t)dt + \gamma\vec{v} \int_0^{TE} \vec{G}(t)tdt + \cdots$$

The Taylor series integrals are named the M_n moments, where M_0 is the zeroth moment of the Taylor expansion and describes the static protons, and M_1 is the first moment, describing the protons moving at constant velocity. The higher order (p>1) terms that characterize the protons' motion (acceleration, jerk, etc.) are considered negligible, and therefore are not included in this simplified demonstration. An additional term has also been neglected from this expansion, which is the unknown gradient-dependent phase error contribution, derived mainly from Maxwell phase and eddy-current-induced background phase. This phase contribution, although removed in the rest of this demonstration, is usually corrected after image reconstruction, by means of polynomial fitting tools[76].

From the equation above, one can infer that the annulment of the gradient moment M_0 could enable the detection of phase information that is proportional to the motion of the hydrogen protons. Using the bipolar gradient setup introduced above (Figure 3), M_0 is canceled:

$$\phi(\vec{r}, TE) = \phi_0 + \gamma\vec{v}M_1$$

In this bipolar gradient setup, there is still the additional unknown ϕ_0 term that adds phase information, limiting the true correlation between phase information and proton velocity. Nevertheless, this term is constant and independent of gradient waveform, thus it could be eliminated by acquiring this setup twice using symmetric bipolar gradient shapes (Figure 10), and then subtracting the phase accumulated in two acquisitions:

$$\begin{aligned}\phi^+ - \phi^- = \Delta\phi &= (\phi_0 + \gamma\vec{v}{M_1}^+) - (\phi_0 + \gamma\vec{v}{M_1}^-) \\ &= \gamma\vec{v}\left({M_1}^+ - {M_1}^-\right) = \gamma\vec{v}\Delta M_1\end{aligned}$$

From this equation, the velocity information is finally given by:

$$\vec{v} = \frac{\Delta\phi}{\gamma\Delta M_1} = \frac{\Delta\phi}{\pi} venc$$

where $venc = \frac{\pi}{\gamma\Delta M_1}$ defines the parameter that can be tuned using the strength of the bipolar gradients to establish the velocity limits in each phase-contrast dataset. This term needs to be chosen with caution, because a low $venc$ would cause phase wrapping (or aliasing), but a too high $venc$ will cause loss in to velocity-to-noise ratio[12].

The two bipolar velocity-encoding gradients can be used to acquire 2D PC-MRI information across a vessel with velocity-encoded in one direction, commonly perpendicularly to the imaging slice (through-plane)[12]. Additionally, albeit less often, 2D PC-MRI can also be acquired such that is encodes velocity information in three orthogonal dimensions, but for that a minimum of four velocity encoding gradient combinations are required (see Figure 12)[12], which doubles the scan time. Nonetheless, encoding velocity information in three orthogonal dimensions is very useful, particularly when moving to volumetric PC-MRI solutions[12].

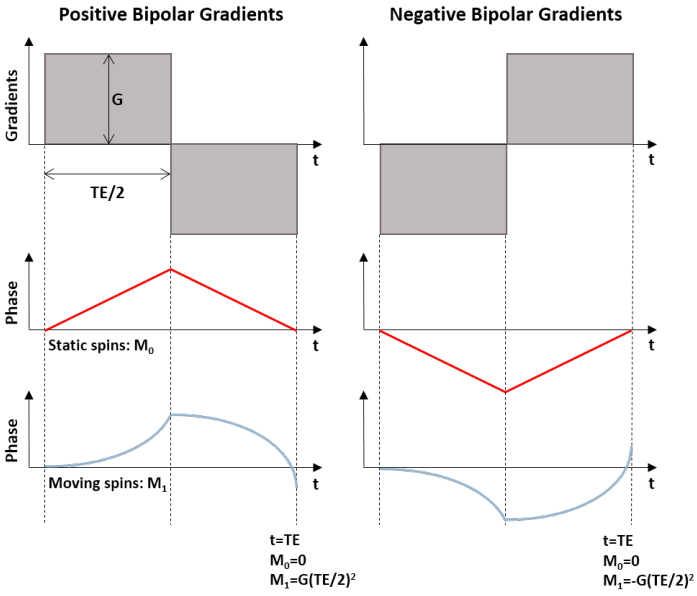

Figure 10. Two-point velocity encoding design. The bipolar gradients are encoded with two symmetric designs. The acquisition of two consecutive readouts, each with one of the following designs, results in two images that, after subtracted with each other, provide phase encoding that is directly proportional to the tissue velocity through a specific direction. The 2-point velocity encoding design is the most common scheme to acquire 2D PC-MRI data, with velocity information encoded through the image acquisition plane. *Figure inspired by Jung et al, Magnetic Resonance Angiography: Phase-Contrast MRI and flow quantification, 2012*[12].

1.4. The growth of multi-dimensional Phase-Contrast MRI

As mentioned in Chapter 1.3, 2D PC-MRI is commonly acquired using a 2-point velocity-encoding scheme that acquires velocity information in the through-plane direction. To maximize the quantification of velocity information in one vessel, each 2D plane needs to be perpendicular to the vessel of interest. Nonetheless, we described in Chapter 1.1 the large diversity of CHD defects with irregular heart anatomies that can affect more than one vessel. In these cases, the number of 2D PC-MRI acquisitions performed will be equivalent to the number of vessels of interest to image, which besides being time consuming also requires highly trained technologists working alongside radiologist and cardiologists to be able to plan all the different 2D slices perpendicularly to the vessels, often with unusual anatomies (Figure 11).

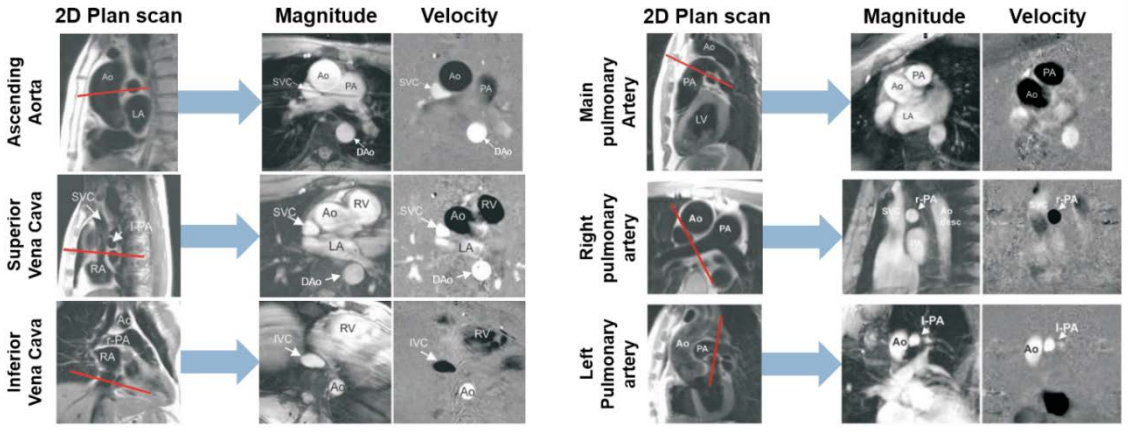

Figure 11. Slice planning of 2D PC-MRI for different vessels of interest and resulting image acquisitions. For each vessel of interest to analyze, a new 2D PC-MRI sequence is required, thus requiring new slice planning. This makes a PC-MRI protocol very challenging and time consuming. Ao: ascending aorta. SVC: superior vena cava. IVC: inferior vena cava. PA: main pulmonary artery. r-PA: right pulmonary artery. l-PA: left pulmonary artery. DAo: descending aorta. LA: left atrium. RV: right ventricle. *Figure extracted from Lotz et al, RadioGraphics, 2002*[14].

In an effort to create a more comprehensive solution to 2D PC-MRI and to address its limitations, a sequence for the comprehensive acquisition of time-resolved 3D and three-directional blood flow measurements was developed[77–80], and has become standardized using the name 4D flow MRI[15,81].

In conventional 4D flow MRI, an imaging volume is acquired over time and velocity information is encoded in three orthogonal dimensions using a 4-point velocity encoding scheme (Figure 12)[82]. In order to resolve cardiac motion, ECG is commonly used to detect cardiac activity and prospectively sort the data into different cardiac phases. To mitigate respiratory motion, 1D diaphragmatic navigators are used to monitor respiratory motion and limit data collection to a manually defined acceptance window during end-expiratory phase[57,58,83]. By encoding the three-directional velocity vector, 4D flow enables calculation of advanced hemodynamic parameters (e.g. wall shear stress, turbulent kinetic energy, helicity, and vorticity), which cannot be measured by any other modality[82].

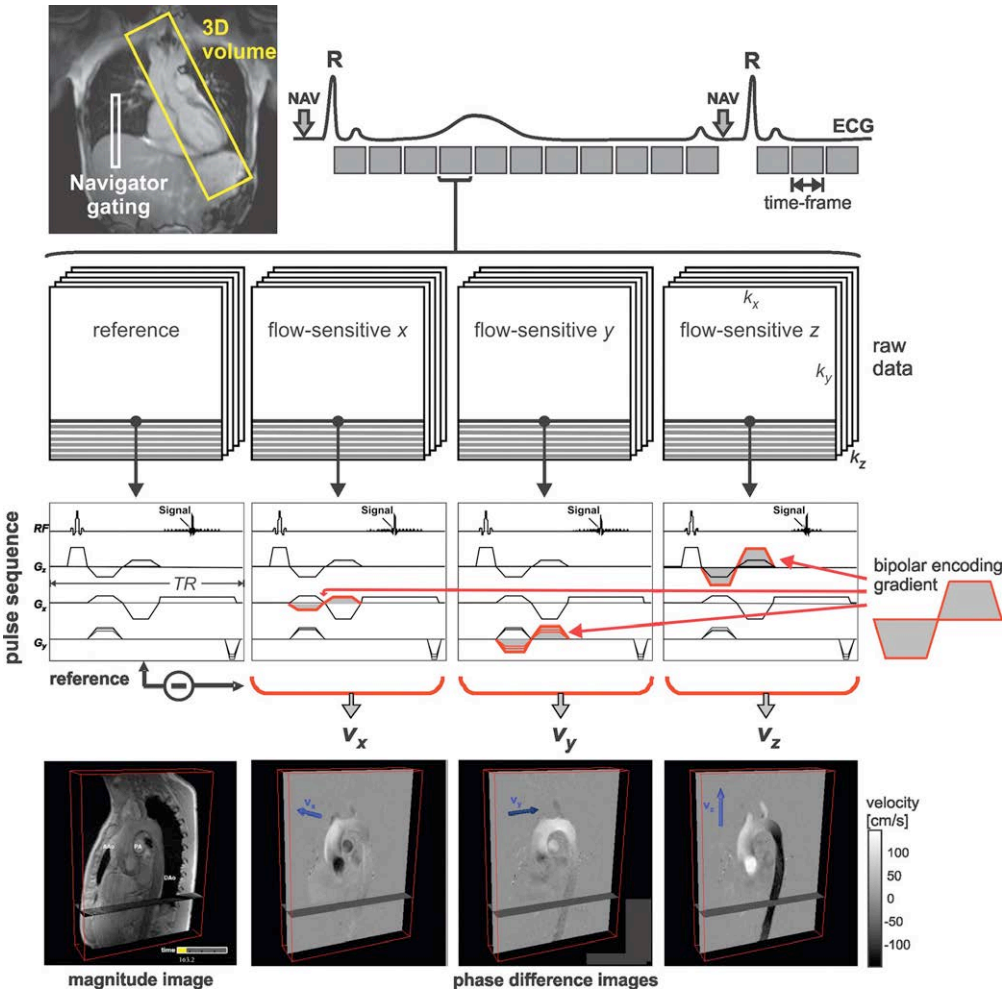

Figure 12. Overall description of the 4D flow MRI framework. For each 3D imaging readout, 4 velocity encoding gradients are acquired, one as reference and three symmetrical bipolar gradients in three orthogonal directions (V_x, V_y, V_z). The data is sorted according to the type of gradient encoding used at each acquisition, and k-space data is filled over time, using electrocardiography for cardiac binning and navigator gating for minimizing respiratory motion artifacts. The magnitude information (anatomy) is retrieved from the reference acquisition, and the phase information in 3 directions (velocity) is obtained by calculating the difference between the reference acquisition and each of the 3 velocity encoding gradients. *Figure extracted from Markl et al, Journal of Magnetic Resonance, 2012*[82].

Despite its reported benefits, the conventional 4D flow MRI sequence also has its own limitations. First, planning the 4D flow MRI sequence is still a complex and time consuming activity, albeit easier than 2D PC-MRI, that still requires highly trained medical staff. Planning a 4D flow MRI scan includes selecting and manipulating the imaging field of view, that might not be isotropic, and setting up the diaphragmatic navigators required for respiratory gating[15]. Moreover, prospectively gating the acquisition to end-expiration discards all the data that could otherwise have been acquired throughout the remainder of the respiratory cycle, leading to a low acquisition efficiency. Additionally the diaphragmatic navigation depends on each subject's breathing patters and creates unpredictable scan times[15]. Finally, beyond imaging efficiency, limiting data acquisition to the end-expiratory phase of the respiratory cycle precludes the evaluation of respiratory-driven changes in hemodynamics, which may have clinical interest in some CHD cohorts, such as single ventricle patients undergoing the Fontan procedure[84].

Considering the limitations of 4D flow MRI, multiple efforts targeted the development of faster and more efficient solutions to acquire 3D PC-MRI in the heart and great vessels[16,17,19–21,64,85]. Mainly, recent studies are targeting respiratory motion compensation tools to ensure predictable scan times and to take advantage of the additional flow information. A number of sequences with alternative k-space trajectories have been proposed including Cartesian[16,64,85], radial [17,19,20], and spiral [21]. In general, each of these proposed methods uses self-gating to track respiratory and/or cardiac motion, by deriving physiological signals from the acquired imaging data or from a repeat non-imaging readout, which also promote a faster and simpler patient setup.

1.5. The free-running Phase-Contrast MRI framework

In an attempt to shift the paradigm of complex CMR exams to whole-heart easy-to-use "push-button" solutions, a free-running framework was recently developed without the need for ECG gating or respiratory navigators[22]. In this framework, a radial sequence[86] acquires data continuously with isotropic resolution during a predictable scan time[22,87,88]. Then, respiratory and cardiac motion signals are retrospectively detected using information from the sequence itself (self-gating)[22,59,87], to then inform an image reconstruction framework that reconstructs the acquired data into multi-dimensional datasets [22,88,89].

The free-running framework has been initially built to provide a multi-dimensional visualization of the cardiac anatomy[22], but has since been extended to different applications, such as angiography[90], flow[19], fat-fraction mapping[91], T1[92] and T2[93] mapping, eye imaging[94] and liver imaging[95]. In particular, to extend this framework to flow imaging, a free-running PC-MRI framework was developed[19], by integrating a 4-point bipolar gradient design to detect velocity encoding in three orthogonal directions, similarly to the design shown in Figure 12 for conventional 4D flow MRI.

The free-running PC-MRI framework is comprised of three main building blocks, which will be described briefly: the imaging sequence, the respiratory and cardiac motion detection and signal extraction, and the image reconstruction.

Imaging sequence

In the free-running PC-MRI framework, the image acquisition follows a free-running 3D radial golden-angle gradient-echo (GRE) research sequence[19,22], wherein radial k-space readouts are acquired continuously using a spiral phyllotaxis pattern[86] (Figure 13A). The acquisition is divided into spiral interleaves that contain a fixed number of radial readouts. Each interleave is rotated by the golden angle about the z-axis relative to its predecessor[86] and is preceded by one k-space signal readout consistently oriented in the superior–inferior (SI) direction, which will be used for respiratory and cardiac motion detection[22,59]. All remaining sequence readouts of the k-space interleave are repeated 4 times in order to encode velocity information in three orthogonal directions[12,19].

Respiratory and cardiac motion detection and signal extraction

The readouts acquired in the SI direction are acquired periodically. They are compiled into 1D vectors and used to detect respiratory and cardiac motion information. This information is converted into signals by means of a sequence of signal extraction steps[19,22]. First, these SI readouts are corrected for trajectory imperfections that are caused by gradient timing delays, eddy currents, and other sources[22]. Then, a principal component analysis is performed to reduce data complexity and to segregate the respiratory and cardiac motion features. Finally, using frequency-based selection, the most prominent respiratory[89,96] and cardiac signals[22] are chosen (Figure 13B). The amplitude of the resulting respiratory signals is used to partition the acquired dataset into different respiratory phases[97], and the information from the estimated cardiac signals is used to identify the beginning and end of each heartbeat, and to retrospectively sort the data into different cardiac phases[22,87].

Image reconstruction

The acquired k-space data, now sorted into respiratory and cardiac phases, as well as into the four different velocity-encoding readouts (Figure 13C). The resulting 6D dataset (x-y-z-respiratory-cardiac-velocity dimensions), contains highly undersampled imaging volumes that share redundant information across the cardiac and respiratory dimension. This dataset is then reconstructed using a k-t sparse SENSE algorithm, which exploits sparsity along both the cardiac and respiratory dimensions[88,98]. The compressed-sensing-based algorithm focuses on solving the following optimization problem:

$$m = \underset{m}{\operatorname{argmin}} \|FCm - s\|_2^2 + \lambda_r \|\nabla_r m\|_1 + \lambda_c \|\nabla_c m\|_1$$

where m is the resultant 5D reconstructed image; F is the non-uniform fast Fourier transform operator; C refers to the coil sensitivities; s refers to the acquired k-space dataset; ∇_r and ∇_c are the first-order difference operators along the cardiac and respiratory dimensions, respectively; and λ_r and λ_c represent the corresponding regularization weights, which are manually optimized for each type of sequence. The optimization problem is solved using a nonlinear conjugate gradient with backtracking line search[22,88,89]. Since all four velocity-encoding readouts are acquired for every k-space sample, the velocity-encoding dimension is fully sampled, and therefore image sparsity will not be explored in this dimension.

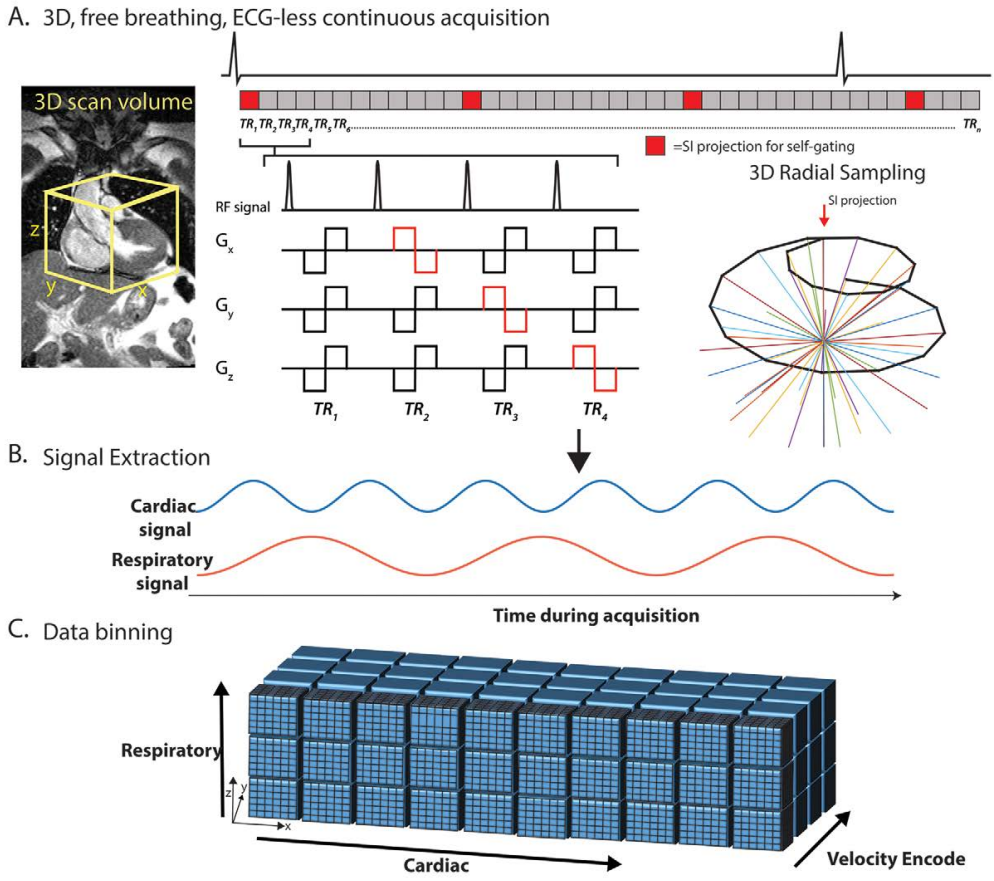

Figure 13. Free-running PC-MRI framework. A) The imaging sequence, **B)** the respiratory and cardiac motion detection and signal extraction, **C)** data binning into a 6-dimensional dataset (x-y-z-respiratory-cardiac-velocity dimensions) for image reconstruction. *Figure retrieved from Ma et al, Radiology Cardiothoracic Imaging. 2020*[19].

The free-running PC-MRI framework has several advantages when compared to the state-of-the-art 2D PC-MRI and the conventional 4D flow MRI[19]. First and foremost, this sequence provides whole-heart coverage with isotropic resolution in a fixed and predictable scan time. Additionally, contrarily to 2D PC-MRI and conventional 4D flow MRI, the quantification of respiratory-resolved flow measurements is now possible, and it allows for the investigation respiratory-dependent hemodynamic changes, which could be interesting to study in certain patient cohorts, such as patients who underwent the Fontan procedure (Chapter 1.1)[19].

Additionally, although the current framework reconstructs data into 5D flow datasets, the versatility of the free-running acquisition scheme is such that the acquired data can be sorted in different ways. For instance, in a study including patients with arrhythmia, the free-running PC-MRI datasets were sorted by the heart-beat duration, to investigate the effects of arrhythmia in flow quantification[99]. Alternatively, flow datasets could be sorted along the cardiac dimension without resolving respiratory motion or vice-versa.

Despite the potential shown by the free-running PC-MRI framework as a paradigm shift in the way PC-MRI is performed, this framework is still under development and, therefore, presents some limitations that need to be investigated. For example, respiratory and cardiac signal extraction strategies are strongly tied to specific sequence parameters, and this coupled interaction limits the optimization of the sequence, that may benefit from new acquisition schemes to reduce scan times, improve image quality, or even acquire higher spatial resolution

data, that is essential to study pediatric congenital heart disease populations. Moreover, the study of respiratory and cardiac motion has not been fully exploited in free-running PC-MRI, and the development of new mechanisms to better mitigate motion-related artifacts could enable better image quality, and benefit sequence and reconstruction optimization efforts. Additionally, while sequence optimization is limited by multiple factors, the overall goal is to generate high quality flow datasets in an easy-to-use fashion at fixed scan times, with high spatial resolution and good image quality for both anatomy and flow information.

1.6. Outline of the Doctoral thesis

In this thesis, novel technical innovations that address practical challenges in 3D PC-MRI are developed, validated, and tested in clinical cohorts. This is in keeping with the goal of improving our ability to quantify blood flow, an important biomarker in the diagnosis and management of cardiovascular disease. In the following chapters:

Chapter 2) **Pilot Tone Navigation** was integrated, for the first time, in to the free-running PC-MRI framework and used to detect cardiac and respiratory signals without the need for external devices while still being fully decoupled from the sequence acquisition, thus simplifying further optimizations of the framework.

Chapter 3) A 3D motion correction tool, called **focused-navigation**, or **fNAV**, was implemented to correct respiratory motion in the free-running PC-MRI framework, for improving image quality and the quantification of flow measurements, as well as for simplifying the current image reconstruction and enable new acceleration strategies.

Chapter 4) Building on the above development of Pilot Tone navigation, where self-navigation and the imaging sequence are now entirely decoupled, and of fNAV, where respiratory motion was successfully corrected to simplify image reconstruction, a novel method for synchronizing two consecutively acquired free-running framework sequences was developed to create a more comprehensive PC-MRI scan with improved image quality and without the need for contrast injection. The technique, called **Synchronization of Neighboring Acquisitions using Physiological Signals**, or **SyNAPS**, synchronizes anatomy and flow information from two separate sequences, enabling a dynamic segmentation of vessels and improved flow assessment

In parallel to these main projects, several complementary avenues were explored in keeping with the goals of addressing practical challenges in the free-running PC-MRI framework:

Chapter 5.1) A study on the effects of contrast agents in the outcome of the free-running PC-MRI framework in a cohort of congenital heart disease patients.

Chapter 5.2) A comparison between blood flow measurements from the free-running PC-MRI framework at two different magnetic field strengths: 1.5T and 3T.

Chapter 5.3) The development of a deep-learning-based algorithm to estimate ECG-like cardiac motion triggers using self-gating readouts of free-running PC-MRI data.

Chapter 6 summarizes the content of this thesis and provides an outlook for future work, including clinical validation of the technical innovations developed in the preceding chapters. Finally, the Supplementary Information Chapter reports all the additional work that was built upon the projects developed in this doctoral thesis.

References

1. Dolk H, Loane M, Garne E. Congenital heart defects in Europe: Prevalence and perinatal mortality, 2000 to 2005. *Circulation*. 2011;123(8):841-849. doi:10.1161/circulationaha.110.958405
2. Moons P, Bovijn L, Budts W, Belmans A, Gewillig M. Temporal trends in survival to adulthood among patients born with congenital heart disease from 1970 to 1992 in Belgium. *Circulation*. 2010;122(22):2264-2272. doi:10.1161/circulationaha.110.946343
3. Wilmot KA, O'Flaherty M, Capewell S, Ford ES, Vaccarino V. Coronary heart disease mortality declines in the United States from 1979 through 2011: Evidence for stagnation in young adults, especially women. *Circulation*. 2015;132(11):997-1002. doi:10.1161/circulationaha.115.015293
4. Schwerzmann M, Schwitz F, Thomet C, Kadner A, Pfammatter JP, Wustmann K. Challenges of congenital heart disease in grown-up patients. *Swiss Med Wkly*. 2017;147(September):w14495. doi:10.4414/smw.2017.14495
5. Hoffmann A, Engelfriet P, Mulder B. Radiation exposure during follow-up of adults with congenital heart disease. *Int J Cardiol*. 2007;118(2):151-153. doi:10.1016/j.ijcard.2006.07.012
6. Fogel MA, Anwar S, Broberg C, Browne L, Chung T, Johnson T, Muthurangu V, Taylor M, Valsangiacomo-Buechel E, Wilhelm C. Society for Cardiovascular Magnetic Resonance/European Society of Cardiovascular Imaging/American Society of Echocardiography/Society for Pediatric Radiology/North American Society for Cardiovascular Imaging Guidelines for the use of cardiovascular magnet. *J Cardiovasc Magn Reson*. 2022;24(1):1-78. doi:10.1186/s12968-022-00843-7
7. Fratz S, Chung T, Greil GF, Samyn MM, Taylor AM, Valsangiacomo Buechel ER, Yoo SJ, Powell AJ. Guidelines and protocols for cardiovascular magnetic resonance in children and adults with congenital heart disease: SCMR expert consensus group on congenital heart disease. *J Cardiovasc Magn Reson*. 2013;15(1):1-26. doi:10.1186/1532-429X-15-51
8. Ismail TF, Strugnell W, Coletti C, Božić-Iven M, Weingärtner S, Hammernik K, Correia T, Küstner T. Cardiac MR: From Theory to Practice. *Front Cardiovasc Med*. 2022;9(March):1-39. doi:10.3389/fcvm.2022.826283
9. Longmore DB, Underwood SR, Hounsfield GN, et al. Dimensional Accuracy of Magnetic Resonance in Studies of the Heart. *Lancet*. 1985;325(8442):1360-1362. doi:10.1016/S0140-6736(85)91786-6
10. Sakuma H, Fujita N, Foo TKF, Caputo GR, Nelson SJ, Hartiala J, Shimakawa A, Higgins CB. Evaluation of left ventricular volume and mass with breath-hold cine MR imaging. *Radiology*. 1993;188(2):377-380. doi:10.1148/radiology.188.2.8327681
11. Korosec FR. Basic Principles of MRI and MR Angiography. In: Carr, J., Carroll T, ed. *Magnetic Resonance Angiography*. Springer, New York, NY; 2012. doi:doi:10.1007/978-1-4419-1686-0_1

12. Jung B, Markl M. Phase-contrast MRI and flow quantification. In: *Magnetic Resonance Angiography*. ; 2012:51–64.
13. Kramer CM, Barkhausen J, Bucciarelli-Ducci C, Flamm SD, Kim RJ, Nagel E. Standardized cardiovascular magnetic resonance imaging (CMR) protocols: 2020 update. *J Cardiovasc Magn Reson*. 2020;22(1):1-18. doi:10.1186/s12968-020-00607-1
14. Lotz J, Meier C, Leppert A, Galanski M. Cardiovascular flow measurement with phase-contrast MR imaging: Basic facts and implementation. *Radiographics*. 2002;22(3):651-671. doi:10.1148/radiographics.22.3.g02ma11651
15. Dyverfeldt P, Bissell M, Barker AJ, et al. 4D flow cardiovascular magnetic resonance consensus statement. *J Cardiovasc Magn Reson*. 2015;17(1):1-19. doi:10.1186/s12968-015-0174-5
16. Pruitt A, Rich A, Liu Y, Jin N, Potter L, Tong M, Rajpal S, Simonetti O, Ahmad R. Fully Self-Gated Whole-Heart 4D Flow Imaging from a Five-Minute Scan. *Magn Reson Med*. 2021;85(3):1222-12236. doi:https://doi.org/10.1002/mrm.28491
17. Kolbitsch C, Vasquez CP, Bastkowski R, Weiss K, Maintz D. Respiratory motion corrected 4D flow using golden radial phase encoding. *Magn Reson Med*. 2019;(June):00:1-10. doi:10.1002/mrm.27918
18. Cheng JY, Hanneman K, Zhang T, Alley MT, Lai P, Tamir JI, Uecker M, Pauly JM, Lustig M, Vasanawala SS. Comprehensive Motion-Compensated Highly Accelerated 4D Flow MRI With Ferumoxytol Enhancement for Pediatric Congenital Heart Disease. *J Magn Reson Imaging*. 2016;43:1355–1368.
19. Ma LE, Yerly J, Piccini D, Sopra L Di, Roy CW, Carr JC, Rigsby CK, Kim D, Stuber M, Markl M. 5D Flow MRI : A Fully Self-gated, Free-running Framework for Cardiac and Respiratory Motion – resolved 3D Hemodynamics. *Radiol Cardiothorac Imaging*. 2020;2(6). doi:10.1148/ryct.2020200219
20. Walheim J, Dillinger H, Kozerke S. Multipoint 5D flow cardiovascular magnetic resonance - Accelerated cardiac- and respiratory-motion resolved mapping of mean and turbulent velocities. *J Cardiovasc Magn Reson*. 2019;21(1):1-13. doi:10.1186/s12968-019-0549-0
21. Bastkowski R, Bindermann R, Brockmeier K, Weiss K. Respiration Dependency of Caval Blood Flow in Patients with Fontan Circulation : Quantification Using 5D Flow MRI. *Radiol - Cardiothorac Imaging*. 2019;1(4):e190005. doi:10.1148/ryct.2019190005
22. Di Sopra L, Piccini D, Coppo S, Stuber M, Yerly J. An automated approach to fully self-gated free-running cardiac and respiratory motion-resolved 5D whole-heart MRI. *Magn Reson Med*. 2019;82(6):2118-2132. doi:10.1002/mrm.27898
23. Katz AM. *Physiology of the Heart*. Fifth Edit. Lippincott Williams & Wilkins, a Wolters Kluwer business; 2011.
24. Teresa Castiello. *Why CMR: Heart Failure*.; 2018.
25. Leung S. *Why CMR: Coronary Artery Disease*.; 2018. doi:10.29309/tpmj/2017.24.10.714
26. Jiang M. *Why CMR: Dilated CMP*.; 2017.
27. Teresa Castiello. *Why CMR: Arrhythmogenic Right Ventricular Cardiomyopathy/Dysplasia*.; 2018. doi:10.1093/eurheartj/ehu284
28. Castiello T. *Why CMR: Hypertrophic Cardiomyopathy*.; 2018. doi:10.1016/j
29. Fidock B, Archer G, Barker N, et al. Standard and emerging CMR methods for mitral regurgitation quantification. *Int J Cardiol*. 2021;331:316-321. doi:10.1016/j.ijcard.2021.01.066
30. Westenberg JJM, Roes SD, Marsan NA, Binnendijk NMJ, Doornbos J, Bax JJ, Reiber JHC, De Roos A, Van Der Geest RJ. Mitral valve and tricuspid valve blood flow: Accurate quantification with 3D velocity-encoded MR imaging with retrospective valve

tracking. *Radiology*. 2008;249(3):792-800. doi:10.1148/radiol.2492080146
31. Wymer DT, Patel KP, Burke WF, Bhatia VK. Phase-contrast MRI: Physics, techniques, and clinical applications. *Radiographics*. 2020;40(1):122-140. doi:10.1148/rg.2020190039
32. Hoffman JIE, Kaplan S. The incidence of congenital heart disease. *J Am Coll Cardiol*. 2002;39(12):1890-1900. doi:10.1016/S0735-1097(02)01886-7
33. Reller MD, Strickland MJ, Riehle-Colarusso T, Mahle WT, Correa A. Prevalence of Congenital Heart Defects in Metropolitan Atlanta, 1998-2005. *J Pediatr*. 2008;153(6):807-813. doi:10.1016/j.jpeds.2008.05.059
34. Didier D, Saint-Martin C, Lapierre C, Trindade PT, Lahlaidi N, Vallee JP, Kalangos A, Friedli B, Beghetti M. Coarctation of the aorta: Pre and postoperative evaluation with MRI and MR angiography; correlation with echocardiography and surgery. *Int J Cardiovasc Imaging*. 2006;22(3-4):457-475. doi:10.1007/s10554-005-9037-8
35. Muzzarelli S, Meadows AK, Ordovas KG, Higgins CB, Meadows JJ. Usefulness of cardiovascular magnetic resonance imaging to predict the need for intervention in patients with coarctation of the aorta. *Am J Cardiol*. 2012;109(6):861-865. doi:10.1016/j.amjcard.2011.10.048
36. Fontan F, Baudet E. Surgical repair of tricuspid atresia. *Thorax*. 1971;26(3):240-248. doi:10.1136/thx.26.3.240
37. Gewillig M. The Fontan circulation. *Heart*. 2005;91(6):839-846. doi:10.1136/hrt.2004.051789
38. Khairy P, Fernandes SM, Mayer JE, Triedman JK, Walsh EP, Lock JE, Landzberg MJ. Long-term survival, modes of death, and predictors of mortality in patients with Fontan surgery. *Circulation*. 2008;117(1):85-92. doi:10.1161/CIRCULATIONAHA.107.738559
39. Piran S, Veldtman G, Siu S, Webb GD, Liu PP. Heart failure and ventricular dysfunction in patients with single or systemic right ventricles. *Circulation*. 2002;105(10):1189-1194. doi:10.1161/hc1002.105182
40. Fallot A. Contribution a l'anatomie pathologique de la maladie bleue (cyanose cardiaque). *Marseillee Med*. Published online 1888:25:77.
41. Campbell M. Incidence of cardiac malformations at birth and later, and neonatal mortality. *Br Heart J*. 1973;35(2):189-200. doi:10.1136/hrt.35.2.189
42. Kolcz J, Pizarro C. Neonatal repair of tetralogy of Fallot results in improved pulmonary artery development without increased need for reintervention. *Eur J Cardio-thoracic Surg*. 2005;28(3):394-399. doi:10.1016/j.ejcts.2005.05.014
43. Al Habib HF, Jacobs JP, Mavroudis C, Tchervenkov CI, O'Brien SM, Mohammadi S, Jacobs ML. Contemporary patterns of management of tetralogy of fallot: Data from the society of thoracic surgeons database. *Ann Thorac Surg*. 2010;90(3):813-820. doi:10.1016/j.athoracsur.2010.03.110
44. Chiu SN, Wang JK, Chen HC, et al. Long-Term survival and unnatural deaths of patients with repaired tetralogy of fallot in an asian cohort. *Circ Cardiovasc Qual Outcomes*. 2012;5(1):120-125. doi:10.1161/circoutcomes.111.963603
45. Cohen MS, Eidem BW, Cetta F, et al. Multimodality Imaging Guidelines of Patients with Transposition of the Great Arteries: A Report from the American Society of Echocardiography Developed in Collaboration with the Society for Cardiovascular Magnetic Resonance and the Society of Cardiovascul. *J Am Soc Echocardiogr*. 2016;29(7):571-621. doi:10.1016/j.echo.2016.04.002
46. Lanzer P, Barta C, Botvinick EH, Wiesendanger HU, Modin G, Higgins CB. ECG-synchronized cardiac MR imaging: Method and evaluation. *Radiology*. 1985;155(3):681-686. doi:10.1148/radiology.155.3.4001369

47. Sievers B, Addo M, Kirchberg S, Bakan A, John-Puthenveettil B, Franken U, Trappe HJ. How much are atrial volumes and ejection fractions assessed by cardiac magnetic resonance imaging influenced by the ECG gating method? *J Cardiovasc Magn Reson*. 2005;7(3):587-593. doi:10.1081/jcmr-200060635
48. Carr JC, Simonetti O, Bundy J, Li D, Pereles S, Finn JP. Cine MR angiography of the heart with segmented true fast imaging with steady-state precession. *Radiology*. 2001;219(3):828-834. doi:10.1148/radiology.219.3.r01jn44828
49. Oster J, Clifford GD. Acquisition of electrocardiogram signals during magnetic resonance imaging. *Physiol Meas*. 2017;38(7). doi:10.1088/1361-6579/aa6e8c
50. Kording F, Schoennagel B, Lund G, Ueberle F, Jung C, Adam G, Yamamura J. Doppler ultrasound compared with electrocardiogram and pulse oximetry cardiac triggering: A pilot study. *Magn Reson Med*. 2015;74(5):1257-1265. doi:10.1002/mrm.25502
51. Larson AC, White RD, Laub G, McVeigh ER, Li D, Simonetti OP. Self-Gated Cardiac Cine MRI. *Magn Reson Med*. 2004;51(1):93-102. doi:10.1002/mrm.10664
52. Vahle T, Bacher M, Rigie D, Fenchel M, Speier P, Bollenbeck J, Schäfers KP, Kiefer B, Boada FE. Respiratory Motion Detection and Correction for MR Using the Pilot Tone: Applications for MR and Simultaneous PET/MR Examinations. *Invest Radiol*. 2020;55(3):153-159. doi:10.1097/RLI.0000000000000619
53. Wang Y, Grimm RC, Rossman PJ, Debbins JP, Riederer SJ, Ehman RL. 3D coronary MR angiography in multiple breath-holds using a respiratory feedback monitor. *Magn Reson Med*. 1995;34(1):11-16. doi:10.1002/mrm.1910340104
54. Liu YL, Riederer SJ, Rossman PJ, Grimm RC, Debbins JP, Ehman RL. A monitoring, feedback, and triggering system for reproducible breath-hold MR imaging. *Magn Reson Med*. 1993;30(4):507-511. doi:10.1002/mrm.1910300416
55. Dyverfeldt P, Ebbers T. Comparison of respiratory motion suppression techniques for 4D flow MRI. *Magn Reson Med*. 2018;78(5):1877-1882. doi:10.1002/mrm.26574
56. Denecken E, Sotelo J, Arrieta C, Andia ME, Uribe S. Impact of Respiratory Gating on Hemodynamic Parameters from 4D Flow MRI. *Appl Sci*. 2022;12:2943. doi:https://doi.org/10.3390/app12062943
57. Wang Y, Rossman PJ, Grimm RC, Riederer SJ, Ehman RL. Navigator-echo-based real-time respiratory gating and triggering for reduction of respiration effects in three-dimensional coronary MR angiography. *Radiology*. 1996;198(1):55-60. doi:10.1148/radiology.198.1.8539406
58. Ehman RL, Felmlee JP. Adaptive technique for high-definition MR imaging of moving structures. *Radiology*. 1989;173(1):255-263. doi:10.1148/radiology.173.1.2781017
59. Stehning C, Bo¨rnert P, Nehrke K, Eggers H, Stuber M. Free-Breathing Whole-Heart Coronary MRA With 3D Radial SSFP and Self-Navigated Image Reconstruction. *Magn Reson Med*. 2005;54:476-480.
60. Bailes DR, Gilderdale DJ, Bydder GM, Collins AG, Firmin DN. Respiratory ordered phase encoding (ROPE): A method for reducing respiratory motion artefacts in MR imaging. *J Comput Assist Tomogr*. 1985;9(4):835-838. doi:10.1097/00004728-198507010-00039
61. Markl M, Harloff A, Bley TA, Zaitsev M, Jung B, Weigang E, Langer M, Hennig J, Frydrychowicz A. Time-Resolved 3D MR Velocity Mapping at 3T: Improved Navigator-Gated Assessment of Vascular Anatomy and Blood Flow. *J Magn Reson Imaging*. 2007;25:824 –831.
62. Ma LE, Markl M, Chow K, Huh H, Forman C, Vali A, Greiser A, Carr J, Schnell S, Barker AJ, Jin N. Aortic 4D flow MRI in 2 minutes using compressed sensing, respiratory controlled adaptive k-space reordering, and inline reconstruction. *Magn Reson Med*. 2019;81(6):3675-3690. doi:10.1002/mrm.27684

63. Cheng JY, Zhang T, Ruangwattanapaisarn N, Alley MT, Uecker M, Pauly JM, Lustig M, Vasanawala SS. Free-breathing pediatric MRI with nonrigid motion correction and acceleration. *J Magn Reson Imaging*. 2015;42(2):407-420. doi:10.1002/jmri.24785
64. Cheng JY, Zhang T, Alley MT, Uecker M, Lustig M, Pauly JM, Vasanawala SS. Comprehensive Multi-Dimensional MRI for the Simultaneous Assessment of Cardiopulmonary Anatomy and Physiology. *Sci Rep*. 2017;7(1):1-15. doi:10.1038/s41598-017-04676-8
65. Schrauben EM, Lim JM, Goolaub DS, Marini D, Seed M, Macgowan CK. Motion robust respiratory-resolved 3D radial flow MRI and its application in neonatal congenital heart disease. *Magn Reson Med*. 2020;83(2):535-548. doi:10.1002/mrm.27945
66. Cheng JY, Hanneman K, Zhang T, Alley MT, Lai P, Tamir JI, Uecker M, Pauly JM, Lustig M, Vasanawala SS. Comprehensive motion-compensated highly accelerated 4D flow MRI with ferumoxytol enhancement for pediatric congenital heart disease. *J Magn Reson Imaging*. 2016;43(6):1355-1368. doi:10.1002/jmri.25106
67. Blanken CPS, Schrauben EM, Peper ES, Gottwald LM, Coolen BF, van Wijk DF, Piek JJ, Strijkers GJ, Planken RN, van Ooij P, Nederveen AJ. Coronary Flow Assessment Using Accelerated 4D Flow MRI With Respiratory Motion Correction. *Front Bioeng Biotechnol*. 2021;9(August):1-11. doi:10.3389/fbioe.2021.725833
68. Roy CW, Heerfordt J, Piccini D, Rossi G, Pavon AG, Schwitter J, Stuber M. Motion compensated whole-heart coronary cardiovascular magnetic resonance angiography using focused navigation (fNAV). *J Cardiovasc Magn Reson*. 2021;23(1):1-17. doi:https://doi.org/10.1186/s12968-021-00717-4
69. Mansfield P, Maudsley A. Medical imaging by NMR. *Br J Radiol*. 1977;50:188-194.
70. Carr H. Y ., Purcell EM. Effects of diffusion on free precession in nuclear magnetic resonance experiments. *Phys Rev*. 1954;94(3):630.
71. Hahn EL. Detection of sea-water motion by nuclear precession. *J Geophys Res*. 1960;65(2):776-777.
72. Paul R Moran. A flow velociy zeugmatographic interlace for NMR imaging in humans. *Magn Reson Imaging*. 1982;1:197-203.
73. Bryant DJ, Payne JA, Firmin DN, Longmore DB. Measurement of Flow With NMR Imaging Using a Gradient Pulse and Phase Difference Technique. *J Comput Assist Tomogr*. 1984;8(4):588-593.
74. van Dijk P. Direct cardiac NMR imaging of heart wall and blood flow velocity. *J Comput Assist Tomogr*. 1984;8(3):429-436.
75. Nayler GL, Firmin DN, Longmore DB. Blood flow imaging by Cine Magnetic Resonance. *J Comput Assist Tomogr*. 1986;10(5):715-722.
76. Walker PG, Cranney GB, Scheidegger MB, Waseleski G, Pohost GM, Yoganathan AP. Semiautomated method for noise reduction and background phase error correction in MR phase velocity data. *J Magn Reson Imaging*. 1993;3(3):521-530.
77. Firmin D, Gatehouse P, Konrad J, Yang G, Kilner P, Longmore D. Rapid 7-dimensional imaging of pulsatile flow. *Comput Cardiol IEEE Comput Soc L*. 1993;14:353–356. doi:10.1109/CIC.1993.378431
78. G.Bogren H, H.Mohiaddin R, Z.Yang G, J.Kilner P, N.Firmin D. Magnetic resonance velocity vector mapping of blood flow in thoracic aortic aneurysms and grafts. *J Thorac Cardiovasc Surg*. 1995;110(3):704-714. doi:10.1016/S0022-5223(95)70102-8
79. Wigström L, Sjöqvist L, Wranne B. Temporally resolved 3D phase-contrast imaging. *Magn Reson Med*. 1996;36(5):800-803. doi:10.1002/mrm.1910360521
80. Markl M, Chan FP, Alley MT, Wedding KL, Draney MT, Elkins CJ, Parker DW, Wicker R, Taylor CA, Herfkens RJ, Pelc NJ. Time-Resolved Three-Dimensional Phase-Contrast MRI. *J Magn Reson Imaging*. 2003;17:499-506. doi:10.1002/jmri.10272

81. Markl M, Schnell S, Barker AJ. 4D flow imaging: Current status to future clinical applications. *Curr Cardiol Rep*. 2014;16(5). doi:10.1007/s11886-014-0481-8
82. Markl M, Frydrychowicz A, Kozerke S, Hope M, Wieben O. 4D flow MRI. *J Magn Reson Imaging*. 2012;36:1015-1036. doi:10.1007/978-3-319-65924-4_9
83. McConnell M, Khasgiwala B, Savord B, Chen M, Chuang M, Edelman R, Manning W. Comparison of Respiratory Suppression Methods and Navigator Locations for MR Coronary Angiography. *Am J Roentgenol*. 1997;168(May):1369-1375.
84. Rutkowski DR, Barton G, François CJ, Bartlett HL, Anagnostopoulos P V., Roldán-Alzate A. Analysis of cavopulmonary and cardiac flow characteristics in fontan Patients: Comparison with healthy volunteers. *J Magn Reson Imaging*. 2019;49(6):1786-1799. doi:10.1002/jmri.26583
85. Bollache E, Barker AJ, Dolan RS, Carr JC, van Ooij P, Ahmadian R, Powell A, Collins JD, Geiger J, Markl M. k-t accelerated aortic 4D flow MRI in under two minutes: Feasibility and impact of resolution, k-space sampling patterns, and respiratory navigator gating on hemodynamic measurements. *Magn Reson Med*. 2018;79(1):195-207. doi:10.1002/mrm.26661
86. Piccini D, Littmann A, Nielles-vallespin S, Zenge MO. Spiral Phyllotaxis : The Natural Way to Construct a 3D Radial Trajectory in MRI. *Magn Reson Med*. 2011;66:1049-1056. doi:10.1002/mrm.22898
87. Coppo S, Piccini D, Bonanno G, Chaptinel J, Vincenti G, Feliciano H, Van Heeswijk RB, Schwitter J, Stuber M. Free-running 4D whole-heart self-navigated golden angle MRI: Initial results. *Magn Reson Med*. 2015;74(5):1306-1316. doi:10.1002/mrm.25523
88. Feng L, Axel L, Chandarana H, Block KT, Sodickson DK, Otazo R. XD-GRASP: Golden-angle radial MRI with reconstruction of extra motion-state dimensions using compressed sensing. *Magn Reson Med*. 2016;75(2):775-788. doi:10.1002/mrm.25665
89. Feng L, Coppo S, Piccini D, Yerly J, Lim RP, Masci PG, Stuber M, Sodickson DK, Otazo R. 5D whole-heart sparse MRI. *Magn Reson Med*. 2017;79(2):826-838. doi:10.1002/mrm.26745
90. Heerfordt J, Whitehead KK, Bastiaansen JAM, Di Sopra L, Roy CW, Yerly J, Milani B, Fogel MA, Stuber M, Piccini D. Similarity-driven multi-dimensional binning algorithm (SIMBA) for free-running motion-suppressed whole-heart MRA. *Magn Reson Med*. 2021;86(1):213-229. doi:10.1002/mrm.28713
91. Mackowiak ALC, Roy CW, Yerly J, Sopra L Di, Falcão MBL, Bacher M, Speier P, Piccini D, Stuber M, Bastiaansen JAM. Whole-Heart Motion-Resolved Multi-Peak Fat-Fraction Mapping using Free-Running 3D Radial Multi-Echo GRE and Pilot Tone. *Proc Intl Soc Mag Reson Med*. 2021;29(0755).
92. Di Sopra L, Roy CW, Bastiaansen JAM, Yerly J, Piccini D, Arn L, Stuber M, van Heeswijk R. Fully Self-Gated Cardiac and Respiratory Motion-Resolved Isotropic 5D T1 Mapping of the Heart : Preliminary Results. *Proc Intl Soc Mag Reson Med*. 2019;27(0785).
93. Rumac S, Roy CW, Yerly J, Falcao MBL, Bustin A, Bacher M, Speier P, Stuber M, Heeswijk RB van. Free-running isotropic whole-heart T2 mapping with ECG-free Pilot Tone navigation. In: *30th International Society for Magnetic Resonance in Medicine*. ; 2022.
94. Franceschiello B, Di Sopra L, Minier A, Ionta S, Zeugin D, Notter MP, Bastiaansen JAM, Jorge J, Yerly J, Stuber M, Murray MM. 3-Dimensional magnetic resonance imaging of the freely moving human eye. *Prog Neurobiol*. 2020;194(October 2019):101885. doi:10.1016/j.pneurobio.2020.101885
95. Mackowiak AL, Roy CW, Falcao MB, Bustin A, Bacher M, Speier P, Piccini D, Stuber M, Vietti-Violi N, Bastiaansen JA. Pilot Tone Guided Focused Navigation for Free-

Breathing Whole-Liver Water-Fat Quantification. In: *Proc Intl Soc Mag Reson Med*. ; 2022.
96. Pang J, Sharif B, Fan Z, Bi X, Arsanjani R, Berman DS, Li D. ECG and navigator-free 4D whole-heart coronary MRA. *J Cardiovasc Magn Reson*. 2015;17(Suppl 1):1-3.
97. Piccini D, Feng L, Bonanno G, Coppo S, Yerly J, Lim RP, Schwitter J, Sodickson DK, Otazo R, Stuber M. Four-dimensional respiratory motion-resolved whole heart coronary MR angiography. *Magn Reson Med*. 2017;77(4):1473-1484. doi:10.1002/mrm.26221
98. Lustig M, Donoho D, Pauly JM. Sparse MRI: The application of compressed sensing for rapid MR imaging. *Magn Reson Med*. 2007;58(6):1182-1195. doi:10.1002/mrm.21391
99. Ma L, Yerly J, Di Sopra L, Piccini D, Lee J, DiCarlo A, Passman R, Greenland P, Kim D, Stuber M, Markl M. Using 5D flow MRI to decode the effects of rhythm on left atrial 3D flow dynamics in patients with atrial fibrillation. *Magn Reson Med*. 2021;85(6):3125-3139. doi:10.1002/mrm.28642

Chapter 2.
Pilot tone navigation for respiratory and cardiac motion-resolved free-running 5D flow MRI

2.1. Overview

The detection of respiratory and cardiac signals in 3D PC-MRI is usually performed separately, with diaphragmatic navigators being the most common tools to monitor respiratory motion, and ECG being the gold standard to record the heart's electrical activity. Nevertheless, the efficiency of the diaphragmatic navigators depends on the patient's physiology and anatomy, causing unpredictable scan times. Additionally, adding the ECG introduces additional setup time, and its signal can sometimes be corrupt, due to limitations in ECG lead placement, or physiological features of the patients, or even due to MR-derived magneto hydrodynamic effects and gradient switching that can induce additional electrical currents, all which compromise the ECG signal detection.

Alternatively, self-gating tools have been shown to provide an accurate detection of both respiratory and cardiac signals, but their performance is sequence dependent. In the free-running PC-MRI framework, the use of self-gating readouts creates a large interdependency between a good imaging trajectory, the need to repeat each readout multiple times for velocity encoding, and the sampling frequency of the self-gating readouts. For these reasons, it would be of interest to find a solution that entirely decouples the imaging part of the sequence and physiological signal extraction.

In this study, we explored the integration of the Pilot Tone Navigation system into the free-running PC-MRI framework to detect respiratory and cardiac motion signals. Pilot Tone is a recently developed MR image-independent motion detection system that has been shown to provide accurate detection of physiological signals. A signal extraction framework was implemented using Pilot Tone to inform a respiratory and cardiac motion resolved 5D flow image reconstruction that was shown to yield equivalent flow measurements with respect to 5D flow reconstructions of the same data using self-gating. Moreover, Pilot Tone was shown to be unaffected by parameter changes in the imaging sequence, which may prompt new sequence trajectory optimizations of the free-running PC-MRI framework.

2.2. Personal contribution

Among the main contributions for this project, I was the primary investigator in this study. I implemented and optimized the full signal extraction framework for Pilot Tone and interfaced it with the free-running sequences. Together with the last two authors, Dr. Christopher W. Roy, PhD, and Prof. Matthias Stuber, PhD, we defined the study pipeline and the hypothesis we wanted to test. I performed the entire data analysis and acquired all the volunteer data at the scanner. All the remaining authors were valuable contributors in advising and/or providing patient data.

2.3. Article Peer-Reviewed

Two abstracts related to this work were presented at two international scientific conferences (Supplementary Information A3.1 and A3.2). The first abstract was presented at the 23rd SCMR meeting in 2020 with the title "*5D Flow using Pilot Tone for cardiac and respiratory self-gating*", where it was selected as one of the best posters to display at SCMR/ISMRM Co-Provided Workshop. The second abstract, named "*5D Flow – A quantitative in vivo comparison between Self Gating and Pilot Tone Gating*", was presented at the 30th ISMRM International meeting in 2020, where it was awarded a 2nd place at the Flow and Motion Study group. The main study has since been peer-reviewed and published in the Journal of Magnetic Resonance in Medicine in February 2022, with the title "*Pilot tone navigation for respiratory and cardiac motion-resolved free-running 5D flow MRI*". Since its publication, this work has already been cited by 15 additional studies, according to the Google Scholar search engine.

Received: 18 June 2021 | Revised: 17 August 2021 | Accepted: 3 September 2021

DOI: 10.1002/mrm.29023

RESEARCH ARTICLE

Magnetic Resonance in Medicine

Pilot tone navigation for respiratory and cardiac motion-resolved free-running 5D flow MRI

Mariana B. L. Falcão[1] | **Lorenzo Di Sopra**[1] | **Liliana Ma**[2,3] | **Mario Bacher**[1,4,5] | **Jérôme Yerly**[1,6] | **Peter Speier**[4] | **Tobias Rutz**[7] | **Milan Prša**[8] | **Michael Markl**[2,3] | **Matthias Stuber**[1,6] | **Christopher W. Roy**[1]

[1]Department of Diagnostic and Interventional Radiology, Lausanne University Hospital (CHUV) and University of Lausanne (UNIL), Lausanne, Switzerland

[2]Department of Radiology, Feinberg School of Medicine, Northwestern University, Chicago, Illinois, USA

[3]Department of Biomedical Engineering, Northwestern University, Chicago, Illinois, USA

[4]Siemens Healthcare GmbH, Erlangen, Germany

[5]Advanced Clinical Imaging Technology, Siemens Healthcare AG, Lausanne, Switzerland

[6]Center for Biomedical Imaging (CIBM), Lausanne, Switzerland

[7]Service of Cardiology, Centre de Resonance Magnétique Cardiaque (CRMC), Lausanne University Hospital and University of Lausanne, Lausanne, Switzerland

[8]Woman-Mother-Child Department, Lausanne University Hospital and University of Lausanne, Lausanne, Switzerland

Correspondence
Christopher W. Roy, Lausanne University Hospital (CHUV), Rue de Bugnon 46, BH-7-84, 1011 Lausanne, Switzerland.
Email: christopher.roy@chuv.ch

Funding information
Supported by the Swiss National Science Foundation (SNSF), grant/award 173129; and the National Institutes of Health (NIH), grants R01HL115828 and F30HL137279

Purpose: In this work, we integrated the pilot tone (PT) navigation system into a reconstruction framework for respiratory and cardiac motion-resolved 5D flow. We tested the hypotheses that PT would provide equivalent respiratory curves, cardiac triggers, and corresponding flow measurements to a previously established self-gating (SG) technique while being independent from changes to the acquisition parameters.

Methods: Fifteen volunteers and 9 patients were scanned with a free-running 5D flow sequence, with PT integrated. Respiratory curves and cardiac triggers from PT and SG were compared across all subjects. Flow measurements from 5D flow reconstructions using both PT and SG were compared to each other and to a reference electrocardiogram-gated and respiratory triggered 4D flow acquisition. Radial trajectories with variable readouts per interleave were also tested in 1 subject to compare cardiac trigger quality between PT and SG.

Results: The correlation between PT and SG respiratory curves were 0.95 ± 0.06 for volunteers and 0.95 ± 0.04 for patients. Heartbeat duration measurements in volunteers and patients showed a bias to electrocardiogram measurements of, respectively, 0.16 ± 64.94 ms and 0.01 ± 39.29 ms for PT versus electrocardiogram and of 0.24 ± 63.68 ms and 0.09 ± 32.79 ms for SG versus electrocardiogram. No significant differences were reported for the flow measurements between 5D

flow PT and from 5D flow SG. A decrease in the cardiac triggering quality of SG was observed for increasing readouts per interleave, whereas PT quality remained constant.

Conclusion: PT has been successfully integrated in 5D flow MRI and has shown equivalent results to the previously described 5D flow SG technique, while being completely acquisition-independent.

KEYWORDS

5D flow MRI, cardiac motion, free-running, pilot tone, respiratory motion

1 | INTRODUCTION

4D flow MRI provides a quantitative evaluation of hemodynamics across an entire 3D volume, allowing for simultaneous assessment of flow in multiple vessels and cardiac chambers.[1,2] As a result, 4D flow has become an integral part of the diagnosis and patient management for disorders such as congenital heart disease (CHD) and valvar abnormalities.[3,4] Typically, diaphragmatic navigators are used to monitor respiratory displacement and discard data acquired during inspiration, thus eliminating blurring artifacts caused by respiratory motion. However, the efficiency of these respiratory navigators depends on the patient's physiology and anatomy, causing unpredictable scan times.[5] Consequently, it becomes challenging to routinely acquire 4D flow datasets covering the heart and great vessels (whole-heart coverage) in a clinically acceptable time (<10 min).

To improve scanning efficiency, several methods have been proposed to collect flow data throughout the entire respiratory cycle and either retrospectively trigger,[6] correct,[7] or resolve respiratory motion.[8–11] Here, as in other studies, we refer to respiratory and cardiac motion-resolved volumetric flow imaging as 5D flow imaging.

Existing approaches for 5D flow imaging take advantage of self-gating (SG), where physiological motion can be directly derived from the acquired imaging data. To resolve respiratory motion, the datasets are binned according to the amplitude of a SG respiratory curve, whereas cardiac motion is resolved by binning data according to time points derived from SG cardiac triggers, effectively removing the need for electrocardiography (ECG) placement and thereby promoting a faster and simpler patient setup.[8–11]

The main drawback behind SG strategies is their dependence on the periodic sampling of either a point or a 1D readout,[6–11] which if not sampled frequently enough may limit the precision of the SG respiratory curves and, especially, cardiac triggers. Likewise, for the SG strategies requiring the repetition of 1D readouts, the limitations of gradient hardware and the need to minimize both eddy current effects and sequence dependent artifacts[12,13] limit our ability to arbitrarily switch between imaging and SG readouts without impacting scanning efficiency and the final image quality. This issue is further confounded by flow sequences, which repeat each readout multiple times for velocity encoding. It would therefore be of interest to find a reliable alternative to extract respiratory curves and cardiac triggers with high sampling rate without impacting the image acquisition scheme.

Recently, the pilot tone (PT) navigation system was proposed as an MR image-independent motion detection system.[14] The PT navigation system, implemented by Speier et al.,[14–16] consists of a small loop antenna, integrated inside a chest coil array, that transmits a continuous-wave RF signal into the magnet bore at a frequency outside of the frequency band of the MR imaging signal, ergo not disturbing the image acquisition but still inside the useable receiver bandwidth. This signal is then captured by all active receiver coils after having been modulated by the underlying motion. From this signal, it is possible to extract respiratory curves in agreement with conventional MR navigators,[14,17] as well as cardiac triggers comparable to ECG gating,[15,16] all in parallel to the MRI acquisition. Thus, PT may be a valuable alternative to the aforementioned MR data-driven SG approaches by providing signals with a higher sampling rate that are independent from the image acquisition.

The goal of this work was the integration of the PT navigation system into a recently proposed free-running radial flow framework for respiratory- and cardiac motion-resolved radial 5D flow imaging.[9,18] PT was compared to the previously described SG method and was validated in the 5D flow framework for healthy subjects and patients with CHD. As a reference measurement, 5D flow reconstructions were additionally compared to conventional ECG-triggered and respiratory navigated Cartesian 4D flow acquisitions. We tested the following 3 hypotheses: 1) PT provides equivalent respiratory curves and cardiac triggers to SG as part of a published 5D flow protocol; 2) 5D

flow image reconstruction using PT yields equivalent flow measurements with respect to 5D flow reconstructions of the same data using SG; 3) PT signals, unlike SG, are unaffected by changes to the underlying 3D radial sequence trajectory.

2 | METHODS

2.1 | Study cohort and data acquisition

A cohort of 15 healthy adults (7 female, age 23-34 years) and 9 patients (3 female, age 13-55 years) with CHD (pathologies listed in Supporting Information Table S1) were scanned on a 1.5T Magnetom Sola (Siemens Healthcare, Erlangen, Germany) using a 12-channel body coil array with an integrated PT generator. All subjects participating in this study, or their legal guardians in case of minors, provided written informed consent compliant with our institutional guidelines and approved by the local research ethics committee.

For each subject, a prototype free-running radial 3D whole-heart flow sequence — hereafter referred to as *5D flow sequence*[9] — was acquired, and PT data was recorded with every readout of the flow sequence by activating the system's integrated PT signal detection functionality. For reference, a conventional ECG gated respiratory navigated Cartesian 4D flow sequence covering the aorta was also acquired.[5] Scan parameters are provided in Table 1.

2.2 | 5D flow pulse sequence

The 5D flow framework implemented in the present study[9] is based on a previously reported free-running framework for 5D radial whole-heart imaging[18] that continuously samples k-space following a 3D radial spiral phyllotaxis sampling pattern.[19] In the 5D flow setup, several spiral interleaves are acquired sequentially and rotated by the golden angle. Each interleave includes a readout orientated along the superior-inferior (SI) direction for subsequent extraction of SG respiratory curves and cardiac triggers,[18] followed by a series of radial imaging readouts spiraling down k-space. Every imaging readout, aside from the SI readouts, was repeated 4 times for balanced 4-point velocity encoding. In order to ensure a sufficient sampling rate of the SI projections for extracting cardiac motion, the number of radial angles sampled per interleave (excluding SI readouts) was established as 5, resulting in a total of 21 readouts per interleave (1 SI + (5 readouts × 4 velocity encoding)). The described 5D flow framework has been previously validated both in vitro and in vivo in a cohort of patients with aortic disease.[9] In addition to using SI readouts for SG (sampling frequency of 10.2 Hz), PT signals were extracted at every readout in parallel to the image acquisition (sampling frequency of 214.1 Hz), and gold standard ECG signals (sampling frequency of 400 Hz) were also recorded throughout the 5D flow scan for subsequent cardiac triggering comparisons.[18]

TABLE 1 Scan parameters for 5D flow and reference 4D flow acquisitions

	5D flow		4D flow reference	
Trajectory	3D radial		3D Cartesian	
Respiration	Gated		Triggered	
Cardiac gating	ECG/SG/PT		ECG	
TE/TR	2.93/4.67 ms		2.33/5.08 ms	
RF excitation angle	7°		7°	
Coverage	Whole heart		Aortic arch	
Acquisition efficiency	100%		32– 97%	
Acceleration rate	R = 43-75		GRAPPA, R = 2	
	Healthy cohort	**Patient cohort**	**Healthy cohort**	**Patient cohort**
Venc	150 cm/s	150-200 cm/s	150 cm/s	150 cm/s
Temporal resolution	38.3-40 ms	38.5-40 ms	21.6-38.1 ms	39.9-40.8 ms
Spatial resolution	$2.5 \times 2.5 \times 2.5$ mm^3	[2.1-2.5] × [2.1-2.5] × [2.1-2.5] mm^3	$2.5 \times 2.5 \times 2.5$ mm^3	$2.5 \times 2.5 \times 2.5$ mm^3
FOV	$240 \times 240 \times 240$ mm^3	(200-240) × (200-240) × (200-240) mm^3	(200-300) × (360-420) × (75-90) mm^3	(166.7-240) × (300-360) × (83.2-110) mm^3
Acquisition time	7:53 min	7:53-8:55 min	4:25-12:34 min	4:42-9:29 min

Scan time in CHD patients was adapted for each clinical case, depending on resolution, FOV, and maximum venc.

CHD, congenital heart disease; ECG, electrocardiogram; PT, pilot tone; SG, self-gating; venc, velocity encoding.

2.3 | Physiological signal extraction

The approach for both PT and SG signal extraction frameworks was based on the work by Di Sopra et al.[18] for the free-running 5D framework, which is summarized in Figure 1. This signal extraction pipeline was implemented in MatLab R2018b (MathWorks, Natick, MA). First, for SG, the SI readouts extracted from the imaging data were corrected for trajectory-dependent imperfections caused by eddy currents, gradient timing delays, and the magnetohydrodynamic effect. The effect of these trajectory imperfections in the SG signal is related to the chosen trajectory architecture for image acquisition.[18] Conversely, the PT signals, emitted at a different frequency, are not affected by the same confounding effects in the current setup; thus, no correction algorithm was performed on those signals. The frequency spectrum for both SG and PT signals in 1 representative subject, before (PT and SG) and after (only SG) correcting for the trajectory imperfections, is shown in Supporting Information Figure S1.

The remaining signal extraction steps were identical for both PT and SG pipelines. Principal component analysis was applied to reduce data complexity and to segregate the respiratory and cardiac components. From the first ten principal components, an estimate of the subject-specific frequency range of the respiratory motion was retrieved, and the principal component with the strongest modulation over the identified range was selected to describe the respiratory curve. To extract cardiac motion, independent component analysis was performed on top of the previously extracted principal components. Pre-applying principal component analysis to these high dimensional datasets reduces computational complexity and enhances independent component analysis performance.[20,21] Then, the subject-specific frequency range of cardiac motion was estimated, and the independent component with the strongest modulation in the defined range was singled out to represent the cardiac signal. From the SG cardiac signals, similarly to the implementation by Di Sopra et al.,[18] cardiac triggers were marked at the zero-crossing time points. Conversely, for PT gating, the local minima was chosen as the trigger point.[15]

2.4 | Data sorting

For each signal extraction type (PT and SG), the individual readouts were assigned to bins independently of their position in the originally acquired interleave; however, to ensure consistency, velocity encodes for a given readout were assigned to the same respiratory and cardiac phase, creating 6D arrays (k_x-k_y-k_z-respiratory-cardiac-velocity encode). The resulting 5D flow datasets sorted using PT and using SG will be hereafter referred to as 5D flow PT and 5D flow SG, respectively. For both PT and SG, the extracted respiratory curve was used to partition the acquired 5D flow data into 4 equally distributed respiratory motion states, ranging from end-inspiration to

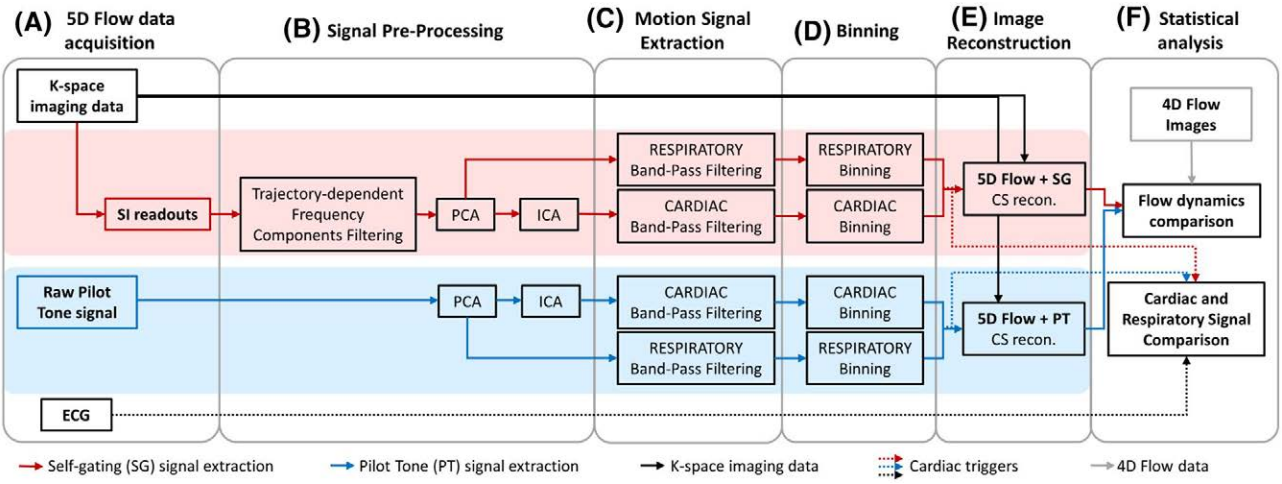

FIGURE 1 Schematic of the pipeline used for this work. (A) The acquired 5D flow datasets were used to extract SG respiratory curves and cardiac triggers. In parallel, PT signals were also used to extract respiratory curves and cardiac triggers. (B) SG signals were corrected for trajectory dependent artifacts. Both SG and PT signals were preprocessed using principal component analysis and independent component analysis. (C) The range of respiratory and cardiac motion was used to find the best representation of each modulation. The extracted respiratory curves from SG and PT were compared with each other, and cardiac triggers were compared with each other as well as with ECG triggers (F). (D) Finally, the 5D flow dataset was binned into respiratory and cardiac phases based on the PT signals (5D flow PT), SG signals (5D flow SG), and (E). XD-GRASP was used to reconstruct both datasets. (F) Finally, flow hemodynamics of the 5D flow PT and 5D flow SG were compared with conventional 4D flow. ECG, electrocardiogram; PT, pilot tone; SG, self-gating

end-expiration, according to the amplitude of signal at each time point. Similarly, data were also assigned to different cardiac phases using the extracted cardiac triggers. The width of each cardiac bin was fixed to 40 ms, resulting in a variable number between 19 and 31 cardiac phases obtained from binning, depending on the individual heart rate of each subject.

2.5 | Image reconstruction

5D flow PT and 5D flow SG images were reconstructed offline using the previously described free-running framework,[18] wherein a multidimensional compressed sensing algorithm enforces sparsity along both respiratory and cardiac dimensions.[22,23] All SI projections, previously used for SG, were removed prior to image reconstruction. Respiratory and cardiac regularization weights were set to 0.005 and 0.0075, respectively, matching those used previously.[9] All 5D flow reconstructions were performed using MatLab R2018b (MathWorks) on a workstation equipped with 2 Intel Xeon CPUs (Intel, Santa Clara, CA), 512GB of RAM, and a NVIDIA Tesla GPU (Nvidia, Santa Clara, CA). Reconstruction time for each 5D flow dataset varied from 8-13 h, depending on the number of cardiac phases and the number of active receiver channels. Conversely, reference 4D flow image reconstructions were directly provided by the scanner reconstruction pipeline during the examination.

2.6 | Analysis of respiratory curves and cardiac triggers

To test our first hypothesis, that PT provides equivalent physiological signals to SG, quantitative comparison of respiratory curves extracted using PT and SG was performed by measuring the consistency between data binned with PT and SG gating, respectively, defined by the percentage of coinciding (overlapping) data points between respiratory phases. Additionally, for each 5D flow PT and 5D flow SG reconstruction, the end-expiration and end-inspiration images were rigidly coregistered over a region of interest containing the lung–liver interface using NiftyRegv1.3.9Ad (University College London, United-Kingdom).[24,25] The resulting displacement measure along the SI direction was used to quantitatively compare respiratory motion detection from the PT and SG signals.

Quantitative comparison of cardiac triggers was performed by comparing the time between consecutive triggers (heartbeat interval duration) derived from PT and SG to gold standard ECG. Additionally, the trigger jitter was defined and calculated as the standard deviation across the trigger delays between every pair of corresponding triggers for either PT or SG versus ECG.[13] To exclude missed triggers from the analysis, rejection of individual triggers was performed using an outlier rejection strategy described previously.[18] This strategy excludes heartbeat intervals that are 1.5 times longer or 0.5 times shorter than the median heartbeat estimated for 20 consecutive heartbeats around each interval.[18] Two subjects had more than 1% of reported corrupted ECG cardiac triggers and were therefore excluded from the cardiac trigger comparison. For the remaining subjects, only individual ECG triggers were excluded.

2.7 | Analysis of flow measurements

To test our second hypothesis, that PT enables equivalent flow measurements to SG, the images reconstructed from 5D flow and 4D flow datasets were first preprocessed using noise filters, background phase correction, and antialiasing correction. A second-order 3D background phase correction model was implemented for 5D flow imaging,[9] whereas a first order correction was used for 4D flow acquisitions.[1,2] The order of each correction model differed because the phase offset is derived from eddy currents, and this offset depends on the type of trajectory used (Cartesian, radial, etc.).

For this analysis, only the end-expiratory phase images of 5D flow PT and 5D flow SG were used because the focus of this study was not to understand the differences in respiratory hemodynamics but instead to validate PT as a valid alternative to SG for 5D flow imaging. The acquired 4D flow datasets were included in the analysis as a reference measurement. For each flow dataset included in this study, the time-averaged phase-contrast angiogram was calculated using the magnitude and phase images of each dataset. From these phase-contrast angiogram images, a segment of the aorta was selected based on image thresholding.

Four aortic 2D planes were manually selected for our comparison. The first plane was located at the lower ascending aorta, slightly above the aortic root. The second plane was located at the upper ascending aorta, before the aortic arch. The third plane was located at the end of the aortic arch (Arch), and the final plane was located at the distal descending aorta (DAo) between the third plane and the diaphragm. The flow rate was computed for each 2D plane across the entire cardiac cycle. Net flow (flow volume across a cardiac cycle), peak flow rate, and peak velocity were calculated per slice for all 5D flow datasets, as well as for the control 4D flow datasets. All segmentations and measurements were computed using the

Siemens 4D Flow v2.4 software (Siemens Healthcare, Erlangen, Germany).

2.8 | Impact of sequence parameters on PT and SG signals

To test our third hypothesis, that PT signals are not impacted by acquisition parameters that otherwise affect SG signals, 6 back-to-back 5D flow acquisitions with a reduced scan time (2:03 min) were performed in 1 healthy subject. Each acquisition used a different phyllotaxis trajectory architecture by varying the number of readouts acquired per interleave but keeping the total number of readouts constant (Table 2). Each interleave included 1 SI readout for self-gating and a remaining set of readouts (varying for each acquisition), repeated 4 times for velocity encoding. Increasing the number of readouts acquired per interleave has the effect of decreasing the gradient strength required to move through k-space but also lowers the sampling rate of SG signals. To assess the impact of eddy-currents induced in each acquisition, the mean background velocity contained in manually selected static structures near the heart was measured. Additionally, PT and SG cardiac triggers were extracted; the sampling frequency was calculated; and the heartbeat interval and trigger jitters were computed using ECG as a reference. Note that this analysis was performed after an upgrade of our MRI system, which improved the PT sampling rate (2000 Hz).

2.9 | Statistical analysis

Agreement between PT and SG respiratory curves was assessed in healthy subjects and CHD patients by measuring the Pearson correlation coefficient. Quantitative measurements of liver displacement from 5D flow PT and 5D flow SG images were statistically compared using a paired *t* test.

Heartbeat intervals from PT and SG were compared to the corresponding ECG heartbeat intervals, which were automatically estimated throughout the scan (PT vs. ECG and SG vs. ECG) across all subjects using Bland-Altman plots. From those Bland-Altman plots, the mean and SD of the bias between each 2 modalities were reported. The cardiac trigger jitter measurements were compared between PT versus ECG and SG versus ECG using a paired *t* test.

In order to compare flow measurements between 5D flow PT and 5D flow SG, we calculated the net flow, peak flow rate, and peak velocity in the 5D flow PT datasets at each plane (aortic root, aortic arch, Arch, DAo) and by comparing these measurements to the 5D flow SG datasets as well as to the reference 4D flow using a paired

TABLE 2 Impact of sequence parameters on PT and SG signals

Nread	ECG Heartbeat duration (ms)	SG Heartbeat Duration (ms)	PT Heartbeat Duration (ms)	SG Trigger Jitter (ms)	PT Trigger Jitter (ms)	SG Sampling Frequency (Hz)	PT Sampling Frequency (Hz)	Average Background Velocity (cm/s)
13	983 ± 68	981 ± 65	981 ± 72	10.6	19.2	16.4	2000	1.10
21	993 ± 77	994 ± 67	994 ± 72	12.4	9.9	10.2	2000	0.62
45	962 ± 69	954 ± 93	962 ± 67	20.6	11.9	4.7	2000	0.46
69	883 ± 58	890 ± 113	883 ± 58	60.1	9.8	3.1	2000	0.17
93	956 ± 48	960 ± 81	957 ± 39	109.9	12.6	2.3	2000	0.15
189	915 ± 54	2330 ± 99	914 ± 51	-	14.7	1.1	2000	0.08

Six back-to-back 5D flow acquisitions with a variable Nread are shown. Overall, increasing Nread leads to decreased background velocity error but also decreased SG sampling rate and accuracy, precluding identification of cardiac triggers for high values of Nread. Conversely, PT sampling rate and accuracy remains unaffected by the underlying k-space trajectory.

Nread, number of readouts acquired per interleave.

t test between every 2 datasets (5D flow PT vs. 5D flow SG, 5D flow PT vs. 4D flow, and 5D flow SG vs. 4D flow). Bonferroni correction was performed to compensate for the 3 flow dataset comparisons. Finally, net flow and peak flow rate were compared for bias between each 2 datasets for all planes using Bland-Altman plots.

3 | RESULTS

3.1 | Analysis of respiratory curves

The respiratory curve analysis from the healthy cohort (Table 3) revealed some small differences in binning when using PT versus SG. The average percentage of overlapping respiratory bins between the 2 modalities was 84.2% in end-expiration, 75.1% and 81.9% in the 2 mid-respiratory phases, and 90.7% in end-inspiration. Results from the patient cohort revealed similar (albeit lower) agreement between PT and SG respiratory bins (Table 3), with an average overlapping percentage of 80.8% for end-expiration 69.3% and 74.9% in the 2 mid-respiratory phases and 86.9% for end-inspiration. Binning mismatch between PT and SG was mostly distributed across the neighboring bins with a distribution between 8.6% and 18.7%.

The Pearson correlation coefficient between the extracted PT and SG respiratory curves was 0.95 ± 0.06 for healthy subjects and 0.95 ± 0.04 for patients. The PT and SG respiratory curves for a representative healthy subject reporting high signal correlation (0.99, $P < .05$) are shown in Figure 2A, B. depicts the PT and SG respiratory curves from the healthy subject reporting the lowest signal correlation (0.81, $P < .05$), where signal baseline drifts of different amplitude are found for both modalities.

The mean displacement of the liver measured between end-expiratory and end-expiratory 5D flow PT and 5D flow SG images were comparable in both the healthy volunteers (PT: 11.19 ± 3.66 mm, SG: 10.65 ± 3.81 mm, $P = .57$) and patient (PT: 9.45 ± 3.70 mm, SG: 9.14 ± 3.54 mm, $P = .25$) cohorts.

3.2 | Analysis of cardiac triggers

One subject reported 4 missed ECG triggers, which were excluded from the remainder of the analysis. Additionally, 1 subject reported 3 missed PT triggers, and another subject reported 2 missed SG triggers. Overall, both PT and SG heartbeat interval duration measures showed a low bias with ECG (Figure 3). Bias values for each Bland-Altman plot were 0.16 ± 64.94 ms for PT versus ECG and 0.24 ± 63.68 ms for SG versus ECG in healthy subjects, and were 0.01 ± 39.29 ms for PT versus ECG and 0.09 ± 32.79 ms for SG versus ECG in patients. Figure 2C shows 3 cardiac signals (PT, SG, and ECG) together with their respective triggers extracted for 1 representative subject during a 5D flow acquisition.

Trigger jitter measurements did not show significant differences ($P > .05$) between PT versus ECG and SG versus ECG. Values reported in healthy subjects were 13.9 ± 8.2 ms for PT versus ECG and 17.0 ± 4.6 ms for SG versus ECG. These values correspond to 1.4 ± 0.7 % and 1.7 ± 0.4 % of the average heartbeat duration, respectively. The same measurements in patients reflected similar results, being 13.0 ± 5.7 ms for PT versus ECG and 17.3 ± 4.9 ms for SG versus ECG, or equivalently representing 1.3 ± 0.6% and 1.7 ± 0.4% of the average heartbeat duration.

3.3 | Analysis of flow measurements

Figure 4 depicts 3D aortic streamlines at peak systole of 2 representative healthy subjects and 1 CHD patient (Marfan syndrome) for the 5D flow PT, 5D flow SG, and 4D flow imaging datasets. A comparison of the magnitude and phase images from 5D flow PT and 5D flow SG

TABLE 3 Respiratory binning consistency assessment between SG and PT datasets across all 15 healthy subjects and 9 CHD patients

		PT Binning							
		Healthy Subjects				CHD Patients			
		End-exp	Mid-exp	Mid-insp	End-insp	End-exp	Mid-exp	Mid-insp	End-insp
SG binning	End-exp	**84.2 %**	15.1 %	0.5 %	0.2 %	**80.8 %**	18.7 %	0.4 %	0.3 %
	Mid-exp	15.6 %	**75.1 %**	8.8 %	0.5 %	18.6 %	**69.3 %**	11.9 %	0.2 %
	Mid-insp	0.1 %	9.3 %	**81.9 %**	8.6 %	0.5 %	11.7 %	**74.9 %**	12.8 %
	End-insp	0.03 %	0.5 %	8.8 %	**90.7 %**	0 .01%	0 .3%	12.8 %	**86.9 %**

The percentage of overlapping data points was measured for every pair of PT and SG bins. In general, non-overlapped bins from the same respiratory phase were assigned to the neighboring phases.

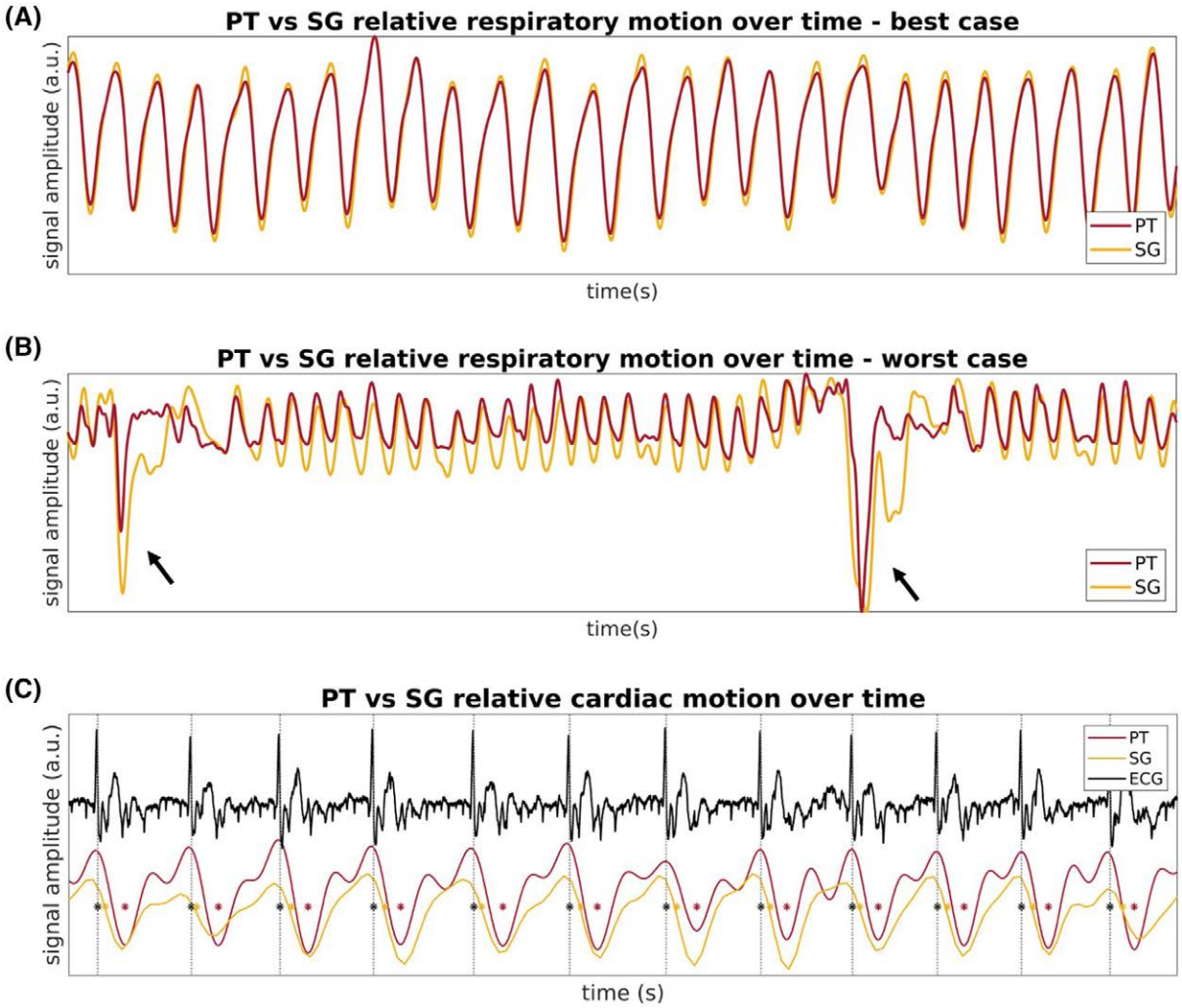

FIGURE 2 Respiratory and cardiac signals extracted from PT and SG plotted for a set of representative subjects. (A) Representation of the PT and SG relative respiratory curves over time for the healthy subject who had the highest reported Pearson correlation coefficient between PT and SG signals (0.99). (B) PT and SG relative respiratory curves over time for the healthy subject reporting the lowest Pearson correlation coefficient. Black arrows denote instances during the scan where the subject took deep breaths at irregular intervals (0.81). (C) Visualization of the PT and SG cardiac signals and their corresponding ECG signal for 1 representative subject demonstrating similar, albeit out-of-phase periodic detection of cardiac motion. Cardiac triggers for each modality are marked with colored asterisks (*)

reconstructions of a representative subject are included in Supporting Information Figure S2. The 2 healthy subjects selected (Figure 4A,B) correspond to the ones shown in Figure 2A,B (highest and lowest respiratory correlation). Figure 4 also depicts the location of the 2D analysis planes for each case. For each streamline image, white arrows highlight differences between aortic flow streamlines when comparing the two 5D flow and the reference 4D flow datasets. For the 2 healthy subjects, the largest differences between 4D flow streamlines and the remaining ones were reported in the descending aorta, whereas the largest difference reported for the 22-year-old CHD patient was at the level of the ascending aorta. Figure 5 shows the flow rate curves of the same subjects using 5D flow PT, 5D flow SG, and 4D flow. In general, the flow rate curves overlap between 5D flow PT and 5D flow SG reconstructions.

The analysis of the different flow measurements across the 2 cohorts (Figure 6) reported similar results to what had already been reported in the flow rate curves for the previous representative cases. In the cohort of healthy subjects, there were no significant differences reported for any of the flow measurements (net flow, peak flow rate, and peak velocity) when comparing the images from 5D flow PT and from 5D flow SG. Conversely, there were some significant differences between 5D flow PT and 4D flow measurements (net flow of DAo, peak flow rate of Arch and DAo, peak velocity of DAo; $P < .05$), and there were also reported significant differences between 5D flow SG and 4D flow measurements (net flow of DAo,

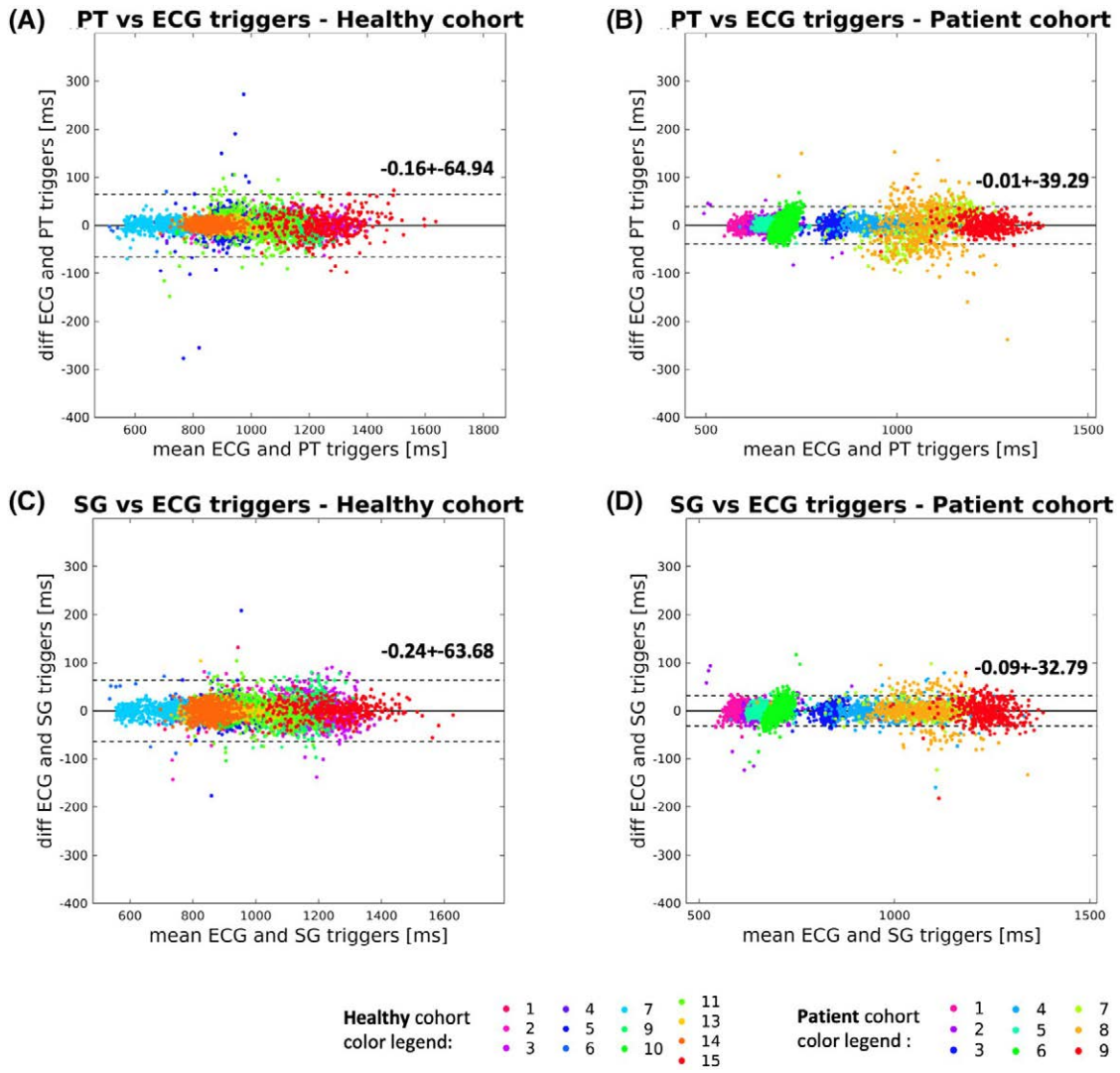

FIGURE 3 Quantitative comparison of heartbeat estimations from 13 healthy subjects (2 subjects were excluded from this analysis) and 9 patients. Each Bland –Altman plot compares differences between the ECG heartbeat interval duration for all cardiac intervals and the corresponding heartbeat duration estimated from PT (A,B) and SG (C,D) cardiac triggers. The linear correlation between the heartbeat durations in both healthy subjects (A,C) and patients (B,D) is excellent $r^2 > 0.95$. The 2 healthy subjects excluded from this analysis had limited ECG quality (>1% of reported corrupted triggers)

peak flow rate of aortic root, Arch and DAo, peak velocity of Arch and DAo; $P < .05$). Likewise, the analysis of the CHD patient cohort showed a good agreement between 5D flow PT and 5D flow SG measurements, and some discrepancies when compared to 4D flow datasets (net flow of DAo for 5D flow SG, and peak velocity of Arch and DAo for both 5D flow reconstructions vs. 4D flow; $P < .05$).

Bland-Altman plots on the healthy cohort analyzing net flow (Figure 7A-C) reported a bias of -0.5 ± 10.7 ml for 5D flow PT versus 5D flow SG, 4.8 ± 31.6 ml for 5D flow PT versus 4D flow, and 5.3 ± 31.4 ml for 5D flow SG versus 4D flow. Regarding peak flow measurements (Figure 7D-F), Bland-Altman plots showed biases of 0.6 ± 23.7 ml/s for 5D flow PT versus 5D flow SG, 6.2 ± 35.0 ml/s for 5D flow PT versus 4D flow, and 5.6 ± 38.3 ml/s for 5D flow SG versus 4D flow. Overall, these results showed good agreement between 5D flow PT and 5D flow SG measurements, and some underestimations relative to the 4D flow reference.

3.4 | Impact of sequence parameters on PT and SG signals

The average background velocity decreased as the number of readouts acquired per interleave was increased (Table 2). Accordingly, the corresponding decrease in SG sampling frequency led to progressively worse estimations of heartbeat interval duration and trigger jitter. Conversely, the

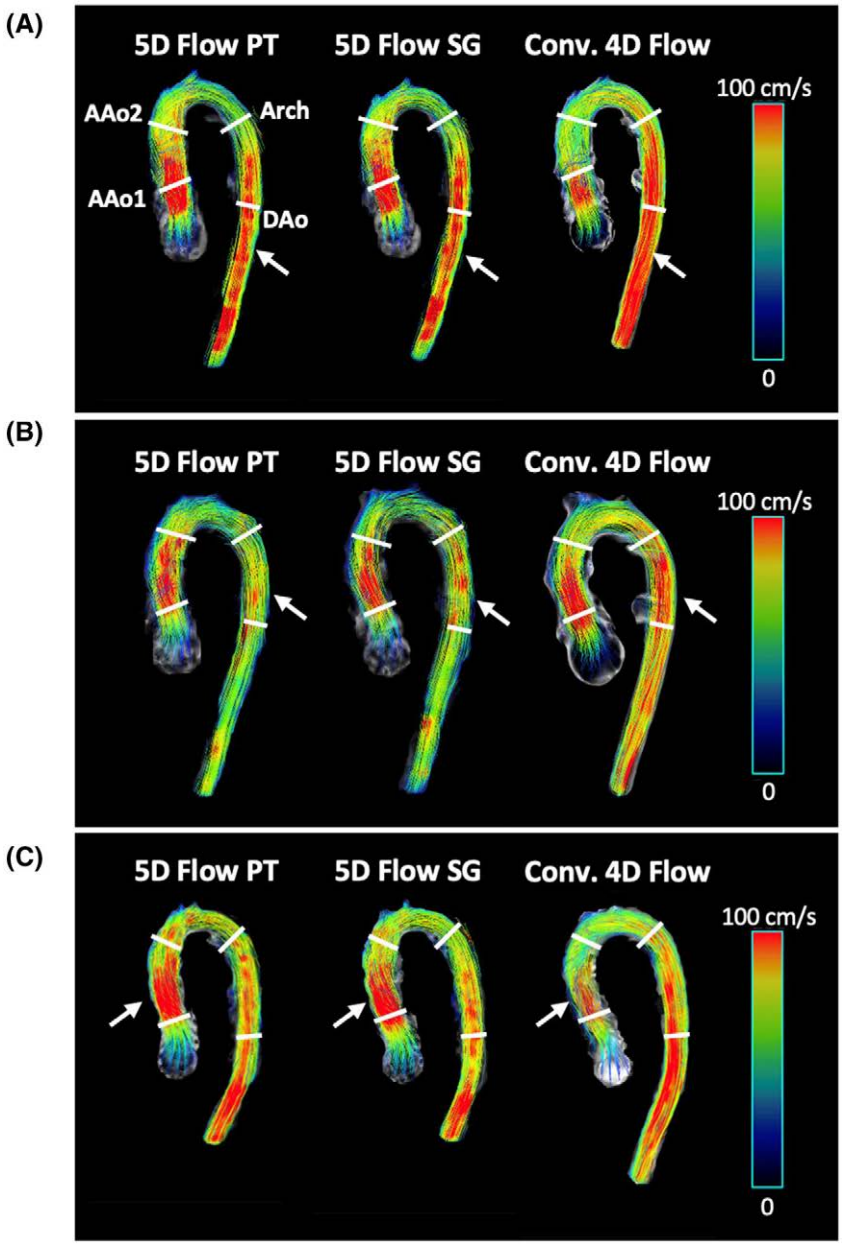

FIGURE 4 Flow streamlines in the aorta. Flow streamlines are displayed for 2 representative healthy volunteers (A-B) and 1 representative patient (C). Four 2D segments (ascending aorta: AAo1, ascending aorta pre-aortic arch: AAo2, end of aortic arch: Arch, and descending aorta: DAo) were drawn for each of the flow datasets (5D flow PT, 5D flow SG, and conventional 4D flow). The velocity streamlines depicted in A correspond to the subject whose respiratory motion had the highest correlation between PT and SG (see Figure 2A), whereas the subject depicted in B is the subject showing the lowest respiratory signal correlation between PT and SG (see Figure 2B). White arrows in the figure denote for each subject 1 location in the aorta where both 5D flow reconstructions show similar streamline patterns while differing from the reference 4D flow. AAo1, aortic root; AAo2, aortic arch; DAo, descending aorta

sampling rate of PT remained constant for each configuration of k-space sampling.

4 | DISCUSSION

In this study, PT-based estimation of physiological motion was successfully integrated into the 5D flow framework. With this approach, the extraction of respiratory curve and cardiac triggers, as well as the subsequent flow quantification, were shown to provide equivalent results to the previously described SG framework. Furthermore, we demonstrated both the sensitivity of SG and the insensitivity of PT to changes in the data acquisition, thus highlighting the potential of using PT to further optimize radial 5D flow acquisitions or free-running whole-heart imaging in general.

This study details the first use of PT for fully self-gated whole-heart imaging, as well as the first comparison between PT and an established SG protocol for both respiratory curve and cardiac trigger extraction. We demonstrated that PT could be successfully applied to both a cohort of healthy individuals and a cohort of CHD patients.

Both PT and SG have been previously individually validated as respiratory-tracking sources.[14,26,27] Consequently, we observed a significantly strong positive correlation between PT and SG respiratory curves, as well as no statistically significant differences in liver displacement measurements. Still, the binning distribution variability in the 2 methods suggests there are small differences stemming

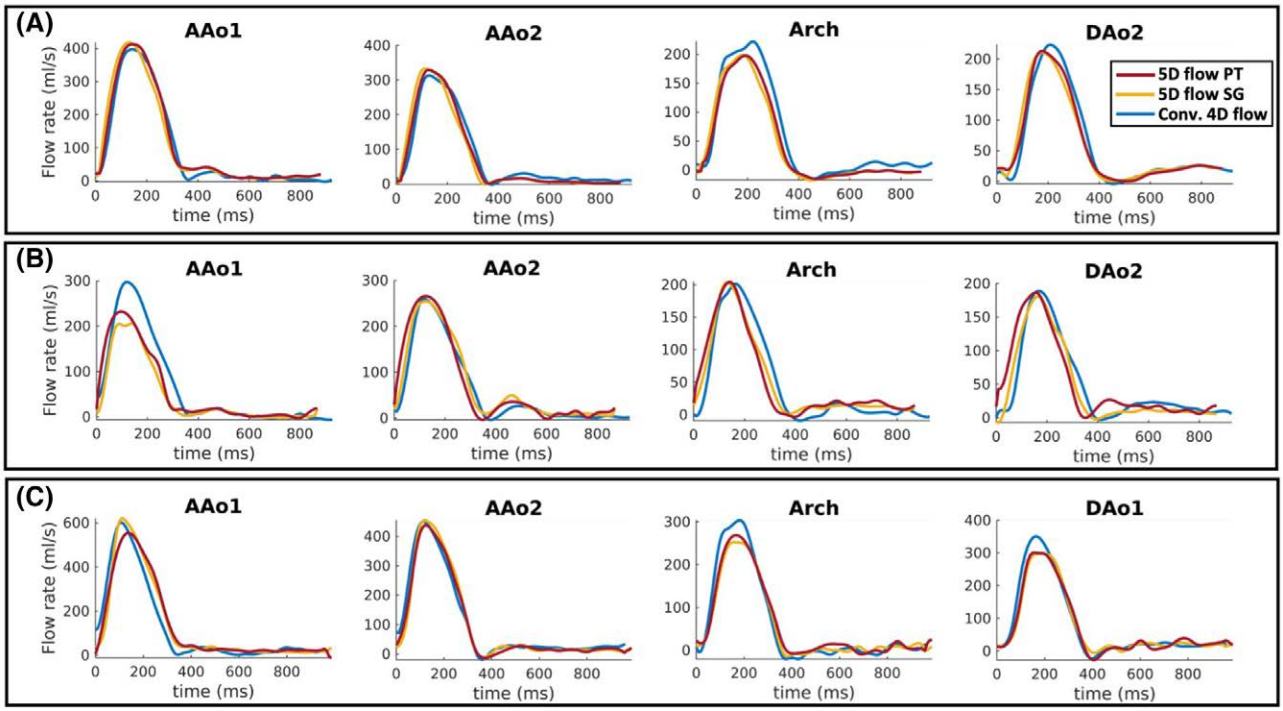

FIGURE 5 Comparison of aortic blood flow measurements in 3 representative subjects. Flow rate curves for 2 healthy volunteers (A-B) and 1 patient (C) are shown for 4 regions of interest (ascending aorta: AAo1, ascending aorta pre-aortic arch: AAo2, end of aortic arch: Arch, and descending aorta: DAo), using 5D flow PT, 5D flow SG, and conventional 4D flow. The flow rate curves depicted in A correspond to the subject whose respiratory motion had the highest correlation between PT and SG (see Figure 2A), whereas the subject depicted in B is the subject showing the lowest respiratory signal correlation between PT and SG (see Figure 2B)

from the ways in which PT and SG are sensitive to motion. In fact, SG extracts motion from the imaging volume,[26] and the modulation of the PT is caused by eddy current variations in moving tissues.[17] Furthermore, the sampling frequencies of the 2 signals are different, as well as the number of data points used for each time sample. The described differences between SG and PT may emphasize some of the disparities obtained after extracting each respiratory curve and cardiac triggers, as discussed below. However, these small differences did not yield any significant quantitative differences for the flow measurements in this work. Furthermore, the reported binning differences appear to be correlated to the range of amplitudes assigned to each respiratory bin, that is, that bins with narrower amplitude ranges (such as end-expiratory bins) will naturally have fewer overlapping readouts between PT and SG and more matches across the neighboring bins. Therefore, larger binning differences are found in readouts that have similar estimated respiratory amplitudes and as a result cause low motion blur if misplaced.

Prior to comparing the PT and SG cardiac triggers, ECG signal quality assessment revealed a failure to accurately record ECG signals during the 5D flow acquisition in 2 healthy subjects. This may have been caused by inadequate electrode placement, the subject's physiological features, or by the magnetohydrodynamic effect, as previously reported.[18,28] Regardless of the cause, this further demonstrates the importance of alternative cardiac gating options for the current 5D flow framework. For the remainder of the subjects, quantitative analysis of cardiac triggers derived from PT and SG showed good agreement with ECG. The heartbeat interval duration measurements showed significant correlation values to ECG, and no significant bias was reported in the trigger jitter measurements between SG versus ECG and PT versus ECG. Additionally, the reported trigger jitter measurements were lower than the temporal resolution; therefore, in the worst-case scenario, any misplaced bin was only shifted into its neighboring cardiac phase. The results obtained in this comparative analysis clearly show that the integration of PT into the 5D flow sequence presents similar performance to the SG framework. In fact, when looking at the trigger jitter results, we can see a small (and nonsignificant) improvement in jitter measurements for PT when comparing to SG, which could be related to the sharper trigger detection mechanism chosen for PT, as well as to the increased sampling frequency used. Still, the features used for triggering in both the PT and SG pipelines are expected to be less well-defined than the established R-wave peak used in ECG triggering. Further understanding of the link between the PT signal and its underlying cardiac physiology may help provide additional improvements to

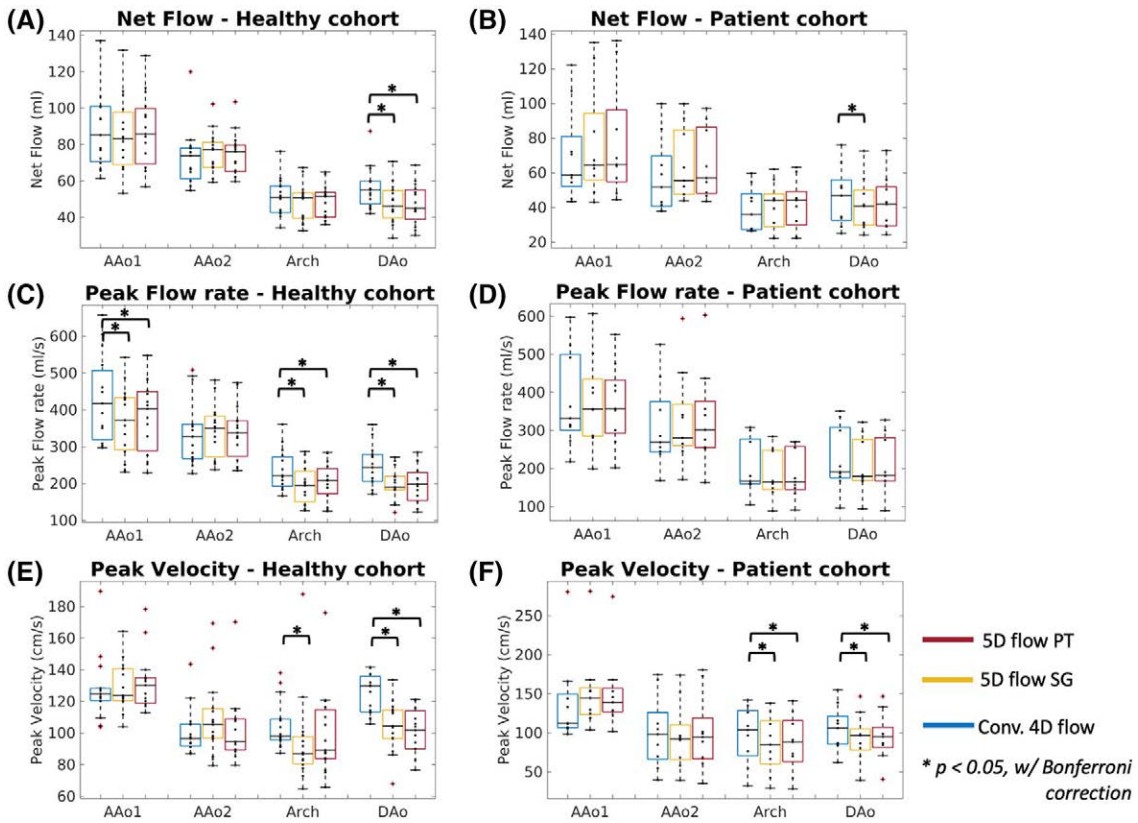

FIGURE 6 Quantitative evaluation of flow metrics from 15 healthy volunteers and 9 congenital heart disease patients. Net flow (A,B), peak flow rate (C,D), and peak velocity (E,F) measurements from 5D flow PT, 5D flow SG, and 4D flow for the healthy cohort (A,C,E) and patient cohort (B,D,F). No significant differences are reported between the 5D flow PT and 5D flow SG flow measurements for either the healthy or patient cohorts. Both 5D flow PT and 5D flow SG reported significant differences in the flow measurements when compared to 4D flow in both cohorts of the study (main differences in Arch and DAo). Interquartile range is drawn by the box limits; black lines correspond to the sample median; the box whiskers delineate 99.3% coverage assuming a Gaussian distribution of the data; and outliers are marked with a red cross. AAo1: ascending aorta, AAo2: ascending aorta pre-aortic arch, Arch: end of aortic arch, DAo: descending aorta. *$P < .05$

the current framework. Of note, when varying the trajectory architecture setup, PT trigger jitter remained constant relative to decreasing SG performance, which further highlights the potential advantages of PT.

Blood flow measurements derived from 5D flow PT, 5D flow SG, and 4D flow datasets were successfully performed in all 15 healthy subjects and 9 patients with CHD. When comparing 5D flow PT to 5D flow SG, no statistically significant bias was found in their respective net flow and peak flow rate measurements across the 4 examined regions of interest. The peak flow measurements did show a relatively large SD, which may be attributed to the inherent sensitivity to noise relative to the average flow rate. When comparing both methods used for 5D flow image reconstruction to 4D flow datasets, consistent underestimations were observed at the aortic isthmus and the descending aorta. Such discrepancies in flow measurements have been previously reported for 5D flow SG, both in vitro and in vivo.[9]

Phase wraps were reported in a small amount of 5D flow and 4D flow reconstructions, possibly caused by uncorrected aliasing or — in the case of 5D flow datasets — by regularization effects from the compressed sensing reconstruction, as well as possibly the existence of noisy voxels at the edge of the aortic segmentation. However, for a given subject, phase wraps were present in both the PT and SG reconstructions of the same data and therefore did not impact the quantitative comparison of flow measurements.

The radial phyllotaxis sampling trajectory employed in this work has been extensively used for structural and functional imaging[18] but has only recently been applied to flow-sensitive imaging.[9] As such, the sampling scheme that is required to ensure adequate sampling of the SI readout for SG may be adversely affecting the sensitivity to flow by introducing unintended artifacts and effect the background phase. This problem, however, is not unique to our design because other respiratory and cardiac-resolved 3D anatomical phase contrast protocols implemented by other research groups[8,10,11,29,30] are also dependent on self-gating information to extract physiological information and therefore have limited trajectory options for sampling.

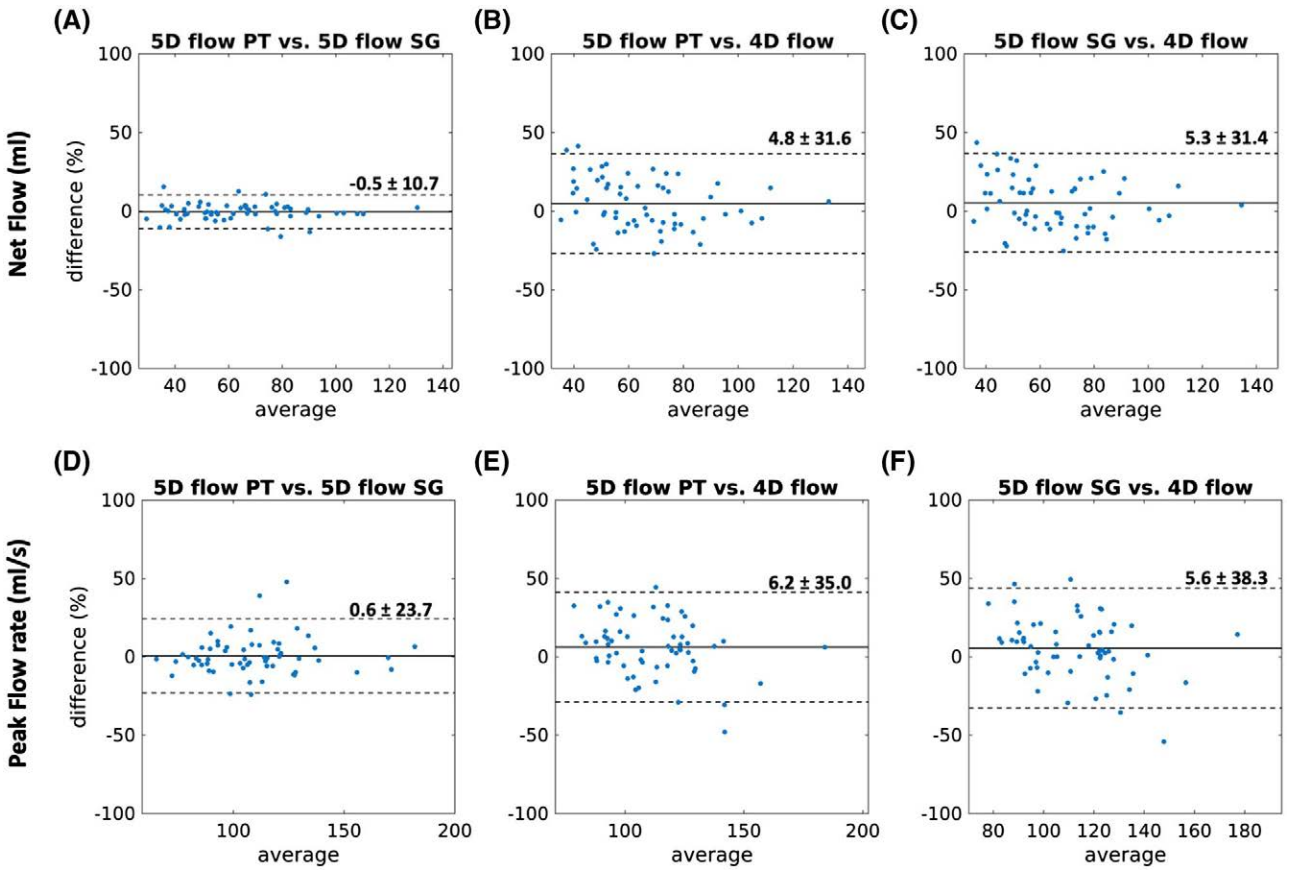

FIGURE 7 Bland-Altman plots of average net flow (A-C) and peak flow rate (D-F), between 5D flow PT versus 5D flow SG (A,D), 5D flow PT versus 4D flow (B,E), and 5D flow SG versus 4D flow (C,F). Biases reported for each comparison showed a low variability between 5D flow PT and 5D flow SG

In this study, we briefly investigated the issue by varying the number of readouts acquired per interleave but keeping the total number of readouts constant (Table 2). This experiment demonstrated, albeit in 1 subject, that by increasing the number of readouts per interleave, we can in fact decrease the background velocity error at the expense of SG cardiac trigger accuracy but without affecting the quality of PT signals. Therefore, PT allows us to decouple the trajectory design from the signal gating methodology and therefore enables the study of different trajectory designs that, for example, would allow for smaller jumps in k-space and reduce the effect of eddy currents and trajectory related artifacts. Additionally, using the protocol described in this work, the removal of the SI projection required for SG would lead to a ~5% reduction in scan time. Future work should continue to investigate such optimizations and their effect on flow measurements.

The current study was limited by the acquisition time of the conventional 4D flow sequence, which precluded whole-heart coverage and constrained us to quantitative comparison of flow in the aorta. Nevertheless, the 5D flow framework had already been validated for whole-heart coverage[9]; thus, our flow analysis on the aorta still provided us with a thorough comparison of PT and SG. Additionally, the lack of an independent ground truth measurement for respiratory motion limited our ability to assess the true accuracy of PT and SG respiratory curves. As a result, we were only able to perform a relative comparison between the 2 signal sources and to evaluate the similarities and differences between them. Finally, an upgrade to the PT system during the course of our study resulted in an increased sampling frequency for the PT signals. This improved system was not available during volunteer and patient scanning but was used to interrogate the impact of sequence parameters on PT and SG signals. Investigating the potential advantages of the increased PT sampling frequency and its impact on respiratory curves, cardiac triggers, and subsequent flow measurements would be of interest for future work.

5 | CONCLUSION

In this work, the PT navigation system was successfully integrated with the free-running 5D flow framework as a method for extracting respiratory curves and cardiac triggers to use in the framework's reconstruction pipeline, providing

equivalent results to the previously described self-gated 5D flow technique in both healthy subjects and CHD patients. Preliminary results also suggest that, in contrast to self-gating, the PT performance for the extraction of respiratory curves and cardiac triggers may not be affected by the type of radial trajectory chosen for the framework. Therefore, PT may provide new opportunities for trajectory design and sampling schemes in 5D flow MRI with the overarching goal of improving the accuracy of flow measurements in an efficient, predictable, and clinically acceptable scan time.

CONFLICT OF INTEREST

Dr. Matthias Stuber receives nonmonetary research support from Siemens Healthcare (Erlangen, Germany). Dr. Peter Speier and Mario Bacher are employees of Siemens Healthcare (Erlangen, Germany). The other authors have no relevant conflicts of interest to declare.

DATA AVAILABILITY STATEMENT

All datasets used during the current study, as well as all the code used for the study, are available on request to the corresponding author.

ORCID

Mariana B. L. Falcão https://orcid.org/0000-0002-4996-0331
Lorenzo Di Sopra https://orcid.org/0000-0003-3426-9457
Liliana Ma https://orcid.org/0000-0001-8834-8519
Mario Bacher https://orcid.org/0000-0002-5529-3598
Jérôme Yerly https://orcid.org/0000-0003-4347-8613
Peter Speier https://orcid.org/0000-0003-0449-1145
Tobias Rutz https://orcid.org/0000-0001-5899-291X
Milan Prša https://orcid.org/0000-0002-9483-7957
Matthias Stuber https://orcid.org/0000-0001-9843-2028
Christopher W. Roy https://orcid.org/0000-0002-3111-8840

REFERENCES

1. Markl M, Frydrychowicz A, Kozerke S, Hope M, Wieben O. 4D flow MRI. *J Magn Reson Imaging*. 2012;36:1015–1036.
2. Calkoen EE, Roest AAW, Van Der Geest RJ, De Roos A, Westenberg JJM. Cardiovascular function and flow by 4-dimensional magnetic resonance imaging techniques: new applications. *J Thorac Imaging*. 2014;29:185-196.
3. Srichai MB, Lim RP, Wong S, Lee VS. Cardiovascular applications of phase-contrast MRI. *Am J Roentgenol*. 2009;192:662-675.
4. Kramer CM, Barkhausen J, Bucciarelli-Ducci C, Flamm SD, Kim RJ, Nagel E. Standardized cardiovascular magnetic resonance imaging (CMR) protocols: 2020 update. *J Cardiovasc Magn Reson*. 2020;22:17.
5. Dyverfeldt P, Bissell M, Barker AJ, et al. 4D flow cardiovascular magnetic resonance consensus statement. *J Cardiovasc Magn Reson*. 2015;17:72.
6. Pruitt A, Rich A, Liu Y, et al. Fully self-gated whole-heart 4D flow imaging from a five-minute scan. *Magn Reson Med*. 2020;85:1222-1236.
7. Kolbitsch C, Bastkowski R, Schäffter T, et al. Respiratory motion corrected 4D flow using golden radial phase encoding. *Magn Reson Med*. 2020;83:635-644.
8. Cheng JY, Zhang T, Alley MT, et al. Comprehensive multi-dimensional MRI for the simultaneous assessment of cardiopulmonary anatomy and physiology. *Sci Rep*. 2017;7:5330.
9. Ma LE, Yerly J, Piccini D, et al. 5D flow MRI: a fully self-gated, free-running framework for cardiac and respiratory motion—resolved 3D hemodynamics. *Radiol Cardiothorac Imaging*. 2020;2:e200219.
10. Walheim J, Dillinger H, Kozerke S. Multipoint 5D flow cardiovascular magnetic resonance—accelerated cardiac- and respiratory-motion resolved mapping of mean and turbulent velocities. *J Cardiovasc Magn Reson*. 2019;21:42.
11. Bastkowski R, Bindermann R, Brockmeier K, Weiss K. Respiration dependency of caval blood flow in patients with Fontan circulation: quantification using 5D flow MRI. *Radiol Cardiothorac Imaging*. 2019;1:e190005.
12. Schmitt F. The gradient system. In Proceedings of the 10th Annual Meeting of ISMRM, Honolulu, Hawaii, USA, 2013. pp. 477-486.
13. Hidalgo-Tobon SS. Theory of gradient coil design methods for magnetic resonance imaging. *Concepts Magn Reson Part A*. 2010;36A:223-242.
14. Speier P, Fenchel M, Rehner R. PT-Nav: a novel respiratory navigation method for continuous acquisitions based on modulation of a pilot tone in the MR-receiver. In Proceedings of the 32nd Annual Scientific Meeting of ESMRMB, Edinburgh, UK, 2015;129:97-98.
15. Bacher M, Speier P, Bollenbeck J, Fenchel M & Stuber M Pilot tone navigation enables contactless prospective cardiac triggering: initial volunteer results for prospective cine. In Proceedings of the 26th Annual Meeting of ISMRM, Paris, France, 2018. p. 2960.
16. Bacher M, Speier P, Bollenbeck J, Fenchel M, Stuber M. Model-based lag free processing of pilot tone navigator data enables prospective cardiac triggering. In Proceedings of the 26th Annual Meeting of ISMRM, Paris, France, 2018. p. 4913.
17. Vahle T, Bacher M, Rigie D, et al. Respiratory motion detection and correction for MR using the pilot tone: applications for MR and simultaneous PET/MR examinations. *Invest Radiol*. 2020;55:153-159.
18. Di Sopra L, Piccini D, Coppo S, Stuber M, Yerly J. An automated approach to fully self-gated free-running cardiac and respiratory motion-resolved 5D whole-heart MRI. *Magn Reson Med*. 2019;82:2118-2132.
19. Piccini D, Littmann A, Nielles-vallespin S, Zenge MO. Spiral phyllotaxis: the natural way to construct a 3D radial trajectory in MRI. *Magn Reson Med*. 2011;66:1049-1056.
20. Draper BA, Baek K, Bartlett MS, Beveridge JR. Recognizing faces with PCA and ICA. *Comput Vis Image Underst*. 2003;91:115-137.
21. Hyvarinen A. Family of fixed-point algorithms for independent component analysis. IEEE International Conference on Acoustics, Speech, and Signal Processing, 1997;5:3917-3920.
22. Feng LI, Coppo S, Piccini D, et al. 5D whole-heart sparse MRI. *Magn Reson Med*. 2017;79:826-838.
23. Feng L, Axel L, Chandarana H, Block KT, Sodickson DK, Otazo R. XD-GRASP: golden-angle radial MRI with reconstruction of extra motion-state dimensions using compressed sensing. *Magn Reson Med*. 2016;75:775-788.

24. Roy CW, Heerfordt J, Piccini D, et al. Motion compensated whole-heart coronary magnetic resonance angiography using focused navigation (fNAV). *J Cardiovasc Magn Reson*. 2021;23:33.
25. Modat M, Ridgway GR, Taylor ZA, et al. Fast free-form deformation using graphics processing units. *Comput Methods Programs Biomed*. 2010;98:278-284.
26. Coppo S, Piccini D, Bonanno G, et al. Free-running 4D whole-heart self-navigated golden angle MRI: initial results. *Magn Reson Med*. 2015;74:1306-1316.
27. Piccini D, Feng LI, Bonanno G, et al. Four-dimensional respiratory motion-resolved whole heart coronary MR angiography. *Magn Reson Med*. 2017;77:1473-1484.
28. Fischer SE, Wickline SA, Lorenz CH. Novel real-time R-wave detection algorithm based on the vectorcardiogram for accurate gated magnetic resonance acquisitions. *Magn Reson Med*. 1999;42:361-370.
29. Bastkowski R, Weiss K, Maintz D, Giese D. Self-gated golden-angle spiral 4D flow MRI. *Magn Reson Med*. 2018;80:904-913.
30. Rutkowski DR, Barton G, François CJ, Bartlett HL, Anagnostopoulos PV, Roldán-Alzate A. Analysis of cavopulmonary and cardiac flow characteristics in Fontan patients: comparison with healthy volunteers. *J Magn Reson Imaging*. 2019;49:1786-1799.

SUPPORTING INFORMATION

Additional Supporting Information may be found in the online version of the article at the publisher's website.

FIGURE S1 Power spectral density (PSD) of self-gating and Pilot Tone and the influence of trajectory dependent imperfections. For a set of representative raw self-gating signals, it is possible to visualize a high-amplitude frequency component (A.) overlapping with the cardiac frequency range of the signal (0.7-3Hz). After correcting the signals for trajectory-related imperfections, the high-amplitude frequency component disappears from the signal spectrum (B.). Conversely, this peak is not observed in the raw Pilot Tone data (C.), and therefore there is no need for trajectory-related corrections

FIGURE S2 Comparison between 5D flow PT and 5D flow SG reconstructions for one sagittal slice in peak systole during end-expiration. Columns depict (from left to right) the 5D flow PT reconstructed dataset, the 5D flow SG reconstructed dataset and the percent difference between the two datasets. Rows depict (from top to bottom) Magnitude images, velocity images in the y direction, velocity images in the x direction, and velocity images in the z direction

TABLE S1 List of all congenital heart disease patients included in this study and their corresponding clinical conditions

How to cite this article: Falcão MBL, Di Sopra L, Ma L, et al. Pilot tone navigation for respiratory and cardiac motion-resolved free-running 5D flow MRI. *Magn Reson Med*. 2021;00:1–15. doi:10.1002/mrm.29023

2.4. Conclusions and Outlook of this work

The successful integration of the Pilot Tone Navigation system within the free-running PC-MRI framework provides the benefits of self-gating (imaging without ECG placement or diaphragmatic navigators) but in a way that is independent of the underlying sequence parameters. This in turn motivates the investigation of alternative k-space trajectories in the interest of improving the quantification of flow measurements and reducing scanning time, without the constraints imposed by periodically sampling data points for self-gating. While the work presented in this chapter has demonstrated the utility of Pilot Tone for flow imaging, its broader application to other free-running techniques, with variations in contrast and sampling regimes, is currently being investigated.

For instance, in Chapter 4, Pilot Tone empowered the successful synchronization of two sequentially acquired sequences, one anatomical free-running sequence and one free-running PC-MRI sequence. The use of this synchronization technique, named SyNAPS led to the development of a comprehensive "anatomy + flow" multidimensional dataset that improved the quantification of flow measurements without the need for injection of contrast agents. This work was awarded a Suma Cum Laude Merit Award at the 30th ISMRM Annual Meeting in 2022 with an abstract entitled "*Free-running 3D anatomical and flow MRI using Synchronization of Neighboring Acquisitions by Physiological Signals (SyNAPS)*". The corresponding scientific manuscript is shown in Chapter 4 and is currently under internal review to be soon submitted to a peer-reviewed academic journal in the field.

Pilot Tone has since then been integrated into a free-running multi-echo GRE framework to acquire respiratory and cardiac-resolved fat-water quantification of the heart, because it can provide a sequence-independent highly sampled detection of the motion, while self-gating would underperform due to the need to acquire 8 echoes within the same readout. This work was presented at the ISMRM & SMRT Annual Meeting & Exhibition in 2021, by Adèle LC Mackowiak with the title "*Whole-Heart Motion-Resolved Multi-Peak Fat-Fraction Mapping using Free-Running 3D Radial Multi-Echo GRE and Pilot Tone*", where it received a Magna Cum Laude Merit Award. Additionally, the work is currently being peer-reviewed in a relevant scientific journal in the field, by the same first author, with title "*Whole-heart motion-resolved multi-peak fat-fraction mapping using Free-Running 3D radial Multi-Echo GRE and Pilot Tone*".

Under the same topic, Pilot Tone has also been used to obtain respiratory-resolved fat-water quantification of the liver using the free-running multi-echo GRE framework. This work has also been presented by Adèle L.C. Mackowiak at the Joint ISMRM-ESMRMB Annual Meeting in 2022, with title "*Pilot Tone-guided focused navigation for free-breathing whole-liver fat-water quantification*".

For whole-heart T2 mapping, Simone Rumac was able to demonstrate the benefits of performing respiratory and cardiac signal extraction using Pilot Tone, while using self-gating in this context is practically inconceivable, due to the wide range of image contrasts required to perform T2 mapping. This work was shown in an abstract presented at the Joint ISMRM-ESMRMB Annual Meeting in 2022, with a study entitled "*Free-running isotropic whole-heart T2 mapping with ECG-free Pilot Tone navigation".*

Chapter 3.
Focused Navigation for respiratory-motion corrected free-running radial 4D flow MRI

3.1. Overview

Conventional 4D flow MRI uses prospective respiratory navigation to limit data collection to the end-expiratory respiratory phase. However, as mentioned before, this option often leads to unpredictable scan times and does not take advantage of information throughout the entire respiratory cycle. In order to acquire PC-MRI throughout the respiratory cycle, additional respiratory compensation tools are needed to ensure reliability of flow measurement quantification and overall good visualization of the vessels of interest.

In this study, we integrated a respiratory motion correction technique, named focused navigation (fNAV), to correct free-running PC-MRI datasets and enable a 4D flow reconstruction. We validated the motion corrected 4D flow dataset against state-of-the art flow imaging techniques and tested the hypotheses that fNAV can estimate and correct motion of the heart due to respiration.

The use of fNAV to collapse the respiratory dimension in free-running 4D flow datasets produces individual 4D flow volumes that contain overall more imaging samples that when reconstructing 5D flow volumes, which increases the image quality of the obtained images, and could eventually be a helpful tool to further optimize the free-running sequence, accelerate it, and/or to increase its spatial resolution.

3.2. Personal contribution

In this study, I was the primary investigator, and together with the last author, Dr. Christopher W. Roy, PhD, we integrated the fNAV correction framework into the free-running PC-MRI reconstruction framework to estimate respiratory displacements from self-gated respiratory signals. Together with Dr. Christopher W. Roy, we defined the study pipeline and the hypothesis we wanted to test. I performed the entire data analysis and followed the patient

acquisitions over time. All the remaining authors were valuable contributions in advising and/or providing patient data.

3.3. Article Peer-Reviewed

The study described in this section has been initially presented at the 31st ISMRM International meeting in 2021 with the title "*Correcting vs resolving respiratory motion in accelerated free-running whole-heart radial flow MRI using focused navigation (fNAV)*" (Supplementary Information A3.3), where it received a Magna Cum Laude Award (top 10%). It has since then been peer-reviewed and accepted at the Journal of Magnetic Resonance in Medicine in February 2023, with the title "*Focused Navigation for respiratory-motion corrected free-running radial 4D flow MRI*".

Received: 25 August 2022 | Revised: 21 February 2023 | Accepted: 21 February 2023

DOI: 10.1002/mrm.29634

RESEARCH ARTICLE

Magnetic Resonance in Medicine

Focused navigation for respiratory–motion-corrected free-running radial 4D flow MRI

Mariana B. L. Falcão[1] | Giulia M. C. Rossi[1] | Tobias Rutz[2] | Milan Prša[3] | Estelle Tenisch[1] | Liliana Ma[4,5] | Elizabeth K. Weiss[4,5] | Justin J. Baraboo[4,5] | Jérôme Yerly[1,6] | Michael Markl[4,5] | Matthias Stuber[1,6] | Christopher W. Roy[1]

[1]Department of Diagnostic and Interventional Radiology, Lausanne University Hospital (CHUV) and University of Lausanne (UNIL), Lausanne, Switzerland

[2]Service of Cardiology, Centre de Resonance Magnétique Cardiaque (CRMC), Lausanne University Hospital and University of Lausanne, Lausanne, Switzerland

[3]Woman-Mother-Child Department, Lausanne University Hospital and University of Lausanne, Lausanne, Switzerland

[4]Department of Radiology, Feinberg School of Medicine, Northwestern University, Chicago, Illinois USA

[5]Department of Biomedical Engineering, Northwestern University, Chicago, Illinois USA

[6] Center for Biomedical Imaging (CIBM), Lausanne, Switzerland

Correspondence
Christopher W. Roy, Lausanne University Hospital (CHUV), Rue de Bugnon 46, BH-7-84, 1011, Lausanne, Switzerland.
Email: christopher.roy@chuv.ch

Funding information
National Institutes of Health, Grant/Award Number: T32EB025766; Swiss National Science Foundation, Grant/Award Numbers: 173129, 201292, PZ00P3_202140

Purpose: To validate a respiratory motion correction method called focused navigation (fNAV) for free-running radial whole-heart 4D flow MRI.

Methods: Using fNAV, respiratory signals derived from radial readouts are converted into three orthogonal displacements, which are then used to correct respiratory motion in 4D flow datasets. Hundred 4D flow acquisitions were simulated with non-rigid respiratory motion and used for validation. The difference between generated and fNAV displacement coefficients was calculated. Vessel area and flow measurements from 4D flow reconstructions with (fNAV) and without (uncorrected) motion correction were compared to the motion-free ground-truth. In 25 patients, the same measurements were compared between fNAV 4D flow, 2D flow, navigator-gated Cartesian 4D flow, and uncorrected 4D flow datasets.

Results: For simulated data, the average difference between generated and fNAV displacement coefficients was 0.04 ± 0.32 mm and 0.31 ± 0.35 mm in the x and y directions, respectively. In the z direction, this difference was region-dependent (0.02 ± 0.51 mm up to 5.85 ± 3.41 mm). For all measurements (vessel area, net volume, and peak flow), the average difference from ground truth was higher for uncorrected 4D flow datasets (0.32 ± 0.11 cm^2, 11.1 ± 3.5 mL, and 22.3 ± 6.0 mL/s) than for fNAV 4D flow datasets (0.10 ± 0.03 cm^2, 2.6 ± 0.7 mL, and 5.1 ±0.9 mL/s, $p < 0.05$). In vivo, average vessel area measurements were 4.92 ± 2.95 cm^2, 5.06 ± 2.64 cm^2, 4.87 ± 2.57 cm^2, 4.87 ± 2.69 cm^2, for 2D flow and fNAV, navigator-gated and uncorrected 4D flow datasets, respectively. In the ascending aorta, all 4D flow datasets except for the fNAV reconstruction had significantly different vessel area measurements from 2D flow. Overall, 2D flow datasets demonstrated the strongest correlation to fNAV 4D flow for both net volume ($r^2 = 0.92$) and peak flow ($r^2 = 0.94$), followed by navigator-gated 4D flow ($r^2 = 0.83$ and $r^2 = 0.86$, respectively), and uncorrected 4D flow ($r^2 = 0.69$ and $r^2 = 0.86$, respectively).

Conclusion: fNAV corrected respiratory motion in vitro and in vivo, resulting in fNAV 4D flow measurements that are comparable to those derived from 2D flow and navigator-gated Cartesian 4D flow datasets, with improvements over those from uncorrected 4D flow.

KEYWORDS
4D flow MRI, fNAV, focused navigation, free-running 3D radial PC-MRI, motion correction

1 | INTRODUCTION

Three-dimensional phase-contrast (PC) MRI or "4D flow MRI" permits a quantitative evaluation of blood flowing throughout the heart and vessels.[1–5] Increasingly, 4D flow MRI is used in the clinical assessment of heart disease,[6–8] but despite advances in 4D flow imaging,[9–18] the achievable volumetric coverage, ease-of-use, and acquisition time remain largely constrained by the need to compensate for respiratory motion. Conventional 4D flow acquisitions use a Cartesian sampling trajectory and a 1D navigator echo, prescribed along the lung liver interface, to limit data collection to a manually defined acceptance window during the end-expiratory respiratory phase.[19,20] Therefore, acquisition efficiency is highly driven by the breathing pattern of each patient, leading to unpredictable scan times. In practice, 4D flow MRI can be acquired without navigators and throughout the respiratory cycle to improve efficiency or reduce scan times, but without additional respiratory compensation there will be a decrease in the accuracy of flow measurements and overall visualization of the vessels of interest.[21,22]

Recently, a respiratory-motion correction technique called focused navigation (fNAV), which estimates displacement from the data itself without the need for additional hardware, was developed for electrocardiogram (ECG)-triggered radial whole-heart cardiac magnetic resonance angiography (CMRA).[23] Using fNAV, a 1D respiratory signal derived from a periodically sampled readout is converted into respiratory displacement measurements that span the entire acquisition along all three spatial dimensions using an auto-focusing algorithm.[24,25] In this way, data can be used from the entire respiratory cycle while minimizing motion related artifacts, therefore, providing a more efficient acquisition and reconstruction of free-breathing data when compared to the conventional 1D navigator approach.

The goal of this work is to extend the fNAV methodology to a free-running 3D radial whole-heart PC-MRI acquisition.[10,26–28] The use of fNAV for respiratory motion correction presents several potential advantages for free-running 3D radial PC-MRI. First, it does not require any additional scans to calibrate respiratory displacement.[29] Second, it is capable of correcting motion for each individual readout, which generally cannot be done using motion correction methods that must first bin the data into respiratory phases.[30] Finally, the 1D respiratory signal is readily derived from the radial imaging data itself and therefore, does not require significant modification[17] or interruption[31] of the imaging sequence to produce navigator data.

In this work, we adapted the fNAV methodology for use in the reconstruction of free-running 3D radial PC-MRI data, resulting in 4D flow images, hereafter, referred to as fNAV 4D flow datasets. We performed a comprehensive validation study in a numerical simulation based on data from a programmable pulsatile flow phantom, wherein displacement due to respiratory motion was simulated retrospectively. We, then, demonstrated the feasibility of this approach in a diverse cohort of patients with congenital heart disease (CHD). We tested the hypotheses that, first, fNAV can estimate and correct for the translational displacement of the heart because of respiration, and second, that fNAV 4D flow datasets produce comparable flow measurements to those from separately acquired reference standard 2D flow datasets and with a reduction in bias when compared to those derived from 4D flow datasets reconstructed without motion correction. We compared the vessel area, net volume, and peak flow measurements from fNAV 4D flow datasets to those from uncorrected 4D flow reconstructions of the same data, as well as to conventional navigator-gated Cartesian 4D flow MRI and to reference standard 2D flow MRI.

2 | METHODS

2.1 | fNAV 4D flow framework

A schematic overview of the proposed pipeline for the reconstruction of fNAV 4D flow datasets is shown in Figure 1. Free-running 3D radial PC-MRI data were acquired (Figure 1A) as previously described,[27] wherein readouts followed a spiral phyllotaxis sampling pattern with each interleave rotated by the golden angle relative to the previous one.[32–34] At the beginning of each interleave, one readout oriented along the superior–inferior (SI) direction was acquired for subsequent extraction of respiratory and cardiac self-gating signals (Figure 1B).[28,34] The SI readout is only acquired for one velocity encode, whereas the imaging readouts were repeated four times for balanced four-point velocity encoding.[27,28]

To reconstruct the acquired data, the fNAV framework, previously developed for ECG-triggered 3D radial CMRA, was adapted for free-running 3D radial PC-MRI with the following four steps. First, a unitless respiratory curve was extracted from the concatenated SI readouts using principal component analysis.[28,34] Second, the respiratory-dependent displacement of the heart in millimeters was modeled along all three spatial dimensions, by multiplying the extracted respiratory curve with three fNAV coefficients describing the maximum amplitude of respiratory motion in three orthogonal directions (A_x, A_y, A_z).

The goal of fNAV is to find the optimal coefficients (A_x, A_y, A_z) that best represent the displacement in each

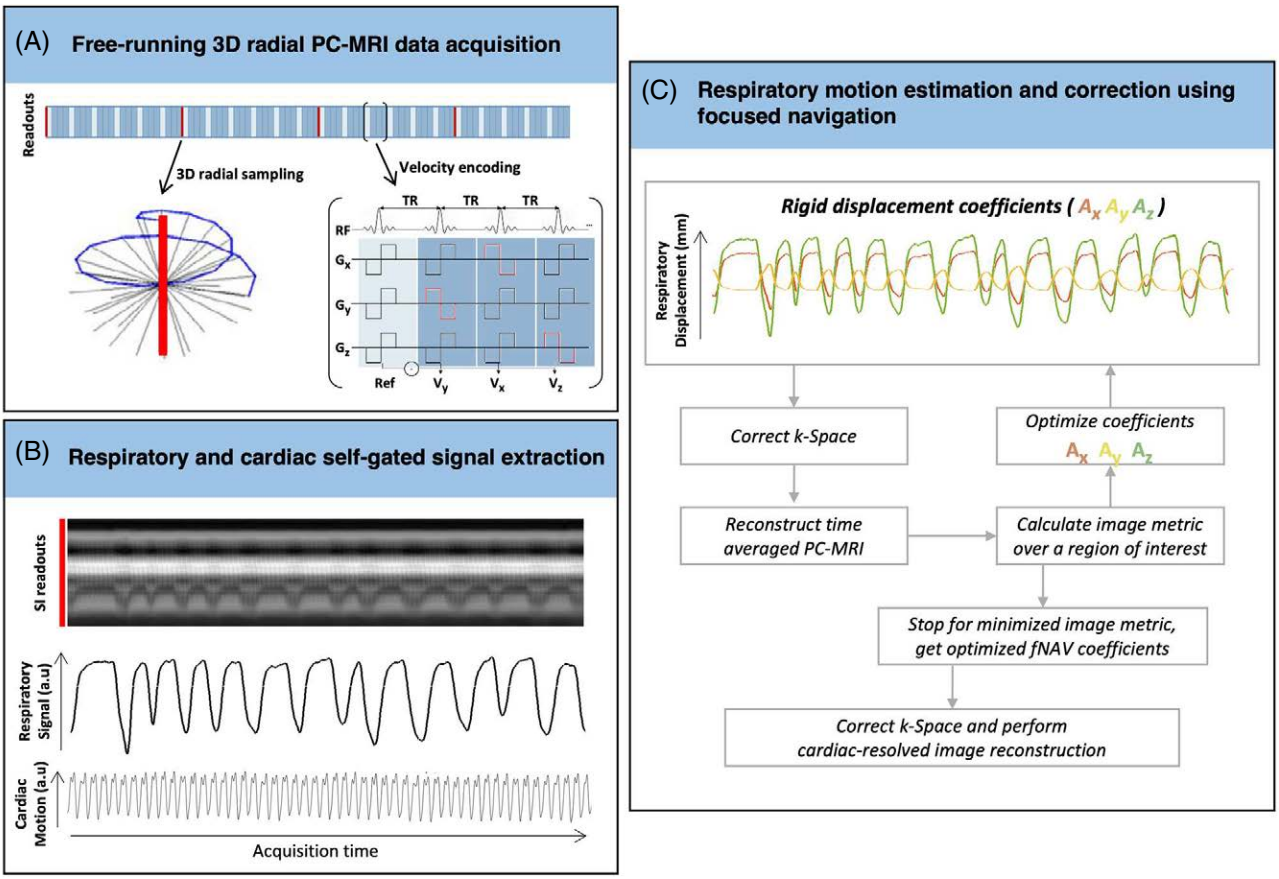

FIGURE 1 Summary of the focused navigation (fNAV) 4D flow pipeline. (A) From continuously acquired free-running 3D radial phase-contrast (PC)-MRI data, (B) respiratory and cardiac motion signals are extracted using self-gating. (C) Using the 1D respiratory self-gating curve, the displacement of the heart because of respiration along all three spatial dimensions was modeled as the product of the respiratory curve and three initially unknown fNAV coefficients (A_x, A_y, A_z). The 3D translational motion determined by the product of the respiratory curve and fNAV coefficients was applied to the acquired k-space. The coefficients were then iteratively adjusted to minimize a metric based on the entropy of the image. The final optimized fNAV coefficients were used to correct the k-space data, which was reconstructed using a k-t sparse SENSE algorithm.[47]

dataset. Therefore, in a third step, the fNAV coefficients were iteratively estimated: the product of the respiratory curve and fNAV coefficients was applied as a phase shift to the acquired k-space data (Figure 1C), an intermediate 4D flow dataset with the current translational motion correction was reconstructed using a non-uniform Fourier transform, and a time-averaged phase-contrast magnetic resonance angiogram (PC-MRA) was calculated by multiplying the sum of squares of the magnitude and phase images. Next, a metric for blur (entropy of the gradient image) was calculated over a region of interest (ROI) automatically placed at the approximate center of the heart, by calculating the center of mass of the PC-MRA[23,25] and used to update the coefficients. The phase shifts corresponding to the optimized fNAV coefficients that minimize the image metric were applied to the acquired k-space.

In addition to correcting respiratory motion, cardiac self-gating was used as previously described.[27,28,34] Notably, the uninterrupted gradient echo sequence that the 3D radial PC-MRI sequence is based on has been shown to interfere with the ECG signal and therefore, self-gating has been shown to be more reliable.[35] Finally, a k-t sparse SENSE algorithm[27,28] was used to reconstruct the final fNAV 4D flow images with corrected respiratory motion and resolved cardiac motion (x-y-z-cardiac-velocity dimensions). After first normalizing each acquisition by the maximum signal from a gridded image reconstruction, regularization parameters for reconstructing the fNAV 4D flow datasets were 0.0075 for total variation applied along the cardiac dimension and 0.015 for total variation applied along the spatial dimension.[28]

2.2 | Optimization of fNAV coefficients

The PC-MRA, as described above, was chosen in place of the magnitude images used in the original fNAV study as

it provided separation between the cardiac anatomy and background allowing for an automated ROI selection as described above, and improved detection of rigid translational movement of the heart without being impacted by non-cardiac anatomy. The size of the ROI was empirically chosen to be one third the acquisition field of view (FOV), which in general provided adequate coverage of the heart.

The entropy of the gradient image (H) was chosen as a blur metric based on previous work and is described by the following[23]:

$$H = -\sum_x \sum_y \sum_z p_{xyz} \log_2 \left(p_{xyz}\right),$$

$$p_{xyz} = \frac{g_{xyz}}{\sum_{xyz} g_{xyz}}, \text{and}$$

$$g_{xyz} = \sqrt{|\nabla_x I|^2 + |\nabla_y I|^2 + |\nabla_z I|^2}$$

where (x, y, z) define a 3D region, (p) is the normalized voxel intensity from the gradient (g) of the intermediate image (I), and ∇ is approximated by 1D finite differences.[17,25,36,37] Optimized fNAV coefficients were found using a steepest descent algorithm where the gradient of H as a function of the fNAV coefficients was approximated numerically.[23]

2.3 | Validation using a numerical simulation

2.3.1 | In vitro acquisitions

An MRI-compatible pulsatile flow pump (delivering flow rates of ~250 mL/s) connected to a U-shaped polyvinyl-chloride pipe, representing a simplified aorta model,[38] was scanned on a 1.5 MAGNETOM Aera scanner (Siemens Healthcare, Erlangen, Germany). The U-pipe contained a section with variable diameter to mimic stenosis, and as a result to create non-uniform flow profiles. The cardiac frequency simulated was ~60 cycles per minute (~1 Hz). To simulate a contrast-enhanced flow scan, gadolinium enhanced water was used as fluid. A fully sampled conventional navigator-gated Cartesian 4D flow sequence was acquired with the following scan parameters: TE = 2.3 ms, TR = 5.1 ms, 15° RF excitation angle, FOV = $54 \times 351.5 \times 370\,mm^3$, base resolution = $24 \times 152 \times 160$, isotropic spatial resolution = $(2.3\,mm)^3$, maximum velocity encoded = 150 cm/s, total scan time of 8.1 min.

2.3.2 | Generating simulated data

To mimic the effects of realistic respiratory motion on our phantom data, a non-rigid deformation field was modeled with uniform displacement along the x and y directions, but linearly increasing displacement along the z direction (Figure 2A). Each deformation field was multiplied by a time-varying respiratory curve modeled from a healthy volunteer acquisition with approximate respiratory peak frequency of ~0.15 Hz. We, then, generated simulated 3D radial k-space readouts after applying the deformation field to the in vitro images. The 3D radial k-space readouts were simulated to match the same sampling scheme and undersampling factor from the in vivo acquisitions (4820 spiral interleaves and 21 radial readouts per interleave, see in vivo section). A total of 100 unique variations of the maximum 3D displacement for each direction (A_x: 0–5 mm, A_y: 0–10 mm, A_z: 0–20 mm) were generated using this pipeline, resulting in 100 corresponding simulated "free-breathing" radial 4D flow acquisitions.[23]

2.3.3 | Accuracy of respiratory motion correction

Using the fNAV 4D flow framework described above, a 3D region of interest was manually selected (fNAV region, Figure 2B), and estimated 3D displacements (fNAV coefficients) were obtained for all 100 simulated 4D flow datasets. Four 2D ROIs were manually selected. The error between ground-truth simulated displacement and fNAV coefficients for each ROI was quantified in terms of mean and SD, as well as using linear regression and Pearson correlation measures.

2.3.4 | Influence of respiratory motion

To study the influence of respiratory motion on both image quality and flow quantification, a subset ($n = 20$) of the simulated acquisitions were chosen such that they spanned the range of the previously generated maximum translational displacements and used for 4D flow image reconstruction, both with correction from the estimated fNAV coefficients (fNAV 4D flow) and without motion correction (uncorrected 4D flow). Additionally, the simulated 4D flow data that did not include any displacement because of respiratory motion, was reconstructed and used as the ground-truth reference.[21]

For each of the four ROIs described above, the vessel area was used as a surrogate measure of blur because of

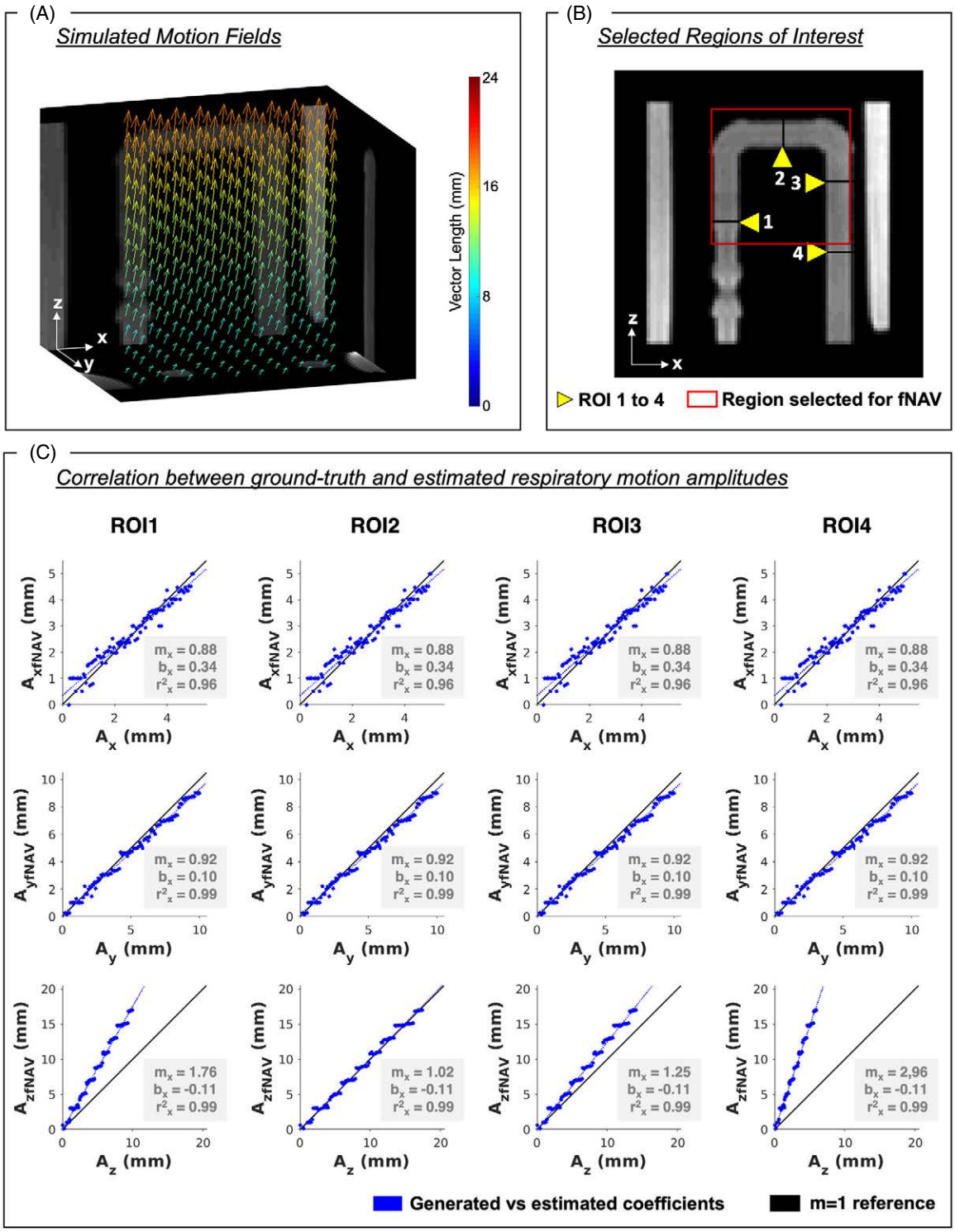

FIGURE 2 Phantom validation of focused navigation (fNAV) for rigid respiratory motion correction. Using the fNAV framework, 3D fNAV coefficients were estimated for each translational displacement of 100 simulated datasets. Vector length describes the 3D direction and amplitude of the voxel-wise motion field. Displacement along the z-direction was simulated to be larger at the top of the phantom and smaller at the bottom. (A) The 3D figure shows the motion fields oriented from top to bottom (B) For four regions of interest (ROI), (C) the correlation between the generated coefficients (A_x, A_y, A_z) and the estimated coefficients (A_{xfNAV}, A_{yfNAV}, A_{zfNAV}) was strong for the three directions of displacement ($r^2 > 0.9$). ROI 3 was the region with the best 1–1 correlation between A_z and A_{zfNAV}, with differences between A_z and A_{zfNAV} increasing with the distance from ROI 3. Yellow arrows point to the ROIs used for this analysis. The red square marks the region chosen for the fNAV correction. The blue lines describe regression lines, and black lines show the identity line. m, slope; b, intercept; ρ, Pearson correlation coefficient.

respiratory motion and was calculated as the sum of all voxels included in the ROI, multiplied by the area of each voxel. The vessel area was calculated for the ground-truth dataset, as well as for all uncorrected and fNAV 4D flow datasets. The mean and SD of the vessel area for each ROI was calculated across the entire range of displacements reconstructed ($n = 20$), for uncorrected and fNAV 4D flow datasets separately. The difference of vessel area from the ground-truth was also compared between the two groups.

For each reconstructed dataset and for each ROI, net volume and peak flow measurements were compared with the ground-truth reference. Mean and SD measures were calculated for each flow measurement and for each ROI. The differences from the ground-truth were calculated for uncorrected and fNAV 4D flow datasets.

2.4 | Feasibility in a cohort of CHD patients

2.4.1 | In vivo acquisitions

A cohort of 25 CHD patients (age, 7–60 years, 12 female) was included in this study (see Table S1 for demographics). Each study participant or their legal guardian provided written informed consent compliant with institutional guidelines. All images were acquired on a 1.5 T Magnetom Sola (Siemens Healthcare, Erlangen, Germany).

Patients underwent a gadolinium-enhanced (Gadobutrol, Bayer, Switzerland, 0.4 mmol/kg) MRI protocol for CHD, that included three standard 2D flow acquisitions placed on the ascending aorta (AAo), descending aorta (DAo), and main pulmonary artery (MPA). Sequence parameters for the 2D flow acquisitions were as follows: TE = 3.0–3.6 ms, TR = 5.25–6.14 ms, 20° RF excitation angle, FOV = (136–234) × (288–340) mm^2, base resolution = (132–136) × (192–288), spatial resolution = (1.0–1.8) × (1.0–1.8) × (4.0–6.0) mm^3, velocity encoding = 150–200 cm/s. Additionally, a standard Cartesian 4D flow acquisition with respiratory navigation (nav-gated 4D flow) was included to obtain a reference 4D flow dataset. Sequence parameters were the following: TE = 2.2–2.3 ms, TR = 4.6–5.1 ms, 7–12° RF excitation angle, FOV = (125–258) × (188–308) × (200–400) mm^3, base resolution = (50–103) × (75–123) × (96–160) isotropic spatial resolution = $(2.1\,mm)^3$–$(2.5\,mm)^3$, maximum velocity encoding = 150–200 cm/s, total scan time of 1.8–11.5 min.

At the end of each clinical exam, a free-running 3D radial PC-MRI sequence (Figure 1A) was acquired. Sequence parameters were as follows: TE = 2.9–3.1 ms, TR = 4.7–4.9 ms, 7° RF excitation angle, FOV = $(220\,mm)^3$–$(240\,mm)^3$, base resolution = $(96)^3$ isotropic spatial resolution = $(2.3\,mm)^3$ – $(2.5\,mm)^3$, maximum velocity encoding = 150–200 cm/s, total scan time of 7.93–8.23 min, 4820 spiral interleaves and 21 radial readouts per interleave (1 SI + [5 readouts × 4-point velocity encoding]). Differences in scan time were because of changes in velocity encoding and FOV.

2.4.2 | Four dimensional flow image reconstruction

Free-running 3D radial PC-MRI acquisitions from all patients were reconstructed into fNAV 4D flow datasets, as described in Figure 1, and into 4D flow datasets without any type of respiratory compensation (uncorrected 4D flow). For fNAV 4D flow, the respiratory motion amplitudes estimated from fNAV were recorded and used for motion correction. Next, to reconstruct fNAV and uncorrected 4D flow datasets, data were binned into 17 to 30 cardiac phases (temporal resolution = 23.8–42.2 ms) and reconstructed using the k-t sparse SENSE algorithm described previously.[27,28] Spatial resolution of the reconstructed datasets matched the acquired spatial resolution, $(2.3\,mm)^3$–$(2.5\,mm)^3$. All reconstructions of fNAV and uncorrected 4D flow datasets were performed in MATLAB (The MathWorks, Natick, MA) and took on average 2.8 ± 0.3 h to reconstruct including 2.5 min for fNAV. The nav-gated 4D flow datasets were reconstructed at the scanner during the examination using the vendor-provided reconstruction pipeline for these datasets. Streamlines derived from fNAV, nav-gated and uncorrected 4D flow datasets were visually compared.

2.4.3 | Comparison of vessel area and flow measurements

The 2D flow and three 4D flow datasets (i.e., fNAV 4D flow, nav-gated 4D flow, and uncorrected 4D flow) were segmented and flow measurements were analyzed using cvi42, Circle (Calgary, AB, Canada). The flow analysis was performed by one observer that was not blinded to the type of data being analyzed. To assess and compare the accuracy of flow measurements from fNAV 4D flow relative to 2D flow and to the remaining 4D flow datasets, vessel planes were manually placed to match the same location of the 2D flow acquisitions covering the AAo, DAo, and MPA. Similarly to in vitro, the

vessel area was used as a surrogate metric for blur because of respiratory motion and was compared between the 2D flow datasets and fNAV, nav-gated, and uncorrected 4D flow datasets. Net volume and peak flow measurements were calculated for every 4D/2D flow dataset. Four dimensional flow measurements (fNAV, nav-gated, and uncorrected) were compared to their analogous 2D flow measurement.

2.5 | Statistical analysis

Each group of measurements was tested for normality using a Lilliefors test. In case of rejection of the null hypothesis at the 5% significance level, measures were compared using a nonparametric Wilcoxon signed rank test. Otherwise, a paired *t* test was used to compare the similarity between datasets. For the patient cohort, differences in net volume and peak flow measurements between 2D flow and 4D flow datasets (fNAV, nav-gated, and uncorrected) were estimated using Bland–Altman analysis. Additionally, the correlation between 2D flow measurements and measurements from all 4D flow datasets was calculated using linear regression and Pearson correlation measures, and the significance level of the correlation was given as a *p*-value, from testing the hypothesis of no correlation.

3 | RESULTS

3.1 | Validation in a pulsatile flow phantom

3.1.1 | Accuracy of respiratory motion correction

The fNAV 4D flow framework was able to estimate displacement because of respiratory motion in all 100 simulated 4D flow acquisitions. The error (mean and SD) in x and y directions was consistent across all four ROIs (A_x–A_{xfNAV} = 0.04 ± 0.32 mm, A_y–A_{yfNAV} = −0.31 ± 0.35 mm) because of the uniform displacement generated in those directions. However, the error in the z direction was greater in ROIs where the true non-rigid displacement diverges from the rigid translational correction provided by fNAV, yielding excellent agreement for ROI 2 (A_z-A_{zfNAV} = 0.02 ± 0.51 mm), followed by increasing average error for ROI 3 (A_z–A_{zfNAV} = 1.71 ± 1.16 mm), ROI 1 (A_z–A_{zfNAV} = 3.78 ± 2.26 mm) and finally ROI 4 (A_z–A_{zfNAV} = 5.85 ± 3.41 mm).

The linear regression measurements calculated between the generated displacements and those estimated by fNAV for the four ROIs corroborates this trend when considering the slope (m), intercept (b), and Pearson correlation coefficient (ρ) respectively along each spatial dimension (Figure 2C).

3.1.2 | Influence of respiratory motion on vessel area

In general, the vessel area for each measured ROI in simulated radial 4D flow data is overestimated (Figure 3B) by uncorrected reconstructions because of motion blur, when compared to the ground-truth reference (Table 1). Conversely, fNAV 4D flow vessel area yielded a better agreement with the ground-truth reference area. This is further demonstrated by the differences in vessel area between uncorrected 4D flow and the ground-truth dataset, which were significantly higher than those measured between the fNAV 4D flow and the ground-truth datasets in all four ROIs (ROI 1: 0.11 ± 0.17 cm^2 vs. 0.04 ± 0.14 cm^2, ROI 2: 0.61 ± 0.43 cm^2 vs. 0.18 ± 0.10 cm^2, ROI 3: 0.15 ± 0.26 cm^2 vs. 0.00 ± 0.09 cm^2, ROI 4: 0.42 ± 0.22 cm^2 vs. 0.18 ± 0.07 cm^2, $p < 0.05$). The average vessel area difference between uncorrected and ground-truth 4D flow datasets (0.32 ± 0.11 cm^2) was significantly different from the average vessel area difference between fNAV and ground-truth 4D flow datasets (0.10 ± 0.03 cm^2, $p < 0.05$).

3.1.3 | Influence of respiratory motion on flow quantification

Overall, simulated datasets with uncorrected respiratory motion resulted in flow measurements that were significantly different from the ground-truth values, whereas fNAV 4D flow datasets showed better agreement with the ground-truth. Still, the quantitative comparison of net volume and peak flow measurements showed different effects of motion across the 4 ROIs (Figure 4, Table 1).

Net volume average differences from the ground-truth were, for uncorrected and fNAV 4D flow datasets, respectively, 11.1 ± 3.5 mL vs. 2.6 ± 0.7 mL. Specifically, for ROI 2 and ROI 3, placed within the fNAV region, the net volume differences from the ground-truth were 22.4 ± 15.4 mL and 2.5 ± 8.3 mL for uncorrected 4D flow and 6.6 ± 3.7 mL and −1.6 ± 2.6 mL for fNAV 4D flow. ROI 1, located at the edge of the fNAV region, reported a net volume difference of 5.1 ± 8.4 mL for uncorrected 4D flow and 0.4 ± 3.8 mL for fNAV 4D flow. Net volume differences from ROI 4 were reduced from 14.3 ± 8.4 mL for uncorrected 4D flow to 5.0 ± 2.4 mL when correcting with fNAV. For

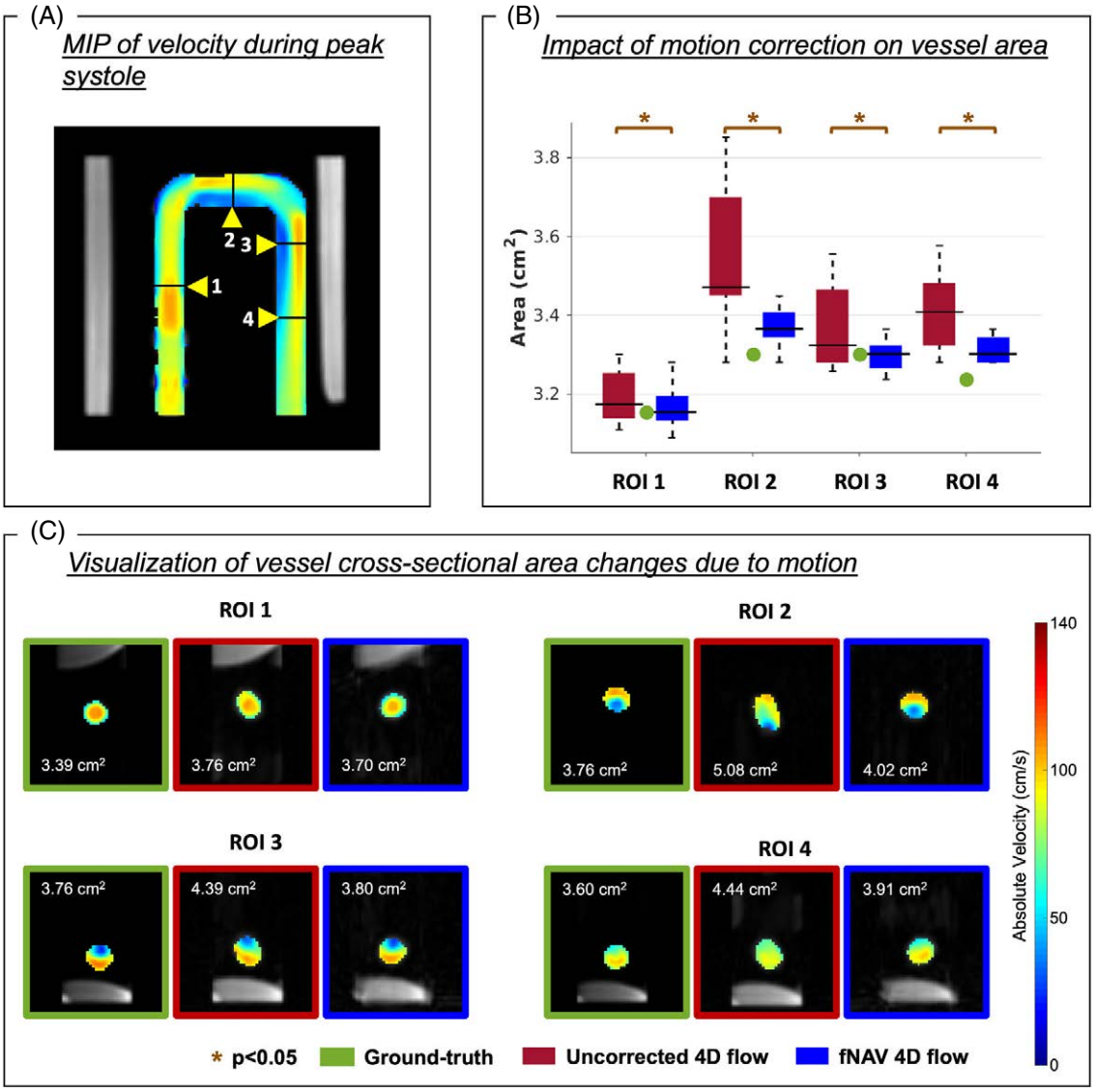

FIGURE 3 Influence of motion on the vessel area for four regions of interest (ROI). (A) Coronal view of the pulsatile flow phantom with the maximum intensity projection (MIP) of the velocity at peak systole shown and the four ROIs marked. (B) After focused navigation (fNAV) correction (blue), the area of each ROI became closer in agreement to the ground-truth ROI area (green), when compared to the uncorrected cases (red). (C) Cross-sectional visualization of the velocity in each ROI at peak systole for one example, showing ground-truth (green), uncorrected 4D flow (red) and fNAV 4D flow (blue) datasets. The area of each cross section is shown at the top left corner of each image. A visible vessel degradation is shown in uncorrected cases. In this example, the largest simulated motion displacement is shown for each ROI. *p*, *p*-value.

peak flow, the same trend was reported (ROI 1: 11.0 ± 18.2 mL/s vs. −0.6 ± 6.9 mL/s; ROI 2: 43.9 ±29.5 mL/s vs. 13.4 ± 7.2 mL/s; ROI 3: 6.6 ± 19.8 mL/s vs. −3.7 ± 5.1 mL/s; ROI 4: 27.6 ±15.7 mL/s vs. 11.2 ± 6.2 mL/s, uncorrected vs. fNAV 4D flow, respectively). The average difference in peak flow measurements was 22.3 ± 6.0 mL/s for uncorrected 4D flow and 5.1 ± 0.9 mL/s for fNAV 4D flow. Overall the average difference in net volume and peak flow measurements was significant between the two comparisons ($p < 0.05$). For individual ROIs, all flow measurements were significantly different between uncorrected and fNAV 4D flow datasets ($p < 0.05$), except in ROI 3 ($p = 0.13$ for net volume and $p = 0.07$ for peak flow).

3.2 | Feasibility in a cohort of CHD patients

3.2.1 | 4D flow image reconstruction

Respiratory motion amplitudes estimated using fNAV were obtained for all patient datasets with a mean

TABLE 1 Mean and SD measurements for vessel area, net volume, and peak flow obtained for each of the four ROIs selected in the phantom.

Measurement	4D flow reconstruction	ROI 1	ROI 2	ROI 3	ROI 4
Vessel area (cm^2)	Ground-truth	3.39	3.76	3.76	3.60
	Uncorrected	3.50 ± 0.17	4.37 ± 0.43	3.91 ± 0.26	4.02 ± 0.22
	fNAV	3.43 ± 0.14	3.93 ± 0.10	3.76 ± 0.09	3.77 ± 0.07
Net volume (mL)	Ground-truth	123.0	148.4	135.5	142.7
	Uncorrected	128.1 ± 8.4	170.9 ± 15.4	137.9 ± 8.3	157.1 ± 8.4
	fNAV	123.4 ± 3.8	155.1 ± 3.7	133.8 ± 2.6	147.7 ± 2.4
Peak flow (mL/s)	Ground-truth	253.7	273.1	271.3	268.6
	Uncorrected	264.7 ± 18.2	317.0 ± 29.5	277.9 ± 19.8	296.3 ± 15.7
	fNAV	253.1 ± 6.9	286.4 ± 7.2	267.6 ± 5.1	279.9 ± 6.2

Note: The reference 4D flow reconstruction (without motion) is used as ground-truth for comparison with 4D flow reconstructions of different respiratory motion displacements without (uncorrected 4D flow) and with (fNAV 4D flow) motion correction.
Abbreviations: ROI, region of interest; fNAV, focused navigation.

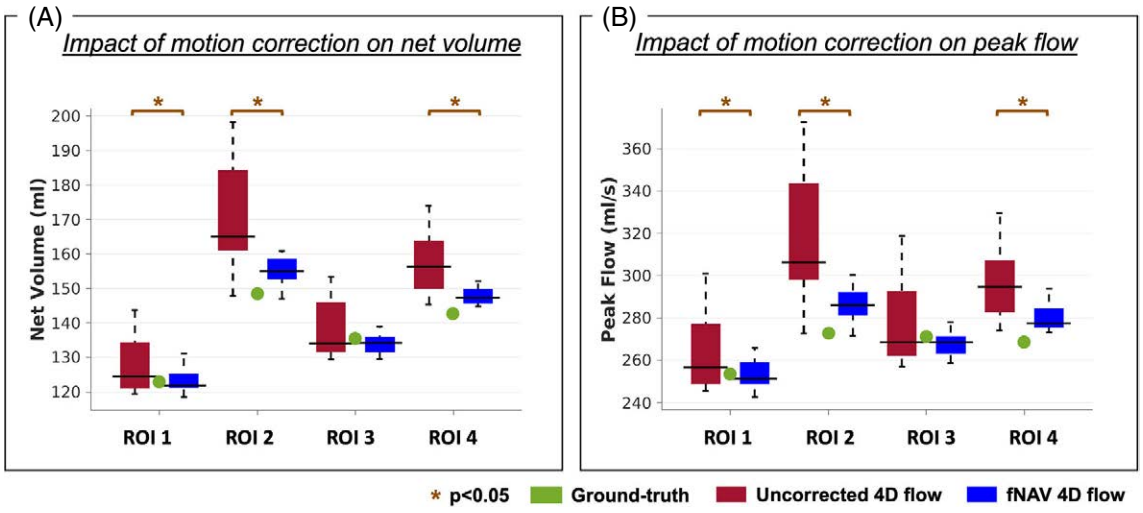

FIGURE 4 Influence of respiratory motion on flow quantification in a pulsatile flow phantom. Net volume (A) and peak flow rate (B) measurements calculated from focused navigation (fNAV) 4D flow and uncorrected 4D flow reconstructions of the simulated datasets ($n = 20$) across the same four ROIs shown in Figures 2 and 3. The ground-truth value for each ROI is marked in green and statistically significant differences between fNAV and uncorrected 4D flow measurements are denoted by orange stars.

and SD of: $A_x = 2.5 \pm 2.0$ mm, $A_y = 2.5 \pm 2.2$ mm, $A_z = 7.2 \pm 3.6$ mm, and ranging between $A_x = 0.4$–7.8 mm, $A_y = 0$–8.9 mm, $A_z = 0.1$–16.4 mm. These values are within the range of values tested in vitro.

Streamline visualizations of all 4D flow datasets (fNAV, nav-gated, and uncorrected) are shown for two representative patients in Figure 5. Overall image quality is comparable between the three 4D flow datasets, including in regions of larger turbulence (yellow arrows). Red arrows highlight locations with small differences in the velocity streamlines between reconstructions, where the uncorrected 4D flow streamlines are visually the most different when compared to fNAV 4D flow and nav-gated 4D flow streamlines.

3.2.2 | Comparison of vessel area and flow measurements

Six MPA segmentations were excluded from the study, two because of poor visualization of the vessel from 2D flow datasets and four because of poor visualization overall, on all flow datasets. One nav-gated 4D flow dataset was corrupted and therefore, was also excluded from the analysis.

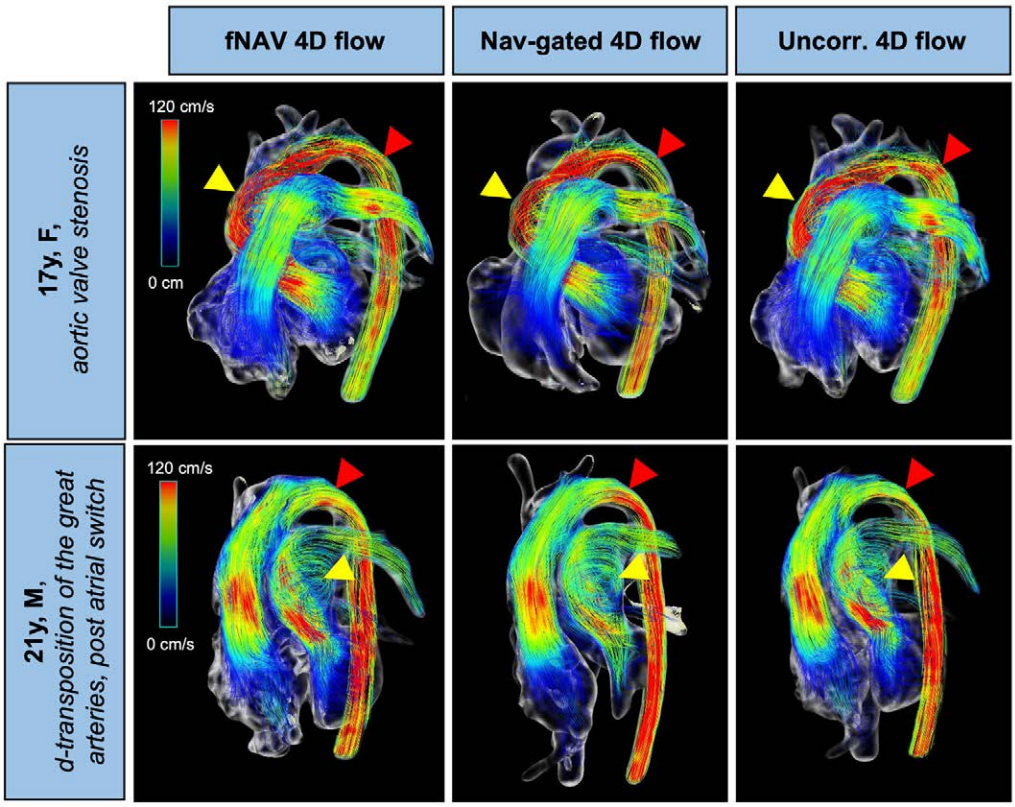

FIGURE 5 Visualization of flow streamlines in two patients with congenital heart disease using focused navigation (fNAV), nav-gated and uncorrected 4D flow datasets. Yellow arrows point to regions of large turbulence for each case, where image quality appears to be similar for both reconstructions. Red arrows point to regions with different flow streamlines, where the uncorrected 4D flow reconstructed dataset has larger differences to the nav-gated 4D flow dataset when compared to fNAV 4D flow. Uncorr. 4D flow, uncorrected 4D flow; F, female; M, male.

From the remaining data, a total of 264 vessels segmented from all the 2D/4D flow datasets were included in the comparison.

In the absence of a ground-truth measurement of vessel area, comparison between fNAV, nav-gated, and uncorrected 4D flow datasets to the reference 2D flow datasets (Figure 6) demonstrated variable agreement depending on the vessel of interest. The average vessel area measurements across all vessels were $4.92 \pm 2.95\,cm^2$ for 2D flow, $5.06 \pm 2.64\,cm^2$ for fNAV 4D flow, $4.87 \pm 2.57\,cm^2$ for nav-gated 4D flow, and $4.87 \pm 2.69\,cm^2$ for uncorrected 4D flow. No significant difference in AAo vessel area was found between fNAV 4D flow datasets ($7.24 \pm 2.63\,cm^2$) and 2D flow datasets ($7.39 \pm 2.64\,cm^2$, $p = 0.38$), but a significant underestimation as compared to 2D flow vessel area measurements was observed for nav-gated 4D flow ($7.10 \pm 2.50\,cm^2$, $p < 0.05$) and uncorrected 4D flow ($6.91 \pm 2.64\,cm^2$, $p < 0.05$). Conversely, DAo vessel area measurements from fNAV 4D flow ($2.88 \pm 0.85\,cm^2$), nav-gated 4D flow ($2.60 \pm 0.77\,cm^2$) and uncorrected 4D flow ($2.57 \pm 0.84\,cm^2$) datasets were significantly ($p < 0.05$) overestimated relative to those from 2D flow datasets ($2.22 \pm 0.67\,cm^2$). No significant differences were found in the

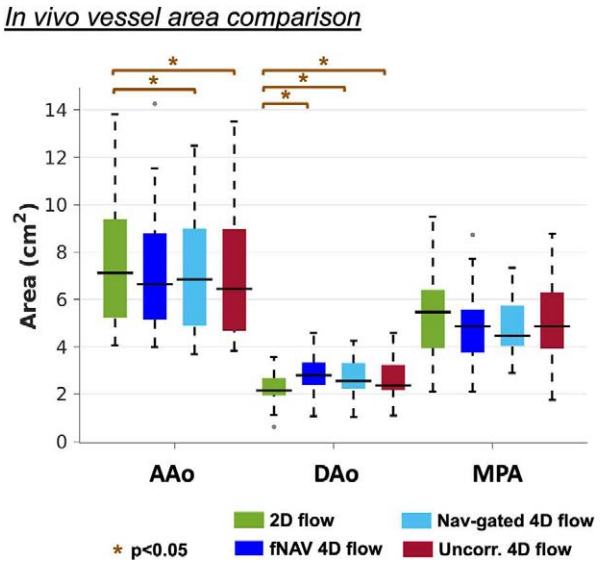

FIGURE 6 Comparison of vessel area from in vivo datasets. 2D flow (green), and focused navigation 4D flow (dark-blue), nav-gated 4D flow (light-blue) and uncorrected 4D flow (red) measurements are included for all patients. AAo, ascending aorta; DAo, descending aorta; MPA, main pulmonary artery; Uncorr. 4D flow, uncorrected 4D flow; *p*, *p*-value.

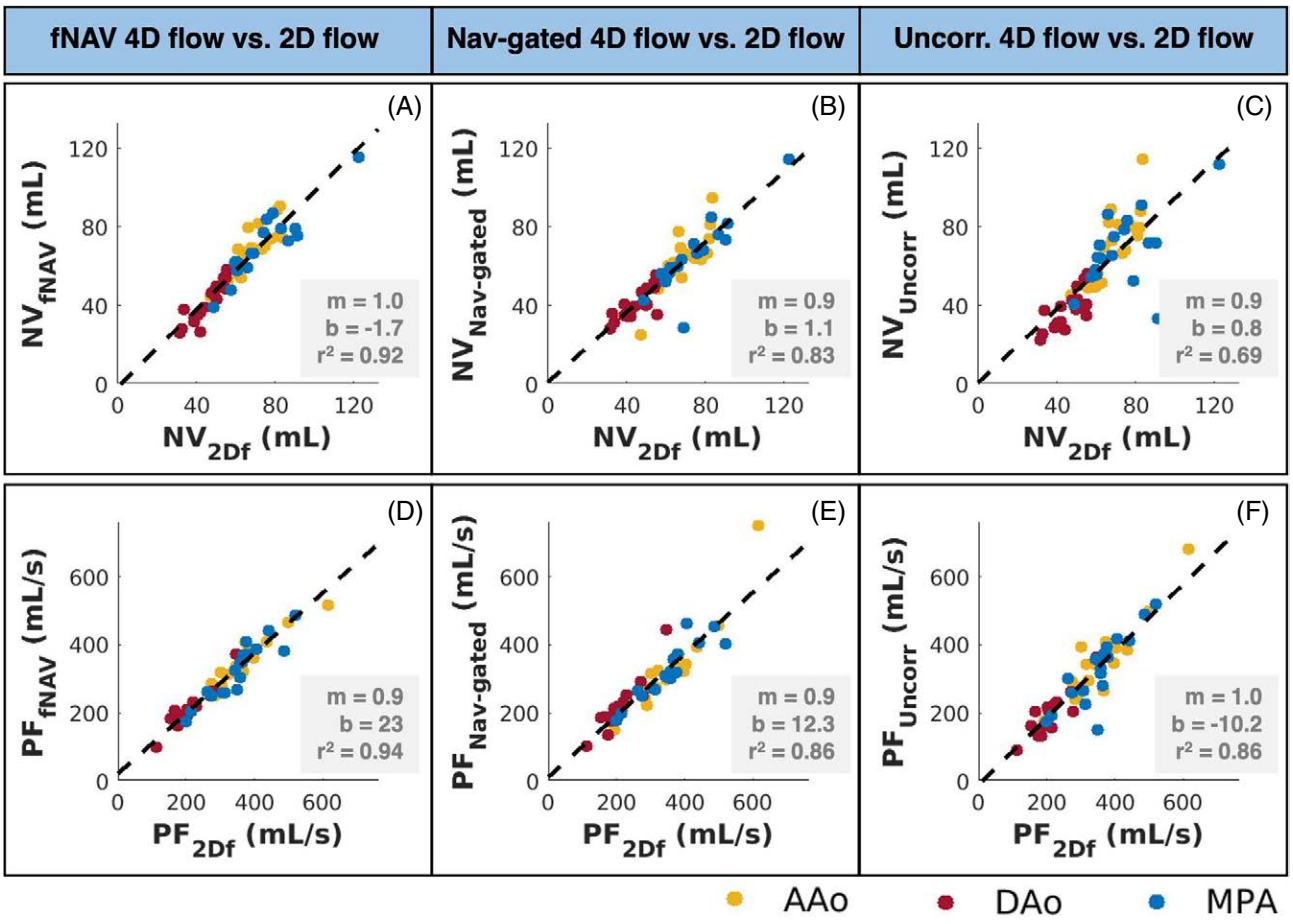

FIGURE 7 Linear regression of net volume (A–C) and peak flow (D–F) measurements between each 4D flow dataset and the reference standard 2D flow datasets. Overall, focused navigation (fNAV) 4D flow net volume and peak flow measurements (A and D) were the strongest correlated measures to 2D flow, when compared to nav-gated 4D flow (B and E) and uncorrected 4D flow (C and F) datasets. NV, net volume; PF, peak flow rate. r^2, squared Pearson correlation coefficient. 2Df, 2D flow; fNAV, fNAV 4D flow; Nav-gated, nav-gated 4D flow; Uncorr, uncorrected 4D flow.

MPA vessel area for fNAV ($5.07 \pm 1.72\,cm^2$, $p = 0.29$), nav-gated ($4.91 \pm 1.31\,cm^2$, $p = 0.17$) and uncorrected ($5.24 \pm 1.97\,cm^2$, $p = 0.74$) 4D flow datasets when compared to 2D flow ($5.25 \pm 2.04\,cm^2$).

Linear regression results between 2D flow and fNAV 4D flow net volume measurements ($r^2 = 0.92$) (Figure 7A) were overall the strongest correlation results when comparing 2D flow with other 4D flow datasets ($r^2 = 0.83$ for comparison to nav-gated 4D flow) (Figure 7B) ($r^2 = 0.69$ for comparison to uncorrected 4D flow) (Figure 7C). Similarly, 2D flow peak flow measurements had a larger correlation with fNAV 4D flow peak flow measurements (Figure 7D–F) ($r^2 = 0.94$, $r^2 = 0.86$, $r^2 = 0.86$, respectively).

Compared to 2D flow, fNAV 4D flow datasets showed the lowest bias in net volume and peak flow across all 4D flow datasets ($-3.5 \pm 19.8\%$ for net volume, $-2.9 \pm 17.2\%$ for peak flow) (Figure 8), although all 4D flow net volume and peak flow measurements were significantly different from 2D flow measurements, with $p < 0.05$, with the exception of the net volume comparison between 2D flow and uncorrected 4D flow ($-4.9 \pm 43.0\%$, $p = 0.06$).

4 | DISCUSSION

In this study, we extended the use of a previously described fNAV method for respiratory motion correction of free-running 3D radial PC-MRI acquisitions to obtain fNAV 4D flow datasets. The proposed fNAV 4D flow approach does not require image navigators or ECG-gating and can be acquired with simplified scan planning and a fixed scan time. Using fNAV, translational motion of the heart is estimated and used to correct all acquired readouts in radial 4D flow MRI. We validated the fNAV 4D flow framework in simulated data generated from non-rigid respiratory motion fields applied to a pulsatile flow phantom and demonstrated its feasibility in a cohort of patients with CHD. We successfully confirmed our hypotheses that: (1)

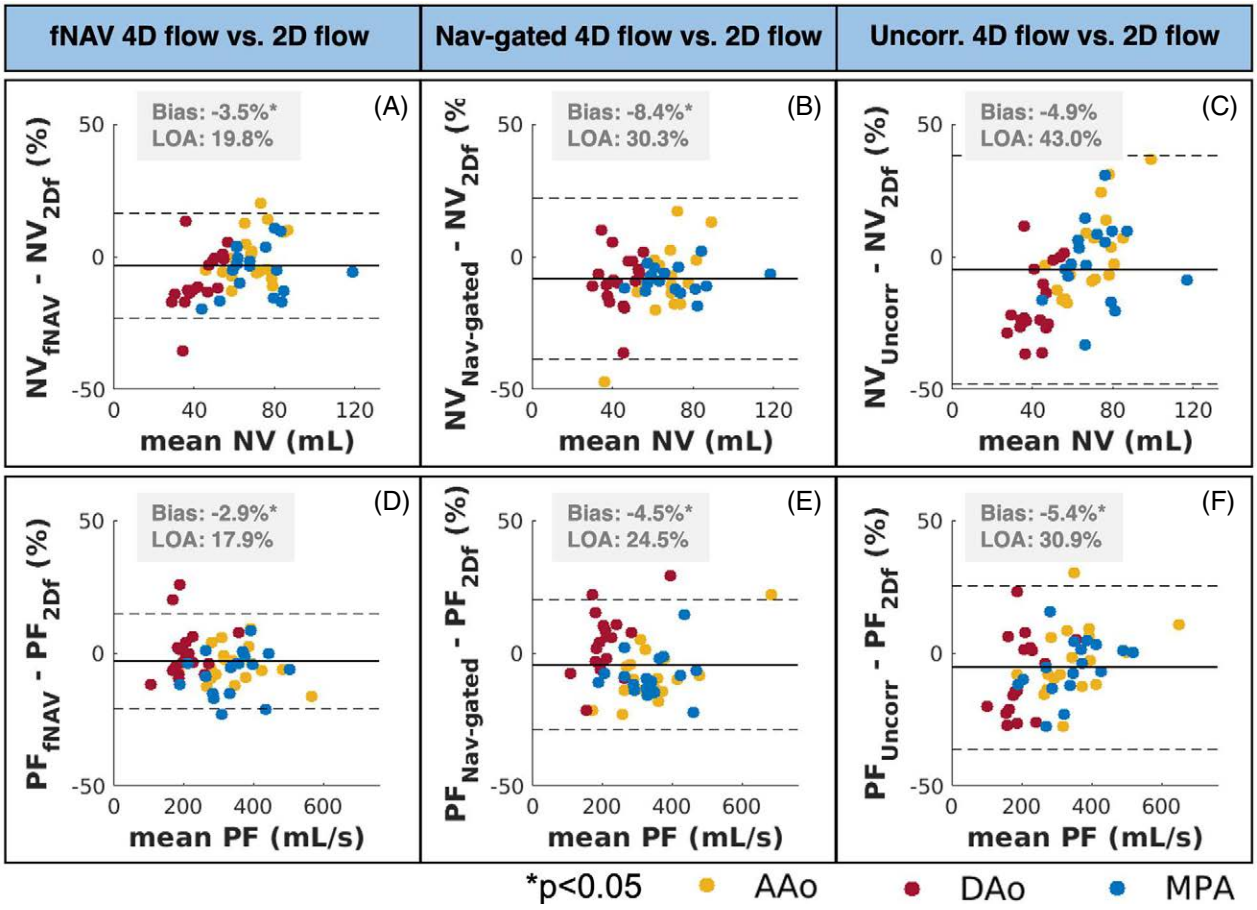

FIGURE 8 Bland–Altman results of net volume (A–C) and peak flow (D–F) measurements between each 4D flow dataset and the reference standard 2D flow datasets. Comparing to 2D flow datasets, focused navigation (fNAV) 4D flow net volume and peak flow measurements (A and D) had smaller biases compared to measures from nav-gated 4D flow (B and E) and uncorrected 4D flow (C and F) datasets. NV, net volume; PF, peak flow rate. LOA, limits of agreement. 2Df, 2D flow, fNAV, fNAV 4D flow; Nav-gated, nav-gated 4D flow; Uncorr, uncorrected 4D flow.

fNAV can estimate respiratory motion from free-running 3D radial PC-MRI acquisitions, and that (2) the resulting fNAV 4D flow datasets produce comparable flow measurements to separately acquired reference measurements, and with a reduction in bias when compared to uncorrected 4D flow datasets. Although a regional variation in the accuracy of respiratory motion and resulting vessel area and flow measurements was observed because of the translational correction applied to a non-rigid underlying motion, overall fNAV 4D flow produced comparable results to the reference standard flow datasets and significantly improved uncorrected data.

4.1 | Validation in a pulsatile flow phantom

In the first part of our study, we validated the use of fNAV for correction of respiratory motion in a numerical simulation based on data obtained from a pulsatile flow phantom. The data acquisition was performed without any physical displacement of the phantom during the scan. Instead, a retrospective approach was chosen to enable a well-controlled simulation of a large number of non-rigid displacements, which not only enabled the direct comparison of estimated fNAV coefficients with generated values, but it also enabled the direct comparison of all datasets induced with motion to the non-motion corrupted counterpart (ground-truth), removing any acquisition-related bias. This comparison demonstrated that respiratory motion impacts both the measured area of the vessel-like structure of the phantom and subsequent flow. These results corroborate previous studies, which also demonstrated a decrease in the accuracy of flow measurements and overall image quality when no respiratory compensation is considered.[21,22]

When using fNAV in vitro, the resulting vessel area and flow measurements demonstrated that fNAV can accurately measure and correct for rigid translational

respiratory motion providing an overall improvement in accuracy relative to uncorrected data but with variation depending on the degree of underlying non-rigid motion. For instance, for ROI 2 and ROI 3, the estimated fNAV displacement measures matched with high correlation the generated displacements, enabling motion corrected 4D flow reconstructions that yielded area and flow measurements in strong agreement with the ground-truth, therefore, confirming our first hypothesis. Moreover, the estimated fNAV coefficients corrected the generated displacements simulated in ROI 1 and ROI 4 with lower accuracy, and, as a result, there were larger differences in the area of these ROIs when comparing fNAV 4D flow datasets to the ground-truth. These results are a consequence of using a rigid motion correction in a non-rigid structure. Nevertheless, the net volume and peak flow measures were still improved by applying motion correction, implying that motion correction, even if not perfect, is still beneficial when compared to the uncorrected counterpart. Nevertheless, at higher spatial resolution, these discrepancies may have greater impact on flow quantification.

The numerical simulation provided valuable insight on how the rigid fNAV correction of free-running 3D radial PC-MRI acquisitions would adapt to an *in vivo* setting, where motion is non-rigid. Still, increasing the complexity of the current phantom setup by including physical motion during the scan (for example with a moving cart) could help us further understand the limits of this technique for correcting respiratory motion in free-running 3D radial PC-MRI acquisitions. Additionally, a more rigorous validation in healthy volunteers that can be given instructions (i.e., periods of shallow or deep breathing) throughout the acquisition may be worth investigating in the future.

4.2 | Feasibility in a cohort of CHD patients

To demonstrate the feasibility and evaluate the performance of the proposed fNAV 4D flow approach in vivo, we compared fNAV 4D flow datasets from a cohort of CHD patients to 2D flow datasets, nav-gated 4D flow datasets, and to uncorrected 4D flow reconstructions of the same data, in terms of vessel area and the resulting flow measurements.

The overall image quality obtained from fNAV 4D flow reconstructions in terms of the PC-MRA volumes and the velocity streamlines visualized at peak systole was comparable between the fNAV, nav-gated and uncorrected 4D flow datasets. Nevertheless, small differences in the velocity streamlines were observed (see Figure 5, red arrows). These discrepancies may have been caused by the anatomical segmentation, or because of SNR differences between acquisitions and reconstructions. However, given the lack of a ground-truth for comparison, understanding these subtle changes can be challenging.

In the absence of a ground-truth measurement, in vivo vessel areas from fNAV, nav-gated, and uncorrected 4D flow datasets were compared to 2D flow and yielded some discrepancies depending on the vessel of interest. These in vivo results are consistent with those from the numerical simulation where the agreement with respect to ground-truth varied according to the position of the ROI, suggesting that our in vivo results are also affected by the translational correction used in the presence of non-rigid motion. Nonetheless, the fNAV 4D flow vessel area showed better overall agreement with 2D flow than to nav-gated and uncorrected 4D flow datasets, again highlighting the fact that fNAV provides an accurate correction of rigid respiratory motion, but may be limited in areas more greatly impacted by the underlying non-rigid motion.

When comparing fNAV, nav-gated, and uncorrected 4D flow measurements of net volume and peak flow to the reference 2D flow, fNAV 4D flow had a lower bias and slightly improved limits of agreement. These results may suggest that the respiratory motion correction provided by fNAV is more representative of the breath-hold performed for the 2D flow acquisitions, when also compared to nav-gated 4D flow, as this technique usually includes a large acceptance window for respiratory motion.

In this proof-of-concept study, 3D translational respiratory-derived displacement of the heart was estimated with fNAV and used to correct the acquired k-space data. Although the corrected data yielded similar vessel segmentations and flow measurements to the reference 2D flow and nav-gated 4D flow acquisitions, the main limitation of the current approach is that it does not account for rotational motion or the more general non-rigid behavior of respiratory motion. In principle, additional fNAV coefficients could be included to account for rotational motion, and the same fNAV approach used in this work can be modified to perform non-rigid correction using the localized auto-focusing method as previously described.[23,25,39] This approach is potentially prohibitive because of increases in computational time as separate reconstructions are required for different motion states, but this may be overcome by reconstructing the different motion states using parallel processing. Given the accurate performance of fNAV demonstrated in this work for specific regions, further investigation into the localized auto-focusing approach is warranted.

The current fNAV 4D flow approach could also be used to improve the quality of previously described respiratory motion-resolved 5D flow reconstructions[27] by correcting

translational intra-bin motion or could be combined with a more generalized strategy for inter-bin motion compensation using motion fields.[30,40–43] Additionally, alternative strategies have been proposed to compensate rather than correct for respiratory motion in 4D flow MRI such as adaptive navigator gating[14,21,44,45] and soft-gating,[18,39,46] but may have limitations in the presence of significant respiratory motion or variability. As new advances in both acquisition and reconstruction methods enable higher spatial resolution, it is likely that a combination of these aforementioned methods including fNAV is needed to truly compensate for the complex non-rigid motion of the heart because of respiration and provide accurate estimations of blood flow. Regardless, of the potential improvements to and future applications of fNAV, validation of the method showing that it can accurately estimate respiratory motion and correct for it to produce high quality visualizations and quantifications of flow has been achieved in this work.

5 | CONCLUSION

Respiratory motion correction for free-running 3D radial PC-MRI acquisitions has successfully been achieved using fNAV, both in a pulsatile flow phantom and in a cohort of patients with congenital heart disease. The resulting fNAV 4D flow datasets yielded accurate estimates of translational displacements of the heart because of respiration, resulting in similar vessel segmentations and flow measurements as those from both reference standard 2D flow and navigator-gated Cartesian 4D flow datasets. Using this approach, a quantitative evaluation of blood flow in the heart and its great vessels can be obtained in a fixed scan time, without the uncertainty in scan duration related to navigator efficiency, and without the need for respiratory navigators or ECG-gating.

FUNDING INFORMATION

M.S. is the Principal Investigator on Swiss National Science Foundation Grants 173129 and 201292 that funded part of this research. C.W.R. is the Principal Investigator on Swiss National Science Foundation Grant PZ00P3_202140 that funded part of this research. M.M. is the Principal Investigator on Grant T32EB025766 from the National Institute of Biomedical Imaging And Bioengineering of the National Institutes of Health that funded part of this research.

ACKNOWLEDGEMENT

Open access funding provided by Universite de Lausanne.

ORCID

Mariana B. L. Falcão https://orcid.org/0000-0002-4996-0331
Tobias Rutz https://orcid.org/0000-0001-5899-291X
Milan Prša https://orcid.org/0000-0002-9483-7957
Liliana Ma https://orcid.org/0000-0001-8834-8519
Justin J. Baraboo https://orcid.org/0000-0001-7301-0005
Jérôme Yerly https://orcid.org/0000-0003-4347-8613
Matthias Stuber https://orcid.org/0000-0001-9843-2028
Christopher W. Roy https://orcid.org/0000-0002-3111-8840

REFERENCES

1. Firmin D, Gatehouse P, Konrad J, Yang G, Kilner P, Longmore D. Rapid 7-dimensional imaging of pulsatile flow. *Proc Comput Cardiol Conf*. 1993;14:353-356.
2. Bogren HG, Mohiaddin RH, Yang GZ, Kilner PJ, Firmin DN. Magnetic resonance velocity vector mapping of blood flow in thoracic aortic aneurysms and grafts. *J Thorac Cardiovasc Surg*. 1995;110:704-714.
3. Wigström L, Sjöqvist L, Wranne B. Temporally resolved 3D phase-contrast imaging. *Magn Reson Med*. 1996;36:800-803.
4. Markl M, Chan FP, Alley MT, et al. Time-resolved three-dimensional phase-contrast MRI. *J Magn Reson Imaging*. 2003;17:499-506.
5. Markl M, Frydrychowicz A, Kozerke S, Hope M, Wieben O. 4D flow MRI. *J Magn Reson Imaging*. 2012;36:1015-1036.
6. Dyverfeldt P, Bissell M, Barker AJ, et al. 4D flow cardiovascular magnetic resonance consensus statement. *J Cardiovasc Magn Reson*. 2015;17:1-19.
7. Leiner T, Bogaert J, Friedrich MG, et al. SCMR position paper (2020) on clinical indications for cardiovascular magnetic resonance. *J Cardiovasc Magn Reson*. 2020;22:1-37.
8. Zhong L, Schrauben EM, Garcia J, et al. Intracardiac 4D flow MRI in congenital heart disease: recommendations on behalf of the ISMRM Flow & Motion Study Group. *J Magn Reson Imaging*. 2019;50:677-681.
9. Johnson KM, Markl M. Improved SNR in phase contrast velocimetry with five-point balanced flow encoding. *Magn Reson Med*. 2010;63:349-355.
10. Gu T, Korosec FR, Block WF, et al. PC VIPR: a high-speed 3D phase-contrast method for flow quantification and high-resolution angiography. *Am J Neuroradiol*. 2005;26:743-749.
11. Bastkowski R, Weiss K, Maintz D, Giese D. Self-gated golden-angle spiral 4D flow MRI. *Magn Reson Med*. 2018;80:904-913.
12. Schrauben EM, Macgowan CK, Lim JM. Motion robust respiratory—resolved 3D radial flow MRI and its application in neonatal congenital heart disease. *Magn Reson Med*. 2019;83:1-14.
13. Bollache E, Barker AJ, Dolan RS, et al. k-t accelerated aortic 4D flow MRI in under two minutes: feasibility and impact of resolution, k-space sampling patterns, and respiratory navigator gating on hemodynamic measurements. *Magn Reson Med*. 2018;79:195-207.

14. Ma LE, Markl M, Chow K, et al. Aortic 4D flow MRI in 2 minutes using compressed sensing, respiratory controlled adaptive k-space reordering, and inline reconstruction. *Magn Reson Med*. 2019;81:3675-3690.
15. Walheim J, Dillinger H, Kozerke S. Multipoint 5D flow cardiovascular magnetic resonance—accelerated cardiac- and respiratory-motion resolved mapping of mean and turbulent velocities. *J Cardiovasc Magn Reson*. 2019;21:1-13. doi:10.1186/s12968‐019‐0549‐0
16. Peper ES, Gottwald LM, Zhang Q, et al. Highly accelerated 4D flow cardiovascular magnetic resonance using a pseudo-spiral cartesian acquisition and compressed sensing reconstruction for carotid flow and wall shear stress. *J Cardiovasc Magn Reson*. 2020;22:1-15.
17. Cheng JY, Hanneman K, Zhang T, et al. Comprehensive motion-compensated highly accelerated 4D flow MRI with ferumoxytol enhancement for pediatric congenital heart disease. *J Magn Reson Imaging*. 2016;43:1355-1368.
18. Pruitt A, Rich A, Liu Y, et al. Fully self-gated whole-heart 4D flow imaging from a five-minute scan. *Magn Reson Med*. 2021;85:1222-1236. doi:10.1002/mrm.28491
19. Wang Y, Rossman PJ, Grimm RC, Riederer SJ, Ehman RL. Navigator-echo-based real-time respiratory gating and triggering for reduction of respiration effects in three-dimensional coronary MR angiography. *Radiology*. 1996;198:55-60.
20. Ehman RL, Felmlee JP. Adaptive technique for high-definition MR imaging of moving structures. *Radiology*. 1989;173:255-263.
21. Dyverfeldt P, Ebbers T. Comparison of respiratory motion suppression techniques for 4D flow MRI. *Magn Reson Med*. 2018;78:1877-1882.
22. Denecken E, Sotelo J, Arrieta C, Andia ME, Uribe S. Impact of respiratory gating on hemodynamic parameters from 4D flow MRI. *Appl Sci*. 2022;12:2943.
23. Roy CW, Heerfordt J, Piccini D, et al. Motion compensated whole-heart coronary cardiovascular magnetic resonance angiography using focused navigation (fNAV). *J. Cardiovasc. Magn. Reson.* 2021;23:1-17.
24. Atkinson D, Hill DLG, Stoyle PNR, Summers PE, Keevil SF. Automatic correction of motion artifacts in magnetic resonance images using an entropy focus criterion. *IEEE Trans Med Imaging*. 1997;16:903-910.
25. Cheng JY, Alley MT, Cunningham CH, Vasanawala SS, Pauly JM, Lustig M. Nonrigid motion correction in 3D using autofocusing with localized linear translations. *Magn Reson Med*. 2012;68:1785-1797.
26. Schrauben EM, Anderson AG, Johnson KM, Wieben O. Respiratory-induced venous blood flow effects using flexible retrospective double-gating. *J Magn Reson Imaging*. 2015;42:211-216.
27. Ma LE, Yerly J, Piccini D, et al. 5D flow MRI: a fully self-gated, free-running framework for cardiac and respiratory motion—resolved 3D hemodynamics. *Radiol Cardiothorac Imaging*. 2020;2:2.
28. Falcão MBL, Di Sopra L, Ma L, et al. Pilot tone navigation for respiratory and cardiac motion-resolved free-running 5D flow MRI. *Magn Reson Med*. 2022;87:718-732.
29. Blanken CPS, Schrauben EM, Peper ES, et al. Coronary flow assessment using accelerated 4D flow MRI with respiratory motion correction. *Front Bioeng Biotechnol*. 2021;9:1-11.
30. Kolbitsch C, Vasquez CP, Bastkowski R, Weiss K, Maintz D. Respiratory motion corrected 4D flow using golden radial phase encoding. *Magn Reson Med*. 2019;83:635-644 . doi:10.1002/mrm.27918
31. Henningsson M, Koken P, Stehning C, Razavi R, Prieto C, Botnar RM. Whole-heart coronary MR angiography with 2D self-navigated image reconstruction. *Magn Reson Med*. 2012;67:437-445.
32. Piccini D, Littmann A, Nielles-vallespin S, Zenge MO. Spiral phyllotaxis: the natural way to construct a 3D radial trajectory in MRI. *Magn Reson Med*. 2011;66:1049-1056.
33. Feng L, Axel L, Chandarana H, Block KT, Sodickson DK, Otazo R. XD-GRASP: Golden-angle radial MRI with reconstruction of extra motion-state dimensions using compressed sensing. *Magn Reson Med*. 2016;75:775-788.
34. Di Sopra L, Piccini D, Coppo S, Stuber M, Yerly J. An automated approach to fully self-gated free-running cardiac and respiratory motion-resolved 5D whole-heart MRI. *Magn Reson Med*. 2019;82:2118-2132.
35. Roy CW, Di Sopra L, Whitehead KK, et al. Free-running cardiac and respiratory motion-resolved 5D whole-heart coronary cardiovascular magnetic resonance angiography in pediatric cardiac patients using ferumoxytol. *J Cardiovasc Magn Reson*. 2022;24:1-12.
36. Ingle RR, Wu HH, Addy NO, et al. Nonrigid autofocus motion correction for coronary MR angiography with a 3D cones trajectory. *Magn Reson Med*. 2014;72:347-361.
37. McGee KP, Manduca A, Felmlee JP, Riederer SJ, Ehman RL. Image metric-based correction (autocorrection) of motion effects: analysis of image metrics. *J Magn Reson Imaging*. 2000;11:174-181.
38. Lorenz R, Benk C, Bock J, et al. Closed circuit MR compatible pulsatile pump system using a ventricular assist device and pressure control unit. *Magn Reson Med*. 2012;67:258-268.
39. Cheng JY, Zhang T, Ruangwattanapaisarn N, et al. Free-breathing pediatric MRI with nonrigid motion correction and acceleration. *J Magn Reson Imaging*. 2015;42:407-420.
40. Batchelor PG, Atkinson D, Irarrazaval P, Hill DLG, Hajnal J, Larkman D. Matrix description of general motion correction applied to multishot images. *Magn Reson Med*. 2005;54:1273-1280.
41. Odille F, Vuissoz PA, Marie PY, Felblinger J. Generalized reconstruction by inversion of coupled systems (GRICS) applied to free-breathing MRI. *Magn Reson Med*. 2008;60:146-157.
42. Usman M, Atkinson D, Odille F, et al. Motion corrected compressed sensing for free-breathing dynamic cardiac MRI. *Magn Reson Med*. 2013;70:504-516.
43. Bustin A, Ginami G, Cruz G, et al. Magnetic resonance in medicine five-minute whole-heart coronary MRA with sub-millimeter isotropic resolution, 100% respiratory scan efficiency, and 3D- PROST reconstruction. *Magn Reson Med*. 2019;81:102-115.
44. Bailes DR, Gilderdale DJ, Bydder GM, Collins AG, Firmin DN. Respiratory ordered phase encoding (ROPE): a method for

reducing respiratory motion artefacts in MR imaging. *J Comput Assist Tomogr*. 1985;9:835-838.
45. Markl M, Harloff A, Bley TA, et al. Time-resolved 3D MR velocity mapping at 3 T: improved navigator-gated assessment of vascular anatomy and blood flow. *J Magn Reson Imaging*. 2007;25:824-831.
46. Cheng JY, Zhang T, Alley MT, et al. Comprehensive multi-dimensional MRI for the simultaneous assessment of cardiopulmonary anatomy and physiology. *Sci Rep*. 2017; 7:1-15.
47. Falcão MBL, Rossi GMC, Ma L, et al. Correcting vs resolving respiratory motion in accelerated free-running whole-heart radial flow MRI using focused navigation (fNAV). *Proc Intl Soc Mag Reson Med*. 2021;29:635-644.

SUPPORTING INFORMATION

Additional supporting information may be found in the online version of the article at the publisher's website.

Table S1. Patient cohort, age, gender, and diagnosis.

How to cite this article: Falcão MBL, Rossi GMC, Rutz T, et al. Focused navigation for respiratory–motion-corrected free-running radial 4D flow MRI. *Magn Reson Med*. 2023;1-16. doi: 10.1002/mrm.29634

3.4. Conclusions and Outlook of this work

In this study, fNAV was shown to successfully estimate respiratory motion from free-running PC-MRI data, which led to 4D flow reconstructions that produced comparable flow measurements to reference standard measurements without the need for diaphragmatic navigators and in a predictable scan time.

The free-running PC-MRI framework used in this work is the same one used in Chapter 2. However, in this work, we correct respiratory motion (4D flow) rather than resolve it (5D flow). As a result, the number of readouts per imaging volume is increased, which in turn increases the baseline image quality. This increase in data sampling provided by a 4D flow reconstruction with fNAV could enable new tests to further accelerate the free-running PC-MRI sequence, which would, in turn, reduce scan times.

A preliminary study investigating the effects of acceleration on both 4D flow fNAV and 5D flow reconstructions of the same free-running PC-MRI data was presented and was awarded a Magna Cum Laude Merit Award at the 30th ISMRM International Meeting in 2021. The study (included as supplementary information A3.3) demonstrated that, using 4D flow fNAV, the imaging sequence could be further accelerated by a factor of 1.67 without sacrificing the accuracy of flow measurements whereas 5D flow measurements had a decrease in accuracy beyond the baseline acceleration factor.

In contrast to the potential acceleration strategy described above, the gain in overall samples per volume provided by correcting respiratory motion could enable higher resolution acquisitions of free-running PC-MRI, which could be especially interesting to diagnose and monitor pediatric cohorts. Additionally, increased spatial resolution may allow for the assessment of anatomical structure, ventricular function, and flow all within a single free-running PC-MRI sequence providing an efficient and comprehensive CMR acquisition.

Chapter 4.
Free-running 3D anatomical and flow MRI using Synchronization of Neighboring Acquisitions by Physiological Signals (SyNAPS)

4.1. Overview

In Chapter 2, Pilot Tone navigation was successfully used to extract cardiac and respiratory motion signals from free-running PC-MRI datasets, and afterwards from other free-running-derived sequences such as multi-echo GRE and T2 mapping. More importantly, Chapter 2 demonstrated that Pilot Tone provides physiological signals that are independent of sequence contrast and parameters and, therefore, Pilot Tone could potentially be used to synchronize two or more sequences together and enable a multi-dimensional/multi-contrast comprehensive CMR framework.

The work presented in this chapter focused on implementing a novel technique for combining image information from multiple acquisitions without restrictions on native contrast or sequence timing parameters, called Synchronization of Neighboring Acquisitions by Physiological Signals (SyNAPS). SyNAPS uses Pilot Tone to extract cardiac and respiratory motion signals that are used to inform a synchronized cardiac motion-resolved and respiratory motion-corrected 4D flow reconstruction. We validated SyNAPS using one free-running anatomical sequence and one free-running PC-MRI sequence and tested the hypothesis that synchronizing these two sequences enables a dynamic segmentation of vessels and improved flow assessment.

4.2. Personal contribution

In this study, I was once again the primary investigator, albeit with increased independence from supervision when compared to the previous two peer-reviewed studies. With support from Dr. Christopher W. Roy, PhD, I designed the study, acquired the data, and performed the

analysis. The remaining co-authors have contributed mainly by helping with the acquisition of volunteer and patient data.

4.3. Article under Internal Review

The study described in this section has been presented at the 32nd ISMRM International meeting in 2022 with the title "*Free-running 3D anatomical and flow MRI using Synchronization of Neighboring Acquisitions by Physiological Signals (SyNAPS)*" (Supplementary Information A3.4), where it received a Summa Cum Laude Award (top 5%). The study is currently under internal review to be submitted to a peer-reviewed scientific journal, with the title "*Free-running 4D anatomical and flow MRI using Synchronization of Neighboring Acquisitions by Physiological Signals (SyNAPS)*".

Free-running 3D anatomical and flow MRI using Synchronization of Neighboring Acquisitions by Physiological Signals (SyNAPS)

Mariana B.L. Falcão[1], Adèle L.C. Mackowiak[1,5,6], Simone Rumac[1], Mario Bacher[1,2], Giulia M. C. Rossi[1], Jessica Bastiaansen[5,6], Ruud Van Heeswijk[1], Peter Speier[2], Michael Markl[4,5], Matthias Stuber[1,6], Christopher W. Roy[1]

[1]Department of Diagnostic and Interventional Radiology, Lausanne University Hospital (CHUV) and University of Lausanne (UNIL), Lausanne, Switzerland.

[2] Siemens Healthcare GmbH, Erlangen, Germany.

[3]Woman- Mother- Child Department, Lausanne University Hospital and University of Lausanne, Lausanne, Switzerland.

[4]Service of Cardiology, Centre de Resonance Magnétique Cardiaque (CRMC), Lausanne University Hospital and University of Lausanne, Lausanne, Switzerland.

[5]Department of Diagnostic, Interventional and Pediatric Radiology (DIPR), University hospital Bern (Inselspital), Bern Switzerland.

[6] Translational Imaging Center, sitem-insel, Bern, Switzerland.

[7]Department of Radiology, Feinberg School of Medicine, Northwestern University, Chicago, Illinois, USA.

[8] Department of Biomedical Engineering, Northwestern University, Chicago, Illinois, USA.

[9] Center for Biomedical Imaging (CIBM), Lausanne, Switzerland

Corresponding Author:

Christopher W. Roy, PhD, Lausanne University Hospital (CHUV), Rue de Bugnon 46, BH-7-84, 1011 Lausanne, Switzerland. Email: christopher.roy@chuv.ch

Funding Source:

MS is the PI on Swiss National Science Foundation Grants 173129 and 201292 that funded part of this research.

CWR is the PI on Swiss National Science Foundation Grant PZ00P3_202140 that funded part of this research

MM is the PI on Grant T32EB025766 from the National Institute Of Biomedical Imaging And Bioengineering of the National Institutes of Health, that funded part of this research.

Abstract

Background: In this work, we introduce a novel technique for combining multiple whole-heart acquisitions without restrictions on native contrast or sequence timing parameters. The proposed technique, **Sy**nchronization of **N**eighboring **A**cquisitions by **P**hysiological **S**ignals (**SyNAPS**), uses Pilot Tone (PT) Navigation to extract cardiac and respiratory motion signals, which are then leveraged to provide a synchronized cardiac motion-resolved and respiratory motion-corrected reconstruction of back-to-back acquisitions. We validate SyNAPS using a free-running 3D radial fast interrupted steady-state sequence (FISS) for anatomy and free-running 3D radial PC-MRI sequence for flow and test the hypothesis that synchronizing these two sequences enables a dynamic segmentation of vessels and improved blood flow measurements.

Methods: Eight healthy volunteers were scanned without contrast agents using free-running anatomical and flow sequences acquired back-to-back. Two conventional breath-held 2D flow sequences in the ascending and descending aorta were also acquired for reference. Using SyNAPS, PT cardiac and respiratory signals spanning the two free-running sequences were extracted for subsequent respiratory motion correction and cardiac binning. After SyNAPS and image reconstruction, the magnitude images from free-running FISS and the phase images from free-running PC-MRI were combined to create SyNAPS 4D flow datasets. Net volume, peak flow and dynamic vessel area were used to compare SyNAPS 4D flow with 4D flow (without the anatomical information from FISS) and 2D flow.

Results: The blood-to-myocardium contrast ratio of SyNAPS 4D flow magnitude images (1.5±0.4) demonstrated a clear improvement over 4D Flow (0.7±0.1, $p<0.01$), and is comparable to the 2D Flow images (2.0±0.9, $p=0.55$), which benefit from in-flow enhancement. The Pearson correlation coefficient between the dynamic vessel area of SyNAPS 4D flow and 2D flow was 0.72±0.27 for the AAo and 0.82±0.09 for the DAo, whereas the correlation between 4D flow and 2D flow was lower, 0.09±0.37 for the AAo and 0.12±0.44 for the DAo. Net volume (0.94) and peak flow (0.95) linear correlation measurements between SyNAPS 4D flow and 2D flow was stronger than the net volume (0.9) and peak flow (0.88) correlation between 4D flow and 2D flow. Bland-Altman analysis showed a lower bias and limits of agreement between SyNAPS 4D flow and 2D Flow, relative to 4D Flow.

Discussion and Conclusion: We developed and demonstrated the initial feasibility and utility of SyNAPS for joint whole-heart anatomical and flow MRI that does not require ECG gating, respiratory navigators, or contrast agents. We show that the high-contrast anatomical imaging sequence can be leveraged to improve 4D flow measurements that often suffer from poor delineation of the vessel boundaries in the absence of contrast agents. These promising results motivate further evaluation in a larger clinical cohort with the overarching goal of creating a fully comprehensive cardiac MRI framework tools without the need for contrast agents in the diagnosis and management of heart disease.

Background

4D flow MRI is increasingly used in the diagnosis and management of cardiovascular disease [1]. It provides a quantitative evaluation of blood flow in the heart and vessels with 3D volumetric coverage. When compared to conventional 2D flow MRI, simultaneous and

retrospective interrogation of multiple vessels with 4D flow provides a significantly simplified scan protocol that is less user-dependent [2,3]. Unfortunately, 4D flow MRI, which typically employs gradient recalled echo (GRE) readouts, suffers from low contrast-to-noise when compared to 2D flow MRI, due to the smaller voxel sizes (2D flow MRI typically uses thick slices) and the absence of in-flow enhancement.

As a result, 4D flow sequences are often acquired after injection of contrast agents, such as Gadolinium or Ferumoxytol to improve SNR and blood-myocardium contrast. Nevertheless, there is a growing effort to limit the use of contrast agents, due to their reported side effects. Gadolinium, for instance, carries toxicity risk, particularly for renal function [4]. Similarly, Ferumoxytol has been associated with the anaphylactic reactions [5], which in turn has led to restrictions on its use and availability in some countries [6]. Therefore, using native contrast in 4D flow MRI is a preferred yet challenging solution.

In this work, we introduce and validate a novel technique for acquiring and reconstructing 4D flow data without the need for contrast injection. Using, the proposed technique called **Sy**nchronization of **N**eighboring **A**cquisitions by **P**hysiological **S**ignals (**SyNAPS**), two free-running [7] 3D radial datasets are acquired back-to-back with the first providing high contrast anatomical images [8] and the second providing 4D flow images [9]. The free-running data are continuously acquired without the need for ECG-gating or respiratory navigators. In parallel to the acquisition, Pilot Tone navigation [10,11] is used to retrospectively synchronize the two acquisitions and inform a joint cardiac motion-resolved and respiratory motion-corrected 4D image reconstruction of the data.

We validated this technique in a cohort of healthy subjects and compare 4D flow measurements using SyNAPS (SyNAPS 4D flow) to 4D flow datasets reconstructed only from free-running 3D radial PC-MRI data (4D flow), and to a 2D flow reference standard. We tested the hypotheses that synchronizing these two sequences enables an improved visualization of the cardiac anatomy and great vessels, enables a dynamic segmentation of vessels, and improves 4D flow measurements of net volume and peak flow Relative to the 2D flow reference standard.

Methods

Synchronization of Neighboring Acquisitions by Physiological Signals (SyNAPS)

The SyNAPS framework consists of 6 steps as illustrated by Figure 1. First, a sequence with high blood-myocardium contrast (free-running 3D radial fast interrupted steady-state sequence, or FISS [8,12,13]) and a sequence with flow encoding (free-running 3D radial PC-MRI sequence [9]) are acquired back-to-back. To track cardiac and respiratory motion over the total acquisition time (~14 minutes), a 12-channel body coil array with an integrated Pilot Tone generator (Siemens Healthcare, Erlangen, Germany) is used [10,11], and the raw Pilot Tone data collected during each sequence are combined for subsequent signal extraction (Figure 1A).

Second, cardiac and respiratory signals are estimated from the Pilot Tone data based on a previously described framework for free-running 3D radial acquisitions but modified to accommodate multiple sequences acquired back-to-back (Figure 1B) [10,14]. In effect, the Pilot

Tone signals that span the two acquisitions are treated as continuous to facilitate extraction of cardiac triggers and respiratory curves as follows.

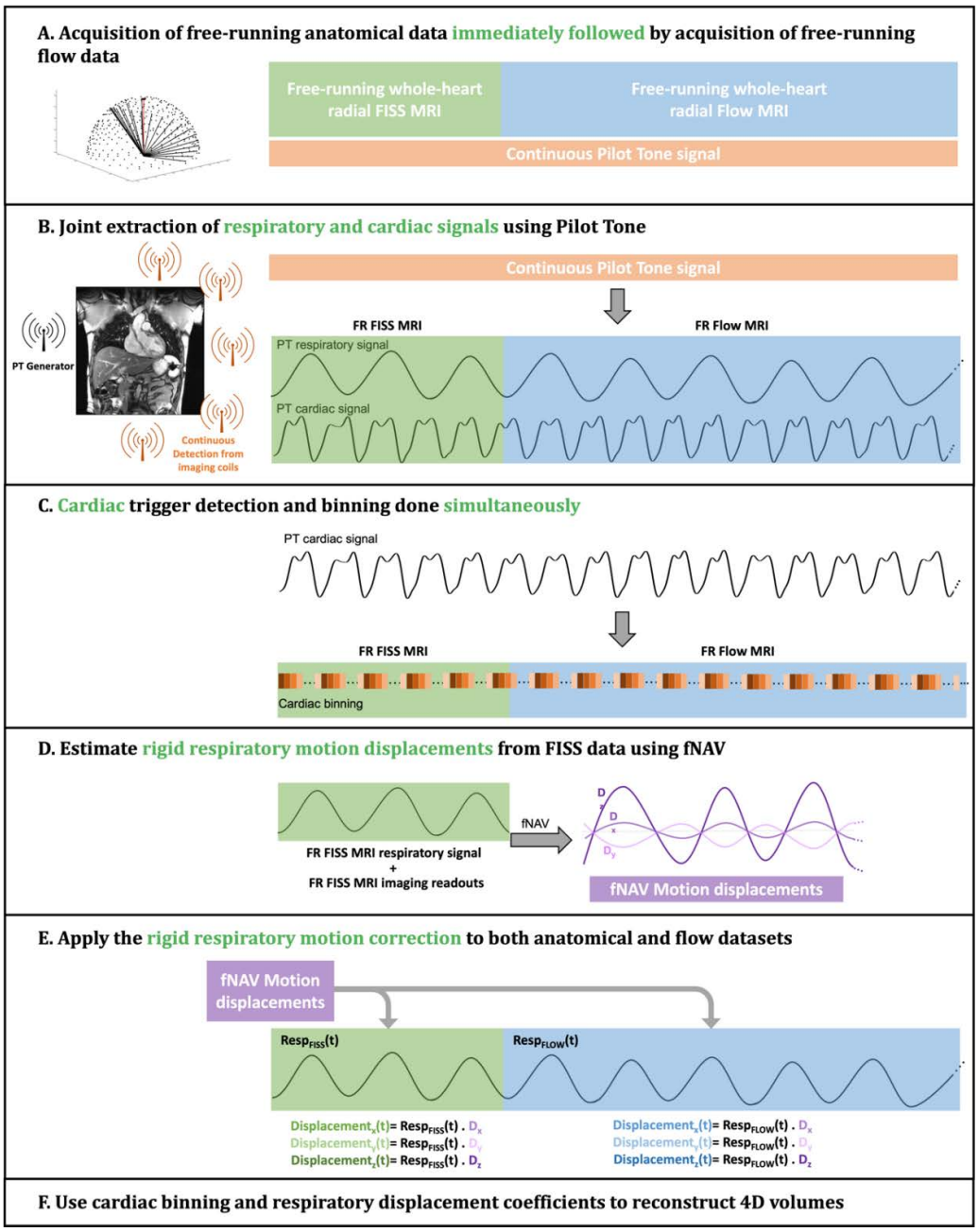

Figure 1. SyNAPS framework for synchronization of two free-running 3D radial MRI sequences. A) One free-running 3D radial fast interrupted steady-state sequence (FISS) [14–16], for a contrast free and natively fat suppressed whole-heart anatomical acquisition, and one free-running 3D radial PC-MRI sequence (FLOW) were acquired sequentially [1,24]. **B)** Cardiac and respiratory signals are extracted from the continuously acquired Pilot Tone (PT) signals. **C)** From the extracted cardiac signals, triggers were selected to then perform cardiac binning of the data over time. **D)** From the respiratory curves extracted, respiratory motion displacements are obtained from the FISS data using fNAV [23], **E)** and are applied to both sequences. **F)** The resulting cardiac binning and respiratory correction information is used to inform a k-t-sparse SENSE reconstruction adapted to each sequence to obtain 4D imaging volumes. In this study, the resulting Magnitude images from 4D FISS and Phase images from 4D Flow are then combined to create 4D Flow SyNAPS.

Third, cardiac triggers are obtained by applying both principal component and independent component analysis to the raw Pilot Tone data followed by adaptive filtering that targets frequencies within physiologically plausible ranges for cardiac motion. The local minima of the cardiac signal then define triggers which allows us to bin readouts from both acquisitions into 20 cardiac phases with synchronization between sequences and without the need for interpolation of cardiac time-points (Figure 1C).

Fourth, respiratory curves are obtained using principal component analysis, followed by adaptive low pass filtering that targets frequencies within physiologically plausible ranges for respiratory motion and detrending to reduce potential offsets between the two sequences or signal drift [7]. The bulk translational motion of the heart due to respiration is then corrected for both free-running FISS and free-running PC-MRI datasets, using focused navigation (fNAV) as previously described [15,16]. Briefly, the unitless respiratory curve derived from Pilot Tone is multiplied by three initially unknown coefficients that describe the maximum displacement in millimeters of the heart over time along the three spatial dimensions. These coefficients are iteratively updated according to a metric for image blur (entropy of the gradient image) calculated over a region-of-interest containing the heart in the FISS images (Figure 1D).

Fifth and finally, the optimized displacement measurements are applied to the corresponding k-space data as a phase shift for both the FISS and PC-MRI acquisitions to correct for respiratory motion (Figure 1E). The data are binned into cardiac phase as described in the third step, and synchronized 4D FISS and 4D Flow images are reconstructed using k-t-sparse SENSE (Figure 1F), that has been previously described for free-running FISS and free-running PC-MRI [7,9,17].

Study cohort

Eight healthy volunteers (4F, ages 23-32) were scanned on a 1.5T MAGNETOM Sola system (Siemens Healthcare, Erlangen, Germany) using the 12-channel body coil array with an integrated PT transmitter. All subjects provided written informed consent compliant with our institutional guidelines and approved by the local research ethics committee.

MR Image Acquisition

As described in the previous section, free-running 3D radial FISS [8] and PC-MRI [9] sequences were acquired back-to-back, for a non-contrast and natively fat suppressed whole-heart anatomical acquisition, and whole-heart acquisition with velocity encoding respectively. Both sequences are derived from a free-running 3D golden-angle radial research sequence [7,18,19], where data is continuously acquired over time, using a spiral phyllotaxis readout pattern [20].

The trajectory is partitioned into interleaves, which contain radial readouts spiraling down k-space [7,10]. Each new interleave is rotated by the golden angle with respect to the previous one. The trajectory (i.e. the number of interleaves and the number of readouts per interleave) has been adapted differently for both sequences used in this study (FISS or flow), to account for the repeated velocity encoded readouts in the flow sequence.

For the free-running FISS sequence, a total of 12000 radial interleaves were acquired, each with 24 readouts and 6 readouts per FISS module. For each readout, TR= 2.94 ms and TE= 1.5 ms, and the scan time was 3:45 min [8]. For the free-running 3D radial PC-MRI sequence, 4820

interleaves were acquired, where imaging readouts were repeated 4 times for balanced 4-point velocity encoding [9,10]. A total of 21 radial readouts was acquired per interleave (1 SI + (5 readouts x 4-point velocity encoding)). For each readout, TR= 5.3 ms, TE= 3.5 ms, venc= 150 cm/s, and scan time=8:59 min. Both free-running FISS and PC-MRI were acquired with the same field of view of $(220mm)^3$, spatial resolution $(2.0mm)^3$ and same prescription of the acquisition volume

In addition to the free-running sequences, two reference standard breath-held 2D flow datasets at end-expiration were acquired for comparison, in the ascending (AAo) and descending aorta (DAo). Sequence parameters for the 2D flow acquisitions were as follows: TR/TE=5.1/2.9ms, venc=150cm/s, FOV=380x260mm^2, spatial resolution= 2.0x2.0x6.0mm^3, Scan time=0:15min.

Free-running image reconstruction

All volunteer data were reconstructed using the SyNAPS framework on a workstation equipped with 2 Intel Xeon CPUs (Intel, Santa Clara, CA), 512GB of RAM, and a NVIDIA Tesla GPU (Nvidia, Santa Clara, CA). For the k-t-sparse SENSE reconstruction [7,9,17],after first normalizing each acquisition by the maximum signal from a gridded image reconstruction, regularization parameters for reconstructing free-running FISS datasets were 0.03 for total variation applied along the cardiac dimension and 0.015 for total variation applied along the spatial dimension, and regularization parameters for free-running PC-MRI were 0.0075 in the cardiac dimension and 0.015 in the spatial dimension [16]. The free-running FISS reconstructions resulted in 4-dimensional (4D) FISS datasets (x-y-z-cardiac); reconstructions of free-running PC-MRI data returned 4D flow datasets (x-y-z-cardiac-velocity encode).

Data Analysis

After reconstruction, the high blood-myocardium contrast images from 4D FISS (magnitude images) were combined with the phase images from the 4D flow datasets to create SyNAPS 4D flow datasets. In both 4D flow datasets (with and without SyNAPS) vessel planes were manually placed to match the same location as the 2D flow acquisitions in the AAo, DAo, and were analyzed using the Circle cvi42 software (Calgary, Canada). In the planes selected for the descending aorta, a cardiac frame was selected so it included a portion of the myocardium. To quantify blood-to-myocardium contrast, two regions of interest were manually drawn, one in the descending aorta and one in the myocardium, and the ratio of the signal intensity between these two regions was calculated.

Dynamic vessel tracing was performed for all flow datasets, based on magnitude and phase images and was semi-automatically adjusted. The absolute difference in vessel area was estimated between each 4D flow segmentation and the reference 2D flow segmentation for each time point, and the mean and standard deviation of the absolute vessel area difference was then estimated across all subjects. Additionally, the Dice similarity coefficient was computed between each 4D flow and 2D flow dynamic vessel segmentations.

The flow rate curve over the cardiac cycle was obtained for each segmentation, and net volume and peak flow measurements were calculated. Differences in net volume and peak flow were estimated between each 4D flow dataset and the 2D flow reference.

Linear regression and Bland-Altman analysis were used to compare SyNAPS 4D flow, 4D flow and 2D flow measurements. A Wilcoxon signed rank test was performed to assess the significant value of the differences measured.

Results

Figure 2 shows two representative examples from healthy subjects, with AAo and DAo segmentations placed in the same location in SyNAPS 4D flow, 4D flow and 2D flow. In both cases, the main visual differences shown from SyNAPS 4D flow are the increase in blood image contrast in the magnitude information when compared to 4D flow. Additionally, the image contrast provided by FISS has enabled the clear visualization of moving cardiac structures, including the segmented vessels, and it shows similar tissue contrast to the 2D flow images, which benefit from in-flow effects. The estimated blood-to-myocardium contrast ratio from SyNAPS 4D flow (1.5±0.4) approaches the ratio from 2D flow (2.0±0.9, p=0.55), while 4D flow datasets had the lowest contrast ratio (0.7±0.1, p<0.01).

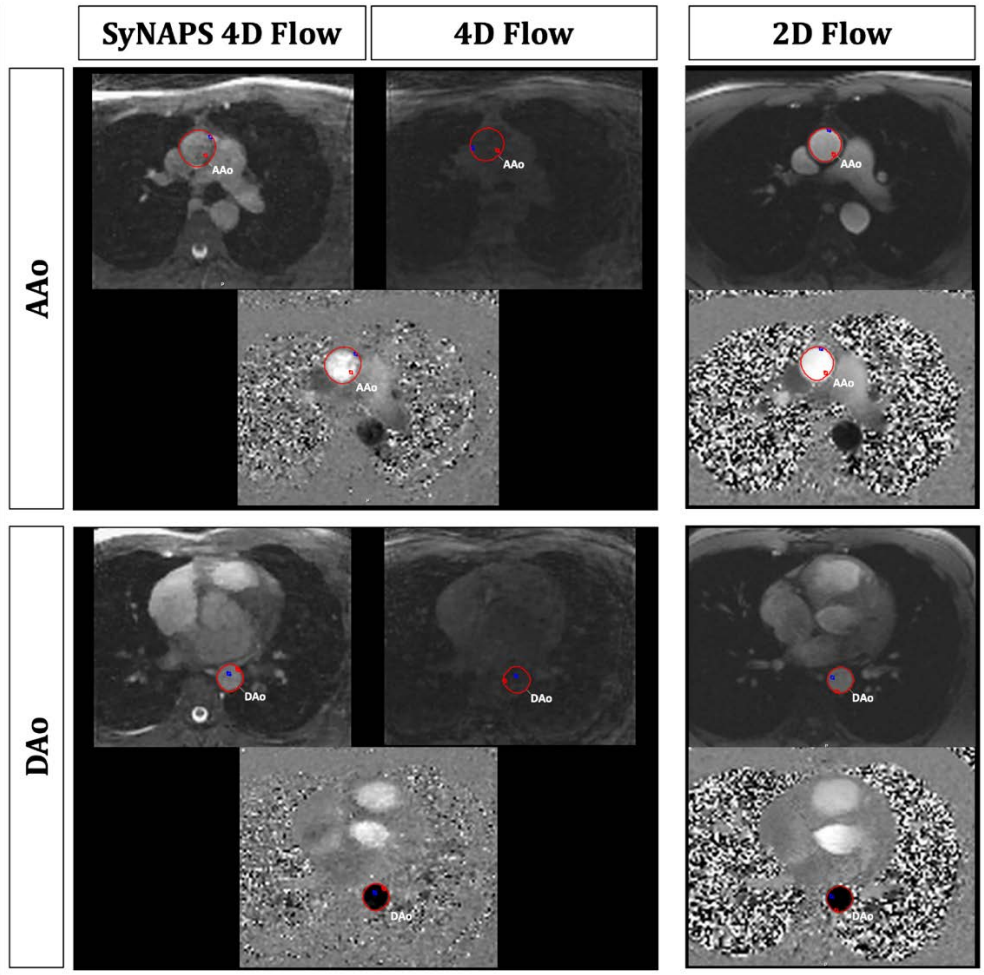

Figure 2. Comparison of SyNAPS 4D Flow to 4D Flow and to the reference 2D Flow for one representative healthy volunteer. The anatomical images integrated in SyNAPS 4D Flow increase the image contrast when compared to 4D Flow MRI. Additionally, heart and vessel structures are better depicted in SyNAPS 4D Flow, with similar contrast to the one from 2D Flow MRI. *AAo: base of the ascending aorta; DAo: the mid descending aorta. Images and vessel segmentations were captured from the image processing software, and blue and red dots inside the vessel segmentation represent maximum and minimum velocity voxels.*

Moreover, when looking at the magnitude images over time, we observed that the delineation of the vessel borders in SyNAPS 4D flow was constant throughout the cardiac cycle, while 2D flow magnitude images, due to the in-flow effects, showed clear fluctuations in signal intensity, reducing vessel visibility. In 2D flow, a higher signal intensity is reported in the blood during mid-systole, with a reduction in signal intensity along the rest of the cardiac cycle until reaching mid-diastole, when the blood velocity in the main vessels is largely reduced. This effect can be visualized in Figure 3, which also shows the consistently low signal level from the 4D flow magnitude images. Moreover, Supplementary Video S1 shows this effect across the cardiac cycle, for four subjects.

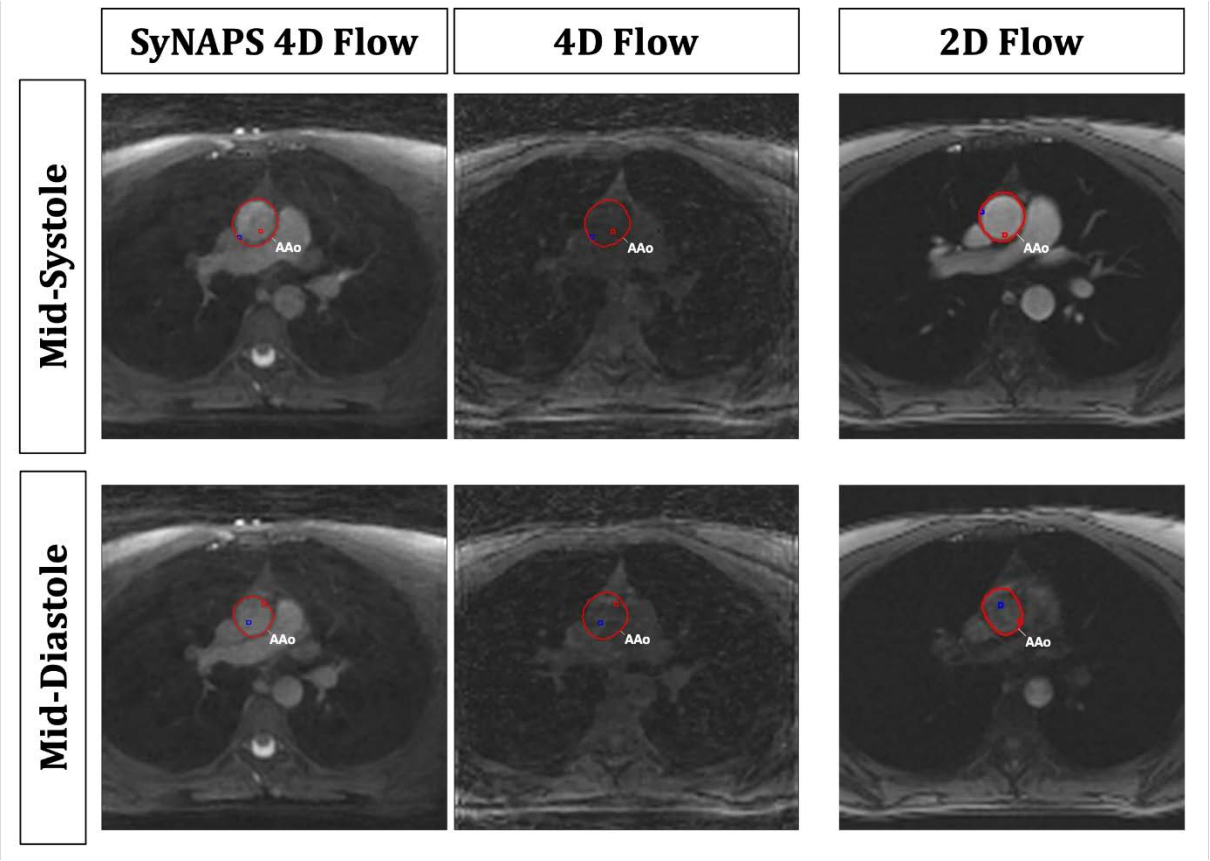

Figure 3. Image contrast between mid-systolic and mid-diastolic phases of the cardiac cycle in the magnitude images for SyNAPS 4D flow, 4D flow and 2D flow datasets of a healthy 26 years old female subject. Image contrast varied in 2D flow, due to inflow effects, while in SyNAPS 4D flow it remains constant. 4D flow provided the worst image contrast of the three techniques. *AAo: base of the ascending aorta; DAo: the mid descending aorta. Images and vessel segmentations were captured from the image processing software, and blue and red dots inside the vessel segmentation represent maximum and minimum velocity voxels.*

For the resulting vessel segmentations, changes in vessel area are observed over time for SyNAPS 4D flow, as well as for the reference 2D flow results, while vessels segmented using 4D flow were mainly static segmentations, as shown in Figure 4. The absolute difference in vessel area (across all time points and volunteers) between SyNAPS 4D flow and 2D flow was 61.1±26.7 mm^2 for AAo ($p=0.08$) and 58.3±20.2 mm^2 for DAo ($p=0.02$). Conversely, when comparing 4D flow with 2D flow, differences in vessel area were 90.5±18.8 mm^2 for AAo

(p=0.008) and 103.4±58.9 mm^2 for DAo (p=0.008). The Dice similarity coefficient between SyNAPS 4D flow and 2D flow vessel segmentations was 0.88±0.05 for the AAo and 0.88±0.04 for the DAo, whilst the Dice similarity coefficient between vessel segmentations of 4D flow and 2D flow was 0.83±0.08 for the AAo and 0.85±0.07 for the DAo. Differences between the SyNAPS 4D flow vs. 2D flow and 4D flow vs. 2D flow dice scores were statistically significant (p≤0.01). The Pearson correlation coefficient between the dynamic vessel area of SyNAPS 4D flow and 2D flow was 0.72±0.27 for the AAo and 0.82±0.09 for the DAo, and the correlation values obtained between 4D flow and 2D flow were lower, 0.09±0.37 for the AAo and 0.12±0.44 for the DAo.

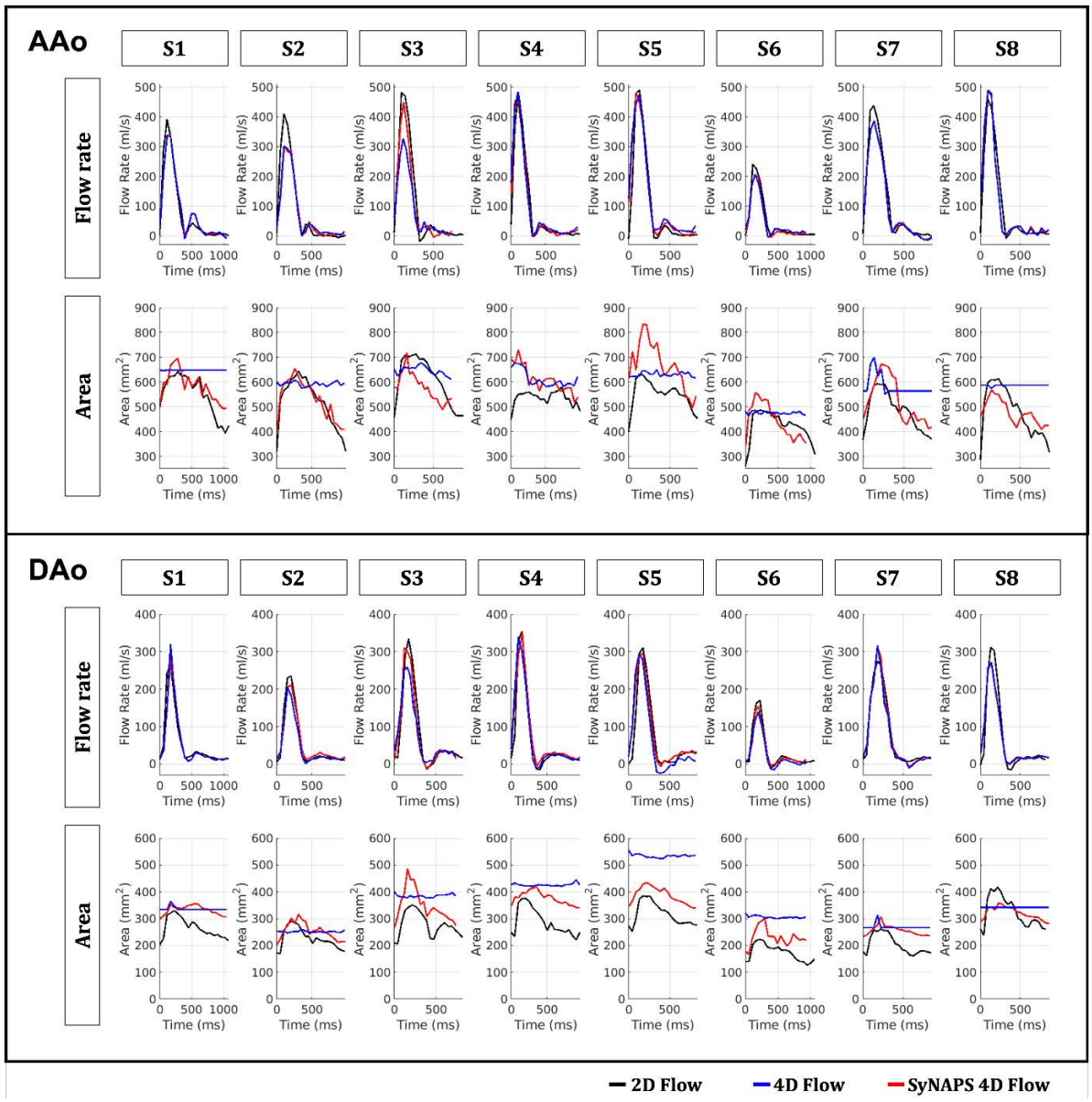

Figure 4. Visualization of flow rate and vessel area across the cardiac cycle for 2D flow, 4D flow, and SyNAPS 4D flow. For all healthy volunteers included in this study, two vessel locations were chosen, one at the base of the ascending aorta (AAo), and another one in the mid descending aorta (DAo). *Black: 2D flow; Blue: 4D flow; Red: SyNAPS 4D flow.*

Figure 4 shows the flow rate curves over time for 2D flow, 4D flow and SyNAPS 4D flow. Across all vessels analyzed, it is possible to visualize cases where the flow curves agree between the three flow datasets (e.g. S4 in AAo), but there are also cases where both SyNAPS 4D flow and 4D flow underestimate the flow rate at peak systole when compared to 2D flow (e.g. S8 in DAo), and some cases show an improvement in flow rate of SyNAPS 4D flow, with a closer agreement to 2D flow when compared to 4D flow curves (e.g. S3 in AAo). Measurements of net volume and peak flow rate are compared among approaches in Figure 5, with linear regression results showing similar significant correlation between all flow datasets ($p<0.05$). Moreover, Bland-Altman analysis showed a lower bias and limits of agreement between SyNAPS 4D flow and 2D Flow relative to 4D Flow vs 2D flow.

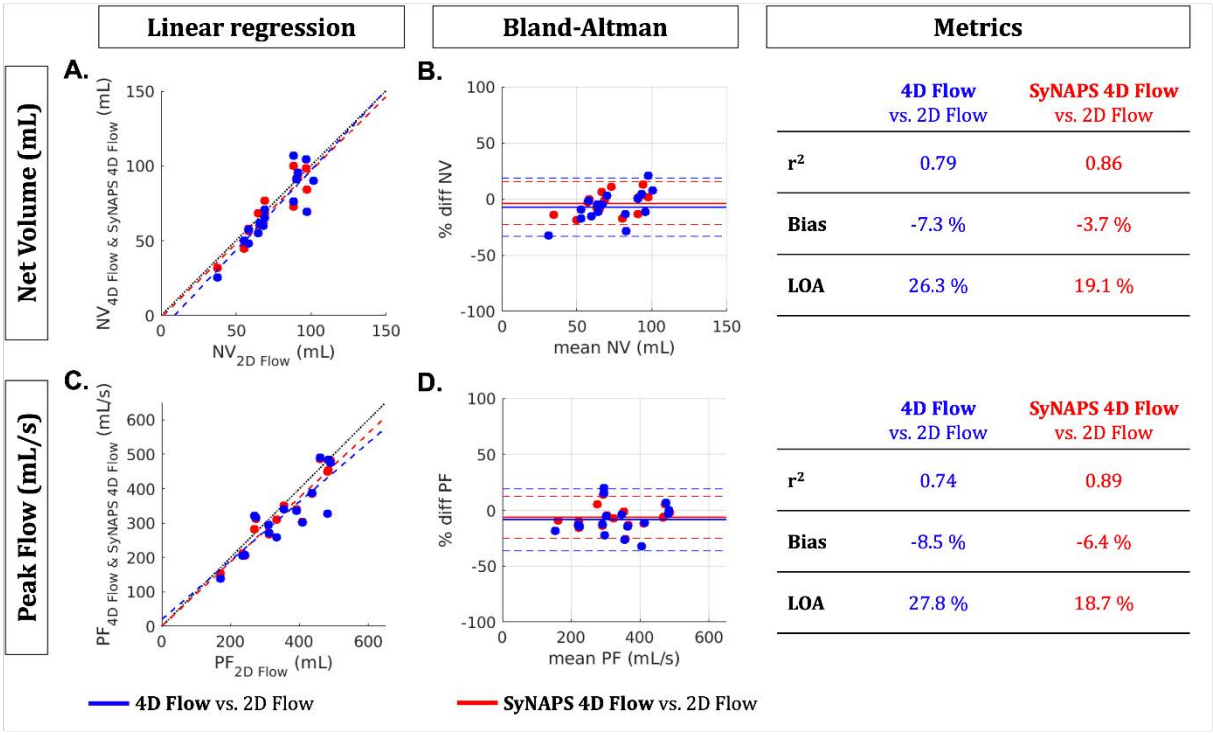

Figure 5. Comparison of net flow (A-B) and peak flow (C-D) measurements between 4D Flow vs. 2D Flow as well as between SyNAPS 4D Flow vs. 2D Flow. Linear regression **(A,C)** and Bland Altman **(B,D)** plots show smaller biases when using SyNAPS 4D Flow. **A,C.** Black dotted lines represent the ideal linear regression trend (slope=1) and color dashed lines represent the linear regression outcome for each pair. **B,D.** bias is depicted in solid lines; limits of agreement (LOA) are represented by dashed lines. *Blue: 4D Flow vs. 2D Flow; Red: SyNAPS 4D Flow vs. 2D Flow. r2: coefficient of determination.*

Discussion

In this work, we introduced SyNAPS, a novel technique for synchronizing and reconstructing consecutively acquired free-running radial whole-heart MRI sequences. Using SyNAPS we combined free-running anatomical (FISS) and flow (PC-MRI) sequences to reconstruct SyNAPS 4D flow images that enable a better overall visualization of the cardiovascular anatomy, with improved dynamic segmentation of blood vessels, resulting in a more accurate assessment of flow without the need for contrast agents.

In SyNAPS 4D flow, the phase information is derived from the free-running flow sequence, just like in 4D flow datasets, however, here the magnitude information, obtained from 4D FISS, provides improved anatomical image contrast. Therefore, the main difference between a SyNAPS 4D flow dataset and a standard 4D flow dataset pertains to the fact that on the first case there is an improved anatomical visualization of cardiac structures, which change dynamically over the cardiac cycle, empowering a dynamic segmentation of the vessels of interest and consequently enhancing the quantification accuracy of flow measurements in those vessels. This unfortunately is not easily achieved solely with 4D flow as the magnitude information provides very low blood-myocardium contrast when performing image acquisition without contrast agent injection. When comparing SyNAPS 4D flow to 4D flow, we can observe that the magnitude information is clearly improved, and additionally comparable to the magnitude information extracted from the 2D flow datasets, which benefit from in-flow enhancement. Additionally, because the in-flow enhancement is sensitive to blood velocity, vessels visibility appear to be more consistent across the cardiac cycle for SyNAPS 4D flow than for 2D flow.

Previous studies have also explored the possibility of leveraging a separately acquired 3D anatomical scan to improve vessel and ventricular segmentation, and thus empower a more accurate flow quantification when combined with a Cartesian 4D flow acquisition [12,13]. These studies used retrospective ECG-gating to synchronize reconstructions to the underlying heart rate and interpolation to provide the same number of cardiac phases for each sequence. To account for respiratory motion, strategies using multiple-averages [12] or prospective respiratory gating to limit data-acquisition to end-expiration [13] have been proposed. The later also investigated image registration to account for residual respiratory motion due to differences in the navigator signals derived from the two sequences, and used a gadolinium-based contrast agent to enhance image quality [13]. Compared to these studies, SyNAPS did not require contrast agents for providing good delineation of anatomical structures, while using Pilot Tone enabled the synchronization of acquisitions without the need for performing multiple averages or interpolating cardiac phases. Moreover, we are no longer limited by differences in the navigator signals, which are typically sequence dependent, to obtain co-registered volumes. The extraction of the respiratory curves and cardiac triggers from the Pilot Tone signals that span the two acquisitions ensures that the signals go through the same post-processing framework and therefore are treated similarly to ensure consistency between signals.

The present study has some limitations. First, there is no absolute validation tool to guarantee that SyNAPS is synchronizing the acquired anatomy and flow datasets. Our current assessment of data synchronization comes from the fact that the combined vessel area comparison and flow results from SyNAPS 4D flow have a good agreement with the reference 2D flow. Nevertheless, small unnoticeable errors may exist, that could have been caused by a drift in the respiratory signal. A more in-depth in vitro study could help understand possible sources of asynchrony to expect in SyNAPS, but random sources of signal corruption may be too complex to simulate. Additionally, image registration could help quantify any possible shift between datasets, however the magnitude data from free-running 3D PC-MRI has considerably lower contrast compared to free-running FISS, which may hinder this computation.

A second limitation of this study is the use of fNAV to correct respiratory motion. In this study, fNAV is only correcting translational bulk motion, and, as a result, does not account for

rotational motion or the more general non-rigid behavior of respiratory motion. This can lead to small motion correction errors in the final imaging datasets. Further developments aim at extending fNAV to non-rigid motion correction in SyNAPS data. Nevertheless, fNAV is not an essential component to the SyNAPS framework, and the synchronized datasets can instead be reconstructed into several respiratory phases to create synchronized 5D imaging volumes [7,9].

Finally, the use of free-running FISS as the anatomical dataset to integrate in SyNAPS 4D flow was chosen because, like a bSSFP sequence, it provides a good blood to myocardium image contrast, but also has native fat suppression that should decrease streaking artifacts in the resulting anatomical image. However, for higher spatial resolutions, other free-running anatomical sequences, such as a bSSFP sequence with fat saturation pulses [7,18] or a bSSFP sequence incorporating LIBRE pulses [21], might provide alternative options for visualizing the cardiovascular anatomy, and would be easily integrated in the SyNAPS framework, due its intentional independence from the underlying contrast or sequence parameters.

Despite the presented limitations of this study, the introduction of SyNAPS as a solution to having both cardiac and respiratory synchronization in cardiac MRI could enable a more comprehensive cardiac MRI evaluation, where all free-running and volumetric sequences are connected. These promising initial results motivate further validation of the framework, especially in the context of heart-rate variability and respiratory drift. Using SyNAPS, a contrast-free whole-heart 4D flow acquisition with good blood-to-myocardium contrast that enables the dynamic segmentation of the vessels for improved quantification of blood flow intake in vessels can now be acquired within a fixed scan time. This easy-to-use setup, which does not require respiratory navigators, could possibly become an alternative to conventional 4D flow techniques to increase image quality without the need for contrast agents. Moreover, SyNAPS could also be applied to other branches of the free-running framework, such as T1 [14] mapping, T2 [22] mapping or fat fraction mapping [23], to create a highly comprehensive MRI-based tool for a synchronized assessment of the structure, function, flow, and tissue properties of the heart, for an improved clinical assessment of heart disease.

Conclusion

This work introduces SyNAPS, a novel framework that builds towards comprehensive whole-heart MRI without the need for contrast agents, by synchronizing free-running acquisitions. We demonstrated the initial feasibility and utility of SyNAPS on a setup for joint whole-heart anatomical and flow MRI that does not require ECG gating or respiratory navigators. We show that the high-contrast anatomical imaging sequence can be leveraged to improve 4D flow measurements that often suffer from poor delineation of the vessel boundaries in the absence of contrast agents.

References

1. Leiner T, Bogaert J, Friedrich MG, Mohiaddin R, Muthurangu V, Myerson S, et al. SCMR Position Paper (2020) on clinical indications for cardiovascular magnetic resonance. J Cardiovasc Magn Reson [Internet]. 2020;22:1–37. Available from: https://doi.org/10.1186/s12968-020-00682-4

2. Markl M, Frydrychowicz A, Kozerke S, Hope M, Wieben O. 4D flow MRI. J Magn Reson Imaging. 2012;36:1015–36.
3. Calkoen EE, Roest AAW, Van Der Geest RJ, De Roos A, Westenberg JJM. Cardiovascular function and flow by 4-dimensional magnetic resonance imaging techniques: New applications. J Thorac Imaging. 2014;29:185–96.
4. Do C, DeAguero J, Brearley A, Trejo X, Howard T, Escobar GP, et al. Gadolinium-Based Contrast Agent Use, Their Safety, and Practice Evolution. Kidney360. 2020;1:561–8.
5. DeLoughery TG. Risk of Anaphylaxis With Intravenous Iron Products. JAMA [Internet]. 2016;315:2232. Available from: https://www.pdr.net/fda-drug-safety-communication/feraheme?druglabelid=1201
6. U.S. Food and Drug Administration: Feraheme (ferumoxytol): Drug safety communication - warnings strengthened and prescribing instructions changed. 2015.
7. Di Sopra L, Piccini D, Coppo S, Stuber M, Yerly J. An automated approach to fully self-gated free-running cardiac and respiratory motion-resolved 5D whole-heart MRI. Magn Reson Med. 2019;82:2118–32.
8. Bastiaansen JAM, Piccini D, Sopra L Di, Roy CW, Heerfordt J, Edelman RR, et al. Natively fat-suppressed 5D whole-heart MRI with a radial free-running fast-interrupted steady-state (FISS) sequence at 1.5T and 3T. Magn Reson Med. 2019;00:1–11.
9. Ma LE, Yerly J, Piccini D, Sopra L Di, Roy CW, Carr JC, et al. 5D Flow MRI : A Fully Self-gated, Free-running Framework for Cardiac and Respiratory Motion – resolved 3D Hemodynamics. Radiol Cardiothorac Imaging. 2020;2.
10. Falcão MBL, Di Sopra L, Ma L, Bacher M, Yerly J, Speier P, et al. Pilot tone navigation for respiratory and cardiac motion-resolved free-running 5D flow MRI. Magn Reson Med. 2021;00:1–15.
11. Vahle T, Bacher M, Rigie D, Fenchel M, Speier P, Bollenbeck J, et al. Respiratory Motion Detection and Correction for MR Using the Pilot Tone: Applications for MR and Simultaneous PET/MR Examinations. Invest Radiol. 2020;55:153–9.
12. Koktzoglou I, Edelman RR. Radial Fast Interrupted Steady-State (FISS) Magnetic Resonance Imaging. Magn Reson Med. 2018;79:2077–2086.
13. Edelman RR, Serhal A, Pursnani A, Pang J, Koktzoglou I. Cardiovascular cine imaging and flow evaluation using Fast Interrupted Steady-State (FISS) magnetic resonance. J Cardiovasc Magn Reson. Journal of Cardiovascular Magnetic Resonance; 2018;20:1–9.
14. Di Sopra L, Roy CW, Bastiaansen JAM, Yerly J, Piccini D, Arn L, et al. Fully Self-Gated Cardiac and Respiratory Motion-Resolved Isotropic 5D T1 Mapping of the Heart : Preliminary Results. Proc Intl Soc Mag Reson Med. 2019;27.
15. Roy CW, Heerfordt J, Piccini D, Rossi G, Pavon AG, Schwitter J, et al. Motion compensated whole-heart coronary cardiovascular magnetic resonance angiography using focused navigation (fNAV). J Cardiovasc Magn Reson. BioMed Central; 2021;23:1–17.
16. Falcão MBL, Rossi GMC, Ma L, Heerfordt J, Piccini D, Yerly J, et al. Correcting vs resolving respiratory motion in accelerated free-running whole-heart radial Flow MRI using focused navigation (fNAV). Proc Intl Soc Mag Reson Med. 2021;29.
17. Feng L, Axel L, Chandarana H, Block KT, Sodickson DK, Otazo R. XD-GRASP: Golden-angle radial MRI with reconstruction of extra motion-state dimensions using compressed sensing. Magn Reson Med. 2016;75:775–88.

18. Coppo S, Piccini D, Bonanno G, Chaptinel J, Vincenti G, Feliciano H, et al. Free-running 4D whole-heart self-navigated golden angle MRI: Initial results. Magn Reson Med. 2015;74:1306–16.
19. Feng L, Coppo S, Piccini D, Yerly J, Lim RP, Masci PG, et al. 5D whole-heart sparse MRI. Magn Reson Med. 2017;79:826–38.
20. Piccini D, Littmann A, Nielles-vallespin S, Zenge MO. Spiral Phyllotaxis : The Natural Way to Construct a 3D Radial Trajectory in MRI. Magn Reson Med. 2011;66:1049–56.
21. Masala N, Bastiaansen JAM, Di Sopra L, Roy CW, Piccini D, Yerly J, et al. Free-running 5D coronary MR angiography at 1.5T using LIBRE water excitation pulses. Magn Reson Med. 2020;84:1470–85.
22. Rumac S, Roy CW, Yerly J, Falcao MBL, Bustin A, Bacher M, et al. Free-running isotropic whole-heart T2 mapping with ECG-free Pilot Tone navigation. 30th Int Soc Magn Reson Med. 2022.
23. Mackowiak ALC, Roy CW, Yerly J, Sopra L Di, Falcão MBL, Bacher M, et al. Whole-Heart Motion-Resolved Multi-Peak Fat-Fraction Mapping using Free-Running 3D Radial Multi-Echo GRE and Pilot Tone. Proc Intl Soc Mag Reson Med. 2021;29.
24. Pruitt A, Rich A, Liu Y, Jin N, Potter L, Tong M, et al. Fully Self-Gated Whole-Heart 4D Flow Imaging from a Five-Minute Scan. Magn Reson Med. 2021;85:1222–12236.
25. Kolbitsch C, Vasquez CP, Bastkowski R, Weiss K, Maintz D. Respiratory motion corrected 4D flow using golden radial phase encoding. Magn Reson Med. 2019;00:1-10.
26. Walheim J, Dillinger H, Kozerke S. Multipoint 5D flow cardiovascular magnetic resonance - Accelerated cardiac- and respiratory-motion resolved mapping of mean and turbulent velocities. J Cardiovasc Magn Reson. Journal of Cardiovascular Magnetic Resonance; 2019;21:1–13.
27. Bastkowski R, Bindermann R, Brockmeier K, Weiss K. Respiration Dependency of Caval Blood Flow in Patients with Fontan Circulation : Quantification Using 5D Flow MRI. Radiol - Cardiothorac Imaging. 2019;1:e190005.
28. Ma L, Yerly J, Di Sopra L, Piccini D, Lee J, DiCarlo A, et al. Using 5D flow MRI to decode the effects of rhythm on left atrial 3D flow dynamics in patients with atrial fibrillation. Magn Reson Med. 2021;85:3125–39.

4.3. Conclusions and Outlook of this work

In this study, a novel technique was developed to synchronize and combine two sequentially acquired free-running sequences. Using the proposed SyNAPS method, one anatomical free-running sequence and one free-running PC-MRI sequence were combined into one comprehensive 4D 'anatomy + flow' imaging dataset, which provided improved anatomical image quality compared to simple 4D flow reconstructions of the same data without the need for contrast injection. The improvement in the visualization of cardiovascular structures enabled a dynamic segmentation of vessels, which in turn increased the precision of flow quantification.

The development of SyNAPS was only possible thanks to the two projects described in Chapters 2 and 3, demonstrating that addressing different limitations of the free-running PC-MRI framework has a direct positive impact in its improvement over time. Particularly, using Pilot Tone to perform a sequence independent respiratory and cardiac motion detection was the key element to enable the synchronization of two different free-running sequences.

Moreover, connecting anatomical information with flow information improved the comprehensibility of the 4D flow dataset without the need for contrast injection. The advantages to not using any contrast agents are broad, from reducing medical costs and setup time to reducing the risk of contrast-derived comorbidities, particularly common in Gadolinium-based contrast agents.

Despite its initial validation for 4D "anatomy + flow" datasets, the long-term advantages go beyond synchronizing only these two modalities. Using SyNAPS could enable information sharing between multiple sequences (anatomy, flow, T1 mapping, T2 mapping, etc.), creating a more comprehensive multi-dimensional CMR exam. The sharing of information between sequences could also be used in the future to further accelerate scan times, and to develop reconstruction algorithms that explore the sparsity across sequences to improve image quality.

Chapter 5.
Complementary projects

While the main focus of this doctoral thesis was to improve the overall ease of use and quality of the free-running PC-MRI framework, either by establishing new modalities for signal extraction or by including motion correction algorithms within the framework, over time different questions arose, that in turn became small research projects. None of these projects has so far been extended to article format, but they were submitted to peer-reviewed conferences: two of them were presented in past years and the third one was submitted to a conference for next year.

Although each project focuses on a different question, they still have one main goal in mind: improve our understanding of the free-running PC-MRI framework when acquired in different contexts. In each sub-chapter, a different technical question was addressed:

Chapter 5.1) How can different contrast agents influence the flow outcome in 5D flow reconstructions of free-running PC-MRI data?

Chapter 5.2) What are the effects of different field strengths (1.5T vs. 3T) in 5D flow reconstructions of free-running PC-MRI data?

Chapter 5.3) Can we extract features of the ECG signal from the free-running PC-MRI self-gating data using a deep-learning network?

5.1. On the effects of contrast agents in free-running whole-heart 5D flow Imaging

5.1.1. Overview and Personal Contribution

In Chapter 4, SyNAPS was developed to synchronize back-to-back acquisitions, that when validated using one anatomical and one flow sequence yielded 4D flow datasets with improved anatomical blood-to-myocardium contrast, which enabled dynamic vessel segmentation and, thus, improved flow quantification without the need to use contrast agents. Alternatively, using contrast agents may improve the signal quality of PC-MRI datasets, and could possibly benefit the optimization of sequence parameters, and further reduce scan times. The injection of contrast agents such as Gadolinium-based or Ferumoxytol-based compounds shortens the relaxation time of tissues within the body that are capable of absorbing these contrast agents to their medium. As a result, using particular sequences, these tissues can have a larger contrast from the remaining tissues that have not absorbed the contrast agent, improving the visualization of some anatomical structures. These contrast agents can be used to visualize vessels, and, additionally, Gadolinium is commonly used to visualize the myocardial scar formation and regional myocardial fibrosis.

This study focuses on comparing the use of contrast agents in the flow performance of the free-running 3D radial PC-MRI framework, with 5D flow reconstructed datasets, in a cohort of congenital heart disease patients. Since using contrast agents increases the signal detected in the bloodstream, they are expected to enable a better flow quantification than when compared to native contrast (no-contrast). Similar work has since been reported by *Kollar et al. at the Journal of Cardiovascular Magnetic Resonance 2022 (doi:10.1186/s12968-022-00886-w)*. Nevertheless, this hypothesis had not been tested in the free-running 3D radial PC-MRI framework, and therefore we performed an initial study to try to compare 5D flow images reconstructed from patients with native contrast to those with either Gadolinium or Ferumoxytol.

The results of this study were submitted as an abstract at the Society for Magnetic Resonance Angiography (SMRA) 34th Annual International Conference in 2022, where it was accepted as a Power Pitch. The investigation of how contrast agents can influence the quality of multi-dimensional PC-MRI imaging is highly relevant to ensure robustness of the techniques, clinical protocol definition, and their impact on clinical assessment.

5.1.2. Abstract

On the effects of contrast agents in free-running whole-heart 5D flow Imaging

Mariana B. L. Falcão[1], Tobias Rutz[2], Milan Prša[3], Estelle Tenisch[1], Liliana Ma[4,5], Michael Markl[4,5], Matthias Stuber[1,5], Christopher Roy[1]

[1]Department of Diagnostic and Interventional Radiology, Lausanne University Hospital (CHUV) and University of Lausanne (UNIL), Lausanne,
Switzerland

[2]Service of Cardiology, Centre de resonance magnétique cardiaque (CRMC), Lausanne University Hospital (CHUV) and University of Lausanne (UNIL), Lausanne, Switzerland

[3]Woman-Mother-Child Department, Lausanne University Hospital (CHUV) and University of Lausanne (UNIL), Lausanne, Switzerland

[4]Department of Radiology, Feinberg School of Medicine, Northwestern University, Chicago, Illinois, USA

[5]Department of Biomedical Engineering, Northwestern University, Chicago, Illinois, USA

[4]Siemens Healthcare GmbH, Erlangen, Germany

[5]Center for Biomedical Imaging (CIBM), Lausanne, Switzerland

Purpose

In free-running whole-heart radial phase-contrast (PC) MRI[1], fully self-gated respiratory and cardiac motion-resolved 3D images are reconstructed with velocity sensitivity across three orthogonal directions (5D flow MRI)[1, 2]. Compared to the current clinical gold standard 2D PC MRI[3], this framework improves scanning efficiency as well as ease-of-use[1]. However, to date, the effect of using contrast in 5D flow MRI has not been investigated. In this study, we compared flow measurements from 5D flow datasets collected without contrast agent, with Ferumoxytol, and with Gadolinium. 2D PC MRI was acquired as reference. We tested the hypothesis that post-contrast 5D flow MRI improves the accuracy of flow measurements relative to no contrast.

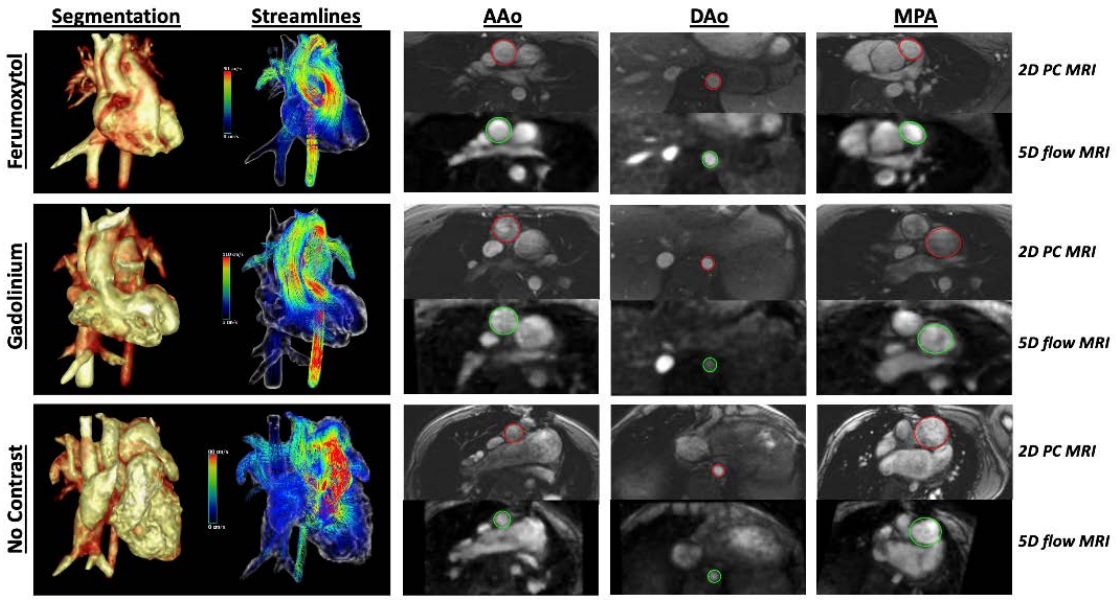

Figure 1. Comparison between three CHD patients acquired with 5D flow MRI. Top to bottom: Ferumoxytol (19y, M, Marfan syndrome), Gadolinium (21y, M, transposition of the great arteries, post-atrial switch), and no contrast (34y, M, tricuspid atresia). Left to right: 3D Segmentation, 3D Streamlines, and 2D contours of AAo, DAo, and MPA.

Methods

15 congenital heart disease (CHD) patients (age 22.5±11.4, 4 F) were scanned on a 1.5T MAGNETOM Sola system (Siemens Healthcare, Erlangen, Germany) using the 5D flow MRI sequence[1]. Additionally, 2D PC MRI was acquired in the proximal ascending aorta (AAo), descending aorta (DAo) and main pulmonary artery (MPA). Prior to the scanning, five subjects received Gadolinium, and five subjects received Ferumoxytol. The five remaining subjects were scanned without a contrast agent. 2D PC MRI contours were drawn on magnitude images. Using a compressed-sensing-based image reconstruction framework [1,2], end-expiratory 5D flow images were selected. 3D vessel segmentation was based on retrospectively computed phase-contrast angiography images for each 5D flow dataset. Orientations and anatomical levels from the 2D PC MRI planes (AAo, DAo, MPA) were used for reformatting and comparison with the 2D images, using Circle's cvi42 (Calgary, Canada) post-processing software. 5D flow segmentation and flow streamlines were visually inspected during the analysis. Net volumes and peak flow rates were measured, and Bland-Altman analysis was used to compare 5D flow MRI and 2D PC MRI. A Wilcoxon signed-rank test was used for statistical analysis.

Results

Segmentation and streamline visualization were qualitatively similar between each contrast group (**Fig.1**). Good agreement between 5D flow MRI and 2D PC MRI net volume measurements (**Fig.2**) can be reported for both Ferumoxytol (p=0.72) and Gadolinium groups (p=0.17), while significant differences were found when acquiring without contrast (p=0.03). Significant peak flow rate biases were identified in the Gadolinium group (p=0.001) and in the no contrast group (p=0.00006), but not for Ferumoxytol (p=0.17). Overall, flow measurements showed better agreement with 2D PC MRI in the Ferumoxytol group followed by its Gadolinium and no contrast counterpart.

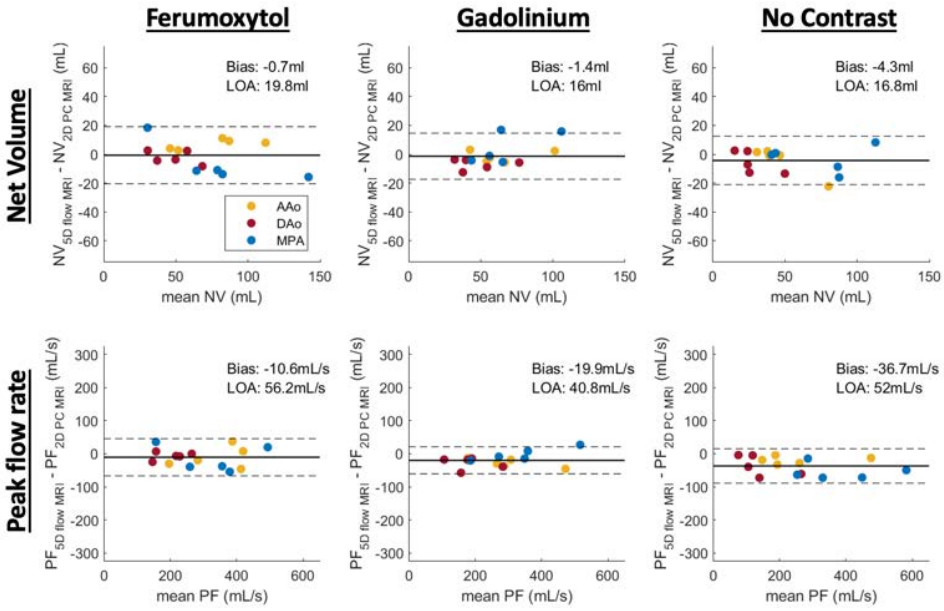

Figure 2. Bland–Altman plots between 5D flow MRI and 2D PC MRI measurements, for each contrast group. Top to bottom: net volume (NV) and peak flow rate (PF). Left to right: Ferumoxytol, Gadolinium and no contrast. Black continuous lines: bias. Black dashed lines: limits of agreement (LOA). AAo, DAo and MPA are visualized in different colors.

Discussion

In this preliminary study, we tested the effects of different types of contrast agents on 5D flow MRI measurements. We report that Ferumoxytol leads to an improvement in 5D flow assessment with respect to the reference 2D PC MRI, while 5D flow MRI without contrast agent showed the least favorable results. This confirms our hypothesis that contrast injection improves the quantification of flow measurements in 5D flow MRI, with regard to 2D PC MRI. The significant differences reported in the no contrast group suggests a larger sensitivity to noise, which is reduced when using Gadolinium, and even more so with Ferumoxytol. This study did not include a quantitative evaluation of signal-to-noise ratio, but future work will focus on adding related metrics and on scanning more subjects.

References

1. Ma LE, et al. 5D Flow MRI: A Fully Self-gated, Free-running Framework for Cardiac and Respiratory Motion – resolved 3D Hemodynamics. Radiol. Cardiothorac. Imaging 2020;2(6).

2. Di Sopra, et al. An automated approach to fully self-gated free-running cardiac and respiratory motion-resolved 5D whole-heart MRI. Magn. Reson. Med. 2019:1–15.

3. Kramer CM, et al. Standardized cardiovascular magnetic resonance imaging (CMR) protocols: 2020 update. J. Cardiovasc. Magn. Reson. 2020;22:1–18.

5.1.3. Conclusions and Outlook of this work

In this preliminary study including 15 patients, 5 for each contrast group, the results suggest a clear influence of contrast agents on the accuracy of flow measurements. Non-contrast data were in general visibly noisier, followed by Gadolinium and Ferumoxytol data, the latter showing the best agreement with reference flow measurements. These results may be largely affected by the image segmentation since non-contrast datasets showed an overall deterioration of anatomical blood-to-myocardium contrast. If that were the case, SyNAPS would provide an easy solution by integrating anatomical information into the flow datasets and grant a dynamic segmentation of vessels that would improve flow quantification.

Additionally, the use of SyNAPS could be extended to cases acquired with Gadolinium or Ferumoxytol, to understand if the flow quantification could be even further improved. If so, using contrast agents together with SyNAPS could then be used to accelerate the acquisition of free-running flow and anatomy datasets, which could become a powerful tool for a fast comprehensive MRI scan.

5.2. Fully self-gated respiratory and cardiac motion-resolved 5D flow: comparison at 1.5T and 3T

5.2.1. Overview and Personal Contribution

So far, we have described two ways to increase the image contrast and consequently improve flow quantification in the free-running PC-MRI framework. First, we introduced the SyNAPS tool that prompted the synchronization of two back-to-back acquisitions and enabled the creation of a joint 4D flow "anatomy + flow" reconstruction that provided improved anatomical blood-to-myocardium contrast and subsequently improved flow quantification. Secondly, we studied how using contrast agents may yield better signal quality and, therefore, improve flow quantification.

One additional way to increase signal quality is to acquire sequences at higher field strengths. So far, all the work presented in this doctoral dissertation has acquired imaging data at a 1.5T field strength. Studying the free-running PC-MRI framework at 3T could benefit from the higher signal-to-noise ratio (SNR) properties of higher field strengths, which could contribute to improving spatial or temporal resolution and decrease acquisition time. The free-running PC-MRI framework has a good set of ingredients that could enable a successful 3T application, but to date it has not been tested in this context.

In this study, we recruited a cohort of healthy subjects and compared 5D flow reconstructions of free-running PC-MRI data in back-to-back scans at 3T and 1.5T. We studied the differences and similarities between the flow outcomes in the two field strengths.

Together with Dr. Christopher Roy, I recruited all subjects for this study. I performed all image reconstructions and analyses. This study was submitted as an abstract at the SCMR 24th Annual Scientific Sessions in 2021, where it was accepted as an oral presentation.

5.2.2. Abstract

Fully self-gated respiratory and cardiac motion-resolved 5D flow: comparison at 1.5T and 3T

Mariana B. L. Falcão[1], Liliana Ma[2,3], Lorenzo Di Sopra[1], Jérôme Yerly[1,4], Michael Markl[2,3], Matthias Stuber[1,4], Christopher W. Roy[1]

[1]Department of Diagnostic and Interventional Radiology, Lausanne University Hospital (CHUV) and University of Lausanne (UNIL), Lausanne, Switzerland

[2]Department of Radiology, Feinberg School of Medicine, Northwestern University, Chicago, Illinois, USA

3Department of Biomedical Engineering, Northwestern University, Chicago, Illinois, USA

[4]Center for Biomedical Imaging (CIBM), Lausanne, Switzerland

Background

Motion-resolved 4D flow MRI is a powerful tool for evaluating hemodynamics in the heart and great vessels[1,2]. Recently, a framework for fully self-gated (SG) free-running radial 3D phase-contrast MRI (5D flow) was developed for respiratory and cardiac motion-resolved flow

imaging with 100% scan efficiency[3,4]. 5D flow MRI was validated on 1.5 T scanners and has shown comparable performance to conventional 4D flow MRI[4,5]. In this work, we extended the 5D flow framework to 3T and performed the first comparison of 5D flow MRI in back-to-back scans of the same subjects at 1.5 and 3T. Our goal was to test the hypothesis that the 5D flow framework can be performed at both 1.5T and 3T and allows for comparable quantification of aortic hemodynamics.

Methods

Eleven healthy subjects (7F, age 23-34) were scanned on 1.5T and 3T clinical scanners (Siemens Healthcare) using 5D flow MRI (5D flow 1.5T and 5D flow 3T)[4], as previously reported[5]. Additionally, ECG and respiratory gated Cartesian 4D flow MRI at 1.5T (4D flow) was used as a reference standard. From the 5D flow data, respiratory and cardiac signals were extracted for data binning[3,5,6] and images were reconstructed using a sparse SENSE algorithm[3,7,8]. To assess cardiac signal extraction quality, the triggering variability between SG and ECG signals was calculated[3]. Two 2D planes (ascending aorta, AAo, and descending aorta, DAo) were selected from each of the flow datasets and used to measure stroke volume, net flow, peak flow, and peak velocity. Variability across the three flow datasets was measured using paired t-tests.

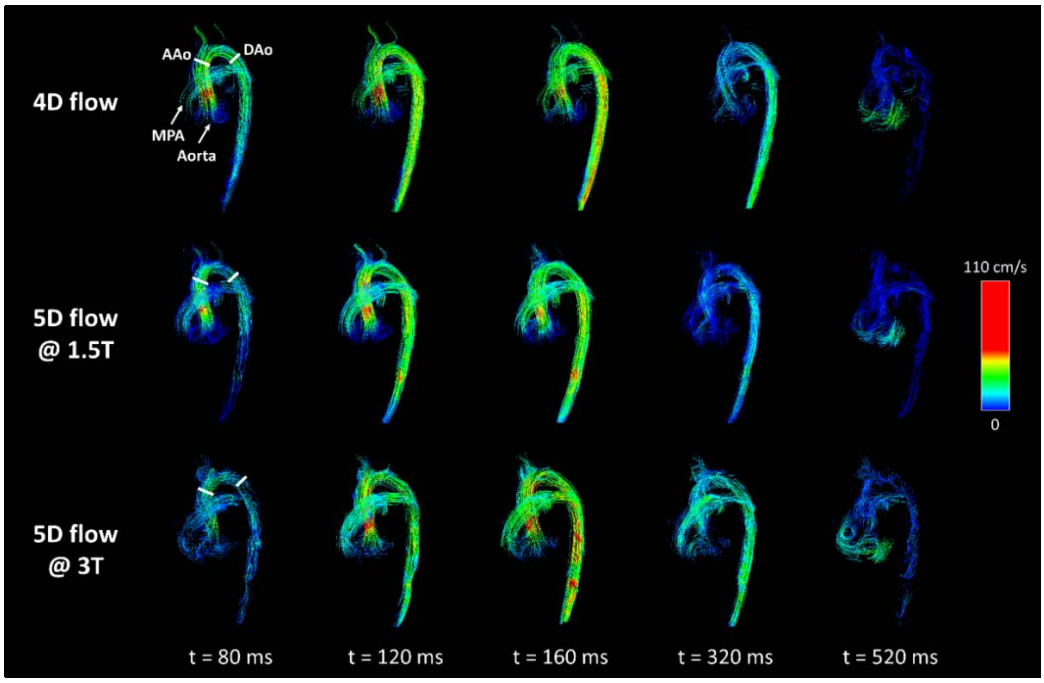

Figure 1. Comparison of flow streamlines over time for 4D flow 1.5T, 5D flow 1.5T and 5D flow 3T in one representative volunteer.

Results

Comparison of cardiac SG signals to the gold standard ECG showed non-significant differences in triggering variability between the two field strengths (16.6 ± 3.9 ms at 1.5T and 13.8 ± 4.2 ms at 3T, $p>0.05$). Overall, the flow measurements from 4D flow, 5D flow 1.5 T and 5D flow 3T were comparable. **Fig.1** and **Fig.2** depict flow streamlines and flow curves over time in a subset of representative volunteers. Significant differences were found between 4D flow and 5D flow 1.5T (**Fig.3**) and were reported in the AAo measures of peak velocity

(100.0±16.7cm/s vs. 113.8±21.3cm/s, p=0.04) and in the DAo measures of peak flow (240.6±73.9ml/s vs. 217.9±56.7ml/s, p=0.03) and peak velocity (107.6±18.6cm/s vs. 93.6±20.3cm/s, p=0.02).

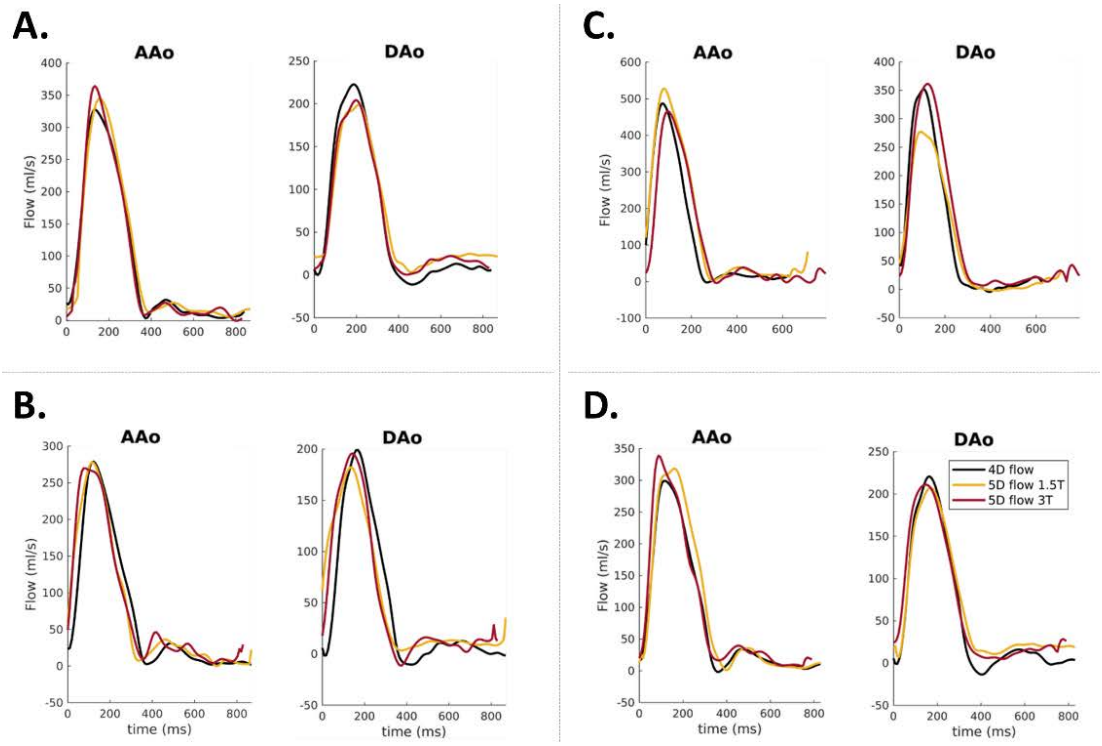

Figure 2. Flow curves comparison between conventional 4D flow at 1.5T, 5D flow at 1.5T and 5D flow at 3T. **A.-D.** Flow curves measured at one 2D segment of the ascending aorta (AAo) and one 2D segment of the descending aorta (DAo) in four representative volunteers.

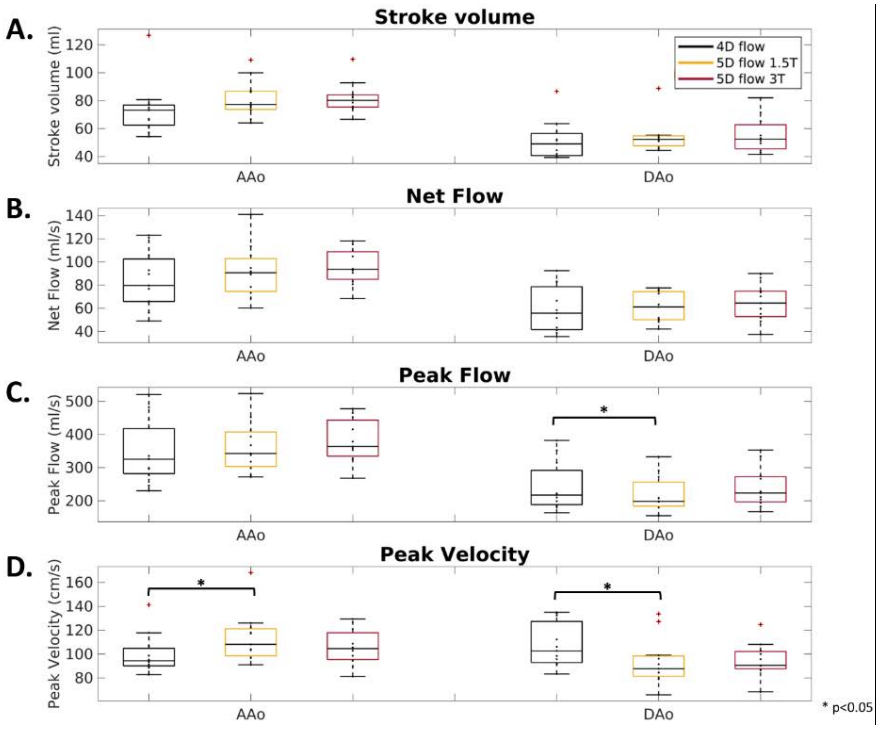

Figure 3. Comparison of flow measurements between 4D flow at 1.5T, 5D flow at 1.5T and 5D flow at 3T for AAo and DAo. **A.** Stroke volume. **B.** Net flow. **C.** Peak flow. **D.** Peak velocity. Significant differences ($p<0.05$) are reported with a black asterisk (*). Outliers are indicated with a red cross (+).

Discussion and Conclusion

Fully self-gated free-running 5D flow MRI at 3T yielded similar results to both conventional 4D and 5D flow measurements at 1.5T. The finding that peak flow and peak velocity using 5D flow MRI at 3T were not significantly different from 4D flow measurements at 1.5T, whereas the opposite was reported for 5D flow MRI at 1.5T vs 4D flow MRI, may be an indicator that increased SNR at 3T could be causing lower flow underestimation, as described in [9]. These promising results warrant further investigation of 5D flow MRI at 3T in patient cohorts in order to further establish the utility of this free-running volumetric flow acquisition with 100% scanning efficiency.

References

1. Srichai MB, Lim RP, Wong S, Lee VS. Cardiovascular applications of phase-contrast MRI. Am J Roentgenol. 2009;192:662–75.

2. Dyverfeldt P, Bissell M, Barker AJ, Bolger AF, Carlhäll CJ, Ebbers T, et al. 4D flow cardiovascular magnetic resonance consensus statement. J Cardiovasc Magn Reson [Internet]. Journal of Cardiovascular Magnetic Resonance; 2015;17:1–19. Available from: http://dx.doi.org/10.1186/s12968-015-0174-5

3. Di Sopra L, Piccini D, Coppo S, Stuber M, Yerly J. An automated approach to fully self - gated free - running cardiac and respiratory motion - resolved 5D whole - heart MRI. 2019;1–15.

4. Ma L, Yerly J, Piccini D, Di Sopra L, Roy CW, Carr J, et al. 5D flow MRI: A free-running, fully self-gated, radial imaging framework for cardiac and respiratory motion-resolved assessment of 3D blood flow dynamics. Radiol Cardiothorac Imaging. 2020;In Press.

5. Falcão M, Ma L, Di Sopra L, Bacher M, Piccini D, Yerly J, et al. 5D Flow MRI using Pilot Tone for Cardiac and Respiratory Self-Gating. Proc 23rd Annu SCMR Sci Sess. 2020;1583–6.

6. Coppo S, Piccini D, Bonanno G, Chaptinel J, Vincenti G, Feliciano H, et al. Free-running 4D whole-heart self-navigated golden angle MRI: Initial results. Magn Reson Med. 2015;74:1306–16.

7. Feng L, Axel L, Chandarana H, Block KT, Sodickson DK, Otazo R. XD-GRASP: Golden-angle radial MRI with reconstruction of extra motion-state dimensions using compressed sensing. Magn Reson Med. 2016;75:775–88.

8. Feng L, Coppo S, Piccini D, Yerly J, Lim RP, Masci PG, et al. 5D whole-heart sparse MRI. Magn Reson Med. 2017;79:826–38.

9. Lotz J, Döker R, Noeske R, Schüttert M, Felix R, Galanski M, et al. In vitro validation of phase-contrast flow measurements at 3 T in comparison to 1.5 T: Precision, accuracy, and signal-to-noise ratios. J Magn Reson Imaging. 2005;21:604–10.

5.2.3. Conclusions and Outlook of this work

Testing the free-running PC-MRI framework at 3T has shown promising results, and future sequence developments could focus on optimizing this sequence to this specific field strength, which would further increase the SNR. However, moving to 3T can also increase the magnetic field and radiofrequency inhomogeneities, as well as the susceptibility effects, all which, in turn, may reduce image quality. Nonetheless, most of these drawbacks can be attenuated by higher order shimming, choice of the sequences used, between other technical changes. Therefore, the SNR benefits of 3T should be further investigated and taken advantage of for improving the sequence design in the free-running PC-MRI framework, particularly for increasing spatial resolution.

The expansion to 3T could also be accelerated by using contrast agents to further improve signal quality, or by integrating anatomy with flow information using SyNAPS to increase the anatomical blood-to-myocardium contrast to assist in vessel segmentations.

5.3. A deep learning framework for cardiac self-gating in free-running radial 4D flow MRI

5.3.1. Overview and Personal Contribution

Throughout this thesis, the importance and utility of extracting respiratory and cardiac signals to either resolve or correct motion has been demonstrated. However, for cardiac signals derived from either Pilot Tone or self-gating, the features used to bin data according to a desired time-point in the cardiac cycle can be quite different from the well-established features of the gold-standard ECG. The ECG signal describes the heart's electrical activity as a sequence of electrical depolarizations and repolarizations, and in a healthy scenario it is characterized by three main waves:

- P wave - represents atrial depolarization
- QRS complex - represents ventricular depolarization
- T wave – represents ventricular repolarization

The peak of the QRS complex (R-wave) is usually much larger in amplitude than the remaining waves, so in MRI it is used as the cardiac feature to segregate consecutively acquired heart beats, and to either trigger off or sort the imaging data.

Self-gating, unlike ECG gating, does not use the heart's electrical activity but is instead based of changes in image intensity due to the presence of motion, mainly describing the bulk movement of the heart due to respiration as well as the heart's contraction and relaxation. While ECG and self-gating are correlated to each other, as they are capturing information of the same heart at the same period of time, their cardiac gating features do not necessarily overlap. As a result, and as shown in Chapter 2, there may be a shift between the ECG and the self-gating trigger points, hampering a direct and reproducible link between reconstruction frames and physiology, and leading to asynchrony when comparing multiple SG images to gold-standard ECG-gated images, which limits the translation and validation of SG techniques to clinical practice.

In a deliberate effort to close the synchronization gap between cardiac time-points derived from ECG and self-gating Giulia MC Rossi and I worked together to create a deep neuronal network that would predict R-wave peaks from self-gating data using the free-running PC-MRI. The results are shown in the following abstract that was accepted at the 2023 ISMRM & ISMRT Annual Meeting and Exhibition as an oral presentation.

5.3.2. Abstract

A deep learning framework for cardiac self-gating in free-running radial 4D flow MRI

Mariana B.L. Falcão[1] & Giulia M.C. Rossi[1], Jonas Richiardi[2], Xavier Sieber[1], Tobias Rutz[3], Milan Prša[4], Estelle Tenisch[1], Pierre Monney[3], Anna Giulia Pavon[5], Panagiotis Antiochos[3], Matthias Stuber[1,6], Christopher W Roy[1]

[1]Department of Radiology, Lausanne University Hospital (CHUV) and University of Lausanne (UNIL), Lausanne, Switzerland;

[2]University of Lausanne (UNIL), Lausanne, Switzerland;

[3]Service of Cardiology, Centre de Resonance Magnétique Cardiaque (CRMC), Lausanne University Hospital and University of Lausanne, Lausanne, Switzerland.

[4]Woman- Mother- Child Department, Lausanne University Hospital and University of Lausanne, Lausanne, Switzerland.

[5]Cardiology Division, Cardiocentro Ticino Institute, Lugano, Switzerland

[6]CIBM Center for Biomedical Imaging, Lausanne, Switzerland;

Introduction

Accurate detection of cardiac motion is essential for producing high-quality MR images of the heart. Electrocardiography (ECG) is currently the gold-standard to trigger the acquisition or to perform retrospective cardiac gating, as the peaks of the R-waves can be reliably identified. However, ECG placement may be time consuming, and the signal is prone to corruption by magnetohydrodynamic effects or gradient switching. Alternatively, self-gating (SG) techniques use the acquired MRI data to derive a signal related to the underlying motion that can be used for retrospective cardiac gating[1]. Nevertheless, features of SG signals do not usually correspond to ECG R-wave peaks, hampering a direct and reproducible link of reconstruction frames with physiology[2]. This can lead to asynchrony when comparing multiple SG images to gold-standard ECG-gated images, limiting the translation of SG techniques to clinical practice.

Previous studies have demonstrated the feasibility of training neural networks to find R-wave peak timepoints using SG signals, both for angiography[3,4] and MRI[5–7]. To our knowledge, no network has so far been developed for 4D flow MRI.

The aim of our study was therefore to train, validate, and test a network for predicting R-wave peak timepoints using repeated readouts from free-running radial 4D flow data. We performed our analysis in a cohort of heart disease patients, compared our deep-learning-based predictions against ground-truth ECG, and demonstrated the feasibility of using deep-learning-based self-gating to reconstruct radial 4D flow data.

Methods

Acquisitions. Free-running 3D radial Phase-Contrast MRI (PC-MRI)[8] data were acquired in 75 consenting patients (3-82 years; 47 M) on a 1.5T MAGNETOM Sola (Siemens Healthcare, Erlangen, Germany), while recording ECG. Each interleaf of the 3D radial trajectory9 was preceded by a readout along the superior-inferior (SI) direction for subsequent self-gating (**Fig.1A**).

Data preparation. Datasets were split into training (55), validation (10) and testing (10) sets. For each dataset, the extracted SI readouts were inverse-Fourier-transformed and subdivided into 3-second windows (**Fig.1B**). Each window was temporally interpolated (N_t=60

timepoints, temporal resolution=48ms), spatially cropped (N_p=128 samples), and underwent coil compression (N_c=10 virtual coils). Ground-truth binary labels (R_{ECG}), indicating the true temporal location of R-wave peaks (R_{ECG} triggers), were obtained for each window from ECG.

Network architecture and training. A fully convolutional neural network (FCNN)[7] was designed to predict from each SI projection a probability of correspondence to an R-wave peak (**Fig.1C**). Network weights (2458540 trainable parameters) were learned on training data by minimizing the weighted binary cross-entropy loss between R_{ECG} and the predicted probabilities (60 epochs, Adam optimizer, learning rate 0.0005).

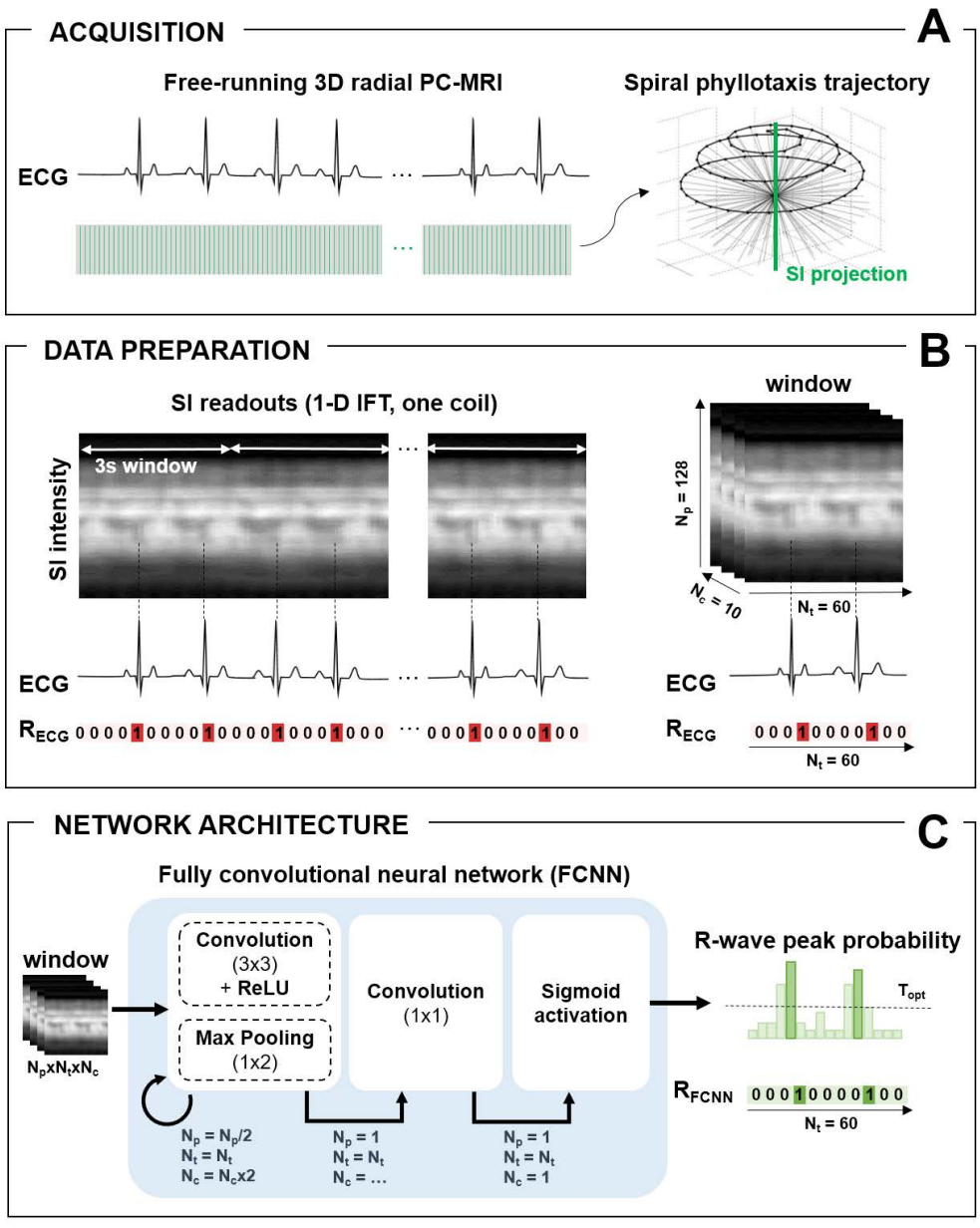

Figure 1. Study Framework A. Free-running 3D radial PC-MRI data were acquired, while recording the ECG. **B.** Inverse-Fourier-transformed SI readouts were divided into 3s windows (N_t=60 timepoints, N_p=128 samples, N_c=10 virtual coils). **C.** The FCNN repeatedly applies blocks of convolutional layers (3x3), rectified linear unit activations and max-pooling (1x2). At each iteration, N_p is halved, N_c is doubled, and N_t is preserved, until N_p=1 is reached. N_c is reduced to 1 within a last convolutional block (1x1), and a sigmoid activation yields a final vector of R-wave peak probabilities.

Model selection. Validation data were used for a Youden Index-based selection of the best model ($M_{opt} \in [0\ 60]$) and optimal threshold ($T_{opt} \in [0\ 1]$) for the conversion of probabilities into binary labels (R_{FCNN}) predicting exact R-wave peak timepoints (R_{FCNN} triggers).

Performance evaluation. The performance of M_{opt} in combination with T_{opt} was evaluated by predicting R_{FCNN} for the validation (biased) and testing (unbiased) sets and comparing against R_{ECG}. For each subject, outlier R_{FCNN} and R_{ECG} triggers (missed and additional R-wave peaks) were counted and excluded from further analysis[2]. The timing between consecutively detected triggers (RR intervals) was compared, and trigger shifts and jitters were computed. For one subject, two 4D flow reconstructions[10] using either R_{FCNN} or R_{ECG} triggers were performed, and flow measurements were compared.

Results

Predictions from the selected model M_{opt} (epoch 47) in combination with T_{opt} (0.00003) were overall in good agreement with R_{ECG}, both for validation and testing (**Fig.2A,C-D**), with five visually assessed failure cases (validation=2, test=3, **Fig.2B**) that were excluded from further analysis.

Despite the larger number of bad RFCNN triggers (**Tab.1**), the model proved capable of identifying R-wave peak timepoints even when the latter were missed in R_{ECG} (**Fig.2D**). After exclusion of bad triggers, R_{FCNN} triggers showed a good concordance with R_{ECG}, with average trigger shifts and jitters close to the temporal resolution of the data (12.8±18.9ms and 52.7±28.5ms for validation, 40.5±30.3ms and 84.2±79.5ms for testing, **Tab.1**).

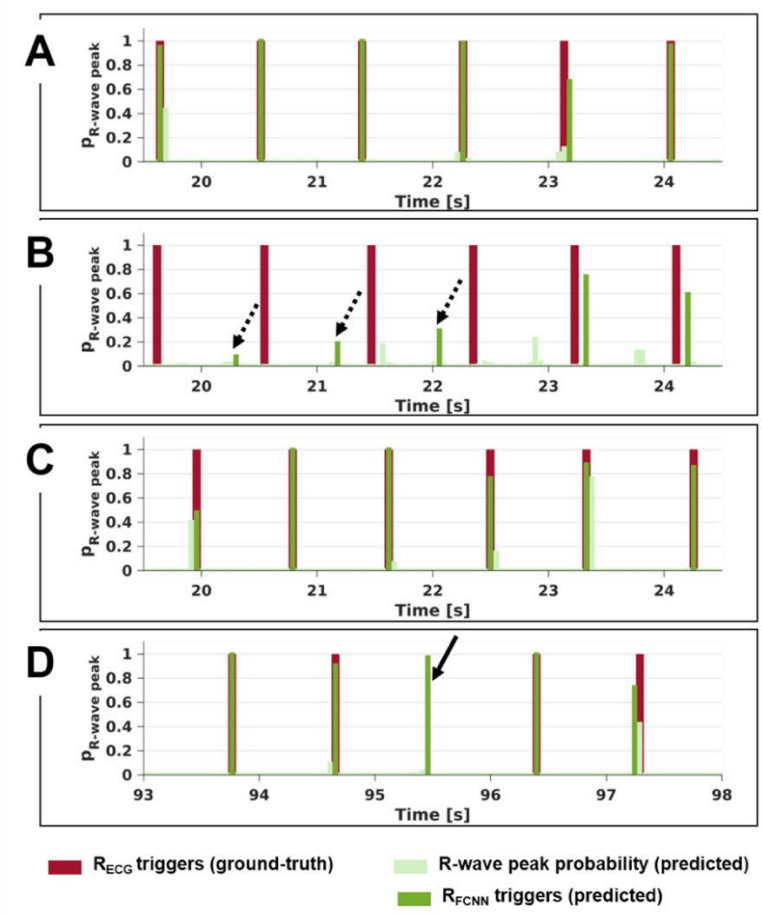

Figure 2. Comparison of FCNN predictions to ground-truth ECG. Examples of accurate (**A,C,D**) and erroneous (**B**) FCNN predictions (light green: R-wave peak probability, dark green: R_{FCNN} triggers) as compared to ground-truth ECG (dark red: R_{ECG} triggers) for two subjects belonging to the validation (**A-B**) and test (**C-D**) sets. Dashed arrows: inaccurate R_{FCNN} triggers. Solid arrow: R_{FCNN} detecting a missed R_{ECG} trigger.

	Av. RR_{ECG} interval (ms)	Av. RR_{FCNN} interval (ms)	Trigger shift (ms)	Trigger Jitter (ms)	% bad R_{ECG} triggers	% bad R_{FCNN} triggers
V1	1057.5	1056.1	7.8	56.2	0.2%	26.5%
V2	919.5	919.2	3.6	23.6	0.9%	1.1%
V4	934.0	936.0	7.2	33.9	5.1%	7.4%
V5	894.0	890.9	2.7	94.2	1.3%	19.9%
V7	828.8	849.5	58.4	89.9	0.0%	20.6%
V8	1055.5	1055.9	15.5	23.4	0.0%	0.2%
V9	926.8	920.9	2.3	65.8	0.8%	11.9%
V10	704.3	708.3	4.6	34.6	1.9%	1.3%
		Mean ± std	**12.8±18.9**	**52.7±28.5**	**1.3±2.0%**	**11.1±10.0%**
T1	880.4	880.1	2.5	23.4	1.4%	1.4%
T2	755.7	743.2	44.4	76.2	3.0%	17.8%
T4	830.2	836.2	58.7	72.6	8.5%	11.8%
T5	733.5	724.6	76.9	119.3	1.2%	24.9%
T7	724.2	724.4	18.0	24.1	0.0%	0.0%
T8	925.2	924.2	10.8	28.0	1.2%	10.8%
T10	889.9	888.7	72.4	245.6	0.0%	4.9%
		Mean ± std	**40.5±30.3**	**84.2±79.5**	**2.2±3.0%**	**10.2±9.0%**

Table 1. Quantitative comparison of FCNN prediction to ground-truth ECG. For both R_{ECG} and R_{FCNN}, the resulting average RR interval (RR_{ECG} and RR_{FCNN}) as well as the percentage of bad triggers (missed and additional R-wave peaks) are reported together with the trigger shifts and jitters (bad triggers excluded). Five visually assessed FCNN failure cases were excluded from this analysis. V, T: subjects belonging to the validation (V) and testing (T) sets.

The distribution of RR_{FCNN} and RR_{ECG} intervals was comparable (**Fig.3A**), confirmed by the low bias and limits of agreement (1.98±104.19ms for validation, -1.79±109.56ms for testing, **Fig.3B-C**).

4D flow reconstructions using both R_{FCNN} and R_{ECG} triggers showed good synchronization of flow rate curves, with comparable net volume (NV) and peak flow (PF) measurements in the ascending (NV_{FCNN}=58.03mL, NV_{ECG}=57.35mL, PF_{FCNN}=347.64mL/s, PF_{ECG}=345.93mL/s) and descending aorta (NV_{FCNN}=38.49mL, NV_{ECG}=37.57mL, PF_{FCNN}=215.61mL/s, PF_{ECG}=215.19mL/s).

Discussion and conclusion

We have shown the feasibility of extracting R-wave peak timepoints from SG readouts in free-running radial 4D flow data using deep learning. The detected timepoints agreed with ground-truth ECG (shifts and jitters close to temporal resolution, comparable RR intervals), and allowed for the generation of 4D flow images with reliable flow measurements. Despite these preliminary results, the temporal resolution of the datasets used for training the network (48ms) had limited the precision. Additionally, the relatively small number of patients included resulted in a low variability in terms of image contrasts and resolution, possibly explaining failure cases.

An extension of the network to other free-running sequences is envisaged, with the aim of achieving a reliable synchronization of SG reconstructions to gold-standard ECG-gated images, further validating the use of SG as an ECG-free alternative for cardiac gating, and simplifying the clinical workflow of cardiac MRI.

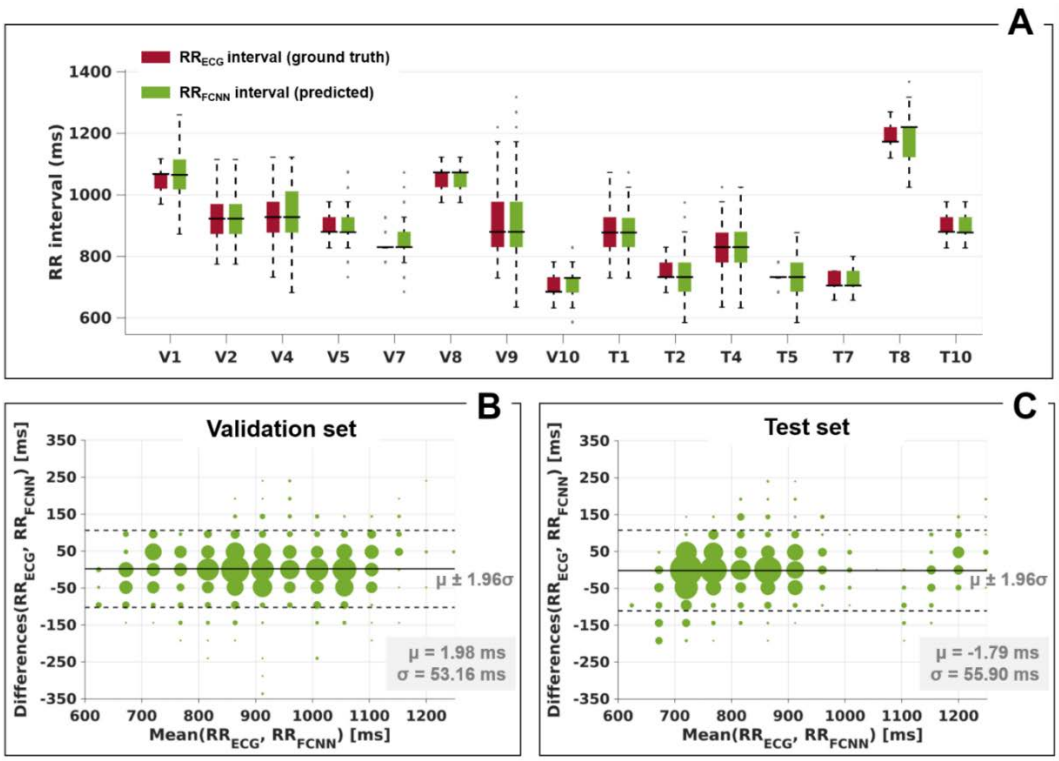

Figure 3. Comparison of RR intervals. A. Box plots showing the distribution of RR intervals in RFCNN (green) and RECG (red). **B-C.** Bland-Altman plots of RR intervals in RFCNN and RECG for the validation (**B**) and test (**C**) sets. The size of the points is proportional to their relative occurrence. Five visually assessed FCNN failure cases were excluded from this analysis.

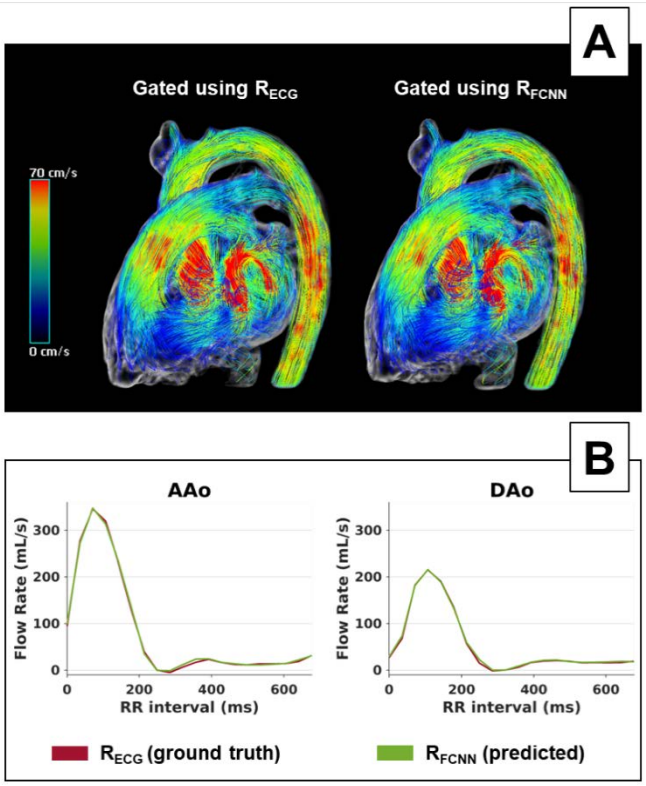

Figure 4. Comparison of 4D flow reconstructions of one dataset using either RFCNN or RECG triggers for cardiac gating. The patient shown (T7 in **Tab.1**) is a 69 years old Mitral Regurgitation female patient (degree 3). **A.** Streamline visualization in peak systole showing comparable image quality. **B.** Flow rates in the ascending (AAo) and descending (DAo) aorta. A good synchronization of the two triggering techniques, as well as a good agreement in the flow curves is shown.

References

1. Larson AC, White RD, Laub G, McVeigh ER, Li D, Simonetti OP. Self-Gated Cardiac Cine MRI. Magn Reson Med. 2004;51(1):93-102. doi:10.1002/mrm.10664

2. Di Sopra L, Piccini D, Coppo S, Stuber M, Yerly J. An automated approach to fully self-gated free-running cardiac and respiratory motion-resolved 5D whole-heart MRI. Magn Reson Med. 2019;(June):1-15. doi:10.1002/mrm.27898

3. Ciusdel C, Turcea A, Puiu A, et al. TCT-231 An artificial intelligence based solution for fully automated cardiac phase and end-diastolic frame detection on coronary angiographies. J Am Coll Cardiol. 2018;72(13):B96-B97. doi:10.1016/j.jacc.2018.08.1356

4. Ciusdel C, Turcea A, Puiu A, et al. Deep neural networks for ECG-free cardiac phase and end-diastolic frame detection on coronary angiographies. Comput Med Imaging Graph. 2020;84:101749. doi:10.1016/j.compmedimag.2020.101749

5. Usman M, Atkinson D, Kolbitsch C, Schaeffter T, Prieto C. Manifold learning based ECG-free free-breathing cardiac CINE MRI. J Magn Reson Imaging. 2015;41:1521–1527.

6. Ahmed AH, Aggarwal H, Nagpal P, Jacob M. Dynamic MRI using Deep Manifold Self-Learning. Proc IEEE Int Symp Biomed Imaging. 2020:1052–1055. doi:doi:10.1109/ isbi45749.2020.9098382.

7. Hoppe E, Wetzl J, Yoon SS, et al. Deep Learning-Based ECG-Free Cardiac Navigation for Multi-Dimensional and Motion-Resolved Continuous Magnetic Resonance Imaging. IEEE Trans Med Imaging. 2021;40(8):2105-2117. doi:10.1109/TMI.2021.3073091

8. Ma LE, Yerly J, Piccini D, et al. 5D Flow MRI : A Fully Self-gated, Free-running Framework for Cardiac and Respiratory Motion – resolved 3D Hemodynamics. Radiol Cardiothorac Imaging. 2020;2(6). doi:10.1148/ryct.2020200219

9. Piccini D, Littmann A, Nielles-vallespin S, Zenge MO. Spiral Phyllotaxis : The Natural Way to Construct a 3D Radial Trajectory in MRI. Magn Reson Med. 2011;66:1049-1056. doi:10.1002/mrm.22898

10. Falcão MBL, Rossi GMC, Ma L, et al. Correcting vs resolving respiratory motion in accelerated free-running whole-heart radial Flow MRI using focused navigation (fNAV). Proc Intl Soc Mag Reson Med. 2021;29(0304). doi:10.1002/mrm.27918

5.3.3. Conclusions and Outlook of this work

This preliminary work demonstrated that using free-running PC-MRI self-gated data we were able to create a deep neuronal network that is capable of predicting the location of R-wave peak timepoints. Albeit preliminary, the reported results are very promising, and bring down the barrier of asynchrony when comparing multiple SG images to gold-standard ECG-gated images. Further optimization of this work will, thus, contribute to the validation of self-gating techniques and to their translation to clinical practice.

Chapter 6.
Conclusion and Outlook

This doctoral thesis has addressed several practical challenges and limitations of the free-running PC-MRI framework in an effort to improve its clinical utility in CMR for the diagnosis and monitoring of congenital heart diseases.

First, Chapter 2 integrated an MR image-independent motion detection system called Pilot Tone with the free-running PC-MRI framework and used it to detect respiratory and cardiac motion signals. Using Pilot Tone, the imaging sequence and the self-navigation signals are entirely decoupled from each other, which offers new opportunities for improving the acquisition (e.g. accelerating scan times, improving resolution) without jeopardizing the signal extraction accuracy. Additionally, the implemented sequence-independent signal extraction framework can be easily adapted to detect respiratory and cardiac motion in other free-running branches, such as whole-heart and whole-liver fat-water quantification imaging (using free-running multi-echo GRE), T2 mapping (using free-running T2 mapping), and ultra-short echo time (using free-running UTE) sequences. Some of these applications have been successfully implemented and presented at international conferences (see Chapter 7 and Supplementary Information material).

In Chapter 3, respiratory motion correction tool called focused navigation (fNAV) was implemented in the free-running PC-MRI framework. The positive results reported in the quantification of flow measurements, and the increase in sampling per imaging volume when compared to the previously used respiratory-resolved alternative, encourages new developments in sequence design to reduce scan times, improve spatial resolution and further improve image quality in free-running PC-MRI.

Finally, in Chapter 4, the knowledge gained from the studies presented in Chapters 2 and 3 was combined and used to create the SyNAPS technique, which enabled the synchronization of two sequences acquired back-to-back, one anatomical free-running sequence and one free-running PC-MRI sequence. Using Pilot Tone navigation, which is decoupled from the imaging sequence, the respiratory and cardiac motion extraction can be combined for both sequences together. Moreover, the motion correction provided by the fNAV algorithm facilitated the overlap of the imaging volumes. Synchronizing and combining the two free-running sequences using SyNAPS led to the creation of 4D “anatomy + flow’ imaging datasets that have increased anatomical blood-to-myocardium image contrast in the flow datasets, which improved dynamic vessel segmentation for a more accurate quantification of flow measurements.

The impact of the work presented has led to new clinical collaborations that investigate the impact of the free-running PC-MRI framework in different cardiovascular diseases.

One study at the University of New South Wales in Sydney, Australia, has acquired 100 patients, 71 of those with pulmonary hypertension, to study and derive invasive hemodynamic measures (pulmonary vascular resistance, mean pulmonary arterial pressure, and mean pulmonary arterial wedge pressure) from 5D flow data using machine-learning tools. This study has been accepted to the 2023 Society for Cardiovascular Magnetic Resonance (SCMR) international meeting, with title "*Cardiovascular MR and supervised machine learning in the derivation of pulmonary vascular hemodynamics in pulmonary hypertension*" see Chapter 7 & and Supplementary Information A2.2.7 for abstract's content).

In a second collaborative study, a diverse CHD patient cohort (N=60) undergoing CMR was recruited at the University Hospital of Lausanne, and blood flow was quantified across all major vessels (aorta, pulmonary arteries, pulmonary veins and caval veins) using the reference standard 2D PC-MRI, the conventional 4D flow MRI and the free-running PC-MRI framework reconstructed to 5D flow datasets. The goal of the study is to compare the three PC-MRI acquisitions to evaluate which acquisition provides a better internal consistency in flow measurements across these major vessels. The preliminary results of this study were accepted as a power pitch at the 2023 Society for Cardiovascular Magnetic Resonance (SCMR) international meeting under the title "*Comparison of free-running whole-heart 5D and 4D compressed sensed flow imaging to standard 2D phase contrast in patients with right-sided congenital heart disease*" (see Chapter 7 & and Supplementary Information A2.2.8 for abstract's content). Figure 1 shows one example from this patient cohort (left), where one 5D flow image volume captured at end-systole and end-expiration shows the presence of stenosis in a patient with coarctation of the aorta after aortic resection.

Additionally, a cohort of patients (N=40) with mild to severe mitral regurgitation is being recruited at the University Hospital of Lausanne, where the free-running PC-MRI framework is being acquired together to the gold standard CMR exam for mitral regurgitation. This study will test the hypothesis that 5D flow reconstructions from the free-running PC-MRI framework can quantify the degree of severity of mitral regurgitation with a comparable outcome to the gold standard CMR exam, as well as to the gold standard echocardiography. In Figure 1 (right) is it possible to visualize one severe mitral regurgitation case with a hypertrophic left atrium, and the regurgitant flow jet pattern at end- systole and end-expiration.

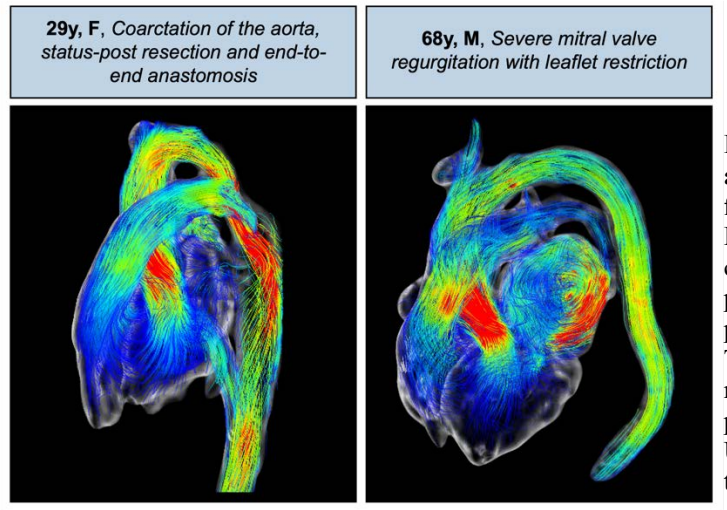

Figure 1. Examples of two clinical datasets acquired with the free-running PC-MRI framework reconstructed into 5D flow MRI images. The first case, on the left, is a congenital heart disease 29 years old female patient with coarctation of the aorta, status post resection and end-to-end anastomosis. The second patient, on the right, is a severe mitral regurgitation 68 years old male patient. Both datasets were acquired at the University Hospital of Lausanne with my technical support for two separate studies.

Beyond the clinical collaborations, this doctoral thesis has also enabled new scientific discoveries and developments that are presented in the Supplementary Information Chapter.

Across all techniques investigated, this doctoral thesis has enabled me to have my own contribution to the field of multi-dimensional PC-MRI through the development of SyNAPS as an innovative solution for a more comprehensive MRI exam.

When compared to the conventional respiratory navigated 4D flow MRI, 4D flow SyNAPS has whole-heart coverage with good blood-to-myocardium contrast, which enabled a dynamic segmentation of the vessels for improved flow quantification. Moreover, planning the acquisition of 4D flow SyNAPS is easier, without needing to place navigators or to adjust imaging volumes. Additionally, 4D flow SyNAPS acquired anatomy and flow information in a fixed scan time under 15 min, with possible future improvements towards faster scan times. Alternatively, the conventional 4D flow MRI requires a complex setup, has unpredictable and long scan times when acquiring whole heart coverage, and may not acquire data using an isotropic resolution due to image quality constraints, which limits the flow quantification in some orientations. 4D flow SyNAPS is therefore a promising alternative to 4D flow MRI.

The development of SyNAPS demonstrates the benefits of resolving practical limitations of the free-running PC-MRI framework. Implementing and validating Pilot Tone was particularly decisive to enable the synchronization and combination of back-to-back acquisitions because it is sequence independent. SyNAPS also addresses some practical limitations, such as the improvement of cardiovascular anatomical contrast without the need for contrast agent injection, as well as the improvement in vessel segmentation, that can now be dynamic, all which contribute to a more accurate and robust quantification of flow measurements.

Moreover, 4D flow SyNAPS has so much untapped potential that can empower innovative tools for CMR. For instance, the possibility to synchronize and combine two, or more, sequentially acquired acquisitions. The benefits of sequence synchronization drives interconnectedness and information sharing between different imaging sequences, that, just like in the case of 4D “anatomy + flow” datasets, may create more comprehensive MRI datasets. Using SyNAPS, cardiovascular MRI could be reimagined to be an easy-to-perform protocol that acquires 3D sequences consecutively and fully synchronized, which, once reconstructed, would be merged into a large multi-dimensional dataset containing in itself all different types of imaging information acquired, pertaining to anatomy, flow, tissue properties, perfusion, etc. This push-button comprehensive CMR solution could help deploying CMR to new clinical centers without the need for specialized CMR training and would improve the current clinical workflow by removing the unpredictable time constrains, derived from, for example, ECG, slice, and navigator placement.

Nevertheless, for this push-button comprehensive CMR solution to succeed, it is also important to address the current limitations relative to the imaging software analysis. This has not been mentioned at large because it was not the focus of this doctoral dissertation; nonetheless, it is a very important component for a long-term usage of multi-dimensional free-running sequences, and in particular for the free-running PC-MRI framework. At present time, there is a small number of software tools capable of handling 4D data, but as information grows towards higher dimensionality, it becomes harder to find a software that is able to connect all the different dimensions together. Therefore, this gap needs to be solved by creating new image

analysis solutions in order to be able to analyze these multi-dimensional datasets. The aforementioned analysis tools need to be intuitive and easy to use, to ensure that they are well received by the clinical community and to facilitate its global use. Moreover, the scientific community that focuses on developing multi-dimensional MRI would greatly benefit from joining forces to develop an open-source image analysis solution to visualize and analyses these multi-dimensional datasets.

In conclusion, this doctoral dissertation has addressed a number of practical challenges of the free-running PC-MRI framework that will drive new optimizations of the framework in the future, such as improving spatial resolution and reducing scan time. The implementation of new strategies for the free-running PC-MRI framework has enabled the development of a novel technique called SyNAPS that synchronizes two sequentially acquired free-running sequences, and combines them to create 4D "anatomy + flow" datasets. The resulting datasets provide an improved visualization of cardiovascular structures in flow data, which enables a dynamic vessel segmentation and improves flow quantification without the need for contrast injection. Future work on SyNAPS will simplify CMR protocols that will consequently help in the broader use of CMR to diagnose and manage CHD in adult and pediatric populations.

Chapter 7.
List of Academic Achievements

Peer-reviewed articles

Falcão MBL, Di Sopra L, Ma L, Bacher M, Yerly J, Speier P, Rutz T, Prša M, Markl M, Stuber M, Roy CW. *Pilot tone navigation for respiratory and cardiac motion-resolved free-running 5D flow MRI.* Magnetic Resonance in Medicine. 2021; 87: 718– 732. doi:10.1002/mrm.29023

Anna Giulia Pavon AG, Guglielmo M, Mennilli P, **Falcão MBL**, Bergamaschi L, Costantin DF, Vivaldo M, Leo LA, Schlossbauer S, Roy CW, Stuber M, Pedrazzini G, Faletra F, *The Role of Cardiovascular Magnetic Resonance in patients with Mitral Regurgitation*, Journal of Cardiovascular Development and Disease. 2022, 9(11), 399. doi:10.3390/jcdd9110399

- My contribution: Have contributed with research and writing in the 4D flow chapter of this manuscript.

Si-Mohamed S, Romanin L, **Falcão MBL**, Yerly J, Tenisch E, Rutz T, Schwitter J, De Bourguignon C , Stuber M, Roy CW , Prsa M, *Ferumoxytol-enhanced free-running 5D whole-heart MRI: a glimpse of a "one-stop shop" modality for cardiac function and morphology*, MAGNETOM Flash SCMR 2023 edition, Siemens Healthineers.

Falcão MBL, Rossi GMC, Rutz T, Prša M, Tenisch E, Ma L, Weiss EW, Baraboo JJ, Yerly J, Markl M, Stuber M, Roy CW, *Focused Navigation for respiratory-motion corrected free-running radial 4D flow MRI*, Magn Reson Med. 2023;1–16. Doi: 10.1002/mrm.29634

Articles in preparation

Mackowiak ALC, Roy CW, Yerly J, **Falcão MBL**, Bacher M, Speier P, Piccini D, Stuber M, Bastiaansen JAM, *Whole-heart motion-resolved multi-peak fat-fraction mapping using Free-Running 3D radial Multi-Echo GRE and Pilot Tone*, under second round of revisions in the Journal of Magnetic Resonance in Medicine.

- My contribution: I implemented the signal extraction framework this work is based on, and I have provided support to the first author regarding this framework.

Falcão MBL, Mackowiak ALC, Rumac S, Bacher M, M. C. Rossi GMC, Ferincz R, Prša M, Rutz T, Tenisch E, Monney P, Patagonis A, Bastiaansen JAM, Van Heeswijk R, Speier P, Markl M, Stuber M, W. Roy CW, *Free-running 3D anatomical and flow MRI using Synchronization of Neighboring Acquisitions by Physiological Signals (SyNAPS)*, Under internal review.

Conference abstracts as 1st author

Falcão MBL, Ma L, Di Sopra L, Bacher M, Piccini D, Yerly J, Speier P, Markl M, Stuber M, Roy CW, *5D Flow MRI using Pilot Tone for Cardiac and Respiratory Self-Gating*, SCMR 23rd Annual Scientific Sessions, 2020, Orlando Florida, SCMR/ISMRM Co-Provided Workshop Poster.

Falcão MBL, Di Sopra, L, Ma, L, Bacher, Piccini D, Yerly J, Speier P, Rutz T, Prša, M, Markl M, Stuber M, Roy CW, *5D Flow – A quantitative in vivo comparison between Self Gating and Pilot Tone Gating*, ISMRM & SMRT Virtual Conference & Exhibition, 2020, Electronic Poster in the conference & selected for Oral Presentation in ISMRM Flow & Motion Study Group.

Falcão MBL, Ma L, Di Sopra L, Yerly J, Markl M, Stuber M, Roy CW, *Fully self-gated respiratory and cardiac motion-resolved 5D flow: comparison at 1.5T and 3T*, SCMR 24th Annual Scientific Sessions, 2021, Oral Presentation.

Falcão MBL, Rossi GMC, Ma L, Heerfordt J, Piccini D, Yerly J, Prša, M, Rutz T, Tenisch E, Markl M, Stuber M, Roy CW, Correcting vs resolving respiratory motion in accelerated free-running whole-heart radial flow MRI using focused navigation (fNAV), ISMRM & SMRT Annual Meeting & Exhibition, 2021, Oral Presentation.

Falcão MBL, Mackowiak ALC, Rumac S, Bacher M, Rossi GMC, Prša, M, Tenisch E, Rutz T, Bastiaansen JAM, Van Heeswijk RB, P. Speier, Markl M, Stuber M, Roy CW, *Free-running 3D anatomical and flow MRI using Synchronization of Neighboring Acquisitions by Physiological Signals (SyNAPS)*, Joint ISMRM-ESMRMB Annual Meeting, 2022, Oral Presentation.

Falcão MBL, Rutz T, Prša M, Tenisch E, Ma L, Markl M, Stuber M, Roy CW, *On the effects of contrast agents in free-running whole-heart 5D flow Imaging*, SMRA 34th Annual International Conference, Power Pitch.

Falcão MBL and Rossi GMC, Richiardi J, Sieber X, Rutz T, Prša M, Tenisch E, Monney P, Pavon AG, Antiochos P, Stuber M, Roy CW, *A deep learning framework for cardiac self-gating in free-running radial 4D flow MRI*, submitted to ISMRM Annual Meeting 2023.

Awards

Conference abstract: *5D Flow – A quantitative in vivo comparison between Self Gating and Pilot Tone Gating*, at ISMRM & SMRT Virtual Conference & Exhibition, 2020:

- ISMRM 2020 Educational Stipend. Waived registration to conference
- ISMRM 2020 Flow and Motion Study Group 2nd place. Cash award of USD 250.

Conference abstract: *Correcting vs resolving respiratory motion in accelerated free-running whole-heart radial flow MRI using focused navigation (fNAV)*, ISMRM & SMRT Annual Meeting & Exhibition, 2021:

- ISMRM 2021 Magna Cum Laude Merit Award (top 10%).

Conference abstract: *Free-running 3D anatomical and flow MRI using Synchronization of Neighboring Acquisitions by Physiological Signals (SyNAPS)*, Joint ISMRM-ESMRMB Annual Meeting, 2022.

- ISMRM 2022 Educational Stipend. Cash award of USD 475 for waived registration and USD 100 for travel costs.
- ISMRM 2022 Summa Cum Laude Merit Award (top 5%).

Conference abstract: *On the effects of contrast agents in free-running whole-heart 5D flow Imaging*, SMRA 34th Annual International Conference.

- SMRA 2022 Travel Award funded by the Martin Prince Foundation. Cash award of USD 430 for conference hotel costs

Conference abstract: *A deep learning framework for cardiac self-gating in free-running radial 4D flow MRI*, ISMRM & ISMRT Annual Meeting & Exhibition, 2023.

- ISMRM 2023 Educational Stipend. Cash award of USD 475 for waived registration and USD180 for travel costs.

Conference abstracts as co-author

Mackowiak ALC, Roy CW, Yerly J, Di Sopra L, **Falcão MBL**, Bacher M, Speier P, Piccini D, Stuber M, Bastiaansen JAM, *Whole-Heart Motion-Resolved Multi-Peak Fat-Fraction Mapping using Free-Running 3D Radial Multi-Echo GRE and Pilot Tone*, ISMRM & SMRT Annual Meeting & Exhibition, 2021.

Weiss EK, Rigsby C, Robinson J, Baraboo J, Ma L, **Falcão MBL**, Roy CW, Stuber M, Markl M, *Free-Running 5D Flow MRI: Impact of Respiratory State Resolution on Image Quality and Flow Quantification*, SCMR 25th Annual Scientific Sessions, 2022.

Baraboo J, Weiss EK, Ma L, Hwang J, Gunasekaran S, **Falcão MBL**, Roy CW, Stuber M, Passman R, Kim D, Markl M, *RR-Resolved 5D flow for Decoding the Impact of Cardiac Rhythm on Left Atrial Flow Dynamics in Atrial Fibrillation and Stroke*, SCMR 25th Annual Scientific Sessions, 2022.

Bacher M, Speier P, **Falcão MBL**, Roy CW, Prša, M, Rutz T, Stuber M, *On the Influence of Respiratory State on Pilot Tone Derived Cardiac Triggers*, SCMR 25th Annual Scientific Sessions, 2022.

Mackowiak ALC, Roy CW, **Falcão MBL**, Bustin A, Bacher M, Speier P, Piccini D, Stuber M, Vietti-Violi N, Bastiaansen JAM, *Pilot Tone-guided focused navigation for free-breathing whole-liver fat-water quantification*, Joint ISMRM-ESMRMB Annual Meeting, 2022.

Rossi GMC, Romanin L, **Falcão MBL**, Milani B, Piccini D, Yerly J, Schwitter J, Prša, M, Rutz T, Tenisch E, Stuber M, Roy CW, Free-running contrast-enhanced ultra-short TE (UTE) for cardiac and respiratory motion-resolved flow artifact-free 5D whole-heart MRI, Joint ISMRM-ESMRMB Annual Meeting, 2022.

Weiss EK, Rigsby CK, Robinson JD, Baraboo J, Ma L, **Falcão MBL**, Roy CW, Stuber M, Markl M, *Free-Running 5D Flow MRI: Impact of Cardiac Temporal Resolution on Flow Quantification*, Joint ISMRM-ESMRMB Annual Meeting, 2022.

Rumac S, Roy CW, Yerly J, **Falcão MBL**, Bustin A, Bacher M, Speier P, Stuber M, Van Heeswijk RB, *Free-running isotropic whole-heart T2 mapping with ECG-free Pilot Tone navigation*, Joint ISMRM-ESMRMB Annual Meeting, 2022.

Yerly J, Roy CW, Milani B, Piccini D, Bustin A, **Falcão MBL**, Van Heeswijk RB, Stuber M, Numerical optimization of 5D cardiac and respiratory motion-resolved CMR imaging for the assessment of left ventricular function, Joint ISMRM-ESMRMB Annual Meeting, 2022.

Ma L, Berhane H, Baraboo Sugimura JM, Roy CW, **Falcão MBL**, Yerly J, Stuber M, Markl M, *A 3D Dense-U-Net for fully automated 5D flow MRI segmentation*, Joint ISMRM-ESMRMB Annual Meeting, 2022.

Baraboo J, Weiss EK, Pradella M, Ma L, Hwang J, Gunasekaran S, **Falcão MBL**, Roy CW, Stuber M, Passman R, Kim D, Markl M, *RR-Resolved 5D flow for Decoding the Impact of Cardiac Rhythm on Left Atrial Flow Dynamics in Atrial Fibrillation and Stroke*, Joint ISMRM-ESMRMB Annual Meeting, 2022.

Rutz T, Tenisch E, **Falcão MBL**, Roy CW, Faessler S, Rodrigues D, Ma L, Markl M, Stuber M, Piccini D, Schwitter J, Prša M, *Comparison of free-running whole-heart 5D and 4D compressed sensed flow imaging to standard 2D phase contrast in patients with right-sided congenital heart disease*, SCMR 26th Annual Scientific Sessions, 2023.

Weiss EW, Rigsby CK, Robinson JD, Baraboo J, Ma LE, **Falcão MBL**, Roy CW, Stuber M, Markl M, *Respiratory-Resolved flow in Congenital Heart Disease: A 5D flow MRI Study*, SCMR 26th Annual Scientific Sessions, 2023.

Kearney K, Pouliopoulos J, Olsen N, John J, Adji A, Hungerford S, Kessler Iglesias C, Song N, Macdonald P, Muthiah K, Keogh A, Hayward C, Grenier J, Thompson R, Roy CW, **Falcão MBL**, Stuber M, Lau E, Puranik R, Ugander M, Kotlyar E, Jabbour A, *Cardiovascular MR and supervised machine learning in the derivation of pulmonary vascular hemodynamics in pulmonary hypertension*, SCMR 26th Annual Scientific Sessions, 2023.

Weiss EW, Baraboo J, Ma LE, **Falcão MBL**, Roy CW, Robinson JD, Stuber M, Rigsby CK, Markl M, *Respiration-resolved 5D flow MRI: Impact of the number of respiratory states of blood flow quantification in congenital heart disease patients*, ISMRM & ISMRT Annual Meeting & Exhibition, 2023.

Weiss EW, Baraboo J, Ma LE, **Falcão MBL**, Roy CW, Stuber M, Markl M, *Dual Venc 5D flow MRI with Increased Velocity Dynamic Range: An in-vitro and in-vivo Validation and Feasibility Study*, ISMRM & ISMRT Annual Meeting & Exhibition, 2023.

Si-Mohamed SA, Romanin L, **Falcão MBL**, Yerly J, Tenisch E, Rutz T, De Bourguignon C, Stuber M, Roy CW, Prsa M, *Free-running 5D whole-heart MRI with ferumoxytol enhancement to evaluate cardiac function in congenital heart disease*, ISMRM & ISMRT Annual Meeting & Exhibition, 2023.

Ferincz R, **Falcão MBL**, Secinaro A, Buonincontri G, Alamo L, Tenisch E, Prsa M, Piccini D, Yerly J, Stuber M, Roy CW, *Motion-corrected free-running 4D MRI of the fetal heart - from in silico to in vivo*, ISMRM & ISMRT Annual Meeting & Exhibition, 2023.

Safarkhanlo Y, Yerly J, **Falcão MBL**, Mackowiak ALC, Piccini D, Stuber M, Jung B, Gräni C, Bastiaansen JAM, *Off-resonance encoded fat suppression methods for 5D whole-heart free-running cardiac MRI at 1.5T*, ISMRM & ISMRT Annual Meeting & Exhibition, 2023.

Master Students Supervised

Master thesis co-advisor of Sara Fässler, for the degree of Master of Medicine at the University of Bern.

A1. Supplementary Information:
Peer-reviewed articles which I have co-authored

A1.1. The Role of Cardiovascular Magnetic Resonance in Patients with Mitral Regurgitation - Peer-Reviewed Article

Article published at the Journal of Cardiovascular Development and Disease.
My contribution: I contributed with the knowledge on multi-dimensional phase-contrast magnetic resonance imaging applications to patients with mitral regurgitation.

Journal of
Cardiovascular
Development and Disease

MDPI

Review

The Role of Cardiovascular Magnetic Resonance in Patients with Mitral Regurgitation

Anna Giulia Pavon [1,†], Marco Guglielmo [2,*,†], Pierpaolo Mattia Mennilli [1], Mariana B. L. Falcão [3], Luca Bergamaschi [1,4], David Filip Costantin [1], Michele Vivaldo [1], Laura Anna Leo [1], Susanne Schlossbauer [1], Christopher W. Roy [3], Matthias Stuber [3,5], Giovanni Pedrazzini [1] and Francesco Faletra [1]

1 Division of Cardiology, Cardiocentro Ticino Institute, Ente Ospedaliero Cantonale, Via Tesserete, 48, 6900 Lugano, Switzerland
2 Department of Cardiology, Division of Heart and Lungs, University Medical Center Utrecht, Utrecht University, 3584 CX Utrecht, The Netherlands
3 Department of Radiodiagnostic and Interventional Radiology, University Hospital of Lausanne and University of Lausanne, 1012 Lausanne, Switzerland
4 Unit of Cardiology, IRCCS Policlinico St. Orsola-Malpighi, Department of Experimental, Diagnostic and Specialty Medicine-DIMES, University of Bologna, 40138 Bologna, Italy
5 Center for Biomedical Imaging (CIBM), 1012 Lausanne, Switzerland
* Correspondence: m.guglielmo@umcutrecht.nl
† These authors contributed equally to this work.

Abstract: The 2019 Global Burden of Disease (GBD) study estimated that there were approximately 24.2 million people affected worldwide by degenerative mitral regurgitation (MR), resulting in 34,200 deaths. After aortic stenosis, MR is the most prevalent VHD in Europe and the second-most common VHD to pose indications for surgery in western countries. Current ESC and AHA/ACC guidelines for the management of VHD emphasize the importance of an integrative approach for the assessment of MR severity, which is of paramount importance in dictating the timing for surgery. Transthoracic echocardiography (TTE) and transesophageal echocardiography (TEE) are the first-line imaging modalities; however, despite the technological advancement, sometimes, the final diagnosis on the degree of the disease may still be challenging. In the last 20 years, CMR has emerged as a robust technique in the assessment of patients with cardiac disease, and, recently, its role is gaining more and more importance in the field of VHD. In fact, CMR is the gold standard in the assessment of cardiac volumes, and it is possible to accurately evaluate the regurgitant volume. The purpose of this review is to outline the current state-of-the-art management of MR by using Cardiac Magnetic Resonance (CMR).

Keywords: mitral valve; cardiovascular magnetic resonance

Citation: Pavon, A.G.; Guglielmo, M.; Mennilli, P.M.; Falcão, M.B.L.; Bergamaschi, L.; Costantin, D.F.; Vivaldo, M.; Leo, L.A.; Schlossbauer, S.; Roy, C.W.; et al. The Role of Cardiovascular Magnetic Resonance in Patients with Mitral Regurgitation. *J. Cardiovasc. Dev. Dis.* **2022**, *9*, 399. https://doi.org/10.3390/jcdd9110399

Academic Editor: Toshiro Kitagawa

Received: 30 September 2022
Accepted: 16 November 2022
Published: 18 November 2022

1. How to "MRI" a Mitral Valve?

The first-line examination for MR remains transthoracic echocardiography (TTE); however, CMR can be of help in many clinical settings [1–3]. The aim of a CMR examination focused on MV includes the assessment of MV anatomy and function to quantify the regurgitation and its hemodynamic repercussion on cardiac chambers. Finally, the scanning protocol includes myocardial tissue characterization in order to identify focal and diffuse myocardial fibrosis [4] (Figure 1).

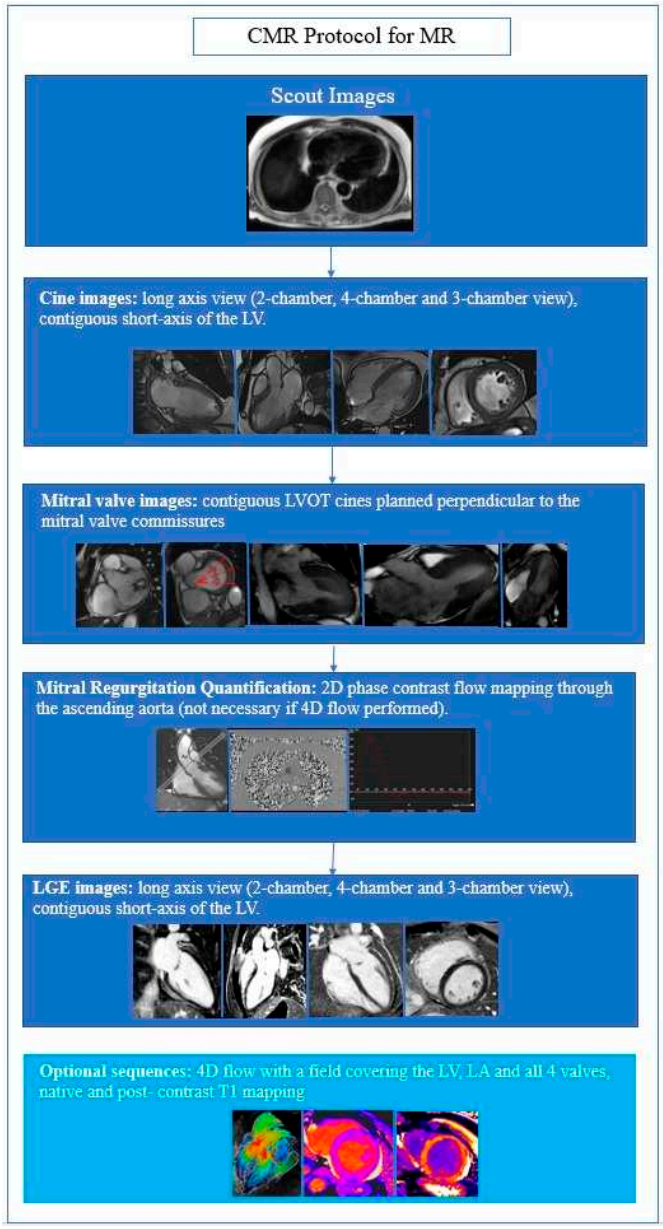

Figure 1. CMR protocol to image a mitral valve. LA: Left atrium; LV: left ventricle; LVOT: left ventricle outflow tract.

1.1. Mitral Valve Apparatus Assessment

MRI can be used to assess leaflets' anatomy and movement. The steady-state free precession (SSFP) pulse sequence is commonly used in this setting since it provides a good assessment of valve morphology and function [5]. Image acquisition is ECG-gated, and each slice is obtained during a single breath-hold of 5–8 s [5]. A visual assessment should be made of all four components of the mitral valve: the anterior leaflets, the posterior leaflets, the annulus, and the sub-valvular apparatus enclouding the papillary muscles [5]. Contiguous, long-axis, left ventricular outflow tract SSFP images should be acquired to visualize and assess all the mitral valve cusps (A1-P1, A2-P2, and A3-P3) [4] (Figure 2A). In this way, it is possible to detect the mechanism of the MR, detecting the presence of prolapsing leaflets or a functional MR. Nevertheless, it must be pointed out that small, thin structures (i.e., fibroelastomas or vegetations) may not be correctly visualized due to spatial resolution.

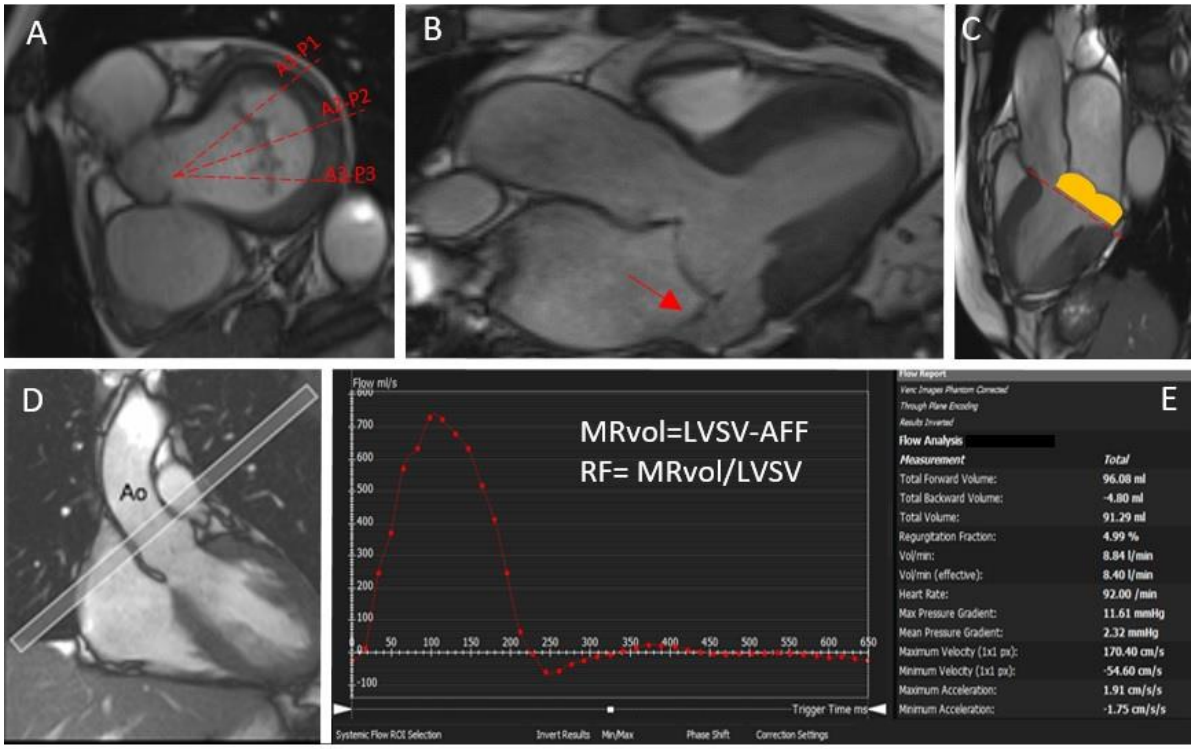

Figure 2. A short axis view of the mitral valve with scallops. Contiguous, long-axis, left ventricular outflow tract SSFP images should be acquired to visualize and assess all the mitral valve cusps following the red lines (**A**). A three-chamber view of a patient with bileaflet mitral valve prolapse in systole (**B**) showing the regurgitant jet (red arrow). A three-chamber view showing the volume of the prolapse that is typically not considered when calculating the ejection fraction ((**C**), orange box). The mitral annular plane is highlighted in red lines. The slice position for the phase-contrast velocity mapping sequence (**D**). (**E**) is showing a flow curve (mL/s) through the ascending aorta to calculate the aortic forward flow. MRvol = mitral regurgitant volume; AFF = aortic forward flow; LVSV = left ventricle stroke volume.

1.2. Ventricular Volume and Function

Correctly imaging the left ventricular (LV) volume and function is of paramount importance in assessing the hemodynamic repercussion of the valvulopathy and avoiding the progression through cardiac dysfunction. Finally, therefore, it is essential to decide on the timing for surgical intervention [1,2] (Figure 2B). Notably, CMR is the gold-standard imaging technique for evaluating LV volume, mass, and function. LV imaging should be assessed according to SCMR guidelines [5]. Ventricular volumes are calculated from a short-axis stack of 6–8 mm thick slices with an interslice gap of 4 mm [5]. It must be taken into account that, in patients with prominent mitral valve prolapse (MVP), the echocardiographic quantification made by Simpson's method may underestimate the LV end-systolic volume (LVESV), as it only considers the volume located between the apex and the mitral annulus and neglects the ventricular volume that is displaced into the left atrium but is contained within the prolapsed mitral leaflets at the end systole [6]. This may lead to an underestimation of LVESV, with a consequent overestimation of mitral regurgitation [7]. The recent series published by Vincenti G et al. [8] highlighted how, for patients with severe bileaflet prolapse, the correction of the LVSV considering the prolapse volume leads to a lower LV ejection fraction, and it also modifies the assessment of MR severity by one grade in a large portion of patients (Figure 2C). However, whether this has prognostic value still needs further validation.

1.3. Tissue Characterization

CMR is the only cardiac imaging technique allowing for the evaluation of myocardial composition. The cornerstone of this aspect is Late Gadolinium contrast-enhanced (LGE) imaging, which is typically obtained 10–15 min after contrast media injection [5]. Since gadolinium contrast media are able to reduce the T1 relaxation time and have a different wash-out in the normal myocardium compared to the pathological myocardial area, it highlights the presence of a damaged myocardium. The latter has a brighter signal, in contrast with the dark healthy myocardium [9]. Another technique that allows for a more quantitative approach to tissue characterization is T1 mapping. Higher native T1 relaxation times may be caused by edema, fibrosis, or protein accumulation. Finally, post-contrast T1 mapping, together with the hematocrit levels, is essential for extracellular volume (ECV) quantification [5].

1.4. Mitral Regurgitation Quantification

The quantification of the MR is a fundamental part of the CMR examination [1,4]. Several qualitative and quantitative methods are available. Starting from qualitative assessment, the MR jet can be visualized using both cine and 2D phase-contrast CMR. This is a visual approach which relies on spin dephasing in cine images. However, it must be pointed out that, given its susceptibility and the important intra-observer and inter-observer variability, this method should be used only to assess the presence of MR, while any estimation of the degree of severity should be performed only quantitatively [4].

1.4.1. 2D Phase Contrast (PC) Velocity Mapping

2D PC velocity mapping is the cornerstone of flow imaging and represents the standard approach to MR quantification [9]. The preferred sequence parameters of 2D PC imaging include a though-plane image placed at the sino-tubular junction in the end-diastole to quantify forward flow (Figure 2D,E). This plane should be perpendicular to the vessel. The baseline velocity encoding for aortic flow is 2.0–2.5 m/s, and the temporal resolution is 25–45 ms. The standard method to calculate the MR volume lies in 2D PC velocity mapping and accounts for the difference between the LV stroke volume calculated using the planimetry of SSFP and the forward volume obtained by 2D PC images [5]. In this way, it is possible to calculate the regurgitant volume and the regurgitant fraction. The mitral regurgitant volume (MRvol) is expressed as the difference between the left ventricular stroke volume (LVSV) and the aortic forward flow (AFF), and the regurgitant fraction (RF) is the MRvol divided by the LVSV, expressed as a percentage. According to both American and European recommendations, an RF > 50% or an MRvol > 60 mL identifies patients with severe MR. As can be imagined, the crucial advantages of this method account for the easy measurement, the lack of a need for geometric assumption, the lack of a contrast agent application, and the short investigation time [10]. However, it must be noted that the accuracy of the PC measurement can be reduced in cases of irregular rhythm or patient motion. Additionally, this standard 2D-based approach does not allow for visualizing or quantifying the 3D structure of the regurgitant jets, as, for instance, echocardiography does.

1.4.2. Quantitative Assessment of MR with CMR

The MRvol and MR RF can be measured according to different methods using a combination of 2D phase contrast velocity mapping and cine images.

1. The standard approach implies the quantification of MRvol and MR RF considering the difference between the LV stroke volume calculated using the planimetry of SSFP images and the aortic (systolic) forward volume obtained by phase-contrast images (AoPC).
2. If no other valve regurgitation or haemodynamically significant shunt are present, the MRvol can be derived by the difference between the LV stroke volume and the RV stroke volume calculated using the planimetry of SSFP images. It must be noted that, given the relatively lower precision with which the RV stroke volume is quantified

compared with the LV stroke volume, intra- and inter-observed variability is lower compared with other methods [11].

3. The difference between the mitral inflow stroke volume and the AoPC. If this method is suitable for patients with multiple valve regurgitations, the fact that 2D phase-contrast CMR requires static imaging planes and cannot adapt to valve motion may result in some inaccuracy [12].
4. Finally, if 4D-flow is available, a direct quantification of the MR flow with retrospective mitral valve tracking can also be performed. MR jets are quantified by defining a systolic reformatted plane perpendicular to the single jet or individually for multiple jets. Otherwise, a reconstructed aortic plane using the retrospective valve-tracking method can be used to quantify AoPC. This measurement can then be used to quantify the MR volume or fraction using the standard LVSV–AoPC method.

1.4.3. 4D Flow

4D flow velocity-encoded CMR imaging is an emerging technique that involves phase-contrast acquisition with flow encoding in all three spatial directions and to the dimension of time. New advances in 4D flow MRI [13] are growing, enabling a more in-depth quantification of MR. Research on this modality has been growing over the past years, and it has enabled not only the quantification of aortic forward flow but also the valve tracking, indirect regurgitant flow tracking, regurgitant jet quantification, and computation of mitral forward flow [14,15]. In a study by Fidock et al. in 2021 [16], 35 patients with different levels of MR severity were recruited for CMR, including the acquisition of 2D cines and 4D flow, and four different methods for MR quantification were compared. Patients were distributed into three groups: having Primary MR, having secondary MR, and having had mitral valve replacement (MPV). The most reproducible technique was reported to be regurgitation assessment based on the correlation between the mitral inflow and aortic inflow, both measured directly from 4D flow MRI data. In 2020, Blanken et al. [17] compared valve tracking and flow tracking semiautomatic quantification techniques to investigate the reproducibility of each measurement in 34 MR patients with different MR severity diagnoses, and they concluded that flow tracking of the regurgitation jets provided more accurate quantification of MR in terms of agreement with the indirect reference measurement, particularly for severe MR cases [17]. Notably, with the advances in accelerated 4D flow MRI, the scan time could possibly be reduced whilst maintaining the accuracy in results. For instance, in 2022, Blanken et al. [18] introduced a new sampling pattern for acquiring a faster 4D flow CMR for valvular quantification, enabling whole heart acquisitions in a short scan time (<10 min) with reliable MR quantification. Additionally, the introduction of the so-called free-running techniques could become a valuable aid in simplifying the scanning workflow, as they acquire imaging data without interruptions over a fixed period and without the need for complex slice positions or navigator placement [18,19]. Nevertheless, a validation of these techniques for MR quantification is still lacking.

However, in contrast to the previous decade, several options of analysis tools for 4D flow are available, and, to date, a standardized analysis process that allows for a uniform workflow and will generate reproducible and comparable quantification is lacking [4].

Clearly, in clinical settings, 4D flow will not replace echocardiography, but since it can provide a reliable quantification of MR when compared with 3D transesophageal echocardiography and has the direct advantages of a non-invasive technique that does not require sedation, it should be considered as a compliment technique. Additionally, it can be used in patients with comorbidities that prevent the use of transesophageal echocardiography [12].

2. Echocardiography and Cardiovascular Magnetic Resonance: Friends or Foes?

In patients with MR, agreement between CMR and the echocardiographic guidelines algorithm was suboptimal. Several studies have shown that echocardiography has limitations in distinguishing non-severe MR from severe MR [20]. Frequently, there could

be discordance among the echocardiographic parameters of MR severity, and there was no guideline-defined hierarchy for weighing individual parameters [20–22]. Recently, S. Uretsky et al. found that, among patients identified as having severe MR by the American Society of Echocardiography algorithm, less than half had severe MR by concomitant CMR evaluations [23]. This finding is consistent with prior studies that have shown a significant discordance between CMR and echocardiography, with absolute agreement values ranging from 36% to 63% [24,25].

The 'internal coherence' of the various measures is of paramount importance in the assessment of thr LV volume and quantitative parameters of MR grading. In fact, in routine echocardiographic practice, the occurrence of these discrepancies between effective stroke and regurgitant volume are not infrequent. In this setting, the CMR evaluation could improve the internal coherence in the MR assessment thanks to its high accuracy and reproducibility through a combination of LV volumetric measurements and aortic flow quantification with phase-contrast velocity mapping or with newer tools such as 4D flow cardiac MRI [3].

Finally, regurgitant volume by CMR seems to be the most reliable method for identifying patients with severe MV, as it is an independent predictor of LV reverse remodelling after mitral valve correction compared to other echocardiographic parameters [23].

The main remaining pitfalls in the assessment of MR by CMR are the fact that current severity thresholds are derived from echocardiographic data and the lack of standard cut-off values. However, recent studies suggest that CMR-specific thresholds may be more appropriate and more closely related to outcome [26], and the increased reproducibility and accuracy of LV and MR quantification may pave the way for the routine use of CMR in the assessment of mitral valve disease [27].

3. What Is the Role of CMR in Primary Mitral Regurgitation?

In both European and AHA/ACC guidelines for the management of MR, CMR is considered only in cases of an inconclusive echocardiography [1,2]. Moreover, no specific indications regarding additional information that can be provided by CMR according to the aetiology of MR are provided.

It must be noticed that, to date, if CMR is superior in assessing cardiac volume and function compared to echocardiography, a gold standard in the quantification of MR severity is still lacking [1]. Surely, echocardiography remains the first-line examination to evaluate primary MR; however the quantification of MR may be challenging, since it strongly relies on an acoustic window and geometric assumptions [1]. To date, only a few studies have tried to compare the degree of severity of primary MR detected in TTE with CMR, showing no conclusive results [28,29]. As mentioned, Uretsky et al. [20] recently demonstrated that there is limited concordance between the echocardiographic parameters of MR severity, and the discordance was worse with more severe MR, highlighting the challenges facing echocardiographers when assessing the severity of MR and emphasizing the need for using an integrated approach that incorporates multiple components. Moreover, the evaluation of MR in CMR has been proven to have a prognostic role. The first larger prospective study in primary MR was published by Myerson et. al. in 2016 [26]. In this landmark paper, patients with moderate or severe primary MR detected in TTE were followed up for a mean time of 2.5 $\pm$ 1.9 years. In this cohort of 109 asymptomatic patients, the presence of a regurgitant volume > 55 mL was found to be associated with the appearance of symptoms and the need for surgery [26]. Moreover, an MR regurgitant volume >55 mL was also found to be the best predictor of mortality in a prospective, multicentric study involving 258 asymptomatic patients with moderate or severe primary MR [27].

Arrhythmic Mitral Valve Prolapse

MVP is a common cardiac condition, with an estimated prevalence between 1% and 3% [30]. Most of the patients with this condition have a benign course, but ever since its initial description, mitral valve prolapse has been associated with higher risk of complex

ventricular arrhythmia and sudden cardiac death [31]. Arrhythmogenesis in patients with mitral valve prolapse is a complex interplay between different factors which is still not completely deciphered. The fundamental role of cardiac imaging is to highlight the presence of high-risk features, which possibly expose patients to a higher risk of arrhythmic complications [32]. The echocardiographic "high-risk" features include the presence of a bileaflet MVP (defined as the presence of a displacement >2 mm beyond the long-axis annular plane, with >5 mm leaflet thickening [33]) accompanied by morphofunctional abnormalities of the mitral annulus such as mitral annular disjunction (MAD) and systolic curling [31]. Conventionally, MAD is defined as the apparent systolic separation of the mitral leaflet insertion from the ventricular myocardium, typically evaluated in a three-chamber view [34]. However, it must be pointed out that the presence of MAD has a circumferential extension, and, sometimes, its identification with TTE will be challenging [31]. On the contrary, the extent of the longitudinal MAD distance located in the posterolateral wall is easily assessed by CMR. Essayagh et al. compared TTE and CMR for the detection of MAD and found a low sensitivity (65%) but a high specificity (96%) for TTE [35]. A recent study compared TTE, TEE, and CMR and showed only a moderate agreement between TTE and CMR, while a good agreement was found between TEE and CMR [36]. Notably, no specific analysis on the patho-morphomogy of MAD exists so far. Recently, evidence for the fact that MAD can also be present in normal hearts has been described and highlights the fact that the role of MAD in arrhythmogenesis may be in need of further analysis [37,38]. In particular, it is possible to distinguish two scenarios: the first scenario with "pseudo-MAD" (sited on P2 insertion), in which MAD is detected only in the systole and actually does not exist, it being formed from the juxtaposition of the belly of the billowing posterior leaflet on the adjacent left atrial wall, giving the illusion that a disjunction is present, but a normal attachment of the leaflet can be observed in the diastolic phase. A second scenario is a "true-MAD", in which the disjunction can be seen in both the systole and diastole, and it is linked to an abnormal attachment of the leaflet in the atrial wall. However, how these two entities may correlate with arrhythmias still needs further study [39].

The other fundamental feature defining the "arrhythmic mitral valve prolapse" is the presence of fibrosis, traditionally detected in LGE sequences at the level of the inferior wall, the infero-lateral wall, and papillary muscles in the landmark paper of Basso C et al. [40], confirmed in several following studies [41,42] (Figure 3). The fact that MVP influences the ventricular remodeling has recently been confirmed by Costant Dit Beaufils et al. [43], showing that replacement myocardial fibrosis was present in 28% of patients with various degrees of MVP and that it was especially located in the basal inferolateral wall or papillary muscle. The myocardial fibrosis prevalence was 13% in trace-mild MR, 28% in moderate MR, and 37% in severe MR, and it was associated with specific features of the mitral valve apparatus, a more dilated LV, and more frequent ventricular arrhythmias (45% vs. 26%, $p < 0.0001$) [43]. The study highlights how the presence of fibrosis, associated with mitral valve apparatus alterations, was finally associated with a more dilated LV, a higher MR degree, and ventricular arrhythmia—all features that are independent risk factors for adverse cardiovascular events.

The future holds promising scenarios, and, apart from localized areas of fibrosis demonstrated on LGE, the presence of interstitial fibrosis evaluated by native T1 mapping or ECV has also been recently analyzed for better arrhythmic risk stratification [41,44,45]. In this setting, patients with MVP were found to have a higher degree of ventricular remodeling, going beyond what can be detected in LGE sequences, evidenced by the higher native T1 relaxation time or higher ECV. Moreover, an ECV > 33% was found to have the same predictive value regarding out-of-hospital cardiac arrest as LGE [41].

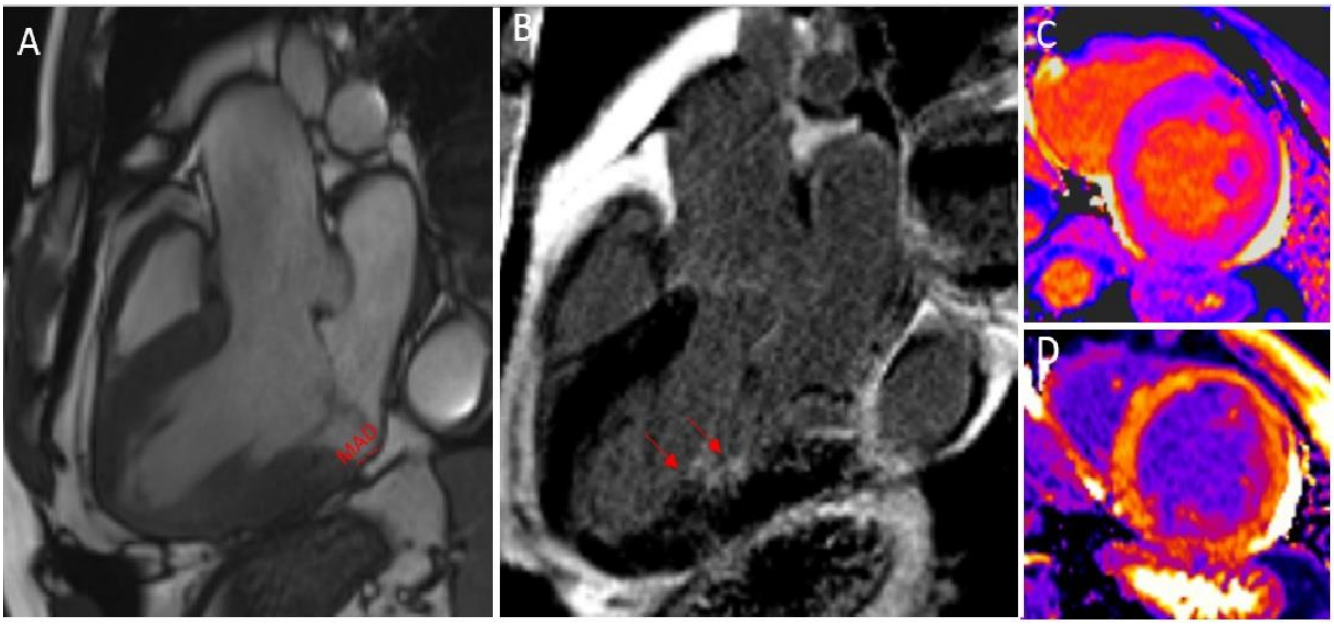

Figure 3. CMR in a patient with MVP. MAD can be clearly diagnosed in an SSFP three-chamber view in the systole (red lines) (**A**). The presence of fibrosis on the tip of papillary muscles (red arrow) is highlighted in LGE (**B**); finally, higher levels of interstitial fibrosis can be identified by higher levels of native T1 mapping (**C**) and ECV after post-contrast T1 mapping (**D**).

4. What Is the Role of MRI in Secondary Mitral Regurgitation?

Secondary MR is the result of LV dysfunction that can be due to various diseases, following myocardial infarction most of the time [1]. In this setting, CMR examinations can provide an accurate assessment of LV dysfunction, highlighting the presence of myocardial scar/necrosis and the viability of myocardial segments and providing important clues that are useful in the work-up of dilated cardiomyopathies [4,46]. This is particularly important for patients who are candidates for surgical revascularization, in which a concomitant surgical treatment of the MV is also suggested. In a pilot study published in 2009, it was first highlighted how posterior papillary muscle region scarring severity correlated with decreased segmental wall motion and a poorer mitral regurgitation correction after coronary revascularization and annuloplasty, suggesting that routinely assessing scar burden may help to identify patients for whom annuloplasty alone is insufficient to eliminate mitral regurgitation [47]. Moreover, it must be noticed that the progression of ischemic mitral regurgitation was also found to be independently associated with adverse LV remodeling and infarct size [48].

It is well known that ischemic mitral regurgitation is typically associated with poor outcomes [1]. In this context, it can be speculated that knowing the viability of the myocardial wall and the possible improvement of myocardial contraction after revascularization may also lead to an improvement in the degree of the MR. However, to date, no specific large studies have been published regarding how the use of CMR may influence clinical management in this specific clinical setting.

Finally, it must be considered that, in recent years, the percutaneous treatment of MR with the MitraClip^{TM} system has also become more and more available in patients with secondary MR [1]. Given the fact that the procedure is relatively new, no studies regarding the use of CMR in the work-up of possible candidates have been published so far [49]. However, in a small series of patients, CMR has been shown to perform very well in the quantitation of MR after MitraClip^{TM} insertion, with an excellent reproducibility compared to echocardiographic methods. Moreover, the evidence that MitraClip^{TM} implantation may be associated with LV reverse remodeling may open the question on the role of CMR tissue characterization in the screening of possible candidates that can benefit from the procedures

5. Future Steps

The role of CMR in the setting of MR evaluation is rapidly expanding as a complement technique to echocardiography to improve the patient's evaluation. Surely, the novelty of 4D flow, allowing for the quantification of flow and regurgitation in many novel ways, will be of help in the future. These methods could include particle tracing component analysis, intra-cavity energetics, retrospective valve tracking to quantify forward and regurgitant jets, 4D flow-derived parameters, semi-quantitative streamline visualization, and intra-cavity hemodynamic forces [50,51]. However, the possible role of these methods and their prognostic relevance still need to be validated.

Moreover, if, on the one hand, it is well known that CMR is the gold reference standard for evaluating volume and function with the possibility for MR quantification that conveys information, and it is possible to quantify MR with a clinical outcome benefit over echocardiography, it must be noted that it still remains unclear which method for MR quantification is more reliable in clinical practice. Finally, despite the fact that the 4D flow technique has also shown promising results, future studies are needed to prospectively evaluate the clinical outcome benefit of using 4D flow CMR for MR quantification in challenging situations.

6. Conclusions

CMR has become a robust and reliable imaging modality, not only for the assessment of ventricle structure and function but also for the quantification of MR. Growing evidence shows that CMR could be an accurate complementary method to echocardiography for grading regurgitation severity. Using comprehensive techniques, CMR allows for an accurate measurement of valvular regurgitant volume (Rvol) and regurgitant fraction (RF), independent of jet morphology and direction. Furthermore, due to its unique ability to assess focal and diffuse LV fibrosis, CMR provides potential information in the clinical evaluation of MR for planning and deciding on the timing and indication of a specific therapy or intervention. Accordingly, taking into consideration the potential accurate uses of CMR in the evaluation of MR, this imaging modality could be useful in the assessment of the unclear severity of valvular regurgitation measured by echocardiography.

Author Contributions: All authors have read and agreed to the published version of the manuscript.

Funding: This research received no external funding.

Institutional Review Board Statement: Not applicable.

Informed Consent Statement: Not applicable.

Data Availability Statement: Not applicable.

Conflicts of Interest: The authors declare no conflict of interest.

References

1. Vahanian, A.; Beyersdorf, F.; Praz, F.; Milojevic, M.; Baldus, S.; Bauersachs, J.; Capodanno, D.; Conradi, L.; De Bonis, M.; De Paulis, R.; et al. 2021 ESC/EACTS Guidelines for the management of valvular heart disease. *Eur. Heart J.* **2021**, *43*, 561–632. [CrossRef] [PubMed]
2. Doherty, J.U.; Kort, S.; Mehran, R.; Schoenhagen, P.; Soman, P. ACC/AATS/AHA/ASE/ASNC/HRS/SCAI/SCCT/SCMR/STS 2017 Appropriate Use Criteria for Multimodality Imaging in Valvular Heart Disease: A Report of the American College of Cardiology Appropriate Use Criteria Task Force, American Association for Thoracic Surgery, American Heart Association, American Society of Echocardiography, American Society of Nuclear Cardiology, Heart Rhythm Society, Society for Cardiovascular Angiography and Interventions, Society of Cardio-vascular Computed Tomography, Society for Cardiovascular Magnetic Resonance, and Society of Thoracic Surgeons. *J. Am. Coll. Cardiol.* **2017**, *70*, 1647–1672. [CrossRef] [PubMed]
3. Landi, A.; Faletra, F.F.; Pavon, A.G.; Pedrazzini, G.; Valgimigli, M. From secondary to tertiary mitral regurgitation: The paradigm shifts, but uncertainties remain. *Eur. Heart J. Cardiovasc. Imaging* **2021**, *22*, 835–843. [CrossRef] [PubMed]
4. Garg, P.; Swift, A.J.; Zhong, L.; Carlhäll, C.-J.; Ebbers, T.; Westenberg, J.; Hope, M.D.; Bucciarelli-Ducci, C.; Bax, J.J.; Myerson, S.G. Assessment of mitral valve regurgitation by cardiovascular magnetic resonance imaging. *Nat. Rev. Cardiol.* **2019**, *17*, 298–312. [CrossRef] [PubMed]

5. Kramer, C.M.; Barkhausen, J.; Bucciarelli-Ducci, C.; Flamm, S.D.; Kim, R.J.; Nagel, E. Standardized cardiovascular magnetic resonance imaging (CMR) protocols: 2020 update. *J. Cardiovasc. Magn. Reson.* **2020**, *22*, 17. [CrossRef]
6. Le Goffic, C.; Toledano, M.; Ennezat, P.-V.; Binda, C.; Castel, A.-L.; Delelis, F.; Graux, P.; Tribouilloy, C.; Maréchaux, S. Quantitative Evaluation of Mitral Regurgitation Secondary to Mitral Valve Prolapse by Magnetic Resonance Imaging and Echocardiography. *Am. J. Cardiol.* **2015**, *116*, 1405–1410. [CrossRef]
7. Topilsky, Y.; Michelena, H.; Bichara, V.; Maalouf, J.; Mahoney, D.W.; Enriquez-Sarano, M. Mitral valve prolapse with mid-late systolic mitral regurgitation: Pitfalls of evaluation and clinical outcome compared with holosystolic regurgitation. *Circulation* **2012**, *125*, 1643–1651. [CrossRef]
8. Vincenti, G.; Masci, P.G.; Rutz, T.; De Blois, J.; Prša, M.; Jeanrenaud, X.; Schwitter, J.; Monney, P. Impact of bileaflet mitral valve prolapse on quantification of mitral regurgitation with cardiac magnetic resonance: A single-center study. *J. Cardiovasc. Magn. Reson.* **2017**, *19*, 56. [CrossRef]
9. Pelc, N.J.; Herfkens, R.J.; Shimakawa, A.; Enzmann, D.R. Phase contrast cine magnetic resonance imaging. *Magn. Reson. Q.* **1991**, *7*, 229–254.
10. Nayak, K.S.; Hu, B.S.; Nishimura, D.G. Rapid quantitation of high-speed flow jets. *Magn. Reson. Med.* **2003**, *50*, 366–372. [CrossRef]
11. Kon, M.W.S.; Myerson, S.; Moat, N.E.; Pennell, D.J. Quantification of regurgitant fraction in mitral regurgitation by cardiovascular magnetic resonance: Comparison of techniques. *J. Heart Valve Dis.* **2004**, *13*, 600–607. [PubMed]
12. Calkoen, E.E.; Roest, A.A.; Kroft, L.J.; van der Geest, R.J.; Jongbloed, M.R.; Bsc, P.J.V.D.B.; Blom, N.A.; Hazekamp, M.G.; De Roos, A.; Westenberg, J.J. Characterization and improved quantification of left ventricular inflow using streamline visualization with 4DFlow MRI in healthy controls and patients after atrioventricular septal defect correction. *J. Magn. Reson. Imaging* **2014**, *41*, 1512–1520. [CrossRef] [PubMed]
13. Dyverfeldt, P.; Bissell, M.; Barker, A.J.; Bolger, A.F.; Carlhäll, C.-J.; Ebbers, T.; Francios, C.J.; Frydrychowicz, A.; Geiger, J.; Giese, D.; et al. 4D flow cardiovascular magnetic resonance consensus statement. *J. Cardiovasc. Magn. Reson.* **2015**, *17*, 72. [CrossRef] [PubMed]
14. Gupta, A.N.; Avery, R.; Soulat, G.; Allen, B.D.; Collins, J.D.; Choudhury, L.; Bonow, R.O.; Carr, J.; Markl, M.; Elbaz, M.S.M. Direct mitral regurgitation quantification in hypertrophic cardiomyopathy using 4D flow CMR jet tracking: Evaluation in comparison to conventional CMR. *J. Cardiovasc. Magn. Reson.* **2021**, *23*, 138. [CrossRef] [PubMed]
15. Lee, J.; Gupta, A.N.; Ma, L.E.; Scott, M.B.; Mason, O.R.; Wu, E.; Thomas, J.D.; Markl, M. Valvular regurgitation flow jet assessment using in vitro 4D flow MRI: Implication for mitral regurgitation. *Magn. Reson. Med.* **2021**, *87*, 1923–1937. [CrossRef]
16. Fidock, B.; Archer, G.; Barker, N.; Elhawaz, A.; Al-Mohammad, A.; Rothman, A.; Hose, R.; Hall, I.R.; Grech, E.; Briffa, N.; et al. Standard and emerging CMR methods for mitral regurgitation quantification. *Int. J. Cardiol.* **2021**, *331*, 316–321. [CrossRef]
17. Blanken, C.P.S.; Westenberg, J.J.M.; Aben, J.-P.; Bijvoet, G.P.; Chamuleau, S.A.J.; Boekholdt, S.M.; Nederveen, A.J.; Leiner, T.; Van Ooij, P.; Planken, R.N. Quantification of Mitral Valve Regurgitation from 4D Flow MRI Using Semiautomated Flow Tracking. *Radiol. Cardiothorac. Imaging* **2020**, *2*, e200004. [CrossRef]
18. Ma, L.E.; Yerly, J.; Piccini, D.; Di Sopra, L.; Roy, C.W.; Carr, J.C.; Rigsby, C.K.; Kim, D.; Stuber, M.; Markl, M. 5D Flow MRI: A Fully Self-gated, Free-running Framework for Cardiac and Respiratory Motion–resolved 3D Hemodynamics. *Radiol. Cardiothorac. Imaging* **2020**, *2*, e200219. [CrossRef]
19. Falcão, M.B.L.; Di Sopra, L.; Ma, L.; Bacher, M.; Yerly, J.; Speier, P.; Rutz, T.; Prša, M.; Markl, M.; Stuber, M.; et al. Pilot tone navigation for respiratory and cardiac motion-resolved free-running 5D flow MRI. *Magn. Reson. Med.* **2021**, *87*, 718–732. [CrossRef]
20. Uretsky, S.; Gillam, L.; Lang, R.; Chaudhry, F.A.; Argulian, E.; Supariwala, A.; Gurram, S.; Jain, K.; Subero, M.; Jang, J.J.; et al. Discordance between echocardiography and MRI in the assessment of mitral regurgitation severity: A prospective multicenter trial. *J. Am. Coll. Cardiol.* **2015**, *65*, 1078–1088. [CrossRef]
21. Grayburn, P.A.; Bhella, P. Grading Severity of Mitral Regurgitation by Echocardiography: Science or Art? *JACC Cardiovasc. Imaging* **2010**, *3*, 244–246. [CrossRef] [PubMed]
22. Uretsky, S.; Argulian, E.; Supariwala, A.; Marcoff, L.; Koulogiannis, K.; Aldaia, L.; Chaudhry, F.A.; Wolff, S.D.; Gillam, L.D. A Comparative Assessment of Echocardiographic Parameters for Determining Primary Mitral Regurgitation Severity Using Magnetic Resonance Imaging as a Reference Standard. *J. Am. Soc. Echocardiogr.* **2018**, *31*, 992–999. [CrossRef] [PubMed]
23. Uretsky, S.; Animashaun, I.B.; Sakul, S.; Aldaia, L.; Marcoff, L.; Koulogiannis, K.; Argulian, E.; Rosenthal, M.; Wolff, S.D.; Gillam, L.D. American Society of Echocardiography Algorithm for Degenerative Mitral Regurgitation: Comparison With CMR. *JACC Cardiovasc. Imaging* **2022**, *15*, 747–760. [CrossRef] [PubMed]
24. Sachdev, V.; Hannoush, H.; Sidenko, S.; Saba, S.G.; Sears-Rogan, P.; Bandettini, W.P.; Brofferio, A.; Shanbhag, S.M.; Brenneman, C.L.; Horvath, K.A.; et al. Are Echocardiography and CMR Really Discordant in Mitral Regurgitation? *JACC Cardiovasc. Imaging* **2017**, *10*, 823–824. [CrossRef]
25. Cawley, P.J.; Hamilton-Craig, C.; Owens, D.S.; Krieger, E.V.; Strugnell, W.E.; Mitsumori, L.; D'Jang, C.L.; Schwaegler, R.G.; Nguyen, K.Q.; Nguyen, B.; et al. Prospective Comparison of Valve Regurgitation Quantitation by Cardiac Magnetic Resonance Imaging and Transthoracic Echocardiography. *Circ. Cardiovasc. Imaging* **2013**, *6*, 48–57. [CrossRef]

26. Myerson, S.G.; D'Arcy, J.; Christiansen, J.P.; Dobson, L.E.; Mohiaddin, R.; Francis, J.M.; Prendergast, B.; Greenwood, J.P.; Karamitsos, T.D.; Neubauer, S. Determination of Clinical Outcome in Mitral Regurgitation with Cardiovascular Magnetic Resonance Quantification. *Circulation* **2016**, *133*, 2287–2296. [CrossRef]
27. Uretsky, S.; Argulian, E.; Narula, J.; Wolff, S.D. Use of Cardiac Magnetic Resonance Imaging in Assessing Mitral Regurgitation: Current Evidence. *J. Am. Coll. Cardiol.* **2018**, *71*, 547–563. [CrossRef]
28. Gorodisky, L.; Agmon, Y.; Porat, M.; Abadi, S.; Lessick, J. Assessment of mitral regurgitation by 3-dimensional proximal flow convergence using magnetic resonance imaging: Comparison with echo-Doppler. *Int. J. Cardiovasc. Imaging* **2018**, *34*, 793–802. [CrossRef]
29. Altes, A.; Levy, F.; Iacuzio, L.; Dumortier, H.; Toledano, M.; Tartar, J.; Tribouilloy, C.; Maréchaux, S. Comparison of Mitral Regurgitant Volume Assessment between Proximal Flow Convergence and Volumetric Methods in Patients with Significant Primary Mitral Regurgitation: An Echocardiographic and Cardiac Magnetic Resonance Imaging Study. *J. Am. Soc. Echocardiogr.* **2022**, *35*, 671–681. [CrossRef]
30. Hutchins, G.M.; Moore, G.W.; Skoog, D.K. The Association of Floppy Mitral Valve with Disjunction of the Mitral Annulus Fibrosus. *New Engl. J. Med.* **1986**, *314*, 535–540. [CrossRef]
31. Pavon, A.; Monney, P.; Schwitter, J. Mitral Valve Prolapse, Arrhythmias, and Sudden Cardiac Death: The Role of Multimodality Imaging to Detect High-Risk Features. *Diagnostics* **2021**, *11*, 683. [CrossRef] [PubMed]
32. Han, Y.; Peters, D.C.; Salton, C.J.; Bzymek, D.; Nezafat, R.; Goddu, B.; Kissinger, K.V.; Zimetbaum, P.J.; Manning, W.J.; Yeon, S.B. Cardiovascular Magnetic Resonance Characterization of Mitral Valve Prolapse. *JACC Cardiovasc. Imaging* **2008**, *1*, 294–303. [CrossRef] [PubMed]
33. Mantegazza, V.; Volpato, V.; Gripari, P.; Ali, S.G.; Fusini, L.; Italiano, G.; Muratori, M.; Pontone, G.; Tamborini, G.; Pepi, M. Multimodality imaging assessment of mitral annular disjunction in mitral valve prolapse. *Heart* **2020**, *107*, 25–32. [CrossRef] [PubMed]
34. Marra, M.P.; Basso, C.; De Lazzari, M.; Rizzo, S.; Cipriani, A.; Giorgi, B.; Lacognata, C.; Rigato, I.; Migliore, F.; Pilichou, K.; et al. Morphofunctional Abnormalities of Mitral Annulus and Arrhythmic Mitral Valve Prolapse. *Circ. Cardiovasc. Imaging* **2016**, *9*, e005030. [CrossRef]
35. Sriram, C.S.; Syed, F.F.; Ferguson, M.E.; Johnson, J.N.; Enriquez-Sarano, M.; Cetta, F.; Cannon, B.C.; Asirvatham, S.J.; Ackerman, M.J. Malignant Bileaflet Mitral Valve Prolapse Syndrome in Patients With Otherwise Idiopathic Out-of-Hospital Cardiac Arrest. *J. Am. Coll. Cardiol.* **2013**, *62*, 222–230. [CrossRef]
36. Essayagh, B.; Sabbag, A.; Antoine, C.; Benfari, G.; Yang, L.-T.; Maalouf, J.; Asirvatham, S.; Michelena, H.; Enriquez-Sarano, M. Presentation and Outcome of Arrhythmic Mitral Valve Prolapse. *J. Am. Coll. Cardiol.* **2020**, *76*, 637–649. [CrossRef]
37. Toh, H.; Mori, S.; Izawa, Y.; Fujita, H.; Miwa, K.; Suzuki, M.; Takahashi, Y.; Toba, T.; Watanabe, Y.; Kono, A.K.; et al. Prevalence and extent of mitral annular disjunction in structurally normal hearts: Comprehensive 3D analysis using cardiac computed tomography. *Eur. Heart J. Cardiovasc. Imaging* **2021**, *22*, 614–622. [CrossRef]
38. Zugwitz, D.; Fung, K.; Aung, N.; Rauseo, E.; McCracken, C.; Cooper, J.; El Messaoudi, S.; Anderson, R.H.; Piechnik, S.K.; Neubauer, S.; et al. Mitral Annular Disjunction Assessed Using CMR Imaging: Insights From the UK Biobank Population Study. *JACC Cardiovasc. Imaging* **2022**, *15*, 1856–1866. [CrossRef]
39. Faletra, F.F.; Leo, L.A.; Paiocchi, V.L.; Schlossbauer, S.A.; Pavon, A.G.; Ho, S.Y.; Maisano, F. Morphology of Mitral Annular Disjunction in Mitral Valve Prolapse. *J. Am. Soc. Echocardiogr.* **2021**, *35*, 176–186. [CrossRef]
40. Basso, C.; Marra, M.P.; Rizzo, S.; De Lazzari, M.; Giorgi, B.; Cipriani, A.; Frigo, A.C.; Rigato, I.; Migliore, F.; Pilichou, K.; et al. Arrhythmic Mitral Valve Prolapse and Sudden Cardiac Death. *Circulation* **2015**, *132*, 556–566. [CrossRef]
41. Pavon, A.G.; Arangalage, D.; Pascale, P.; Hugelshofer, S.; Rutz, T.; Porretta, A.P.; Le Bloa, M.; Muller, O.; Pruvot, E.; Schwitter, J.; et al. Myocardial extracellular volume by T1 mapping: A new marker of arrhythmia in mitral valve prolapse. *J. Cardiovasc. Magn. Reson.* **2021**, *23*, 1–13. [CrossRef] [PubMed]
42. Figliozzi, S.; Georgiopoulos, G.; Lopes, P.M.; Bauer, K.B.; Moura-Ferreira, S.; Tondi, L.; Mushtaq, S.; Censi, S.; Pavon, A.G.; Bassi, I.; et al. Myocardial Fibrosis at Cardiac MRI Helps Predict Adverse Clinical Outcome in Patients with Mitral Valve Prolapse. *Radiology* **2022**, 220454. [CrossRef] [PubMed]
43. Beaufils, A.-L.C.D.; Huttin, O.; Jobbe-Duval, A.; Senage, T.; Filippetti, L.; Piriou, N.; Cueff, C.; Venner, C.; Mandry, D.; Sellal, J.-M.; et al. Replacement Myocardial Fibrosis in Patients With Mitral Valve Prolapse: Relation to Mitral Regurgitation, Ventricular Remodeling, and Arrhythmia. *Circulation* **2021**, *143*, 1763–1774. [CrossRef]
44. Guglielmo, M.; Fusini, L.; Muscogiuri, G.; Baessato, F.; Loffreno, A.; Cavaliere, A.; Rizzon, G.; Baggiano, A.; Rabbat, M.G.; Muratori, M.; et al. T1 mapping and cardiac magnetic resonance feature tracking in mitral valve prolapse. *Eur. Radiol.* **2020**, *31*, 1100–1109. [CrossRef]
45. Bui, A.H.; Roujol, S.; Foppa, M.; Kissinger, K.V.; Goddu, B.; Hauser, T.H.; Zimetbaum, P.J.; Ngo, L.H.; Manning, W.J.; Nezafat, R.; et al. Diffuse myocardial fibrosis in patients with mitral valve prolapse and ventricular arrhythmia. *Heart* **2016**, *103*, 204–209. [CrossRef] [PubMed]
46. Kwon, D.H.; Kusunose, K.; Obuchowski, N.A.; Cavalcante, J.L.; Popovic, Z.B.; Thomas, J.D.; Desai, M.Y.; Flamm, S.D.; Griffin, B.P. Predictors and Prognostic Impact of Progressive Ischemic Mitral Regurgitation in Patients with Advanced Ischemic Cardiomyopathy: A Multimodality Study. *Circ. Cardiovasc. Imaging* **2016**, *9*, e004577. [CrossRef] [PubMed]

47. Flynn, M.; Curtin, R.; Nowicki, E.R.; Rajeswaran, J.; Flamm, S.D.; Blackstone, E.H.; Mihaljevic, T. Regional wall motion abnormalities and scarring in severe functional ischemic mitral regurgitation: A pilot cardiovascular magnetic resonance imaging study. *J. Thorac. Cardiovasc. Surg.* **2009**, *137*, 1063–1070.e2. [CrossRef] [PubMed]
48. Spieker, M.; Marpert, J.; Afzal, S.; Scheiber, D.; Bönner, F.; Horn, P.; Kelm, M.; Westenfeld, R. Extent and determinants of left ventricular reverse remodeling in patients with secondary mitral regurgitation undergoing MitraClip implantation. *IJC Heart Vasc.* **2021**, *34*, 100804. [CrossRef] [PubMed]
49. Hamilton-Craig, C.; Strugnell, W.; Gaikwad, N.; Ischenko, M.; Speranza, V.; Chan, J.; Neill, J.; Platts, D.; Scalia, G.M.; Burstow, D.; et al. Quantitation of mitral regurgitation after percutaneous MitraClip repair: Comparison of Doppler echocardiography and cardiac magnetic resonance imaging. *Ann. Cardiothorac. Surg.* **2015**, *4*, 341–351. [CrossRef]
50. Garg, P.; Crandon, S.; Swoboda, P.P.; Fent, G.J.; Foley, J.R.J.; Chew, P.G.; Brown, L.A.E.; Vijayan, S.; Hassell, M.E.C.J.; Nijveldt, R.; et al. Left ventricular blood flow kinetic energy after myocardial infarction—Insights from 4D flow cardiovascular magnetic resonance. *J. Cardiovasc. Magn. Reson.* **2018**, *20*, 61. [CrossRef]
51. van der Geest, R.J.; Garg, P. Advanced Analysis Techniques for Intra-cardiac Flow Evaluation from 4D Flow MRI. *Curr. Radiol. Rep.* **2016**, *4*, 38. [CrossRef]

A1.2. Motion-Resolved Fat-Fraction Mapping with Whole-Heart Free-Running Multiecho GRE - under Peer-review

Article under peer-review at the Journal of Magnetic Resonance in Medicine.

My contribution: I provided the Pilot Tone signal extraction pipeline and helped the first author to adapt it to the Free-Running 3DRadial Multi-Echo GRE datasets.

Adèle L.C. Mackowiak[1,2,3], Christopher W. Roy[3], Jérôme Yerly[3,4], Mariana B.L. Falcão[3], Mario Bacher[3,5], Peter Speier[5], Davide Piccini[3,6], Matthias Stuber[3,4], Jessica A.M. Bastiaansen[1,2]

[1]Department of Diagnostic, Interventional and Pediatric Radiology (DIPR), Inselspital, Bern University Hospital, University of Bern, Switzerland
[2]Translation Imaging Center (TIC), Swiss Institute for Translational and Entrepreneurial Medicine, Bern, Switzerland
[3]Department of Radiology, Lausanne University Hospital (CHUV) and University of Lausanne (UNIL), Lausanne, Switzerland
[4]Center for Biomedical Imaging (CIBM), Lausanne, Switzerland
[5]Siemens Healthcare GmbH, Erlangen, Germany
[6]Advanced Clinical Imaging Technology (ACIT), Siemens Healthcare AG, Lausanne, Switzerland

Abstract

Purpose: To develop a free-running 3D radial whole-heart multiecho GRE framework for cardiac- and respiratory-motion-resolved fat fraction quantification.

Methods: Multiecho (N_{TE}=8) readouts optimized for water-fat separation and quantification were integrated within a continuous non-ECG-triggered free-breathing 3D radial GRE acquisition. Motion resolution was achieved with Pilot Tone (PT) navigation, and extracted cardiac and respiratory signals were compared to those obtained with self-gating (SG). After XD-GRASP-based image reconstruction, FF, R2*, and B_0 maps, as well as fat and water images were generated with a maximum-likelihood fitting algorithm. The framework was tested in a custom fat-water phantom and in 10 healthy volunteers at 1.5T using N_{TE}=4 and N_{TE}=8 echoes. The separated images and maps were compared with a standard free-breathing ECG-triggered acquisition.

Results: The method was validated in vivo, with respiratory and cardiac motion being resolved over all collected echoes. Across volunteers, PT provided respiratory and cardiac signals in agreement (r=0.91 and r=0.72) with self-gating of the first echo, and a higher correlation to the ECG (0.1% of missed triggers for PT vs 5.9% for SG). The framework enabled pericardial fat imaging and quantification throughout the cardiac cycle, revealing a decrease in FF at end-systole by 11.4±3.1% across volunteers (P<0.0001). Motion-resolved end-diastolic 3D FF maps showed good correlation with ECG-triggered measurements (FF bias of -1.06%). A significant difference in free-running FF measured with N_{TE}=4 and N_{TE}=8 was found (P<0.0001 in sub-cutaneous fat and P<0.01 in pericardial fat).

Conclusion: Free-running fat fraction mapping was validated at 1.5T, enabling ME-GRE-based fat quantification with N_{TE}=8 echoes in 6:15min.

1. Introduction

MRI-derived proton-density fat fraction (PDFF) is considered a robust and reproducible noninvasive measure of fat concentration within the MR research community[1]. Cardiac fat quantification canaid the diagnosis of pathologies where adipose cells abnormally develop, within fat depots in dilated cardiomyopathy[2] or within scar tissue of the infracted myocardium leading to an increased risk of arrhythmogenic right ventricular cardiopathy[3,4] and sudden cardiac death[5,6]. Fat fraction (FF) quantification also carries potential to characterize the complex metabolic role of different adipose tissues in obesity[7,8] and diabetes[9,10], where increased amounts of epicardial, pericardial and peri-coronary fat alter the cardiovascular disease risk profile[11,12]. Nevertheless, cardiac fat quantification with MRI is seldom performed in clinical settings, where invasive biopsies remain the standard measurement.

PDFF can be quantified using multi-echo GRE (ME-GRE) MRI sequences that acquire images at different echo times[13]. Multiple echoes are needed to reliably separate the signals in the presence of B_0 magnetic field inhomogeneities, which confounds the detection of fat[14]. Dedicated algorithms take into account effects of B_0[15–18], T1[19,20], T2*[21], or noise[22], and assume a fixed fat spectral model [23–25]. Accurate fat quantification requires a sufficient amount of data points to resolve the multiple resonance peaks of the triglyceride molecule, which lengthens the acquisition time and may limit the clinical translation of the technique. Because of motion, cardiac PDFF quantifications are typically performed during breath-holds and with the use of triggering devices such as electrocardiograms (ECG). Therefore, cardiac PDFF measurements are limited in the number of echoes that can be collected, or restricted in terms of organ coverage. While free-breathing techniques have enabled whole-heart water-fat separation at 1.5T[26,27], 3T[28,29] and 7T[30], they still relied on triggered acquisitions or the sampling of 4 or fewer echoes, and did not focus on fat quantification. Alternatively, approaches that combine fingerprinting[31–33] or deep learning[34] with ME-GRE have shown promising results for fat quantification with various amount of echoes, but still required breath-holding and ECG-triggering with restricted organ coverage. To increase the number of echoes to improve spectral resolution in conjunctionwith scan efficiency, alternative motion management techniques are needed.

Recently introduced free-running concepts using continuous uninterrupted 3D acquisitions enable whole-heart free-breathing MRI where ECG R-wave time stamps help resolve cardiac motion retrospectively[35]. Free-running sequences have a fixed scan time, improve ease-of-use, and applications range from anatomical imaging[36–38], to coronary angiography[39,40], T1 and T2 mapping[41–44], and flow measurements[45]. Advances in respiratory motion compensation extended with a compressed sensing (CS) reconstruction made restrospective cardiac- and respiratory-motion resolved 5D imaging possible[46,47]. The addition of Pilot Tone (PT) technology[48,49] as an alternative to self-gating (SG) for extracting cardiac and respiratory signals[50] permits the sequence-independent monitoring of physiological motion. This development could be particularly suitable for long or repeated echo readouts, such as ME-GRE scans, that typically have lower SNR.

To address the challenge of limited organ coverage and restrictions on the number of echoes that can be acquired, in this work, a 3D ME-GRE free-running approach was developed for fat fraction quantification. The aim of the study was to combine the strength of motion-resolved cardiac MRI and advanced fat-water decomposition techniques to perform multi-peak fitting of 3D images of the whole heart, that are resolved for both cardiac and respiratory motion, without the need for triggering devices

nor breath-holds. The proposed framework combines 1) an extension of the free-running acquisition scheme to higher dimensionality with multiecho sampling, 2) PT technology, 3) a robust CS reconstruction framework and 4) a state-of-the-art multi-peak fitting routine for fat-water separation and quantification, with 8 echoes. Phantom and healthy volunteer experiments were performed to test whether the proposed free-running FF mapping framework can provide 3D motion-resolved parametric maps of cardiac adipose tissue.

2. Methods

MRI experiments were performed at 1.5T (MAGNETOM Sola, Siemens Healthcare, Erlangen, Germany) using a 12-channel body array equipped with an integrated PT generator. Volunteers, N=10 (F=5, M=5, age [21;31] y.o., BMI [19.1;24.7]) provided their informed consent and the study was approved by the local Ethics Committee.

2.1 Data Acquisition, Reconstruction and Post-Processing Framework

2.1.1 Sequence design

A prototype whole-heart 3D radial free-running GRE sequence was modified to incorporate multiple echo readouts for each radial segment using monopolar (fly-back) readout gradients (**Figure 1**). The phyllotaxis k-space trajectory consists of sets of radial segments grouped into interleaved spirals, which are successively rotated by the golden angle[51]. The first radial segment of each interleaf is oriented along the superior-inferior (SI) direction. The multi-echo readout scheme prolongs the time between two subsequent SI segments of the same echo time TE_i ($i=1,\ldots,N_{TE}$) within the echo train (see **Supporting Information Table S1**). Note that these SI segments are used to perfom self-gating (see Section 2.1.3). The ECG signal was logged during the scan period.

An ECG-triggered version of above sequence was also acquired, using the same k-space sampling, with data collection performed only during the diastolic resting phase.

2.1.2 Acquisition parameters

In vitro

A custom fat-water phantom with 14 vials containing different fat concentrations (see **Supporting Information Figure S1** for details on phantom design and a comparison with a Cartesian acquisition scheme) was scanned with two versions of the proposed protocol with $N_{TE}=8$ and $N_{TE}=5$, to mimic respectively the free-running and ECG-triggered sequences, and both with two RF excitation angles $\alpha=12°$ and $\alpha=6°$. Sequence parameters included: a pixel bandwidth of 890Hz/px, a field-of-view (FOV) size of $290mm^3$, an interecho spacing of $\Delta TE=2.05ms$, and $TE_1=1.25ms$. The repetition time was TR=17.02ms in free-running and TR=10.87ms with ECG-triggering.

In vivo

The prototype free-running sequence was designed with an acquisition time (TA) of 6:15min and isotropic resolution of $(2.0mm)^3$ (**Table 1**). Within this fixed duration 8 echoes (N_{TE}) with an inter-echo spacing $\Delta TE=2.05ms$ arecollected with a k-space trajectory of 22 segments per radial interleave. The ECG-triggered protocol has a matching FOV, spatial resolution, RF excitation angle and receiver bandwidth, and a similar acquisition time. The ECG-triggered sequence is heart rate-dependent with

an average scan time of 6:23min. The available time for echo collection is constrained by the cardiac resting phaseperiod. Therefore, the trajectory was set to 12 segments and 437 interleaves in the triggered protocol. This enabled the collection of 5 echoes while producing a similar phyllotaxis pattern as the one used in the free-running protocol (see **Supporting Information Figure S2**), and a slightly higher yet close to the Nyquist sampling factor (**Table 1**).

The proposed free-running sequence induced Specific Absorption Rate (SAR) values ranging from 0.01719 to 0.02197 W/kg in the N=10 volunteers.

MR acquisition	Free-Running	ECG-triggered
FOV size [mm^3]	220 x 220 x 220	220 x 220 x 200
Spatial resoltion [mm^3]	2.0 x 2.0 x 2.0	2.0 x 2.0 x 2.0
RF excitation angle [°]	12	12
Receiver bandwidth [Hz/px]	893	893
TR [ms]	17.02	11.04
N_{TE}	8	5
TE_1 / ΔTE	1.25 / 2.05	1.25 / 2.05
TA [min:s]	6:15	[5:58; 6:64]
$N_{segments}$ x $N_{interleaves}$	22 x 1000	12 x 437
Nyquist sampling factor [%]	5.6	6.4

Table 1. MR sequence parameters for the free-running and ECG-triggered ME-GRE acquisitions. Sequence parameters were chosen to maximize data collection within a scan time of 6 minutes, with matching echo times (TE) and inter-echo spacing ΔTE for the free-running and ECG-triggered acquisitions. The Nyquist sampling factor corresponds to the ratio between the k-space lines within one motion bin and the total amount of lines required for a fully-sampled reconstruction, expressed in %.

2.1.3 Physiological signals extraction

The coil-integrated PT generator emits a continuous-wave RF signal that is modulated by physiological motion. The PT navigator functions at a frequency outside of the MR band (62 MHz), hence not disturbing image acquisition. The PT data was used to compute one-dimensional respiratory and cardiac signals using principal component analysis (**Figure 1**), which were then used to bin the raw imaging data into 2 respiratory and 10-11 cardiac motion states. Respiratory motion was adressed by selecting the radial views in the bin corresponding to end-expiration (around 40%, as was done previously[52]). Compared to previously published single-echo free-running reconstructions [39,47,50], the proposed multiecho framework uses a lower temporal resolution (90ms per cardiac bin) in order to guarantee an acceptable undersampling factor (**Table 1**) for CS reconstruction, as well as sufficient SNR towards the end of the long echo train.

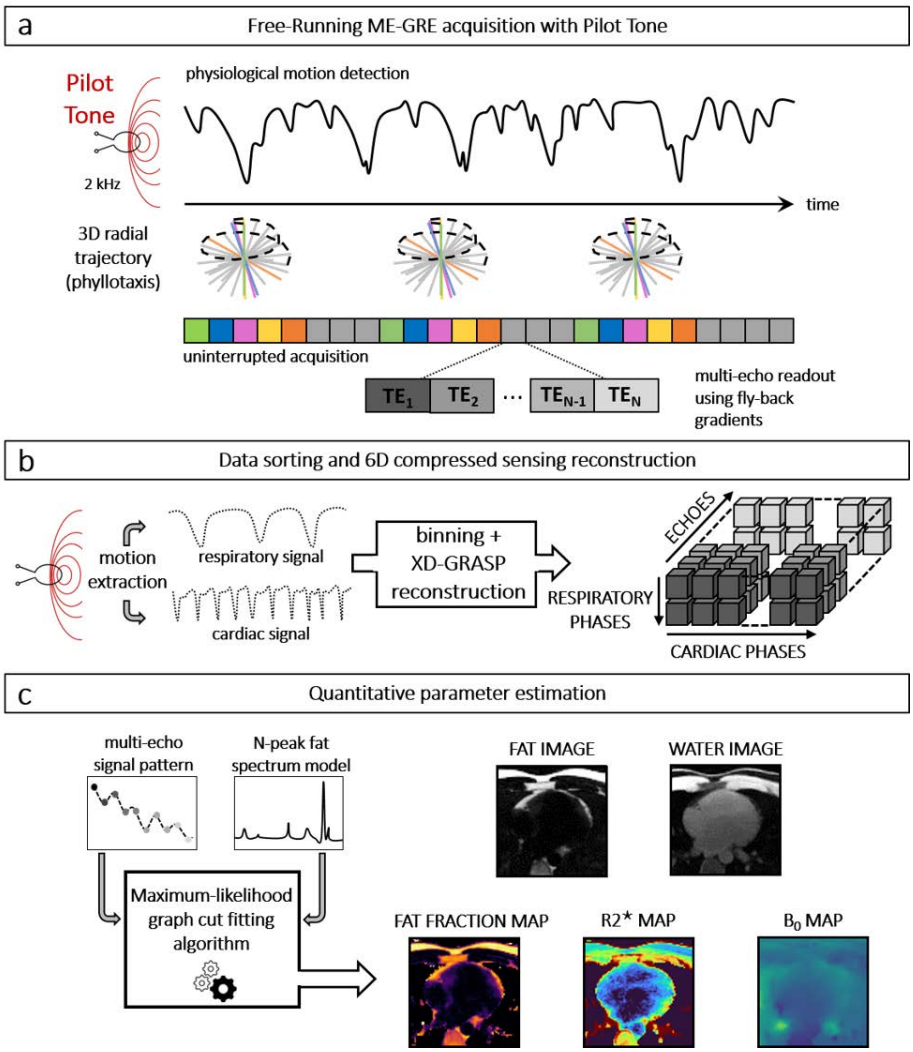

Figure 1. Acquisition, reconstruction and post-processing framework. **a.** The free-running multiecho GRE acquisition uses a 3D radial phyllotaxis trajectory, where each k-space line is repeated N_{TE} times with fly-back gradients. During the whole duration of the uninterrupted data acquisition, the coil-integrated Pilot Tone navigator registers signals at a 2kHz sampling rate, which are modulated by physiological motion. **b.** Acquired signals are used to bin the MR data into cardiac and respiratory motion states. The XD-GRASP algorithm reconstructs the highly undersampled k-space data into 6-dimensional imaging volume. **c.** The signal pattern formed along the echo dimension is fed to a fat-water decomposition algorithm, along with a reference fat spectrum, to produce separated fat and water images, as well as fat fraction (FF), water fraction (WF) and main field deviation (B_0) maps.

2.1.4 Motion-resolved image reconstruction

The acquired k-space data were sorted into 6D (x-y-z-cardiac-respiratory-echo) according to the cardiac and respiratory motion states and echo number. The first 220 radial segments (corresponding to 10 interleaves and 15 of the total acquisition) were discarded from the reocnstruction to eliminate potential transient magnetization effects. The highly undersampled motion-resolved datasets were reconstructed using XD-GRASP[46,53] and the alternating method of multipliers (ADMM)[54]. Regularization using total variation[53] was applied spatially, as well as along the respiratory-resolved and cardiac-resolved dimensions. No regularization was applied along the echo dimension, so that the contrast variations between fat and water signals remain unaltered. The same regularization weights, chosen to maintain a good trade-off between visual image quality and motion compression artifacts, were used for all 6D reconstructions (see **Supporting Information Figure S3**).

All 6D reconstructions were performed using MatLab R2018b (The Mathworks, Inc., Natick, Massachusetts, United States) on a workstation equipped with 2 Intel Xeon CPUs (Intel, Santa Clara, California, United States), 512GB of RAM, and a NVIDIA Tesla GPU (Nvidia, Santa Clara, California, United States). Reconstruction time was recorded using a built-in MatLab clock.

Respiratory-motion-resolved image reconstruction of the ECG-triggered acquisitions was performed using the same XD-GRASP algorithm described above. The regularization weights along the spatial and respiratory-resolved dimensions were matched to that used for free-running reconstructions.

2.1.5 Fat-water separation and quantitative parameters (FF, B_0, R2) estimation*

The reconstructed 6D datasets were post-processed to compute fat- and water-only 5D (x-y-z-cardiac-respiratory) images as well as parametric maps (FF, R2*, B_0) with an iterative graph cut algorithm for fat-water separation[18,55], part of the ISMRM 2012 Fat/Water Toolbox[56]. The algorithm estimates the B_0 field map and computes water and fat fraction maps through fitting of a multi-peak fat model with a single T2* decay component, using a reference 6-peak fat spectrum[23,56]. Parameters for the fitting algorithm were tuned based on phantom experiments and included: a range of [0;100]Hz for R2* estimation, a range of [-400;400]Hz for the B_0 map values, a number n=40 graph cut iterations, and a regularization parameter λ=0.05. A spatial subsampling with factor R=2 was used to accelerate the estimation of the B_0 map.

2.2 Analysis

2.2.1 Comparison of Pilot Tone and Self-Gating for ME-GRE

Physiological signal extraction using PT was compared to a self-gating approach. SG uses principal component analysis on the repeated SI projections that encode motion information. Because 8 subsequent SI projections are acquired, the effect of the choice of SI projection for SG of multiecho acquisitions was tested in all volunteers by performing the SG signal extraction from the eight sets of SI projections (labelled SG TE_i, i=1,…,8) and comparing it to signals extracted from PT and the reference ECG trace. A correlation analysis using Pearson's coefficient *r* was performed to determine which SG TE_i source provides the closest match to PT signals in both respiratory and cardiac dimensions, as well as to determine the variability between the different sources. The influence on the binning into motion states was determined by computing a percentage of binning difference to PT. This metric corresponds to the ratio of k-space segments placed into a different motion bin than the one selected using the PT signal, over the total number of segments. Additionally, a visual comparison was performed on the reconstructed images.

Because SG signals are derived from 3D radial imaging data, they may contain trajectory-made frequency components that are non-physiological and require filtering[47] (see **Supporting Information Figure S4**). To determine the amount of trajectory-dependent information embedded within the SG cardiac signals extracted from each TE, a metric of spectral power removal was used. Spectral power removal corresponds to the percentage of spectral density power removed from the original frequency spectrum after the trajectory-dependent frequency component filtering[47]. This metric informs on the impact of gradient delays and eddy currents on the recorded signal, and therefore could help for the choice of TE for SG signal extraction, as an alternative to PT.

In addition, cardiac signals extracted from all sources (SG TE_i and PT) were compared to the ECG trace recorded during the MRI scan. The mean durations of the cardiac cycle were compared to those measured by the ECG. The number of trigger points throughout the whole free-running acquisition was reported for the ECG and the other sources, and the percentage of missed triggers (w.r.t. ECG triggers) was computed. Moreover, the trigger jitter, i.e. the standard deviation of the difference between the time stamps of the ECG triggers and that of each source, was measured. This last metric informs about the accuracy of cardiac cycle length estimation, as the trigger points of each source are not matched with the ECG trigger time: PT triggering is performed on the local minima of the extracted cardiac signal, while SG triggering is performed on the zero-crossing point of the signal (**Figure 4b**). Therefore, the trigger jitter measures a deviation across trigger delays, across pairs of associated trigger points between the ECG and each evaluated source.

2.2.2 Parametric mapping analysis

To analyze the FF maps, regions of interest (ROIs) were drawn in pericardial fat, and sub-cutaneousfat for a static reference. ROIs were drawn based on the visual assessment of the fat-only images. For each tissue type, two ROIs were drawn, in both free-running and ECG-triggered data. The average and standard deviation of the FF was computed across cardiac motion states, at expiration. The FF from triggered datasets were compared to those from the diastolic resting phase in the free-running data by linear regression and Bland-Altman analyses.

2.2.3 Impact of echo train length

To test the impact of echo train length on fat quantification, free-running data were undersampled in the echo dimension by selecting only the first four echoes (from TE_1 = 1.25 ms to TE_4=7.40 ms). The FF maps obtained with N_{TE} = 4 were compared to those obtained with N_{TE} = 8. The average FF over 10 end-diastolic, expiratory slices in two ROIs in sub-cutaneous fat and two ROIs in pericardial fat were computed. Paired parametric t-tests (GraphPad Prism, version 8.0.2 for Windows, GraphPad Software, San Diego, California, United States) were performed in each tissue to determine statistically significant differences.

2.2.4 Impact T1 bias

Due to the shorter T1 relaxation time of fat compared to water-based tissues, the fat signal measured with GRE imaging is amplified by a factor κ which is dependent on the RF excitation angle[19,22]. When defining the true fat fraction as FF_{true}=F/(W+F) where F and W are the respective amplitudes of fat and water signals, the measured fat fraction $FF_{measured}$ deviates from FF_{true} so that $FF_{measured}$=κF/(W+κF). To evaluate the impact of T1 bias, numerical simulations of the Bloch equations (MatLab 2021a, MathWorks, Natick, MA, USA) and phantom experiments were performed. The signal evolution of myocardial and fat tissues was simulated for both the free-running (TR=17.02ms) and the ECG-triggered (TR=11.04ms) sequences, for a range of RF excitation angles $\alpha \in [1\ ;25]°$. The relaxation times were T1=996ms and T2=47ms for myocardium[57], and T1=343ms and T2=58ms for sub-cutaneous fat at 1.5T[58]. For the simulation of the ECG-triggered sequence, a cardiac cycle length of 900ms was assumed. The measured fraction $FF_{measured}$ was plotted as a function of the true fraction FF_{true} for the choice of RF excitation angle α=12° used in volunteer experiments.

In phantom experiments, the same fat-water separation post-processing was performed as described in volunteer experiments. The average and standard deviation of the FF in the phantom vials was measured across 15 slices and compared to reference values quantified with MR spectroscopy (MRS) performed at 9.4T in each vial. Following the methodology of Yang *et al.*[20], a T1 bias correction was performed using T1 estimates (T1fat=340ms and T1water=1350ms measured with inversion recovery turbo-spin-echo MRI[59]) on the separated fat-water images, and corrected FF values were also calculated and compared with MRS.

In volunteers, T1 bias correction was performed in order to adequately compare the free-running and ECG-triggered FF maps: for each sequence type, the bias estimated from the simulation experiments described above was used.

3. Results

3.1 Numerical Simulations & Phantom Experiments

3.1.1 Numerical Simulations

A fat signal amplification factor of κ=1.5854 was found for an RF excitation angle of 12° (**Figure 2ab**, dashed curves). For the ECG-triggered sequence, this factor was κ=1.1610 (**Figure 2ab**, plain curves). This translated into different correction curves for the free-running and ECG-triggered sequences, where the largest deviation from the true fraction was measured at 11.4% for FF_{true}=44.3% with the free-running sequence, and FF_{true}=48.1% with a deviation of 3.8% (**Figure 2b**).

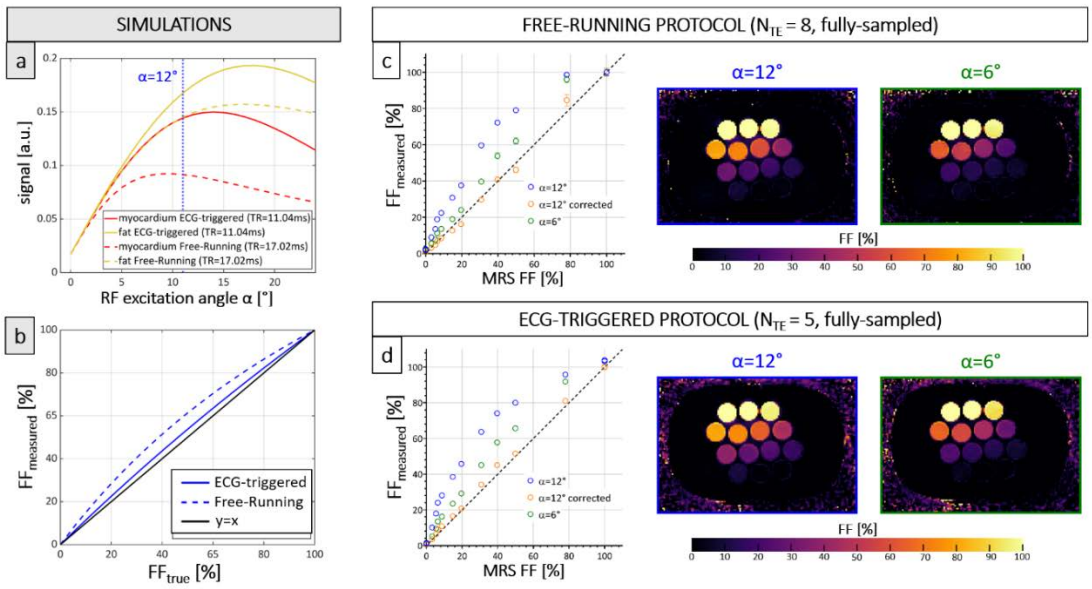

Figure 2. Impact of T1 bias in numerical simulations and in a phantom with controlled fat fractions. Using Bloch simulations, simulated fat and myocardium signals are plotted for different RF excitation angles in a free-running and in an ECG-triggered sequence (**a**). The blue dotted line indicates the expected signal amplitudes in the current study when using an RF excitation angle α=12°. In panel (**b**), the measured FF obtained with α=12° is plotted as a function of the true FF, for the free-running and ECG-triggered sequences. In phantom experiments, the average FF measured in maps obtained with free-running (**c**) and ECG-triggered (**d**) sequences, with RF excitation angles α=12° (blue), α=6° (green), is shown as a function of ground truth FF measured with MRS. T1bias-corrected values from the α=12° protocols are shown in orange on the graphs (**c, d**). Although the reduced flip angle approach reduced the bias of T1 to a certain degree, the correction based on T1 estimates completely eliminated it.

3.1.2 Phantom experiments

Both the free-running and ECG-triggered protocols demonstrated large deviations due to T1 bias. Even with a reduced flip angle approach (α=6°) the bias was not completely eliminated (**Figure 2cd**). After correction of T1 bias with known estimates of T1, the regression analysis with respect to the MRS controlled FF produced a line described by y=1.02x-0.67 (r^2=0.995) for the free-running protocol and y=0.99x+1.73 (r^2=0.998) for the ECG-triggered protocol.

3.2 Motion-Resolved Multi-Echo Image Reconstruction

PT navigation successfully extracted both cardiac and respiratory motion in all 10 healthy volunteers, allowing the echo-specific visualization of motion frames corresponding to the expiration phase of the respiratory cycle, and the end-diastolic phase of the cardiac cycle (**Figure 3, Supporting Information S3**). The mean cardiac cycle length was between [745;1037] ms, which correlated with the ECG derived cycle length [742;1035] ms, with a Pearson correlation coefficient of *r*=0.931 (**Supporting Information Figure S5**). The 10 (11 bins for volunteer V6 who had the longest mean cardiac cycle) cardiac bins had a bin length between [74.5;102.5] ms, with an average bin length of 90.7 ms across volunteers.

The average and standard deviation of the XD-GRASP reconstruction time for the 10 6D free-running datasets was 5h05min±1h10min (on the workstation described in 2.1.4.). For the 10 5D ECG-triggered datasets, the average and standard deviation of the reconstruction time on the same workstation was 26min±4min.

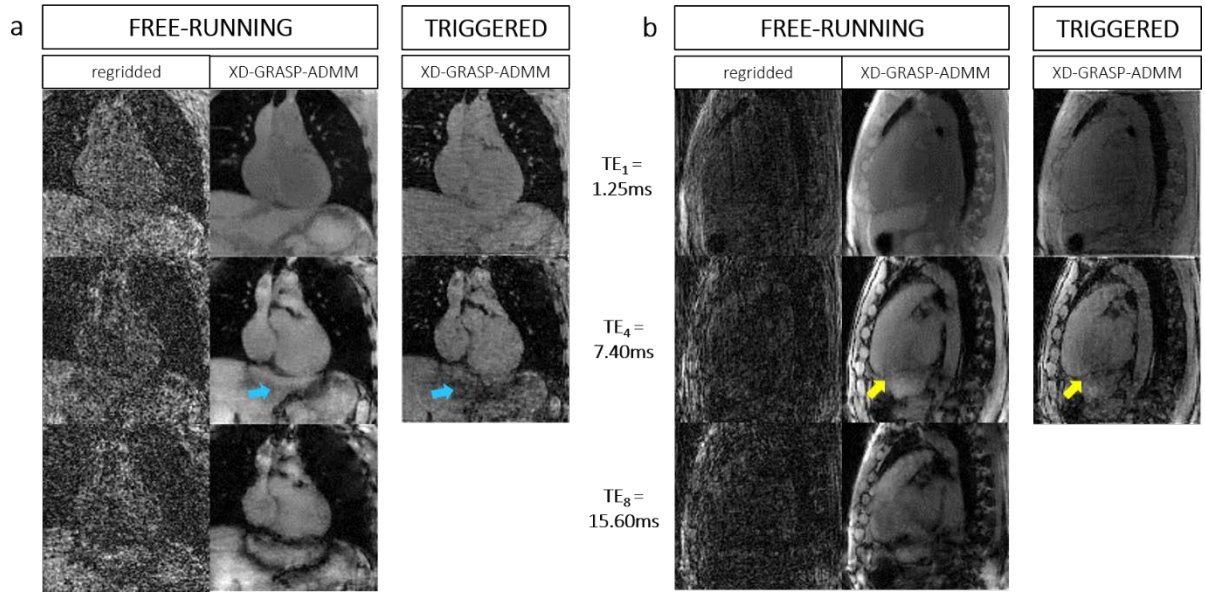

Figure 3. Multi-echo compressed sensing reconstruction with XD-GRASP-ADMM. The effect of XD-GRASP on the different contrast images (at echo times TE_1, TE_4 and TE_8) collected with the PT free-running ME-GRE acquisition is shown in (**a**) the coronal plane in healthy volunteer V6 and (**b**) the sagittal plane on healthy volunteer V7. The framework allows recovering of the anatomy absent from the highly undersampled regridded data (5.6% Nyquist), whilst preserving the contrast change needed for chemical species separation. In comparison, the ECG-triggered 5-echo acquisition (6.4% Nyquist) reconstructed with the same framework displays a slightly higher visual sharpness (**b**, yellow arrows), but is noisier than the free-running images. The ECG-triggered image at TE_4 shows some signal loss and blurriness in the liver that is less visible in the PT free-running data (**a**, blue arrows).

The free-running XD-GRASP images were in visual agreement with the reference ECG-triggered images obtained at the diastolic resting phase in terms of anatomy (**Figure 3**), and showed for each TE anatomical features that cannot be recovered from heavily undersampled data without CS (**Figure 3**, regridded images). In addition to a signal loss along the echo dimension, additional blurriness at organ interfaces (heart-liver, lung-liver) was also observed at TE_8, compared to TE_1 and TE_4. Despite a larger amount of k-space data used for each 3D volume reconstructed from the triggered acquisition (6.4% Nyquist against 5.6% for free-running) and the use of the same respiratory motion correction based on PT, signal losses outside the heart were observed in triggered images that were much attenuated in free-running images (**Figure 3**).

3.3 Comparison of Pilot-Tone and Self-Gating for ME-GRE

For respiratory motion, signals extracted from the different SG sources showed good consistency across echoes, with an average Pearson correlation to PT $r \geq 0.93$ across volunteers(**Table 2**). As illustrated in volunteer V1, the SG respiratory signals from the first two and the last two recorded echoes (i.e. TE_1, TE_2, TE_7 and TE_8) showed good agreement with the PT signal, despite a smaller peak-to-peak amplitude reported for PT over the two respiratory cycles displayed (**Figure 4a**). Higher correlation was found across the volunteers for the first two echoes (Table 2). Only the selection of TE_8 as a source tends to increase the deviation from PT binning (18.6% compared to around 11% for other sources).

For cardiac motion, variability was observed in the main detected frequency f_{CARD} when a different TE source is used, for example in volunteer V1: a main cardiac frequency f_{CARD}=1.03Hz was extracted from SG TE_1 and TE_2, while f_{CARD}=0.75Hz was reported with SG TE_7 (**Figure 4b**). For reference, the ECG recording of volunteer V1 yielded a mean cardiac cycle length of 1005 ms (**Supporting Information Figure S5**), corresponding to a main cardiac frequency of f_{CARD}=1.00Hz. This difference can be seen where selected signals are plotted over a dozen cardiac cycles (**Figure 4b**). Overall, the correlation to PT was poorer for cardiac than respiratory signals, with the best correlation at r=0.72 achieved with SG TE_1, and the weakest correlation at r=0.36 with SG TE_7 across volunteers (**Table 2**). It is worth noting that large standard deviations were observed across volunteers for this metric.

In volunteer V1, despite an average cardiac frequency detected close to that of SG TE_1 and SG TE_2, SG TE_8 showed poorer correlation (r=0.651) to PT as well as to the reference ECG trace, with more missed cardiac triggers and a larger deviation of the estimated cycle.

The percentage of spectral power removal decreased with increasing source echo time (**Table 2**). With SG TE_1 as source, an average of 92% of frequency components were identified as trajectory-dependent and thus filtered out. However using the next echo TE_2 as source, this number dropped to 60%. A steady reduction was seen with the use of successive TEs, with the lowest number reported for TE_7. However, no particular trend across echoes was observed in the percentage of binning difference with respect to PT-based binning (**Table 2**).

The trigger points from the PT cardiac signals had the best match to ECG triggers, with a trigger jitter of (23±14)ms across volunteers and 0.1% of missed triggers (**Table 2**). SG TE_7 had the largest deviation from both the PT source and the ECG signal across volunteers, with an average trigger jitter as large as (118±102)ms.

source	% spectral power removed	Pearson's *r* correlation to PT – respiratory	Pearson's *r* correlation to PT – cardiac	% binning difference to PT – respiratory	% binning difference to PT – cardiac	% missed ECG triggers	ECG trigger jitter [ms]
SG TE_1	92 ± 5	0.96 ± 0.01	0.72 ± 0.32	12 ± 2	15 ± 4	5.9 ± 4.4	69 ± 22
SG TE_2	60 ± 13	0.96 ± 0.03	0.51 ± 0.24	12 ± 2	14 ± 4	6.8 ± 9.6	87 ± 24
SG TE_3	58 ± 10	0.94 ± 0.06	0.54 ± 0.31	12 ± 2	13 ± 4	9.0 ± 12.8	132 ± 92
SG TE_4	32 ± 11	0.93 ± 0.10	0.66 ± 0.26	11 ± 2	12 ± 4	5.4 ± 8.5	68 ± 22
SG TE_5	30 ± 7	0.92 ± 0.11	0.52 ± 0.32	12 ± 2	13 ± 4	10.8 ± 14.1	65 ± 26
SG TE_6	29 ± 7	0.92 ± 0.11	0.60 ± 0.29	11 ± 1	13 ± 4	6.9 ± 9.5	57 ± 16
SG TE_7	21 ± 9	0.92 ± 0.11	0.36 ± 0.31	11 ± 2	13 ± 4	13.9 ± 14.5	118 ± 102
SG TE_8	28 ± 6	0.91 ± 0.12	0.56 ± 0.30	19 ± 3	13 ± 3	8.5 ± 14.0	85 ± 55
Pilot Tone	0	1	1	0	0	0.1 ± 0.1	23 ± 14

Table 2. Comparison of PT-based and SG-based physiological signal extraction parameters in volunteers. The number of SI readouts is repeated by the number of acquired echoes (N_{TE}), which was 8. The cardiac and respiratory signals reconstructed from the 8 different SG and one PT sources are compared by quantification of the following metrics: percentage of spectral power filtered out due to trajectory dependencies (see **Supporting Information Figure S4**), Pearson correlation coefficient w.r.t. PT, percentage of difference in binning w.r.t. PT, percentage of missed trigger points w.r.t. the reference ECG, and ECG trigger jitter. All reported metrics are given as a mean and standard deviation.

No differences in the respiratory positions of the chest could be observed, indicating similarity in respiratory signals used for binningDespite the higher variability in cardiac motion characteristics (**Table 2**), the effect on reconstructed images was minor, but visible in the water-only images identified at end-systole and at mid-diastole for SG TE_1, SG TE_7 and PT (**Figure 4c**). All three sets of images displayed overall good visual agreement and homogenous fat suppression in both the chest and the heart. However, closer inspection of the region containing the right coronary artery (RCA) showed that the images binned based on SG TE_7 signals were blurrier, with a slight loss of contrast in the RCA at diastole.

3.4 Water-Fat Separation and Parametric Mapping

The average post-processing time was 2h43min±7min. For triggered acquisitions, the average computing time was 14min37s±18s.

Water-fat separation with graph cut was successful in all volunteers, without water-fat swaps or motion ghost artifacts. In the FF maps, as well as water fraction (WF) maps (**Figure 5**), no displacement of the expected static (chest, spine) regions was seen, nor ghosting, indicating that respiratory motion compensation was achieved and that cardiac motion compensation did not interfere with organs and tissue in the periphery of the field of view. The displacement of the fatty regions of the heart was clearly observed (**Figure 6**, animated GIF in **Supporting Information Video S1**).

Despite the lack of blood-to-myocardium contrast inherent to GRE imaging, the water-only images provided good visualization of cardiac anatomy, with complete absence of fatty tissue, enabling the visualization of the RCA(**Figure 5a**, top and **Figure 6c**). In the corresponding fat-only images (**Figure 5a**, bottom and **Figure 6d**), 3D visualization of the pericardial fat was possible, particularly in coronal orientation around the right atrium and left ventricle. Sub-cutaneous fat-based tissues appeared brighter than cardiac fat tissues; such differences are more apparent in the co-registered quantitative FF and WF maps displayed with a color gradient (**Figure 5b**).

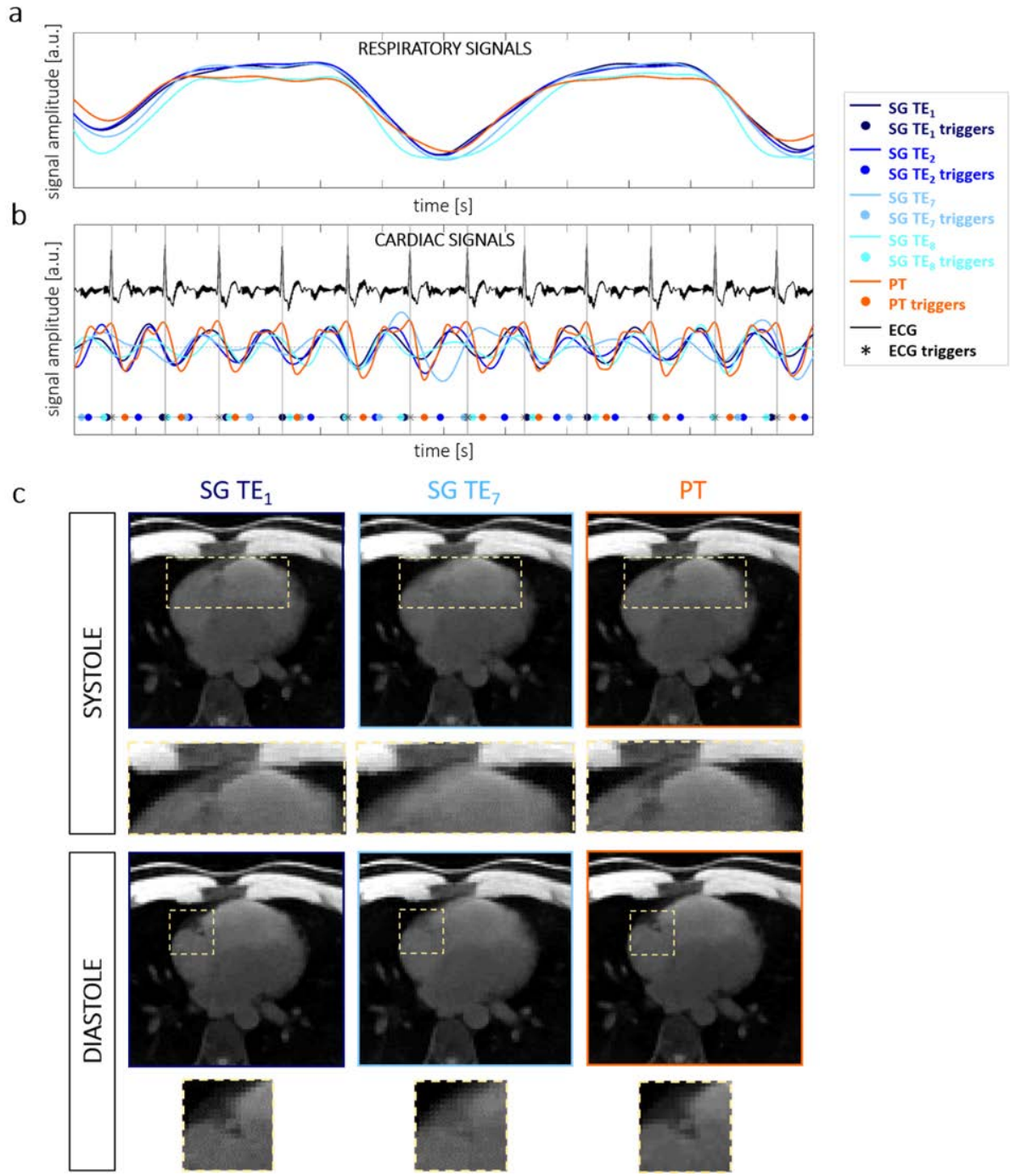

Figure 4. Comparison of PT-based and SG-based physiological signal extraction in V1 and effect on water-only images. (a) Respiratory curves over a 12s time interval for healthy volunteer V1, obtained from PT data and from the SI projections of respective echo times TE_1, TE_2, TE_7 and TE_8. **(b)** Corresponding cardiac signals over the same time interval. While the SG signals from the first two echoes show good correlation with PT, the signals from SG TE_7 and SG TE_8 present an offset w.r.t. PT. SG and PT trigger points extracted from each source are shown on the lower line, alongside with the ECG triggers for reference. ECG trigger points correspond to the R-wave, SG trigger points correspond to the zero-crossing (dotted line) of the extracted SG signal, and PT trigger points correspond to the local minima of the extracted PT signal. **(c)** Transverse mid-systolic and late-diastolic water-only images obtained from the proposed free-running sequence using the SG signals extracted from TE_1 (left), TE_7 (middle) and using PT signals (right). For both cardiac phases, images from all three physiological signal source are in good visual agreement. Close-ups of the regions containing the right coronary artery (RCA) show no difference between SG TE_1 and PT, but loss of contrast and additional blur at SG TE_7.

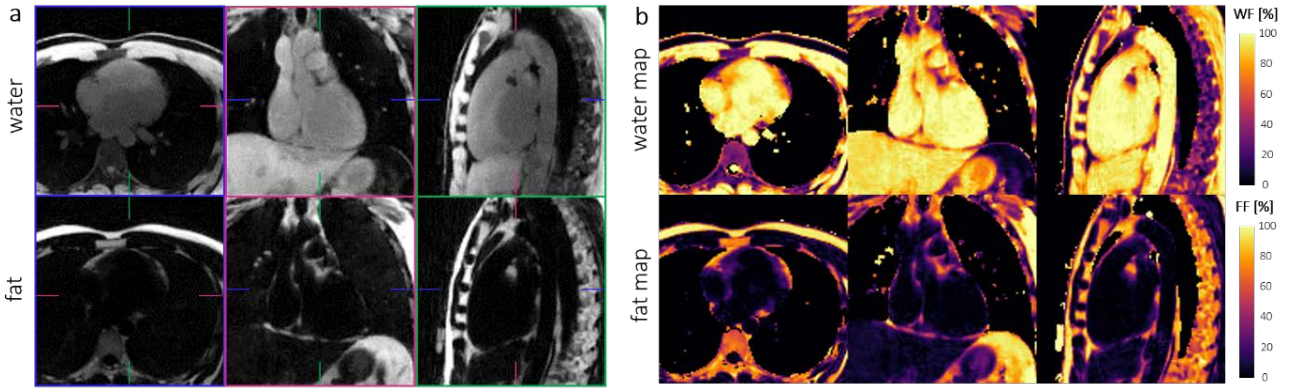

Figure 5. Water-fat separation and quantification obtained with the proposed framework. On panel (**a**), water-only and fat-only images of healthy volunteer V1 are shown, as obtained after post-processing reconstructed 6D imaging volumes with a maximum-likelihood graph cut fitting algorithm. On panel (**b**), the corresponding parametric maps of water fraction and fat fraction are displayed. Slice position with respect to the three traditional MRI views (transversal, coronal and sagittal) is indicated on panel (**a**) by the colored lines.

In addition to fat-water images and maps, the proposed framework produced cardiac and respiratory motion-resolved 3D maps of R2* (**Figure 6c**, **Supporting Information Video S1c**) and B_0 (**Figure 6f**, **Supporting Information Video S1f**). R2* values measured in the myocardium were within the expected range for healthy subjects (R2*<50Hz i.e. T2*>20ms). Elevated values (R2*>70Hz) were detected at the interfaces with the liver and the lungs. Compared to the FF and WF maps, the R2* maps displayed a higher standard deviation across the heart, with a more granular aspect, making cardiac motion slightly less obvious to visualize. The B_0 maps showed good field homogeneity in the heart, without variations across the cardiac cycle. Off-resonance deviations were observed outside the heart, with deviations up to 100Hz seen in the liver. Changes in B_0 across the cardiac bins were only observed within air-filled regions (lungs and FOV periphery).

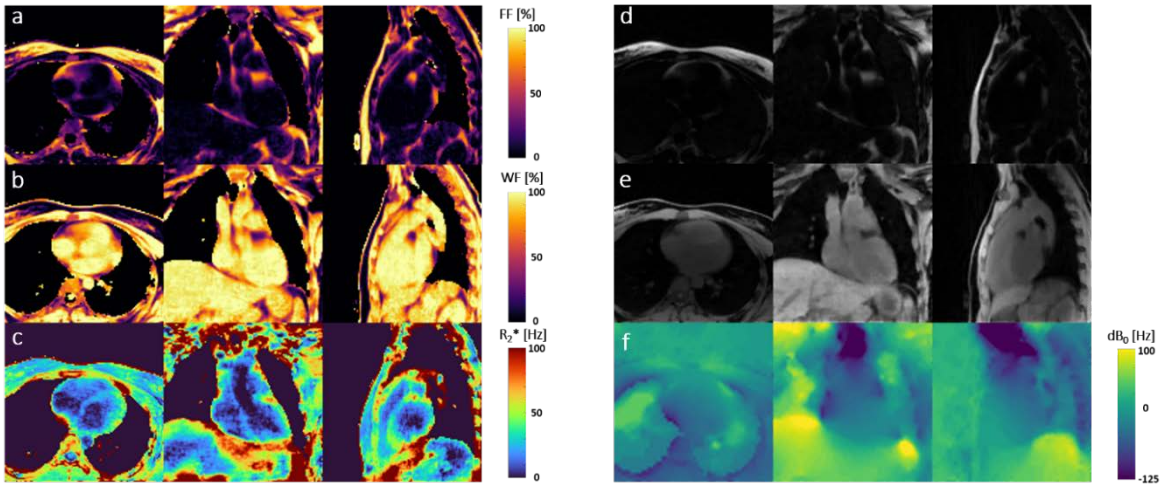

Figure 6. Respiratory and cardiac motion-resolved parametric maps in healthy volunteer V3: (a) fat fraction, (b) water fraction, (c) R2* and (f) B_0, and separated fat-only (d) and water-only (e) images (see Supporting Information S1 for the animation). Transversal, coronal and sagittal views of the heart at end-expiration are displayed in panels (a), (b), (e), (d) and (f), while panel (c) displays a different set of slices, selected to highlight the myocardium delineation in the R2* maps. The animation presented in **Supporting Information Video S1** loops through the cardiac cycle.

Measurements in the sub-cutaneous fat were not affected by the motion binning, with constant FF measured across the cardiac cycle in all volunteers (**Figure 7a)**. However, the FF measured in the pericardial fat varied across bins. A consistent pattern was found in all subjects, although to a different extent, with reduced fat content at end-systole compared to mid-diastole (45.7±8.3% against 59.1±14.9% in V4, 59.0±16.5% against 66.0±10.0% in V10 after T1 bias correction). The average decrease in FF observed during end-systole across volunteers was 11.4±3.1% after T1 bias correction, from the FF measured at mid-diastole. Inspection of the corresponding B_0 maps (**Figure 7c**) revealed no deviations from one cardiac bin to the next, thus excluding B_0 inhomogeneities as cause of the observed variations in the fat fraction measurements. In all subjects, higher standard deviations were reported in the pericardial fat ROIs than in the sub-cutaneous fat. The average FF measured in the ECG-triggered images was elevated with respect to the free-running diastolic images in 6 out of 10 volunteers (**Figure 7a**). A Bland-Altman analysis showed a bias of -1.06% between the average pericardial FF measured in the free running maps identified as diastolic and the ECG-triggered maps, with 95% limits of agreement at [-8.70;6.58]% (**Supporting Information Figure S6**). Smaller standard deviations were also observed in the ECG-triggered FF maps, compared to the free-running ones. Visually, the ECG triggered FF map (**Figure 7b**, left-most image) had an apparent sharper delineation of the pericardial fatty tissue, where the free-running maps showed fatty regions spread over larger areas.

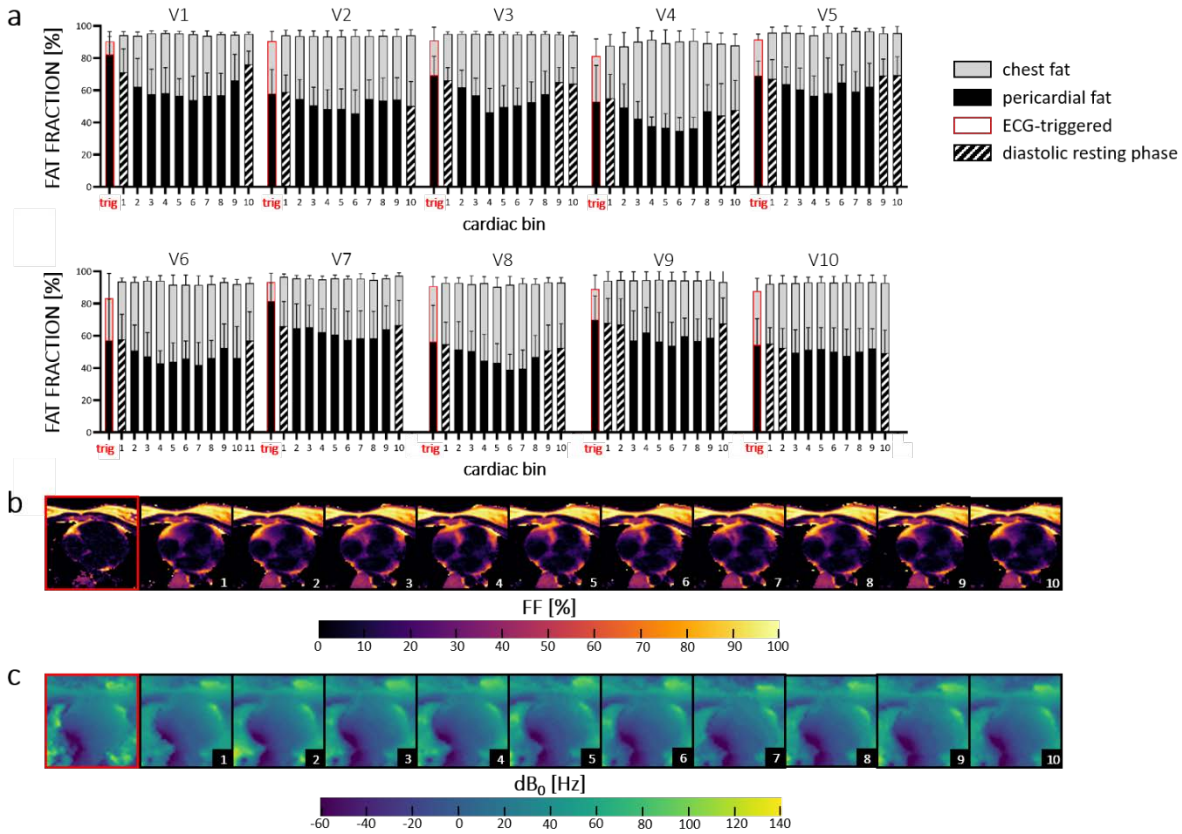

Figure 7. Fat quantification throughout the cardiac cycle, after T1 bias correction. The proposed ME-GRE free-running framework allows quantitative visualization and measurement of cardiac fat content at each phase of the cardiac cycle. **(a)** Average fat fraction and standard deviation measured in ROIs placed within two tissue types: sub-cutaneous fat and pericardial fat, at expiration. TR-adjusted T1 bias correction based on T1 estimates was performed in accordance to the level of bias in the free-running and triggered sequence. In the free-running images, fat fraction was measured in each

of the 10 (resp. 11 for volunteer V6) cardiac phases that were re-ordered to place end-diastole at the start (cardiac bin 1). Diastolic resting phase in the free-running images is identified with the white horizontal striped pattern. The matching ROIs reference measurements in ECG-triggered datasets (corresponding to diastolic resting phase) are shown in red borders on the left-hand side of each sub bar plot, with the label "trig". **(b)** Transversal cardiac FF maps of healthy volunteer V3, at each cardiac bin as labelled in panel **(a)**. The displacement of pericardial fatty regions can be followed throughout the cycle. The corresponding slice of the FF map obtained with the 5-echo ECG-triggered protocol is shown on the left, with red borders. **(c)** Corresponding B_0 maps, which show deviations from the main magnetic field due to system-level imperfections and susceptibility effects. B_0 mapping constitutes an important step of fat quantification techniques with ME-GRE, as the off-resonance caused by the presence of fat has to be decoupled from other sources of off-resonance to be quantified accurately. The corresponding slice of the B_0 map obtained with the 5-echo ECG-triggered protocol is shown on the left, with red borders.

Although the free-running FF maps obtained from processing the first 4 TEs were in visual agreement with their 8 TEs counterparts (**Figure 8a**), a paired t-test performed in both sub-cutaneous and pericardial fat ROIs revealed a significant difference in the average estimated fat fraction (**Figure 8c**) when N_{TE} is reduced. Strong significance was found in the sub-cutaneous fat (P<0.0001), where fat fraction was consistently estimated at a lower value with N_{TE}=4 than N_{TE}=8. The paired t-test performed in pericardial fat yielded a p-value of P=0.084. The influence of a reduced N_{TE} on R2* quantification was directly discernible from the reconstructed maps (**Figure 8b**). Under-sampling in the echo dimension resulted in noisy maps, disrupting the visualization of anatomy such as myocardium delineation that was present in the fully-sampled maps.

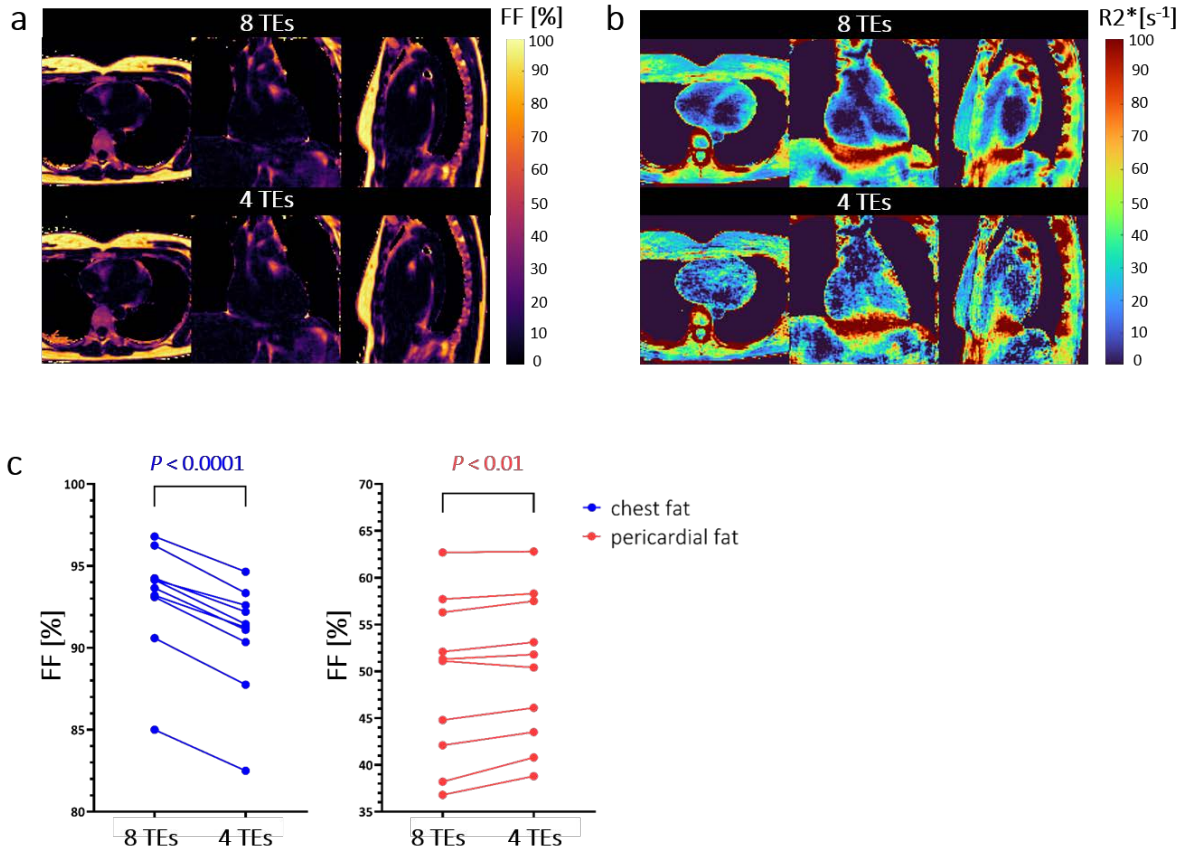

Figure 8. Influence of N_{TE} on fat quantification. (a) 3D fat fraction maps obtained with the proposed ME-GRE free-running framework, using 8 (top) and 4 (bottom) echoes for chemical species separation and quantification, in volunteer V2. Perfect visual agreement between both sets of images can be observed. **(b)** 3D R2* maps obtained with the proposed

ME-GRE free-running framework, using 8 (top) and 4 (bottom) echoes involunteer V2. If a basic delineation of the myocardium muscle is visible in all three orientations with 8 TEs, the undersampled R2* maps lose this sighting due to high granularity. **(c)** Average fat fraction in sub-cutaneous and pericardial fat ROIs measured in10 selected slices, for allvolunteers. The same ROIs were used in both fully sampled (8 TEs) and undersampled (4 TEs) maps. A paired parametric t-test reveals a highly significant difference ($P<0.0001$) in sub-cutaneousfat measurements, with a consistent underestimation of the fat content measured with $N_{TE} = 4$ between volunteers. In pericardial fat, the influence of N_{TE} on fat quantification was also detected, but at a lower level of significance ($P<0.01$).

4. Discussion

This study demonstrates the feasibility of free-running whole-heart ME-GRE based fat fraction mapping using retrospective motion resolutionbased on PT signals and XD-GRASP. The free-running FF mapping approach with PT permits the collection of an unlimited number of echoes, thus theoretically benefiting mapping accuracy. In the current proof-of-concept study, $N_{TE}=8$ echoes were acquired in a relatively short scan time (6:15min) for 3D whole-heart coverage, while only N_{TE} 5 echoes of the same echo train could be acquired in a corresponding ECG-triggered acquisition with similar TA. Signal decay as a result of T2* relaxation provides the only limitation on the number of echoes that can be acquired with the proposed free-running ME-GRE framework.

Physiological cardiac motion signals extracted from PT showed an improved correlation with the reference ECG trace compared with the SG signals, confirming prior findings[50]. PT navigation strategies have several advantages compared to SG strategies. First, PT navigation provides a constant and higher sampling frequency (2kHz) compared with SG, and secondly, PTsignals are insensitive to the underlying trajectory, unlike SG signals which require a correction for trajectory-dependent signal modulation[47]. The last advantage is that scan time could be further shortened by removal of the SI projections. In the current sequence design, the frequency of SI readouts decreases with increasing number of echoes, which affects the temporal resolution of SG. The SG sampling frequency was 2.67Hz, which may hinder cardiac rhythm detection. Although it was not observed to be a limitation in the current healthy volunteer study, it is a potential hurdle for signal extraction in patient populations with abnormal or altered cardiac rhythm. In such cases, PT would remove the need for signal extrapolation otherwise required with SG. Furthermore, the analysis of SG signals extracted from multiple echoes demonstrated that the frequency components extracted from certain echoes, in particular towards the end of the echo train where SNR is decreased, do not accurately depict true cardiac rhythm and therefore introduce motion blurring in the images. Nevertheless, despite differences in cardiac signals from the PT and SG sources, the effect on image quality at the end of the water-fat separation was minor at $(2mm)^3$ spatial resolution. Based on these findings, PT navigation may especially benefit quantification methods where 12 or more echoes are required, such as T2* or complex fat models. Alternative PT-like methods such as Beat-PT[60] have shown promising results for accurate triggering and could be considered to further improve the cardiac signal extraction. Otherwise, self-gating extraction techniques based on k-space center information could be considered as a way to increase the frequency of motion sampling[38,41,42,61].

The use of XD-GRASP in the present study allowed to recover anatomy that is otherwise barely distinguishable with a simple regridded reconstruction of the heavily undersampled ME-GRE radial data. The reconstruction framework also maintained the contrast changes expected from one echo to another in ME-GRE, and images were in agreement with the reference ECG-triggered ones. While other free-running studies make use of bSSFP readouts and report strong aliasing due to bright adipose

tissue in non-fat suppressed highly accelerated scans[38], our reconstructed ME-GRE images did not exhibit such artifacts. The current sequence design did not allow for undersampling in the echo dimension, as was done previously[62], where each subsequent echo had a different trajectory. This approach, as well as rosette-like trajectories[63] where the acquisition of multiple "petals" can essentially be seen as a multiecho scan, could be exploited in the future to reduce scan time.

The free-running ME-GRE framework enabled quantitative fat measurements across the cardiac cycle, and in the current volunteer study, a variable FF pattern was consistently observed as a function of time, indicating an heterogenity of the pericardial fatty tissue. This result suggests that motion-averaged or frozen-motion (i.e. triggered) visualizations might only allow for partial or incomplete tissue characterization, a finding that can be linked to similar reports on the effect of respiratory motion on R2* quantification in the liver[64,65]. It remains to be determined whether the observed variation is physiological, or whether ROI drawing on $(2mm)^3$ spatial resolution maps might have affected the results. Because no B_0 variations were detected in the heart across the cardiac phases, the observation is not related to B_0 main magnetic field. The B_0 maps produced by the framework mainly serve to separate water and fat, but could have the potential to detect and correct errors or artifacts in images acquired during the same CMR exam that are senitive to off-resonance[66]. Despite the visual agreement between FF maps obtained with 4 and 8 echoes, significant differences in FF in both static and moving tissues suggest that higher echo sampling benefits mapping accuracy. This is further corroborated by the difference in sub-cutaneous fat FF measurements between the 5-echo ECG-triggered acquisition and the 8-echo free-running acquisition, even after TR-adjusted correction from T1 bias. If a reduced flip angle approacg is commonly used for T1 bias reduction, the phantom results of the present work suggest that an a posteriori correction based on T1 estimates, while requiring extra information, might be better suited for the proposed framework, as it would allow to maintain higher SNR, following the conclusions of Yang *et al*.[20]. T1 bias could be circumvented with the use of emerging FF quantification methods which employ different ways to encode off-resonance[67], but are not applicable to ME-GRE data.

While the same reference fat spectral model was used throughout all the experiments in this study[56], the sampling of N_{TE}=8 echoes would allow to test different models, including ones with various amounts of peaks (theoretically up to N_{TE}-2=6 peaks[18,23]) or ones based on cardiac fatty tissue. Future investigations could therefore include the use of self-calibrated spectra, as reported by several studies[25,68]. Although not explored in the current study, the R2* quantification and the resulting R2* map suggest that a delineation of the myocardial muscle is possible. The current framework could therefore be used for the simultaneous assessment of myocardial iron overload[69,70], by extending it to bi-exponential relaxation models for a refined estimation[71,72].

Although the water-fat quantification methods (T2*-IDEAL, graph cuts algorithm) have been validated thoroughly in phantoms[24,73], a ground truth measurement for pericardial FF could not be performed in this volunteer study. Besides invasive biopsies and PDFF measured with MRS, which are focal measures, there currently exists no noninvasive reference measurement for whole-heart FF *in vivo*.

To maintain a reasonable scan time, the data was heavily undersampled and therefore the binning limited to 10-11 cardiac and 2 respiratory phases. This limitation could potentially be overcome by performing motion correction in the respiratory domain[74]. Subsequently, this would allow for a cardiac motion-resolved reconstruction with an increased number of cardiac bins[75]. Furthermore, the addition

of motion fields within the reconstruction may provide improved image sharpness and visualization of cardiac fat[26]. The use of a motion-consistent approach based on clustering could also be integrated in this type of golden-angle acquisition[76].

An additional challenge is the absence of large volumes of fat tissue in our volunteers, which at $(2.0\text{mm})^3$ resolution restricts the number of voxels available for quantitative and statistical analysis, as well as renders segmentation more difficult. Future work in patients (displaying wider ranges of FF) would allow for a comparison with invasive biopsies, and may help determine whether the proposed framework, at increased spatial resolution, allows for a distinction of epicardial vs. pericardial fat, as changes of that have been associated with the presence of coronary artery disease[77,78] .

By incorporating an additional echo dimension within the free-running framework, the present study constitutes a preliminary step towards easier access to whole-heart fat quantification, while the presence of cardiac fat as an imaging biomarker undergoes early stage validation.

5. Conclusion

In this study, an MRI framework incorporating a free-running ME-GRE sequence, integrated PT navigation, a robust CS reconstruction and a multi-peak fat fraction mapping routine was proposed for whole-heart water-fat separation and quantification. The framework combines ease-of-use, robustness to motion and whole-organ fat quantification without compromising on the number of echoes to be collected, in a relatively short scan time (6:15min).

Acknowledgements

We acknowledge the use of the Fat-Water Toolbox (http://ismrm.org/workshops/FatWater12/data.htm) for some of the results shown in this article.

The authors thank Diego Hernando for the valuable discussions and input on this work.

This study was supported by funding received from the Swiss National Science Foundation (grants #PCEFP2_194296 and #PZ00P3_167871 to JB), the Unil Bourse Pro-Femmes (JB), the Emma Muschamp Foundation (JB) and the Swiss Heart Foundation (grant #FF18054 to JB).

References

1. Reeder SB, Hu HH, Sirlin CB. Proton density fat-fraction: A standardized mr-based biomarker of tissue fat concentration. J. Magn. Reson. Imaging 2012;36:1011–1014 doi: 10.1002/jmri.23741.

2. Lu M, Zhao S, Jiang S, et al. Fat Deposition in Dilated Cardiomyopathy Assessed by CMR. JACC Cardiovasc. Imaging 2013;6:889–898 doi: 10.1016/j.jcmg.2013.04.010.

3. Burke AP, Farb A, Tashko G, Virmani R. Arrhythmogenic Right Ventricular Cardiomyopathy and Fatty Replacement of the Right Ventricular Myocardium. Circulation 1998;97:1571–1580 doi: 10.1161/01.CIR.97.16.1571.

4. Kellman P, Hernando D, Shah S, et al. Multiecho dixon fat and water separation method for detecting fibrofatty infiltration in the myocardium. Magn. Reson. Med. 2009;61:215–221 doi: 10.1002/mrm.21657.

5. Mordi I, Radjenovic A, Stanton T, et al. Prevalence and Prognostic Significance of Lipomatous Metaplasia in Patients With Prior Myocardial Infarction. JACC Cardiovasc. Imaging 2015;8:1111–1112 doi: 10.1016/j.jcmg.2014.07.024.

6. Baroldi G, Silver MD, De Maria R, Parodi O, Pellegrini A. Lipomatous metaplasia in left ventricular scar. Can. J. Cardiol. 1997;13:65–71.

7. Gorter PM, van Lindert ASR, de Vos AM, et al. Quantification of epicardial and peri-coronary fat using cardiac computed tomography; reproducibility and relation with obesity and metabolic syndrome in patients suspected of coronary artery disease. Atherosclerosis 2008;197:896–903 doi: 10.1016/j.atherosclerosis.2007.08.016.

8. Franz D, Weidlich D, Freitag F, et al. Association of proton density fat fraction in adipose tissue with imaging-based and anthropometric obesity markers in adults. Int. J. Obes. 2018;42:175–182 doi: 10.1038/ijo.2017.194.
9. Rosito GA, Massaro JM, Hoffmann U, et al. Pericardial Fat, Visceral Abdominal Fat, Cardiovascular Disease Risk Factors, and Vascular Calcification in a Community-Based Sample. Circulation 2008;117:605–613 doi: 10.1161/CIRCULATIONAHA.107.743062.
10. Cordes C, Baum T, Dieckmeyer M, et al. MR-Based Assessment of Bone Marrow Fat in Osteoporosis, Diabetes, and Obesity. Front. Endocrinol. 2016;7 doi: 10.3389/fendo.2016.00074.
11. Sironi AM, Petz R, De Marchi D, et al. Impact of increased visceral and cardiac fat on cardiometabolic risk and disease: Visceral, epicardial and/or intrathoracic fat? Diabet. Med. 2012;29:622–627 doi: 10.1111/j.1464-5491.2011.03503.x.
12. Chen O, Sharma A, Ahmad I, et al. Correlation between pericardial, mediastinal, and intrathoracic fat volumes with the presence and severity of coronary artery disease, metabolic syndrome, and cardiac risk factors. Eur. Heart J. - Cardiovasc. Imaging 2015;16:37–46 doi: 10.1093/ehjci/jeu145.
13. Reeder SB, Wen Z, Yu H, et al. Multicoil Dixon chemical species separation with an iterative least-squares estimation method. Magn. Reson. Med. 2004;51:35–45 doi: 10.1002/mrm.10675.
14. Bray TJ, Chouhan MD, Punwani S, Bainbridge A, Hall-Craggs MA. Fat fraction mapping using magnetic resonance imaging: insight into pathophysiology. Br. J. Radiol. 2018;91:20170344 doi: 10.1259/bjr.20170344.
15. Yu H, Reeder SB, Shimakawa A, Brittain JH, Pelc NJ. Field map estimation with a region growing scheme for iterative 3-point water-fat decomposition. Magn. Reson. Med. 2005;54:1032–1039 doi: 10.1002/mrm.20654.
16. Tsao J, Jiang Y. Hierarchical IDEAL: Fast, robust, and multiresolution separation of multiple chemical species from multiple echo times. Magn. Reson. Med. 2013;70:155–159 doi: 10.1002/mrm.24441.
17. Lu W, Hargreaves BA. Multiresolution field map estimation using golden section search for water-fat separation. Magn. Reson. Med. 2008;60:236–244 doi: 10.1002/mrm.21544.
18. Hernando D, Kellman P, Haldar JP, Liang Z-P. Robust water/fat separation in the presence of large field inhomogeneities using a graph cut algorithm. Magn. Reson. Med. 2009:NA-NA doi: 10.1002/mrm.22177.
19. Bydder M, Yokoo T, Hamilton G, et al. Relaxation effects in the quantification of fat using gradient echo imaging. Magn. Reson. Imaging 2008;26:347–359 doi: 10.1016/j.mri.2007.08.012.
20. Yang IY, Cui Y, Wiens CN, Wade TP, Friesen-Waldner LJ, McKenzie CA. Fat fraction bias correction using T1 estimates and flip angle mapping. J. Magn. Reson. Imaging 2014;39:217–223 doi: 10.1002/jmri.24126.
21. Yu H, McKenzie CA, Shimakawa A, et al. Multiecho reconstruction for simultaneous water-fat decomposition and T2* estimation. J. Magn. Reson. Imaging 2007;26:1153–1161 doi: 10.1002/jmri.21090.
22. Liu C-Y, McKenzie CA, Yu H, Brittain JH, Reeder SB. Fat quantification with IDEAL gradient echo imaging: Correction of bias from T1 and noise. Magn. Reson. Med. 2007;58:354–364 doi: 10.1002/mrm.21301.
23. Yu H, Shimakawa A, McKenzie CA, Brodsky E, Brittain JH, Reeder SB. Multiecho water-fat separation and simultaneous R estimation with multifrequency fat spectrum modeling. Magn. Reson. Med. 2008;60:1122–1134 doi: 10.1002/mrm.21737.
24. Hines CDG, Yu H, Shimakawa A, McKenzie CA, Brittain JH, Reeder SB. T1 independent, T2* corrected MRI with accurate spectral modeling for quantification of fat: Validation in a fat-water-SPIO phantom. J. Magn. Reson. Imaging 2009;30:1215–1222 doi: 10.1002/jmri.21957.
25. Kühn J-P, Hernando D, Muñoz del Rio A, et al. Effect of Multipeak Spectral Modeling of Fat for Liver Iron and Fat Quantification: Correlation of Biopsy with MR Imaging Results. Radiology 2012;265:133–142 doi: 10.1148/radiol.12112520.
26. Mayer J, Blaszczyk E, Cipriani A, et al. Cardio-respiratory motion-corrected 3D cardiac water-fat MRI using model-based image reconstruction. Magn. Reson. Med. n/a doi: 10.1002/mrm.29284.
27. Liu J, Nguyen TD, Zhu Y, et al. Self-Gated Free-Breathing 3D Coronary CINE Imaging with Simultaneous Water and Fat Visualization. PLOS ONE 2014;9:e89315 doi: 10.1371/journal.pone.0089315.
28. Taviani V, Hernando D, Francois CJ, et al. Whole-heart chemical shift encoded water–fat MRI. Magn. Reson. Med. 2014;72:718–725 doi: 10.1002/mrm.24982.
29. Munoz C, Cruz G, Neji R, Botnar RM, Prieto C. Motion corrected water/fat whole-heart coronary MR angiography with 100% respiratory efficiency. Magn. Reson. Med. 2019;82:732–742 doi: 10.1002/mrm.27732.
30. Dietrich S, Aigner CS, Mayer J, et al. Motion-compensated fat-water imaging for 3D cardiac MRI at ultra-high fields. Magn. Reson. Med. 2022;87:2621–2636 doi: 10.1002/mrm.29144.

31. Jaubert O, Cruz G, Bustin A, et al. Water–fat Dixon cardiac magnetic resonance fingerprinting. Magn. Reson. Med. 2020;83:2107–2123 doi: 10.1002/mrm.28070.
32. Jaubert O, Cruz G, Bustin A, et al. T1, T2, and Fat Fraction Cardiac MR Fingerprinting: Preliminary Clinical Evaluation. J. Magn. Reson. Imaging 2021;53:1253–1265 doi: 10.1002/jmri.27415.
33. Lima da Cruz GJ, Velasco C, Lavin B, Jaubert O, Botnar RM, Prieto C. Myocardial T1, T2, T2*, and fat fraction quantification via low-rank motion-corrected cardiac MR fingerprinting. Magn. Reson. Med. 2022;87:2757–2774 doi: 10.1002/mrm.29171.
34. Goldfarb JW, Craft J, Cao JJ. Water–fat separation and parameter mapping in cardiac MRI via deep learning with a convolutional neural network. J. Magn. Reson. Imaging 2019;50:655–665 doi: 10.1002/jmri.26658.
35. Coppo S, Piccini D, Bonanno G, et al. Free-running 4D whole-heart self-navigated golden angle MRI: Initial results. Magn. Reson. Med. 2015;74:1306–1316 doi: 10.1002/mrm.25523.
36. Bastiaansen JAM, Piccini D, Di Sopra L, et al. Natively fat-suppressed 5D whole-heart MRI with a radial free-running fast-interrupted steady-state (FISS) sequence at 1.5T and 3T. Magn. Reson. Med. 2020;83:45–55 doi: 10.1002/mrm.27942.
37. Franceschiello B, Di Sopra L, Minier A, et al. 3-Dimensional magnetic resonance imaging of the freely moving human eye. Prog. Neurobiol. 2020;194:101885 doi: 10.1016/j.pneurobio.2020.101885.
38. Küstner T, Bustin A, Jaubert O, et al. Fully self-gated free-running 3D Cartesian cardiac CINE with isotropic whole-heart coverage in less than 2 min. NMR Biomed. 2021;34:e4409 doi: 10.1002/nbm.4409.
39. Masala N, Bastiaansen JAM, Sopra LD, et al. Free-running 5D coronary MR angiography at 1.5T using LIBRE water excitation pulses. Magn. Reson. Med. 2020;84:1470–1485 doi: 10.1002/mrm.28221.
40. Ishida M, Yerly J, Ito H, et al. Optimal Protocol for Contrast-enhanced Free-running 5D Whole-heart Coronary MR Angiography at 3T. Magn. Reson. Med. Sci. 2023;advpub:tn.2022-0086 doi: 10.2463/mrms.tn.2022-0086.
41. Qi H, Bustin A, Cruz G, et al. Free-running simultaneous myocardial T1/T2 mapping and cine imaging with 3D whole-heart coverage and isotropic spatial resolution. Magn. Reson. Imaging 2019;63:159–169 doi: 10.1016/j.mri.2019.08.008.
42. Qi H, Jaubert O, Bustin A, et al. Free-running 3D whole heart myocardial T1 mapping with isotropic spatial resolution. Magn. Reson. Med. 2019;82:1331–1342 doi: 10.1002/mrm.27811.
43. Shaw JL, Yang Q, Zhou Z, et al. Free-breathing, non-ECG, continuous myocardial T1 mapping with cardiovascular magnetic resonance multitasking. Magn. Reson. Med. 2019;81:2450–2463 doi: 10.1002/mrm.27574.
44. Christodoulou AG, Shaw JL, Nguyen C, et al. Magnetic resonance multitasking for motion-resolved quantitative cardiovascular imaging. Nat. Biomed. Eng. 2018;2:215–226 doi: 10.1038/s41551-018-0217-y.
45. Ma LE, Yerly J, Piccini D, et al. 5D Flow MRI: A Fully Self-gated, Free-running Framework for Cardiac and Respiratory Motion–resolved 3D Hemodynamics. Radiol. Cardiothorac. Imaging 2020;2:e200219 doi: 10.1148/ryct.2020200219.
46. Feng L, Coppo S, Piccini D, et al. 5D whole-heart sparse MRI. Magn. Reson. Med. 2018;79:826–838 doi: 10.1002/mrm.26745.
47. Di Sopra L, Piccini D, Coppo S, Stuber M, Yerly J. An automated approach to fully self-gated free-running cardiac and respiratory motion-resolved 5D whole-heart MRI. Magn. Reson. Med. 2019;82:2118–2132 doi: 10.1002/mrm.27898.
48. Speier P. PT-Nav: A Novel Respiratory Navigation Method for Continuous Acquisitions Based on Modulation of a Pilot Tone in the MR-Receiver. Proc ESMRMB 2015;129:97–98.
49. Vahle T, Bacher M, Rigie D, et al. Respiratory Motion Detection and Correction for MR Using the Pilot Tone: Applications for MR and Simultaneous PET/MR Exams. Invest. Radiol. 2020;55:153–159 doi: 10.1097/RLI.0000000000000619.
50. Falcão MBL, Di Sopra L, Ma L, et al. Pilot tone navigation for respiratory and cardiac motion-resolved free-running 5D flow MRI. Magn. Reson. Med. 2022;87:718–732 doi: 10.1002/mrm.29023.
51. Piccini D, Littmann A, Nielles-Vallespin S, Zenge MO. Spiral phyllotaxis: The natural way to construct a 3D radial trajectory in MRI. Magn. Reson. Med. 2011;66:1049–1056 doi: 10.1002/mrm.22898.
52. Zhong X, Hu HH, Armstrong T, et al. Free-Breathing Volumetric Liver and Proton Density Fat Fraction Quantification in Pediatric Patients Using Stack-of-Radial MRI With Self-Gating Motion Compensation. J. Magn. Reson. Imaging 2021;53:118–129 doi: 10.1002/jmri.27205.
53. Feng L, Axel L, Chandarana H, Block KT, Sodickson DK, Otazo R. XD-GRASP: Golden-angle radial MRI with reconstruction of extra motion-state dimensions using compressed sensing. Magn. Reson. Med. 2016;75:775–788 doi: 10.1002/mrm.25665.

54. Boyd S, Parikh N, Chu E, Peleato B, Eckstein J. Distributed Optimization and Statistical Learning via the Alternating Direction Method of Multipliers. Found. Trends® Mach. Learn. 2011;3:1–122 doi: 10.1561/2200000016.
55. Boykov Y, Veksler O, Zabih R. Fast approximate energy minimization via graph cuts. IEEE Trans. Pattern Anal. Mach. Intell. 2001;23:1222–1239 doi: 10.1109/34.969114.
56. Hu HH, Börnert P, Hernando D, et al. ISMRM workshop on fat–water separation: Insights, applications and progress in MRI. Magn. Reson. Med. 2012;68:378–388 doi: 10.1002/mrm.24369.
57. Hamilton JI, Pahwa S, Adedigba J, et al. Simultaneous Mapping of T1 and T2 Using Cardiac Magnetic Resonance Fingerprinting in a Cohort of Healthy Subjects at 1.5T. J. Magn. Reson. Imaging 2020;52:1044–1052 doi: 10.1002/jmri.27155.
58. de Bazelaire CMJ, Duhamel GD, Rofsky NM, Alsop DC. MR Imaging Relaxation Times of Abdominal and Pelvic Tissues Measured in Vivo at 3.0 T: Preliminary Results. Radiology 2004;230:652–659 doi: 10.1148/radiol.2303021331.
59. Taylor AJ, Salerno M, Dharmakumar R, Jerosch-Herold M. T1 Mapping: Basic Techniques and Clinical Applications. JACC Cardiovasc. Imaging 2016;9:67–81 doi: 10.1016/j.jcmg.2015.11.005.
60. Anand S, Lustig M. Beat Pilot Tone: Exploiting Preamplifier Intermodulation of UHF/SHF RF for Improved Motion Sensitivity over Pilot Tone Navigators. Proc Intl Soc Mag Reson Med 2021;29:0568.
61. Liu J, Spincemaille P, Codella NCF, Nguyen TD, Prince MR, Wang Y. Respiratory and cardiac self-gated free-breathing cardiac CINE imaging with multiecho 3D hybrid radial SSFP acquisition. Magn. Reson. Med. 2010;63:1230–1237 doi: 10.1002/mrm.22306.
62. Benkert T, Feng L, Sodickson DK, Chandarana H, Block KT. Free-breathing volumetric fat/water separation by combining radial sampling, compressed sensing, and parallel imaging. Magn. Reson. Med. 2017;78:565–576 doi: 10.1002/mrm.26392.
63. Liu Y, Hamilton J, Eck B, Griswold M, Seiberlich N. Myocardial T1 and T2 quantification and water–fat separation using cardiac MR fingerprinting with rosette trajectories at 3T and 1.5T. Magn. Reson. Med. 2021;85:103–119 doi: 10.1002/mrm.28404.
64. Zhong X, Armstrong T, Nickel MD, et al. Effect of respiratory motion on free-breathing 3D stack-of-radial liver relaxometry and improved quantification accuracy using self-gating. Magn. Reson. Med. 2020;83:1964–1978 doi: 10.1002/mrm.28052.
65. Schneider M, Benkert T, Solomon E, et al. Free-breathing fat and R2* quantification in the liver using a stack-of-stars multi-echo acquisition with respiratory-resolved model-based reconstruction. Magn. Reson. Med. 2020;84:2592–2605 doi: 10.1002/mrm.28280.
66. Kellman P, Herzka DA, Arai AE, Hansen MS. Influence of Off-resonance in myocardial T1-mapping using SSFP based MOLLI method. J. Cardiovasc. Magn. Reson. 2013;15:63 doi: 10.1186/1532-429X-15-63.
67. Rossi GM, Hilbert T, Mackowiak AL, Pierzchała K, Kober T, Bastiaansen JA. Fat fraction mapping using bSSFP Signal Profile Asymmetries for Robust multi-Compartment Quantification (SPARCQ). 2020 doi: 10.48550/arXiv.2005.09734.
68. Reeder SB, Robson PM, Yu H, et al. Quantification of hepatic steatosis with MRI: The effects of accurate fat spectral modeling. J. Magn. Reson. Imaging 2009;29:1332–1339 doi: 10.1002/jmri.21751.
69. Triadyaksa P, Oudkerk M, Sijens PE. Cardiac T2* mapping: Techniques and clinical applications. J. Magn. Reson. Imaging 2020;52:1340–1351 doi: 10.1002/jmri.27023.
70. Mavrogeni S. Evaluation of myocardial iron overload using magnetic resonance imaging. Blood Transfus. 2009;7:183–187 doi: 10.2450/2008.0063-08.
71. Juras V, Apprich S, Zbýň Š, et al. Quantitative MRI analysis of menisci using biexponential T2* fitting with a variable echo time sequence. Magn. Reson. Med. 2014;71:1015–1023 doi: 10.1002/mrm.24760.
72. Positano V, Salani B, Pepe A, et al. Improved T2* assessment in liver iron overload by magnetic resonance imaging. Magn. Reson. Imaging 2009;27:188–197 doi: 10.1016/j.mri.2008.06.004.
73. Hernando D, Sharma SD, Aliyari Ghasabeh M, et al. Multisite, multivendor validation of the accuracy and reproducibility of proton-density fat-fraction quantification at 1.5T and 3T using a fat–water phantom. Magn. Reson. Med. 2017;77:1516–1524 doi: 10.1002/mrm.26228.
74. Roy CW, Heerfordt J, Piccini D, et al. Motion compensated whole-heart coronary cardiovascular magnetic resonance angiography using focused navigation (fNAV). J. Cardiovasc. Magn. Reson. 2021;23:33 doi: 10.1186/s12968-021-00717-4.

75. Falcão MBL, Rossi GM, Ma LE, et al. Correcting vs resolving respiratory motion in accelerated free-running whole-heart radial flow MRI using focused navigation (fNAV). Proc Intl Soc Mag Reson Med 2021;29.
76. Heerfordt J, Whitehead KK, Bastiaansen JAM, et al. Similarity-driven multi-dimensional binning algorithm (SIMBA) for free-running motion-suppressed whole-heart MRA. Magn. Reson. Med. 2021;86:213–229 doi: 10.1002/mrm.28713.
77. Ahn S-G, Lim H-S, Joe D-Y, et al. Relationship of epicardial adipose tissue by echocardiography to coronary artery disease. Heart 2008;94:e7–e7 doi: 10.1136/hrt.2007.118471.
78. Guglielmo M, Lin A, Dey D, et al. Epicardial fat and coronary artery disease: Role of cardiac imaging. Atherosclerosis 2021;321:30–38 doi: 10.1016/j.atherosclerosis.2021.02.008.
79. Bush EC, Gifford A, Coolbaugh CL, Towse TF, Damon BM, Welch EB. Fat-Water Phantoms for Magnetic Resonance Imaging Validation: A Flexible and Scalable Protocol. JoVE J. Vis. Exp. 2018:e57704 doi: 10.3791/57704.

A2. Supplementary Information: Conference abstracts which I have co-authored

A2.1. Pilot Tone and Signal extraction related developments

A2.1.1. Whole-Heart Motion-Resolved Multi-Peak Fat-Fraction Mapping using Free-Running 3D Radial Multi-Echo GRE and Pilot Tone

Adèle L. C. Mackowiak[1], Christopher W. Roy[1], Jérôme Yerly[1,2], Lorenzo Di Sopra[1], Mariana B. L. Falcão[1], Mario Bacher[1], Peter Speier[1], Davide Piccini[1,4], Matthias Stuber[1,2], and Jessica A. M. Bastiaansen[1]

[1]Department of Radiology, Lausanne University Hospital (CHUV) and University of Lausanne (UNIL), Lausanne, Switzerland,
[2]CIBM Center for Biomedical Imaging, Lausanne, Switzerland,
[3]Siemens Healthcare GmbH, Erlangen, Germany,
[4]Advanced Clinical Imaging Technology, Siemens Healthcare AG, Lausanne, Switzerland

Synopsis

A free-running multi-echo GRE approach was proposed for whole-heart fat quantification. Retrospective extraction of cardiac and respiratory motion states was achieved using integrated Pilot Tone navigation, enabling a free-breathing non-ECG-triggered acquisition. Following a motion-resolved compressed sensing based image reconstruction of the separate echoes, fat fraction, water fraction, R* and B maps, as well as separated fat and water images, were calculated. Free-running acquisition parameters were optimized in a fat phantom. Volunteer experiments demonstrated the feasibility of motion-resolved free-running fat-fraction mapping technique in a 6-minute scan time.

Introduction

Noninvasive methods for cardiac fat quantification may aid diagnosis in patients suffering from myocardial fat infiltration[1,2], dilated cardiomyopathy[3,4], and help characterize the role of intra-myocardial fat in obesity and diabetes[5,6]. Gold-standard fat-fraction (FF) maps are currently obtained using multi-echo gradient echo (ME-GRE) acquisitions followed by maximum-likelihood fitting[7-10].

Accurate quantification exploits multi-peak fat models[11,12] ($N_{peaks}\geq6$), which can theoretically only be resolved with a minimum number of $N_{TE}=N_{peaks}+2$ acquired echoes[9,12]. In cardiac MRI, respiratory

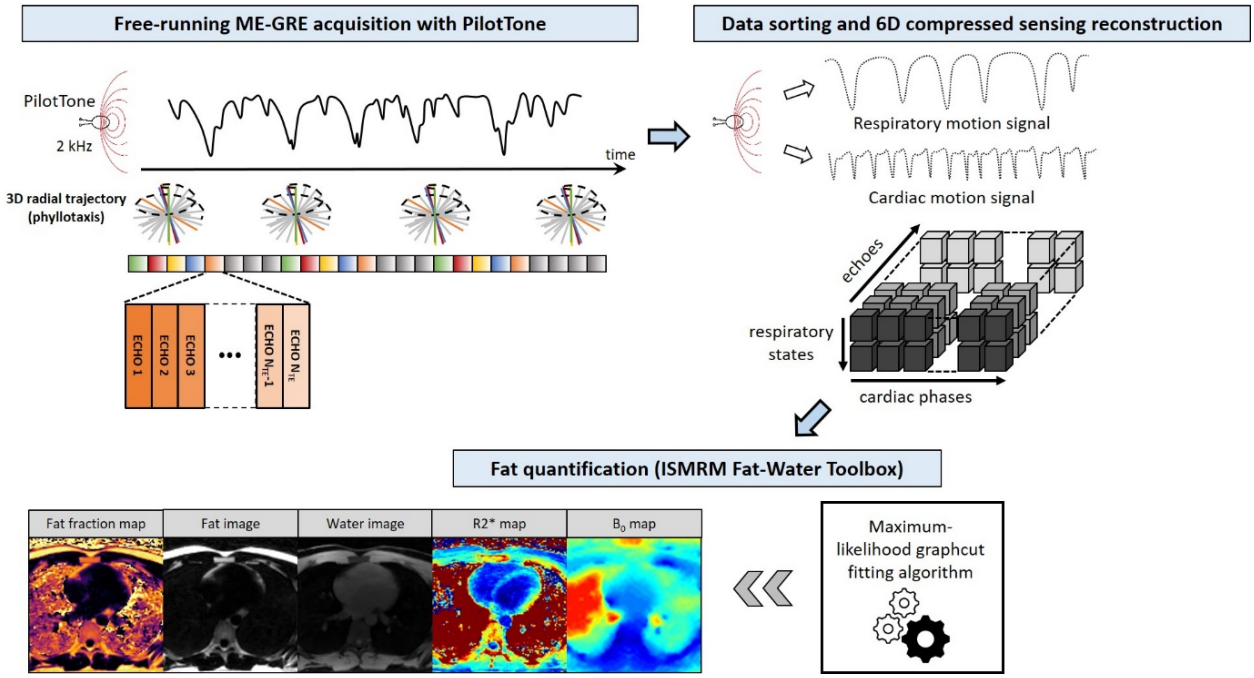

Figure 1. Prototype acquisition, reconstruction and post-processing framework. The uninterrupted whole-heart 3D radial free-running ME-GRE acquisition contains 1000 radial interleaves rotated by the golden angle[22]. Each segment of the spiral is repeated for N_{TE} echoes. The PT signals are used to retrospectively assign acquired segments to specific cardiac and respiratory motion states. After motion-resolved image reconstruction with XD-GRASP-ADMM[20, 21], an N-peak fat spectrum model and graph cut algorithm[7] are used to obtain FF, R_2* and B_0 maps, and fat and water images

motion is often addressed using breath-holds, while ECG triggering and the selection of a quiescent acquisition window helps avoid cardiac motion blurring[13]. Recent developments in free-running cardiac MRI[14,15], with integrated Pilot Tone (PT)[16,17,18,19], make it possible to retrospectively compensate for cardiac and respiratory motion. Free-running developments may benefit FF mapping because 1) an uninterrupted acquisition poses no limits on the amount of echoes, 2) removes the need for external triggering devices or breath-holds and improves ease of use and patient comfort, 3) provides whole-heart coverage, and 4) may simultaneously provide functional information such as ejection fraction. The aim of the study was to propose a novel free-running 3D radial ME-GRE approach for whole-heart fat-fraction mapping, with integrated PT navigation for cardiac and respiratory signal gating. The sequence was optimized in a phantom with fat components. Proof of concept motion-resolved free-running fat-fraction mapping was tested in healthy volunteers.

Methods

All experiments were performed on a 1.5T clinical scanner (MAGNETOM Sola, Siemens Healthcare, Erlangen, Germany) using a 12-channel body coil equipped with a PT transmitter.

Phantom experiments: The prototype free-running 3D radial ME-GRE sequence incorporated a readout of N=8 echoes at each segment of the spiral (**Fig.1**). In a fat phantom (**Fig.2**), the effect of receiver bandwidths and RF excitation angles on the measured fat fraction was tested. Sequence parameter ranges that were tested included RF excitation angles [5;25]°,bandwidths [321;1063] Hz/pixel, monopolar or bipolar readout gradients, and echo spacings [1.29;3.65] ms. Fat fractions

estimated with graph cut maximum-likelihood fitting[7] were compared to values obtained with MR spectroscopy (MRS) (**Fig.2**).

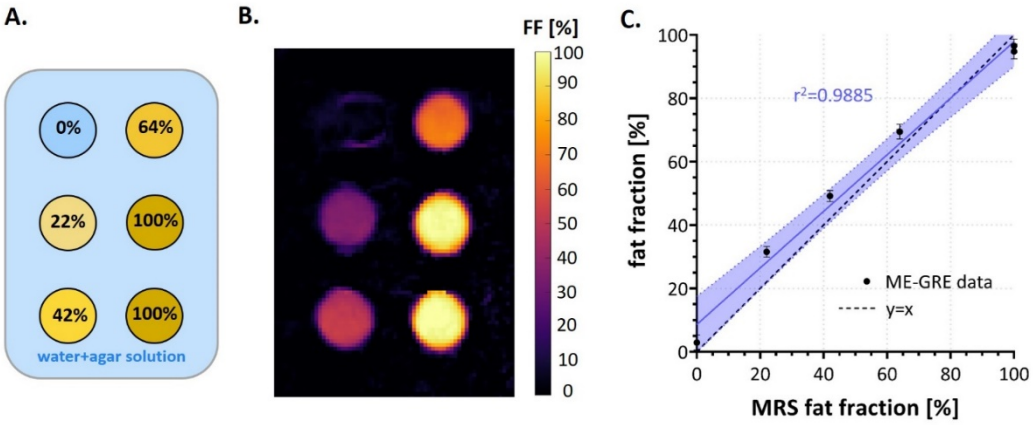

Figure 2. Phantom experiment. A custom-built fat phantom made with peanut oil, agar, and water (A) was used to test the proposed free-running ME-GRE sequence. The fat-fraction map obtained (B) with the maximum-likelihood fitting routine shows good agreement with the gold-standard MRS estimation (C). The shaded blue area represents the 95% confidence interval on the regression line.

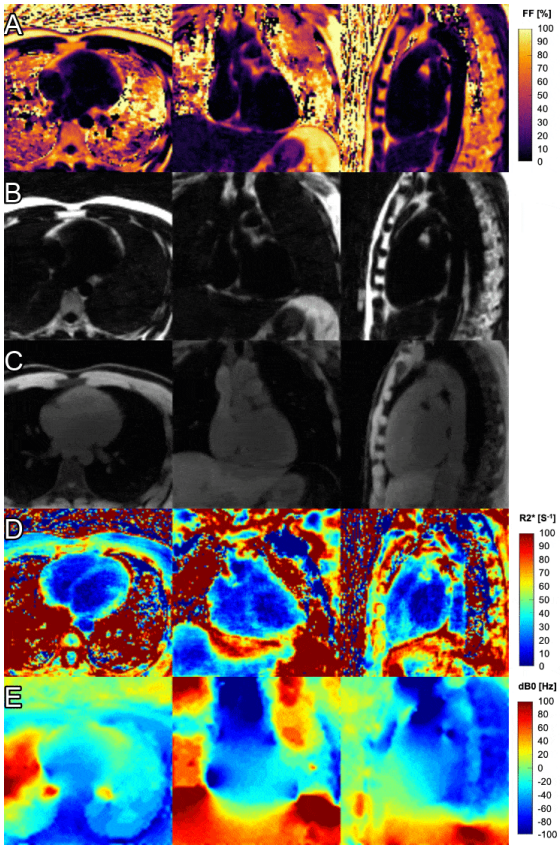

Figure 3. Motion-resolved maps and images of the whole heart in transversal, coronal and sagittal view in one healthy volunteer, visualized for a single cardiac phase in this static context. A. Fat fraction map; **B.** Fat-only image; **C.** Water-only image; **D.** R_2*map; **E.** dB_0 map (deviation from main field strength B_0).

Slices displayed in rows A, B, and C were chosen to highlight fatty regions of the heart. Slices displayed in rows D and E were chosen to highlight blood/myocardium contrast in the R_2* maps and therefore do not match the slices displayed in rows A, B and C.

Volunteer experiments: Free-running ME-GRE was performed in n=5 healthy volunteers after providing informed written consent. Optimized sequence parameters included: (2.0mm) spatial resolution, receiver bandwidth of 893Hz/pixel, RF excitation angle 12°, a monopolar readout gradient, N=8, echo spacing TE=2.05ms, TE=1.25ms. The acquisition time was 6:15min per subject. Cardiac and respiratory signals were retrospectively extracted from PT and used to bin acquired k-space data into 2 respiratory and 10-11 cardiac motion states[15,19]. A compressed sensing reconstruction (similar

to that reported in[15] and based on[20,21]) of our 6-dimensional (x-y-z-cardiac-respiratory-echo) data was used to provide motion-resolved 3D volumes of each echo. Using a 6-peak fat-model and a maximum-

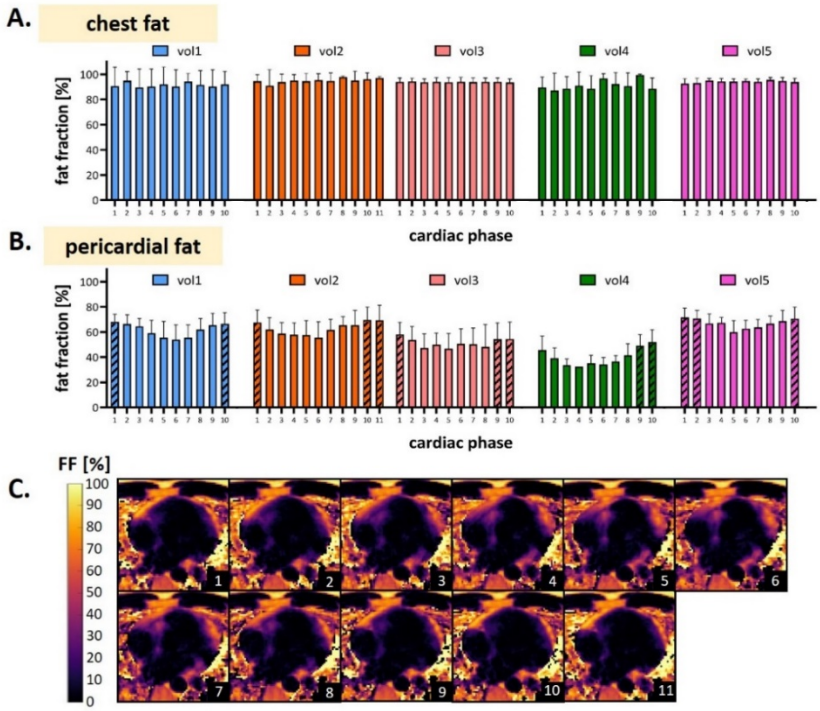

Figure 4. Fat fraction measurements across the cardiac cycle. A. In static chest fat, the fat fraction estimation across the cardiac cycle has little to no variation, across volunteers. **B.** In pericardial fat, a lower fat fraction is measured during the cardiac states identified as systole, with respect to those identified as corresponding to the resting phase of the heart, the latter being indicated by a diagonal pattern. **C.** Transversal view of fat fraction maps in 11 cardiac phases, in a healthy volunteer (vol2).

likelihood graph cut fitting algorithm[7] (ISMRM Fat/Water Toolbox), fat fraction, R_2*, B_0 maps and fat-only and water-only images were reconstructed (**Fig.1**). The influence on fat quantification of the selection of cardiac phase and number of echoes used for the fitting was determined in regions of interest (ROI) placed in chest and pericardial fat. Statistical significance was determined using a paired Student's t-test.

Results

Phantom experiments: Fat quantification was not bandwidth-dependent in our examined range, despite the increase in noise. The free-running ME-GRE sequence parameters yielding the most similar FF estimation with respect to MRS were selected for volunteer experiments, and resulted in fat-fractions with a coefficient of determination of r=0.9885 for a slope with 95% confidence interval in [0.7588;1.026] (**Fig.2**).

Volunteer experiments: PT allowed the successful extraction of motion signal in all volunteers, which enabled motion-resolved reconstructed fat-images, water-images, R_2* maps, and FF maps (**Fig.3**). The analysis of FF maps obtained at different phases of the cardiac cycle (**Fig.4**) revealed a consistent estimation in chest fat fraction yet a decrease in the pericardium during systole. The comparative analysis of maps obtained using four or eight echoes (**Fig.5**) yielded FF maps of similar quality. Quantitatively, while a significant difference (p=0.0252) was observed in the chest fat, the same analysis in pericardial fat showed no difference (p=0.6096). The quality of R_2* maps decreased with fewer echoes.

Discussion

Although GRE typically requires a low receiver bandwidth to mitigate noise, FF quantification was not affected by increasing the receiver bandwidth to 893Hz/pixel, which benefits both shorter

acquisition time as well as echo spacing. The combined use of PT and the free-running approach to cardiac MRI simplifies access to whole-heart fat quantification, as it allows to retrospectively select a

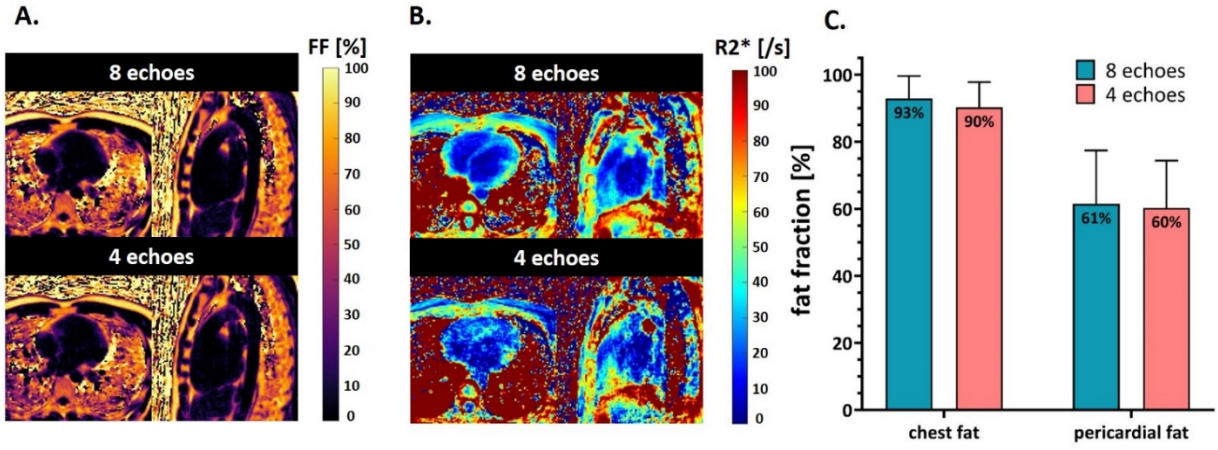

Figure 5. Comparison of mapping results with 8 and 4 echoes. A. Fat fraction maps obtained with 8 and 4 echoes are visually consistent. **B.** R_2* maps obtained with 4 echoes are noisier than those obtained with 8 echoes, altering the visualization of anatomy (myocardium). **C.** Mean estimated fat fraction and standard deviation measured across 5 volunteers, in ROIs selected in the chest fat and in pericardial fat, obtained with the two methods.

cardiac phase and to account for RR fluctuations. It remains to be investigated whether the observed variation in pericardial FF was due to errors in acquisition/ reconstruction/ROI selection, or if it indicates a physiological effect. Although the use of four or eight echoes did not significantly affect the quantification of FF in volunteers, an increased number of echoes would certainly benefit the quantification of lower fat fractions, as more peaks in the fat spectrum could be resolved.

Conclusion

A novel free-running 3D radial ME-GRE acquisition and reconstruction approach was developed with integrated PT navigation that provided motion-resolved whole-heart fat-fraction maps. Free-running ME-GRE neither relies on ECG triggering nor on breath-holds, and allows the acquisition of an arbitrary number of echoes within a fixed scan time.

Acknowledgements

We acknowledge the use of the Fat-Water Toolbox (http://ismrm.org/workshops/ FatWater12/data.htm) for some of the results shown in this article.

This study was supported by the Swiss National Science Foundation (PZ00P3_167871and PCEFP2_194296), the Swiss Heart Foundation (FF18054), the UNIL Bourse Pro Femmes, and the Emma Muschamp Foundation.

References

1. Mordi, Ify, et al. "Prevalence and prognostic significance of lipomatous metaplasia in patients with prior myocardial infarction." JACC: Cardiovascular Imaging 8.9 (2015):1111-1112.

2. Kellman, Peter, et al. "Multiecho dixon fat and water separation method for detecting fibrofatty infiltration in the myocardium." Magnetic Resonance in Medicine: An Official Journal of the International Society for Magnetic Resonance in Medicine 61.1(2009): 215-221.

3. Lu, Minjie, et al. "Fat deposition in dilated cardiomyopathy assessed by CMR." JACC: Cardiovascular Imaging 6.8(2013): 889-898.

4. Kellman, Peter, Diego Hernando, and Andrew E. Arai. "Myocardial fat imaging." Current cardiovascular imaging reports 3.2 (2010): 83-91.
5. McGavock, Jonathan M., et al. "Adiposity of the heart*, revisited." Annals of internal medicine 144.7(2006): 517-524.
6. Sironi, A. M., et al. "Impact of increased visceral and cardiac fat on cardio metabolic risk and disease." Diabetic Medicine 29.5 (2012): 622-627.
7. Hernando, Diego, et al. "Robust water/fat separation in the presence of large field inhomogeneities using a graph cut algorithm." Magnetic Resonance in Medicine: An Official Journal of the International Society for Magnetic Resonance in Medicine 63.1(2010): 79-90.
8. Caussy, Cyrielle, et al. "Optimal threshold of controlled attenuation parameter with MRI-PDFF as the gold standard for the detection of hepatic steatosis." Hepatology 67.4 (2018):1348-1359.
9. Reeder, Scott B., et al. "Multicoil Dixon chemical species separation with an iterative least-squares estimation method." Magnetic Resonance in Medicine: An Official Journal of the International Society for Magnetic Resonance in Medicine 51.1(2004): 35-45.
10.Yu, Huanzhou, et al. "Multiecho reconstruction for simultaneous water-fat decomposition and T2* estimation." Journal of Magnetic Resonance Imaging: An Official Journal of the International Society for Magnetic Resonance in Medicine 26.4 (2007): 1153-1161.
11. Reeder, Scott B., et al. "Quantification of hepatic steatosis with MRI: the effects of accurate fat spectral modeling." Journal of Magnetic Resonance Imaging: An Official Journal of the International Society for Magnetic Resonance in Medicine 29.6(2009): 1332-1339.
12. Yu, Huanzhou, et al. "Multiecho water-fat separation and simultaneous R estimation with multifrequency fat spectrum modeling." Magnetic Resonance in Medicine: An Official Journal of the International Society for Magnetic Resonance in Medicine 60.5(2008): 1122-1134.
13. Jaubert, Olivier, et al. "T1, T2, and Fat Fraction Cardiac MR Fingerprinting: Preliminary Clinical Evaluation." Journal of Magnetic Resonance Imaging (2020).
14. Coppo, Simone, et al. "Free-running 4D whole-heart self-navigated golden angle MRI: initial results." Magnetic resonance in medicine 74.5 (2015):1306-1316.
15. Di Sopra, Lorenzo, et al. "An automated approach to fully self-gated free-running cardiac and respiratory motion-resolved 5D whole-heart MRI." Magnetic resonance in medicine 82.6 (2019): 2118-2132.
16. Speier, P.,M. Fenchel, and R. Rehner. "PT-Nav: a novel respiratory navigation method for continuous acquisitions based on modulation of a pilot tone in the MR-receiver." Proc European Society for Magnetic Resonance in Medicine and Biology 32 (2015): 128.
17. Bacher, M. "Retrospective Evaluation of Pilot Tone Based Cardiac Trigger Quality In A Volunteer Cohort." Book of Abstracts ESMRMB 30 (2017):360-361.
18. Schroeder, L., et al. "Two-dimensional respiratory-motion characterization for continuous MR measurements using pilot tone navigation." Proceedings of the 24th Annual Meeting of ISMRM, Singapore. 2016.
19. Falcão, Mariana BL, et al. "5D Flow–A quantitative in vivo comparison between Self-Gating and Pilot Tone Gating."
20. Feng, L. I., et al. "5D whole-heart sparse MRI." Magnetic resonance in medicine 79.2(2018): 826-838.
21. Sun, Jian, Huibin Li, and Zongben Xu. "Deep ADMM-Net for compressive sensing MRI." Advances in neural information processing systems. 2016.
22. Piccini, Davide, et al. "Spiral phyllotaxis: the natural way to construct a 3D radial trajectory in MRI." Magnetic resonance in medicine 66.4 (2011):1049-1056.

Proceedings **ISMRM & SMRT Annual Meeting & Exhibition** (2021)
Abstract number **0755**
Abstract accepted as an Oral presentation.
Magna Cum Laude Merit Award
My contribution: I provided the Pilot Tone signal extraction pipeline and helped the first author to adapt it to the Free-Running 3DRadial Multi-Echo GRE datasets.

A2.1.2. Free-running contrast-enhanced ultra-short TE (UTE) for cardiac and respiratory motion-resolved flow artifact-free 5D whole-heart MRI

Giulia M.C. Rossi[1], Ludovica Romanin[1,2], Mariana B.L. Falcão[1], Bastien Milani[1], Davide Piccini[1,2], Jérôme Yerly[1,3], Jürg Schwitter[4,5,6], Milan Prša[7], Tobias Rutz[8], Estelle Tenisch[1], Matthias Stuber[1,3], and Christopher W. Roy[1]

[1]Department of Radiology, Lausanne University Hospital (CHUV) and University of Lausanne (UNIL), Lausanne, Switzerland,
[2]Advanced Clinical Imaging Technology (ACIT), Siemens Healthcare AG, Lausanne, Switzerland,
[3]CIBM Center for Biomedical Imaging, Lausanne, Switzerland,
[4]Division of Cardiology, Lausanne University Hospital (CHUV), Lausanne, Switzerland,
[5]Director CMR-Center, Lausanne University Hospital (CHUV), Lausanne, Switzerland,
[6]Faculty of Biology and Medicine, University of Lausanne (UNIL), Lausanne, Switzerland,
[7]Division of Pediatric Cardiology, Woman-Mother-Child Department, Lausanne University Hospital (CHUV) and University of Lausanne (UNIL), Lausanne, Switzerland,
[8]Service of Cardiology, Heart and Vessel Department, Lausanne University Hospital (CHUV) and University of Lausanne (UNIL), Lausanne, Switzerland

Synopsis

Free-running whole-heart MRI can suffer from flow artifacts. Despite the efficiency of 3D radial UTE in minimizing the latter, its integration as a free-running sequence has so far been challenging due to poor-quality self-gating, which has necessitated an inefficient dual-echo approach. In this work we show that self-gating signals from a single-echo ferumoxytol-enhanced free-running 3D radial UTE sequence are comparable to the dual-echo approach, allowing to significantly improve scanning efficiency and produce dynamic images that are free from flow artifacts.

Introduction

In the free-running framework for whole-heart MRI, data are continuously acquired independently from the underlying physiological motion, and retrospectively reconstructed as cardiac and respiratory motion-resolved 5D images using self-gating (SG) signals derived from the data themselves[1]. In addition to providing high-quality dynamic visualizations of cardiac anatomy, this approach meets the need for a simplified and time-efficient workflow for cardiac MR exams. In this context, ferumoxytol-enhanced 5D imaging with a 3D radial gradient echo (GRE) sequence has been shown to provide excellent delineation of cardiac anatomy by enhancing the blood-pool signal[2,3]. Nonetheless, dephasing effects due to blood flow in concert with shortened T2* can produce artifactual signal voids adversely affecting the image quality and potentially hindering the visibility of anatomical structures (e.g. valves, small-sized vessels, aortic dilatation)[4,5]. Previous work demonstrated that ultra-short TE (UTE) sequences are effective in minimizing flow-related dephasing[5,6]. However, in absence of a contrast agent, TE shortening comes at the expense of blood-to-myocardium contrast, negatively affecting anatomical visualization and reliable SG signals extraction (previously addressed by acquiring a second echo at longer TE for self-navigation, at the cost of scan time)[7].

We tested the hypothesis that, by integrating a 3D radial UTE acquisition[7] within the free-running framework[1] in ferumoxytol-enhanced MRI of congenital heart disease (CHD), the inherent advantages (absence of flow artifacts and excellent contrast) can mutually compensate the inherent disadvantages

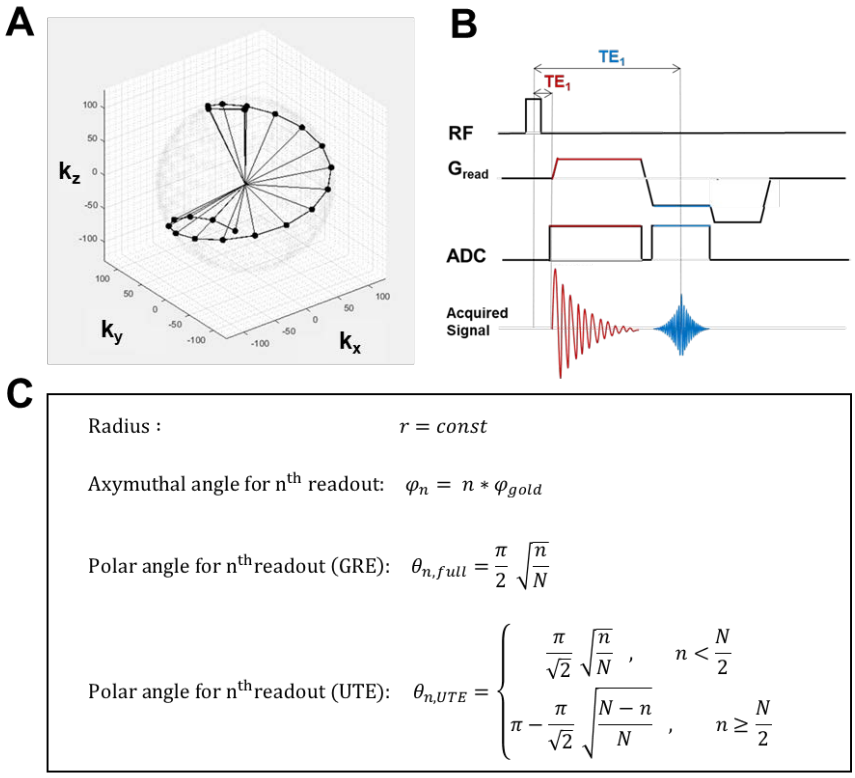

Figure 1. UTE sequence. A: RF pulses are followed by center-out UTE readouts using ramp-sampling. A second full-echo can be acquired for SG. **B-C:** The spiral phyllotaxis trajectory[10] was adapted to ensure full k-space coverage. In our work, sequence parameters were: RF excitation angle=15°, base resolution=192, spatial resolution=(1.14mm), TE_1/TE_2=0.08/2.17ms, half readouts=81906 for dual- and 126478 for single-echo UTE, resulting in constant acquisition time TA_{UTE}=5:20min with 54% more sampling for single-echo UTE. For reference TA_{GRE}=5:59 min (full readouts=126478).

(low contrast and presence of flow artifacts) of the two components. This simultaneously allows for self-navigation within a single-echo UTE acquisition and yields flow artifact-free 5D images with improved visibility of anatomical structures.

Methods

Acquisitions: Seven CHD patients (age: 3-38 y; 5 male) underwent imaging on a 1.5T MAGNETOM Sola (Siemens Healthcare, Erlangen, Germany), after providing IRB-approved written informed consent. For each patient, ferumoxytol-enhanced whole-heart data were acquired with a prototype free-running UTE sequence[7] with an option for multi-echo readouts (TE=0.08ms, n=4 with dual- and n=3 with single-echo UTE, see **Fig.1**) as well as with a previously reported version for free-running GRE[2]. With equal acquisition time TA_{UTE}=5:20min, single-echo UTE had a 54% increase in scanning efficiency as compared to dual-echo UTE. For each dataset and echo, SG signals were extracted and used for data sorting into motion-resolved bins (4 respiratory, 50ms cardiac)[1].

UTE self-gating: To test the hypothesis that the increase in contrast with ferumoxytol allows for reliable SG signals extraction from single-echo UTE acquisitions, SG signals obtained from the two echoes of the dual-echo UTE acquisitions (n=4) were compared[8]. For cardiac SG, the time between consecutively detected triggers (RR intervals) was compared by means of a Bland-Altman analysis and paired-sample t-tests. The similarity between SG respiratory signals was evaluated via the Pearson correlation coefficient, while their concordance in terms of assignments of readouts to respiratory bins was quantified by measuring the percentage of coinciding assignments.

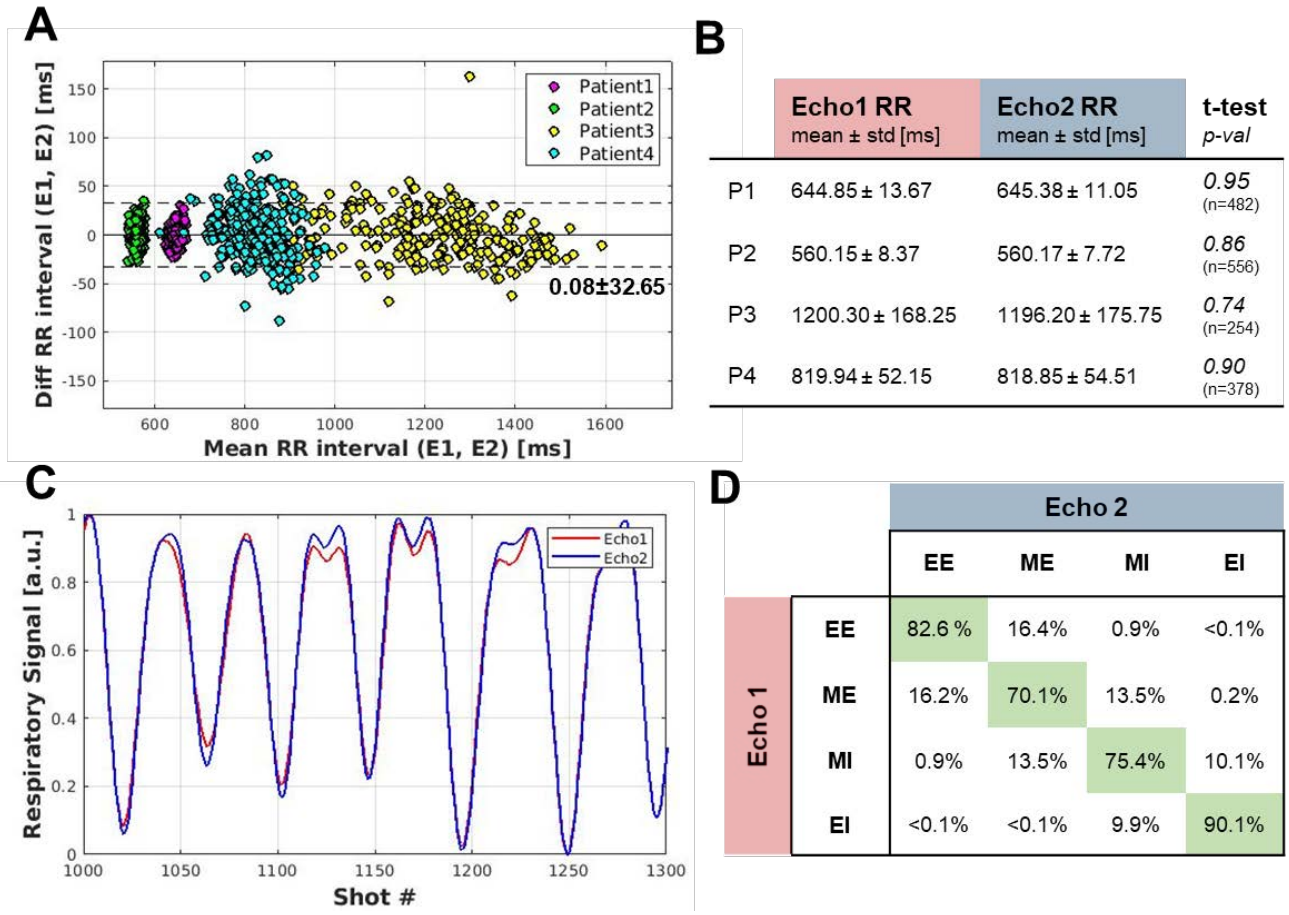

	Echo1 RR mean ± std [ms]	Echo2 RR mean ± std [ms]	t-test *p-val*
P1	644.85 ± 13.67	645.38 ± 11.05	*0.95* (n=482)
P2	560.15 ± 8.37	560.17 ± 7.72	*0.86* (n=556)
P3	1200.30 ± 168.25	1196.20 ± 175.75	*0.74* (n=254)
P4	819.94 ± 52.15	818.85 ± 54.51	*0.90* (n=378)

Figure 2. Comparison of SG signals obtained from the first (E1) and second (E2) echoes of dual-echo UTE acquisitions. A: Bland-Altman analysis of RR intervals from E1 and E2. **B:** RR intervals (mean ± std) from E1 and E2 are reported with the results of paired-sample t-tests. For reference, RR intervals from GRE are reported. **C:** Examples of SG respiratory signals from E1 and E2. **D:** Assignments of readouts to respiratory bins (EE: end- expiration, ME: mid-expiration, MI: mid-inspiration, EI: end-inspiration) based on SG respiratory signals from E1 and E2 (green: coinciding assignments).

Reconstructions: 5D UTE and 5D GRE images were reconstructed[1]. End-expiratory lung-liver sharpness[9] was compared (paired-sample Wilcoxon signed rank test), and the quality of motion-resolution was qualitatively assessed by means of M-mode images.

Flow artifacts in UTE and GRE reconstructions: To test the hypothesis that UTE helps minimizing flow-related dephasing, the severity of flow artifacts in 5D UTE and 5D GRE images was evaluated by computing the standard deviation of the mean signal intensity across cardiac phases in a ROI covering a cross-section of the ascending aorta.

Results

UTE self-gating: Good agreement was found between SG signals obtained from the two echoes of dual-echo UTE acquisitions. For cardiac SG, Bland-Altman analysis of RR intervals revealed low bias and good limits of agreement (0.08±32.65 ms) and t-tests did not reveal statistically significant differences (p_{test}>0.05) albeit in a small cohort (**Fig.2A-B**). Respiratory SG signals were also comparable, both in terms of signal correlation ($r_{Pearson}$=0.94±0.05) and binning (coincidence of 82.6%, 70.1%, 75.4% and 90.1% from end-expiration to end-inspiration), with mismatches mostly due to assignments to neighboring bins (**Fig.2C-D**).

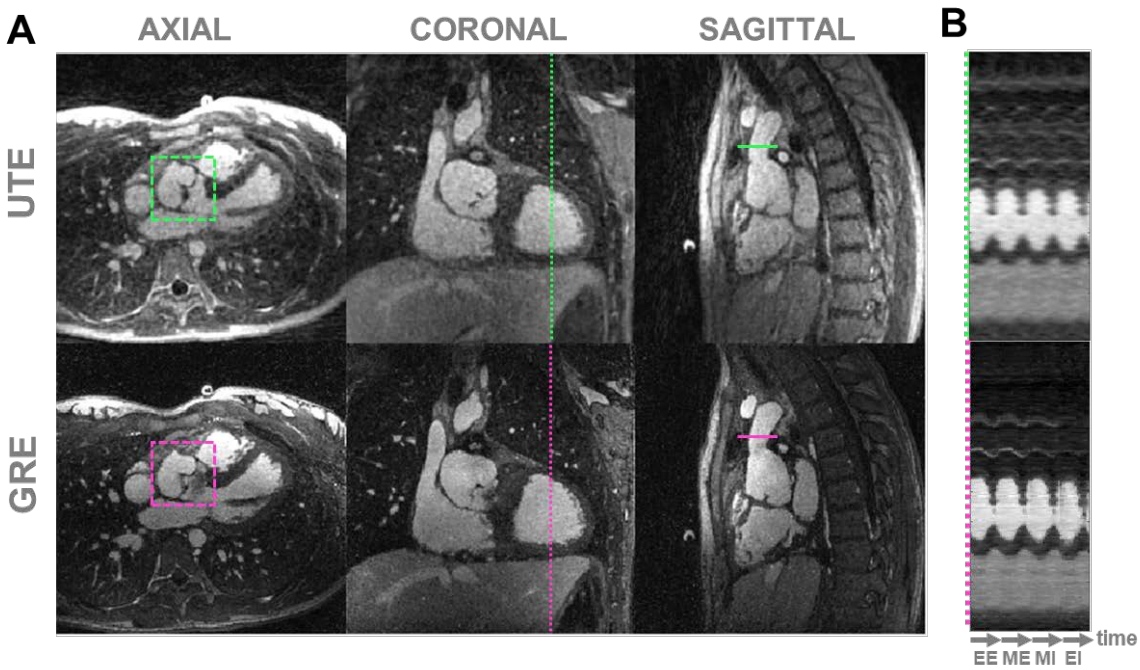

Figure 3. Qualitative comparison of 5D UTE and 5D GRE images. A: Mid-diastolic end-expiration phase of a 5D UTE reconstruction (top) and the reference 5D GRE (bottom). ROIs on the aortic valve (axial, dashed squares) and aortic cross-sections (sagittal, continuous line) indicate the locations selected for flow artifact visualization in Fig.4. **B:** M-mode images showing signal intensity evolution of a line crossing the left ventricle(coronal, dotted line) along cardiac and respiratory cycles (EE: end-expiration, ME: mid-expiration, MI: mid-inspiration, EI: end-inspiration).

Reconstructions: Overall, 5D UTE and 5D GRE reconstructions displayed good delineation of cardiac anatomy, albeit with more blur (s_{UTE}=2.10±0.21, s_{GRE}=2.55±0.36, $p_{Wilcoxon}$<0.05, n=7) in 5D UTE (**Fig.3A** and **Fig.5**). M-mode images suggested a comparable level of motion-resolution (**Fig.3B**).

Flow artifacts in UTE and GRE reconstructions: Visual inspection of 5D images revealed no flow artifacts in 5D UTE images, while they appeared prominent on 5D GRE, affecting the visibility of anatomical structures (**Fig.4A** and **Fig.5**). This was corroborated by quantitative measures (**Fig.4B**).

Discussion and conclusion

In this work, we showed the benefits of integrating a 3D radial UTE acquisition within the free-running framework in ferumoxytol-enhanced MRI. On one hand, we confirmed our first hypothesis that the increased blood-to-myocardium contrast offered by ferumoxytol allows for robust self-navigation based solely on the UTE echo, resulting in time-efficient acquisitions offering potential for increased sampling or reduced acquisition time. On the other hand, we confirmed our second hypothesis that the TE shortening enabled by UTE acquisitions allows for a significant reduction of signal dephasing, yielding flow artifact-free 5D images with improved visibility of dynamic anatomical structures. Additional work on the acquisition (protocol, trajectory optimization) and on the reconstruction side (reconstruction parameters, gradient imperfections correction) is still needed to bring the framework to realize its full potential in the context of ferumoxytol-enhanced imaging of CHD patients.

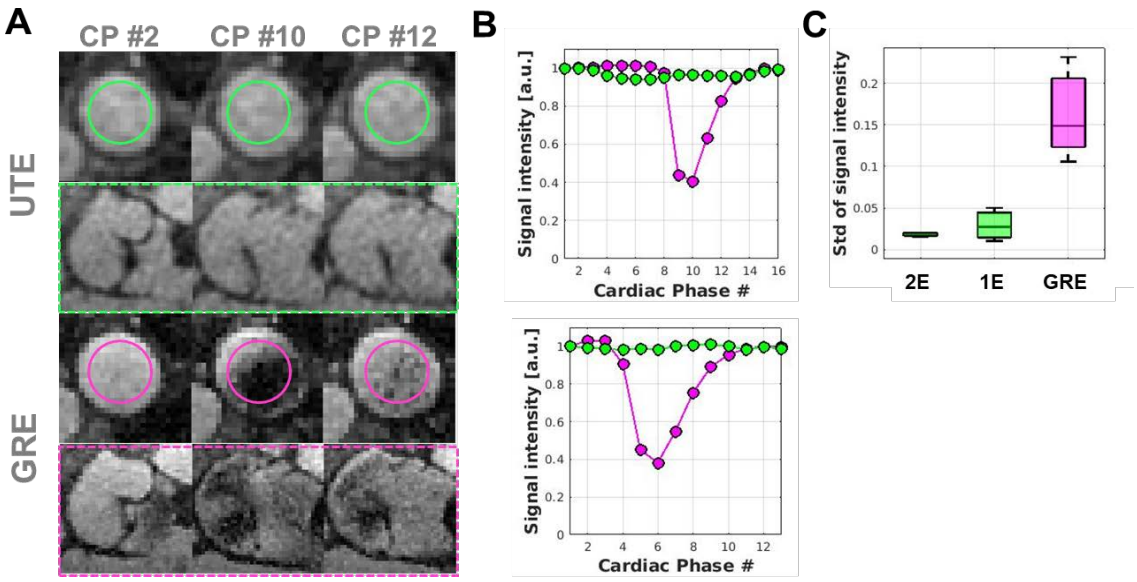

Figure 4. Flow artifacts in 5D UTE and 5D GRE images. A: Comparison of flow artifacts (dashed line: aortic valve; circle: aortic cross section; see Fig.3A) for different cardiac phases (CP) for a 5D UTE (top, green) and the corresponding 5D GRE (bottom, pink) reconstructions. **B:** Evolution of mean signal intensity for a ROI on the aorta for a 5D UTE (top: dual-echo, dataset shown in **A**; bottom: single-echo) and the corresponding 5D GRE (pink) reconstructions. C: Standard deviation of mean signal intensity over CP across all patients (from left to right: dual-echo UTE, single-echo UTE, GRE).

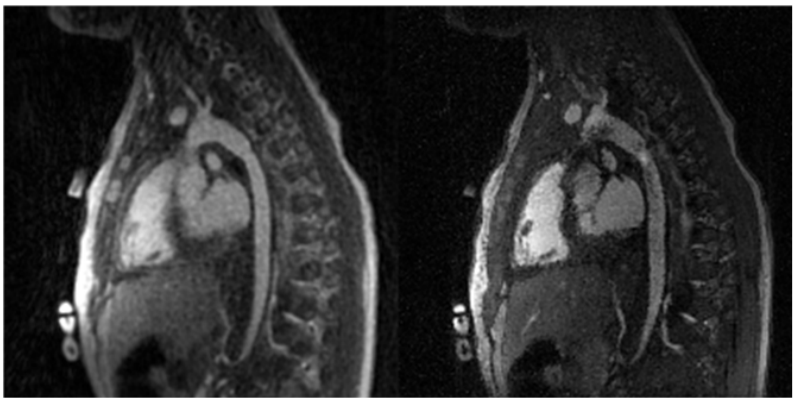

Figure 5. Visualization of cardiac motion and flow artifacts in 5D UTE and 5D GRE images (left and right, respectively) for a patient with a Williams syndrome with aortic stenosis and aortic arch hypoplasia after patch enlargement.*

*Images depicted in this Appendix are static.

Acknowledgements

The work was funded by the Swiss National Science Foundation (SNSF 320030B_201292)

References

1. Di Sopra, L., Piccini, D., Coppo, S., Stuber, M., & Yerly, J. (2019). An automated approach to fully self-gated free-running cardiac and respiratory motion-resolved 5D whole-heart MRI. Magneticresonance in medicine, 82(6), 2118-2132.
2. Di Sopra, L., Roy, C. W., Whitehead K. K., Fogel M. A., Piccini, D., & Stuber, M. Study on the potential acceleration offerumoxytol-enhanced free-running 5D whole-heart MRI in pediatric patients. Proc.Intl. Soc. Mag. Reson. Med. , 749550 (2020).

3. Heerfordt, J., Whitehead, K. K., Bastiaansen, J.A., Di Sopra, L., Roy, C. W., Yerly, J., ... & Piccini, D. (2021).Similarity-driven multi-dimensional binning algorithm (SIMBA) for free-running motion-suppressed whole-heart MRA. Magnetic Resonance in Medicine, 86(1), 213-229.
4. Monney, P., Piccini, D., Rutz, T., Vincenti, G., Coppo, S., Koestner, S. C., ... &Schwitter, J. (2015). Single centre experience of the application of self-navigated3D whole heart cardiovascular magnetic resonance for the assessment of cardiac anatomy in congenital heart disease. Journal of Cardiovascular Magnetic Resonance, 17(1), 1-12.
5. Robson, M. D., Gatehouse, P. D., Bydder, M.,& Bydder, G. M. (2003). Magnetic resonance: an introduction to ultrashort TE (UTE) imaging. Journal of computer assisted tomography, 27(6), 825-846.
6. Herrmann, K. H., Krämer,M., & Reichenbach, J. R. (2016). Time efficient 3D radial UTE sampling with fully automatic delay compensation on a clinical 3T MR scanner. PLoS One, 11(3), e0150371.
7. Delacoste, J.,Chaptinel, J., Beigelman-Aubry, C., Piccini, D., Sauty, A.,& Stuber, M. (2018). A double echo ultra-short echo time (UTE) acquisition for respiratory motion-suppressed high-resolution imaging of the lung. Magnetic resonance in medicine, 79(4), 2297-2305.
8. Falcão, M. B., Di Sopra, L., Ma, L., Bacher, M., Yerly, J., Speier, P., ... & Roy, C. W. (2021). Pilot tone navigation for respiratory and cardiac motion-resolved free-running 5D flow MRI. Magnetic resonance in medicine, 00:1-15.
9. Ahmad, R., Ding, Y., & Simonetti, O. P. (2015). Edge sharpness assessment by parametric modeling: application to magnetic resonance imaging. Concepts in Magnetic Resonance Part A, 44(3), 138-149.
10. Piccini, D., Littmann, A., Nielles-Vallespin, S., & Zenge, M. O.(2011). Spiral phyllotaxis: the natural way to construct a 3D radial trajectory in MRI. Magnetic resonance in medicine, 66(4), 1049-1056.

Proceedings **Joint Annual Meeting ISMRM-ESMRMB & ISMRT 31st Annual Meeting** (2022)
Abstract number **0333**
Abstract accepted as an Oral presentation.
Magna Cum Laude Merit Award
My contribution: I provided the Pilot Tone signal extraction pipeline and helped the first author to adapt it to the free-running contrast-enhanced UTE datasets.

A2.1.3. Pilot Tone-guided focused navigation for free-breathing whole-liver fat-water quantification

Adèle LC Mackowiak[1], Christopher W Roy[1], Mariana BL Falcão[1], Aurélien Bustin[1,2,3], Mario Bacher[1,4], Peter Speier[4], Davide Piccini[1,5], Matthias Stuber[1,6], Naïk Vietti-Violi[1], and Jessica AM Bastiaansen[1,7,8]

[1]Department of Radiology, Lausanne University Hospital (CHUV) and University of Lausanne (UNIL), Lausanne, Switzerland,
[2]Department of Cardiovascular Imaging, Hôpital Cardiologique du Haut-Lévêque, CHU de Bordeaux, Bordeaux, France,
[3]IHU LIRYC, Electrophysiology and Heart Modeling Institute, INSERM U1045, Centre de Recherche Cardio-Thoracique de Bordeaux, Université de Bordeaux, Bordeaux, France,
[4]SiemensHealthcare GmbH, Erlangen, Germany,
[5]Advanced Clinical Imaging Technology, Siemens Healthcare AG, Lausanne, Switzerland,
[6]CIBM Center for Biomedical Imaging, Lausanne, Switzerland,
[7]Department of Diagnostic, Interventional and Pediatric Radiology (DIPR), Inselspital, Bern University Hospital, University of Bern, Bern, Switzerland,
[8]Translational Imaging Center, sitem-insel, Bern, Switzerland

Synopsis

A free-breathing 3D radial multi-echo GRE acquisition for whole-liver fat-water separation and quantification was proposed, which integrated retrospective respiratory motion extraction with Pilot Tone and motion-compensated reconstruction with focused navigation. The proposed framework was tested in 10 healthy volunteers at 1.5T. Post-processing of the 8 reconstructed and denoised echoes with a graphcut algorithm provided fat-water separated images and fat fraction maps of isotropic resolution. Images and maps were compared to breath-held reference 3D and 2D Cartesian acquisitions for validation of the quality of both motion compensation and fat-water separation.

Introduction

Within the non-invasive assessment of liver steatosis using fat fraction (FF), the importance of whole-organ coverage and large region of interest (ROI) selection in multiple slices has been highlighted[1,2], to account for steatosis inhomogeneity. Multi-Echo GRE (ME-GRE) sequences provide reliable fat-water separation and quantification, after fitting the echoes to a multi-peak fat spectral model[3].

Correction for confounders such as B_0 inhomogeneities, noise, and T_1 bias, as well as a high number of echoes for good spectral resolution[3–5], are required. The latter can make high-resolution whole-liver examinations long and require repeated breath-holds. Free-breathing approaches are desirable for improved patient comfort, but can involve complex computational models with long reconstruction times.

We hypothesize that by combining a Pilot Tone-guided ME-GRE acquisition with focused navigation (fNAV), an auto-focusing technique recently validated for cardiac MRI[6], motion-compensated whole-liver fat quantification with a high number of echoes is possible within an acceptable scan time, under free-breathing conditions. The images obtained with the proposed framework are compared

in vivo to a gold-standard 2D 2-point Dixon sequence for fat-water separation and a 3D Cartesian ME-GRE for FF mapping.

MR parameters	3D radial FB	3D Cartesian BH	2p-Dixon VIBE BH
FOV size [mm²]	290x290	290x290	290x290
spatial resolution [mm³]	1.51x1.51x1.51	1.51x1.51x5.0	1.51x1.51x5.0
number of slices	192	8	8
TR [ms]	19.02	19.24	6.70
$\Delta TE/TE_1$ [ms]	2.30/1.38	2.30/1.30	2.38/2.39
number of echoes NTE	8	8	2
flip angle [°]	12	12	10
pixel bandwidth [Hz/px]	898	898	470
gradient readout mode	monopolar	monopolar	bipolar
acceleration	64% Nyquist	none	Parallel Imaging factor 4
acquisition time [min]	02:57	00:20	00:07

Table 1. Acquisition parameters. The prototype free-breathing 3D radial ME-GRE sequence was acquired continuously with a phyllotaxis trajectory made of 424 interleaves composed of 22 segments each with a golden-angle rotation in between interleaves, leading to a 02:57min scan time. Parameters of the 3D Cartesian ME-GRE sequence were selected to match that of the proposed radial sequence as closely as possible, under the constraint of a breath-hold duration of 20sec. The 2p-Dixon sequence parameters were fixed as provided by the manufacturer.

Methods

On a 1.5T clinical scanner (MAGNETOM Sola, Siemens Healthcare, Erlangen, Germany), n=10 healthy volunteers (F=6, ages 23-39yo) who provided informed consent were scanned with a prototype 3D radial ME-GRE sequence with isotropic spatial resolution of $(1.5mm)^3$. Data acquisition was performed during free-breathing, using a prototype free-running 3D golden angle radial trajectory[8] with 8 echoes. A 12-channel chest coil with an integrated PT generator, operating outside the MR frequency range, was used for trajectory-independent monitoring of motion. A respiratory signal was extracted from the PT data[9] and used for estimating fNAV coefficients that describe the amplitude of the respiratory motion at each spatial location. The fNAV coefficients were iteratively optimized to minimize an image quality metric (gradient entropy), then used to correct the separate echoes. Multi-contrast patch-based denoising[10] was performed on the reconstructed 4D volumes. Fat and water images and FF maps were generated using a 6-peak fat model and a maximum-likelihood graphcut algorithm[11] (ISMRM Fat/Water Toolbox[12]).

During the same examination, a 2-point Dixon VIBE sequence provided reference fat and water 2D images directly at the scanner. An anisotropic 3DCartesian ME-GRE sequence was also acquired during breath-holding with 8 echoes, and provided sources images at the scanner that were processed with the same fitting algorithm as to provide reference fat-water separated images and FF maps. Sequence parameters are detailed in **Tab.1**.

The mean and standard deviation of the FF in 3 intra-hepatic ROIs was measured for both radial and Cartesian 3D acquisitions and used to perform a Bland-Altman analysis on the 10 volunteers.

Results

Respiratory PT signals were successfully extracted in all volunteers (**Fig.1A**), which enabled the minimization of motion-induced blurring using fNAV (**Fig.1B-C**), especially visible at the lung-liver interface. The average reconstruction time wih fNAV was 37min ([range 14-62] min) across volunteers. Patch-based denoising (additional computation time of 11min per 4D volume) improved the overall visual image sharpness (**Fig.1C-D**).

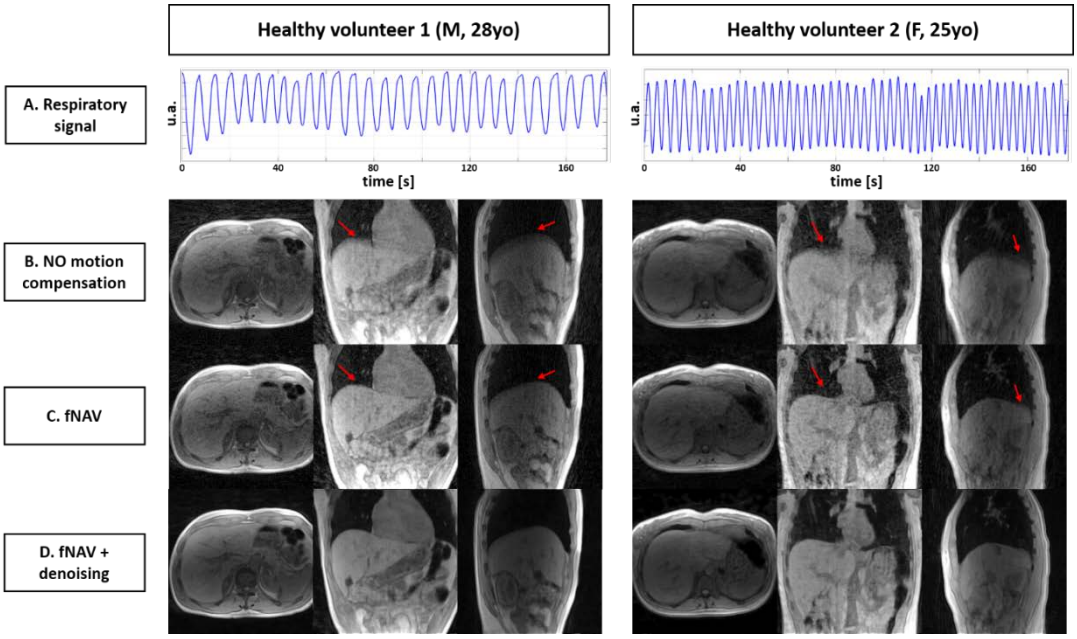

Figure 1. Motion compensation with fNAV in 2 healthy volunteers. The respiratory signal extracted from the Pilot Tone is shown on panel **A**. The source images of the first collected echo with the proposed sequence are shown **B**. reconstructed without motion compensation, **C.** reconstructed with fNAV and **D.** reconstructed with fNAV and denoised. Visible blurring in the superior-inferior direction at the lung-liver interface affects the uncompensated images, which is corrected by fNAV (red arrows). Denoising improved overall image sharpness and quality.

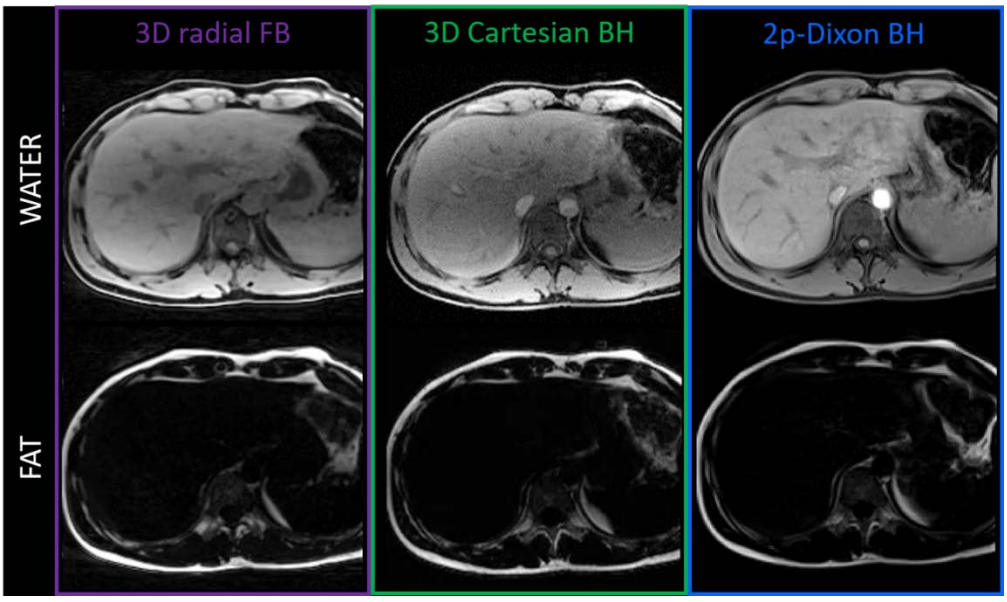

Figure 2. Separated fat and water images in healthy volunteer 3 (M, 28yo). Water-only (top) and fat-only (bottom) images are obtained from fitting the ME-GRE data to a 6-peak liver fat model, in the case of the 3D radial and3D Cartesian (left and middle columns). The 2D 2-point Dixon VIBE acquisition (right column) produces separated images directly at the scanner and provides a gold-standard for fat-water separation. Good agreement and no swaps were observed, although contrast differences between 3D radial and 3D Cartesian can be seen (abdominal aorta).

The comparison of fat-water separated images to breath-held images showed the absence of motion artifacts with our technique, as well as a robust chemical species separation, without swaps (**Fig.2**).

In volunteer 4 (**Fig.3A**), the radial FF maps showed a larger granularity of the fatty regions and elevated FF in ROI1, compared to the breath-held Cartesian ones. Large standard deviations were

A.

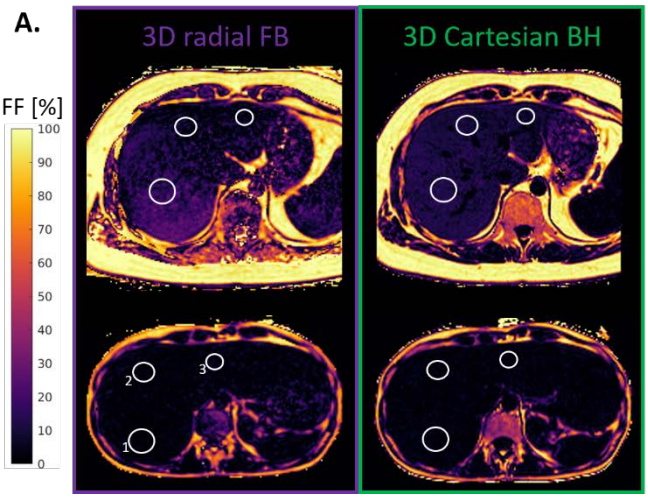

B.

		3D RAD FB	3D CART BH
Healthy volunteer 4 (M, 33 yo)	ROI 1	18.8±3.9	12.1±2.6
	ROI 2	2.6±8.1	9.4±2.9
	ROI 3	3.9±4.9	7.9±2.5
Healthy volunteer 5 (F, 29 yo)	ROI 1	1.7±1.5	2.2±1.5
	ROI 2	2.2±1.9	2.3±1.4
	ROI 3	2.6±1.7	2.0±1.8

Figure 3. Fat fraction maps in 2 healthy volunteers. A. Healthy volunteer 4 (top) and 5 (bottom). The regions of interest (ROI) used for quantitative analysis are indicated by white circles. The labels indicated on the bottom-left map are respectively: 1. Segment VII, 2. Segment IV and 3. Segment II. **B.** Mean and standard deviation of the fat fraction (in %) measured across the ROI in the volumes presented in panel A, for both imaging protocols.

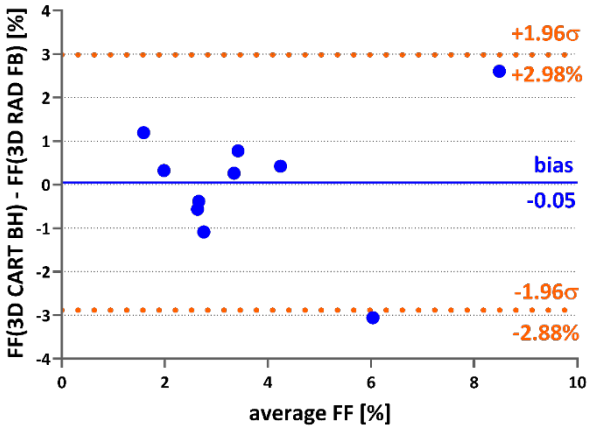

Figure 4. Bland-Altman plot: difference between 3D radial FB and 3D Cartesian BH in 10 healthy volunteers. The 3D Cartesian ME-GRE with NTE=8 echoes analyzed with graph cut provided FF maps that were compared to those obtained with the proposed3D radial framework. A low bias is reported, with small limits of agreements between the 2 imaging protocols, mostly driven by bigger deviations observed in 2 volunteers out of 10. Difference in slice thickness (1.5 vs 5.0mm) could explain these deviations.

measured in all 3 ROIs (**Fig.3B**). Conversely, good agreement between the two protocols was observed in volunteer 5 (**Fig.3B**). This was confirmed in the rest of the cohort, as a Bland-Altman analysis of the mean FF in 10 volunteers revealed an average bias of 0.09% between the Cartesian and proposed radial techniques, with 1.96 standard deviation bounds of [-2.43-2.63]% (**Fig.4**). Out of 10 datasets, only 2 had a mean difference across all ROIs higher than 1%, including volunteer 4 mentioned above.

Discussion

This study demonstrated the feasibility of combining a 3D radial sparse trajectory with a ME-GRE acquisition with 8 echoes using PT and fNAV, reaching isotropic clinical resolution in less than 3 minutes without introducing errors in the fat-water separation nor motion artifacts. Although differences in contrast from the Cartesian references were observed, visualization of global liver anatomy and main hepatic and portal veins was possible.

Global agreement of the parametric FF maps with the Cartesian reference in 80% of the volunteers showed the proposed method is promising, but the low FF content expected in healthy volunteers limited the evaluated range of our study. The deviation of our technique from the Cartesian reference was higher in volunteers with fat content above 5%, which will be investigated. Therefore, extended mapping validation on a standardized phantom, as well as case studies on subjects with elevated fat content would further characterize the accuracy of the technique. Additionally, this work could be extended to include R_2* quantification without prolonging scan time, which would benefit iron deposition assessment.

Conclusion

This work presented a pipeline for free-breathing whole-liver fat imaging, which can be used to retrieve reliable information on the location and quantity of hepatic fat within acceptable scan and reconstruction time for a resolution of $(1.5\text{mm})^3$.

Acknowledgements

The authors acknowledge the use of the ISMRM Fat/Water Toolbox[12] for some of the results shown in this work.

The present study was funded by the Swiss National Science Foundation (grant number #PCEFP2_194296, #PZ00P3_167871), the Unil Bourse Pro-Femmes, the Emma Muschamp Foundation and the Swiss Heart Foundation.

References

1. K.-N. Vu, G. Gilbert, M. Chalut, M. Chagnon, G. Chartrand, and A. Tang, 'MRI-determined liver proton density fat fraction, with MRS validation: Comparison of regions of interest sampling methods in patients with type 2 diabetes', Journal of Magnetic Resonance Imaging, vol. 43, no. 5, pp.1090–1099, May 2016, doi: 10.1002/jmri.25083.

2. C. A. Campo, D. Hernando, T. Schubert, C. A. Bookwalter, A. J. V. Pay, and S. B. Reeder, 'Standardized Approach for ROI-Based Measurements ofProton Density Fat Fraction and R_2* in the Liver', American Journal of Roentgenology, vol. 209, no. 3, pp. 592–603, Sep. 2017, doi:10.2214/AJR.17.17812.

3. H. Yu, A. Shimakawa, C. A. McKenzie, E. Brodsky, J. H. Brittain, and S. B. Reeder, 'Multiecho water-fat separation and simultaneous R_2* estimation with multifrequency fat spectrum modeling', Magnetic Resonance in Medicine, vol. 60, no. 5, pp. 1122–1134, Nov. 2008, doi: 10.1002/mrm.21737.

4. S. B. Reeder, H. H. Hu, and C. B. Sirlin, 'Proton density fat-fraction: A standardized mr-based biomarker of tissue fat concentration', Journal of Magnetic Resonance Imaging, vol. 36, no. 5, pp. 1011–1014, Nov. 2012, doi:10.1002/jmri.23741.

5. S. Meisamy et al., 'Quantification of Hepatic Steatosis with T_1-independent, T_2*-corrected MR Imaging with Spectral Modeling of Fat: Blinded Comparison with MR Spectroscopy', Radiology, vol. 258, no. 3, pp. 767–775, Mar. 2011, doi: 10.1148/radiol.10100708.

6. C. W. Roy et al., 'Motion compensated whole-heart coronary cardiovascular magnetic resonance angiography using focused navigation (fNAV)', Journal of Cardiovascular Magnetic Resonance, vol. 23, no. 1, p. 33, Mar. 2021, doi:10.1186/s12968-021-00717-4.

7. T. Vahle et al., 'Respiratory Motion Detection and Correction for MR Using the Pilot Tone: Applications for MR and Simultaneous PET/MR Exams', Invest Radiol, vol. 55, no. 3, pp. 153–159, Mar. 2020, doi: 10.1097/RLI.0000000000000619.

8. D. Piccini, A. Littmann, S. Nielles-Vallespin, and M. O. Zenge, 'Spiral phyllotaxis: The natural way to construct a 3D radial trajectory in MRI: Spiral Phyllotaxis Radial 3D Trajectory', Magnetic Resonance in Medicine, vol. 66, no. 4, pp. 1049–1056, Oct. 2011, doi: 10.1002/mrm.22898.

9. M. B. L. Falcão et al., 'Pilot tone navigation for respiratory and cardiac motion-resolved free-running 5D flow MRI', Magnetic Resonance in Medicine, vol. n/a, no. n/a, doi: 10.1002/mrm.29023.

10. A. Bustin, G. Lima da Cruz, O. Jaubert, K. Lopez, R. M. Botnar, and C. Prieto, 'High-dimensionality undersampled patch-based reconstruction(HD-PROST) for accelerated multi-contrast MRI', Magnetic Resonance in Medicine, vol. 81, no. 6, pp. 3705–3719, 2019, doi: 10.1002/mrm.27694.
11. D. Hernando, P. Kellman, J. P. Haldar, and Z.-P. Liang, 'Robust water/fat separation in the presence of large field inhomogeneities using a graphcut algorithm', Magnetic Resonance in Medicine, p. NA-NA, 2009, doi: 10.1002/mrm.22177.
12. H. H. Hu et al., 'ISMRM workshop on fat–water separation: Insights, applications and progress in MRI', Magnetic Resonance in Medicine, vol. 68,no. 2, pp. 378–388, 2012, doi: 10.1002/mrm.24369.

Proceedings **Joint Annual Meeting ISMRM-ESMRMB & ISMRT 31st Annual Meeting** (2022)
Abstract number **0114**
Abstract accepted as an Oral presentation.
My contribution: I provided the Pilot Tone signal extraction pipeline and helped the first author to adapt it to the free-running multi-echo GRE datasets.

A2.1.4. Free-running isotropic whole-heart T_2 mapping with ECG-free Pilot Tone navigation

Simone Rumac[1], Christopher W. Roy[1], Jérôme Yerly[1], Mariana B. L. Falcao[1], Aurélien Bustin[1,2,3], Mario Bacher[1,4], Peter Speier[4], Matthias Stuber[1,5], and Ruud B. van Heeswijk[1]

[1]Department of Radiology, Lausanne University Hospital (CHUV) and University of Lausanne (UNIL), Lausanne, Switzerland,
[2]IHU LIRYC, Electrophysiology and Heart Modeling Institute, INSERM U1045, Centre de recherche Cardio-Thoracique de Bordeaux, Université de Bordeaux, Bordeaux, France,
[3]Cardiovascular Imaging, Hôpital Cardiologique du Haut-Lévêque, CHU de Bordeaux, Bordeaux, France,
[4]Siemens Healthcare GmbH, Erlangen,Germany,
[5]CIBM Center for BioMedical Imaging, Lausanne, Switzerland, Lausanne, Switzerland

Synopsis

The most commonly employed T_2 mapping techniques are 2D and make use of ECG-triggering. This may be a limitation in patients with variable heart rate and complex three-dimensional conditions. To address these limitations, we here propose an isotropic free-running 3D T_2 mapping technique that avoids ECG triggering by using Pilot Tone navigation. In three healthy volunteers, our technique produced accurate isotropic T_2 maps when compared to 2D T_2 prepared bSSFP (T_2=41.1±4.8ms vs. 44.9±3.3ms, respectively, p=0.1), and cardiac motion was successfully resolved.

Introduction

Cardiac T_2 mapping is routinely used in clinical MR protocols for the assessment of acute edema[1]. Most commonly employed T_2 mapping techniques are breath-held single-slice 2D acquisitions. This coverage can limit the sensitivity, especially in the case of myocardial pathologies that have heterogeneous 3D patterns throughout the myocardium. To more completely characterize these spatially complex disease patterns, several 3D T_2 mapping techniques have therefore been proposed[2-6]. Moreover, all current 2D and 3D T_2 mapping techniques make use of electrocardiogram (ECG) triggering, which may lead to unpredictable scan times, depends on high-quality ECG signals, may fail in case of arrhythmia, and implies a time-inefficient sampling of k-space. Most of these limitations might be avoided by using a free-running acquisition with retrospective self-gating[7], but robust ECG-free self-gating is very challenging when a wide range of image contrasts is used, as is the case for mapping. To address these limitations, we here propose an isotropic free-running 3D T_2 mapping technique that 1) utilizes Pilot Tone[8] navigation to obtain contrast-independent respiratory and cardiac signals, 2) robustly corrects for respiratory motion through focused navigation (fNAV)[9], 3) fully resolves cardiac motion, 4) produces accurate maps through compressed sensing (CS) combined with patch-based denoising (HD-PROST)[10].

Methods

The acquisition (**Fig.1**) consists of a prototype free-running[7] 3D radial GRE sequence with a phyllotaxis trajectory[11], field of view=$(220\text{mm})^3$, isotropic spatial resolution=$(1.5\text{mm})^3$, TR/TE=4.4/2.2ms, α=5°, four interleaved T_2 preparation times T_2-prep=0/25/40/55ms, 35200 readouts/T_2-prep, and a total acquisition time of 11.3min. All data were acquired on a 1.5T clinical

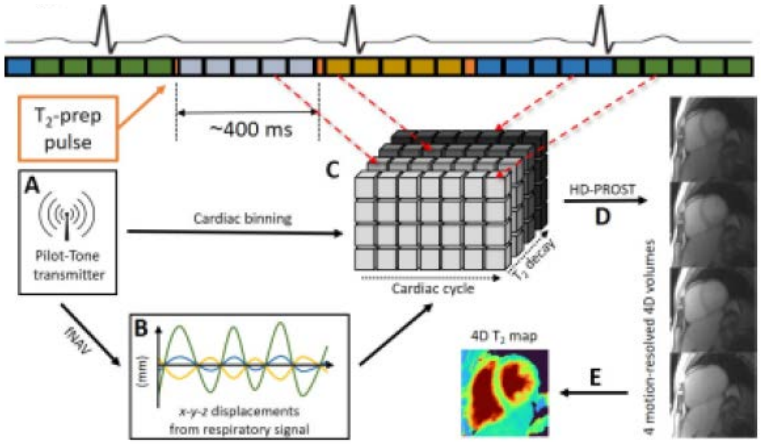

Figure 1. Overview of the proposed technique. A continuous 3D radial GRE acquisition is periodically interleaved with T_2-prep pulses of increasing duration. **A)** The Pilot Tone coil is used to obtain respiratory and cardiac signals. **B)** The extracted signal is converted into a correction factor (fNAV) prior to reconstruction. **C)** A CS reconstruction is performed with resolved cardiac and T_2-prep dimensions. **D)** HD-PROST is applied to denoise the images, thus obtaining four cardiac-motion-resolved 4D volumes with T_2-weighted contrast. **E)** Dictionary matching is used to create a 4D T_2 map.

scanner (MAGNETOM Sola, Siemens Healthcare, Erlangen, Germany). Data-synchronized respiratory and cardiac signals were extracted from the Pilot Tone signal[12]. The respiratory motion was corrected using focused navigation (fNAV)[9], which estimates the amplitude of respiratory motion along all three spatial dimensions in order to scale the respiratory motion signals obtained from the Pilot Tone, and translationally corrects each k-space readout prior to the CS reconstruction, thus reducing the dimensionality of the dataset. Source images were reconstructed with total variation (TV) regularization along the cardiac dimension, and denoising was subsequently performed by applying HD-PROST to improve the T_2 precision. Extended phase graph (EPG)[13] simulations were used to generate a sequence-specific dictionary for a range of T_2 values. A pixel-wise match of the source images with this dictionary then resulted in the T_2 map. The proposed technique was validated in an agar-NiCl-gel phantom designed to mimic the in-vivo range of myocardial relaxation times. Gold-standard values were obtained using a turbo-spin-echo (TSE) sequence with 32 echo times (13-422ms) and TR=10s. Linear regression and Bland-Altman analyses were performed to compare our technique and routine breath-held T_2-prepared T_2 mapping[14] to the TSE relaxation times. Finally, both the proposed technique and the clinical routine scans were applied to the heart of three healthy volunteers (age=33±8y, 1F) with IRB approval and written informed consent. The myocardial T_2 maps were manually segmented, and a Student's t-test was used to compare the average values in the corresponding myocardial area to routine T_2-prepared mapping[14]. We measured the average myocardial T_2 in all cardiac phases and computed its standard deviation as a measure of precision.

Results

The phantom T_2 maps demonstrated a high correlation with the gold standard over the relevant T_2 range ($y=0.98x-4.6$, $R^2=0.98$, **Fig.2**). A small (~6ms) underestimation was observed compared to the TSE T_2 values, which was consistent in the range of interest. The Bland-Altman analysis confirmed the bias but did not reveal other trends. In all in-vivo cases, and despite the periodic interference produced by the T_2-prep modules, Pilot Tone allowed a robust detection of both cardiac and respiratory signals. The fNAV correction successfully aligned the respiratory phases as evidenced by sharp lung-

liver interfaces. The CS-based reconstruction produced well-aligned source images with resolved cardiac motion. The resulting motion-resolved T_2 maps were accurate when compared to routine 2D maps (T_2=41.1±4.8ms vs. 44.9±3.3ms, respectively, p=0.1). Moreover, we found that the average T_2 value remained coherent across the cardiac cycle (**Fig.4**), with the average standard deviation across all phases being lower than 3 ms for all considered subjects.

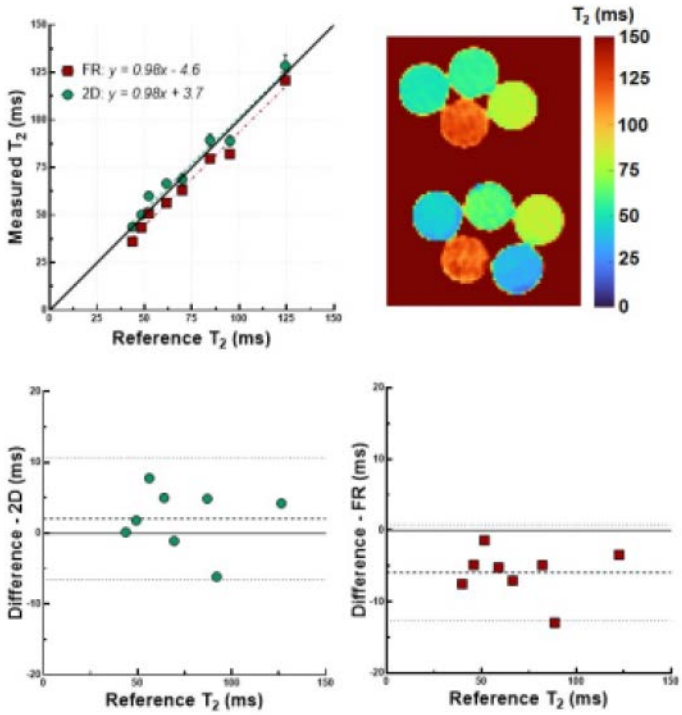

Figure 2. Validation of the technique in the phantom. A) Linear regression plot of the T_2 values obtained with the proposed technique. The T_2 relaxation times show a slight but consistent underestimation when compared to the turbo-spin-echo reference over the entire range of interest (35ms-130ms). **B)** Bland-Altman analysis of routine 2D T_2 mapping. **C)** Bland-Altman analysis of the proposed technique, confirming the ~6ms bias. The dotted lines represent the 95% limits of agreement.

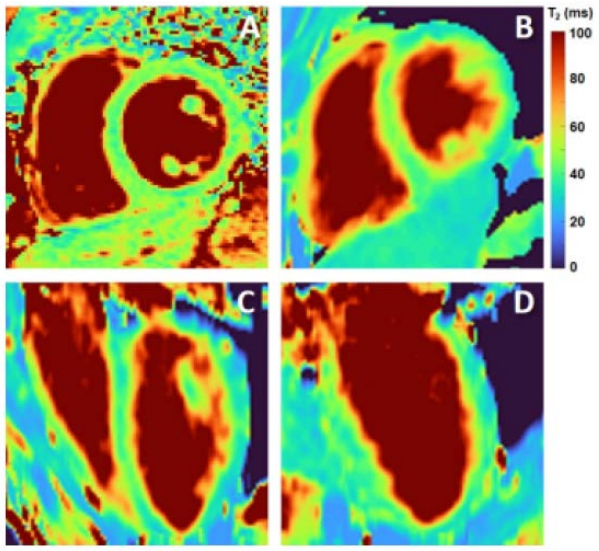

Figure 3. The resulting maps compared to 2D T_2-prepared bSSFP (M, 41 y.o). A) Short-axis breath-held 2D T_2 map acquired with routine T_2-prepared bSSFP. **B)** Short-axis slice obtained with the proposed technique in mid-diastole. **C-D)** The corresponding orthogonal planes (pseudo-4CH and pseudo-2CH).

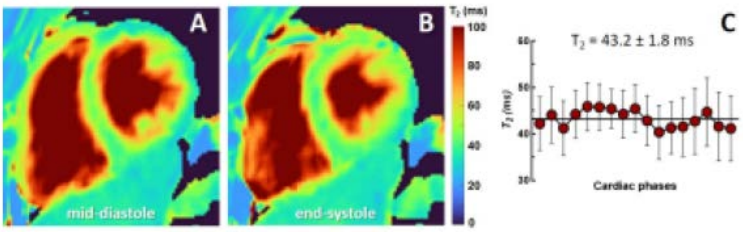

Figure 4. Average myocardial T_2 across the cardiac cycle (M, 41 y.o). A) Mid-diastolic T_2 map. **B)** Corresponding T_2 map in the end-systolic phase. C) The average T_2 measured in the segmented myocardial area. The bars indicate the measured standard deviation.

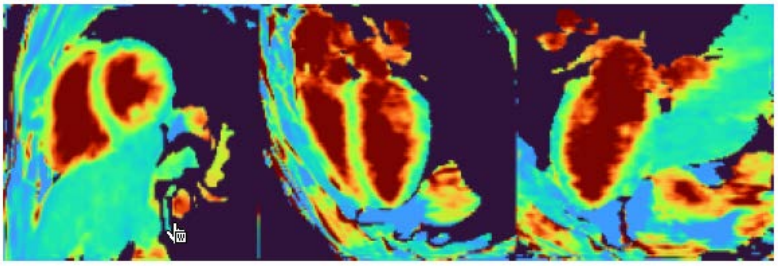

Figure 5. The resulting cardiac-resolved T_2 map (M, 41 y.o). One short-axis, pseudo-4CH and pseudo-2CH slices across the full cardiac cycle.

Discussion

The proposed technique showed high correlation with the gold-standard TSE acquisition in the phantom, but a small T_2 underestimation, which is mostly likely due to stimulated echoes in the TSE and is consistent with what was previously found in dictionary-matching-based techniques. The use of Pilot Tone allows for robust identification of physiological signals regardless of periodic changes in source image contrast. The fNAV correction proved to be a useful tool in order to reduce dimensionality and therefore reduced the computational burden while retaining all information. Finally, the T_2 maps demonstrated high consistency across the different cardiac phases, albeit in a small sample size. Therefore, further optimization is required to improve both accuracy and precision in a larger cohort. In conclusion, we successfully demonstrated the feasibility and preliminary results of an isotropic free-running 3D T_2 mapping technique.

Acknowledgements

No acknowledgement found.

References

1. Messroghli, D. R. et al. Clinical recommendations for cardiovascular magnetic resonance mapping of T1, T2, T2* and extracellular volume: A consensus statement by the Society for Cardiovascular Magnetic Resonance (SCMR) endorsed by the European Association for Cardiovascular Imaging (EACVI). J Cardiovasc Magn Reson 19, 75 (2017).
2. van Heeswijk, R. B. et al. Self-navigated isotropic three-dimensional cardiac T2 mapping. Magn. Reson. Med. 73, 1549–54 (2015).
3. Ding, H. et al. Three-dimensional whole-heart T2 mapping at 3T. Magn. Reson. Med. 74, 803–16 (2015).
4. Milotta, G. et al. 3D Whole-heart free-breathing qBOOST-T2 mapping. Magn. Reson. Med. 83, 1673–1687 (2020).
5. Bustin, A. et al. Accelerated free-breathing whole-heart 3D T 2 mapping with high isotropic resolution. Magn. Reson. Med. 83, 988–1002(2020).
6. Qi, H. et al. Free-running simultaneous myocardial T1/T2 mapping and cine imaging with 3D whole-heart coverage and isotropic spatial resolution. Magn. Reson. Imaging 63, 159–169 (2019).
7. Di Sopra, L., Piccini, D., Coppo, S., Stuber, M. & Yerly, J. An automated approach to fully self-gated free-running cardiac and respiratory motion-resolved 5D whole-heart MRI. Magn. Reson. Med. 82, 2118–2132 (2019).
8. Speier, P., Fenchel, M. & Rehner, R. PT-Nav: A Novel Respiratory Navigation Method for Continuous Acquisition Based on Modulation of aPilot Tone on the MR-Receiver. Magn. Reson. Mater. Phys. Biol. Med. 28, 1–135 (2015).

9. Roy, C. W. et al. Motion compensated whole-heart coronary cardiovascular magnetic resonance angiography using focused navigation(fNAV). J. Cardiovasc. Magn. Reson. 23, 33 (2021).
10. Bustin, A. et al. High-dimensionality undersampled patch-based reconstruction (HD-PROST) for accelerated multi-contrast MRI. Magn. Reson. Med. 81, 3705–3719 (2019).
11. Piccini, D., Littmann, A., Nielles-Vallespin, S. & Zenge, M. O. Spiral phyllotaxis: the natural way to construct a 3D radial trajectory in MRI. Magn. Reson. Med. 66, 1049–1056 (2011).
12. Falcão, M. B. L. et al. Pilot tone navigation for respiratory and cardiac motion-resolved free-running 5D flow MRI. Magn. Reson. Med. (2021)doi:10.1002/mrm.29023.
13. Weigel, M. Extended phase graphs: Dephasing, RF pulses, and echoes - Pure and simple. J. Magn. Reson. Imaging 41, 266–295 (2015).
14. Giri, S. et al. T2 quantification for improved detection of myocardial edema. J. Cardiovasc. Magn. Reson. 11, 56 (2009).
15. Hamilton, J. I. et al. Simultaneous Mapping of T1 and T2 Using Cardiac Magnetic Resonance Fingerprinting in a Cohort of Healthy Subjects at 1.5T. J. Magn. Reson. Imaging (2020) doi:10.1002/jmri.27155.

Proceedings **Joint Annual Meeting ISMRM-ESMRMB & ISMRT 31st Annual Meeting** (2022)
Abstract number **0020**
Abstract accepted as a Power Pitch.
My contribution: I provided the Pilot Tone signal extraction pipeline and helped the first author to adapt it to the free-running whole-heart T2 mapping datasets.

A2.1.5. On the Influence of Respiratory State on Pilot Tone Derived Cardiac Triggers

M. Bacher[1] P. Speier[1]; M. B. L. Falcão[2]; C. Roy[2]; M. Prša[3]; T. Rutz[4]; M. Stuber[2]

[1]DL CARD, Siemens Healthineers, Erlangen, Germany;
[6]Department of radiology, Lausanne University Hospital (CHUV) and University of Lausanne (UNIL), Lausanne, Switzerland, Lausanne, Switzerland;
[3]Woman-mother-child department, Lausanne University Hospital (CHUV) and University of Lausanne (UNIL), Lausanne, Switzerland, Lausanne, Switzerland;
[4]Department of cardiology, Lausanne University Hospital (CHUV) and University of Lausanne (UNIL), Lausanne, Switzerland

Background

Pilot Tone (PT)[1] is a novel, electromagnetic sensing technique capable of remotely sensing respiratory and cardiac motion that has gained popularity in recent years. The PT signal is closely correlated to total cardiac volume[2] and can be used both in real-time or retrospectively to trigger or gate MR acquisitions. We have previously used PT in lieu of self-gating[3] for its high temporal resolution and sequence-independence in a free-running acquisition strategy. PT signals are used to bin the acquired data into respiratory and cardiac bins. Here we aim to investigate how the trigger points derived from the cardiac PT signal change depending on the respiratory position.

Methods

We scanned 12 volunteers (a: 27+/-3y, 7 male, 8 female) and eight patients (a: 24+/-16y, 5 male, 3 female) at 1.5T (MAGNETOM Sola, Siemens Healthcare GmbH, Erlangen, Germany) using a prototype free-running acquisition[3]. From raw PT data (one channel per receive coil) the respiratory and cardiac PT signals $s_{PT,resp}$ and $s_{PT,card}$ were extracted using Blind Source Separation (BSS) (PCA for $s_{PT,resp}$, ICA for $s_{PT,card}$). The cardiac signal was filtered using our Kalman-Filter processing chain[4], where cardiac triggers are detected as zero-crossings of the signals 1st derivative (**Fig.1a**). The respiratory signal $s_{PT,resp}$ was used to bin the data into three respiratory bins (see **Fig.1b**). For each of these bins, triggers were extracted from $s_{PT,card}$ and matched with ECG R-peaks as ground truth (**Fig.1c**). The temporal difference between ECG R-peak and PT triggers, Δtrig (see **Fig.2**) was determined and, to account for the effect of R-R duration changing with respiratory state (respiratory sinus arrythmia), Δtrig was normalized to the mean R-R interval in its corresponding bin and is thus given in percent of the mean R-R interval. This normalization also allows for the pooling of results over subjects. Respiratory bins were then tested for significant differences in $\Delta_{trig,norm}$ using ANOVA. To characterize respiratory amplitude, we used navigators on the liver dome, derived from reconstructed 3D datasets. In total, we analyzed 8550 individual heartbeats in the volunteer- and 3742 heartbeats in the patient cohort.

Results

We found significant differences in $\Delta_{trig,norm}$ between all respiratory states in the volunteer cohort (**Fig.3**) but no significant difference was observed in the patient cohort. Normalized trigger delays are given in **Tab.1**. Respiratory amplitude was significantly higher in the volunteer cohort (16.1+/4.9 mm) than in the patient cohort (9.1+/1.8 mm).

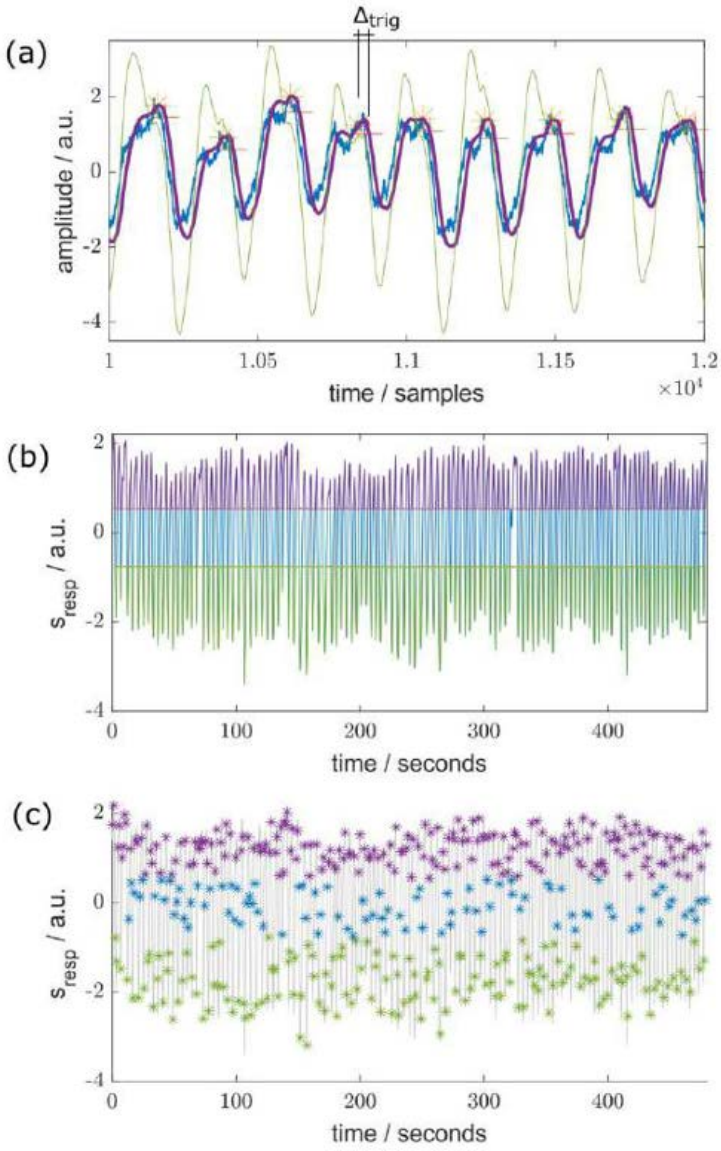

Figure 1. (a) Raw cardiac signal (blue), Kalman Filtered (purple), 1st derivative (green). PT triggers (red +, zero crossings of the 1st derivative) plotted against ECG R-peaks (yellow*). (b) Binning of datapoints into respiratory bins (Green: Expiration, Blue: Mid and Purple: Inspiration). (b) PT derived trigger points found for each bin in (a).

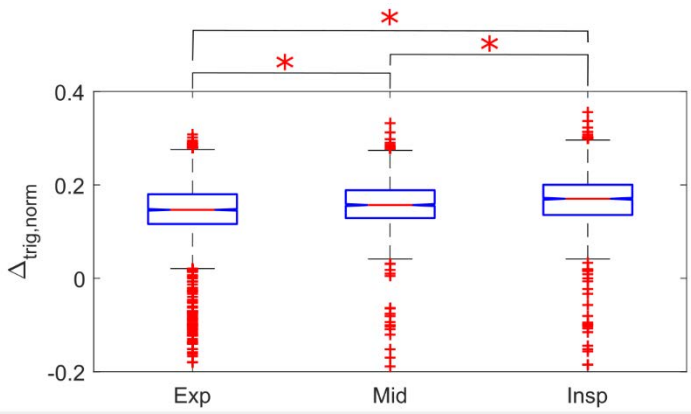

ANOVA Table

Source	SS	df	MS	F	Prob>F
Groups	0.6282	2	0.3141	88.79	6.79588e-39
Error	30.2337	8547	0.00354		
Total	30.8619	8549			

Figure 2. ANOVA results shown as boxplot for the volunteer cohort. $\Delta_{trig,norm}$ differ significantly between groups at the P<0.005 confidence level (red asterisks). Outliers are plotted as red +. No significant differences were observed between respiratory states in the patient cohort.

	Insp	Mid	Exp
Volunteers	in % of mean R-R interval		
mean delta	0.1643	0.1584	0.1462
std delta	0.0638	0.0499	0.0604
Patients			
mean delta	0.1773	0.173	0.1735
std delta	0.072	0.0696	0.0674

Table 1. Means and standard deviation of $\Delta_{trig,norm}$ in Expiration, Mid-respiration and inspiration stratified by volunteer and patient cohort. $\Delta_{trig,norm}$ is given in percent of the mean R-R interval in the corresponding respiratory state.

Conclusions

We found that in subjects with higher respiratory amplitude, trigger points are slightly shifted with respect to R-peak, whereas this effect is not significant when the respiratory amplitude is lower. Falcão et al.[3] found no significant difference in image quality when using PT derived motion data compared to self-gating, but when going to higher temporal resolutions, these small changes will potentially need to be considered. The observed differences in $\Delta_{trig,norm}$ are readily explained by the fact that BSS techniques are statistical in nature and healthy subjects tend to spend more time in expiration. Thus, these data points are weighted more strongly in the separation algorithm when training on free-breathing data. This could be mitigated by introducing data weighting based on respiratory state during this training phase.

References

1. Speier P, Fenchel M, Rehner R. PTNav: a novel respiratory navigation method for continuous acquisitions based on modulation of a pilot tone in the MRreceiver . In: Magnetic Resonance Materials in Physics, Biology and Medicine. Vol. 28. ; 2015. pp. 9798. doi: 10.1007/s1033401504872.

2. Bacher M, Dornberger B, Bollenbeck J, Stuber M, Speier P. Listening in on the Pilot Tone: A Simulation Study. In: Joint Annual Meeting of the ISMRM & ESMRMB, Virtual. ; 2021. p. 1364.

3. Falcão MBL, Di Sopra L, Ma L navigation for respiratory and cardiac motion resolved free, et al. (in press) Pilot Tone running 5D flow Magnetic Resonance Imaging. Magn. Reson. Med. 2021.

4. Bacher M, Gatehouse P, Wage R, et al. Performance Analysis of a Fully Automatic Real Time Capable Pilot Tone Cardiac Triggering Framework. Sess. 2020;63:412Proc. from 23rd Annu. SCMR Sci. 414.

Proceedings **SCMR Virtual Annual Scientific Sessions** (2022)
Abstract number **000215**
Abstract accepted as an Oral presentation.
My contribution: I provided the data for this study.

A2.1.6. Motion corrected free-running 4D MRI of the fetal heart - from in silico to in vivo

Robin Ferincz[1], Mariana B.L. Falcão[1], Aurelio Secinaro[2], Guido Buonincontri[3,4], Leonor Alamo[5], Estelle Tenisch[5], Milan Prsa[6], Davide Piccini[1,8,9], Jerome Yerly[7], Matthias Stuber[1,7], Christopher W. Roy[1]

[1]Department of Radiology, Lausanne University Hospital (CHUV) and University of Lausanne (UNIL), Switzerland
[2]Advanced Cardiothoracic Imaging Unit, Department of Imaging, Bambino Gesù Children's Hospital IRCCS, Rome, Italy
[3]Laboratory of Medical Physics and Magnetic Resonance, IRCCS Stella Maris, Pisa, Italy
[4]Imago 7 Research Center, Pisa, Italy
[5]Department of Radiology and Interventional Radiology, Lausanne University Hospital and University of Lausanne, Lausanne, Switzerland
[6]Woman- Mother-Child Department, Lausanne University Hospital and University of Lausanne, Lausanne, Switzerland
[7]Center for Biomedical Imaging (CIBM), Lausanne, Switzerland
[8]Advanced Clinical Imaging Technology (ACIT), Siemens Healthcare AG, Lausanne, Switzerland
[9]LTS5, École Polytechnique Fédérale de Lausanne (EPFL), Lausanne, Switzerland

Synopsis

MR imaging of the fetal heart is challenging due to resolution requirements and the impact of maternal respiration, fetal cardiac motion, and gross fetal movement. These factors have largely precluded the development of 3D acquisition techniques. In this work, a novel reconstruction algorithm is developed to estimate and correct for displacement of the fetal heart due to maternal respiration and gross fetal movement enabling the first ever motion-corrected time-resolved 4D images of the fetal heart from 3D radial data. Proof-of-concept results are demonstrated using a comprehensive numerical simulation developed for this work and initial data acquired in utero.

Introduction

Technical developments have driven the use of MRI to complement ultrasound in the evaluation of the fetal heart, providing new ways to manage cardiovascular diseases detected in utero [1]. Fetal cardiac MRI acquisitions are designed with the shortest scan times possible to avoid artifacts and blur from maternal respiratory motion, fetal cardiac motion, and gross fetal movement. A balance must therefore be struck between the need for abbreviated scan times, the spatial resolution necessary to visualize the small vessels and chambers of the fetal heart, the temporal resolution needed to resolve the fast fetal heart rate, and the volumetric coverage required to interrogate the complex 3D cardiac anatomy. As a result, a series of 2D images combined with motion-correction, scattered data interpolation and super-resolution algorithms [2,3] provide a surrogate for dynamic 3D (4D) MRI evaluation of the fetal heart. However, 2D acquisitions may be limited by through-plane motion and have a constrained spatial resolution in the slice selection direction. Alternatively, the use of 3D acquisitions has recently been proposed, greatly simplifying scan planning [4,5], but no methods for motion-compensation have been published to date. In this work, we therefore propose a novel reconstruction method for 4D MRI of the fetal heart using a continuous 3D radial acquisition with isotropic spatial resolution. Our proposed reconstruction algorithm retrospectively identifies and corrects both displacement of the fetal heart due to maternal respiration as well as gross fetal movement. To validate our approach and to inform in utero parameter ranges, a complex numerical simulation framework is developed providing a

necessary but not yet available ground truth for developing 3D fetal imaging techniques. Here, we present our initial findings using our numerical phantom and demonstrate the first ever motion-corrected 4D images of the fetal heart from 3D radial data acquired in utero.

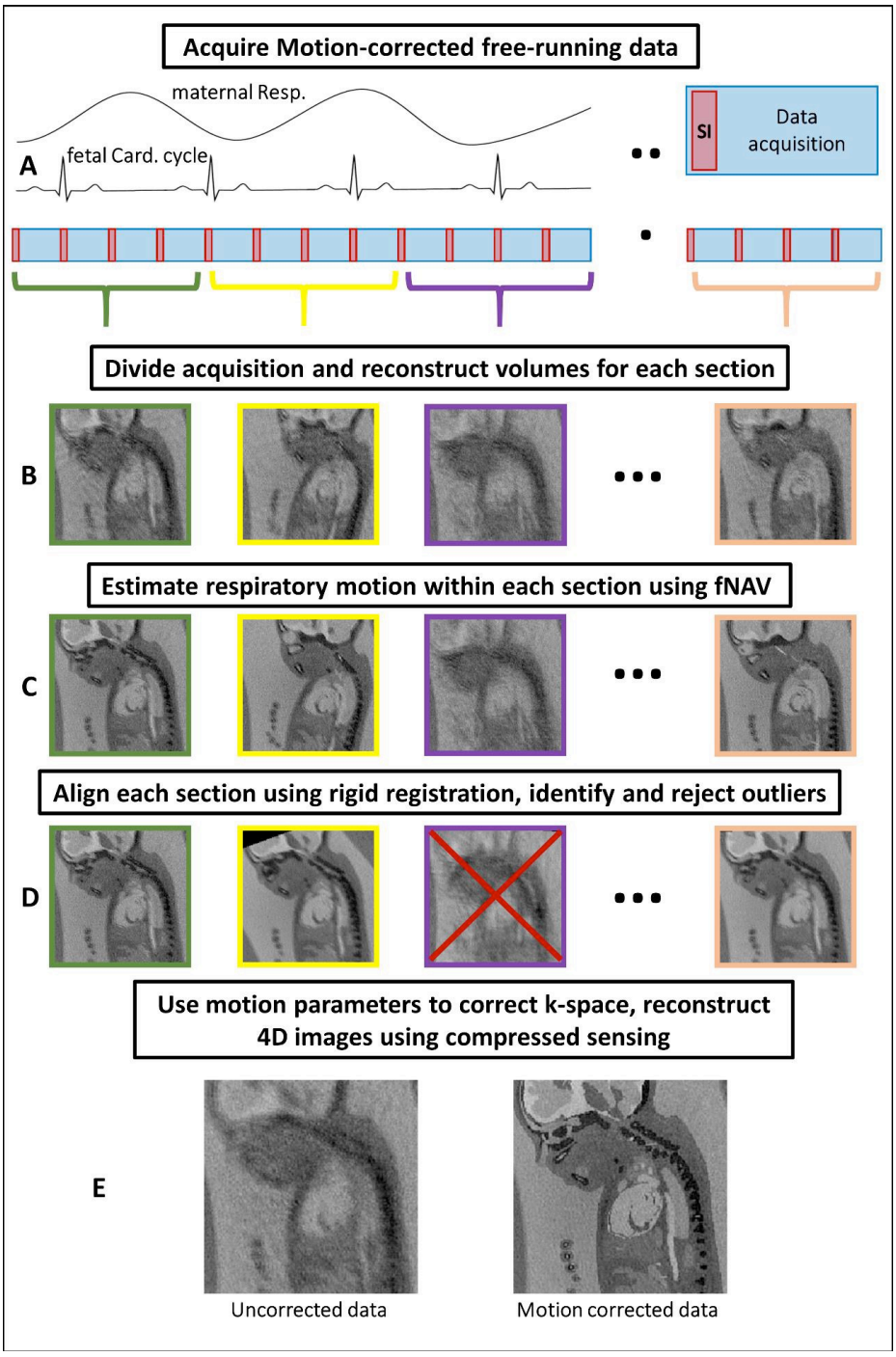

Figure 1. Schematic of the reconstruction algorithm. A continuous 3D radial acquisition (A) is divided into 16 bins of ~15 s each (B), which are then processed, corrected (C) for maternal respiration (fNAV) 6 and (D) bulk fetal movement (rigid registration and outlier rejection). The motion-corrected k-space data are then binned into cardiac phases and reconstructed using compressed sensing to obtain 4D images (E).

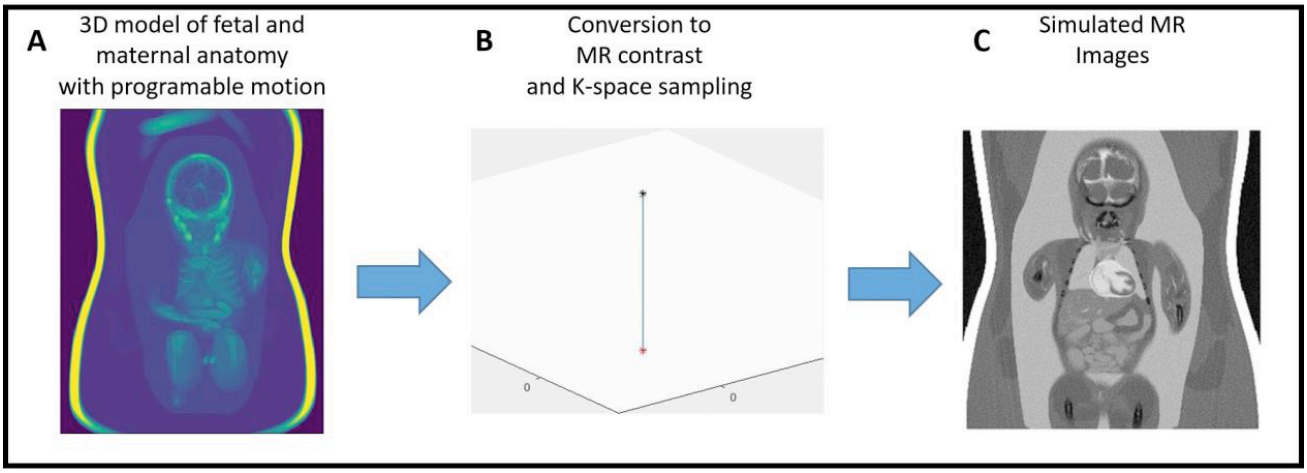

Figure 2. Animated depiction of the numerical simulation framework. (A) Programmable translational and rotational motion are applied to a labeled 3D model of the maternal and fetal anatomy. The labeled data are converted to MRI contrast using an analytical signal equation and (B) sampled with a user-defined k-space trajectory. (C) Finally, simulated MR images are reconstructed.

Methods

Fig.1 outlines the proposed algorithm for estimating displacement of the fetal heart due to maternal respiration [6] and gross fetal movement by exploiting intermediate "real-time" reconstructions of 3D radial data. The motion estimates are used to correct the k-space data and reject outliers [2]. The remaining data are retrospectively binned according to their cardiac phase and reconstructed as 4D images [8]. To characterize this algorithm, we designed a comprehensive numerical simulation of the maternal and fetal anatomy (**Fig.2**) [7]. It includes 3D programmable motion (respiration and bulk movement), MR contrast and 3D k-space sampling schemes. In silico data sets (N=50) were generated with maximum 3D translational motion amplitudes of 10 mm, maximum 3D rotation of 5°, and scan parameters matching in utero data. One pregnant volunteer who gave consent (32 weeks gestational age) was scanned using a previously described free-running 3D radial bSSFP research sequence 8 without fat suppression or ramp-up pulses, on a 1.5T clinical MRI scanner (MAGNETOM Aera, Siemens Healthcare, Erlangen, Germany). For in silico data, motion-corrected, and uncorrected images were compared and the image blur relative to the ground truth was measured [9]. For in utero data retrospective binning in to 20 cardiac phases was performed using an MRI compatible Doppler ultrasound gating device [10] and compressed sensing reconstruction was performed using spatial and temporal regularization weights of 0.001 and 0.05 respectively. 4D in utero images were visually inspected using Circle (cvi42, Circle Cardiovascular Imaging, Calgary, Canada).

Results

Bulk fetal movement is well visualized by real-time reconstructions (**Fig.3a**) of the in silico data, as shown in transversal, sagittal, and coronal orientations. When compared to the motion-free reference (**Fig.3b**), this movement leads to significant blur in the uncorrected images. Conversely, the motion-corrected images recover fine details of the heart despite the underlying maternal respiration and gross fetal movement. Quantitative measurement of image blur corroborates this visual result with corrected images yielding low amounts of blur (0.5±0.3) relative to the uncorrected image (3.3±0.1).

Fig.4 provides a comparison between uncorrected and motion-corrected images obtained in utero. A clear improvement in image quality and delineation of the fetal cardiac anatomy is obtained using

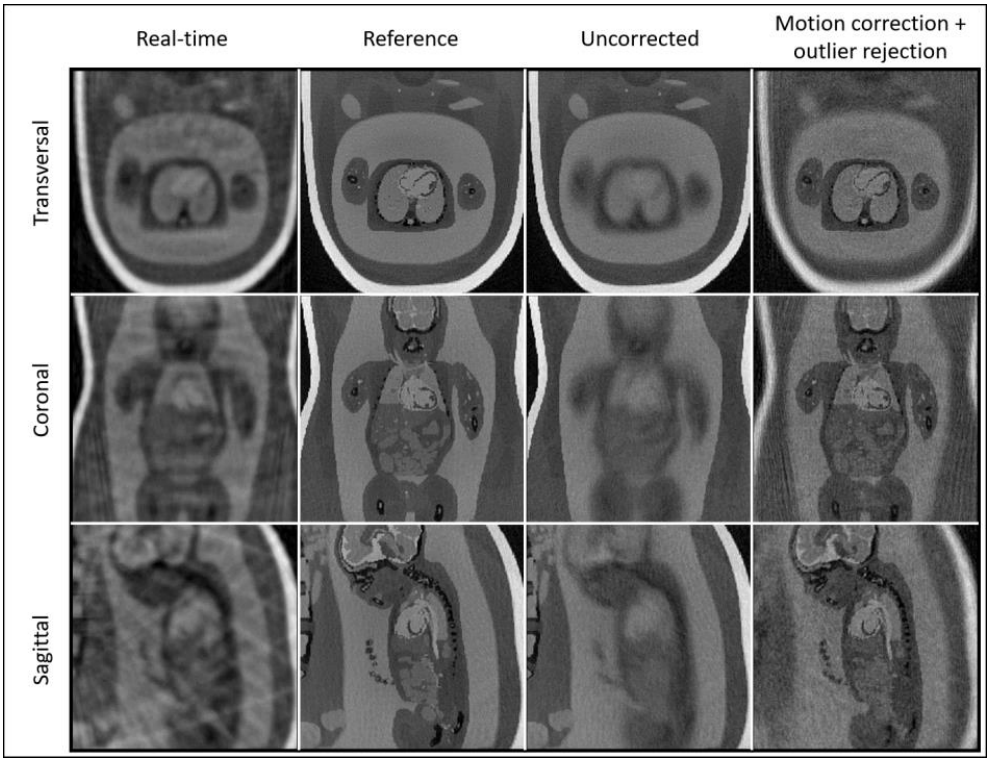

Figure 3. Reconstruction of in silico 3D radial data wherein programmable displacement of the fetus due to maternal respiration and bulk fetal movement is visualized by a real-time reconstruction (A). Final reconstructed images are also shown in transversal, sagittal, and coronal views with (D) and without (C) the proposed motion-correction algorithm in comparison to the ground truth motion-free reference (B).

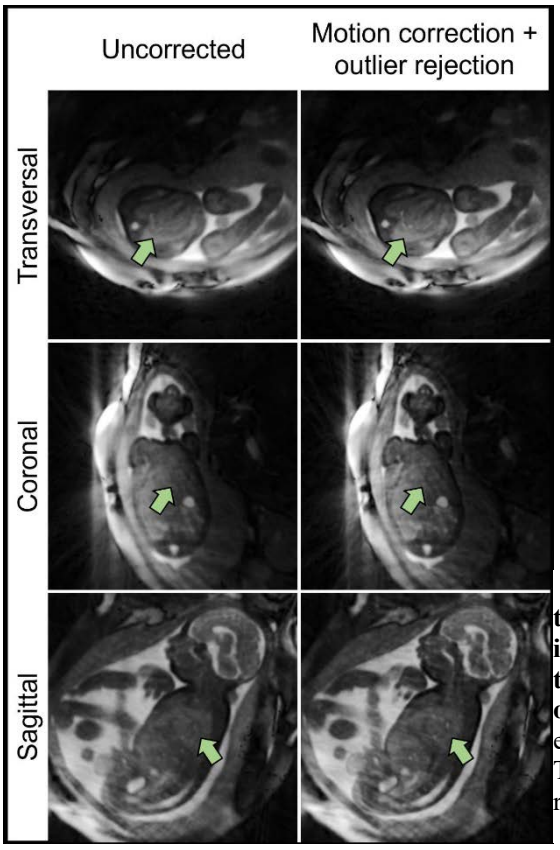

Figure 4. Reconstruction of in vivo 3D radial data. Images in transversal, sagittal, and coronal views demonstrated a clear improved visualization of the fetal heart (green arrows) using the proposed motion-correction algorithm relative to the original uncorrected data. Relevant scan parameters include RF excitation angle: 50°, resolution: (1.5 mm)3, FOV (288 mm)3, TE/TR: 1.44/2.88 ms, readout bandwidth: 814 Hz/pixel, 87494 radial readouts, and total scan time: ~ 6 minutes.

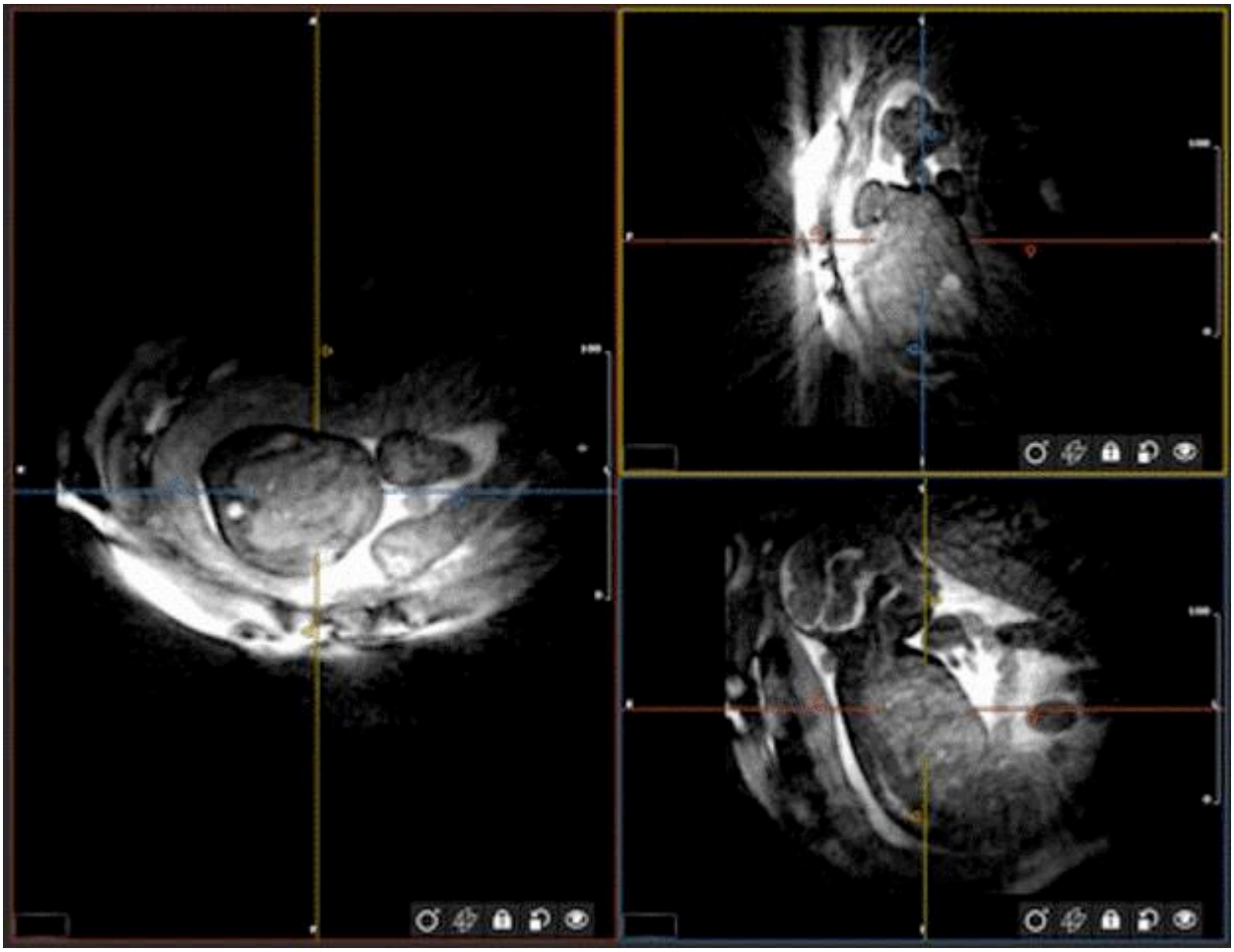

Figure 5. Animation of 4D images of the fetal heart using the proposed reconstruction algorithm. Beginning with a transverse view (left), coronal view (top right), and sagittal view (bottom right), synchronized movement between the 3 scan planes is shown, highlighting the ability to retrospectively interrogate the dynamic 3D data, finally reaching a short-axis view in the top right, due to the isotropic spatial resolution provided by this technique.

motion-correction, corroborating the in-silico result. However, streaking artifact originating from the high maternal fat signal remains. Finally, **Fig.5** provides an animation of the final 4D image reconstructions from in utero data highlighting the ability to retrospectively interrogate the dynamic anatomy of the fetal heart in arbitrary scan planes due to the 3D isotropic spatial resolution and large volumetric coverage achieved by this technique.

Discussion and Conclusion

A novel algorithm for motion-corrected dynamic volumetric imaging of the fetal heart was developed. Its initial use was investigated using a numerical simulation and its feasibility was demonstrated in utero providing the first ever motion-corrected 4D images of the fetal heart from a continuous 3D radial acquisition. Further investigation is required to determine the degree of motion that can be accurately corrected. Additionally, improvements to the acquisition are needed to reduce artifacts unrelated to motion. Nevertheless, the numerical simulation provided by this work already creates a tool for exploring the impact of motion, as well as future optimizations. This is all in keeping with the goal of providing a high resolution volumetric assessment of the fetal heart for continued improvement in our ability to manage cardiovascular disease discovered in utero.

References

1. Roy CW, van Amerom JFP, Marini D, Seed M, Macgowan CK. Fetal Cardiac MRI: A Review of Technical Advancements. Top Magn Reson Imaging. 2019 Oct;28(5):235-244.
2. van Amerom JFP, Lloyd DFA, Deprez M, Price AN, Malik SJ, Pushparajah K, van Poppel MPM, Rutherford MA, Razavi R, Hajnal JV. Fetal whole-heart 4D imaging using motion-
corrected multi-planar real-time MRI. Magnetic Resonance in Medicine. 2019 May;82(3):1055-1072.
3. Roberts TA, van Amerom JFP, Uus A, Lloyd DFA, van Poppel MPM, Price AN, Tournier JD, Mohanadass CA, Jackson LH, Malik SJ, Pushparajah K, Rutherford MA, Razavi R, Deprez M, Hajnal JV. Fetal whole heart blood flow imaging using 4D cine MRI. Nature Communications. 2020 Oct;11(4992).
4. Piek M, Ryd D, Töger J, Testud F, Hedström E, Aletras AH. Fetal 3D cardiovascular cine image acquisition using radial sampling and compressed sensing. Magn Reson Med. 2022 Sep;1-11.
5. Knapp J, Tavares de Sousa M, Lenz A, Herrmann J, Zhang S, Kording F, Hergert B, Adam G, Bannas P, Schoennagel BP. Fetal 4D flow MRI of the great thoracic vessels at 3 Tesla using Doppler-ultrasound gating: a feasibility study. Eur Radiol. 2022 Oct.
6. Roy CW, Heerfordt J, Piccini D, Rossi G, Pavon AG, Schwitter J, Stuber M. Motion compensated whole-heart coronary cardiovascular magnetic resonance angiography using focused navigation (fNAV). J Cardiovasc Magn Reson. 2021 Mar;23(1):33.
7. Roy CW, Marini D, Segars WP et al. Fetal XCMR: a numerical phantom for fetal cardiovascular magnetic resonance imaging. J Cardiovasc Magn Reson. 2019 May;21(29).
8. Di Sopra L, Piccini D, Coppo S, Stuber M, Yerly J. An automated approach to fully self-gated free-running cardiac and respiratory motion-resolved 5D whole-heart MRI. Magn Reson Med. 2019 Dec;82(6):2118-2132.
9. Roy CW, Seed M, Kingdom JC, Macgowan CK. Motion compensated cine CMR of the fetal heart using radial undersampling and compressed sensing. J Cardiovasc Magn Reson. 2017 Mar;19(29).
10. Kording F, Yamamura J, de Sousa MT, Ruprecht C, Hedström E, Aletras AH, Ellen Grant P, Powell AJ, Fehrs K, Adam G, Kooijman H, Schoennagel BP. Dynamic fetal cardiovascular magnetic resonance imaging using Doppler ultrasound gating. J Cardiovasc Magn Reson. 2018 Mar;20(1):17.

Proceedings **ISMRM & ISMRT Annual Meeting & Exhibition** (2023)
Abstract number **6595**
Abstract accepted as an Oral presentation at a combined Educational and Scientific session.
My contribution: I provided counseling on the interpretation of the results and I helped in the signal extraction pipeline.

A2.2. Free-running PC-MRI framework related developments

A2.2.1. Free-running 5d Flow MRI: Impact of Respiratory States Resolution on Image Quality and Flow Quantification

E. Weiss[1]; C. Rigsby[2]; J. Robinson[3]; J. Baraboo[1]; L. Ma[1]; M. B. L. Falcão[4]; C. Roy[4]; M. Stuber[4]; M. Markl[1]

[1]Department of radiology, Northwestern University Feinberg School of Medicine, Chicago, United States of America;
[2]Medical imaging, Ann & Robert H. Lurie Children's Hospital of Chicago, Chicago, United States of America;
[3]Pediatric cardiology, Ann & Robert H. Lurie Children's Hospital of Chicago, East Chicago Avenue, Chic ago, United States of America;
[4]Department of Radiology, Lausanne University Hospital (CHUV) and University of Lausanne (UNIL), Lausanne, Switzerland,

Background

Free running 5D flow MRI is a novel technique that enables fully self-gated (cardiac and respiration) measurement of respiratory resolved blood flow. This may be particularly useful in patients with venous abnormalities, such as those with a Fontan connection, where respiration is a known driver of flow[1]. While previous studies have used 4 respiratory state (RS) bins, it is not clear how many bins are necessary to characterize respiratory driven flow. The reduction of the number of RS bins to 2 or 3 would allow for reduced scan time and/or improved image quality (increased number of k-space per bin). The purpose of this study was to systematically investigate the impact of number of RS on image quality and ability to measure respiration driven flow changes.

Methods

5D flow MRI[2], a radially sampled, fully self-gated scan, was acquired in 5 patients with congenital heart disease who received ferumoxytol for a clinically indicated CMR study. All data sets were reconstructed with 2, 3 and 4 RS bins (9 bins per patient) where each reconstructed bin is a full 4D flow data set (TR=40ms, spatial resolution=2x2x2 mm). 5D flow data analysis included background phase correction, velocity anti-aliasing and quantification of net flow across 2D planes at the following anatomic locations: main pulmonary artery (MPA) or left and right pulmonary arteries (LPA and RPA) in subject 2, ascending aorta (AAo), descending aorta (DAo) at the level of the MPA, inferior vena cava (IVC), and superior vena cava (SVC), bilaterally if applicable. The range of the net flow (max flow-min flow) was measured for each vessel in each reconstruction. Image quality was qualitatively assessed between reconstructions.

Results

One patient was excluded due to poor image quality. The remaining cohort (10.8+5.3y, 1 female) is described in **Table 1**. Example images for subject 4 are shown in **Fig.1a-f**. These demonstrate improved image quality, as evidenced by qualitatively sharper vessel boundaries, when reconstructed with fewer RS bins. With respect to respiratory resolved net flow, the trend for respiration driven changes was consistent within each patient across the 3 reconstructions (ex. **Fig.1h-i**). Across all subjects and vessels, there was a significant decrease in the range captured between the 4 bin and the

2 bin reconstructions (3.2mL p<0.001, **Fig.2**), but flow changes were similar between the 4 bin and 3 bin reconstructions (1.4mL decrease, p=0.054, **Fig.2**). Similar findings were observed when only caval veins and MPA, which have expected respiratory driven flow, were included in the comparison (4.1mL, p=0.005, **Fig.2**).

Subject	GA	Age (y)	Gender	Anatomy
1	Y	2.9	M	Partial anomalous pulmonary venous return and large superior sinus venosus septal defect with left to right shunting
2	N	13.9	M	Hypoplastic left heart syndrome status-post Fontan procedure and coarctation of the aorta
3	N	13.7	M	Loeys-Dietz Syndrome status-post valve sparing aortic root replacement for aortic root dilation
4	N	12.5	F	Closed superior sinus venosus ASD, partial anomalous pulmonary venous return status-post warden procedure, left SVC patent and drains to coronary sinus

Table 1. Summary of cohort included in analysis.

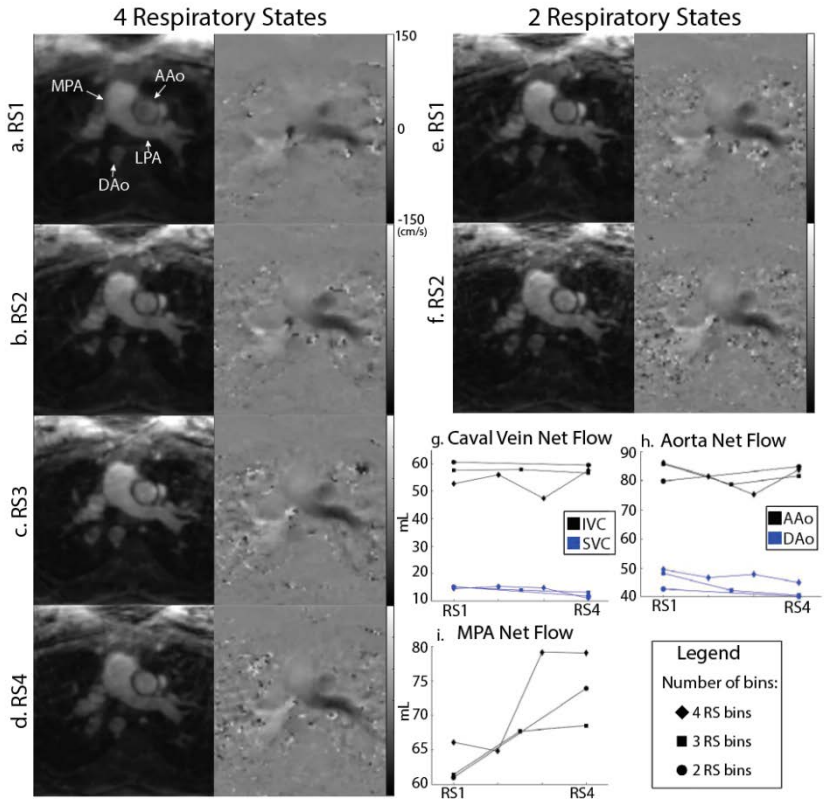

Figure 1. Magnitude and right-left phase images for subject 4 reconstructed using 4 (a-d) and 2 bins (e-f). There was increased sharpness in the 2 RS bin reconstructions. Increased MPA flow was visualized as respiration progressed. Absolute net flow values are reported for each vessel and reconstruction (g-i).

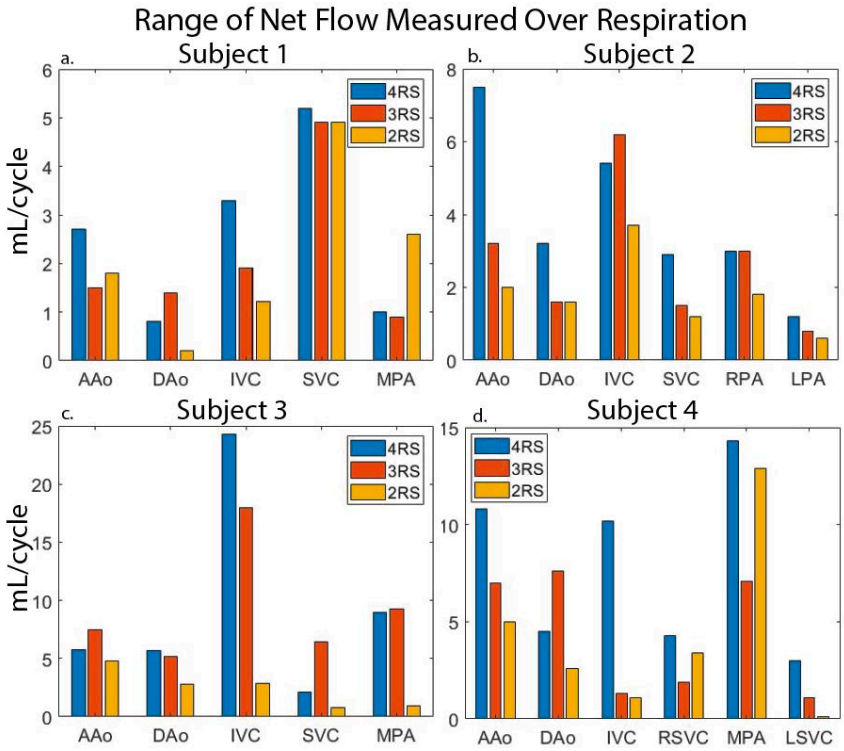

Figure 2. The range of net flow measured across the respiratory cycle for each vessel measured in all 4 patients (a-d) across all 3 reconstructions.

Conclusions

The number of RS reconstructed impacts the ability to measure respiration driven flow. Two RS bins were insufficient whereas respiratory driven net flow differences for 3 bins were equivalent to 4 bins in our small feasibility study cohort. Using 3 RS bins instead of 4 allows for a shorter scan time or increased data per bin to improve image quality which was qualitatively seen in all patients. Future studies in larger cohorts are needed to assess reconstruction impact on other flow metrics such as peak velocity.

References

1. van der Woude, S. F., Rijnberg, F. M., Hazekamp, M. G., Jongbloed, M. R., Kenjeres, S., Lamb, H. J., ... & Wentzel, J. J. (2021). The influence of respiration on blood flow in the Fontan circulation: insights for imaging-based clinical evaluation of the total cavopulmonary connection. Frontiers in Cardiovascular Medicine, 8.

2. Ma, L. E., Yerly, J., Piccini, D., Di Sopra, L., Roy, C. W., Carr, J. C., ... & Markl, M. (2020). 5D flow MRI: a fully self-gated, free-running framework for cardiac and respiratory motion–resolved 3D hemodynamics. Radiology: Cardiothoracic Imaging, 2(6), e200219.

Proceedings **SCMR Virtual Annual Scientific Sessions** (2022)
Abstract number **000187**
Abstract accepted as an Oral presentation.
Early career Award Finalist.

My contribution: I provided counseling on the analysis and interpretation of the different reconstructions performed with a different number of respiratory phases.

A2.2.2. RR-Resolved 5D flow for Decoding the Impact of Cardiac Rhythm on Left Atrial Flow Dynamics in Atrial Fibrillation and Stroke

J. Baraboo[1]; E. Weiss[1]; L. Ma[1]; J. Hwang[1]; S. Gunasekaran[1]; M. B. L. Falcão[2]; C. Roy[2]; M. Stuber[2]; R. Passman[6]; D. Kim[7]; M. Markl (1)
E. Weiss[1]; C. Rigsby[2]; J. Robinson[3]; J. Baraboo[1]; L. Ma[1]; M. B. L. Falcão[4]; C. Roy[4]; M. Stuber[4]; M. Markl[1]

[1]Department of radiology, Northwestern University Feinberg School of Medicine, Chicago, United States of America;
[2]Department of Radiology, Lausanne University Hospital (CHUV) and University of Lausanne (UNIL), Lausanne, Switzerland,
[3]Department of cardiology, Northwestern University Feinberg School of Medicine, Chicago, United States of America
[4]Room 1600, University Northwestern, Evanston, United States of America

Background

Atrial fibrillation (AF) is the most common sustained cardiac arrhythmia. Impaired left atrium (LA) hemodynamics, slow blood flow velocities and blood stasis, have been implicated in increased risk for LA thrombus formation and cardioembolic stroke[1,2]. RR-resolved 5D flow is a novel MRI technique to acquire time-varying 3D anatomic and velocity measures for varied RR-interval durations during cardiac arrhythmia (**Fig.1**)[3]. LA peak velocities and blood stasis can be measured across a range of RR interval durations to assess the impact of changes of heart rates on atrial hemodynamics. The purpose of this study was to apply RR-resolved 5D flow MRI in a cohort of AF patients with and without a history of stroke. We hypothesize that AF patients with prior stroke will have greater impaired RR-resolved LA hemodynamics (lowered peak velocities, higher LA stasis) than AF patients who have not had a stroke.

Methods

24 AF patients (68 ± 8 years old, 5 female) undergoing cardiac MRI with RR-resolved 5D Flow were retrospectively enrolled (venc = 100 cm/s, FOV = 250×250×250 mm3, TE/TR = 2.93/4.70 ms, flip angle= 7°, temporal resolution = 40 ms, spatial resolution= 2.5x2.5x2.5 mm3). 8 AF patients had a history of stroke and 16 had no stroke history. RR-resolved 5D flow reconstruction included sorting k-space data based on RR-interval where each RR bin had the same number of RR-intervals (RR1 to RR4, **Fig.1**). The RR distribution coefficient of variation (RR-std/RR-mean, CoV) was calculated per patient. RR-resolved 5D flow data analysis included background phase correction, velocity anti-aliasing, and manual 3D segmentation of the LA (Mimics, Materialise, Belgium). Blood stasis was calculated per voxel as the percentage of cardiac time with absolute LA velocity < 10 cm/s and then averaged over the segmented LA region to determine mean stasis. Peak velocities were calculated as the mean of the top 5% of velocities. T-test or Wilcoxon ranksum test was used to determine significant differences ($\alpha = .05$).

Results

The RR variability during acquisition was similar between stroke and no-stroke groups (RR distribution CoV not significantly different between groups, 0.18 ± 0.10 vs 0.14 ± .07, p = 0.34). RR-resolved 5D flow derived mean stasis and peak velocities demonstrated trends, though non-significant,

for lowered peak velocities (represented in **Fig.2**) and higher stasis per RR bin comparison for the stroke history AF subgroup compared to the no stroke AF subgroup (**Fig.3**). Stasis and peak velocity percent differences between groups ranged from 4% to 16%. Largest differences were observed for RR1 bin between AF stroke history vs no stroke history for peak velocity (0.21 ± 0.04 m/s vs 0.24 ± .05 m/s, 16% percent difference, p = 0.10) and stasis (69 ± 12% vs 66 ± 14%, 11% percent difference, p = 0.17, **Fig.3**).

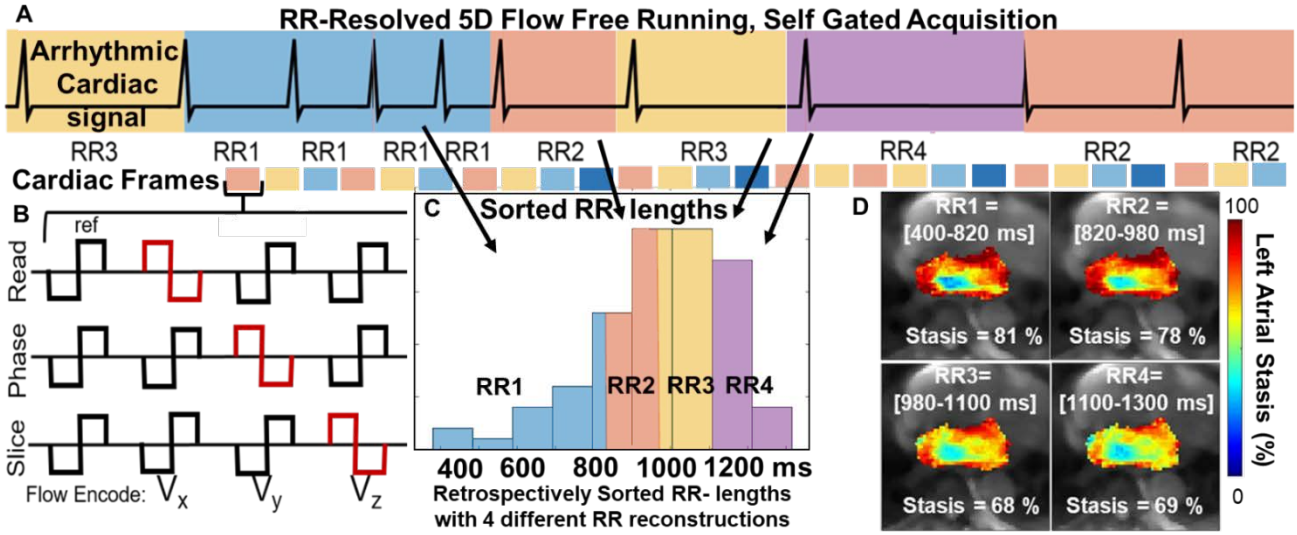

Figure 1. A) RR-Resolved 5D Flow is a free running acquisition that retrospectively determines RR interval duration and cardiac time frames. B) 3D time varying velocity is encoded through bipolar gradients. C) RR-durations are sorted into 4 RR-bins (RR1 to RR4) for reconstruction. D) Stasis (shown: 2D axial maps) and peak velocity are derived per bin.

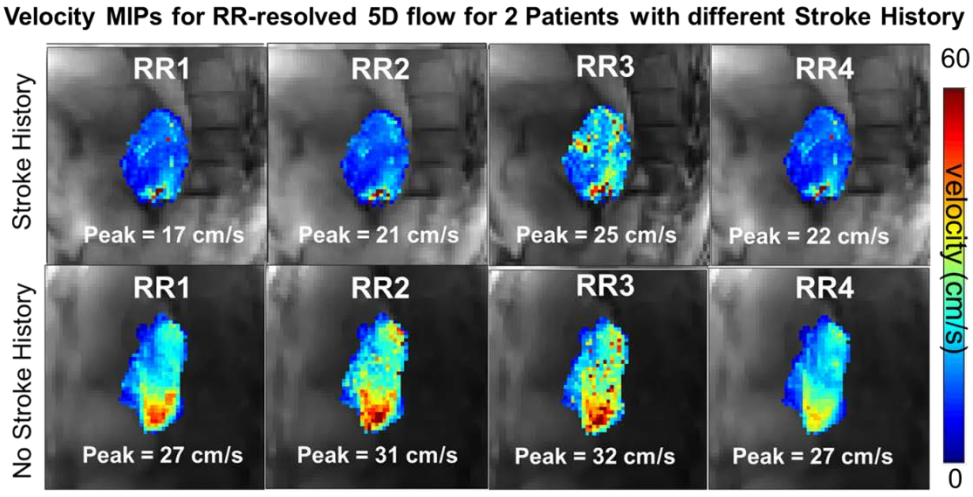

Figure 2. RR-resolved left atrial (LA) peak velocity maps (sagittal maximum intensity projections) for AF patients with stroke history (top) and no stroke (bottom). Most pronounced differences in LA velocities were seen for the shortest RR-interval duration (RR1 bin) with diminishing differences for longer RR-intervals (RR2-4 bins).

Conclusions

We demonstrated a trend towards lowered LA peak velocities and higher stasis in AF patients with a stroke history compared to those with no stroke history. Largest, though still non-significant, percent

differences were in shorter RR intervals (RR1 bin) likely to be either rejected or averaged with less discriminatory heartbeat hemodynamics by other non RR-interval resolved acquisitions. This study was limited due CoV heterogeneity with more patients needed for further rhythm (maintaining sinus v acquisition) stratification and examination.

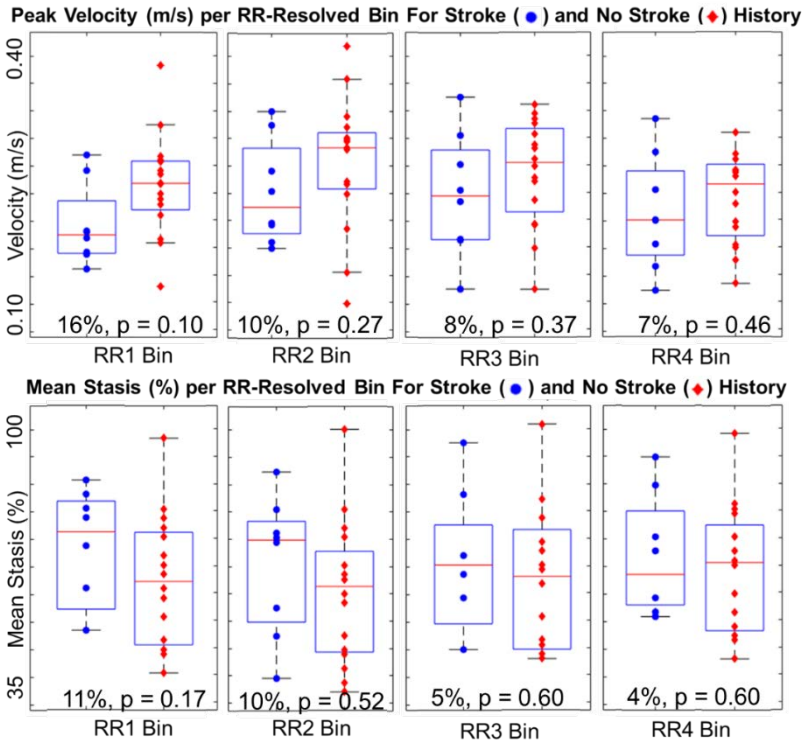

Figure 3. Left atrial peak velocity (top) and mean stasis (bottom) boxplots per RR bin for AF patients with stroke history (n = 8, blue circles) and with no stroke history (n = 16, red diamonds). Absolute mean percent differences are shown with p- values. Peak velocities trended lower and stasis trended higher for AF patients with prior stroke.

References

1. Handke M, Harloff A, Hetzel A, Olschewski M, Bode C, Geibel A. Left Atrial Appendage Flow Velocity as a Quantitative Surrogate Parameter for Thromboembolic Risk: Determinants and Relationship to Spontaneous Echocontrast and Thrombus Formation-– A Transesophageal Echocardiographic Study in 500 Patients with Cerebral Ischemia. J Am Soc Echocardiogr. 2005;18(12):1366 1372. doi:10.1016/J.ECHO.2005.05.006

2. Lowe GDO. Virchow's Triad Revisited: Abnormal Flow. Pathophysiol Haemost Thromb. 2003;33(56):455457. doi:10.1159/000083845

2. Ma L, Yerly J, Sopra L Di, et al. Using 5D flow MRI to decode the effects of rhythm on left atrial 3D flow dynamics in patients with atrial fibrillation. Magn Reson Med. 2021;85(6):3125 3139. doi:10.1002/MRM.28642

Proceedings **SCMR Virtual Annual Scientific Sessions** (2022)
Abstract number **000428**
Abstract accepted as an Oral presentation.
My contribution: I provided counseling on the interpretation of the results.

A2.2.3. Free-Running 5D Flow MRI: Impact of Cardiac Temporal Resolution on Flow Quantification

Elizabeth K. Weiss[1,2], Cynthia K. Rigsby[3], Joshua D. Robinson[3], Justin Baraboo[1,2], Liliana Ma[1,2], Mariana B. L. Falcão[4], Christopher W. Roy[4], Matthias Stuber[4], and Michael Markl[1,2]

[1]Biomedical Engineering, Northwestern University, Evanston, IL, United States, Radiology,
[2]Feinberg School of Medicine, Chicago, IL, United States,
[3]Medical Imaging, Lurie Children's Hospital, Chicago, IL, United States,
[4]Radiology, Lausanne University Hospital (CHUV) and University of Lausanne (UNIL), Lausanne, Switzerland

Synopsis

The flexible reconstruction of 5D flow MRI data may be particularly beneficial in pediatric cases where cardiac cycle length varies greatly. We compared flow measurements from 5D flow and 2D phase contrast. 5D flow data was reconstructed using either a cardiac bin width of 40ms or that matching the 2D phase contrast reconstruction. We find excellent correlation of both 5D flow reconstructions with 2D phase contrast. There is overestimation of arterial flow measures by 5D flow, with most overestimation by the short temporal resolution reconstruction. Further study should additionally compare with 4D flow MRI.

Introduction

Free-running 5D flow MRI is a novel technique that enables fully self-gated cardiac and respiratory motion-resolved measurements of blood flow over a 3D volume[1]. Data acquisition utilizes highly accelerated radial k-space sampling, followed by sorting of k-space lines in flexible user defined cardiac and respiratory bins, and subsequent compressed sensing reconstruction (5D = 3D + cardiac time + respiration). Several previous 5D flow studies have used similar cardiac temporal resolution - approximately 40ms, and 4 respiratory states (end-expiration to inspiration)[2-4]. However, the impact of the selection of the 5D flow cardiac temporal resolution on the accuracy of flow quantification has not been systemically investigated. Since 5D flow is a useful tool in studying congenital heart disease (CHD), such as single ventricle physiology[1], this may be particularly relevant in young pediatric patients with known higher heart rates. It is thus important to investigate the impact of cardiac phase resolution on flow measurement in the pediatric population. We aimed to investigate whether increasing the temporal resolution in pediatric patients with CHD would improve 5D flow agreement with the clinically standard 2D phase contrast MRI.

Methods

5D flow MRI[2] was acquired in 6 patients with CHD who received ferumoxytol during a clinically indicated cardiac MR study. All patients received 2D phase contrast (PC) MRI in at least two vessels. 2D-PC MRI (spatial resolution: 1.1-1.3x1.1-1.3mm, temporal resolution: 16.1-28ms, venc: 80-250cm/s) was acquired over 1 minute during a breath hold if under general anesthesia or free breathing otherwise and the images were retrospectively cardiac gated using EKG (**Fig.1a**). Each 5D flow dataset (FOV: 150-200x150-200mm, spatial resolution: 1.5mm-2mm isotropic, venc: 150cm/s) was reconstructed twice: once with 40ms cardiac temporal resolution (T_s) and once with a higher temporal resolution, matching that of the 2D-PC MRI reconstructed images (herein called short T_s

reconstruction). 2D-PC temporal resolutions are listed in **Table 1**. All 5D-flow reconstructions used 4respiratory states (RS, **Fig.1b**). Net flow and peak flow were measured in each vessel with a corresponding 2D-PC MRI measurement (**Fig.2a**) using commercial software (Circle CVI, Calgary, Canada). Bland Altman analysis was used to assess agreement between 2D-PC and each of the RS bins of5D flow MRI. Results were reported as percent difference bias ± limits of agreement (LOA). Data was stratified on vessel type (vein/artery).

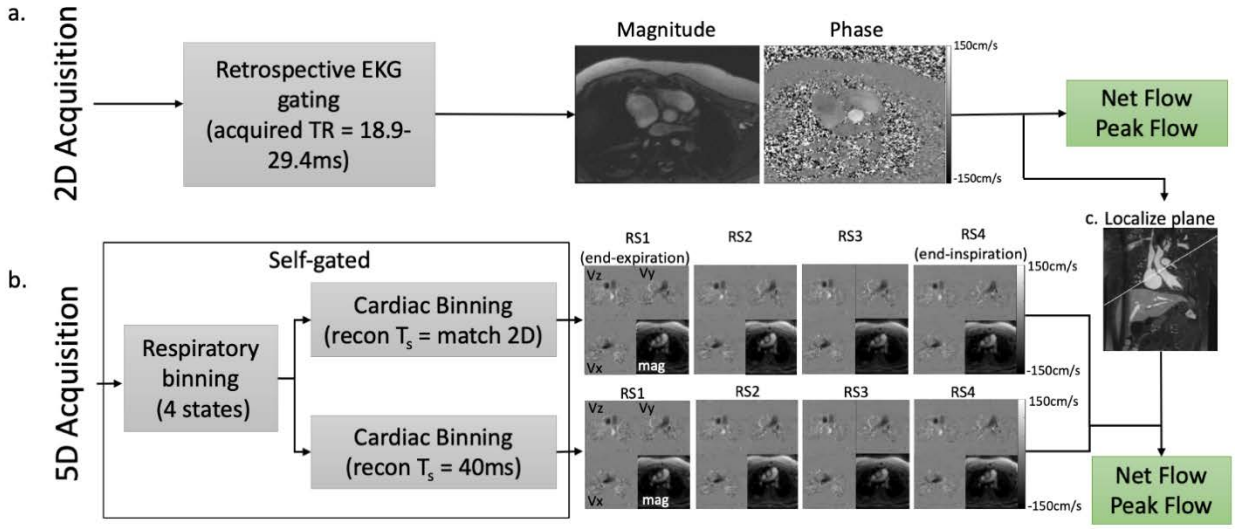

Figure 1. Acquisition, reconstruction, and analysis workflow schematic. 2D phase contrast **(a)** was acquired with retrospective EKG gating and net flow and peak flow were measured. 5D flow acquisition **(b)** was followed by off-line reconstruction using 4 respiratory states (RS) and a T_s= 40ms and with a temporal resolution matching that of the 2D phase contrast acquisition (short T_s reconstruction). Cross-referenced MR angiograms **(c)** were used to localize the 2D acquisitions to enable flow measurement in the comparable location in the 5D flow MRI data set.

Sub	GA	Age (yrs)	G	2D-PC recon T_s (ms)	Locations with 2D-PC	Anatomy
1	Y	2.9	M	27.2	AV, PV	Partial anomalous pulmonary venous return and large superior sinus venosus septal defect with left to right shunting
2	N	13.9	M	28.0	AV, LPA*, IVC, SVC	Hypoplastic left heart syndrome status-post Fontan procedure and coarctation of the aorta
3	N	13.7	M	16.1	AV, PV	Loeys-Dietz Syndrome status-post valve sparing aortic root replacement for aortic root dilation
4	N	12.5	F	18.1	AV, PV, LPA, RPA	Closed superior sinus venosus atrial septal defect, partial anomalous pulmonary venous return status-post warden procedure, left SVC patent and drains to coronary sinus
5	Y	2.2	M	26.6	AV, LPA, RPA, IVC, SVC, DAo	Double inlet left ventricle, status-post pulsatile Glenn procedure
6	Y	7	M	20.8	AV, PV, LPA, RPA	Left pulmonary artery sling, status-post repair

Table 1. Summary of cohort included in analysis (GA=general anesthesia, G=gender, T_s= temporal resolution). Anatomical Abbreviations: AV – above aortic valve, PV – above pulmonic valve, LPA – left pulmonary artery, RPA – right pulmonary artery, IVC – inferior vena cava, SVC – superior vena cava, DAo– descending aorta. *RPA 2D-PC was acquired incorrectly in the LPA and was excluded.

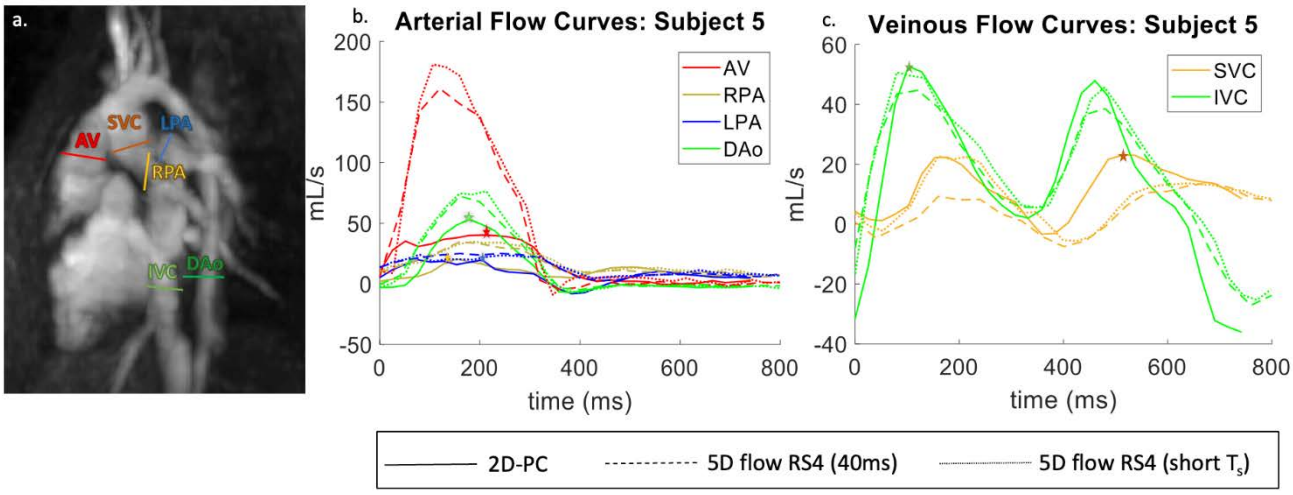

Figure 2. Planes were placed on a 5D flow derived 3D MR angiogram to correspond with 2D-PC plane placement (a). Example flow curves from subject 5 are shown for arteries **(b)** and veins **(c)** measured. Net flow, area under the curve, and peak flow, marked by a star, were measured. Initial Bland-Altman analysis is stratified by venous vs arterial measurement. Anatomical Abbreviations: AV – above aortic valve, LPA – left pulmonary artery, RPA – right pulmonary artery, IVC – inferior vena cava, SVC – superior vena cava.

Results

The study cohort (8.7±5.4yrs, 1 female, HR: 91±22 bpm) demographics are described in **Table 1**. Flow curves for subject 5 are shown in **Fig.2**, demonstrating the distinct difference in flow for arterial and venous measurements. In arteries, we found that both 5D flow reconstructions significantly overestimated 2D-PC net flow. Further, the short T_s reconstruction overestimated arterial peak flows in all RS bins (**Table 2**). Correlation of 5D flow with 2D-PC MRI was excellent in arterial measures ($R^2 > 0.91$). In veins, there was no significant bias for any reconstruction or metric. Good correlation was seen in venous measures (net flow: $R^2 > 0.72$; peak flow: >0.97). Across both metrics and vessel types, RS3 had the narrowest average LOA for the short T_s 5D flow reconstruction whereas RS2 had the narrowest average LOA for the 40ms reconstruction (table 2). Bland-Altman plots from RS3 are shown in **Fig.3**.

When comparing the 5D flow reconstructions, we found that the short T_s reconstruction had an average percent increase of 8.6% in net flow and 10.4% in peak flow. There was excellent correlation between the reconstructions in all bins (R^2>0.97).

Discussion

We demonstrate that in a cohort of pediatric CHD patients, 5D flow derived net flow and peak flow had excellent correlation with 2D-PC measurements. Overall, we observed few significant biases in the 40ms reconstruction whereas the short T_s reconstruction generally overestimated arterial flow measures. This overestimation may be due to reduced smoothing in the signal over time or may be due to the compressed sensing (CS) being poorly tuned to reconstruction on cardiac bins with fewer lines of acquired k-space. We also found that RS2 and RS3 had the narrowest LOAs for arterial and venous measures, suggesting that these bins may most closely match the 2D-PC MRI respiratory state. This study was limited by its heterogeneous cohort and variable velocity encodes and breathing status during 2D-PC acquisition. Additionally, it faces the inherent challenge of exactly replicating the places from 2D-PC acquisition within the 3D volume of the 5D flow data. Future work should include a larger cohort, emphasizing inclusion of venous measurements, and comparisons to 4D flow MRI.

		Arteries (n=18)				Veins (n=4)			
	T_s	RS1	RS2	RS3	RS4	RS1	RS2	RS3	RS4
Net Flow (mL)	40 ms	5.4±24.0 (0.94***)	4.1±24.4 (0.93***)	6.0±26.8 (0.93***)	**6.1±22.7*** (0.95***)	0.7±7.4 (0.75)	0.1±10.3 (0.72)	-1.1±3.3 (0.94*)	-2.0±6.9 (0.87)
	Short T_s	**7.2±23.0*** (0.96***)	6.0±26.7 (0.91***)	**6.8±21.2*** (0.95***)	**7.6±22.7*** (0.95***)	0.5±8.1 (0.73)	1.3±7.8 (0.75)	1.1±7.2 (0.92*)	1.2±9.7 (0.92*)
Peak flow (mL/s)	40 ms	12.4±98.8 (0.96***)	-9.0±52.8 (0.97***)	-5.2±64.5 (0.96***)	0.8±64.2 (0.96***)	0.0±4.9 (0.98**)	1.5±8.4 (0.98*)	-4.4±7.0 (0.98**)	-4.0±5.7 (0.98*)
	Short T_s	**38.0±130.8*** (0.96***)	19.2±110.1 (0.94***)	**22.6±80.6*** (0.97***)	**23.9±91.7*** (0.97***)	0.7±6.5 (0.99**)	3.5±6.4 (0.98*)	3.3±10.1 (0.99**)	0.4±11.1 (0.97*)

Table 2. Bland Altman results are reported as absolute difference bias ± limits of agreement (LOA) where a positive bias indicates overestimation by 5D flow. The R^2 for the linear regression is reported in parenthesis. The analysis was performed separately for venous and arterial measures. Both 5D flow reconstructions overestimated arterial net flow and the short T_s reconstruction additionally overestimated arterial peak flow. Asterisks indicates a statistically significant bias or R^2. Bolding indicates significant bias. P-value legend: * $p<0.05$, ** $p<0.01$, *** $p<0.001$.

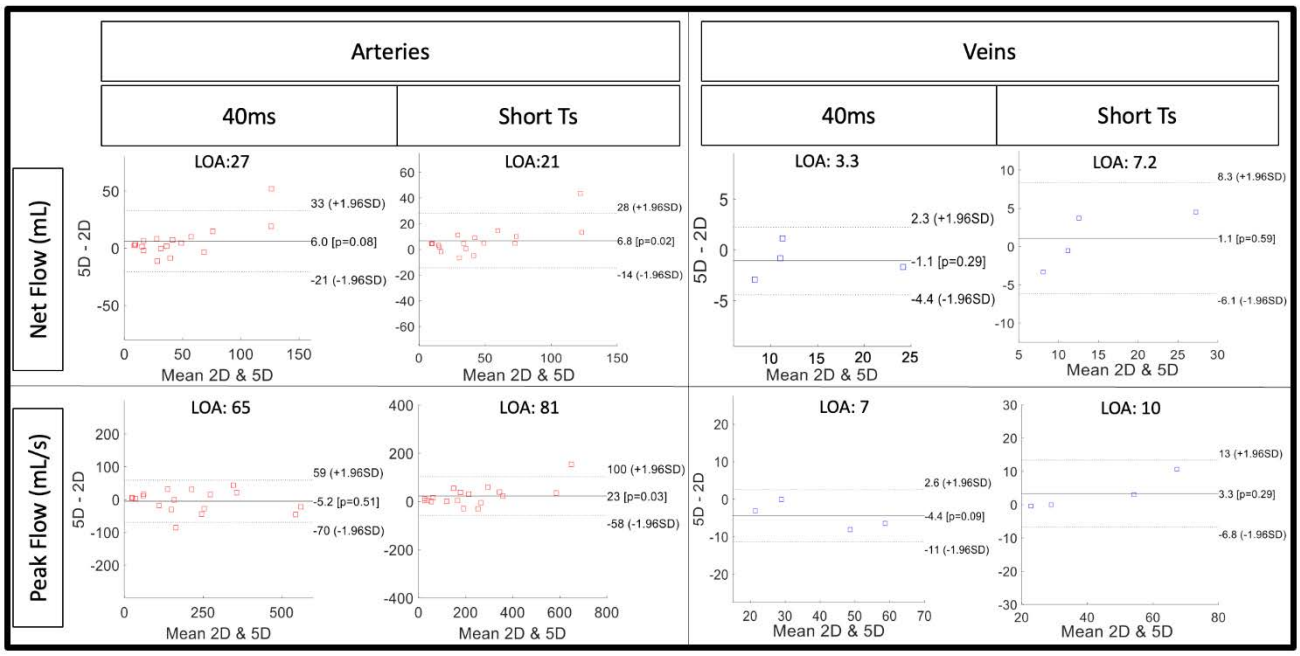

Figure 3. Bland-Altman plots comparing 2D-PC to the third respiratory state (inspiration) of 5D flow. Comparison with the 40ms reconstruction and short T_s reconstruction are shown for both net flow and peak flow. Bias ± limits of agreement (LOA) are reported in bottom of each plot.

Conclusion

Pediatric patients have a wide range of heart rates, and thus may benefit from the flexible reconstruction of 5D flow MRI to ensure sufficient cardiac phase resolution. We demonstrated that, in a heterogenous cohort of pediatric CHD patients, both standard 40ms and reduced T_s reconstructions had excellent agreement with 2D-PC. However, there is additional significant bias in the short T_s

reconstruction compared to the standard 40ms reconstruction. It is unclear if these biases reflect uncaptured flow in the clinical-standard and these differences will require further investigation.

Acknowledgements

No acknowledgement found.

References

1. van der Woude, S. F., Rijnberg, F. M., Hazekamp, M. G., Jongbloed, M. R., Kenjeres, S., Lamb, H. J., ... & Wentzel, J. J. (2021). The influence of respiration on blood flow in the Fontan circulation: insights for imaging-based clinical evaluation of the total cavopulmonary connection. Frontiers in Cardiovascular Medicine, 8.

2. Ma, L. E., Yerly, J., Piccini, D., Di Sopra, L., Roy, C. W., Carr, J. C., ... & Markl, M. (2020). 5D flow MRI: a fully self-gated, free-running framework for cardiac and respiratory motion–resolved 3D hemodynamics. Radiology: Cardiothoracic Imaging, 2(6), e200219.

3. Falcão, M. B., Di Sopra, L., Ma, L., Bacher, M., Yerly, J., Speier, P., ... & Roy, C. W. (2021). Pilot tone navigation for respiratory and cardiac motion-resolved free-running 5D flow MRI. Magnetic resonance in medicine.

4. Ma, L., Yerly, J., Di Sopra, L., Piccini, D., Lee, J., DiCarlo, A., ... & Markl, M. (2021). Using 5D flow MRI to decode the effects of rhythm on left atrial3D flow dynamics in patients with atrial fibrillation. Magnetic resonance in medicine, 85(6), 3125-3139.

Proceedings **Joint Annual Meeting ISMRM-ESMRMB & ISMRT 31st Annual Meeting** (2022)

Abstract number **0896**

Abstract accepted as a Poster.

Best trainee abstract in pediatrics finalist.

My contribution: I provided counseling on the analysis and interpretation of the different reconstructions performed with different cardiac temporal resolutions.

A2.2.4. RR-Resolved 5D flow for Decoding the Impact of Cardiac Rhythm on Left Atrial Flow Dynamics in Atrial Fibrillation and Stroke

Justin Baraboo[1], Elizabeth Weiss[1], Maurice Pradella[1], Liliana Ma[1], Julia Hwang[1], Suvai Gunasekaran[1], Mariana Falcão[2], Christopher W Roy[2], Matthias Stuber[2], Rod Passman[1], Daniel Kim[1], and Michael Markl[1]

[1]Northwestern University, Chicago, IL, United States,
[2]University of Lausanne, Lausanne, Switzerland

Synopsis

RR-resolved 5D flow is a novel MRI technique that can acquire time-resolved 3D hemodynamics for varying RR-interval durations during atrial fibrillation (AF) (5D = 3D + cardiac time + RR-interval duration). The purpose of this study was to apply RR-resolved 5D flow MRI in a cohort of AF patients with and without a prior history of stroke. We saw significantly lowered left atrial peak velocities and trends toward higher atrial blood stasis in AF patients with previous stroke history vs no previous stroke history who underwent arrhythmia during MRI acquisition. RR-resolved 5Dflow may be a promising approach for cardiovascular imaging in arrhythmic patients.

Introduction

Atrial fibrillation (AF) is the most common sustained cardiac arrhythmia[1]. Impaired left atrial (LA) hemodynamics, slow blood flow velocities and blood stasis, are implicated in increased risk of thrombus formation and cardioembolic stroke in AF patients[2,3]. Echocardiographic and 4D flow MRI have shown atrial velocities in AF patients with cardiac arrhythmia are lower compared to AF patients maintaining sinus rhythm. However, each modality has limitations: echocardiography lacks 3D volumetric coverage to fully capture complex LA flow dynamics; atrial 4D-flow MRI is ill-suited to study beat-to-beat flow changes during arrhythmia[4,5]. RR-resolved 5D flow[6] is a novel MRI technique with inherent self-gating that can acquire time-resolved 3D hemodynamics for varying RR-interval durations during cardiac arrhythmia (5D = 3D + cardiac time + RR-interval duration, **Fig.1**).Peak velocities and blood flow stasis are measured across a range of RR intervals, assessing the impact of varying heart rates on atrial 3D hemodynamics. The purpose of this study was to apply RR-resolved 5D flow MRI in a cohort of AF patients with and without a prior history of stroke. We hypothesize that 1) variable RR-interval duration during arrhythmia will impact atrial flow measures and 2) AF patients with prior stroke will have impaired RR-resolved LA hemodynamics (lowered peak velocities, higher LA stasis).

Methods

32 AF patients (**Table 1**) undergoing cardiac MRI with RR-resolved 5D Flow were retrospectively enrolled (1.5T, venc=100 cm/s, FOV=250×250×250mm3, TE/TR =2.93/4.70ms, flip angle=7°, temporal resolution=40ms, spatial resolution= 2.5x2.5x2.5 mm3). 16 AF patients had a history of prior stroke (stroke+) and 16 had no previous stroke history (stroke-).

RR-resolved 5D flow reconstruction used a self-gating algorithm to retrospectively identify RR-interval duration and cardiac state (**Fig.1A**) for each k-space line. A RR-interval duration histogram (**Fig.1C**) was constructed where all unique RR-interval lengths were sorted from shortest to longest.

Parameter	Stroke History	No Stroke History
Number	16	16
Age (years)	70 ± 7	65 ± 8
Sex	14 Male, 2 Female	12 Male, 4 Female
Race	9 Caucasian, 7 African American	14 Caucasian, 2 African American
RR Distribution Coefficient of Variation	.17 ± .08	.15 ± .07

Table 1. Patient Demographics and Coefficient of Variation distributions.

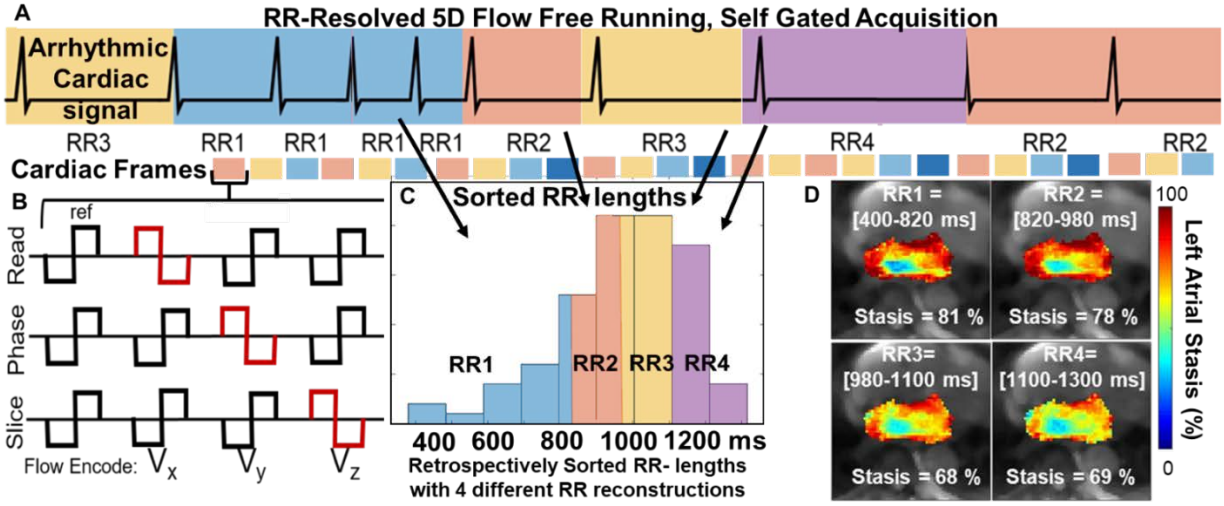

Figure 1. A) RR-Resolved 5D Flow is a free running acquisition that uses a self-gating algorithm to retrospectively determine RR-interval duration and cardiac time frames. **B)** 3D time varying velocity is encoded through bipolar gradient encodings. **C)** RR-interval durations are sorted into 4 RR-bins (short to long) for the reconstructions of four sets of cardiac time-resolved velocity data per RR-bin. **D)** Hemodynamic parameters such as 2D axial mean stasis projection maps are derived for each RR-interval duration RR1 to RR4.

Four non-overlapping RR-interval bins, where each bin had the same number of RR-intervals, were reconstructed using compressed sensing. Imager construction resulted in four sets of 5D flow MRI data sets representing four RR-intervals durations (RR1 to RR4, **Fig.1D**)[6].

To quantify heart rate variability during acquisition, the RR-interval histogram (**Fig.1C**) was used to calculate the RR-interval duration coefficient of variation (RR-std/RR-mean, CoV) for each patient. To account for heart rate variability differences, patients were classified as high heart rate variability (HRV-high) or low heart rate variability (HRV-low). From previous results for detecting AF via RR histograms and CoV[7], HRV-high was defined as a CoV of 0.15-0.32, and HRV-low was defined as CoV less than 0.15. Two patients were excluded due to elevated CoV (> 0.40, possibly linked to non-AF arrhythmias) and one patient for poor image and data quality.

RR-resolved 5D flow data analysis included pre-processing of each RR bins data set (**Fig.2**). The LA was manually segmented from a derived phase contrast angiogram from RR3 bin (Mimics, Materialise, Belgium) and used for each RR bin. Blood stasis was calculated per voxel (percentage of cardiac time velocity < 10 cm/s) and mean stasis over the entire LA was calculated for each RR bin. Peak velocities were calculated as the mean of the top 5% of velocities to mitigate noise. Stasis and peak velocities were visualized by mean and maximum intensity projections (MIPs) and were compared between stroke+ and stroke- cohorts for high and low heart rate variability (**Fig.3**). Mean absolute percent differences between RR1 stasis and peak velocities and RR3 and RR4 were calculated within each patient for HRV-high and HRV-low stroke+ and stroke- groups.

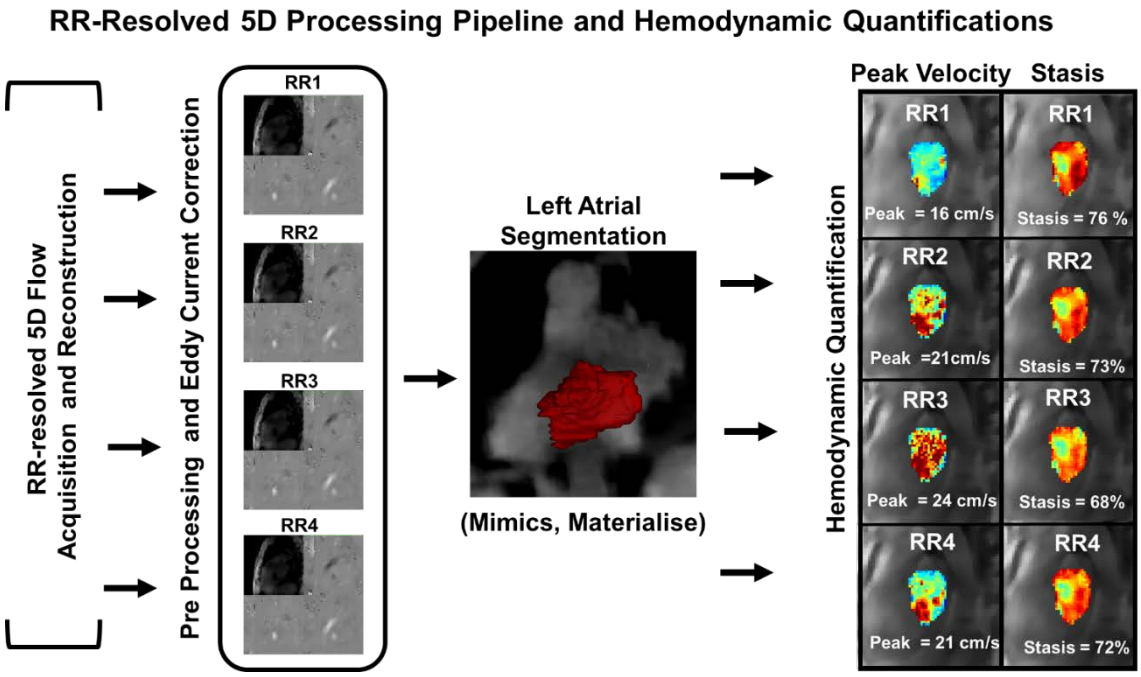

Figure 2. Following extraction of self-gating signals, sorting of data into 4 RR-interval bins (RR1 to RR4), and CS image reconstruction, RR-resolved 5D flow MRI data underwent pre-processing (eddy current correction, velocity antialiasing) for each RR bin. The left atrium was segmented from the 5D flow MRI data for one RR bin using commercial software (Mimics, Materialise, Belgium) and used as static segmentation mask for all RR bins. Peak velocity and stasis maps were created for each RR bin and used to calculate mean LA stasis and LA peak velocity.

Results

CoV analysis identified 13 patients with marked cardiac arrhythmia (HRV-high: 6 stroke+ and 7 stroke-) and 16 patients with low heart rate variability (HRV-low: 8 stroke+ and 8 stroke-). HRV-high had larger RR-variable differences (RR1 vs RR3/4) ranging from 9-18% mean absolute percent differences for peak velocity and stasis vs HRV-low RR (5-14% mean absolute percent differences). RR-resolved 5D flow demonstrated, overall, trends for lowered peak velocities and higher stasis per each RR bin in HRV-high and HRV-low for stroke+ and stroke- cohorts. More pronounced differences in LA flow measures were seen for shorter RR-interval bins (RR1,RR2) with significantly reduced peak velocities for HRV-high stroke+ vs. stroke- AF patients (0.21±0.04 m/s vs. 0.27±0.05 m/s, $p<0.05$). Stasis and peak velocity differences ranged from 8%-16% for stasis and 9-33% for peak velocity in the HRV-high cohort and 11-18% for stasis and 2-10% for peak velocity in the HRV-low cohort.

Discussion

The findings of this study demonstrate that RR-resolved 5D Flow MRI was sensitive to detect changes in RR-interval dependent LA hemodynamics which may yield important information for understanding risks for atrial thrombus formation in patients with varying heart rates. Largest differences in peak velocity and stasis were observed between stroke history groups in the HRV-high cohort, potentially signaling an effect of arrhythmia, itself, on atrial hemodynamics and thus thromboembolic risk.

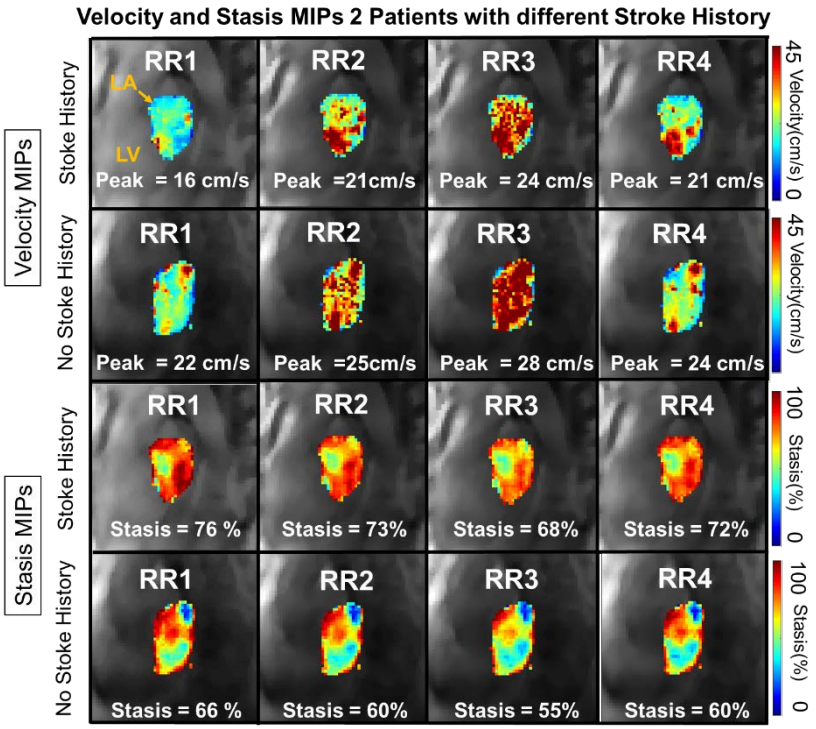

Figure 3. RR-resolved left atrial (LA) peak velocity (PV, top) and stasis (below) maps (sagittal maximum intensity projections) for two AF patients with and without history of embolic stroke. In the individual patient, the impact of arrhythmic changes in heart rate on atrial flow measures is clearly evident (peak velocity and stasis difference of up to 8cm/s and 11% between RR interval bins). Most pronounced stroke+ vs. stroke- differences in LA velocities were seen for the shortest RR-interval duration (RR1 bin) with diminishing differences for longer RR-intervals (RR2-4 bins).

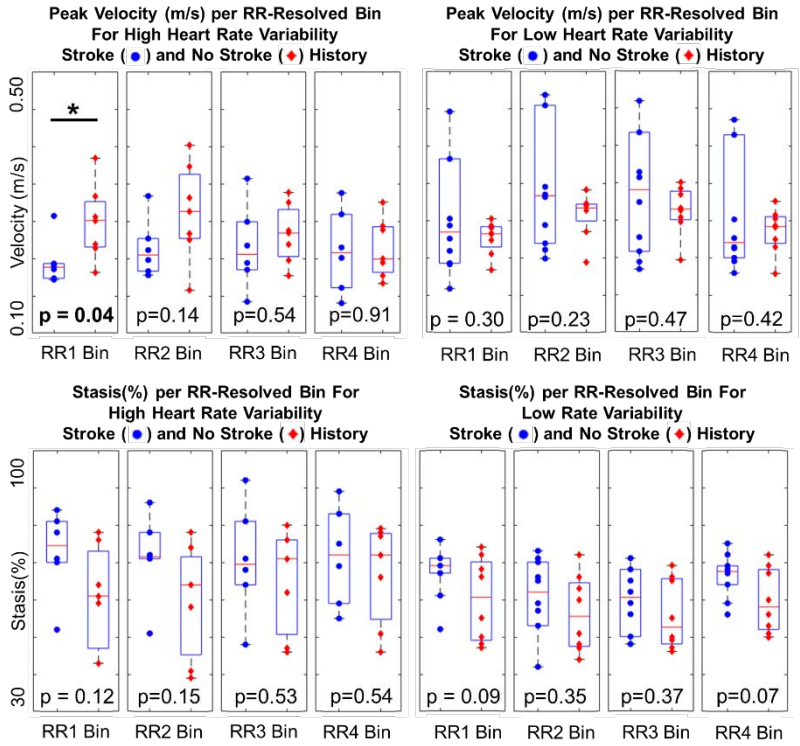

Figure 4. Left atrial peak velocity (top) and mean stasis (bottom) boxplots per RR bin for HRV-high (left) stroke+ (n = 6, blue circles) and stroke- (n = 7,red diamonds) and HRV-low (right) stroke+ (n=8, blue circles) and stroke- (n=8, red diamonds). Peak velocities were significantly lower for HRV-high stroke+ AF patients than stroke- AF patients ($p < .05$). Stasis trended higher for stroke+ AF patients than stroke- for all RR bins and HRV but was not significant.

Conclusion

RR-resolved 5D flow detected differences in LA flow for different RR-interval durations where most pronounced stroke vs no stroke differences for peak velocity and stasis were observed for RR1 bins. These RR-resolved difference cannot be detected by conventional 4D-flow imaging. RR-resolved 5D flow may thus be a promising novel approach for cardiovascular imaging in arrhythmic patients with potential to improve stroke risk.

Acknowledgements

Research reported in this publication was supported by the National Institute Of Biomedical Imaging And Bioengineering of the National Institutes of Health under Award Number T32EB025766 and R21AG055954-02

References

1. AHA/ACC/HRS Guideline for the Management of Patients With Atrial Fibrillation: A Report of the American College of Cardiology/American Heart Association Task Force on Clinical Practice Guidelines and the Heart Rhythm Society in Collaboration With the Society of Thoracic Surgeons. Circulation. 2019; 140(2): e125-e151. doi:10.1161/CIR.0000000000006652.

2. Shen MJ, Arora R, Jalife J. Atrial Myopathy. JACC Basic to Transl Sci. 2019; 4(5): 640-654.doi:10.1016/J.JACBTS.2019.05.0053.

3. Markl M, Hennig J. Phase contrast MRI with improved temporal resolution by view sharing: K-space related velocity mapping properties. Magn Reson Imaging. 2001;19(5):669-676.doi:10.1016/S0730-725X(01)00386-14.

4. Markl M, Lee DC, Furiasse N, et al. Left Atrial and Left Atrial Appendage 4D Blood Flow Dynamics in Atrial Fibrillation. Circ Cardiovasc Imaging. 2016; 9(9): e004984.doi:10.1161/CIRCIMAGING.116.0049845.

5. Handke M, Harloff A, Hetzel A, Olschewski M, Bode C, Geibel A. Left Atrial Appendage Flow Velocity as a Quantitative Surrogate Parameter for Thromboembolic Risk: Determinants and Relationship to Spontaneous Echo contrast and Thrombus Formation–A Transesophageal Echocardiographic Study in 500 Patients with Cerebral Ischemia. J Am Soc Echocardiogr. 2005; 18(12): 1366-1372. doi:10.1016/J.ECHO.2005.05.0066.

6. Ma L, Yerly J, Sopra L Di, et al. Using 5D flow MRI to decode the effects of rhythm on left atrial 3D flow dynamics in patients with atrial fibrillation. Magn Reson Med. 2021; 85(6): 3125-3139. doi:10.1002/MRM.286427.

7. Tateno K, Glass L. Automatic detection of atrial fibrillation using the coefficient of variation and density histograms of RR and ΔRR intervals. Med Biol Eng Comput. 2001; 39(6): 664-671.doi:10.1007/BF02345439

Proceedings **Joint Annual Meeting ISMRM-ESMRMB & ISMRT 31st Annual Meeting** (2022)
Abstract number **0216**
Abstract accepted as an Oral presentation.
Summa Cum Laude Merit Award

My contribution: I provided counseling on the interpretation of the results.

A2.2.5. A 3D Dense-U-Net for fully automated 5D flow MRI segmentation

Liliana E. Ma[1,2], Haben Berhane[1,2], Justin Baraboo[1,2], Michael Sugimura[3], Christopher W. Roy[4], Mariana Falcão[4], Jérôme Yerly[4], Matthias Stuber[4,5], and Michael Markl[1,2]

[1]Department of Radiology, Northwestern University, Feinberg School of Medicine, Chicago, IL, United States,
[2]Department of Biomedical Engineering, Northwestern University, Evanston, IL, United States,
[3]Self-employed, Chicago, IL, United States,
[4]Department of Radiology, Lausanne University Hospital (CHUV) and University of Lausanne (UNIL), Lausanne, Switzerland,
[5]Center for Biomedical Imaging, Lausanne, Switzerland

Synopsis

Recently, a free-running 5D flow framework was introduced and validated. However, some 5D flow MRI is based on 3D radial imaging, which is limited by reduced SNR that can result in challenges with 3D segmentation. A number of previous studies have investigated automatic segmentation for 4D flow MRI, however these have been traditionally optimized for Cartesian datasets, which are typically acquired over much smaller spatial matrices and cover only one respiratory position. The purpose of this study was thus to adapt and expand a deep-learning framework to cardiac 5D flow MRI data for automatic segmentation of the thoracic aorta.

Introduction

Recently, a fully self-gated, 3D radial, free-running 5D flow (4D flow + respiration) framework was introduced and validated for the assessment of respiratory and cardiac motion-resolved 3D hemodynamics[1,2]. While 5D flow MRI attempted to address traditional limitations associated with respiration control, ECG gating, and scan inefficiency, it is based on 3D radial imaging, which is limited by reduced SNR that can result in challenges related to data post-processing such as the 3D segmentation of cardiac chambers and vessels. Manual 3D segmentation of the thoracic aorta, for example, can take up to 20-30 minutes, and in 5D flow imaging, needs to be repeated for each reconstructed respiratory time point. A number of previous studies have investigated 3D autosegmentation for 4D flow MRI, however these have been traditionally optimized for Cartesian 4D flow datasets, which are typically acquired over much smaller spatial matrices and cover only one respiratory position[3,4]. Kolarik et al. recently introduced an open source 3D Dense-U-Net network that was optimized for high-resolution datasets on accessible hardware, with 99% accuracy on autosegmentation of anatomic brain MRI and thoracic vertebrae CT datasets[5]. The purpose of this study was thus to adapt and expand this framework to cardiac 5D flow MRI data for deep learning-based automatic segmentation of the thoracic aorta for evaluation of respiratory and cardiac-resolved hemodynamics.

Methods

The study included 20 previously described patients with aortic valve/aortic disease who underwent a prototype 5D flow MRI scan (mean age, 49 ±17 years, 18 men, ~8 minute scan time)[2]. 5D flow MRI (vx, vy, vz + cardiac + respiration) data can also be considered as four separate 4D flow (vx, vy, vz + cardiac) datasets corresponding to four different respiratory positions. A cardiac time point-averaged 3D phase-contrast MRA was calculated using both magnitude and velocity data (**Fig.1a**) for each

respiratory phase (Resp1-4, end-expiration to end-inspiration) and used to manually segment the thoracic aorta. In total, 4 x 20 patients = 80 aorta segmentations were thus available as labeled ground truth data for network training and testing. A 3D Dense U-Net (**Fig.1b**) was trained on an Alienware m17 R3 personal laptop with 6 cores, 16 Gb RAM, and Nvidia GeForce RTX2070 GPU. 16 patient datasets were used for training, while 4 were used for testing. Respiratory phases were treated as separate datasets (i.e., 16patients*4 respiratory phases = 64 datasets used for training, 4 patients*4=16 for testing). Dice similarity coefficients (DSC) were used to evaluate segmentation accuracy. Hemodynamic parameters based on both manual and automated segmentations were evaluated using 2D peak systolic velocity maximum intensity projections (MIP, **Fig.4a**), where peak systolic velocities were calculated in the ascending aorta (AAo), arch, and descending aorta (DAo) for all testing datasets. Time-resolved absolute velocity time curves were calculated by averaging the absolute velocity ($\sqrt{v_x^2 + v_y^2 + v_z^2}$) over the entire segmentation volume, and plotting this value for each cardiac time point (**Fig.4b**).

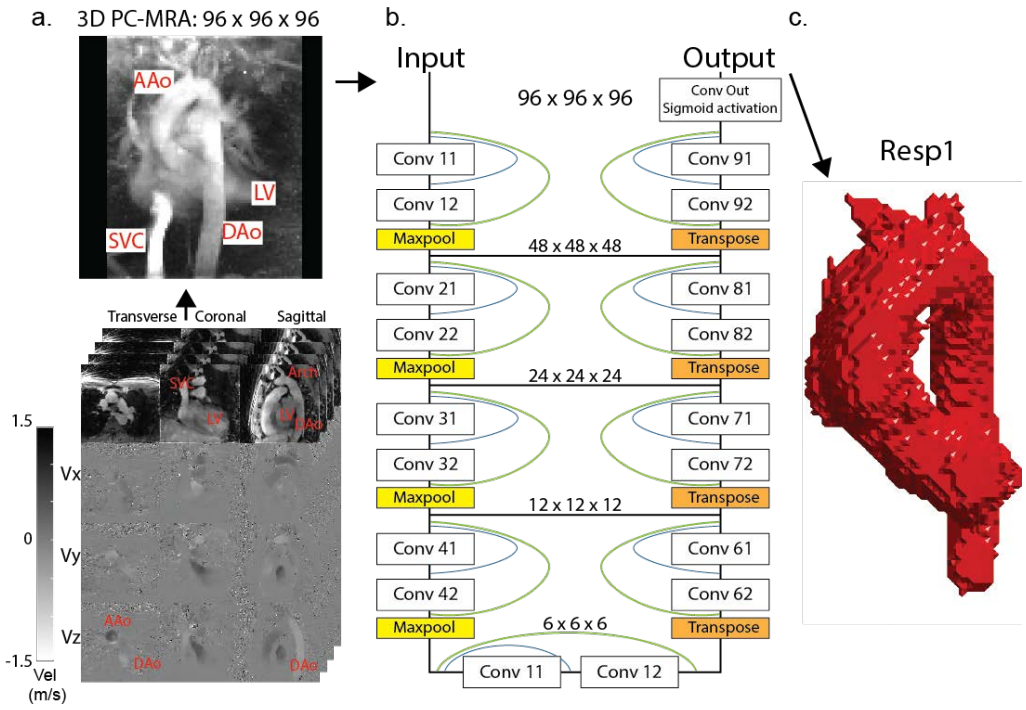

Figure 1. Analysis workflow. (a), 3D phase-contrast MR angiogram (PC-MRA) was calculated from velocity and magnitude data and fed as the inputinto a dense U-Net model **(b).** U-Net architecture (adapted from figure 6 from Koralnik et al.) Residual interconnections are represented by greenlines, dense connections blue. Sigmoid activation was used on the output network layer, and thus all pixels with values <0.5 were labelled as 0 and≥ 0.5 as 1 for a binary mask output **(c).** Note: example autosegmentation in this figure is for one respiratory position (end-expiration).

DSC scores across all test sets				
	Patient 1	**Patient 2**	**Patient 3**	**Patient 4**
Resp 1 (End expiration)	0.79	0.84	0.82	0.82
Resp 2	0.79	0.84	0.83	0.78
Resp 3	0.80	0.83	0.81	0.81
Resp 4 (end inspiration)	0.78	0.83	0.78	0.80

Figure 2. DSC scores across all 4 patient test sets. DSC scores were consistent across all respiratory phases, with potentially a slight decrease in performance for end-inspiration. Manual segmentation of the thoracic aorta served as the ground truth data.

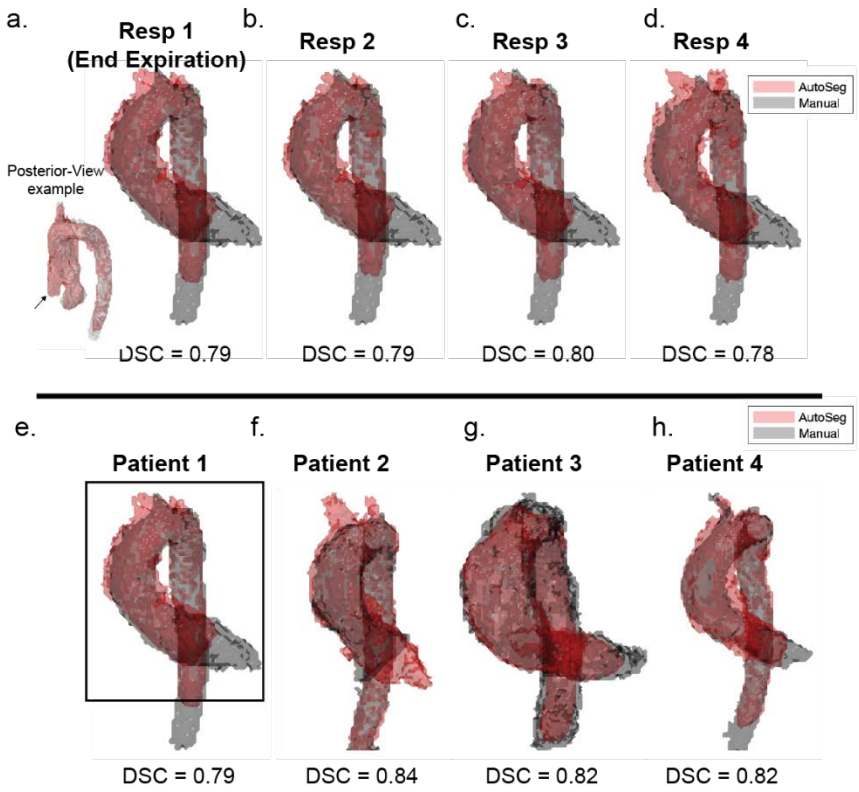

Figure 3. Deep learning-based automatic segmentation (AutoSeg) versus manual results. (a-d), segmentation results for all respiratory positions fora single representative patient. Note the protrusion at the posterior view near the aortic root **(a)**. **(e-h),** segmentation results for all four test patients for at end-expiration (Resp1). The black box represents cropping of distal DAo for subsequent hemodynamic quantification comparisons.

Results

The 3D Dense U-Net architecture was adapted to 5D flow data and trained in a single batch for 50 epochs (training time=35.6 minutes). Automated segmentation of all testing datasets was performed in 5.7 seconds. DSC scores for all patients and respiratory phases ranged from 0.78 to 0.83 (**Fig.2**). End-expiratory (Resp1) automated and manual segmentations for all patients in the testing group are shown in **Fig.3b**. Automated segmentations tended to crop the distal DAo relative to manual segmentations. Thus, manual segmentations were cropped to comparable points of the distal DAo for quantitative comparisons (**Fig.3e**, black box).

Peak velocity MIPs showed excellent visual agreement between automated and manual segmentations (**Fig.4a**). Regional peak velocities also showed good-to-excellent agreement between automatic and manual segmentations (auto vs. manual, AAo: 2.56±0.47 m/s vs. 2.56±0.44 m/s , Arch:1.12±0.26 vs. 1.13 ±0.25, DAo: 1.16±0.31 vs. 1.16±0.30, $p>0.05$). Bland-Altman analysis demonstrated increasing limits of agreement (LOA) from AAo to DAo (**Fig.5**). Autosegmentation-derived absolute velocity showed good agreement over velocity time curves (**Fig.4b**). Bland-Altman analysis of absolute velocity over all patients further demonstrated good agreement (**Fig.4c**), but a statistically significantly decrease over all respiratory phases and time points compared to manual segmentation (auto: 0.267±0.163 m/s, manual: 0.275±0.168 m/s, $p<0.05$).

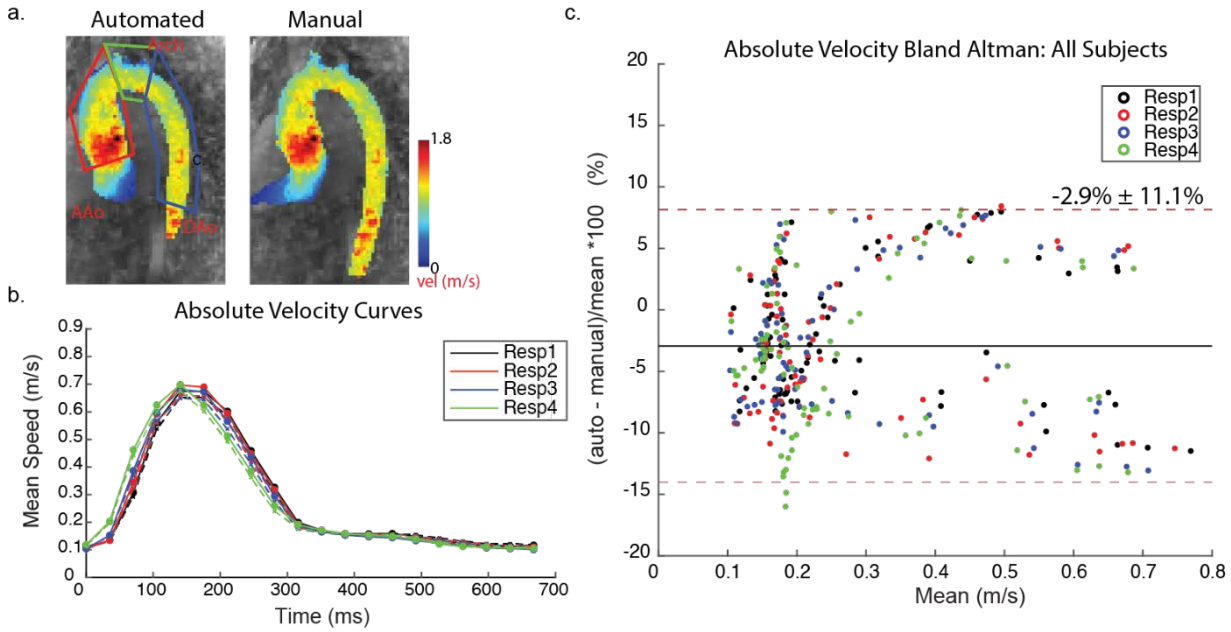

Figure 4. Hemodynamic analyses. (a) representative peak systolic velocity MIPs based on auto vs. manual segmentations for representative patient during end-expiration. **(b)** example absolute velocity curves for the same patient show small variations between automatic (solid line) and manual (dashed) segmentation-derived curves, however the relative shapes are preserved. **(c)** Bland-Altman of absolute velocity over all time points for all testing datasets. Black solid lines represent mean bias, with red dotted lines representing limits of agreement.

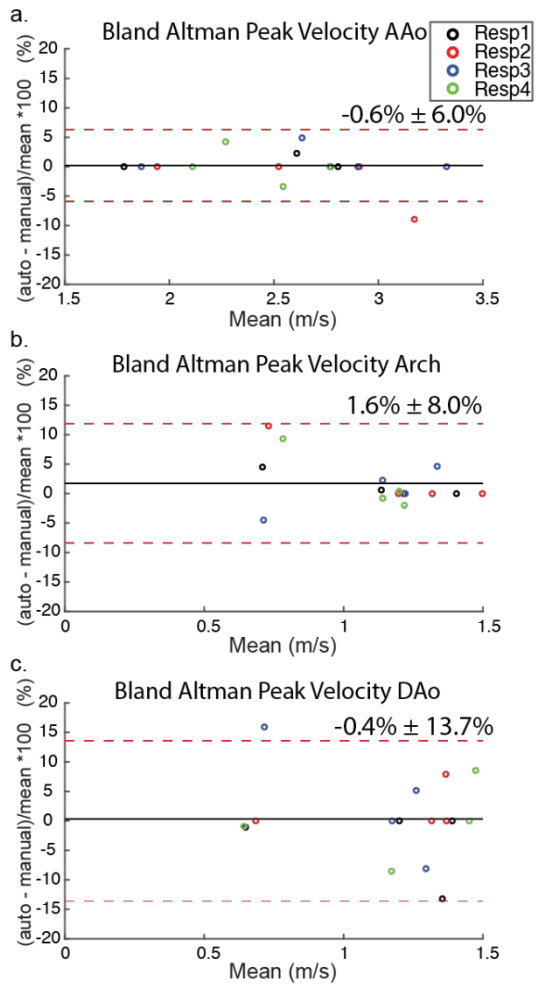

Figure 5. Bland-Altman of peak velocities for AAo (a), Arch (b), and DAo (c). Black solid line represents mean bias, with red dotted lines representing limits of agreement, with numerical values represented in percentage on the top right corner of each plot.

Discussion/Conclusions

This study demonstrated the feasibility of expanding a 3D Dense U-Net for fully automated 3D segmentation of 5D flow MRI data for investigation of cardiac and respiratory-resolved hemodynamics on commercially available hardware. While mean absolute velocities tended to be underestimated by the autosegmentation, this underestimation was well within 10% of the manually-derived values. In addition, peak velocity LOA was increased in the DAo, potentially due the fact that peak velocities in the distal aorta are often closer to the vessel wall, increasing susceptibility to eroded contours as well as segmentation size.

While the initial results are promising, this study was limited by the small sample size. In addition, high pressure systems like the thoracic aorta are not primarily influenced by respiratory variation, with major respiratory effects seen primarily in the low-pressure pulmonary circulation. Future studies will include larger sample sizes, K-fold cross-validation, optimization of hyperparameters, as well as segmentation of additional vascular structures included in the 5D flow MR volume.

Acknowledgements

Grant support by NHLBI R01HL115828, NHLBI F30HL137279, NHLBI R21AG055954, and SNF 320030-173129.

References

1. Di Sopra, L., et al., An automated approach to fully self-gated free-running cardiac and respiratory motion-resolved 5D whole-heart MRI. Magnetic resonance in medicine, 2019

2. Ma, L.E., et al., 5D flow MRI: a fully self-gated, free-running framework for cardiac and respiratory motion–resolved 3D hemodynamics. Radiology: Cardiothoracic Imaging, 2020. 2(6): p. e200219.

3. Berhane, H., et al., Fully automated 3D aortic segmentation of 4D flow MRI for hemodynamic analysis using deep learning. Magnetic resonance in medicine, 2020. 84(4): p. 2204-2218.

4. Bustamante, M., et al., Atlas-based analysis of 4D flow CMR: automated vessel segmentation and flow quantification. Journal of Cardiovascular Magnetic Resonance, 2015. 17(1): p. 1-12.

5. Kolařík, M., et al., Optimized high resolution 3D dense-U-Net network for brain and spine segmentation. Applied Sciences, 2019. 9(3): p. 404.

Proceedings **Joint Annual Meeting ISMRM-ESMRMB & ISMRT 31st Annual Meeting** (2022)
Abstract number **0331**
Abstract accepted as an Oral presentation.
My contribution: I provided counseling on the interpretation of the results.

A2.2.6. Respiratory-Resolved flow in Congenital Heart Disease: A 5D flow MRI Study

Elizabeth K. Weiss[1,2], Cynthia K. Rigsby[3], Joshua D. Robinson[3], Justin Baraboo[1,2], Liliana Ma[1,2], Mariana B. L. Falcão[4], Christopher W. Roy[4], Matthias Stuber[4], and Michael Markl[1,2]

[1]Biomedical Engineering, Northwestern University, Evanston, IL, United States, Radiology,
[2]Feinberg School of Medicine, Chicago, IL, United States,
[3]Medical Imaging, Lurie Children's Hospital, Chicago, IL, United States,
[4]Radiology, Lausanne University Hospital (CHUV) and University of Lausanne (UNIL), Lausanne, Switzerland

Background

Respiration has been shown to drive hemodynamic changes in healthy individuals[1] and those with congenital heart disease (CHD).[2] However, conventional flow methods are typically limited to acquisition during a single respiration state (e.g. breath-hold, navigator-gated). 5D flow MRI[3] is a new, free-running, and self-gated technique that enables quantification of 3D velocities over both the cardiac and respiratory cycle. This study aimed to develop a novel physiology-driven respiratory gating method to assess the impact of respiration in CHD patients using 5D flow MRI.

Methods

22 patients with CHD (17±11 yrs, 45% female) undergoing a clinically indicated CMR with ferumoxytol were consented for an 8.5-minute 5D flow add-on. The cohort was divided into 3 anatomical subgroups (**Fig.1d**): single ventricle disease (SVD, n=5), pulmonary artery disease (PA, n=7), and shunt (n=5). Frequent superior-inferior readouts were used to extract cardiac and respiratory signals for retrospective gating. Using a peak- finding algorithm (**Fig.1b**), the 5D flow MRI data was sorted into 4 respiratory states (RS): end-expiration, end-inspiration, active inspiration, and active expiration. Net flow was measured at the following locations (**Fig.1c**): ascending aorta (Ao), main pulmonary artery (MPA), left and right pulmonary arteries (LPA & RPA), and inferior and superior vena cava (IVC & SVC). The range of net flow over respiration was normalized to the mean over respiration. Median flow curves were normalized to end- expiration.

Results

Overall, the caval veins (IVC & SVC) had larger respiratory driven flow changes than the pulmonary arteries (MPA, RPA & LPA) and aorta (40% vs 17% & 12%, $p<0.001$). The pulmonary arteries had larger flow changes across the 4 RS than the Ao (17% vs 12%, $p=0.008$; **Fig.2b**). In sub-group analysis, we found that the Ao of SVD patients had less respiratory driven flow than the pulmonary arteries and caval veins (9% vs 34% & 51%, $p<0.01$). In shunt patients, respiration had a larger impact in the caval veins than the pulmonary arteries and the Ao (28% vs 13% & 11%, $p<0.01$, **Fig.2a**). We also noted that, in the IVC of SVD and shunt patients (**Fig.3d**), active inspiration had a large, positive percent change in flow while active expiration had a large, negative percent change.

Discussion

We demonstrated a novel respiratory gating method, based on physiologic respiratory phases, was able to detect respiration driven flow changes in CHD patients. We found that pulmonary arteries and caval

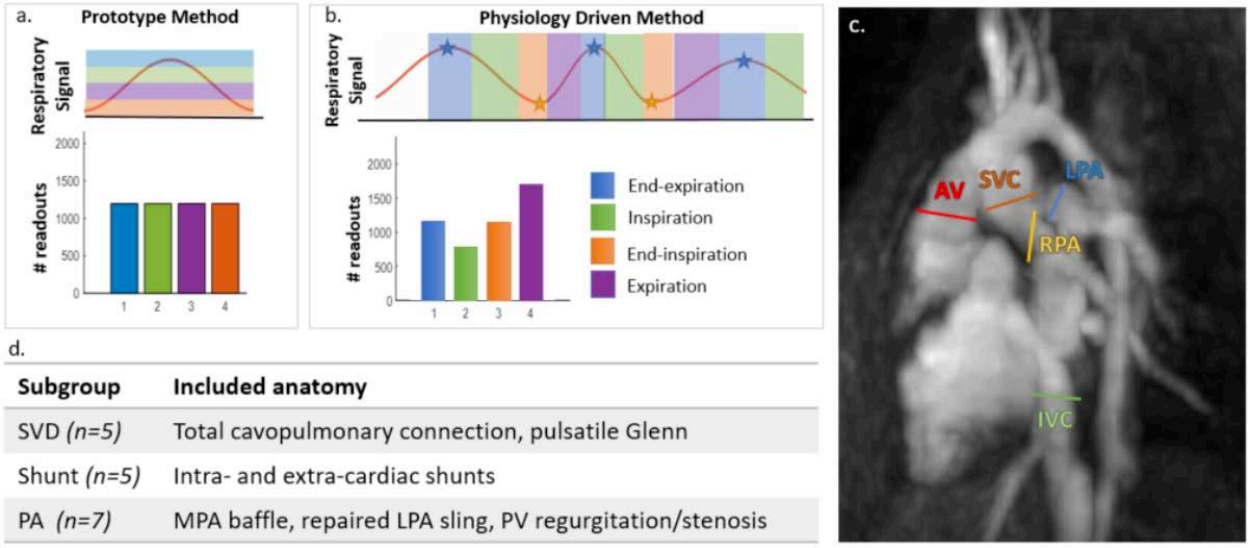

d.

Subgroup	Included anatomy
SVD *(n=5)*	Total cavopulmonary connection, pulsatile Glenn
Shunt *(n=5)*	Intra- and extra-cardiac shunts
PA *(n=7)*	MPA baffle, repaired LPA sling, PV regurgitation/stenosis

Figure 1. Methods overview. The prototype respiratory gating method (a) used the signal magnitude and is shown for reference. The newly proposed method used in this study (b) uses physiologic respiratory phases for each individual breath. Locations of 2D, time resolved ROIs to measure net flow in a Fontan patient (c) are shown and additional details for the 3 anatomical subgroups are given (d).

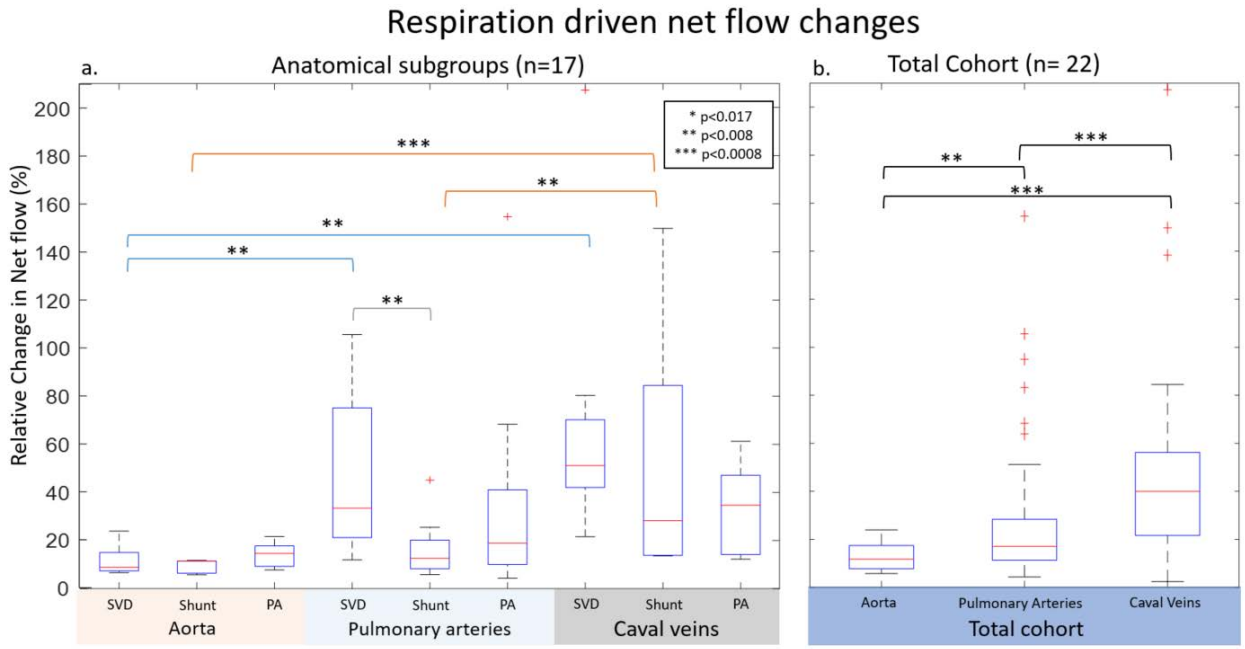

Figure 2. Degree of respiration driven changes in net flow in each anatomical subgroup (a) and in the total cohort (b). Asterisks indicate significance of comparison.

veins had more respiratory driven flow than the aorta. Additionally, we found that anatomy played a role. In shunt patients, pulmonary arteries did not have more respiratory driven flow than the Ao, but in SVD patients, where the pulmonary arteries are passively filled, there was a large, significant difference. We also found that in many cases, the change in flow during active inspiration and expiration were opposite. This suggests that the prior method, which grouped data from these phases, would be inadequate.

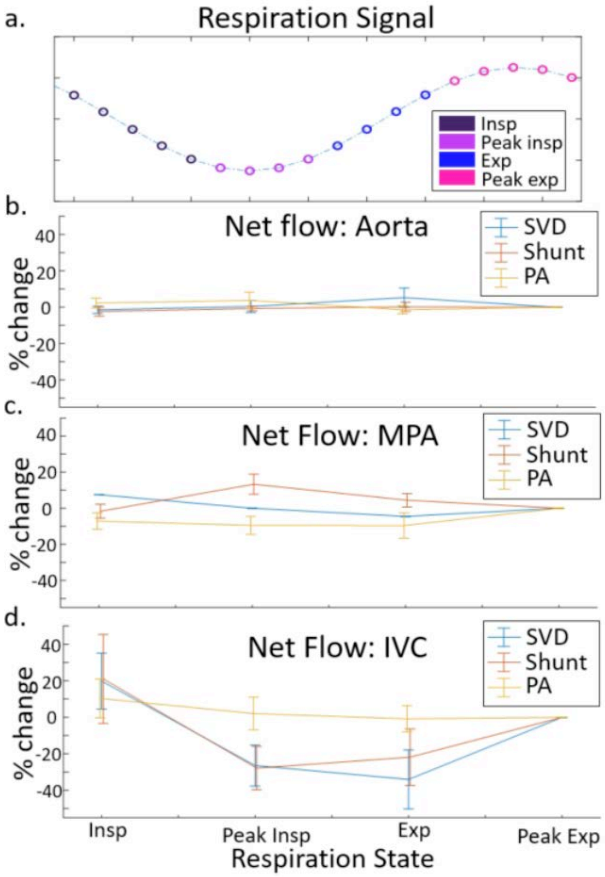

Figure 3. Median net flow curves normalized to end-expiration for all 3 anatomical groups in 3 selected vessels: aorta (b), MPA (c), and IVC (d). A single respiratory gated breath is shown for reference (a).

References:

1. Körperich, H., Barth, P., Gieseke, J., Müller, K., Burchert, W., Esdorn, H., ... & Laser, K. T. (2015). Impact of respiration on stroke volumes in paediatric controls and in patients after Fontan procedure assessed by MR real-time phase-velocity mapping. European Heart Journal-Cardiovascular Imaging, 16(2), 198-209.

2. Wei, Z., Whitehead, K. K., Khiabani, R. H., Tree, M., Tang, E., Paridon, S. M., ... & Yoganathan, A. P. (2016). Respiratory effects on Fontan circulation during rest and exercise using real-time cardiac magnetic resonance imaging. The Annals of thoracic surgery, 101(5), 1818-1825.

3. Ma, L. E., Yerly, J., Piccini, D., Di Sopra, L., Roy, C. W., Carr, J. C., ... & Markl, M. (2020). 5D flow MRI: a fully self-gated, free-running framework for cardiac and respiratory motion–resolved 3D hemodynamics. Radiology: Cardiothoracic Imaging, 2(6).

Proceedings **SCMR 26th Annual Scientific Sessions** (2023)
Abstract number **1343621**
Abstract accepted as an Oral presentation.
Early career Award Finalist.

My contribution: I provided counseling on the analysis and interpretation of the different reconstructions performed with a different number of physiologic respiratory phases.

A2.2.7. Cardiovascular MR and supervised machine learning in the derivation of pulmonary vascular hemodynamics in pulmonary hypertension

K Kearney[1], J Pouliopoulos[1], N Olsen[2], J John[1], A Adji[1], S Hungerford[3], C Kessler Iglesias[1], N Song[1], P Macdonald[1], K Muthiah[1], A Keogh[1], C Hayward[1], J Grenier[4], R Thompson[4], J Yerly[5], C Roy[5], MBL Falcão[5], E Lau[6], R Puranik[6], M Ugander[7], E Kotlyar[1], A Jabbour[1]

[1]St Vincent's Hospital, Sydney
[2]University of New South Wales, Sydney
[3]Royal North Shore Hospital
[4]University of Alberta
[5]Lausanne University Hospital (CHUV) and University of Lausanne (UNIL)
[6]Royal Prince Alfred Hospital, University of Sydney
[7]University of Sydney

Background

Right heart catheterization (RHC) is the gold standard for assessing cardiac physiology. Cardiac magnetic resonance (CMR) imaging has not yet been shown to reliably quantify invasive haemodynamic measures such as pulmonary vascular resistance (PVR), mean pulmonary arterial pressure (mPAP) and mean pulmonary arterial wedge pressure (mPAWP). This study aimed to derive these variables using CMR and supervised machine learning (SML).

Methods

Patients undergoing RHC were recruited for same-day CMR sequences involving cine imaging, 2D flow, 5D flow (respiratory gated 4D flow), T1/T2 mapping, and lung water density. The dataset was split into training and test components. Cross validation was used to tune models. Generalised linear regression and decision-tree analyses using XGBoost were performed in R.

Results

100 patients underwent same-day RHC and CMR. The mean age was 57±17 years, 68% female. Pulmonary hypertension (PH) classification: 35 precapillary, 16 combined pre and postcapillary, 20 postcapillary and 29 controls with normal pressures. CMR-derived PVR (mr-PVR) correlated well with RHC values, with test data from R2 of 0.72 as described in **Tab.1**. **Fig.2** shows the Bland-Altman analysis for mrPVR. CMR derived mPAP (mr-mPAP) likewise correlated well, with test data R2 of 0.70. CMR-derived mPAWP (mr-mPAWP) achieved an R2 of 0.48 in the test cohort.

Elevated PVR was correctly identified on CMR with an accuracy (ratio n correct predictions:total predictions) of 1.0 in both the test and train cohorts. CMR was able to classify 3 subtypes of PH or normal pressures with an accuracy of 0.60 in the train cohort and 0.53 in the test.

Conclusion

CMR-derived pulmonary hemodynamics measures utilising supervised machine learning algorithms correlated closely with invasive RHC. CMR shows promise to reduce the burden of invasive RHC.

Model	PVR XGBoost	MPAP XGBoost	MPAWP XGBoost
Train data R^2	0.99	0.99	0.94
Train RMSE	5.2	0.75	1.68
Test data R^2	0.72	0.70	0.48
Test RMSE	220.2	7.3	5.6

Table 1. Summary of best performing models for PVR, mPAWP and mPAP.

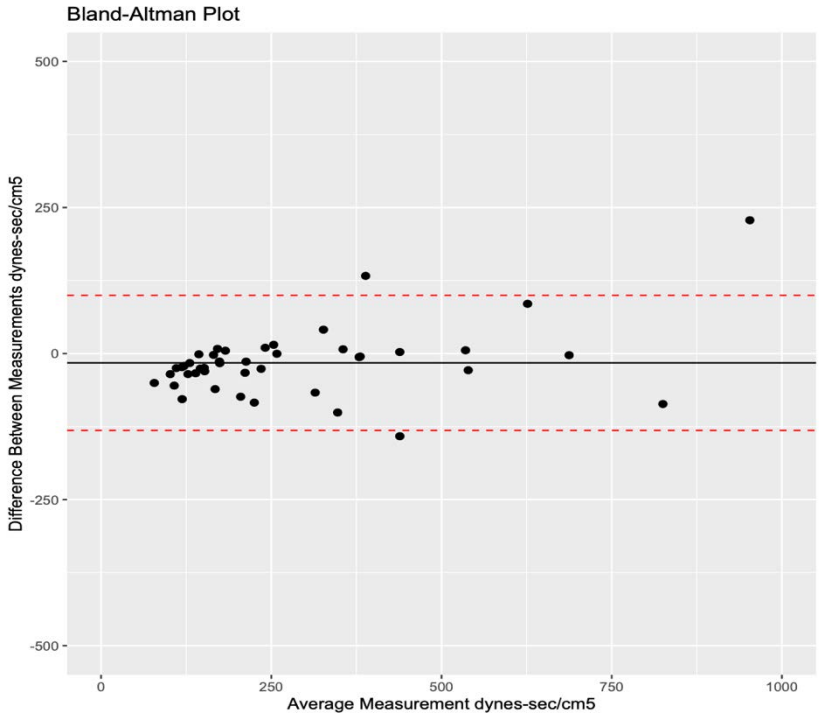

Figure 2. Bland-Altman plot of test dataset mr-PVR.

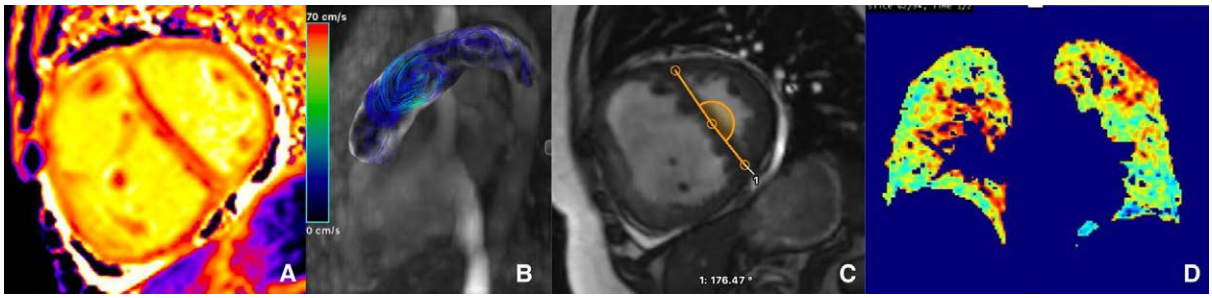

Figure 3. Example images obtained in precapillary pulmonary hypertension. A: T1 mapping B: 4D flow vortices C: Ventricular septal angle measurement D: Lung water density mapping.

Proceedings **SCMR 26th Annual Scientific Sessions** (2023)
Abstract number **1351872**
Abstract accepted as an Oral presentation.
My contribution: I helped in the image reconstruction framework for the first ~20 datasets and provided counseling on the interpretation of the results.

A2.2.8. Comparison of free-running whole-heart 5D and 4D compressed sensed flow imaging to standard 2D phase contrast in patients with right-sided congenital heart disease

Tobias Rutz[1], Estelle Tenisch[2], Mariana B.L. Falcão[2], Christopher W. Roy[2], Sara Faessler[1], David Rodrigues[2], Liliana Ma[3,4], Michael Markl[3,4], Matthias Stuber[2,5], Davide Piccini[2], Jürg Schwitter[1], Milan Prša[6]

[1]Service of Cardiology, Centre de resonance magnétique cardiaque (CRMC), Lausanne University Hospital and University of Lausanne, Lausanne, Switzerland.
[2]Department of Diagnostic and Interventional Radiology, Lausanne University Hospital and University of Lausanne, Lausanne, Switzerland.
[3]Department of Radiology, Feinberg School of Medicine, Northwestern University, Chicago, IL, United States.
[4]Department of Biomedical Engineering, Northwestern University, Chicago, IL, United States.
[5]Center for Biomedical Imaging (CIBM), Lausanne, Switzerland
[6]Pediatric Cardiology Unit, Woman-Mother-Child Department, Lausanne University Hospital and University of Lausanne, Lausanne, Switzerland.

Background:

Flow quantification by cardiac magnetic resonance (CMR) is particularly important in right-sided congenital heart disease (CHD). 2D phase contrast (2DPC) flow sequences are limited by the need for precise prescription of image planes, long scan time and impreciseness in the presence of valvulopathies[1]. Recently introduced accelerated free-breathing 3D whole heart flow sequences promise to simplify CMR exam allowing faster image acquisition and retrospective flow measurements. This study compares therefore standard 2DPC to an accelerated 4D flow sequence with prospective respiratory navigation[2] and a free-running radial fully self-gated respiratory and cardiac motion-resolved 5D flow[3,4].

Methods:

Patients with right-sided CHD were scanned on a 1.5T MAGNETOM Sola system (Siemens Healthcare, Erlangen, Germany). 2DPC was performed in the ascending, descending aorta (AA, DA), main, right and left pulmonary artery (MPA, RPA, LPA) and superior vena cava (SVC). A prototype whole-heart free-running 3D radial PC CMR sequence was also acquired[3]. Using a compressed-sensing-based image reconstruction framework[3,4], 5D flow images were obtained, and the end-expiratory phase was used for analysis. Finally, 4D flow data were collected.2 3D vessel segmentation was based on retrospectively computed phase-contrast angiography images for each 5D and 4D flow datasets. Flow rate was measured in the AA, DA, MPA, RPA, LPA and SVC on images obtained with all three sequences.

Results:

Fifteen patients (age 31±3 years, 7 women, tetralogy of Fallot 10, Ross operation 4, pulmonary valvuloplasty 1) were included. Mean pulmonary regurgitation fraction (PR) was 16 ± 4 % (range 1; 51) and peak velocity of MPA/ right ventricle to pulmonary artery conduit was 2.0 ± 0.2 m/s (range 0.9; 3.5).

	2DPC	4DCS	5D flow	p
AA, l/min	4.9 ± 1.0	4.6 ± 1.9	4.7 ± 0.9	0.850
DA, l/min	2.6 ± 0.8	2.6 ± 0.7	2.5 ± 0.8	0.943
MPA, l/min	4.6 ± 1.4	3.9 ± 1.2	4.2 ± 1.1	0.423
RPA, l/min	2.7 ± 0.7[1]	1.9 ± 0.5	2.4 ± 0.4	0.004
LPA, l/min	2.1 ± 0.7[2]	1.6 ± 0.5	1.8 ± 04	0.048
SVC, l/min	1.5 ± 0.4	1.2 ± 0.3	1.2 ± 0.4	0.066

Table 1. Comparison of absolute flow rate values (l/min) between 2DPC vs. 4DCS and 5D flow. [1]p=0.04 2DPC vs. 4DCS, [2]p=0.052 2DPC vs. 4DCS. *Abbreviation: AA = ascending aorta, DA = descending aorta, MPA = main pulmonary artery, RPA = right pulmonary artery, LPA = left pulmonary artery, SVC = superior vena cava.*

	2DPC vs. 4DCS	2DPC vs. 5D flow	p
AA	0.18 (-2.77, 3.14)	0.19 (-1.52, 1.90)	0.999
DA	0.07 (-1.99, 1.9)	0.16 (-2.55, 2.24)	0.723
MPA	0.77 (-1.01, 2.60)	0.52 (-1.9, 3.0)	0.397
RPA	0.73 (-0.14, 1.56)	0.30 (-0.64, 1.24)	<0.001
LPA	0.45 (-0.49, 1.40)	-0.27 (-95, 1.48)	0.347
SVC	0.29 (-0.13, 0.71)	0.26 (-0.14, 0.65)	0.636

Table 2. Bias 2DPC vs. 4DCS and 5D flow. Data shown are bias (l/min) (lower, upper limit of agreement). *Abbreviation: AA = ascending aorta, DA = descending aorta, MPA = main pulmonary artery, RPA = right pulmonary artery, LPA = left pulmonary artery, SVC = superior vena cava.*

Compared to 2DPC, both 4D and 5D flow generally tended to underestimate absolute flow rate with significant reduction in the RPA and LPA for 4D (**Tab 1**).

Analysis of RPA flow revealed a significantly smaller bias for the comparison of 2DPC vs. 5D flow rate compared to 2DPC vs. 4D flow rate (**Tab 2**).

The bias i.e. the difference of RPA flow rate between 2DPC vs. 4D as well as 2DPC vs. 5D flow, was directly related to the RPA peak velocity (RPA PV, **Fig 1**): RPA PV to RPA 2DPC vs. 4D: r2=0.413, p=0.013, RPA PV to 2DPC vs. 5D: r2=0.317, p=0.045. The bias of RPA flow rate between 2DPC vs. 4D flow correlated to the MPA PR: r2=0.308, p=0.039. There were no similar observations for other vessels.

Conclusion:

4D and 5D flow provide results comparable to 2DPC, however, both sequences showed a trend to lower absolute flow values which is particularly true for the pulmonary arteries. Flow turbulences due to the pulmonary valvulopathies could explain these observations, as their severity appears to influence the agreement between 2DPC and both 4D and 5D flow sequences.

Larger studies are planned to better elucidate the reasons for our results and to understand which sequences determine most accurately the true flow rate.

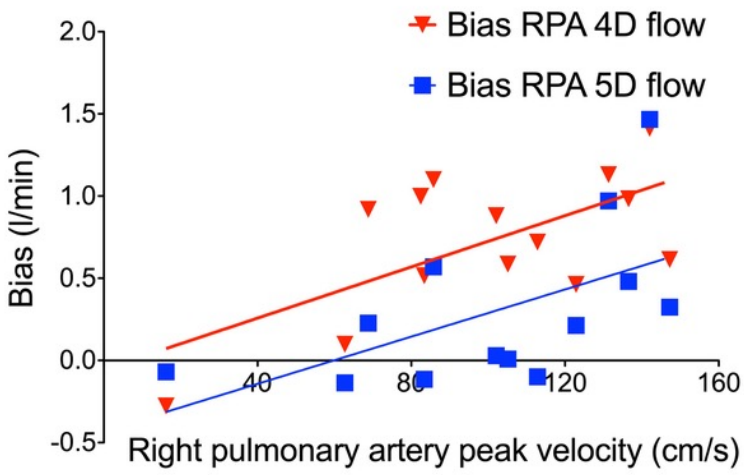

Figure 1. Correlation of bias of 2DPC vs. 4D flow (red line) and 2DPC vs. 5D flow (blue line) measurements in right pulmonary artery (RPA) to right pulmonary artery peak velocity

References

1. Rutz T, et al. Comparison of MR flow quantification in peripheral and main pulmonary arteries in patients after right ventricular outflow tract surgery: A retrospective study. J Magn Reson Imaging. 2017;46(6):1839-1845.
2. Ma LE, et al. 5D Flow MRI: A Fully Self-gated , Free-running Framework for Cardiac and Respiratory Motion – resolved 3D Hemodynamics. Radiol. Cardiothorac. Imaging 2020;2(6).
3. Di Sopra, et al. An automated approach to fully self-gated free-running cardiac and respiratory motion-resolved 5D whole-heart MRI. Magn. Reson. Med. 2019:1–15.
4. Ma LE, et al. Aortic 4D flow MRI in 2 minutes using compressed sensing, respiratory controlled adaptive k-space reordering, and inline reconstruction. Magn Reson Med 2019;81(6):3675-3690.

Proceedings **SCMR 26th Annual Scientific Sessions** (2023)
Abstract number **1353476**
Abstract accepted as a Power Pitch.
My contribution: I helped in the data acquisition, image reconstruction and data preparation for analysis of all datasets.

A2.2.9. Dual Venc 5D flow MRI with Increased Velocity Dynamic Range: An in-vitro and in-vivo Validation and Feasibility Study

Elizabeth Weiss[1,2], Justin Baraboo[1,2], Liliana Ma[1,2], Mariana B. L. Falcão[3], Christopher W. Roy[3], Matthias Stuber[3,4], and Michael Mark[1,2]

[1]Biomedical Engineering, Northwestern University, Evanston, IL, United States, Radiology,
[2]Feinberg School of Medicine, Chicago, IL, United States,
[3]Department of Radiology, Lausanne University Hospital (CHUV) and University of Lausanne (UNIL), Lausanne, Switzerland,
[4]CIBM Center for Biomedical Imaging, Lausanne, Switzerland,

Synopsis

We illustrate a pilot study of the first implementation of dual-venc 5D flow MRI. We found excellent voxel-wise agreement with single-venc 5D flow in a pulsatile phantom. In two healthy controls, we find good agreement, but identify unexpected aliasing in the dual venc 5D flow which requires further investigation.

Introduction

Respiration has been shown to be an important driver of hemodynamics in patients post-Fontan repair[1]. 5D flow MRI[2] is a new, free-running, self-gated, highly accelerated method to measure respiration driven 3D blood flow velocities over the cardiac and respiratory cycles. However, a single velocity encode (venc) in 5D flow MRI limits the velocity dynamic range. This is problematic when both venous and arterial flows must be measured (e.g., aortopulmonary collateral quantification). To address this limitation, we developed dual-venc 5D flow MRI which takes advantage of high velocity-to-noise ratio (VNR) of low venc acquisitions while correcting aliasing with high venc data. The goal of this study was to validate the technique in vitro and demonstrate its feasibility in healthy volunteers.

Methods

The proposed dual venc (DV) 5D flow MRI sequence utilized a 7-point velocity encoding scheme to measure both low venc (LV) and high venc (HV) velocity data (**Fig.1a**). The acquisition (2.5x2.5x2.5mm^3, TE/TR: 4.1/34.9ms) was free-running, radially sampled, and retrospectively self-gated using respiratory and cardiac signals extracted from superior-inferior readouts.

The LV and HV data were reconstructed in parallel using compressed sensing (CS) and were separately preprocessed for background-phase corrections. A difference image (HV-LV) was used to identify and correct velocity aliasing in the LV data as previously described[3] (**Fig.1b**). This preserved the favorable VNR of the LV images while correcting aliasing using the HV images.

DV 5D flow (venc=60/120cm/s) was acquired in an established pulsatile flow phantom[2] (60bpm, U-tube shape, Gd enhanced water) for validation. The respiratory dimension was collapsed in this experiment. Single venc (SV) 5D flow (venc=120cm/s) and 4D flow (venc=120cm/s) were also acquired. Both 5D flow scans had set scan times (SV: 8.5min, DV: 18min) that acquired 4820 radial spokes with 6 subshots for velocity encoding (4 gradients in SV, 7 in DV).

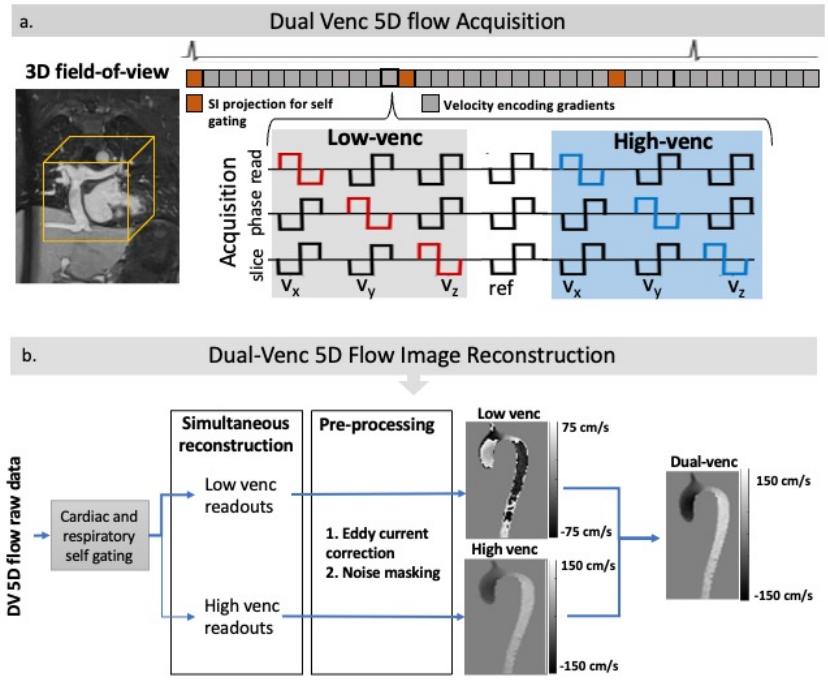

Figure 1. Dual Venc 5D flow acquisition and reconstruction. A 7-point gradient velocity encoding scheme is used in addition to interspersed superior-inferior readouts for self-gating (a). The raw dual venc 5D flow data is gated along the respiratory and cardiac dimension. The LV and HV images are reconstructed in parallel, separately preprocessed, and combined using a difference image (b).

Net flow and peak velocity were measured in several 2D regions of interest (Fig3a). VNR (Eq1) was calculated in both SV and DV 5D flow images (water bottles used as static tissue).

$$\text{VNR}=\text{mean}(\text{velocity 3D segmentation})/\text{SD}(\text{velocity static tissue}) \quad [\text{EQ1}]$$

DV (venc=75/150cm/s) and SV (venc=150cm/s) 5D flow were also acquired in 2 healthy adults. Voxel-wise comparisons were made in a region with velocity aliasing in the LV, but not HV, data. VNR in the caval veins was calculated in both SV and DV 5D flow images (spine segmented for static tissue). Only end-expiration was compared in this study.

Results

In-vitro validation: Aliasing was seen in LV images (**Fig.2a**) that was corrected in the DV images (**Fig.2c**). Bland-Altman analysis revealed good agreement with 4D flow for net flow (limits of agreement [LOA]: 2.9mL, 10% of mean net flow) and peak velocity (LOA: 6.7cm/s, 10% of mean peak velocity) (**Fig.3**). However, there was significant overestimation by DV 5D flow compared to 4D flow in both net flow (1.7mL, p=0.02, 6% of mean net flow) and peak velocity (4.2cm/s, p=0.01, 7% of mean peak velocity). Bland-Altman analysis for voxel-wise comparisons of SV and DV velocities had significant bias (<1cm/s, p<.01) and LOA of <6cm/s in all velocity directions (7% of peak velocity and 13% of mean velocity at peak flow, **Fig.4**). VNR increased 69% in DV images compared to SV images.

In-vivo feasibility: In both volunteers, there was unexpected aliasing near the aortic valve in HV images (Fig5a) and was thus uncorrected in the DV images. However, there was appropriate correction

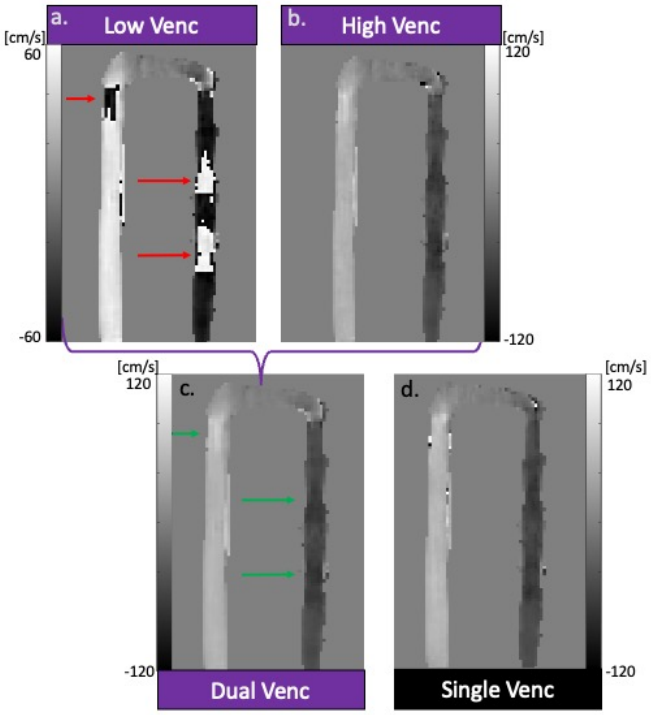

Figure 2. Aliasing (red arrows) is clearly shown in a slice from the low venc reconstruction (a). These voxels are not aliased in the high venc image (b) and thus, aliasing was corrected in the combined dual venc image (green arrows, c). Qualitatively, the velocities are similar to the single venc image (d).

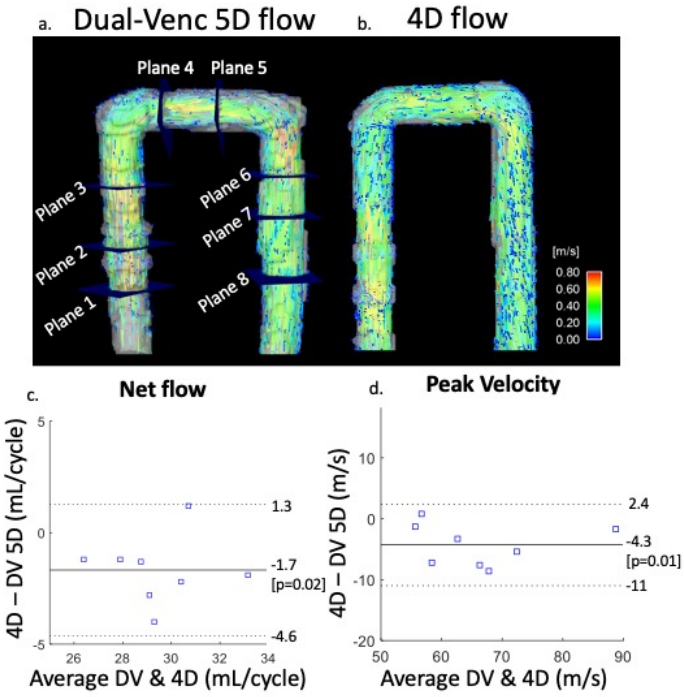

Figure 3. Net flow and peak velocity were measured at several locations in the phantom (a). Qualitatively, pathlines are similar between the DV 5D flow (a) and 4D flow (b) acquisitions. There was good agreement in net flow (c) and peak velocity (d) between these acquisitions with slight overestimation by DV 5D flow. There was similar plane to plane variability in net flow between DV 5D flow and 4D flow.

of aliasing in other regions, such as the descending aorta (**Fig.5b**), which had good agreement of velocity magnitude in both subjects between SV and DV 5D flow (LOA: 11 & 9cm/s, bias <1cm/s p<.01, **Fig.5b**). This was 11% and 10% of peak velocity in the DAo respectively. Additionally, the DV images had an 80% increase and 109% increase in VNR in each subject, respectively.

Discussion

We demonstrate the first implementation of DV 5D flow MRI. The acquisition improved VNR >65% compared to SV 5D flow which is greater than what could be achieved from simply increasing the

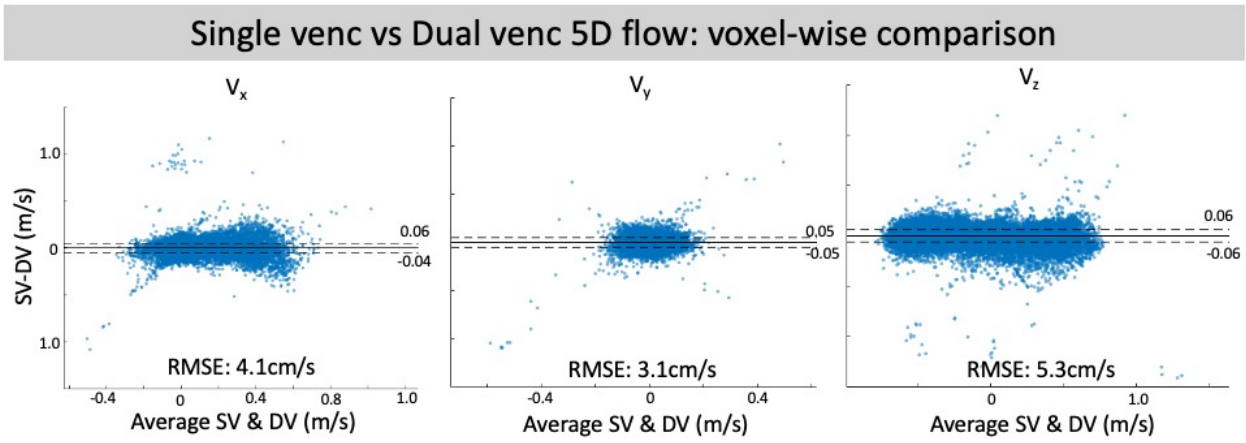

Figure 4. Voxel-wise comparison between dual venc 5D flow and single venc 5D flow over all time points in the phantom. There is excellent agreement in all velocity directions with bias <1cm/s and limits of agreement £ 6cm/s. RMSE = root mean square error.

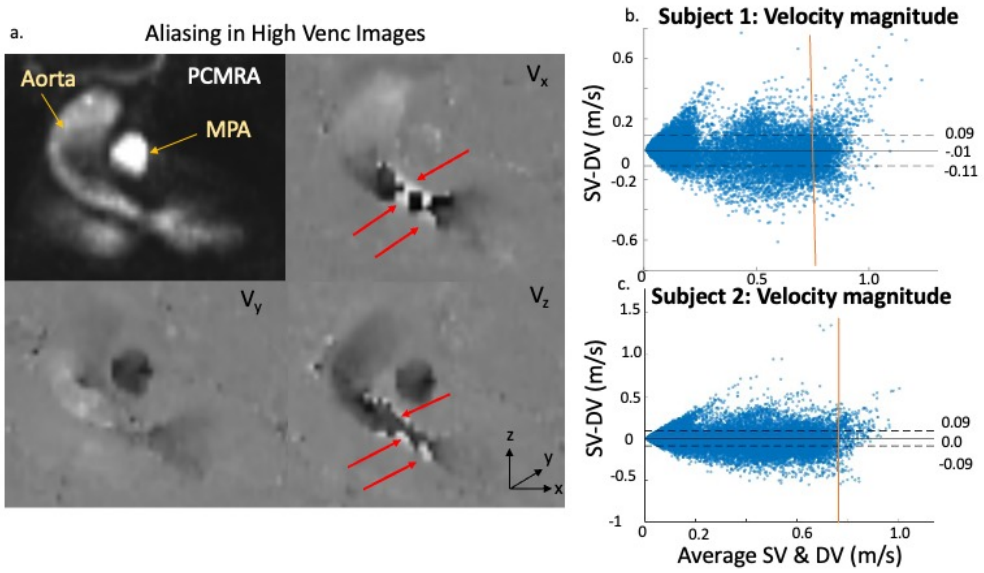

Figure 5. Dual venc 5D flow in healthy volunteers. Example images demonstrate aliasing (red arrows) occurring near the aortic valve in the HV images (a). Voxel-wise comparison of DV 5D flow and SV 5D flow in the descending aorta for both subjects demonstrate good agreement (b-c), even in velocities above the low venc (orange line, 75 cm/s) where aliasing would occur in the LV images. Some variability between scans may be due to imperfect alignment of cardiac rhythm. PCMRA = phase contrast MR angiogram, MPA = main pulmonary artery.

scan time to 18 minutes (45% increase). The theoretical VNR increase due to halving the venc was ~100%. Variation from this may be due to the high acceleration, imperfect background phase correction, or CS regularization. The increased VNR will improve the utility of 5D flow in Fontan patients. For example, slow, venous flow has been shown to vary with respiration.2 However, selecting a venc to best measure this precludes analysis in narrowed pulmonary arteries, a possible cause of Fontan failure.4 While these are promising results, in vivo data suggests that further investigation is necessary to prevent aliasing seen near the aortic valve. This artefact may reflect increased noise due to imbalanced distribution of the first magnetic moment in the HV gradients or increased motion noise due to long scan times. This study served to establish in vitro validation and in vivo feasibility of dual venc 5D flow MRI. Additional studies are necessary to investigate the impact of DV 5D flow on respiratory driven hemodynamics

Conclusion

We illustrated a pilot study of the first implementation of dual-venc 5D flow MRI. We found good agreement with single venc 5D flow and 4D flow in a pulsatile phantom in addition to increased VNR.

References

1. Wei, Z., Whitehead, K. K., Khiabani, R. H., Tree, M., Tang, E., Paridon, S. M., ... & Yoganathan, A. P. (2016). Respiratory effects on Fontan circulation during rest and exercise using real-time cardiac magnetic resonance imaging. The Annals of thoracic surgery, 101(5), 1818-1825.
2. Ma, L. E., Yerly, J., Piccini, D., Di Sopra, L., Roy, C. W., Carr, J. C., ... & Markl, M. (2020). 5D flow MRI: a fully self-gated, free-running framework for cardiac and respiratory motion–resolved 3D hemodynamics. Radiology: Cardiothoracic Imaging, 2(6).
3. Schnell, S., Ansari, S. A., Wu, C., Garcia, J., Murphy, I. G., Rahman, O. A., ... & Markl, M. (2017). Accelerated dual-venc 4D flow MRI for neurovascular applications. Journal of Magnetic Resonance Imaging, 46(1), 102-114.
4. Amodeo, A., Galletti, L., Marianeschi, S., Picardo, S., Giannico, S., Di Renzi, P., & Marcelletti, C. (1997). Extracardiac Fontan operation for complex cardiac anomalies: seven years' experience. The Journal of thoracic and cardiovascular surgery, 114(6), 1020-1031.

Proceedings **ISMRM & ISMRT Annual Meeting & Exhibition** (2023)
Abstract number **4229**
Abstract accepted as a Power pitch.
My contribution: I provided counseling on the interpretation of the results.

A2.2.10. Respiration-resolved 5D flow MRI: Impact of the number of respiratory states of blood flow quantification in congenital heart disease patients

Elizabeth Weiss[1,2], Justin Baraboo[1,2], Liliana Ma[1,2], Mariana B. L. Falcão[3], Christopher W. Roy[3], Joshua D. Robinson[4], Matthias Stuber[3,5], Cynthia K. Rigsby[4], and Michael Mark[1,2]

[1]Biomedical Engineering, Northwestern University, Evanston, IL, United States, Radiology,
[2]Feinberg School of Medicine, Chicago, IL, United States,
[3]Department of Radiology, Lausanne University Hospital (CHUV) and University of Lausanne (UNIL), Lausanne, Switzerland,
[4]Medical Imaging, Lurie Children's Hospital, Chicago, IL, United States,
[5]CIBM Center for Biomedical Imaging, Lausanne, Switzerland,

Synopsis

We adapted our novel respiratory gating method to evaluate the impact of respiratory state (RS) resolution on respiratory driven flow measured by 5D flow MRI. We found that the impact of respiratory state resolution was both anatomy and vessel dependent. Caval veins and measurements in single ventricle disease patients were most impacted by the reduction of respiratory states. Shunt patients and pulmonary artery measurements were more robust to reduced RS and may be able to take advantage of the decreased acceleration associated with fewer RS. 5D flow MRI is well suited for this variable need as respiratory gating is retrospective.

Introduction

Respiration has been shown to drive hemodynamic changes in healthy individuals1 and patients with congenital heart disease (CHD).2 Yet, conventional flow methods including 2D phase contrast and 4D flow MRI are often limited to acquisition during a single respiration state (breath-hold, navigator-gated). 5D flow MRI3 is a new free-running, self-gated technique that enables 3D velocity quantification over both cardiac and respiratory cycles. However, the original respiratory gating method (Fig1a) did not reflect the physiology of respiration. Additionally, while four respiratory states (RS) were typically reconstructed, it is unclear if this respiratory resolution is optimal. 5D flow uses highly accelerated, radial sampling combined with compressed sensing (CS) reconstruction. Reduction of RS may decrease acceleration, enabling improved image quality or shorter scan time. We aimed to assess the impact of RS resolution on respiratory driven flow measurements in a novel physiology driven gating method.

Methods

11 patients with CHD (15.6±11.7yrs, M/F: 5/6) undergoing a clinically indicated CMR with ferumoxytol were consented for an 8.5-minute 5D flow add-on (res: 1.5-2.5mm isotropic, cardiac res: 40ms). Superior-inferior readouts were used to extract cardiac and respiratory signals for retrospective gating. Scans were reconstructed three times: with 2, 3, or 4 RS. The physiology driven gating method sorted readouts on a per-breath basis, assigning the maximum and minimum 25% of signal to end-expiration and end-inspiration respectively. To define 4 RS, the remaining points were assigned to expiration and inspiration based on slope (Fig1b). To create 3 RS, inspiration and end-inspiration were combined (Fig1c). For 2 RS, end-expiration and expiration were also combined (Fig1d). These reductions aimed to decrease CS acceleration. The acceleration was patient-specific, based on

respiratory gating (Fig2). Net flow was measured in the ascending aorta (Ao), main pulmonary artery (MPA), left and right pulmonary arteries (LPA&RPA), and inferior and superior vena cava (IVC&SVC). Range of net flow over all RS, normalized to the mean over respiration, defined respiratory driven flow changes. Median respiratory resolved flow curves were normalized to end-expiration. The cohort was stratified into two subgroups: single ventricle disease (SVD, n=5) and shunt physiology (n=5). One patient fit neither group.

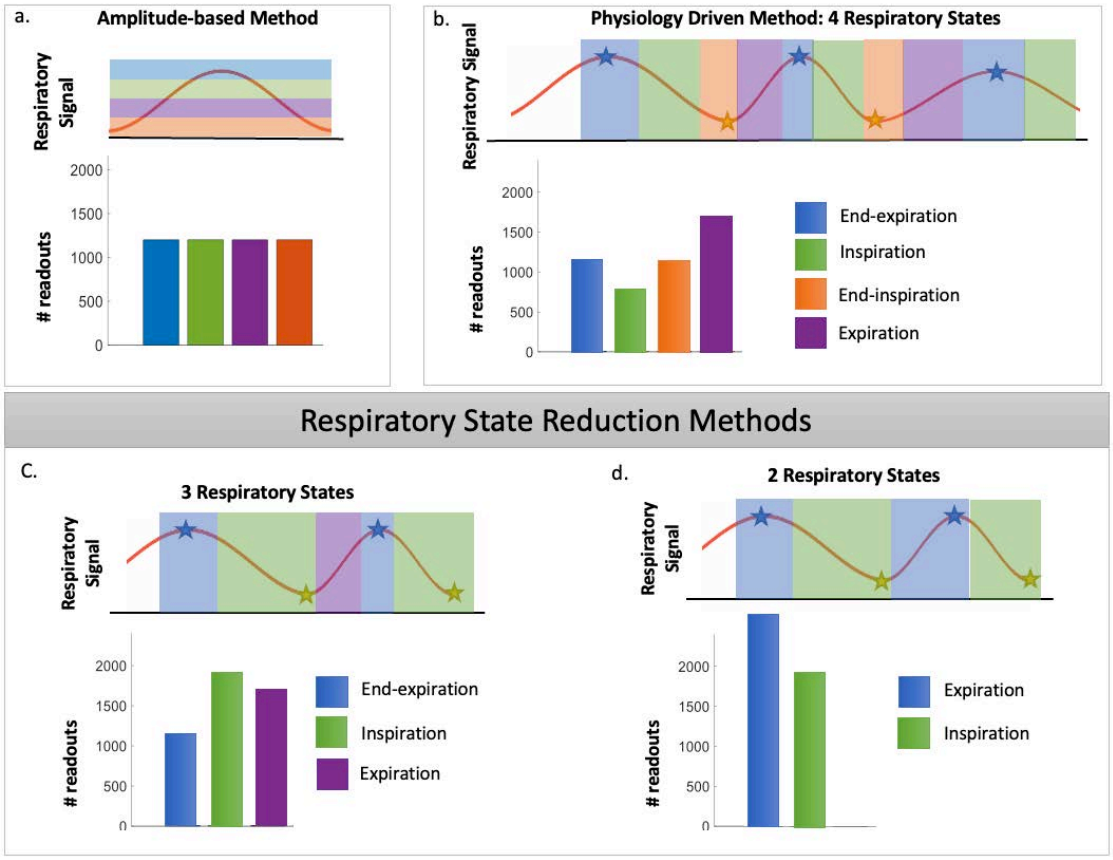

Figure 1. Respiratory gating methods overview. Initial implementation of 5D flow MRI used an amplitude-based method to determine respiratory states (**a**, RS). We have proposed a novel approach, defining a gating method based on physiologic respiratory states (**b**). In this abstract, we propose two methods to reduce the number of respiratory states (**c-d**). The number of readouts per respiratory state is patient specific as determined by the gating method.

Results

Respiratory gating and CS acceleration: Data acquired during expiration and end-expiration covered a significantly larger fraction of the respiratory cycle than inspiration (28% & 29% vs 20%, $p<0.01$) and end-inspiration (28% & 29% vs 23%, $p<0.01$). With reduced RS resolution, the necessary CS acceleration decreased (Fig2).

Respiratory driven net flow changes: Reduced RS resolution decreased respiratory driven flow changes measured in the aorta, pulmonary arteries (PAs, MPA, LPA&RPA), and caval veins (IVC&SVC). Flow changes were significantly larger in 4 RS images compared to 3 and 2 RS images in the aorta (12% vs 8% & 3%, $p<0.017$) and caval veins (59% vs 46% & 28%, $p<0.017$). Caval veins had significantly larger flow changes than the PAs in 4 RS (28% vs 59%, $p<0.017$) and 3 RS (22% vs 46%, $p<0.017$) images, but not in 2 RS images. The aorta had significantly smaller respiratory driven changes than the PAs and caval veins in all images (Fig3).

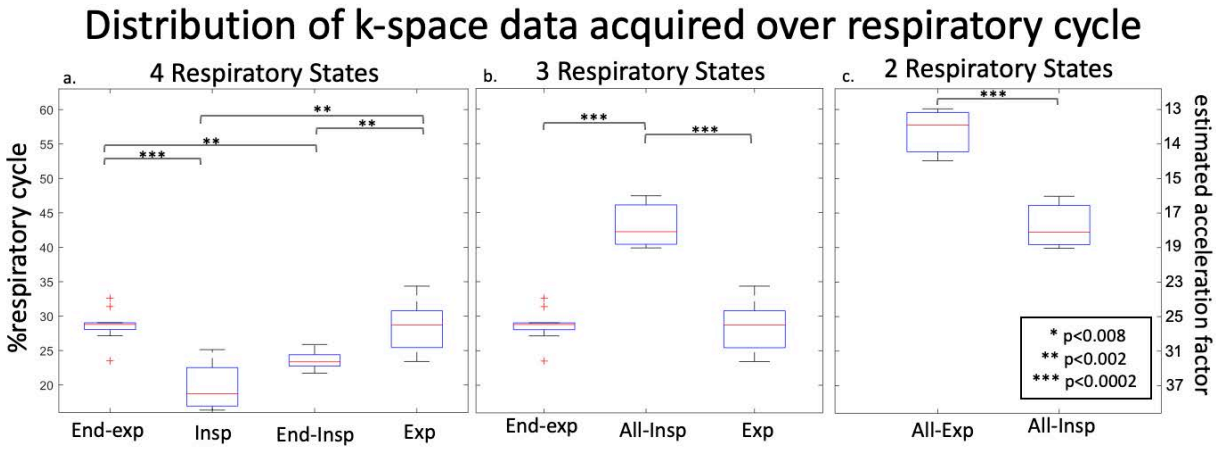

Figure 2. Physiology driven respiratory gating yields unequal distribution of the number of k-space lines assigned to each respiratory state over, and thus, unequal acceleration across respiratory states. Relative distribution over the cohort is shown for 4 RS (**a**), 3 RS (**b**), and 2 RS (**c**). Acceleration factor was estimated assuming 20 equally filled cardiac time frames, a set scan time of 8.5 minutes, and 96x96x96 matrix size.

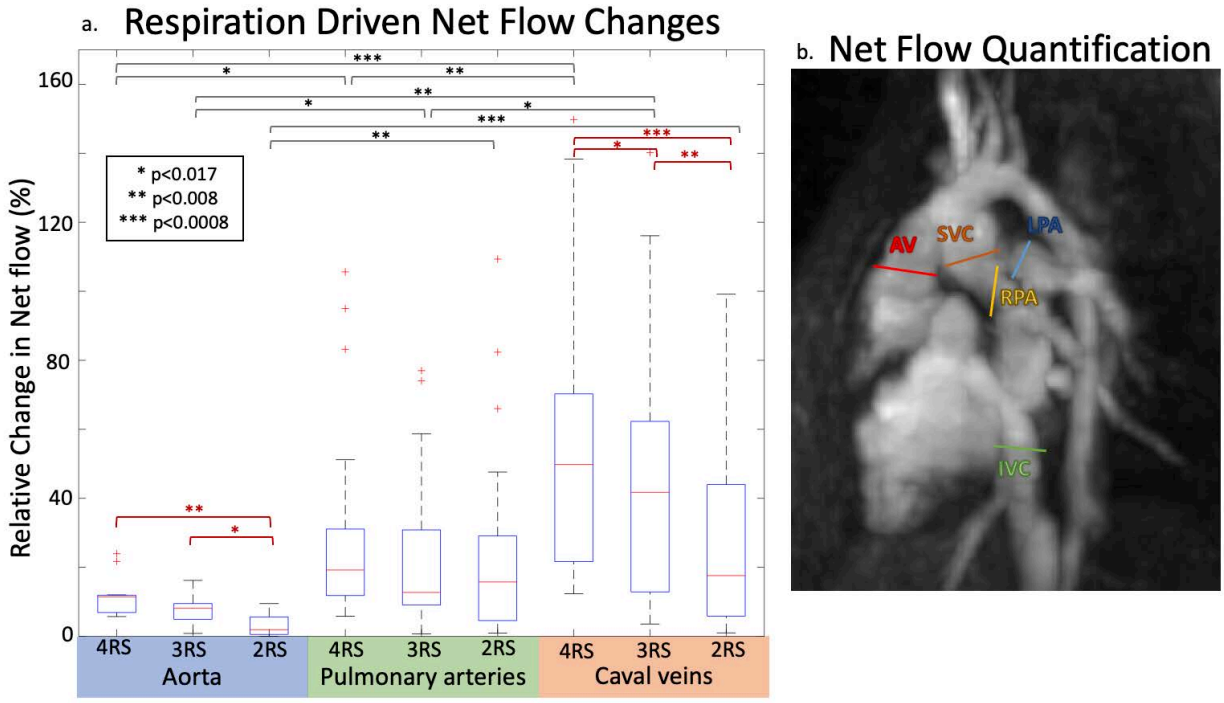

Figure 3. Impact of number of respiratory states on respiratory driven flow in the total cohort (n=11, a). Red comparison bar indicates differences within a vessel group, between respiratory resolutions. Example regions of interest are shown for a patient that was status-post Fontan repair (**b**).

Respiratory resolved flow curves: Timing of changes in flow over respiration were generally conserved with reduced RS (Fig4). However, in the IVC, the relative change in flow during inspiration in 4 RS images was significantly less than in 2 RS images (Fig4c, $p<0.01$).

Sub-group analysis: In 4 RS images, SVD patients had increased flow changes in PAs and caval veins compared to the aorta (Fig5). In shunt patients, caval veins had increased flow changes compared to the aorta and PAs. Only SVD patients had a substantial decrease in respiratory driven flow in caval veins from 3 to 2 RS. Additionally, inter-vessel group differences became insignificant for shunt patients when using <4 RS whereas differences were preserved using 3 RS in SVD patients.

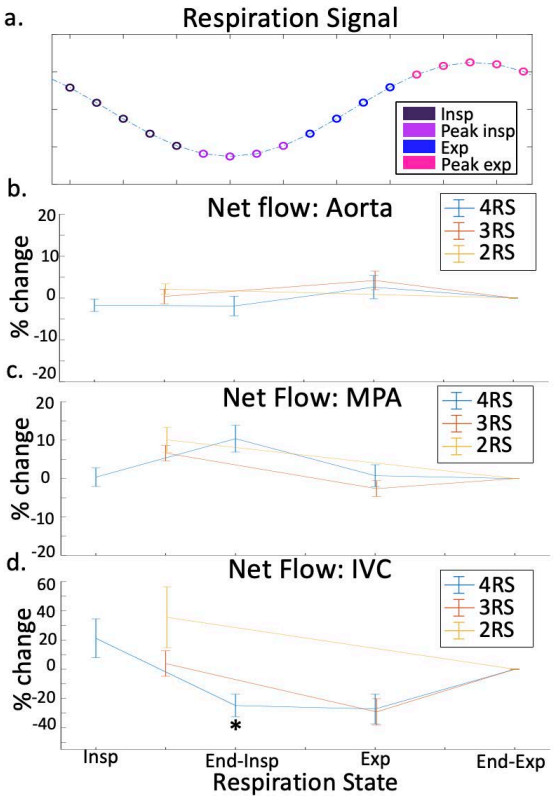

Figure 4. Impact of respiration (a) normalized to end-expiration in the aorta (b), main pulmonary artery (c), and inferior vena cava (d). Changes in flow were normalized to net flow during end-expiration. Asterisks indicates significant difference between 4RS and 2RS ($p<0.05$).

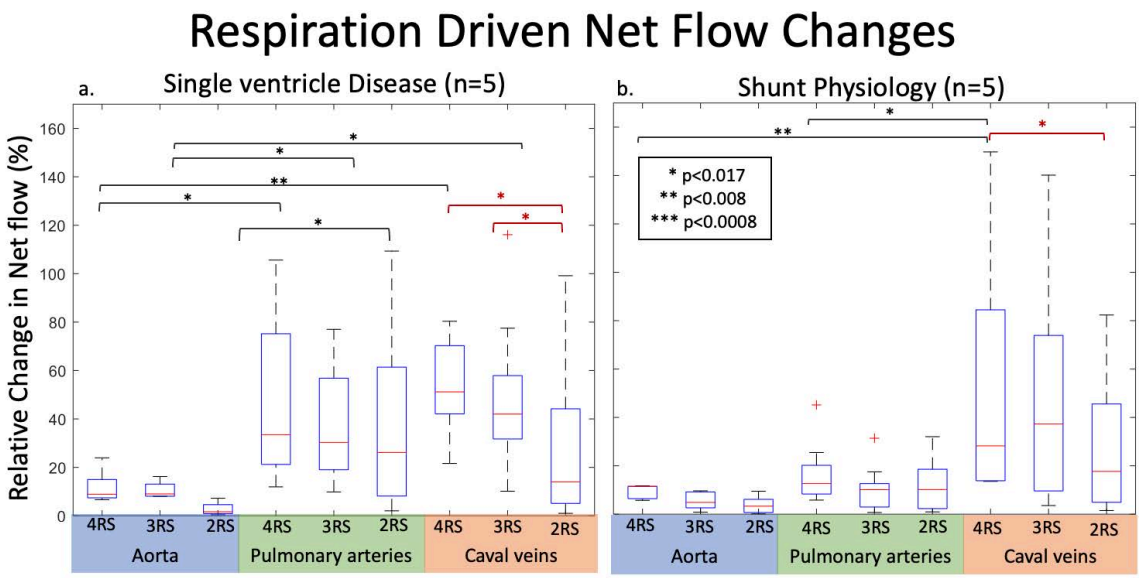

Figure 5. Impact of respiratory resolution in single ventricle disease patients (SVD, a) and shunt patients (b). Red comparison bar indicates differences within a vessel group, between respiratory resolutions.

Discussion

Overall, we found that the impact of respiratory resolution was vessel dependent. Respiratory driven flow decreased with RS resolution in the aorta and caval veins, but not in the PAs. This may be due to similar flow changes during end-inspiration and inspiration, leading to little information loss when combined. Yet, differences between PAs and caval veins were diminished in the 2 RS images. Due to retrospective self-gating, 5D flow is well-suited to the need for variable RS resolution, allowing

reduced CS acceleration in cases where 2 or 3 RS is sufficient. Additionally, in the IVC, end-inspiration and inspiration had different effects on flow. This information was lost in both the 2 and 3 RS images, suggesting 4 RS may be necessary to resolve respiratory driven flow in caval veins. We also showed that SVD anatomy may benefit more from additional RS than shunt anatomy. There was significant change in the caval veins with each respiratory state reduced only in the SVD group. Future studies should include additional CHD types and healthy volunteers to optimize respiratory resolution for each subject group.

Conclusion

We found that impact of respiratory resolution on flow was both anatomical subgroup and vessel dependent. In the caval veins and aorta, but not the PAs, reduction in RS decreased measured respiratory driven flow. Caval vein flow changes diminished with each combined RS in the SVD group only.

References

1. Körperich, H., Barth, P., Gieseke, J., Müller, K., Burchert, W., Esdorn, H., ... & Laser, K. T. (2015). Impact of respiration on stroke volumes in paediatric controls and in patients after Fontan procedure assessed by MR real-time phase-velocity mapping. European Heart Journal-Cardiovascular Imaging, 16(2), 198-209.
2. Wei, Z., Whitehead, K. K., Khiabani, R. H., Tree, M., Tang, E., Paridon, S. M., ... & Yoganathan, A. P. (2016). Respiratory effects on Fontan circulation during rest and exercise using real-time cardiac magnetic resonance imaging. The Annals of thoracic surgery, 101(5), 1818-1825.
3. Ma, L. E., Yerly, J., Piccini, D., Di Sopra, L., Roy, C. W., Carr, J. C., ... & Markl, M. (2020). 5D flow MRI: a fully self-gated, free-running framework for cardiac and respiratory motion–resolved 3D hemodynamics. Radiology: Cardiothoracic Imaging, 2(6).

Proceedings **ISMRM & ISMRT Annual Meeting & Exhibition** (2023)
Abstract number **4227**
Abstract accepted as an Oral presentation.
My contribution: I provided counseling on the interpretation of the results.

A2.3. Additional contributions

A2.3.1. Numerical optimization of 5D cardiac and respiratory motion-resolved CMR imaging for the assessment of left ventricular function

Jérôme Yerly[1,2], Christopher W Roy[1], Bastien Milani[1], Davide Piccini[1,3], Aurélien Bustin[1,4,5], Mariana B.L. Falcão[1], Ruud B. van Heeswijk[1], and Matthias Stuber[1,2]

[1]Radiology, Lausanne University Hospital (CHUV) and University of Lausanne (UNIL), Lausanne, Switzerland,
[2]CIBM Center for Biomedical Imaging, Lausanne, Switzerland,
[3]Advanced Clinical Imaging Technology, Siemens Healthcare, Lausanne, Switzerland,
[4]Electrophysiology and Heart Modeling Institute, IHU LIRYC, Bordeaux, France,
[5]Cardiovascular Imaging, Hôpital Cardiologique du Haut-Lévêque, CHU de Bordeaux, Bordeaux, France

Synopsis

The free-running framework (FRF) was recently proposed to address the limitations of current techniques to assess left ventricular (LV) ejection fraction (LVEF). However, the accuracy of FRF to assess LVEF has yet to be quantitatively examined. This work rigorously quantifies and optimizes the effect of the regularization weights on LVEF and several image quality metrics using a numerical phantom with well-controlled boundary conditions, and validates the results in in-vivo 5D FRF data. The results demonstrated that the combination of regularization weights that are optimal in terms of image quality do not correspond to the optimal weights for LVEF assessment.

Introduction

Left ventricular (LV) ejection fraction (LVEF) is a strong predictor of outcome in patients with heart failure[1]. Cardiac magnetic resonance (CMR) is the gold-standard for LVEF assessment and typically involves the acquisition of a stack of LV short-axis 2D cine-images over multiple breath-holds. However, the low through-plane spatial resolution and coverage may be suboptimal for accurate assessment of LVEF[2]. Moreover, repeated breath-hold acquisitions may lead to poor reproducibility of end-inspiration position, are often challenging for patients, and may even cause Valsalva maneuvers resulting in biased LVEF measurements. In addition, operator involvement remains considerable as several cardiac localizers are still necessary to find the short-axis view. The free-running framework (FRF)[3] was recently proposed to remove these constraints and to simplify workflow of LVEF assessment[4]. However, the accuracy of FRF to assess LVEF has yet to be quantitatively examined. To reconstruct the highly undersampled 3D+cardiac+respiratory motion-resolved (5D) images, FRF requires careful optimization of the regularization weights to find a compromise between residual aliasing and compression of the underlying physiological motion. This work rigorously quantifies and optimizes the effect of the regularization weights on LVEF and several image quality metrics using a numerical phantom with well-controlled boundary conditions, and validates the results in in-vivo 5D FRF data.

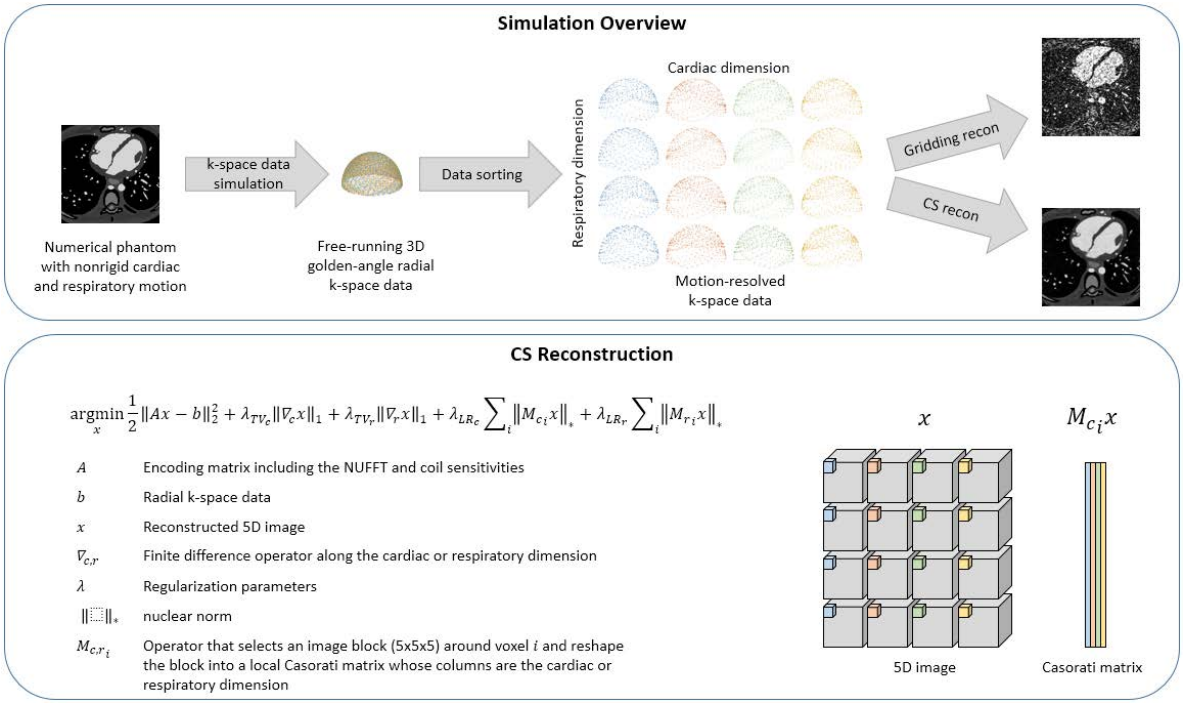

Figure 1. Schematic of the study design. Free-running 3D golden-angle radial k-space data were synthesized from the XCAT phantom, sorted into a 5D (x-y-z-cardiac-respiratory) matrix, and reconstructed with a compressed sensing reconstruction framework using both total variation (TV) and local low-rank (LR) regularization terms. The synthetic sequence parameters were: isotropic voxel size = $(1.1\text{mm})^3$, TR/TE = 3.1ms/1.6ms, RF flip angle = 61, radial interleaves = 5749, and profiles per interleave = 22.

Methods

Numerical Phantom: Free-running 3D golden-angle radial data were synthesized using a previously described numerical simulation[5]. The synthesized data simulated anatomical tissues with realistic nonrigid cardiac and respiratory motion derived from the XCAT phantom[6] and included heart-rate and respiratory motion variability. The simulated LVEF was 63.2%. The n-th radial readout corresponding to the (n-1)*TR timepoint was obtained by computing the 3D volume representing the desired cardiac and respiratory phase using the XCAT software, converting the labelled volume to CMR contrast using a bSSFP signal model with tissue relaxation properties from the literature, simulating 3D coil sensitivities, and computing the inverse NUFFT[5].

Image reconstruction: The synthetic FRF radial data were sorted into a 5D (x-y-z-cardiac-respiratory) matrix and reconstructed with the compressed sensing (CS) reconstruction framework shown in **Fig.1**. The reconstruction implemented total variation (TV) and local low-rank (LR) regularization terms along both the cardiac and respiratory dimensions. The four corresponding regularization weights were the independent variables that were optimized as described below.

Analysis: LVEF was automatically computed for every reconstructed dataset using thresholding and the ground truth position of the aortic and mitral valves. The image quality was quantitatively assessed by the following metrics: mean squared error (MSE), structural similarity index measure (SSIM), peak signal-to-noise ratio (PSNR), and blood-myocardium interface sharpness. The four regularization terms were first optimized individually by setting the other terms to zero. For each term, the two regularization weights that yielded the highest image quality with an LVEF error below 3%when compared to ground truth were selected for further optimization. The 3% limit is well within the range of intra and interobserver variability of LVEF reported in earlier studies[2]. Next, the four regularization terms were optimized by combining the weights previously selected. The optimal

combination of weights was determined by selecting the combination that resulted in the best image quality given a maximum acceptable LVEF error of 3%. Finally, as a proof of concept, the optimized combination was used to reconstruct an in-vivo 5D FRF dataset[4] and the LVEF was compared to a reconstruction using weights that were optimized for image quality only without considering the maximum acceptable error limit for LVEF.

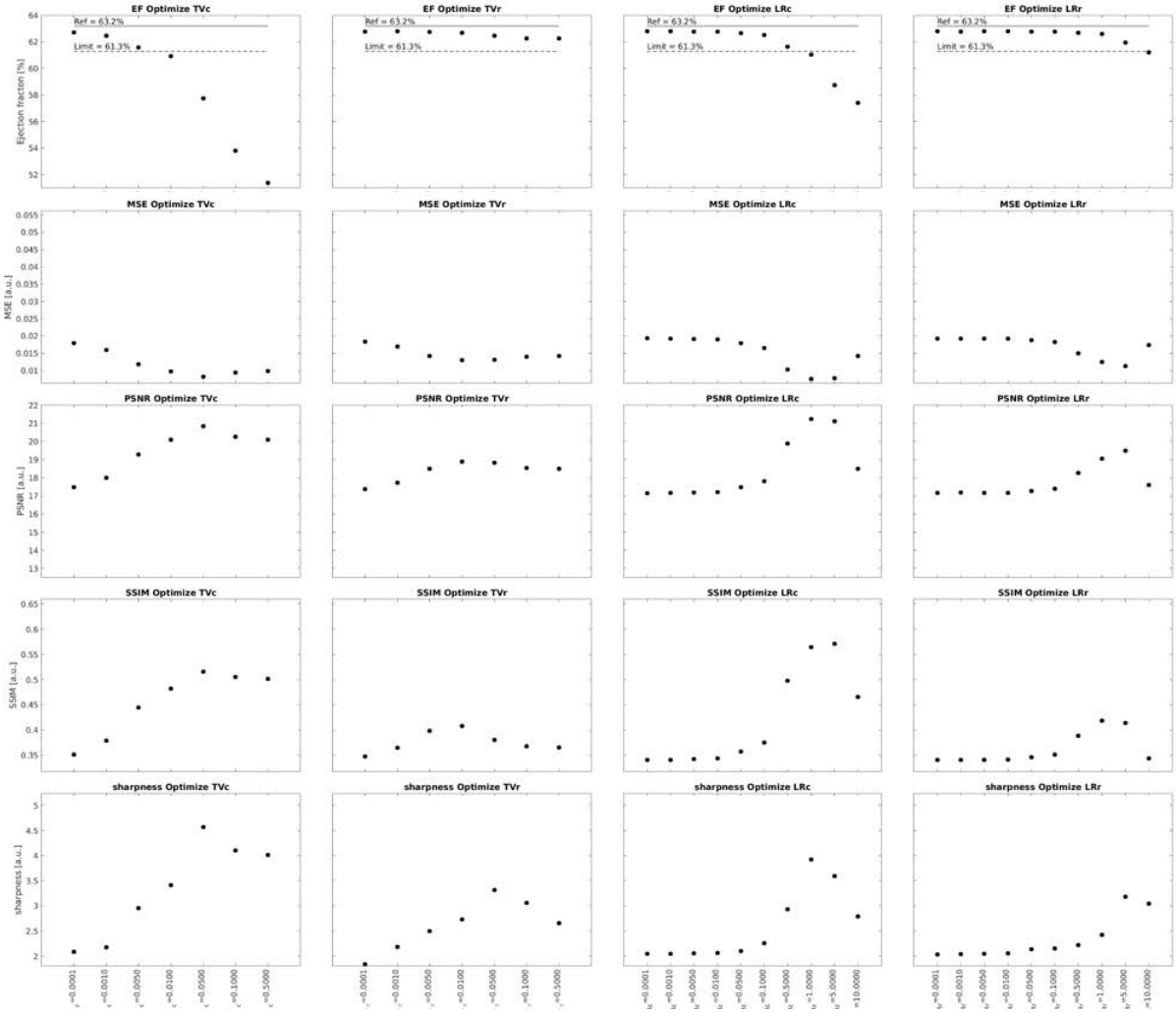

Figure 2. Individual optimization of the weights for the four different regularization terms in the CS reconstruction. For each regularization term, a range of weights was investigated while setting the weights for the other regularization terms to zero. For TV regularization, the weights ranged from 0.0001 to 0.5 and for LR regularization, the weights ranged from 0.0001 to 10. The solid and dashed lines in the LVEF plots indicate the ground truth LVEF (63.2%) and the 3% deviation, respectively.

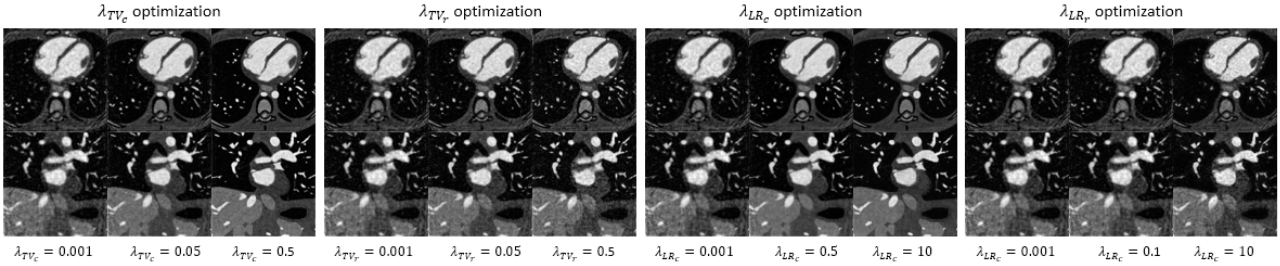

Figure 3. Animated gifs illustrating the cardiac and respiratory motion-resolved reconstructions for some of the regularization weights presented in Figure 2. High cardiac regularization weights did not significantly affect respiratory motion, but they significantly compressed cardiac motion. Similarly, high respiratory regularization weights did not significantly affect cardiac motion, but they significantly compressed respiratory motion.

Results

Increasing the regularization weights generally resulted in a decrease in LVEF and an improvement in image quality to a point beyond which image quality degraded again (**Fig.2**). Regularization along the respiratory dimension had a significantly lower impact on LVEF and image quality than regularization along the cardiac dimension, i.e. lower value spread (**Fig.2**). High respiratory regularization weights had little impact on LVEF, but significantly compressed respiratory motion (almost no visible respiratory motion for λ_{TV_r}=0.5 and λ_{LR_r}=10 in **Fig.3**). The optimization of each individual regularization term resulted in the following weights: λ_{TV_c}={0.001,0.005}, λ_{TV_r}={0.005,0.01}, λ_{LR_c}={0.1,0.5}, and λ_{LR_r}={0.5,1.0}. All possible combinations of the regularization terms with these weights resulted in an LVEF error of less than 3% (**Fig.4**). Among all these combinations, the one that gave the best image quality was (λ_{TV_c}, λ_{TV_r}, λ_{LR_c}, λ_{LR_r})=(0.001,0.01,0.5,0.5). Reconstruction of the in-vivo FRF dataset using this optimized combination of weights resulted in 50.04% LVEF. When using the set of weights that maximizes image quality without considering LVEF error, i.e. (λ_{TV_c}, λ_{TV_r}, λ_{LR_c}, λ_{LR_r})=(0.05,0.01,1.0,1.0), the LVEF was 44.87% in this case.

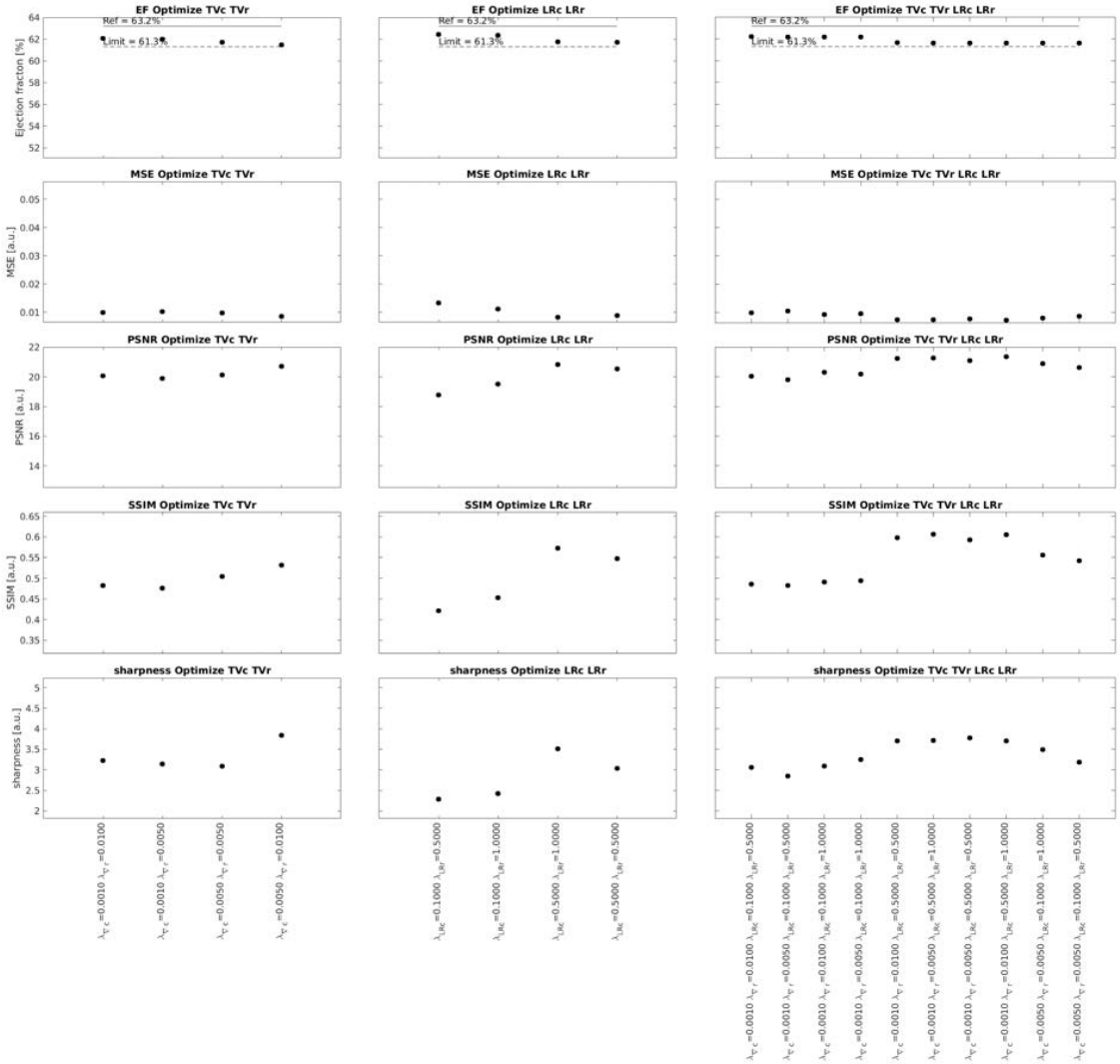

Figure 4. Optimization of the weights for the combined regularization terms in the CS reconstruction. The left column shows the results for reconstructions using only the two TV regularization terms; the middle column shows the results for the reconstructions using only the two LR regularization terms; and the right column shows the results for the reconstructions using all TV and LR regularization terms.

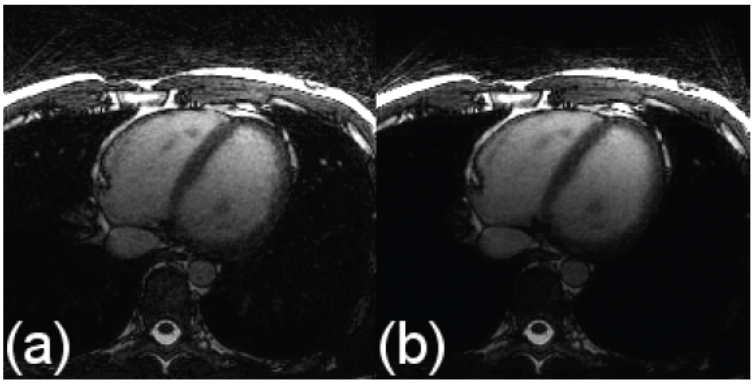

Figure 5. Animated gifs illustrating the cardiac and respiratory motion-resolved reconstructions for an in-vivo dataset using the optimized (a) and sub-optimal (b) combination of regularization weights resulting in LVEF values of 50.04% and 44.87%, respectively.*

* Images depicted in this Appendix are static.

Discussion and Conclusion

This experimental study rigorously quantified and optimized the effect of the regularization weights of a CS reconstruction on the LVEF and several image quality metrics using a numerical phantom with well-controlled boundaries. The results demonstrated that the combination of regularization weights that are optimal in terms of image quality do not correspond to the optimal weights for LVEF assessment. Increasing the regularization weights generally resulted in better image quality, but also decreased LVEF accuracy due to motion compression artifacts. A relatively wide range of parameters provided an acceptable tradeoff between LVEF accuracy and image quality. This study may help guide reconstruction parameters for CS reconstruction of free-running 5D images and may help bridge a gap in validating optimized FRF for LVEF assessment.

References

1. Curtis JP, Sokol SI, Wang Y, Rathore SS, Ko DT, Jadbabaie F, Portnay EL, Marshalko SJ, Radford MJ, Krumholz HM. The association of left ventricular ejection fraction, mortality, and cause of death in stable outpatients with heart failure. J Am Coll Cardiol 2003;42:736–42.

2. Vincenti G, Monney P, Chaptinel J, Rutz T, Coppo S, Zenge MO, Schmidt M, Nadar MS, Piccini D, Chèvre P, Stuber M, Schwitter J. Compressed Sensing Single–Breath-Hold CMR for Fast
Quantification of LV Function, Volumes, and Mass. JACC Cardiovasc. Imaging 2014;7:882–892 doi:10.1016/j.jcmg.2014.04.016.

3. Sopra LD, Piccini D, Coppo S, Stuber M, Yerly J. An automated approach to fully self-gated free-running cardiac and respiratory motion-resolved5D whole-heart MRI. Magn. Reson. Med. 2019;82:2118–2132 doi: 10.1002/mrm.27898.

4. Yerly J, Di Sopra L, Vincenti G, Piccini D, Schwitter J, Stuber M. Fully Self-Gated Cardiac and Respiratory Motion-Resolved 5D MRI for Rapid Assessment of Left Ventricular Function. In:
Montreal; 2019. p. 2106.

5. Roy CW, Heerfordt J, Piccini D, Rossi G, Pavon AG, Schwitter J, Stuber M. Motion compensated whole-heart coronary cardiovascular magnetic resonance angiography using focused navigation (fNAV). J. Cardiovasc. Magn. Reson. 2021;23:33 doi: 10.1186/s12968-021-00717-4.

6. Segars WP, Sturgeon G, Mendonca S, Grimes J, Tsui BMW. 4D XCAT phantom for multimodality imaging research. Med. Phys. 2010;37:4902–4915doi: 10.1118/1.3480985.

Proceedings **Joint Annual Meeting ISMRM-ESMRMB & ISMRT 31st Annual Meeting** (2022)
Abstract number **1650**
Abstract accepted as a Digital Poster.

My contribution: I helped the first author in the ejection fraction analysis of the healthy subject acquisition.

A2.3.2. Free-running 5D whole-heart MRI with ferumoxytol enhancement to evaluate cardiac function in congenital heart disease

Salim Aymeric Si-Mohamed[1,2], Ludovica Romanin[3,4], Mariana Falcao[3], Jerome Yerly[2,3], Estelle Tenisch[3], Tobias Rutz[5], Charles De Bourguignon[6], Jurg Schwitter[7,8,9], Matthias Stuber[2,3], Christopher Roy[3], and Milan Prsa[10]

[1]Radiology department, University of Lyon, Lyon, France,
[2]CIBM Center for Biomedical Imaging, Lausanne, Switzerland,
[3]Department of Radiology, Lausanne University Hospital (CHUV) and University of Lausanne (UNIL), Lausanne, Switzerland,
[4]Advanced Clinical Imaging Technology (ACIT), Siemens Healthcare AG, Lausanne, Switzerland
[5]Service of Cardiology, Heart and Vessel Department, Lausanne University Hospital (CHUV) and University of Lausanne (UNIL), Lausanne, Switzerland
[6] Research radiology department, Hospices Civiles de Lyon, Lyon, France,
[7]Division of Cardiology, Lausanne University Hospital (CHUV), Lausanne, Switzerland,
[8]Director CMR-Center, Lausanne University Hospital (CHUV), Lausanne, Switzerland,
[9]Faculty of Biology and Medicine, University of Lausanne (UNIL), Lausanne, Switzerland,
[10]Division of Pediatric Cardiology, Woman-Mother-Child Department, Lausanne University Hospital (CHUV) and University of Lausanne (UNIL), Lausanne, Switzerland,

Synopsis

Free-running 5D whole-heart imaging (5D CMR) has been proposed as a means of simplifying CMR exams by capturing the entire 3D cardiac anatomy without the need for ECG gating or breath-holds. We demonstrated that 5D CMR enables the evaluation of cardiac function in comparison to ECG gated 2D CINE images in congenital heart disease patients. In addition, it enables evaluation of the cardiac morphology with an improvement of the diagnostic quality in 66% of the cases. This suggests that the free-running approach has the potential for replacing the conventional 2D imaging for evaluation of both cardiac function and morphology.

Background

Cardiac magnetic resonance imaging (CMR) plays a critical role in the management of patients with congenital heart disease (CHD) [1,2]. In a conventional CMR exam, electrocardiogram (ECG) gated 2D CINE images (2D CMR) are the current gold standard for assessing cardiac function, but require a reliable ECG signal, precise prescription of multiple imaging planes, and patient ability to perform breath-holds. Recently, free-running 5D whole-heart imaging (5D CMR) has been proposed as for simplifying CMR exams by capturing the entire 3D cardiac anatomy without the need for ECG gating or breath-holds[3,4]. In this work, and using a gold standard comparison, we demonstrated feasibility and validity of using ferumoxytol-enhanced 5D CMR to evaluate cardiac function in a cohort of patients with CHD.

Methods

Seventeen CHD patients (22±15-years of age, 7 female (41%)) were retrospectively included in this monocentric study, after approval by the IRB. All patients underwent both 2D CMR and research 5D sequence CMR after an injection of 2 mg/kg of ferumoxytol[3,4] on a 1.5T clinical MR scanner (MAGNETOM Sola, Siemens Healthcare, Erlangen, Germany) with a 18-channel phased-array coil.

Relevant scan parameters for both sequences are listed in **Tab.1**. A cardiac radiologist with 7 years of experience reformatted the end-inspiratory images from 5D CMR to match the respiratory phase, orientation and slice thickness of 2D CMR. Two readers without experience of 5D CMR (R1: a radiologist and R2: research engineer with 7 and 9 years of experience in cardiac imaging, respectively) blinded to the patient's identity and condition, independently performed the measurement of end-diastolic and end-systolic cardiac volumes (EDV, ESV) in a random order on a clinical workstation using Circle software (cvi42 5.12.1). Inter- and intrareader reproducibility were assessed with the intraclass correlation coefficient (ICC). A two-way model with measures of consistency was used to calculate ICC values. Reproducibility was defined as poor (ICC<0.400), fair to good (ICC=0.400–0.750), or excellent (ICC>0.750). Two-sided P .05 was considered to indicate a significant difference. Diagnostic image quality was assessed and compared according to a five-point quality scale ranging from 1= insufficient due to blurring and/or breathing motion and/or insufficient contrast, to 5= excellent without blurring or breathing motion and with excellent contrast.

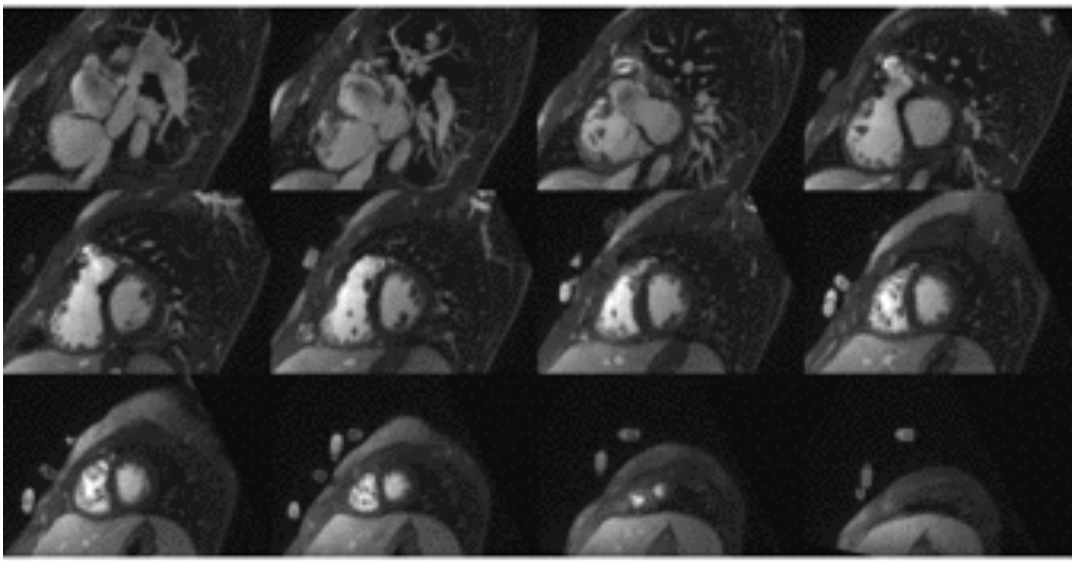

Figure 1. Dynamic high-resolution short-axis 5D CMR of the heart with high temporal resolution (25 phases per cycle) in an 8-year-old-male patient treated for a type II common. The 5D CMR images, from which diagnostic quality was scored as excellent by both readers, allow a great evaluation of the heart contraction particularly inside the septum that is showing an end-diastolic abrupt displacement towards the right ventricle.

Results

All patients were successfully analyzed. Time of acquisition of 5D CMR was significantly reduced by 58±101 seconds in comparison to 2D CMR (5.8±0 min vs 6.8±1.7 min, P<0.02). Absolute mean differences among both readers in left EDV, ESV and LVEF for 5D CMR relative to 2D CMR were 0.6±14.8 mL, 5.8±9.1 mL and 3.6±5.0%. Absolute mean differences among both readers in right EDV,

ESV and LVEF for 5D CMR relative to 2D CMR were 9.9±13.7 mL, 7.1±7.8 mL and 0.1±4.2 %, respectively. Almost perfect correlation between left and right cardiac volumes and volume ejection fraction was observed (all r>0.87) (**Tab.2**). Interreader agreement was excellent for all ejection fraction measures on both 2D and 5D CMR images (all ICC >0.940) with a highest value for LVEF on 5D CMR images (0.989) (**Tab.3**). Similarly, intrareader agreement for both readers was excellent for all ejection fraction measures between 2D and 5D CMR images (all ICC>0.862) with highest values for RVEF (0.944 and 0.954 for R1 and R2, respectively). Diagnostic quality was improved in 35% and 41% of the cases on 5D CMR images for R1 (mean score: 4.4±0.6 vs 4.0±0.8) and R2 (mean score: 4.2±0.5 vs 3.7±0.7), respectively to be found from good to excellent in 94% of the cases (compared to 65% on 2D images) (**Fig.1**).

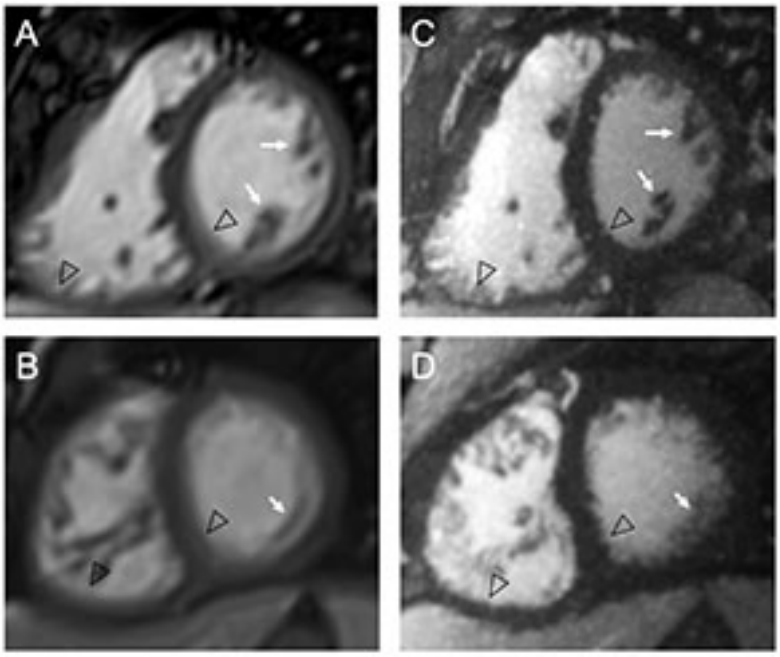

Figure 2. Example case of 8-year-old-male patient treated for a type II common truncus (A-B: short-axis bSSFP 2D, C-D: short-axis GRE 5D). Left and right ventricular ejection fractions were normal and comparable on both images (55% and 53%, respectively). It is noteworthy to mention the improved depiction of the cardiac structures due to higher spatial resolution such as the interface between the cardiac muscle and cavities (black empty head arrows), and the papillary muscle (white arrows). Consequently, diagnostic quality was improved from good to excellent on free-running 5D.

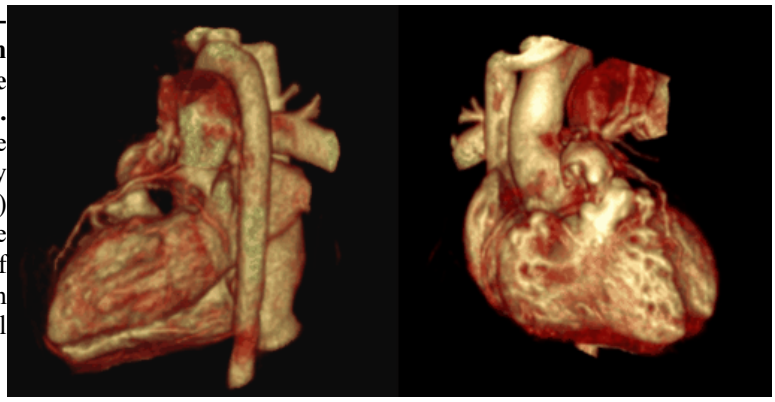

Figure 3. Dynamic high-resolution free-running 3D volume rendering of the heart with high temporal resolution in an 8-year-old-male patient treated for a type II common truncus. (A) Posterior view of the left ventricle shows the cavity motion with a depiction of the left coronary tree implantation and all great vessels. (B) Anterior view of the right ventricle shows the cavity motion with a depiction of the grafting of the pulmonary root. Other cardiac structures such as right coronary tree, aortic root are well identified as well during cardiac cycle.

Discussion

In the present study, we demonstrated in a population of CHD patients the feasibility of using ferumoxytol-enhanced 5D CMR to evaluate both right and left cardiac functions with higher spatial resolution, faster time of acquisition and similar temporal resolution than CINE 2D CMR but without the need for ECG gating or breath-holds. Our results showed an excellent intrareader agreement of the

LVEF and RVEF between 5D and 2D CMR images. The average difference between EF was close to 0% for the right ventricle and slightly higher at 3.6% for the left ventricle. A larger difference for LVEF may be explained by a more difficult delineation of the left cavity in comparison to the right one particularly during systole because of thicker wall and trabeculations of the left myocardium. This anatomical particularity probably explains also the larger difference found for the left ESV compared to EDV between 5D and 2D CMR images. In addition, while our results showed an excellent interreader agreement of LVEF on 5D and 2D CMR images, 5D CMR images showed a higher agreement. This finding is probably explained by the improved diagnostic quality using 5D CMR, such as found in ~40% of the cases due to higher spatial resolution, lower motion artefact and higher contrast. Altogether, this suggests that 5D CMR could reduce the operator dependency of cardiac function analysis while outperforming its feasibility, time of acquisition, convenience and diagnostic quality.

Conclusion

Free-running 5D CMR enabled measurements of LV and RV volumes and function that were comparable to 2D CMR while outperforming the reference standard in terms of image quality.

	2D CMR	5D CMR
Type of sequence	bSSFP	Gradient echo
Acquisition type	2D	3D
Temporal resolution	35 ± 11 ms	53 ± 14 ms
Echo time	1.2 ± 0.1 ms	1.6 ± 0.1 ms
RF excitation Angle	63 ± 10 °	15 ± 0 °
Spatial resolution	1.4 x 1.4 x 5–8 mm	1.1 x 1.1 x 1.1 mm
Number of cardiac phases	25 per cycle	25 per cycle
Field-of-view	168 x 208 mm^2	192 x 192 x 192 mm^3
Breath-holding time	8 – 12 seconds	No breath-holding

Table 1. Sequence parameters for both 2D CMR and free-running 5D CMR protocols.

Cardiac parameters	2D CMR	5D CMR	r	95% confidence interval	P (two-tailed)
Left EDV	139 (±59) mL	138 (±54) mL	0.96	0.89 to 0.99	<0.0001
Left ESV	62 (±30) mL	67 (±31) mL	0.95	0.87 to 0.98	<0.0001
LVEF	**56 (±7) %**	**52 (±8) %**	**0.78**	**0.48 to 0.92**	**< 0.001**
Right EDV	137±54 mL	146 (±54) mL	0.97	0.92 to 0.99	<0.0001
Right ESV	74±32 mL	78±34 mL	0.99	0.96 to 0.99	<0.0001
RVEF	**46 (±9) %**	**47 (±9) %**	**0.89**	**0.72 to 0.96**	**<0.0001**

Footnote– EDV: end-diastolic volume, ESV: end-systolic volume, LVEF: left ventricular ejection fraction, RVEF: right ventricular ejection fraction.

Table 2. Comparison between the cardiac volumes and ventricular ejection fraction calculated by a cardiac radiologist (R1 with 7 years of experience) on short-axis cine-images derived from bSSFP 2D images and GRE 5D free-running images with Pearson correlation analysis.

	Interreader		
Parameter	**ICC**	**95% CI**	
LVEF derived from 2D CMR	0.963	0.897	0.987
LVEF derived from 5D CMR	0.989	0.971	0.996
RVEF derived from 2D CMR	0.954	0.867	0.984
RVEF derived from 5D CMR	0.944	0.839	0.980
	Intrareader		
Parameter	**ICC**	**95% CI**	
R1: LVEF derived from 2D vs 5D CMR	0.875	0.655	0.955
R2: LVEF derived from 2D vs 5D CMR	0.862	0.618	0.950
R1: RVEF derived from 2D vs 5D CMR	0.944	0.839	0.980
R2: RVEF derived from 2D vs 5D CMR	0.954	0.867	0.984

Footnote. R1=first reader, R2=second reader. LVEF: left ventricular ejection fraction, RVEF: right ventricular ejection fraction.

Table 3. Inter- and Intrareader ICC and 95% Confidence Interval of LVEF and RVEF in 17 CHD patients (22±15-years of age, 7 female (41%), body surface area: 1.5 m2 ± 0.6).

References

1. Dorfman AL., Geva T., Samyn MM., et al. SCMR expert consensus statement for cardiovascular magnetic resonance of acquired and non-structural pediatric heart disease. J Cardiovasc Magn Reson 2022;24(1):44. Doi: 10.1186/s12968-022-00873-1.

2. Fratz S., Chung T., Greil GF., et al. Guidelines and protocols for cardiovascular magnetic resonance in children and adults with congenital heart disease: SCMR expert consensus group on congenital heart disease. J Cardiovasc Magn Reson 2013;15(1):51. Doi: 10.1186/1532-429X-15-51.

3. Roy CW., Di Sopra L., Whitehead KK., et al. Free-running cardiac and respiratory motion-resolved 5D whole-heart coronary cardiovascular magnetic resonance angiography in pediatric cardiac patients using ferumoxytol. J Cardiovasc Magn Reson Off J Soc Cardiovasc Magn Reson 2022;24(1):39. Doi: 10.1186/s12968-022-00871-3.

4. Di Sopra L., Piccini D., Coppo S., Stuber M., Yerly J. An automated approach to fully self-gated free-running cardiac and respiratory motion-resolved 5D whole-heart MRI. Magn Reson Med 2019;82(6):2118–32. Doi: 10.1002/mrm.27898.

Proceedings **ISMRM & ISMRT Annual Meeting & Exhibition** (2023)
Abstract number **2265**
Abstract accepted as an Oral presentation.

My contribution: I provided counseling on the analysis and interpretation of the results and I provided data analysis knowledge.

A2.3.3. Off-resonance encoded fat suppression methods for 5D whole-heart free-running cardiac MRI at 1.5T

Yasaman Safarkhanlo[1,2], Jerome Yerly[3,4], Mariana Falcao[3], Adèle LC Mackowiak[2,3,5], Davide Piccini[3,6], Matthias Stuber[3,4], Bernd Jung[2,5], Christoph Gräni[1,2], Jessica AM Bastiaansen[2,5]

[1]Department of Cardiology, University Hospital Bern, Bern, Switzerland
[2]Translation Imaging Center (TIC), Swiss Institute for Translational and Entrepreneurial Medicine, Bern, Switzerland
[3]Department of Diagnostic and Interventional Radiology, Lausanne University Hospital (CHUV) and University of Lausanne (UNIL), Lausanne, Switzerland
[4]Center for Biomedical Imaging, Lausanne Switzerland
[5]Department of Diagnostic, Interventional and Pediatric Radiology (DIPR), Inselspital, Bern University Hospital, University of Bern, Switzerland
[6]Advanced Clinical Imaging Technology, Siemens Healthineers International AG, Lausanne, Switzerland

Synopsis

The presence of fat signals around the heart can affect the diagnostic quality of cardiovascular MR images. There are multiple fat-suppression pulses, such as FISS, and off-resonance water-excitation (WE) pulses, such as BORR, LIBRE, an LIBOR, that have been developed for the free-running balanced Steady-State free-Precession (bSSFP) sequences at low-field MRI (1.5T).

These fat-suppression pulses gave never been thoroughly compared to each other, therefore, in this work, we implemented four different fat-suppression pulses and validated their performance on phantoms and healthy volunteers. Our results indicated LIBOR provided better fat suppression compared to BORR and LIBRE, while having fast acquisition time.

Introduction

Unsuppressed fat signals in cardiac MRI (CMR) can impact the visualization of anatomical structures hampering diagnostic image quality[1]. Because of fast T1 recovery of fat, and k-space center dominated MRI signal weighting, fat signal suppression is challenging in non-Cartesian MRI. Therefore, approaches that focus on water excitation (WE) are favored over fat saturation. Free-running CMR at 1.5T typically uses radial trajectories and is based on bSSFP acquisitions[2,3]. The reconstructed cardiac and respiratory motion-resolved whole-heart data (5D CMR) allow for determining cardiac function and coronary artery imaging[2,3]. Several methods were developed for fat suppression, such as Fast Interrupted Steady-State (FISS)[4,5], which uses an interruption of the bSSFP steady state to generate a wide off-resonance signal stop-band, and short off-resonance WE pulses such as Binomial Off-Resonant Rectangular (BORR)[6], Lipid Insensitive Binomial off-Resonant RF Excitation (LIBRE)[7,8], and a RF-power-optimized Lipid Insensitive Binomial Off-Resonant (LIBOR)[9]. Aforementioned RF pulses can be shortened by increasing their off-resonance frequency, requiring an increase in RF power which can be problematic when combined with bSSFP. Therefore, the aim of this work was to implement BORR and the RF-power-optimized LIBOR pulse and compare them with LIBRE and FISS for free-running CMR at 1.5T.

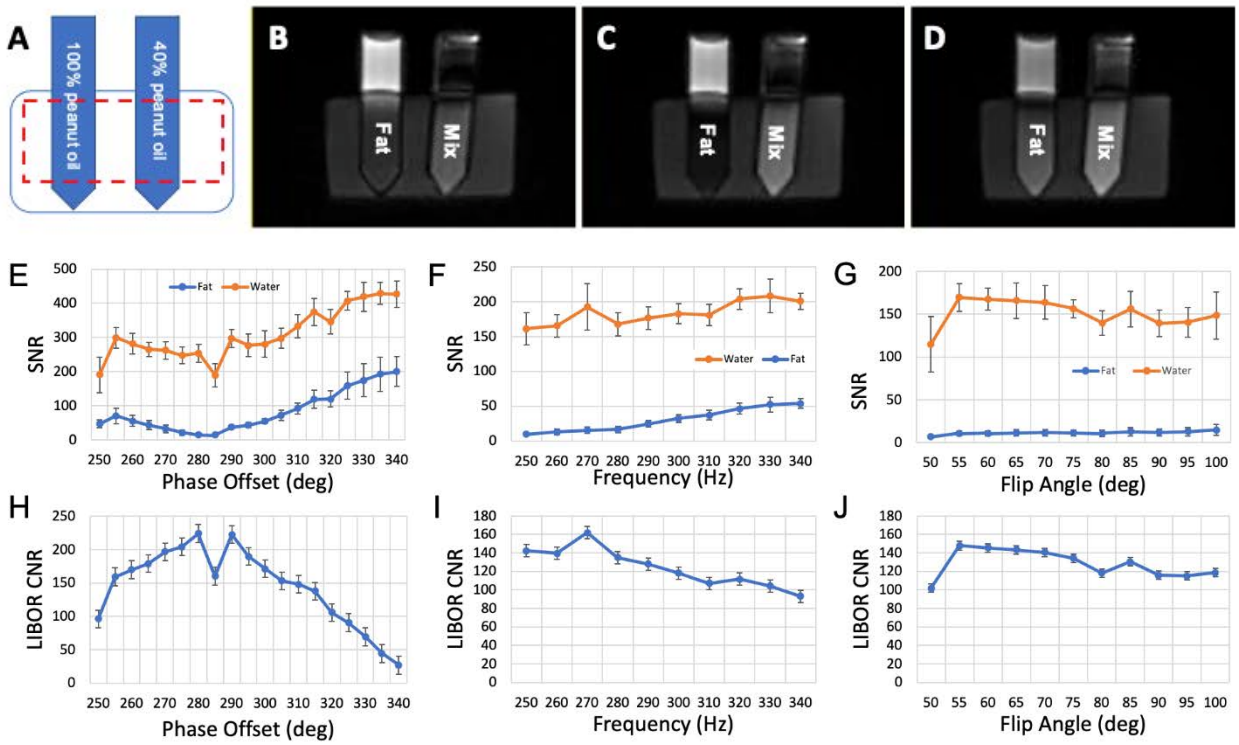

Figure 1. (A) Illustration and LIBOR acquisitions with phase offset of (B) 250°, (C) 285°, and (D) 270°. Red dashed lines indicate the shimming box. Fat and water SNR changes with different phase offsets (fixed frequency of 270Hz and a 78° flip angle) (E), frequencies (fixed phase offset 285° and a 78° flip angle) (F), and flip angles (fixed phase offset of 285° and a frequency of 270Hz) (G). CNR for different phase offsets (H), RF excitation frequencies (I), and flip angles (J). The CNR outlier was a result of noise spike in that particular experiment (E, H).

Methods

Phantom measurements

Research free-running bSSFP sequences using off-resonant LIBOR, BORR, and LIBRE pulses, as well as free-running FISS, were implemented and tested on a 1.5T clinical MRI scanner (MAGNETOM Sola, Siemens Healthcare, Erlangen, Germany). The water and fat signals were quantified as a function of pulse frequency, which was varied from 250 to 340 Hz for LIBOR, and from 400 to 600 Hz for BORR and LIBRE. Since LIBOR is tuned by the phase difference between two subpulses, phase offset was swept from 250° to 340° to confirm previous findings[9]. Additionally, water and fat signals were measured as a function of RF excitation angle, which was varied from 50° to 100° for LIBOR, 90 to 180° for BORR, and 50° to 180° for LIBRE pulse sequence. All measurements were repeated at different dates (n=3). Pulse duration of LIBOR and BORR was fixed to 2.6 ms, to match LIBRE[8].

Remaining sequence parameters were the same, unless specified, for all 4 acquisitions as follows: 2.0 mm^3 isotropic resolution, bandwidth of 992 Hz/pixel, echo time (TE) 2.46 ms, and repetition time (TR) 4.9 ms. FISS TR was 2.47 ms. Acquisition time for phantom studies was around 30 seconds per sequence.

Free-running CMR in volunteers

Four different free-running acquisitions, LIBOR, BORR, LIBRE, and FISS were acquired in healthy volunteers (n=4) who gave written informed consent. Acquisition parameters were identical to

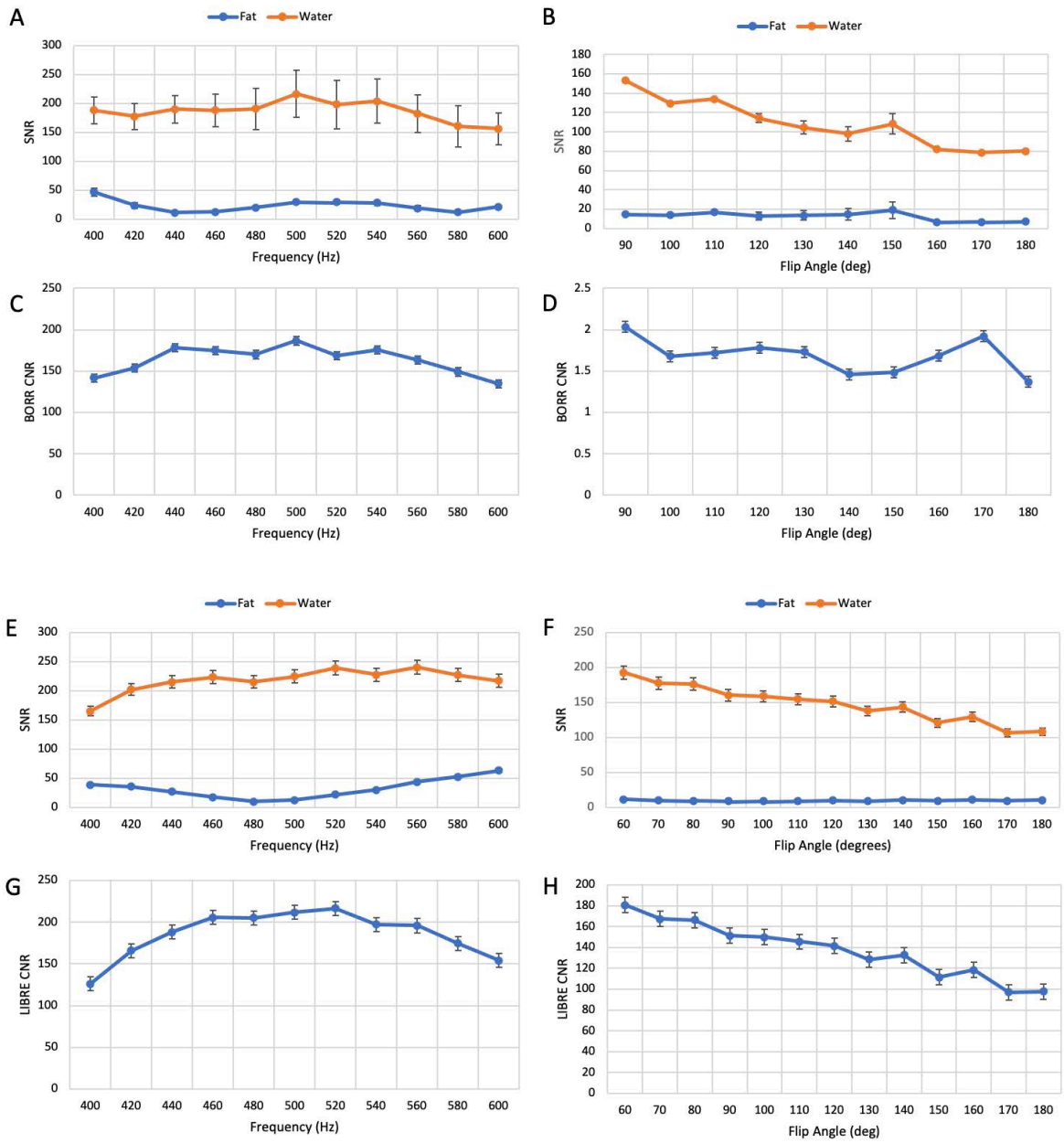

Figure 2. Measured fat and water signal-to-noise ratios (SNR) with different (A) frequencies and constant flip angle of 141°, and (B) different flip angles and constant frequency of 600 Hz. The calculated CNR for BORR sequence with different (C) frequencies, and (D) flip angles. Measured fat (blue) and water (orange) SNR with different (E) frequencies and constant flip angle of 124°, and (F) flip angles and fixed frequency of 500 Hz. The calculated CNR for LIBRE sequence with different (G) frequencies, and (H) flip angles.

phantom comparison experiments besides increasing the number of k-space lines to ~45k. Images were reconstructed with compressed-sensing framework described by Di Sopra et al.[3]. Scan time for in vivo studies was 3:40 minutes per off-resonance WE sequences, and 2:55 minutes for FISS.

Image analysis

Data were analyzed using MATLAB (R2022a, The MathWorks) and ImageJ (NIH, Wisconsin University). Regions of interest (ROIs) were drawn in water and fat vials, and in the background noise. In vivo, ROIs were drawn in chest fat, ventricular blood pool, lungs, and myocardium. Signal-to-noise ratio (SNR) was computed by dividing the average ROI signal by the standard deviation of background

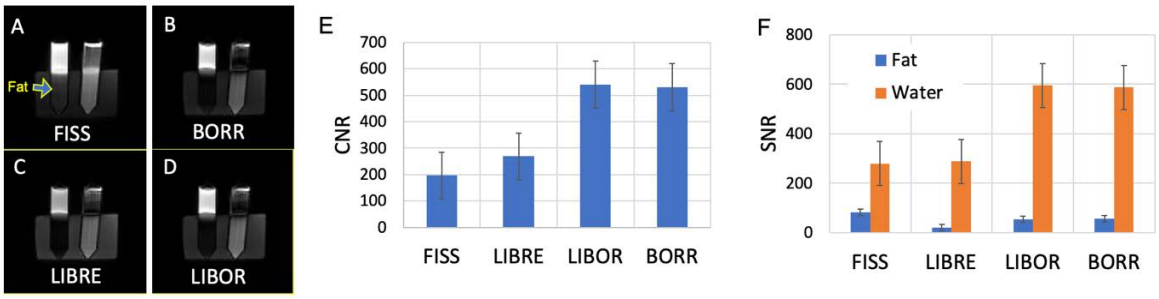

Figure 3. Four different fat-suppression methods, (A) FISS, (B) BORR, (C) LIBRE, and (D) LIBOR, and their (E) CNR and (F) SNR.

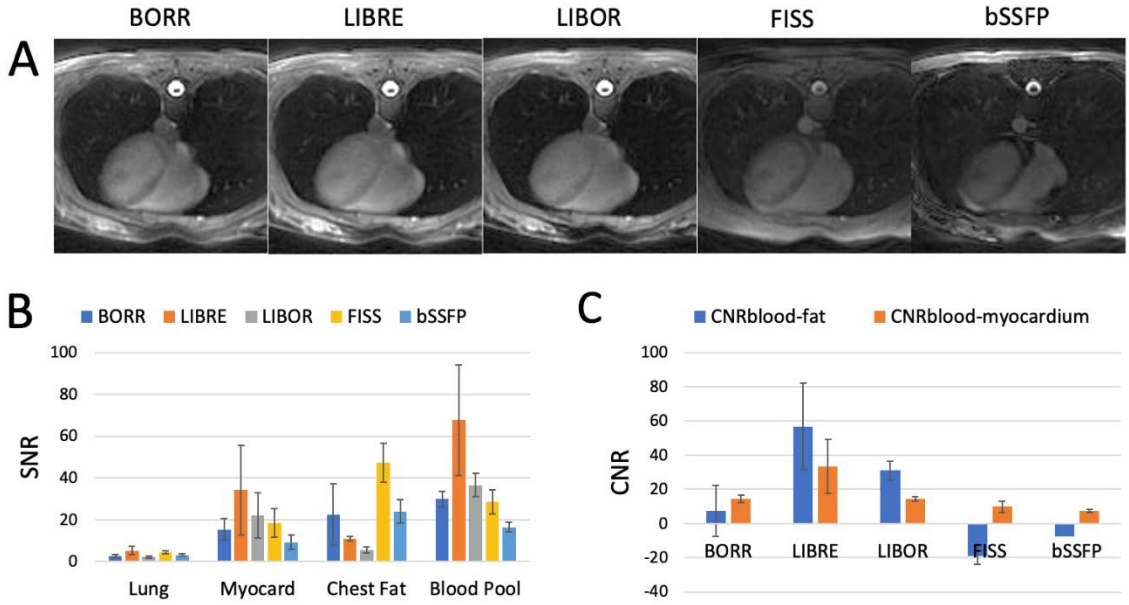

Figure 4. (A) Volunteer data acquired with FISS, BORR, LIBRE, LIBOR, and bSSFP. (B) Signal intensity of lung, myocardium, chest fat, and ventricular blood pool for different acquisition. (C) $CNR_{Blood\text{-}Fat}$ calculated by subtracting $SNR_{Blood\ Pool}$ from $SNR_{Chest\ Fat}$ and $CNR_{Blood\text{-}Myocardium}$ calculated by subtracting $SNR_{Blood\ Pool}$ from $SNR_{Myocardium}$.

noise. To compare different acquisitions in the phantom, contrast-to-noise ratio (CNR) was calculated by subtracting water SNR from fat SNR.

Gridded reconstructions were used for quantitative in vivo comparisons and CNR was calculated between ventricular blood and chest fat ($CNR_{Blood\text{-}Fat}$), as well as blood and myocardium ($CNR_{Blood\text{-}Myocardium}$).

Results and Discussion

The LIBOR phase offset, frequency, and flip angle impact fat signal suppression. Maximum CNR was found with a phase offset of 280°, a frequency of 270 Hz, and a flip angle of 55° for LIBOR (**Fig.1**), pulse frequency of 500 Hz and a flip angle of 90° for BORR, and frequency of 520 Hz and flip angle of 60° for LIBRE (**Fig.2**). These findings corroborate the expected theoretical range of required RF amplitudes (9).

In phantoms, LIBOR provided the largest CNR of all compared techniques, while FISS had the lowest CNR, which indicates that LIBOR efficiently suppresses fat signal without reducing or having a significant impact on water signal (**Fig.3**).

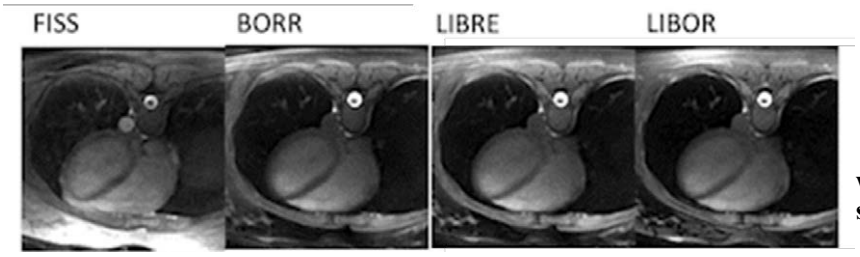

Figure 5. Volunteer data acquired with FISS, BORR, LIBRE, and LIBOR sequences (animation).

For in vivo free-running CMR, LIBRE has the highest SNR in ventricular blood pool and LIBOR the lowest SNR in chest fat. LIBRE displayed the highest $CNR_{Blood\text{-}Fat}$ and $CNR_{Blood\text{-}Myocardium}$ values (**Fig.4**). Across watery tissues, no significant differences were observed between these techniques, as expected. Nevertheless, because chest fat falls outside the shim volume, pericardial fat signals may provide a more stable and appropriate metric for fat signal suppression, which will be further investigated in a larger volunteer cohort. In whole-heart imaging data, a big difference in fat suppression can be observed across techniques and anatomical regions (**Fig.5**).

Conclusion

Different off-resonance water-excitation methods were compared in free-running CMR at 1.5T and is the first report on both LIBOR and BORR pulses. LIBOR enabled effective fat suppression while maintaining a short TR and reducing RF power compared with BORR and LIBRE, conversely, FISS demonstrated the highest CNR of blood and myocardium.

References

1. Munoz C, Bustin A, Neji R et al. Motion-corrected 3D whole-heart water-fat high-resolution late gadolinium enhancement cardiovascular magnetic resonance imaging. Journal of Cardiovascular Magnetic Resonance 2020;22:1-13.
2. Feng L, Coppo S, Piccini D et al. 5D whole-heart sparse MRI. Magn Reson Med 2018;79:826-838.
3. Di Sopra L, Piccini D, Coppo S, Stuber M, Yerly J. An automated approach to fully self-gated free-running cardiac and respiratory motion-resolved 5D whole-heart MRI. Magn Reson Med 2019;82:2118-2132.
4. Bastiaansen JAM, Piccini D, Di Sopra L et al. Natively fat-suppressed 5D whole-heart MRI with a radial free-running fast-interrupted steady-state (FISS) sequence at 1.5T and 3T. Magn Reson Med 2020;83:45-55.
5. Koktzoglou I, Edelman RR. Radial fast interrupted steady-state (FISS) magnetic resonance imaging. Magnetic resonance in medicine 2018;79:2077-2086.
6. Ye Y, Hu J, Haacke EM. Robust selective signal suppression using binomial off-resonant rectangular (BORR) pulses. J Magn Reson Imaging 2014;39:195-202.
7. Bastiaansen JAM, Stuber M. Flexible water excitation for fat-free MRI at 3T using lipid insensitive binomial off-resonant RF excitation (LIBRE) pulses. Magn Reson Med 2018;79:3007-3017.
8. Masala N, Bastiaansen JAM, Di Sopra L et al. Free-running 5D coronary MR angiography at 1.5T using LIBRE water excitation pulses. Magn Reson Med 2020;84:1470-1485.
9. Bastiaansen J, Piccini D, Mackowiak A. Fat-free MRI with fast and power-optimized off-resonant LIBOR pulses. 2022.

Proceedings **ISMRM & ISMRT Annual Meeting & Exhibition** (2023)
Abstract number **0360.**
Abstract accepted as a Digital Poster.
My contribution: I acquired the data used for this study.

A3. Supplementary Information: Conference abstracts not included in the main Thesis

A3.1. 5D Flow using Pilot Tone for cardiac and respiratory self-gating

Mariana B.L. Falcão[1], Liliana Ma[2,3], Lorenzo Di Sopra[1], Mario Bacher[1,4], Davide Piccini[1,5], Jérôme Yerly[1,6], Peter Speier[4], Michael Markl[2,3], Matthias Stuber[1,6], Christopher Roy[1]

[1]Department of Diagnostic and Interventional Radiology, Lausanne University Hospital (CHUV) and University of Lausanne (UNIL), Lausanne,
Switzerland
[2]Department of Radiology, Feinberg School of Medicine, Northwestern University, Chicago, Illinois, USA
3Department of Biomedical Engineering, Northwestern University, Chicago, Illinois, USA
[4]Siemens Healthcare GmbH, Erlangen, Germany
[5]Advanced Clinical Imaging Technology, Siemens Healthcare AG, Lausanne, Switzerland
[6]Center for Biomedical Imaging (CIBM), Lausanne, Switzerland

Background

Current clinical methods for 4D flow MRI rely on ECG gating and respiratory navigators, leading to prolonged and unpredictable scan times. Recent advances have enabled cardiac and respiratory motion-resolved 5D flow with a fixed scan time, using a free-running framework[1, 2]. This protocol employed a 3D radial phyllotaxis trajectory[3], and periodic readouts along the superior-inferior direction allow for both cardiac and respiratory self-gating[1], eliminating the need for an ECG signal and navigator scans. Alternatively, Pilot Tone navigation allows for the extraction of these physiologic signals in parallel to the acquisition[4,5,6]. In this study, we explore the initial feasibility of using Pilot Tone for ECG- and navigator-free 5D flow MRI.

Methods

Six volunteers (4F, age: 28.0±4.8 years) were scanned on a 1.5T MAGNETOM Sola (Siemens Healthcare, Erlangen, Germany), using a 12-channel body coil with an integrated Pilot Tone transmitter. Each volunteer was scanned using a prototype radial 5D Flow MRI sequence covering the whole heart and 4D Flow sequence covering the aorta with the parameters listed in Fig.2. Cardiac and respiratory gating signals were retrospectively extracted from the multi-channel Pilot Tone signals as described by **Fig.1** and subsequently used to bin the data into 4 respiratory and 17-21 cardiac frames,

depending on the subject's heartrate. Cardiac binning accuracy was quantified by the standard deviation of the difference between Pilot Tone and ECG triggers. The resulting 5D flow datasets were

reconstructed using XD-GRASP[7]. Flow curves were calculated for both the 4D and 5D Flow data sets in the ascending aorta, descending aorta and aortic arch using the Siemens 4D Flow v2.4 Software. The net flow volume and the peak flow were compared using the Wilcoxon signed rank test.

Results

The acquisition time was 9min 01s for 5D Flow and 11min 19s ± 4min 24s for 4D Flow. Pilot Tone cardiac triggers matched the ECG triggers with an average error of 4.8±3.4% Aortic flow curves (Fig. 2) derived from 5D flow underestimated peak systolic flow by 23±11%. Net flow and peak flow values (Fig. 3) showed that 5D Flow tends to underestimate the flow measurements by 11±14% and 22±11% respectively ($p < 0.05$ in 4 out of 6 measurements).

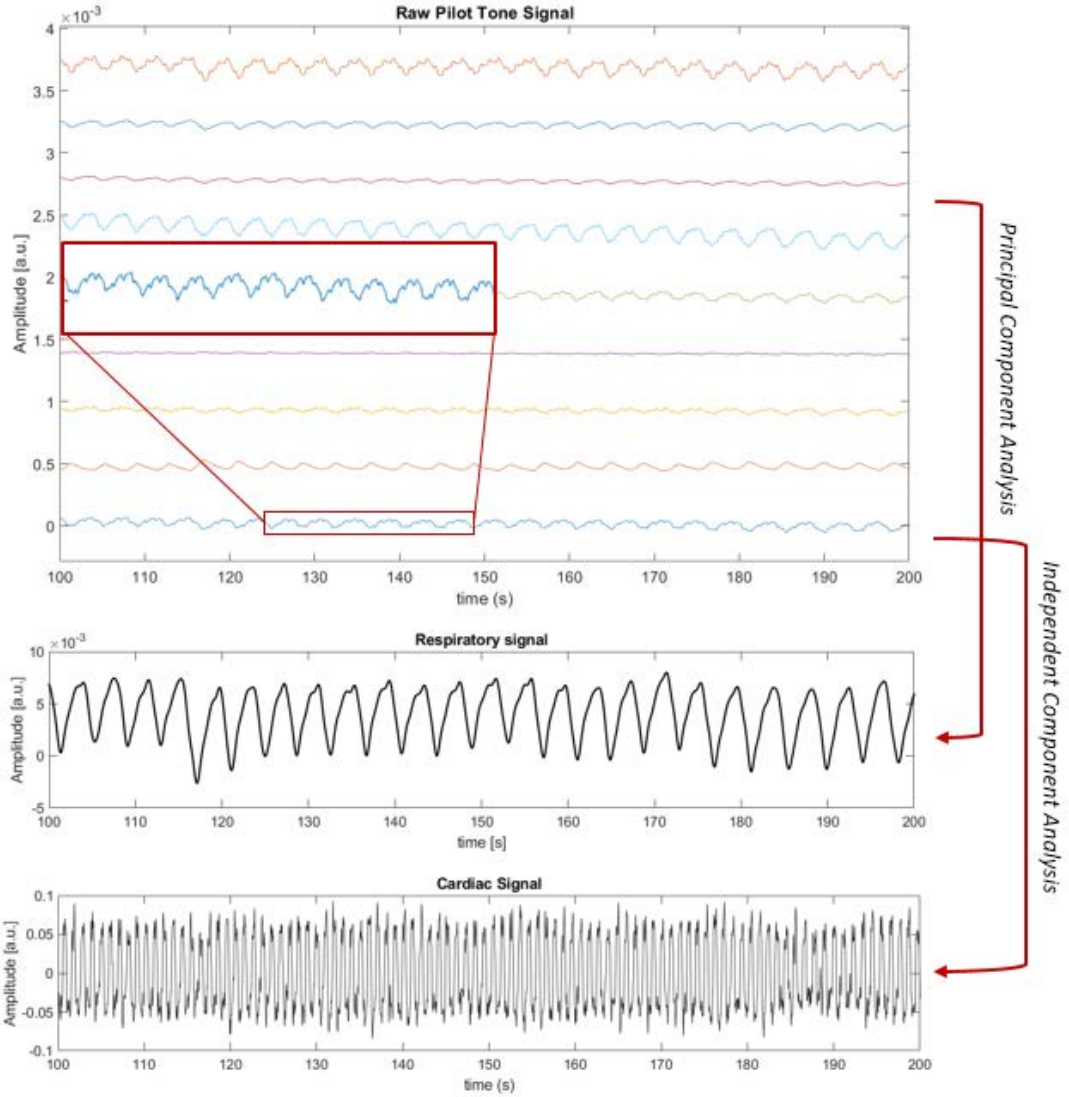

Figure 1. Respiratory and cardiac gating information extracted from the Pilot Tone signals. The Pilot Tone Navigation system consists of a transmitter which, when activated, generates a magnetic field outside the imaging range. The emitted magnetic field is sensitive to modulation due to motion, and therefore its variation can be captured by the receiver coils. This variation had been shown to contain cardiac and respiratory motion[3,4,5], which can be extracted and used for data binning. While the respiratory modulation is obtained from Principal Component Analysis, the cardiac movement is extracted using Independent Component Analysis[1,5].

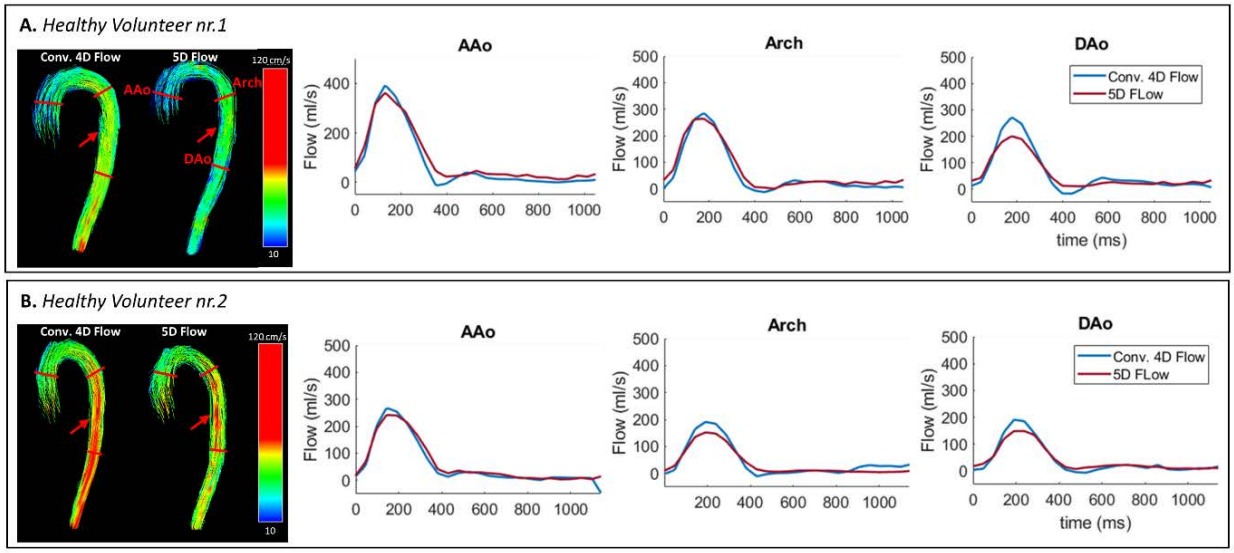

Figure 2. Comparison of the flow curves of two healthy volunteers (A-B) at three planes along the aorta (AAo -ascending aorta, DAo - descending aorta, Arch - aortic arch). Scan parameters 5D: spatial resolution: (2.3mm)3, temporal resolution: 112.8ms, Venc: 150cm/s. Scan parameters 4D: spatial resolution: 2.4x2.4x2.5 mm3, temporal resolution: 38.6-57.9ms, Venc: 150cm/s. 5D flow appears to consistently underestimate peak flows in comparison to conventional 4D flow. (see arrows).

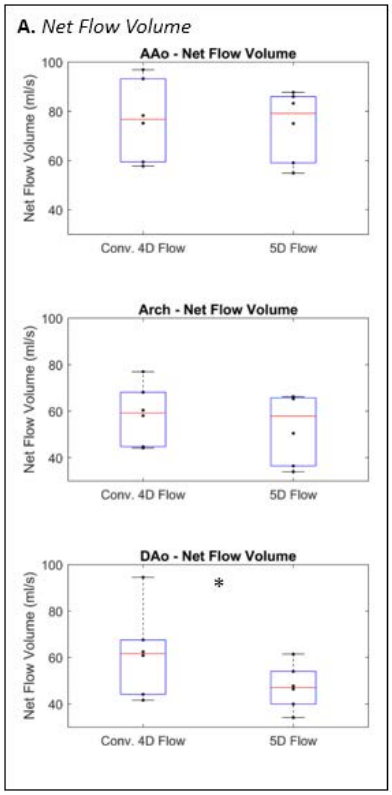

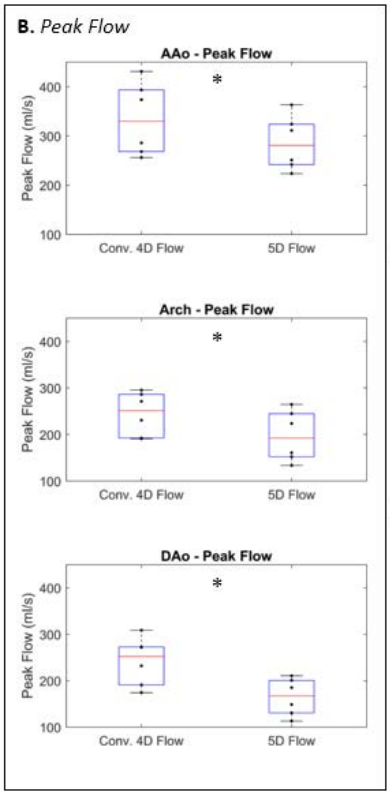

C.

	Average Net Flow Volume values (ml/s)	
	Conv. 4D	5D
AAo	76.8 ± 16.4	74.3 ± 14.2
Arch	58.8 ± 12.9	53.0 ± 15.0
Dao	61.9 ± 19.1	47.3 ± 9.7

D.

	Average Peak Flow values (ml/s)	
	Conv. 4D	5D
AAo	334.7 ± 73.8	285.8 ± 54.9
Arch	244.5 ± 46.6	196.6 ± 54.6
DAo	241.8 ± 52.1	164.9 ± 39.7

E.

	Wilcoxon signed rank test	
	Net Flow Volume	Peak Flow
AAo	0.56	0.03*
Arch	0.09	0.03*
DAo	0.03*	0.03*

* pval<0.05

Figure 3. Net Flow volume (A.) and Peak Flow (B.) boxplots of Conventional 4D Flow and 5D Flow. The interquartile range is shown by the blue boxes. Mean and Standard Deviation values can be found in C. and D., respectively. E. The Wilcoxon Signed rank test shows that 5D flow underestimated flow values in comparison to conventional 4D flow, with the exception of the Net Flow Volume in the AAo. AAo -ascending aorta, DAo - descending aorta, Arch - aortic arch.

Discussion and Conclusions

ECG- and navigator-free cardiac and respiratory motion-resolved 5D Flow with a fixed scan time is feasible using Pilot Tone, providing a means for whole-heart evaluation of hemodynamics with shorter scan time than conventional 4D Flow. The tendency to underestimate flow values in 5D Flow has been reported before[2], and may be caused by temporal undersampling and regularization. While further optimization of acquisition and reconstruction parameters is needed to improve the consistency between 5D flow and the 4D flow reference standard, the use of Pilot Tone gating, which is independent of the acquisition, provides a new method for fully self-gated 5D flow.

References

1. L. Di Sopra et al., An Automated Approach to Fully Self-Gated Free-Running Cardiac and Respiratory Motion-Resolved 5D Whole-Heart MR Imaging. Magn Reson Med 2019, In Press
2. L. Ma et al. 5D flow MRI: A free-running, fully self-gated, radial imaging framework for cardiac and respiratory motion-resolved assessment of 3D blood flow dynamics, Proc. Intl. Soc. Mag. Reson. Med. 27 (2019), 0090.
3. Piccini, D. et al. Spiral Phyllotaxis: The Natural Way to Construct a 3D Radial Trajectory in MRI. Magnetic Resonance in Medicine 2011, 66, 1049–1056.
4. P. Speier et al. PT-Nav: A Novel Respiratory Navigation Method for Continuous Acquisition Based on Modulation of a Pilot Tone in the MR-Receiver, Proc. ESMRMB 129:97-98, 2015.
5. M. Bacher et al. Retrospective Evaluation of Pilot Tone Based Cardiac Trigger Quality In A Volunteer Cohort, Book of Abstracts ESMRMB 2017 30:360- 361.
6. L. Schroeder et al. Two-Dimensional Respiratory-Motion Characterization for Continuous MR Measurements Using Pilot Tone Navigation. In Proc. Intl. Soc. Mag. Reson. Med. 24:3103, 2016.
7. L. Feng et al. 5D whole-heart sparse MRI. Magn Reson Med 2017, 79(2), 826–838.

Proceedings **SCMR 23rd Society Annual Scientific Sessions** (2020)
Abstract number **749530**
Abstract accepted as a Digital Poster
Selected as a poster for the SCMR/ISMRM Co-Provided Workshop

A3.2. 5D Flow – A quantitative in vivo comparison between Self Gating and Pilot Tone Gating

Mariana B.L. Falcão[1], Lorenzo Di Sopra[1], Liliana Ma[2,3], Mario Bacher[1,4], Davide Piccini[1,5], Jérôme Yerly[1,6], Peter Speier[4], Tobias Rutz[7], Milan Prša[7], Michael Markl[2,3], Matthias Stuber[1,6], Christopher Roy[1]

[1]Department of Diagnostic and Interventional Radiology, Lausanne University Hospital (CHUV) and University of Lausanne (UNIL), Lausanne,
Switzerland
[2]Department of Radiology, Feinberg School of Medicine, Northwestern University, Chicago, Illinois, USA
3Department of Biomedical Engineering, Northwestern University, Chicago, Illinois, USA
[4]Siemens Healthcare GmbH, Erlangen, Germany
[5]Advanced Clinical Imaging Technology, Siemens Healthcare AG, Lausanne, Switzerland
[6]Center for Biomedical Imaging (CIBM), Lausanne, Switzerland
[7]Department of Cardiology, Lausanne University Hospital (CHUV), Lausanne, Switzerland

Synopsis

Conventional 4D flow MRI techniques often have prolonged and unpredictable scan times, due to the use of respiratory navigation. To address this, a fully self-gated cardiac and respiratory motion-resolved whole-heart 5D flow protocol with a fixed scan time was recently developed using a free-running framework. This protocol extracts cardiac and respiratory signals from periodic readouts (self-gating). In this study, we explore the use of Pilot Tone signals as an alternative method for cardiac and respiratory signal extraction to reconstruct 5D flow data and compare reconstructions to those using the previously established self-gating method and the conventional 4D flow sequence.

Introduction

Conventional 4D flow MRI techniques often have prolonged and unpredictable scan times, due to the use of respiratory navigation. As a result, acquiring whole-heart 4D flow images in a clinically acceptable scan time (<10min) is challenging. To address this, a fully self-gated cardiac and respiratory motion-resolved whole-heart 5D flow protocol with a fixed scan time was recently developed using a free-running framework[1,2,3]. This method employs a continuous, non-ECG triggered 3D radial acquisition with phyllotaxis sampling[4] and periodic readouts for cardiac and respiratory self-gating (SG)[2]. Pilot Tone signals (PT), acquired in parallel to the MR acquisition, have also been recently proposed for cardiac and respiratory gating. The PT Navigation system consists of a transmitter that generates an alternating magnetic field with a frequency outside the band occupied by the MR signal. The field received by the local MR coils is modulated by motion[5,6]. Both SG and PT potentially replace the ECG signal and navigator scans in 4D/5D flow imaging. In this study, we explore the use of PT signals to reconstruct 5D flow data and compare reconstructions to those using the previously reported SG method[3] as well as a reference standard 4D flow sequence.

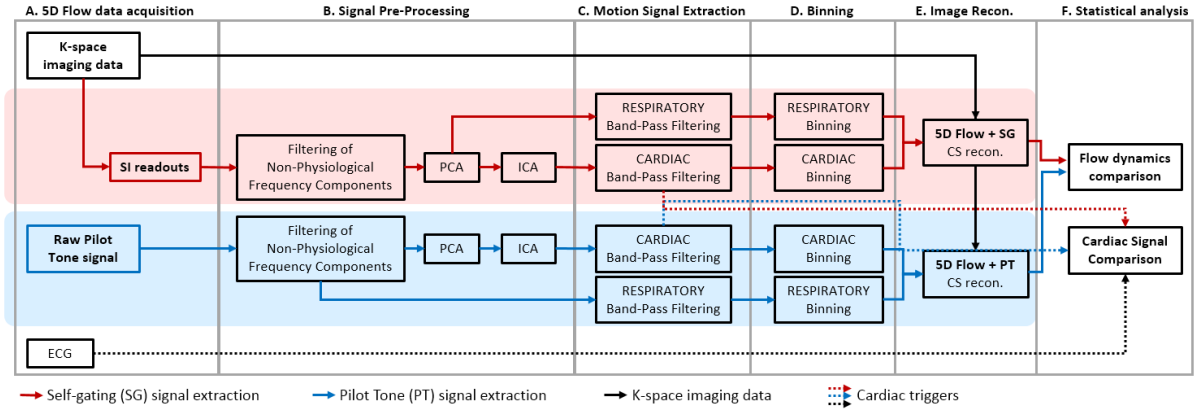

Figure 1. Study Pipeline. A. Free-running 5D flow data were acquired and the ECG signal was recorded for subsequent comparisons (**F.**). **A-C.** Cardiac and respiratory signals were extracted from either periodically acquired SI readouts or Pilot Tone signals. **D-E.** Finally, k-space data were binned and reconstructed with XD-GRASP[8]. **F.** The end-expiratory datasets were used for flow calculations and comparison with 4D flow values.

	A. Acquisition Time (min:sec)		B. Trigger Precision Cardiac Gating Error (%)	
Volunteer	**4D Flow**	**5D Flow**	**ECG vs SG**	**ECG vs PT**
1	13:43	7:53	3.1	3.3
2	14:33	7:53	4.4	5.6
3	16:35	7:53	1.8	2.0
4	7:11	7:53	1.6	2.9
5	5:20	7:53	2.6	1.7
6	10:33	8:43	5.7	5.7
7	6:00	7:50	2.8	3.4
8	5:57	7:50	2.1	2.4
9	12:8	7:52	1.4	2.4
10	8:21	7:50	3.9	4.7
11	12:34	7:50	2.6	2.2
Mean ± SD	10:16 ± *3:55*	7:57 ± *0:15*	2.9 ± 1.3	3.3 ± 1.4
T-Test	0.08		0.08	

Figure 2. A. Acquisition time of the 4D flow and 5D flow sequences for all subjects. Variation in 5D flow acquisitions times are due to field-of-view size. 4D flow times varied due to navigator efficiency and heart rate. B. Cardiac gating error given as the standard deviation of the difference between SG or PT triggers and the recorded R-wave of the ECG, normalized by the mean ECG RR-Interval.

Methods

One navigator gated 4D flow sequence[7] covering the aorta and one prototype free-running radial whole-heart 5D flow sequence[3] were used for imaging in 11 healthy adult volunteers (age: 27.9±3.6 years) who provided written informed consent on a 1.5T MAGNETOM Sola (Siemens Healthcare, Erlangen, Germany), using a 12-channel body coil with an integrated PT transmitter. Scan parameters were: field of view (4D: (200-292.8 mm) x (360-366 mm) x (75-137.4 mm), 5D: $(220mm)^3$-$(260mm)^3$); spatial resolution (4D: 2.4x2.4x2.5 mm^3, 5D: $(2.3mm)^3$); temporal resolution (4D: 38.6-57.9ms, 5D: 50ms); velocity encoding (4D/5D: 150cm/s). Both 4D flow and 5D flow were performed during free-breathing and the ECG signal was measured during 5D flow scans for subsequent comparison. The acquisition time of each sequence was also recorded.

For 5D flow, cardiac and respiratory signals were retrospectively extracted from SG and PT signals using the post-processing steps outlined in **Fig.1**. For both SG and PT, the cardiac gating error was quantified as the standard deviation of the difference between SG or PT triggers and the recorded ECG, normalized by the mean ECG RR-Interval[2].

After signal extraction, the SG and PT 5D flow datasets were binned into 4 respiratory and 17-23 cardiac frames, depending on the subject's heartrate, and reconstructed using XD- GRASP[8]. For the 4D flow datasets and the two 5D flow datasets (with SG and PT), flow curves were calculated in two segments of the ascending aorta (AAo1, AAo2), one segment of the descending aorta (Dao), and one segment of the aortic arch (Arch) using Siemens 4D Flow v2.4. Additionally, the net flow volume and peak flow were computed and compared using the Wilcoxon signed rank test.

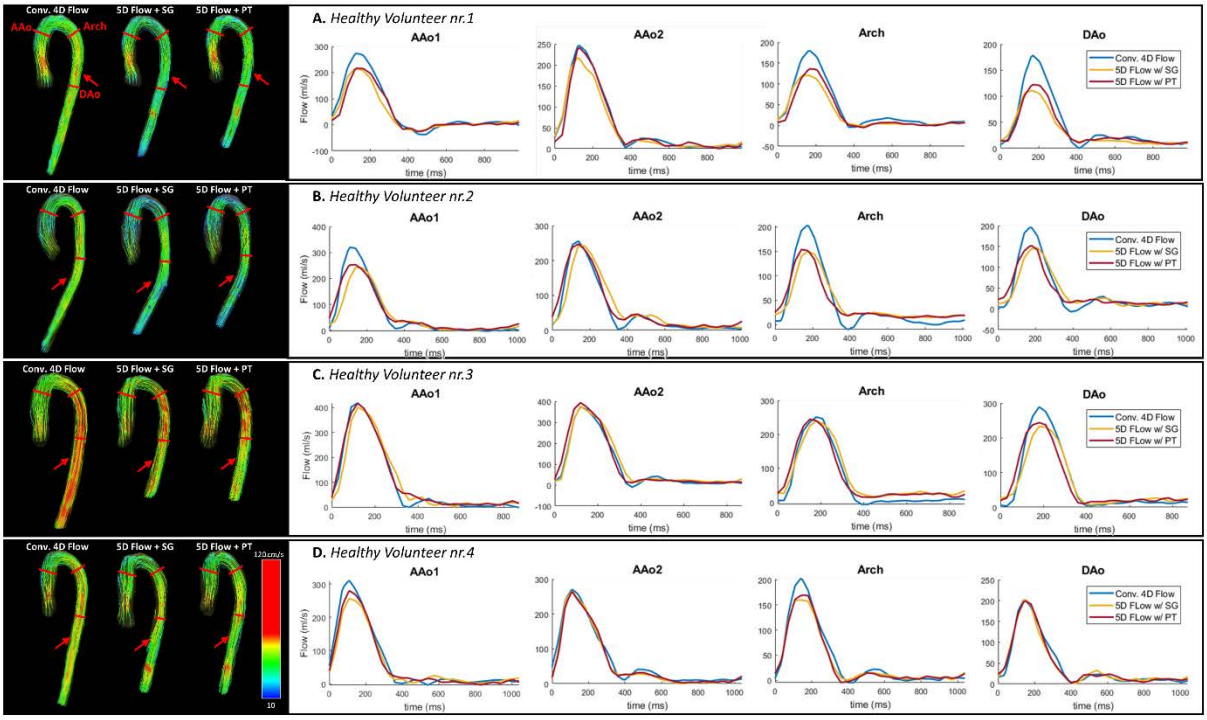

Figure 3. Comparison of flow curves from four healthy volunteers (A-D) originating from four planes along the aorta. The flow curves from the two 5D flow reconstructions (SG and PT signal extraction) show similar temporal evolution, but underestimate peak flows in comparison to 4D flow (see arrows). AAo1: lower segment of the ascending aorta, AAo2: upper segment of the ascending aorta, DAo: descending aorta, Arch: aortic arch.

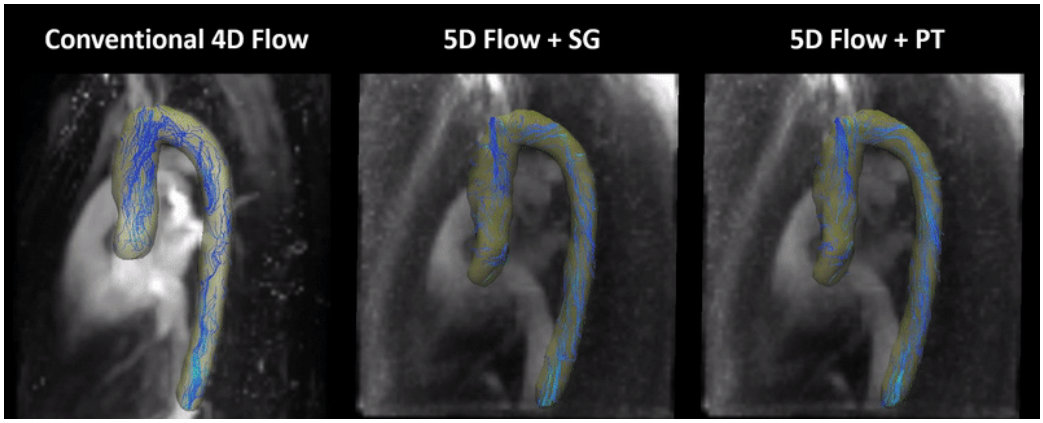

Figure 4. Flow streamlines across one cardiac cycle for 4D flow, 5D flow with SG and 5D flow PT. (animated)

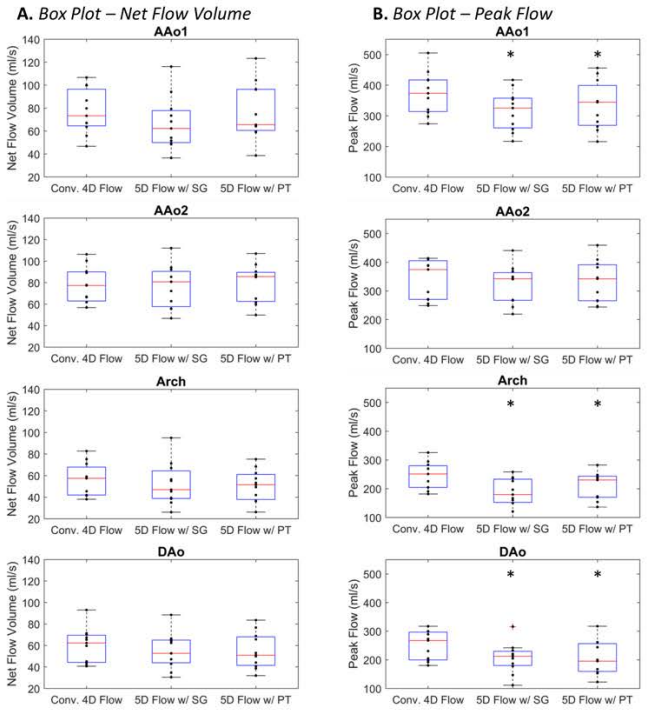

C.

	Average Net Flow Volume values (ml/s)		
	Conv. 4D	5D + SG	5D + PT
AAo1	76.99 ± 19.45	76.97 ± 24.87	66.73 ± 23.14
AAo2	77.29 ± 17.28	79.54 ± 17.74	76.26 ± 19.71
Arch	55.76 ± 15.36	65.69 ± 14.81	52.41 ± 19.60
Dao	60.14 ± 16.08	54.92 ± 16.63	55.21 ± 16.54

D.

	Average Peak Flow values (ml/s)		
	Conv. 4D	5D + SG	5D + PT
AAo1	373.54 ± 69.94	333.27 ± 78.89	316.86 ± 64.78
AAo2	339.14 ± 69.65	332.07 ± 73.36	323.80 ± 66.19
Arch	245.60 ± 47.21	207.86 ± 47.80	182.90 ± 55.32
DAo	250.27 ± 50.17	206.80 ± 58.21	206.55 ± 53.07

E.

	Wilcoxon signed rank test			
	Net Flow Volume		Peak Flow	
	5D + SG	5D + PT	5D + SG	5D + PT
AAo1	0.21	0.97	0.005*	0.01*
AAo2	0.97	0.52	0.21	0.21
Arch	0.46	0.12	0.001*	0.001*
DAo	0.28	0.28	0.01*	0.01*

Figure 5. Net flow volume (A.) and peak flow (B.) population distributions for 4D flow, SG and PT 5D flow reconstructions. The interquartile range is shown by the blue boxes. Mean and Standard Deviation values are shown in C. and D., respectively. E. The Wilcoxon signed-rank test shows that both SG and PT 5D flow underestimated peak flow values in comparison to 4D flow, with the exception of the AAo2. AAo1: lower segment of the ascending aorta, AAo2: upper segment of the ascending aorta, Dao: descending aorta, Arch: aortic arch.

Results

The acquisition time of the 5D flow sequence (7min 57s±15s) was shorter (p=0.08) and less variant than that of the 4D flow protocol (10min 16s±3min 55s) across all subjects (**Fig.2**). The mean and standard deviation of the cardiac gating error across volunteers were 2.9±1.3% for SG and 3.3±1.4% for PT (**Tab.2**, p=0.08). Figure 3 shows flow curves for the four aortic segments in four subjects, as well as flow streamlines immediately after peak systole for 4D flow and 5D flow reconstructed with self-gated and Pilot Tone gated signals. A flow animation for a full cardiac cycle using the three reconstructions is depicted in **Fig.4**. The 3D hemodynamics of the flow streamlines across the same subject were consistent, although some reduced flow values were observed on both 5D flow reconstructions. Regarding the net flow volume (**Fig.5**), there were no significant differences between 4D flow and either SG or PT 5D flow. Nevertheless, compared to the 4D flow measurements, the peak flow was significantly decreased for both SG and PT 5D flow for the lower segment of the ascending aorta, the descending aorta and the aortic arch ($p<0.05$).

Discussion

5D flow scans provided whole-heart coverage in a predictable and shorter scan time, whereas 4D flow suffered from variable efficiency due heart rate and variable navigator efficiency secondary to variability in breathing patterns. The cardiac gating error was consistent between SG and PT and within the range of previously reported values for SG[2], demonstrating the feasibility of PT as an alternative method for cardiac and respiratory gating in 5D flow imaging. While underestimation of the peak flow has been reported before[3] and may be caused by temporal undersampling and regularization, further

investigation is required. Still, the temporal evolution of the flow curves and agreement in net flow volumes suggests 5D flow using SG or PT is a promising alternative to 4D flow, providing whole-heart coverage with matching temporal and spatial resolution predictably in less than 10min.

Conclusions

Pilot Tone signals provide a valuable alternative to self-gating for ECG- and navigator-free cardiac and respiratory motion-resolved 5D flow, while being completely independent of the acquisition. As a result, the feasibility of using Pilot Tone for signal extraction may open new opportunities for improving flow acquisitions, including reduced scan times, and improved k-space sampling.

References:

1. S. Coppo et al. Free-running 4D whole-heart self-navigated golden angle MRI: Initial results. Magnetic Resonance in Medicine 2015, 74(5), 1306–1316.
2. L. Di Sopra et al., An Automated Approach to Fully Self-Gated Free-Running Cardiac and Respiratory Motion-Resolved 5D Whole-Heart MR Imaging. Magn Reson Med 2019, In Press
3. L. Ma et al. 5D flow MRI: A free-running, fully self-gated, radial imaging framework for cardiac and respiratory motion-resolved assessment of 3D blood flow dynamics, Proc. Intl. Soc. Mag. Reson. Med. 27 (2019), 0090.
4. Piccini, D. et al. Spiral Phyllotaxis: The Natural Way to Construct a 3D Radial Trajectory in MRI. Magnetic Resonance in Medicine 2011, 66, 1049–1056.
5. P. Speier et al. PT-Nav: A Novel Respiratory Navigation Method for Continuous Acquisition Based on Modulation of a Pilot Tone in the MR-Receiver, Proc. ESMRMB 129:97-98, 2015.
6. M. Bacher et al. Retrospective Evaluation of Pilot Tone Based Cardiac Trigger Quality In A Volunteer Cohort, Book of Abstracts ESMRMB 2017 30:360- 361.
7. P. Dyverfeldt et al. 4D flow cardiovascular magnetic resonance consensus statement. Journal of Cardiovascular Magnetic Resonance 2015, 17(1), 1–19.
8. L. Feng et al. 5D whole-heart sparse MRI. Magn Reson Med 2017, 79(2), 826–838.

Proceedings **ISMRM & SMRT Virtual Conference & Exhibition** (2020)
Abstract number **2270**
Abstract accepted as a Digital Poster
2nd place in Flow and Motion Study group

A3.3. Correcting vs resolving respiratory motion in accelerated free-running whole-heart radial flow MRI using focused navigation (fNAV)

Mariana B.L. Falcão[1], Giulia M.C. Rossi[1], Liliana Ma[2,3], John Heerfordt[1,4], Davide Piccini[1,4], Jérôme Yerly[1,5], Milan Prša[6], Tobias Rutz[7], Estelle Tenisch[7], Michael Markl[2,3], Matthias Stuber[1,5], Christopher W. Roy[1]

[1]Department of Radiology, Lausanne University Hospital (CHUV) and University of Lausanne (UNIL), Lausanne, Switzerland
[2]Department of Radiology, Feinberg School of Medicine, Northwestern University, Chicago, IL, United States,
[3]Department of Biomedical Engineering, Northwestern University, Chicago, IL, United States,
[4]Advanced clinical imaging technology, Siemens Healthcare AG, Lausanne, Switzerland,
[5]Center for Biomedical Imaging (CIBM), Lausanne, Switzerland,
[6]Woman-Mother-Child Department, Lausanne University Hospital (CHUV) and University of Lausanne (UNIL), Lausanne, Switzerland
[7]Service of Cardiology, Centre de resonance magnétique cardiaque (CRMC), Lausanne University Hospital (CHUV) and University of Lausanne (UNIL), Lausanne, Switzerland

Synopsis

In this work, a free-running radial whole-heart flow sequence was acquired in five congenital heart disease (CHD) patients and images were reconstructed using a) a previously developed 5D flow framework for respiratory and cardiac resolved images, and b) a novel framework for respiratory motion corrected and cardiac resolved 4D flow (fNAV). Image and flow differences were measured across a range of acceleration factors. We showed that the free-running acquisition, which is already undersampled, can be even further accelerated with less signal degradation if it is reconstructed with fNAV 4D flow, compared to using 5D flow.

Introduction

4D flow MRI is typically acquired over several minutes during free-breathing and, therefore, requires respiratory motion compensation. This is typically achieved using respiratory navigators that limit data acquisition to a predetermined respiratory level, resulting in decreased scanning efficiency[1,2]. Alternatively, data acquired throughout the entire respiratory cycle may be used for image reconstruction by either correcting respiratory motion[3,4], or by binning the data into unique phases to resolve respiratory motion, allowing for more predictable scanning times[5–7]. The increased scanning efficiency derived from correcting or resolving respiratory motion may be used for improved resolution, volumetric coverage, or to further accelerate the already undersampled acquisitions[8,9]. In this work, we present a novel approach for respiratory motion correction in free-running radial whole-heart flow MRI based on focused navigation (fNAV)[10]. We compared respiratory corrected fNAV 4D flow to respiratory resolved 5D flow6 reconstructions of the same datasets across a range of undersampling factors, and tested the hypothesis that fNAV 4D flow enables higher acceleration factors than the ones already achieved in free-running flow, as opposed to 5D flow.

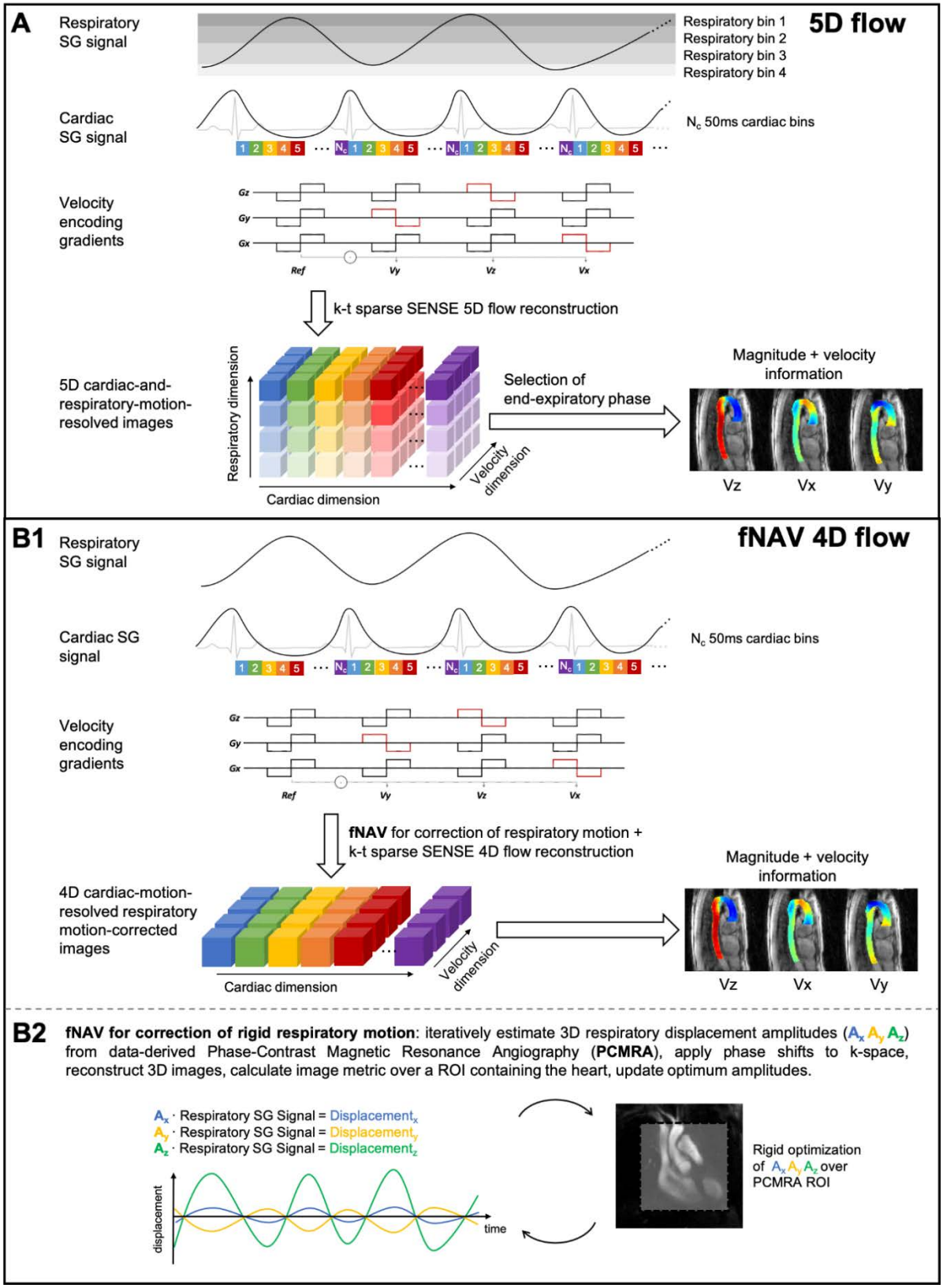

Figure 1. Study outline for reconstructing a free-running flow dataset. A. Reconstruction of motion-resolved 5D flow data uses the motion information to reconstruct images at different respiratory and cardiac phases. **B1.** Cardiac motion-resolved and respiratory motion-corrected fNAV 4D flow reconstructions take advantage of the respiratory motion and of data derived PCMRA images to iteratively estimate the rigid displacement of the heart due to respiration for every readout (**B2**), and use auto-focusing to correct this displacement to the end-expiratory position[10](fNAV).

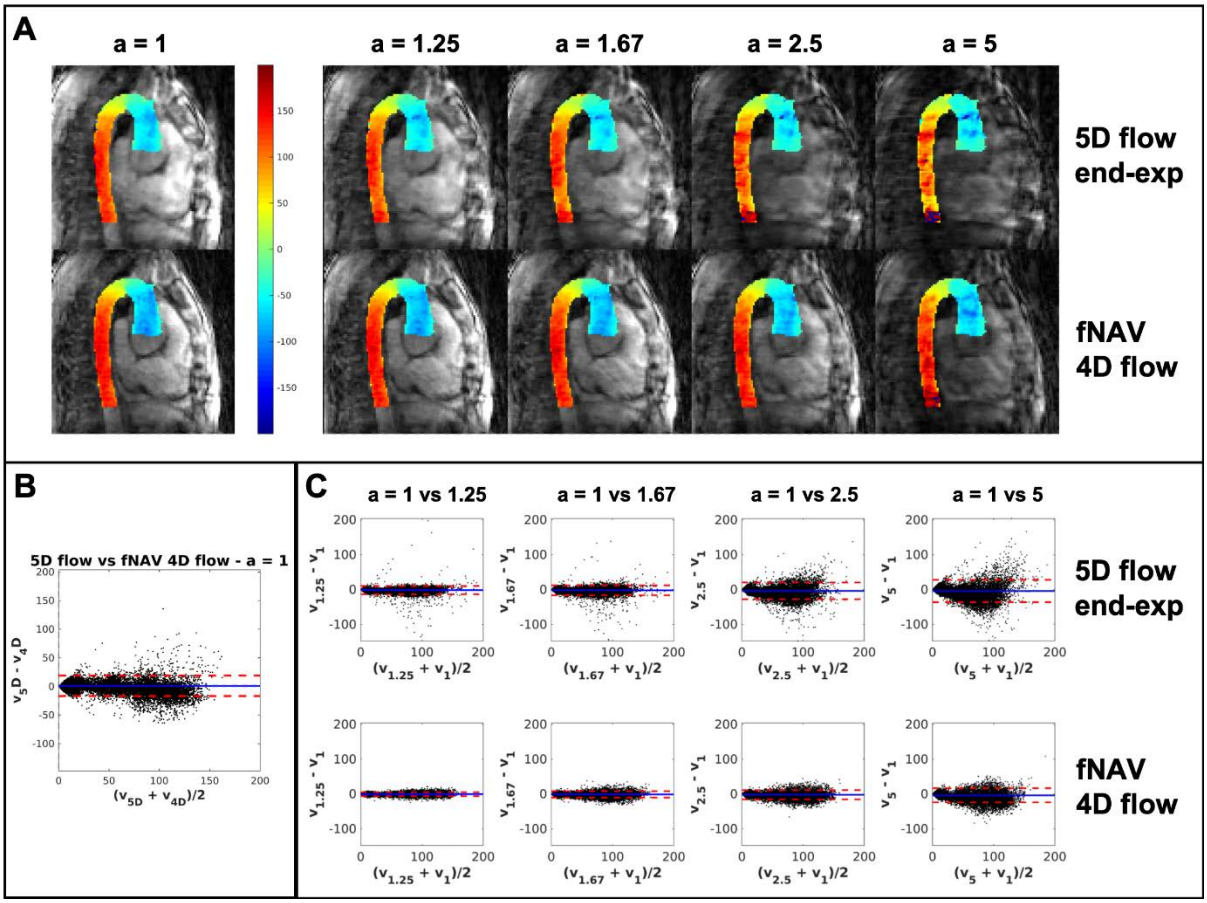

Figure 2. Velocity differences for increasing acceleration factors in one representative subject. A. MIP of the velocity encoded in the z direction (cm/s) for each acceleration factor (a=[1,1.25,1.67,2.5,5]) and reconstruction method (5D flow at end-expiration and 4D flow fNAV). **B.** Voxel-wise velocity bias (in cm/s) in Bland-Altman plot between 4D flow fNAV and 5D flow at (a=1). **C.** Bland-Altman plots of the voxel-wise velocity differences between datasets with (a=1) and (a=[1.25,1.67,2.5,5]) for both 5D flow and 4D flow fNAV in one representative subject.

Methods

Five CHD patients (18-29 years, 3 Female) were scanned after ferumoxytol contrast administration (dose 2mg/kg) on a 1.5T clinical MR system (MAGNETOM Sola, Siemens Healthcare, Erlangen, Germany) using a prototype free-running radial whole-heart flow sequence6,11. The study was approved by the local ethics committee and all patients provided written informed consent compliant with our institutional guidelines. Scan parameters (Scan time=8:08-8:14min, field of view=(220 mm)3-(260 mm)3, spatial resolution=(2.3 mm)3-(2.7 mm)3, temporal resolution=40ms, Venc=200cm/s) were adjusted for each patient. Two reconstruction methods were used: a) extraction of respiratory and cardiac self-gating signals6,12 for data sorting into a motion-resolved 5-dimensional flow array and k-t-sparse SENSE reconstruction6,11(Fig.1A). b) cardiac self-gating signal extraction for data sorting, and respiratory signal extraction to use as input for the auto-focusing algorithm(fNAV) (Fig.1B)10. fNAV 4D flow reconstructions were similar to 5D flow, but without respiratory regularization. 5D flow images at end-expiration were manually selected. To study the acceleration effect, we reconstructed fNAV 4D flow and 5D flow images using [100,80,60,40,20]% of the acquired data (retrospective acceleration factors a=[1,1.25,1.67,2.5,5], relative to originally undersampled datasets[6]). Qualitative comparison of all reconstructions was performed by calculating the maximum intensity projection (MIP) of the dominant velocity direction (z) in a sagittal reformat. Then, using a

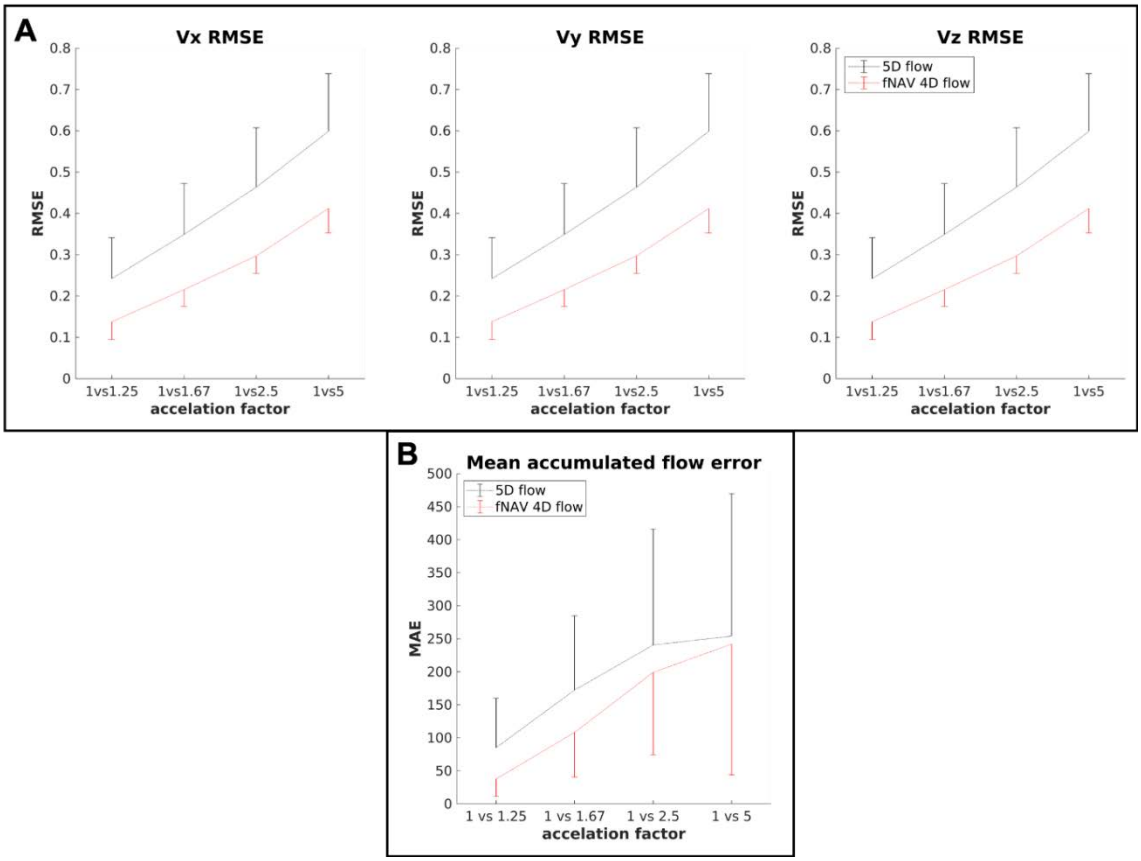

Figure 3. Image reconstruction error and flow error across the entire patient cohort for each acceleration factor. **A.** Population mean and standard deviation of the root mean square error (RMSE) of each flow reconstruction method calculated for each acceleration factor with respect to reconstructions using all acquired data (a=1), and for the three encoded velocities. **B.** Mean accumulated flow error, averaged across five manually selected 2D planes for all patients, with respect to (a=1) for both flow reconstruction methods.

3D segment of the aorta, a voxel-wise Bland-Altman plot was computed to estimate the intra-voxel variability across the different acceleration factors in comparison to (a=1). The root mean square error (RMSE) of all subjects was calculated between every acceleration factor and (a=1), across all voxels and cardiac phases. Five 2D-orthogonal planes were segmented in the descending aorta for each reconstructed image, and the flow curves, net flow, and peak flow measurements were calculated. The mean accumulated flow error13 was computed for each 2D plane as the difference between the flow curves of each acceleration factor with respect to (a=1).

Results

MIP images of the aorta showed good visual agreement between fNAV 4D flow and 5D flow (Fig.2A) for reconstructions using all acquired data (a=1). For increasing acceleration factors, degradation of 5D flow reconstructions is noticeable while fNAV 4D flow remains relatively consistent. These qualitative results are corroborated by the Bland-Altman plots of the velocity vector for increasing acceleration factors (Fig.2B-C), showing an overall larger standard deviation within the 5D flow datasets. RMSE (Fig.3A) and mean accumulated flow error (Fig.3B) increased with acceleration factor for both fNAV 4D flow and 5D flow as expected, but the error was higher overall in magnitude and variability for the 5D flow images. Higher net flow and peak flow measurements (Fig.4) were reported in fNAV 4D flow images, relative to 5D flow, while also being more robust to increasing acceleration factors.

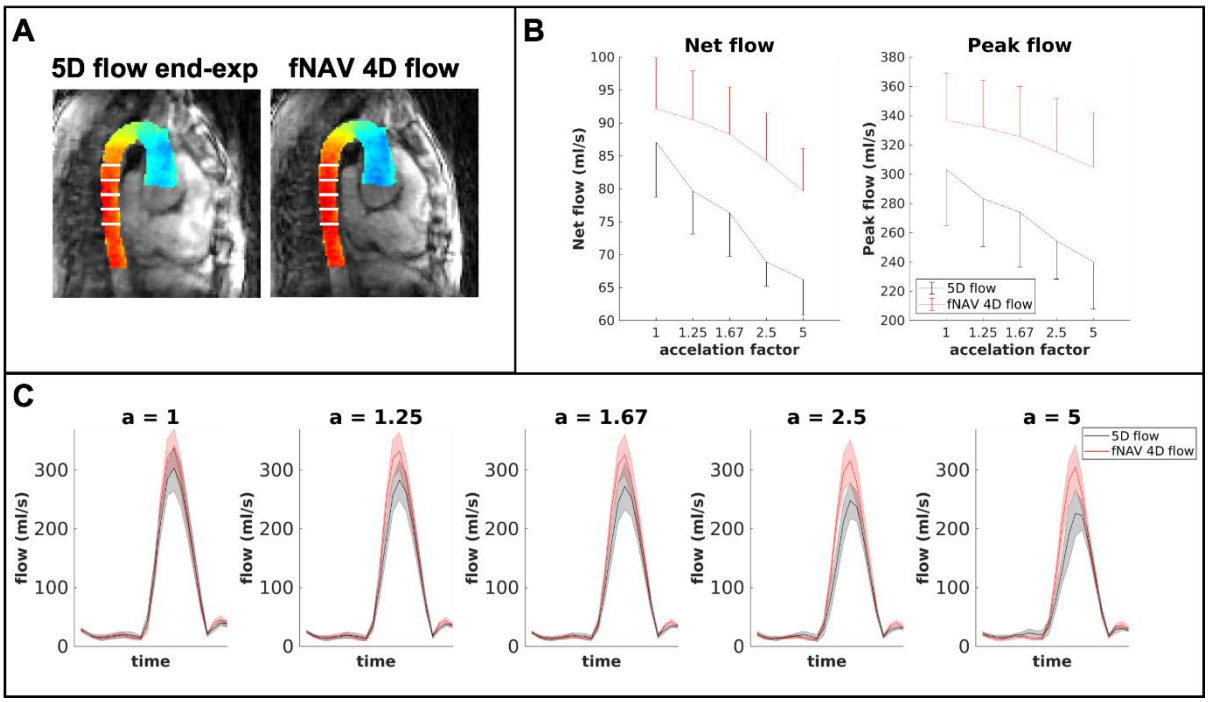

Figure 4. Representative flow measurements for increasing acceleration factors in one representative subject across the five 2D planes. A. Manually selected 2D planes in the descending aorta. **B.** Net flow and peak flow measurements in ml/s reconstructed at different acceleration factors and averaged across the five 2D planes. **C.** Flow curves and their variation across the different 2D planes, for both fNAV 4D flow and 5D flow, and for all acceleration factors.

Discussion

fNAV 4D flow provided comparable, albeit slightly increased net and peak flow measurements, relative to 5D flow, and showed less degradation in overall reconstruction and flow errors for the tested acceleration factors, confirming therefore our original hypothesis. Our results, albeit with a small sample size, suggest that acquisitions reconstructed with fNAV 4D flow could be prospectively accelerated by a larger factor than when using 5D flow, and without significant degradation of image quality or flow measurements. For instance, using 60% of the original data for reconstruction with fNAV 4D flow (a=1.67) would grant similar flow measurements from the original data size, and would provide lower signal corruption and flow variability than a 5D flow reconstruction using only 80% of the data (a=1.25).

Intra-voxel variability was reported between the two reconstructions, so further comparisons to established Cartesian 2D or 4D flow are needed to determine which of these methods better represents ground truth. Nevertheless, 5D flow has previously reported underestimated flow measurements relative to Cartesian 4D flow, possibly due to physiological variation or overregularization from the reconstruction algorithm. fNAV 4D flow may, thus, help elucidate whether increasing the amount of data per cardiac bin improves the agreement between the proposed radial and established Cartesian flow measurements.

Conclusion

Our results suggest the robustness of fNAV 4D flow across the tested acceleration factors in comparison to 5D flow, may enabled faster scan times, improved resolution, or better agreement with the established Cartesian flow measurements.

References

1. Markl, Michael, Alex Frydrychowicz, MD, Sebastian Kozerke MH, Wieben O. 4D flow MRI. J Magn Reson Imaging. 2012;36:1015-1036. doi:10.1007/978-3-319-65924-4_9

2. Dyverfeldt P, Bissell M, Barker AJ, et al. 4D flow cardiovascular magnetic resonance consensus statement. J Cardiovasc Magn Reson. 2015;17(1):1-19. doi:10.1186/s12968-015-0174-5

3. Cheng JY, Hanneman K, Zhang T, et al. Comprehensive motion-compensated highly accelerated 4D flow MRI with ferumoxytol enhancement for pediatric congenital heart disease. J Magn Reson Imaging. 2016;43(6):1355-1368. doi:10.1002/jmri.25106

4. Kolbitsch C, Vasquez CP, Bastkowski R, Weiss K, Maintz D. Respiratory motion corrected 4D flow using golden radial phase encoding. Magn Reson Med. 2019;(June):00:1-10. doi:10.1002/mrm.27918

5. Walheim J, Dillinger H, Kozerke S. Multipoint 5D flow cardiovascular magnetic resonance - Accelerated cardiac- and respiratory-motion resolved mapping of mean and turbulent velocities. J Cardiovasc Magn Reson. 2019;21(1):1-13. doi:10.1186/s12968-019-0549-0

6. Ma LE, Yerly J, Piccini D, et al. 5D Flow MRI : A Fully Self-gated , Free-running Framework for Cardiac and Respiratory Motion – resolved 3D Hemodynamics. Radiol Cardiothorac Imaging. 2020;2(6)(6).

7. Bastkowski R, Bindermann R, Brockmeier K, Weiss K. Respiration Dependency of Caval Blood Flow in Patients with Fontan Circulation : Quantification Using 5D Flow MRI. Radiol - Cardiothorac Imaging. 2019;1(4).

8. Ma LE, Markl M, Chow K, et al. Aortic 4D flow MRI in 2 minutes using compressed sensing, respiratory controlled adaptive k-space reordering, and inline reconstruction. Magn Reson Med. 2019;81(6):3675-3690. doi:10.1002/mrm.27684

9. Giese D, Schaeffter T, Kozerke S. Highly undersampled phase-contrast flow measurements using compartment-based k-t principal component analysis. Magn Reson Med. 2013;69(2):434-443. doi:10.1002/mrm.24273

10. Roy CW, Heerfordt J, Piccini D, et al. Motion Compensated Whole-Heart Coronary Magnetic Resonance Angiography using Focused Navigation (fNAV). 2020:0-2. http://arxiv.org/abs/2010.14206.

11. Di Sopra L, Piccini D, Coppo S, Stuber M, Yerly J. An automated approach to fully self-gated free-running cardiac and respiratory motion-resolved 5D whole-heart MRI. Magn Reson Med. 2019;(June):1-15. doi:10.1002/mrm.27898

12. Falcão M, Ma L, Di Sopra L, et al. 5D Flow MRI using Pilot Tone for Cardiac and Respiratory Self-Gating. Proc 23rd Annu SCMR Sci Sess. 2020:1583-1586.

13. Giese D, Wong J, Greil GF, Buehrer M, Schaeffter T, Kozerke S. Towards highly accelerated Cartesian time-resolved 3D flow cardiovascular magnetic resonance in the clinical setting. J Cardiovasc Magn Reson. 2014;16(42):1-8. doi:10.1186/1532-429X-16-42

Proceedings **ISMRM & SMRT Annual Meeting & Exhibition** (2021)
Abstract number **0304**
Abstract accepted as an Oral Presentation
Magna Cum Laude Award

A3.4. Free-running 3D anatomical and flow MRI using Synchronization of Neighboring Acquisitions by Physiological Signals (SyNAPS)

Mariana B.L. Falcão[1], Adele Mackowiak[1], Simone Rumac[1], Mario Bacher[1,2], Giulia Rossi[1], Milan Prša[3], Estelle Tenisch[1], Tobias Rutz[4], Jessica Bastiaansen[1,5,6], Ruud Van Heeswijk[1], Peter Speier[2], Michael Markl[7,8], Matthias Stuber[1,9], Christopher W. Roy[1]

[1]Department of Diagnostic and Interventional Radiology, Lausanne University Hospital (CHUV) and University of Lausanne (UNIL), Lausanne, Switzerland.
[2]Siemens Healthcare GmbH, Erlangen, Germany.
[3]Woman- Mother- Child Department, Lausanne University Hospital and University of Lausanne, Lausanne, Switzerland.
[4]Service of Cardiology, Centre de Resonance Magnétique Cardiaque (CRMC), Lausanne University Hospital and University of Lausanne, Lausanne, Switzerland.
[5]Department of Diagnostic, Interventional and Pediatric Radiology (DIPR), University hospital Bern (Inselspital), Bern Switzerland.
[6]Translational Imaging Center, sitem-insel, Bern, Switzerland.
[7]Department of Radiology, Feinberg School of Medicine, Northwestern University, Chicago, Illinois, USA.
[8]Department of Biomedical Engineering, Northwestern University, Chicago, Illinois, USA.
[9]Center for Biomedical Imaging (CIBM), Lausanne, Switzerland

Synopsis

We introduce a novel method for combining multiple free-running MRI acquisitions together, through the use of cardiac and respiratory signal extraction with Pilot Tone navigation called Synchronization of Neighboring Acquisitions by Physiological Signals (SyNAPS). We demonstrate the initial feasibility and utility of SyNAPS on a setup for joint reconstruction of back-to-back dynamic anatomical and flow MRI acquisitions, here named 4D flow SyNAPS. Overall, 4D flow SyNAPS enabled an improved structural visualization, when compared to the magnitude images from 4D flow datasets alone, and the resulting flow measurements showed better agreement with reference 2D flow acquisitions.

Introduction

The free-running framework was recently developed for fully self-gated whole-heart MRI[1] and has been extended to angiography[2], flow[3,4], T1[5] and fat fraction[6] mapping. Each of these branches benefit from a simplified workflow and predictable scan times without the need for ECG gating or respiratory navigation. However, self-gating, which extracts cardiac and respiratory motion signals from the data themselves, has been shown to have unpredictable shifts relative to known physiological markers (i.e. R-wave, end-expiratory position), precluding a comprehensive analysis of different free-running branches in the same exam, or requiring additional manual spatial and temporal synchronization of the resulting images[1]. In this work, we present a novel approach for combining multiple free-running acquisitions called Synchronization of Neighboring Acquisitions by Physiological Signals (SyNAPS). In the proposed SyNAPS framework, we use the Pilot Tone (PT) navigation system[4,7,8] to acquire cardiac and respiratory motion signals in parallel to sequential free-running acquisitions. The PT signals, fully independent from the imaging acquisitions, then inform a joint respiratory motion-corrected and cardiac motion-resolved 4D image reconstruction[9,10]. Here, we demonstrate the initial feasibility and utility of SyNAPS using sequentially acquired free-running 3D radial fast interrupted

steady-state (FISS)[11] and free-running 3D radial flow data sets (4D Flow)[3,10]. We test the hypothesis that using SyNAPS, the magnitude images from FISS can be leveraged to improve vessel segmentation and subsequent flow quantification in the free-running 4D Flow data[12]. We compare this approach called 4D Flow SyNAPS to 4D Flow alone, and to a 2D Flow reference standard.

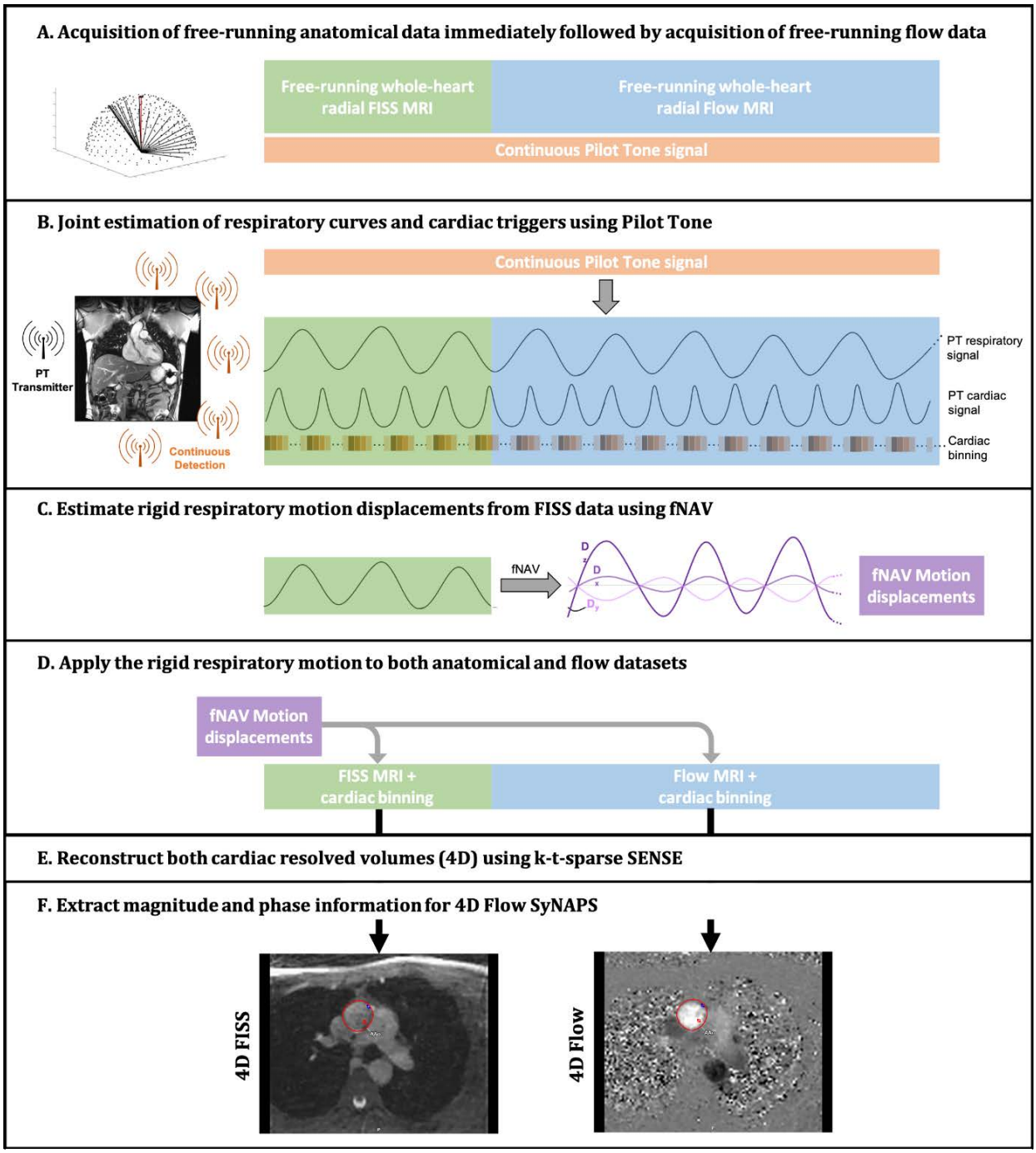

Figure 1. 4D Flow SyNAPS study pipeline with integrated SyNAPS framework (B-E.). A. Two free-running 3D radial MRI sequences are acquired: FISS[11] and Flow[3,10]. PT signals are detected continuously throughout the two acquisitions. **B.** Respiratory and cardiac signals are extracted together. **C.** Respiratory motion displacements are obtained from FISS using fNAV[9], **D.** and are applied to both sequences. **E.** A k-t-sparse SENSE reconstruction creates 4D images for both sequences. **F.** Magnitude and Phase images from 4D FISS and 4D Flow, respectively, create the final 4D Flow SyNAPS.

Methods

Five healthy volunteers (2F, ages 23-32) and two Marfan Syndrome patients (2F, ages 14-18) were scanned on a 1.5T MAGNETOM Sola system (Siemens Healthcare, Erlangen, Germany) using a 12-channel body coil array with an integrated PT transmitter. All subjects provided written informed consent compliant with our institutional guidelines and approved by the local research ethics committee. Two 2D Flow datasets were acquired as reference (ascending and descending aorta (AAo, DAo) (TR/TE=5.1/2.9ms, venc=150cm/s, FOV=380x260mm2, spatial resolution=2.0x2.0x6.0mm3, Scan time=0:15min). Then, two prototype free-running radial whole-heart MRI sequences[1] were ran, the first one was FISS[11] followed immediately by 4D Flow[3,10] (**Fig.1A**). Scan parameters for FISS were TR/TE=2.94/1.5ms, segments=12000, readouts per FISS module=4, number of FISS modules=6, FOV=(220mm)3, spatial resolution=(2.0mm)3, Scan time=3:45min. Scan parameters for 4D Flow (TR/TE=5.3/3.5ms, shots=4820, segments=21, venc=150cm/s, FOV=(220mm)3, spatial resolution=(2.0mm)3, Scan time=8:59min.

SyNAPS was used to connect the reconstruction of the two sequences (**Fig.1B-E**). PT respiratory and cardiac signals spanning the two free-running sequences were extracted for subsequent respiratory motion correction and cardiac binning (**Fig.1B**). Translational respiratory motion correction of the underlying k-space data was performed on both free-running FISS and 4D flow datasets, using focused navigation (fNAV) coefficients estimated from the FISS data (**Fig.1C-D**)[9,10]. Finally, each dataset was reconstructed into cardiac motion-resolved volumes (4D) using a k-t-sparse SENSE algorithm (**Fig.1E-F**). To demonstrate the utility of the SyNAPS framework, the high blood-myocardium contrast images from FISS were combined with the phase images from 4D Flow to create 4D Flow SyNAPS. This was compared to 4D Flow alone, as well as to the reference 2D Flow data by retrospectively extracting matching slice positions. Measurements in the AAo and DAo were quantitatively compared (Circle cvi42, Calgary, Canada), in terms of flow measurements (flow rate, net volume, peak flow) and vessel area over the cardiac cycle.

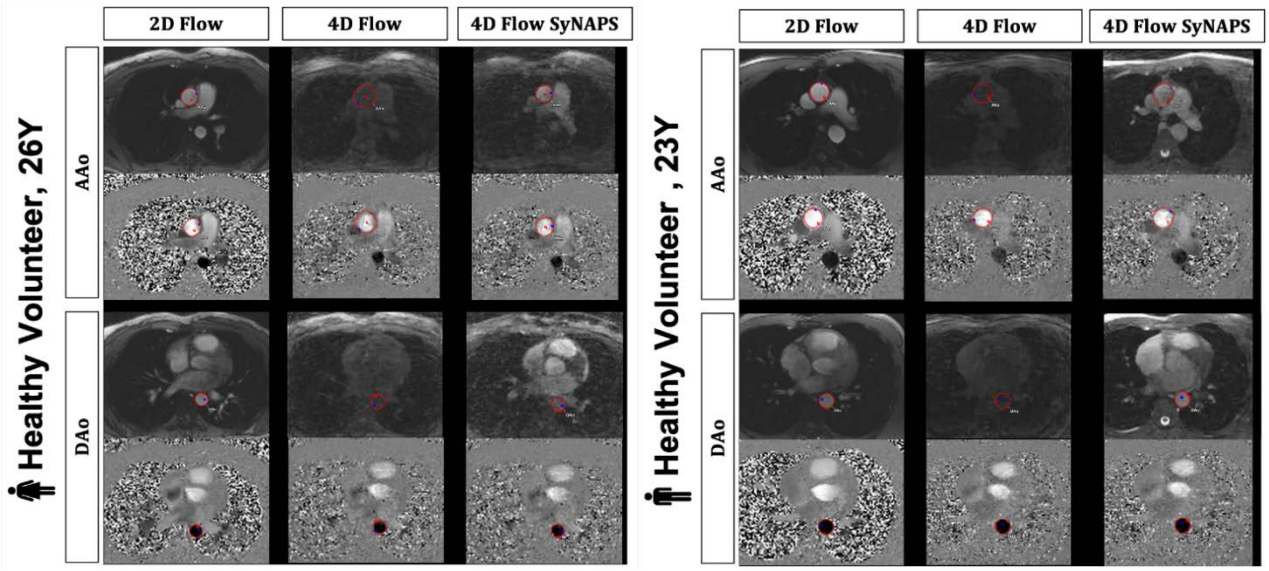

Figure 2. Comparison of reference 2D Flow to 4D Flow and 4D Flow SyNAPS for two representative healthy volunteers. The anatomical images integrated in 4D Flow SyNAPS increase the image contrast when compared to 4D Flow MRI. Additionally, heart and vessel structures are better depicted in 4D Flow SyNAPS, with similar contrast to the one from 2D Flow MRI. AAo: base of the ascending aorta; DAo: the mid descending aorta. Blue and red dots inside vessel segmentation represent maximum and minimum velocity voxels.

Results

The contrast of 4D Flow SyNAPS magnitude images (derived from the FISS sequence) demonstrates a clear improvement over 4D Flow alone (Figure 2), and are comparable to the 2D Flow images, which benefit from in-flow enhancement. For all five healthy volunteers, 4D Flow SyNAPS yielded flow rates and vessel area changes comparable to 2D Flow MRI (Figure 3). Linear regression reported similar significant correlation between all flow datasets ($p<0.05$); Bland-Altman analysis reported a lower bias and limits of agreement between 4D Flow SyNAPS and 2D Flow (Figure 4) relative to 4D Flow alone. For the two patient datasets, fusion of anatomical and flow information (Figure 5) clearly demonstrates the successful synchronization of the two sequences.

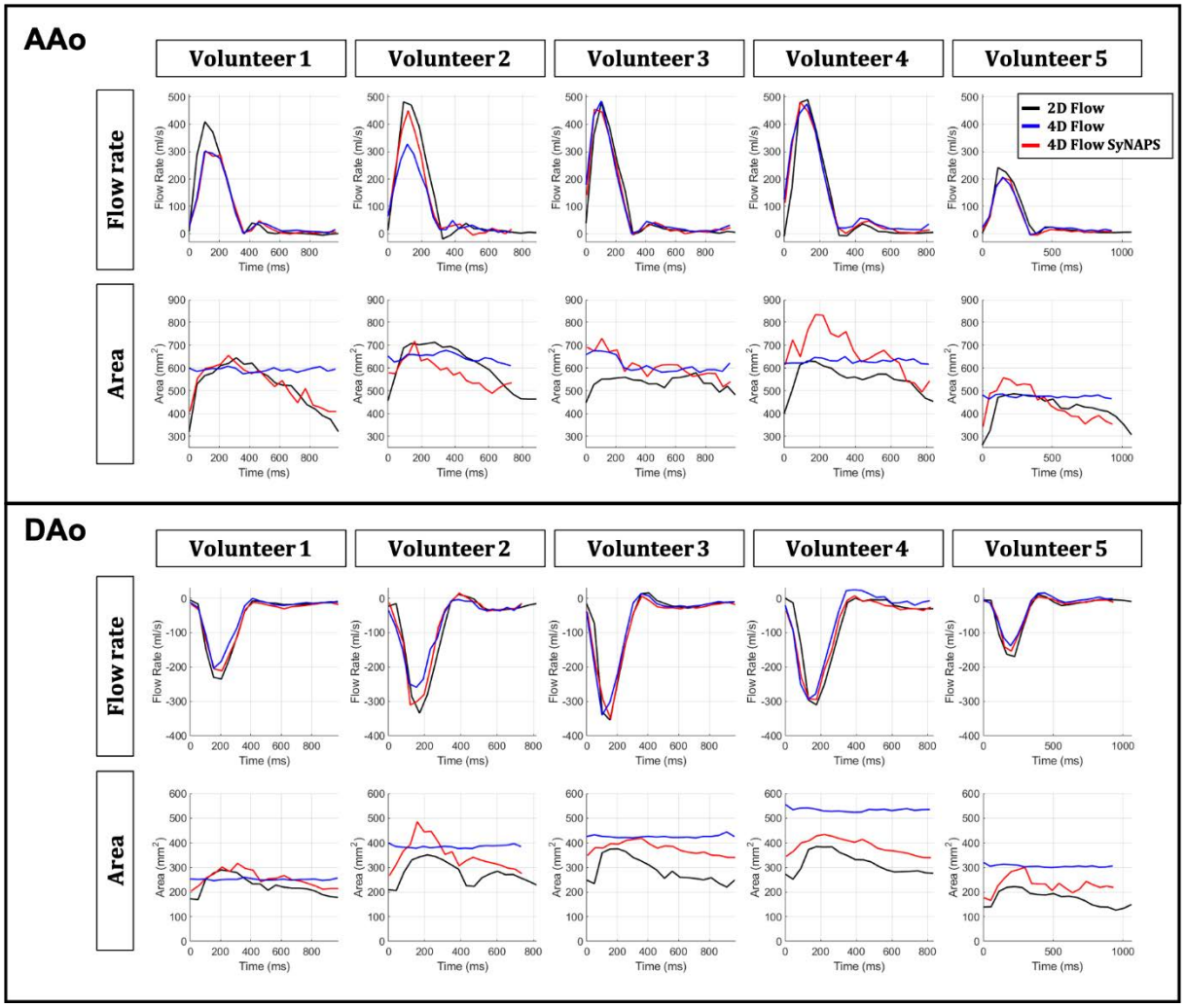

Figure 3. Example respiratory and cardiac signals extracted with SyNAPS (A.) and visualization of flow rate and vessel area across the cardiac cycle, for 2D Flow, 4D Flow, and 4D Flow SyNAPS. For all healthy volunteers included in this study, two vessel locations were chosen, one at the base of the ascending aorta (AAo), and another one in the mid descending aorta (DAo). Black: 2D Flow; Blue: 4D Flow; Red: 4D Flow SyNAPS.

Discussion and Conclusion

This work introduces SyNAPS, a framework that builds towards comprehensive whole-heart MRI by synchronizing different branches of the free-running framework. We demonstrated the initial feasibility and utility of SyNAPS on a setup for joint whole-heart anatomical and flow MRI that does not require ECG gating or respiratory navigators. We show that the high-contrast anatomical imaging

sequence can be leveraged to improve 3D flow measurements that often suffer from poor delineation of the vessel boundaries in the absence of contrast agents [12]. These promising initial results motivate further validation of the framework, especially in the context of heart-rate variability and respiratory drift. While the current implementation used the respiratory signal for motion correction, this framework could be easily extended to respiratory-resolved 5D imaging. Finally, SyNAPS can be readily applied to other branches of the free-running framework in order to create a simplified workflow for a comprehensive assessment of the structure, dynamic function, blood flow, and tissue properties of the heart, with the overarching goal of creating new MRI-based tools in the diagnosis and management of heart disease.

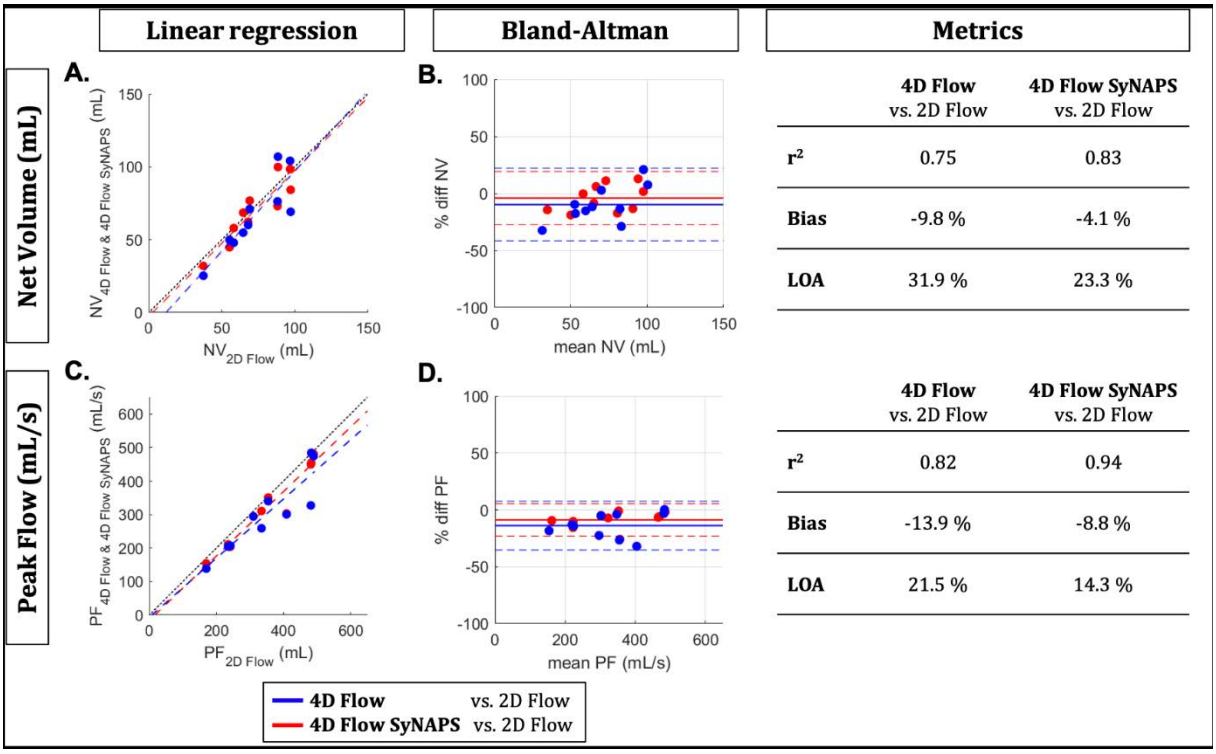

	4D Flow vs. 2D Flow	4D Flow SyNAPS vs. 2D Flow
r^2	0.75	0.83
Bias	-9.8 %	-4.1 %
LOA	31.9 %	23.3 %

	4D Flow vs. 2D Flow	4D Flow SyNAPS vs. 2D Flow
r^2	0.82	0.94
Bias	-13.9 %	-8.8 %
LOA	21.5 %	14.3 %

Figure 4. Comparison of net flow (A-B) and peak flow (C-D) measurements between **4D Flow vs. 2D Flow as well as** between **4D Flow SyNAPS vs. 2D Flow**. Linear regression (**A-C**) and Bland Altman (**B-D**) plots show smaller biases when using 4D Flow SyNAPS. **A-C.** Black dotted lines represent the ideal linear regression trend (slope=1) and color dashed lines represent the linear regression outcome for each pair. **B-D.** bias is depicted in solid lines; limits of agreement (LOA) are represented by dashed lines. Blue: 4D Flow vs. 2D Flow; Red: 4D Flow SyNAPS vs. 2D Flow. r2: coefficient of determination.

References

1. Di Sopra L, Piccini D, Coppo S, Stuber M, Yerly J. An automated approach to fully self-gated free-running cardiac and respiratory motion-resolved 5D whole-heart MRI. Magn Reson Med. 2019;1–15.
2. Heerfordt J, Whitehead KK, Bastiaansen JAM, Di Sopra L, Roy CW, Yerly J, et al. Similarity-driven multi-dimensional binning algorithm (SIMBA) for free-running motion-suppressed whole-heart MRA. Magn Reson Med. 2021;86:213–29.
3. Ma LE, Yerly J, Piccini D, Sopra L Di, Roy CW, Carr JC, et al. 5D Flow MRI : A Fully Self-gated, Free-running Framework for Cardiac and Respiratory Motion – resolved 3D Hemodynamics. Radiol Cardiothorac Imaging. 2020;2(6).
4. Falcão MBL, Di Sopra L, Ma L, Bacher M, Yerly J, Speier P, et al. Pilot tone navigation for respiratory and cardiac motion-resolved free-running 5D flow MRI. Magn Reson Med. 2021;00:1–15.
5. Di Sopra L, Roy CW, Bastiaansen JAM, Yerly J, Piccini D, Arn L, et al. Fully Self-Gated Cardiac and Respiratory Motion-Resolved Isotropic 5D T1 Mapping of the Heart : Preliminary Results. Proc Intl Soc Mag Reson Med. 2019;27.

6. Mackowiak ALC, Roy CW, Yerly J, Sopra L Di, Falcão MBL, Bacher M, et al. Whole-Heart Motion-Resolved Multi-Peak Fat-Fraction Mapping using Free-Running 3D Radial Multi-Echo GRE and Pilot Tone. Proc Intl Soc Mag Reson Med. 2021;29.
7. Speier P, Fenchel M, Rehner R. PT-Nav: A Novel Respiratory Navigation Method for Continuous Acquisitions Based on Modulation of a Pilot Tone in the MR-Receiver. Proc ESMRMB. 2015. p. 129:97-98.
8. Vahle T, Bacher M, Rigie D, Fenchel M, Speier P, Bollenbeck J, et al. Respiratory Motion Detection and Correction for MR Using the Pilot Tone: Applications for MR and Simultaneous PET/MR Examinations. Invest Radiol. 2020;55:153–9.
9. Roy CW, Heerfordt J, Piccini D, Rossi G, Pavon AG, Schwitter J, et al. Motion compensated whole-heart coronary cardiovascular magnetic resonance angiography using focused navigation (fNAV). J Cardiovasc Magn Reson. BioMed Central; 2021;23:1–17.
10. Falcão MBL, Rossi GMC, Ma L, Heerfordt J, Piccini D, Yerly J, et al. Correcting vs resolving respiratory motion in accelerated free-running whole-heart radial Flow MRI using focused navigation (fNAV). Proc Intl Soc Mag Reson Med. 2021;29.
11. Bastiaansen JAM, Piccini D, Sopra L Di, Roy CW, Heerfordt J, Edelman RR, et al. Natively fat-suppressed 5D whole-heart MRI with a radial free-running fast-interrupted steady-state (FISS) sequence at 1.5T and 3T. Magn Reson Med. 2019;00:1–11.
12. Jarvis KB, Wu C, Giri S, Schnell S, Barker AJ, Collins JD, et al. Improved assessment of aortic 3D blood flow with combined k-t accelerated 3D CINE bSSFP & 4D flow MRI. J Cardiovasc Magn Reson. 2016;18:1–2.

Proceedings **Joint Annual Meeting ISMRM-ESMRMB & ISMRT 31st Annual Meeting** (2022)
Abstract number **0215**
Abstract accepted as an Oral Presentation.
Summa Cum Laude Award